CAB

ornl

ORNL/M-2849

OAK RIDGE
NATIONAL
LABORATORY

MARTIN MARIETTA

THE NEW PRODUCTION REACTOR FUEL POST IRRADIATION EXAMINATION DATA REPORT FOR CAPSULES NPR-1, NPR-2 AND NPR-1A

September - 1993

D.R. Harrison
12/11/01

MANAGED BY
MARTIN MARIETTA ENERGY SYSTEMS, INC.
FOR THE UNITED STATES
DEPARTMENT OF ENERGY

ORNL/M-2849

The New Production Reactor Fuel Post Irradiation Examination Data Report for Capsules NPR 1, NPR 2, and NPR 1A

September 1993

Authors

ORNL

C. A. Baldwin
G. L. Bell
G. C. Copeland
L. C. Emerson
M. L. Grossbeck
R. N. Morris
B. F. Myers
N. H. Packan
J. T. Parks
O. M. Stansfield
R. D. Taylor

INEL

R. R. Hobbins

CEGA

R. Acharya
F. C. Montgomery
W. J. Scheffel
C. A. Young

CONTENTS

Page

SUMMARY v

1.0 INTRODUCTION 1-1

2.0 DESCRIPTION OF EXPERIMENT 2-1
2.1 Objectives: 2-1
2.2 Description of Fuel Specimens 2-2
2.2.1 Coated Particles 2-3
2.2.2 Fuel Compacts 2-4
2.2.3 Piggyback Samples 2-12
2.3 Capsule Design 2-27
2.3.1 Description Of Test Articles 2-28
2.3.2 Fuel Compacts 2-28
2.4 Irradiation Facility 2-29
2.4.1 Brief Description of the HFIR 2-29
2.4.2 Materials Irradiation Facility (MIF) 2-30
2.5 References 2-32

3.0 CAPSULE OPERATION AND EVALUATION 3-1
3.1 Operating History 3-1
3.1.1 Operating Temperatures 3-4
3.2 Determination of the Fission Gas Release Rate to Birth Rate Ratios (R/B) 3-54
3.3 Analysis of Flux Dosimeters 3-54
3.3.1 Description 3-56
3.3.2 Disassembly 3-59
3.4 Burnup Determination 3-70
3.5 Thermal Analysis 3-71
3.5.1 Fuel Compact Radial Temperature Distribution 3-71
3.5.2 Piggyback Specimen Temperatures 3-71
3.5.3 Fuel Temperature Uncertainty 3-86
3.7 References 3-99

4.0 POSTIRRADIATION EXAMINATION RESULTS 4-1
4.1 Capsule Disassembly 4-1
4.1.1 Post Irradiation Handling & Shipping 4-1
4.1.2 Visual Examination of Capsules 4-2
4.1.3 Gamma Scanning of Capsules 4-2
4.1.4 Removing Contents of Capsule NPR 1 4-3
4.1.5 Removing Contents of Capsule NPR 2 4-4
4.1.6 Removal of Components from Graphite Bodies 4-4
4.2 Visual Examination 4-6
4.2.1 Visual Examination of Graphite Bodies 4-6
4.2.2 Gamma Scanning of Graphite Bodies with Fuel Compacts 4-6
4.2.3 Visual Examination of Fuel Compacts 4-6
4.2.4 Piggyback Specimen Capsules 4-7

4.3 Dimensional Change Analysis 4-11
4.3.1 Metrology of Fuel Compacts 4-11
4.3.2 Metrology of Graphite Bodies 4-18
4.4 Fission Gas Release 4-22
4.4.1 Methods of Monitoring Fission Gas Release 4-22
4.4.2 Results of Monitoring Fission Gas Release 4-31
4.5 Particle Fission Product Inventory by IMGA 4-57
4.5.1 Particles Unbonded from Fuel Particles 4-58
4.5.2 Compact Deconsolidation Debris and Electrolyte 4-66
4.5.3 Piggyback Particles 4-67
4.6 Ceramographic Examination 4-69
4.6.1 Unirradiated Fuel 4-69
4.6.2 Irradiated Fuel 4-70
4.6.3 Summary Discussion 4-83
4.7 Characterization by Burning and Leaching 4-85
4.7.1 Leach-Burn-Leach 4-85
4.7.2 Burn-Visual Examination 4-95
4.7.3 Burn-Dimensional Change Analysis 4-96
4.8 Analytical Scanning Electron Microscopy on Coated Fuel Particles 4-98
4.8.1 Introduction 4-98
4.8.2 Electron Microprobe Analysis 4-98
4.8.3 Fission Product Distribution Analysis 4-99
4.8.4 Fracture of SiC Layer 4-103
4.9 References 4-199

5.0 DISCUSSION 5-1
5.1 Comparison With Prior Experience 5-1
5.2 Coating Failure Mechanism 5-1
5.3 References 5-4

6.0 CONCLUSIONS 6-1

APPENDIX A A-1

SUMMARY

The NPR 1, NPR 2, and NPR 1A irradiation capsule experiments were carried out to provide a demonstration of the performance of reference NP-MHTGR fuel. The fuel was produced on laboratory scale equipment and contained two new particle design features not previously tested. One feature was a 40% increase in IPyC thickness, and the other feature was a low density PyC protective outer layer. The NPR 1 and NPR 1A tests were designed to provide demonstration at the upper boundaries of burnup, temperature, and fast neutron fluence while NPR 2 exposed the fuel to maximum burnup and fast neutron fluence but at moderate temperatures close to NP-MHTGR expected core average. The NPR 1 and NPR 2 fuel was exposed to accelerated irradiation conditions in the HFIR test facilities at Oak Ridge National Laboratory (ORNL). While NPR 1A was irradiated in the ATR at the Idaho National Engineering Laboratory (INEL). The NPR 1 and NPR 2 capsules were irradiated 170 effective full power days with NPR 1 starting July 25 and NPR 2 on August 28, 1991. The NPR 1A capsule was irradiated 64 days starting October 2, 1991. During irradiation the capsules were purged with a flow of helium and neon gas and the fission gas content of the exhaust gas was monitored to provide a measure of the retentive capability of fuel as irradiation proceeded.

The initial fission gas release from all capsules was extremely low ($<5 \times 10^{-8}$ R/B Kr-85m) which was a reflection of the fact that the exposed heavy metal contamination of the fuel compacts was less than 10^{-5} fraction of the fuel content. However, the fuel began to release fission gas when the fast neutron fluence exceeded about 1.5×10^{25} n/m^2. The fission gas activity of the purge gas increased rapidly to maximum release rates on the order of 10^{-4} R/B Kr85m for the high temperature NPR 1 and 10^{-5} R/B Kr85m for the lower temperature NPR 2. When the NPR 1 and NPR 2 capsules had reached the desired exposure after 8 cycles in HFIR, the irradiation was terminated. The irradiation of capsule NPR 1A which operated at a temperature similar to NPR 1 was terminated when the fission gas release rate approached 2×10^{-5} R/B Kr85m.

The post irradiation examination of NPR 1 and NPR 2 was initiated in the ORNL hot cells in January 1993 and the disassembly of the NPR 1A capsule took place at INEL in May 1993. The compacts were relatively weak but they were extracted from the graphite holders without significant damage or debonding of particles. The compacts in the lower half

of capsules NPR 1 and NPR 2 and all compacts of NPR 1A were shipped to General Atomics, San Diego, CA where fission gas release from individual compacts was determined by activation and heating in TRIGA.

Examination of 8 unbonded (piggyback) fuel particle samples showed that the outer seal coat and perhaps the PPyC had cracked. However, the irradiation induced cracking was not as extensive as in compacts. Ceramography, scanning electron microscopy, gamma analysis of individual particle fission product inventory (IMGA), and leach-burn-leach procedures were carried out at ORNL on selected fuel compacts to characterize fuel condition. The results of ceramography work indicated no SiC failure at low neutron fluence and about 6% of the particles had radial cracks through the SiC layer when the fast neutron exposure exceeded 2×10^{25} n/m^2. The results from leach-burn-leach of compacts NPR 1-B6 showed that the exposed kernel fraction in compacts was about 1.5%. The exposed kernel fraction did not increase significantly when PyC coatings and compact matrix was removed by burning. This observation linked the PyC coating failure with failure of the SiC since (1) PPyC/OPyC, SiC, and IPyC were all failed when SiC was failed and (2) burning the PyC did not increase exposed kernel fraction.

The buffer coatings did not crack but they underwent irradiation induced shrinkage in the radial direction, decreasing thickness by 50%. Swelling of the kernel was observed in several particles where the buffer had been breached and the kernel swelled into the gap between the shrinking buffer and the IPyC which remained attached to the SiC. However, no fission product attack of the SiC was observed even when the swelling kernel contacted the inner surface of the IPyC.

The IPyC coating was firmly bonded to the SiC except in the vicinity of SiC cracks where debonding and IPyC curling away from the SiC was frequently observed. From 10 to 30% of particles with failed IPyC showed cracked SiC. The fact that a crack in the IPyC was usually detected within 100 μm of cracks in the Sic and when the IPyC was intact the SiC was unfailed suggested that the mechanism for failure of those coatings was connected in some manner. The leach-burn-leach results discussed above indicated the OPyC was also failed. A plausible failure mechanism has the following features:

(1) Irradiation induced shrinkage of the PPyC, seals, and OPyC caused those layers to fail at a fast neutron exposure of about 1.8×10^{25} n/m^2. This condition removes a source of compressive force on the SiC.

(2) The IPyC is strongly bonded to the SiC. When the IPyC fails due to irradiation induced shrinkage, a tensile stress is developed in the SiC which significantly increases the probability of SiC failure.

While the PIE provided supporting evidence for failure of the SiC coating from interaction with the IPyC, there was no conclusive evidence for any single failure mechanism.

1.0 INTRODUCTION

The New Production Reactor (NPR) Fuel Development Program was initiated in 1989 as part of a Department of Energy (DOE) task to ensure a long term supply of materials for the US nuclear weapons program. Several reactor concepts were considered for the NPR and programs were put in place by DOE to provide the information needed to select the optimum concept. The Modular High Temperature Gas Cooled Reactor (MHTGR) was one of the candidates proposed as a potential source of the required materials.

The NPR version of the MHTGR, which was named the NP MHTGR, was patterned after the commercial MHTGR and the same coated particle fuel form was adopted to the extent possible. One major difference between the fuel for the commercial MHTGR and the NP MHTGR was that the NP MHTGR fuel contained uranium with 93% U-235 enrichment while the commercial MHTGR had a two particle fertile/fissile fuel with 20% enrichment in the fissile particle. While different forms of highly enriched coated particle fuel had been irradiated previously, new design improvements with regards to kernel composition and coating design developed for the commercial MHTGR were adopted in an attempt to provide the most retentive fuel possible. There were two primary fuel design features adopted; (1) a kernel containing a mixture of UO_2 and UC_2 which was called UCO, and (2) a low density protective pyrocarbon (PPyC) outer layer on the coated particle. The UCO kernel was intended to provide improved thermal stability and the PPyC protected the particle coating from mechanical damage during fuel compact fabrication. The particle design is illustrated in Figure 1.1.

While existing fuel irradiation test data on several different fuel designs provided reason to believe that the reference NP MHTGR fuel would perform as required, no data on the reference NP MHTGR fuel existed. For DOE to properly evaluate the NP MHTGR relative to other NPR candidate reactors it was necessary to demonstrate satisfactory performance of the highly enriched reference coated particle fuel.

In order to provide the required demonstration in a timely manner, accelerated irradiation testing of the fuel was carried out over the 1990 through 1993 time period. Three irradiation tests were conducted to demonstrat performance of MHTGR fuel. Two tests, the NPR 1 and NPR 2 capsules, were irradiated in the HFIR at ORNL. The third test, NPR 1A,

which contained fuel from the same production lot was irradiated in the ATR at Idaho National Engineering Laboratory (INEL) and initial test results are reported elsewhere (Refs. 1.1, 1.2).

The operational phase of the NPR 1 and NPR 2 tests have been reported previously (Ref. 1.3). Results of post irradiation examination (PIE) of the NPR 1 and NPR 2 irradiation tests are reported in this document. Ceramographic, gamma spectroscopy, and leach-burn-leach examination of a limited amount of NPR 1A fuel was also carried out at ORNL and results of that work are also included here.

References

1.1 McIsaac, C. V., et al., "Concentrations of Fission Product Noble Gases Released During the NP-MHTGR Fuel Compact Experiment - 1A," EG&G Idaho (INEL) ST-PHY-92-032 Vol. I and Vol. II, April 1992.

1.2 Martinson, Z. R., et al., "Test NPR 1A Results Report," EG&G Idaho (INEL) EDF-NPR-MHTGR-0656, July 1993

1.3 Bell, G. L., J. T. Parks, K. R. Thoms, L. C. Emerson, G. L. Copeland, B. F. Myers, "The New Production Reactor Fuel Irradiation Experiments NPR 1 and NPR 2 Irradiation Phase Report," ORNL/M-2663, 2/12/93

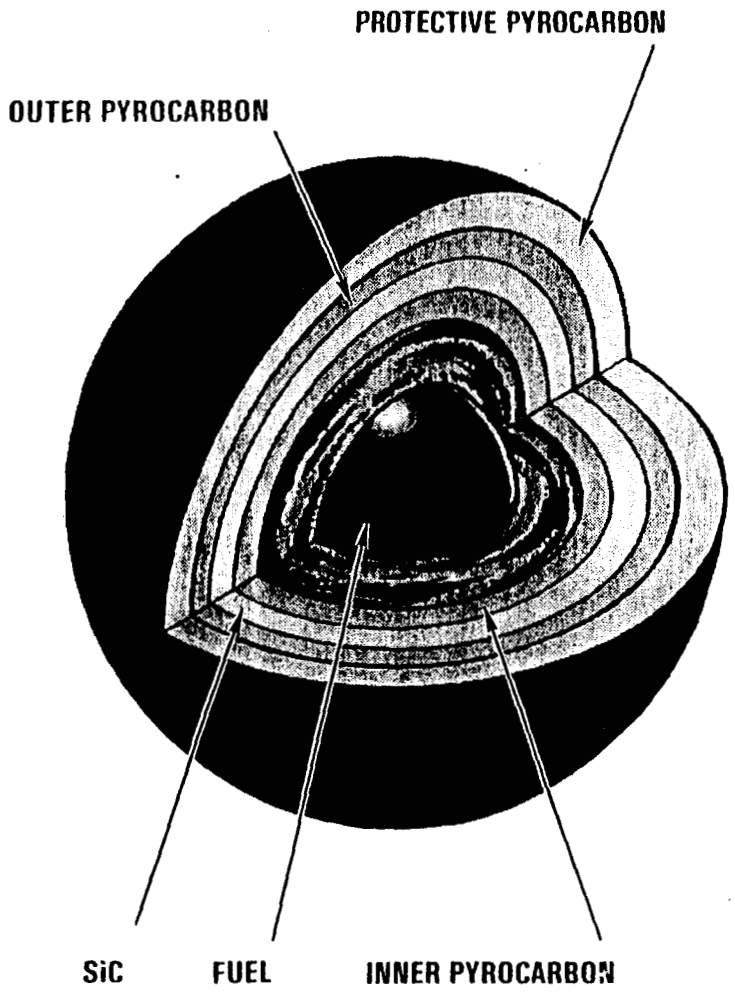

COMPONENT/PURPOSE

- FUEL KERNEL
  - PROVIDE FISSION ENERGY
  - RETAIN SHORT LIVED FISSION PRODUCTS
- BUFFER LAYER (POUROUS CARBON LAYER)
  - ATTENUATE FISSION RECOILS
  - VOID VOLUME FOR FISSION GASES
- INNER PYROCARBON (IPyC)
  - PROVIDE SUBSTRATE FOR SiC DURING MANUFACTURE
  - FISSION PRODUCT BARRIER (EXCEPT Cs AND Sr)
- SILICON CARBIDE (SiC)
  - RETAIN GAS AND METAL FISSION PRODUCTS
  - FISSION PRODUCT BARRIER (INCLUDING Cs AND Sr)
- OUTER PYROCARBON (OPyC)
  - PROVIDE FISSION PRODUCT BARRIER IN PARTICLES WITH DEFECTIVE SiC
- PROTECTIVE PYROCARBON (P-PyC)
  - PROVIDE SOFT, CRUSHABLE LAYER TO PREVENT PARTICLE DAMAGE DURING COMPACT PRODUCTION
  - PROVIDE BONDING SURFACE

Figure 1.1 NP-MHTGR Fuel Design

2.0 DESCRIPTION OF EXPERIMENT

2.1 Objectives:

The primary objective of capsules NPR 1 and NPR 2 was to demonstrate that HEU UCO TRISO particles in fuel compacts fabricated to NP MHTGR specifications would perform as expected under moderate and peak UCO fuel burnups of 78% FIMA, and a fast neutron exposure of at least 2.5×10^{25} neutrons/m^2 ($E > 0.18$MeV). Secondary objectives for the fuel compacts in these capsules were:

1. Provide first in-reactor test of HEU UCO fuel meeting NP MHTGR quality specification and provide a portion of the data base necessary to demonstrate normal operating condition fuel performance models;

2. Provide a portion of the samples needed for conduction cooldown simulation tests designed to demonstrate fuel performance under off normal operating conditions and validate accident condition performance models.

During the irradiation of NPR 1 and NPR 2 there was much greater fuel coating failure and fission gas release than expected. Because of these results the original goals were not achieved and the primary objective of the experiment was changed. The original objectives of the experiments and the PIE work were replaced with the objective to determine the cause of the fuel particle failure under irradiation conditions.

The capsules also contained sealed specimens known as "piggyback experiments" which were of third priority. The objectives of the piggyback experiments were not changed by the unexpected high failure of the reference fuel. The piggyback objectives are listed below:

1. To provide irradiated unbonded HEU UCO particles meeting NP MHTGR specifications for selected PIE investigations to obtain fuel performance statistics of reference fuel under normal operating conditions. Results of these experiments provide for comparison with results from particles irradiated in compacts as well as results from defective particles irradiated in other experiments.

2. To provide irradiated fuel particle specimens for postirradiation heating experiments to evaluate particle performance under accident conditions.

3. To provide well characterized, irradiated, unfueled particles for structural studies. These specimens will provide data for correlating fission product transport and solubility with the microstructure of SiC coatings.

4. To provide well characterized, irradiated, unfueled particles for the study of fission product transport. The tests will be done under nearly isothermal conditions. These tests will provide quantitative information on fission product species uptake and transport under NP MHTGR normal core operating conditions.

5. To provide irradiated, unfueled particles with missing OPyC layers for the study of the effect of SiO_2 layers on the transport of fission products into SiC coatings during normal operating temperatures.

6. To provide well characterized, irradiated, unfueled particles for postirradiation heating tests to investigate fission product behavior during accident conditions.

The particle coating failure and fission gas release observed during irradiation of the three capsules was much larger than expected so the demonstrated retention of fission products was less than originally anticipated. The occurrence of particle failure offered the opportunity for exploration to determine the cause of the failure so that it could be eliminated in the future. This latter objective was added late in the program and guided much of the PIE effort.

2.2 Description of Fuel Specimens

Capsules NPR-1 and NPR-2 each contained 16 fuel compact specimens and 60 unbonded particle samples. The fuel compacts were designed to characterize the performance of reference HEU UCO TRISO-coated particles in fuel compacts which were fabricated with laboratory-scale equipment to MHTGR-NPR product specifications.

The unbonded particle samples consisted of standard fuel particles from the same batch used in the compact, and unbonded inert TRISO particles. The standard fuel particles were included to give information on fuel particle performance statistics for particles without the influence of the compact matrix. The inert particles were included to provide characterization of fission product element solubility and transport rate under a neutron flux.

A detailed description of the fuel specimens tested in the capsules, and the method of preparation is given in Ref. 2.2.1.

2.2.1 Coated Particles

The standard fuel particle is an 8-layer TRISO design, consisting of a high-density UO_2-UC_2 core (UCO) surrounded by concentric layers of low- and high-density pyrolytic carbon and SiC. The reference 200-μm-diameter UCO kernel was fabricated by Babcock & Wilcox using an internal gelation process. Details of this process (given in Ref. 2.?) include

a. Forming a solid microsphere containing uranium oxide and carbon black by internally gelating spherical drops created by pulsed forcing of a broth through needle-type orifices.

b. Removing the volatile impurities from the microspheres by calcining at 340°C.

c. Densifying and adjusting the chemical form of the microspheres by a controlled sintering process which results in a partial carbothermic reduction of the uranium oxide by the internal carbon black.

d. Mechanical screening and separation of imperfectly-shaped and over- and undersize fuel.

The fuel kernels used in NPR-1, NPR-2, and NPR 1A coated particles came from the composite lot no. B10-K-91381. This lot was blended from kernels sintered in 7 separate runs (step c.) from microspheres manufactured by 3 sphere-forming runs (step a.). Although the

broth used in each sphere-forming run was freshly prepared for the run, the ingredients used in the broths came from the same material lots.

A compilation of the quality control test reports generated during fuel kernel manufacture and the conformance certification and material traceability data are given in. A summary of the kernel batch characteristics is given in Table 2-1.

Eight coating layers were deposited around the kernels using chemical vapor deposition (CVD) in a fluidized bed in the General Atomics Laboratory Coater No.2. A total of 72 coating runs were conducted. The details of these processes are described in Ref. 2.2.?. Since, the purpose of these capsule irradiations was to test a reference design particle, the conditions used in the coating manufacturing process were kept reasonably constant. During coating, the temperature of the coating furnace and the coating gas flow rates were maintained at preset values. As shown in Table 2-2, the time necessary to equilibrate the furnace and the particles at the coating temperature varied slightly between runs.

Quality control data were obtained on samples from the individual batch runs and on composite samples. Inspection of individual batch runs was used to give information on the variability of coating characteristics such as the buffer-coating density and buffer % carbon which could not be obtained from the composite batch. Table 2-3 gives a summary of the coating characteristics. The complete quality control data is reported in Ref. 2.2.3.

2.2.2 Fuel Compacts

The fuel compacts tested consisted of coated fuel particles and shim particles bonded in a carbonaceous matrix material. The fuel compacts are right circular cylinders with a typical diameter of about 12.4 mm and a typical length of about 49.4 mm. The uranium loadings in the compacts, given in Table 2-4, were adjusted so that as many particles as possible were irradiated at the design temperature without exceeding a capsule wall temperature of 400 °C.

Two compacts were located in each region of NPR 1 and NPR 2, thus the total number of particles per capsule was about 77,500. These compacts were designated 1A and 1B for region 1, 2A and 2B for region 2, *etc.* The pair of regions located at the same distance from the HFIR midplane made up a zone; such that zone 1 consisted of compacts 1A, 1B, 8A, and 8B, *etc.*, through zone 4 consisting of compacts 4A, 4B, 5A, and 5B.

Fuel compacts were fabricated using a hot injection press. Details of this process are described in Ref. 2.2.1. The basic compact manufacturing process at General Atomics included the following steps:

a. preparation of blended mixtures containing fuel particles and graphite shim.

b. preparation of uncured fuel compacts using hot-injection molding with a pitch-based matrix.

c. carbonizing the matrix by heating the compacts to about 900°C in a graphite crucible under an argon purge.

d. removing impurities and heavy-metal contamination by a high-temperature, gaseous, HCL leaching process at 950°C for 30 minutes.

e. final heat treatment in N_2 at about 1600°C.

QC tests were completed on the finished compacts to ensure that the compacts were within the specifications for HTGR fuel. A general description of the fuel rods irradiated is given in Table 2-5.

TABLE 2-1
GENERAL DESCRIPTION OF KERNEL BATCH USED IN COATED PARTICLES

Sphere forming ID No. B10-CD-	Sintering batch run ID No. B10-SNF-	SIZE (um)	U (wt%)	Density (Mg/M^3)	Carbon (wt%)	Oxygen (wt%)	C/U RATIO	O/U RATIO
91324	91464	196.2 ± 3.6	89.28	10.47	1.72	9.15	0.3772 ± 0.0001	1.5064 ± 0.0021
91324	91465	200.0 ± 3.7	89.07	10.52	1.68	8.98	0.3693 ± 0.0001	1.4819 ± 0.0054
91324	91466	200.0 ± 3.4	89.04	10.52	1.72	9.07	0.3783 ± 0.0032	1.4973 ± 0.0027
91325	91467	204.9 ± 4.7	88.73	10.46	1.58	9.14	0.3475 ± 0.0015	1.5132 ± 0.0035
91325	91468	201.1 ± 3.2	88.88	10.52	1.56	9.13	0.3426 ± 0.0016	1.5108 ± 0.0107
91325	SNF-91469	204.4 ± 3.6	88.94	10.66	1.60	9.01	0.3512 ± 0.0047	1.4891 ± 0.0027
91327	91470	198.6 ± 10.0	88.94	10.74	1.72	8.89	0.3787 ± 0.0001	1.4693 ± 0.0043
COMPOSITE LOT B10-K-91381 B&W Analysis		197.0 ± 4.7	89.28 ± 0.11	10.51 ± 0.01	1.65 ± 0.02	9.17 ± 0.22	0.3617 ± 0.0043	1.5095 ± 0.0358
COMPOSITE LOT B10-K-91381 GA Analysis		200 ± 5	89.44 ± 0.02	10.47 ± 0.06	1.66 ± 0.04	8.68 ± 0.09	0.36	1.43

Table 2-2. General Description of Coating Process Runs

Coating No.	Batch No.	Coating Type	Runs	Charge In (g)	Coater Preheat (min)	Particle Preheat (min)	Orifice Length (mm)	Coating Gas		time (min)
								Cover	Active	
1	FM10-00002 to FM10-00018	Buffer	17	25	15.2 ±3.3	10.7 ±2.4	228.6	Ar	C_2H_2	2.7 (a)
2	FM12-00002 to FM12-00018	first Seal	17	40.0 ±0.6	15.3 ±6.1	9.4 ±2.5	254	Ar	C_3H_6	30
3		IPyC	(b)	(b)			254	Ar	$C_2H_2 + C_3H_6$	24 (c)
4	FM13-00002 to FM13-00018	SiC	17	72.5 ±2.3	22.4 ±8.4	10.8 ±1.4	177.8	H_2	H_2 + MTS	133 ±6.8
5	FM14-00001 to FM14-00010	OPyC	10	122.0 ±0.5	12.2 ±6.9	13.6 ±5.3	254	Ar	$C_2H_2 + C_3H_6$	12 (d)
6	FM17-00001 to FM17-00011	Second Seal	11	139.3 ±4.0 (e)			228.6	Ar	C_3H_6	21.25
7		PPyC	(f)	(f)			228.6	Ar	C_2H_2	2 (g)
8		Third Seal	(f)	(f)			228.6	Ar	C_3H_8	30 (h)

(a) 4 runs at 2.75 min; 13 runs at 2.67 min
(b) continuous from first seal
(c) 1 run at 22.5 min; 3 runs at 23 min; 12 runs at 24 min; 1 run missing run sheet
(d) 1 run at 11.5 min; 9 runs at 12 min
(e) all batches were about 140 g with one batch of 127.5 g
(f) continuous from second seal
(g) 1 run at 127 sec; 10 runs at 120 sec
(h) 1 run at 31.9 min; 10 runs at 30 min

Table 2-3. General Description of Coating Characteristics

Coating Batch		buffer		Buffer Coated Particle		IPyC			SiC	
Identity	coating stage	thick-ness (μm)	density (Mg/m^3)	density (Mg/m^3)	% C	thickness (μm)	density (Mg/m^3)	BAFo	thickness (μm)	density (Mg/m^3)
FM10-0002 to FM10-0018	Buffer	102 ± 10	0.97 ± 0.06	1.96±0.10	45.1 ± 1.1					
FM12-10001 composite	IPyC					53 ± 4	1.92 ± 0.01			
FM13-10001 composite	SiC								35 ± 3	3.23 ± 0.001
FM16-0001 to FM1600009, 10	OPyC									
FM16-10001 composite	OPyC									
FM17-00001 to FM17-00011	PPyC									
FM19-00001 composite	total particle							1.058 ± 0.005		

Table 2-3 (Cont.). General Description of Coating Characteristics

Coating Batch	OPyC layer			OPyC coated particle		PPyC layer			PPyC Coated Particle	Total Particle wt % U: 9.4 ± 0.02 Wt % O: 0.92 ± 0.05			
	thickness (μm)	density	micro-porosity (ml/m2)	diameter (μm)	density (Mg/m^3)	thickness (μm)	density (Mg/m^3)	BAFo	density (Mg/m^3)	diameter (μm)	density (Mg/m^3)	aspect ratio	crush strength (g)
FM10-0002 to FM10-0018													
FM12-10001 composite													
FM13-10001 composite													
FM16-00001 to FM16-0009,10		1.87 ± 0.01	1.0 ± 0.1	654 ± 20	2.23 ± 0.006								
FM16-10001 composite	39 ± 4	1.86 ± 0.01	1.03 ± 0.01	654 ± 20	2.22 ± 0.003								
FM17-00001 to FM17-00011							1.06 ± 0.03		1.83 ± 0.02				
FM19-00001 total particle						47 ± 11	1.06	1.052 ± 0.006		758 ±754	1.84	1.05 ± 0.02	4627 ± 705

TABLE 2-4. Loading per Compact in NPR-1 and NPR-2.

Region	235U (g)	238U (g)	Total U (g)	Approximate Number of Particles
1	0.2144	0.0158	0.2302	6126
2	0.1844	0.0135	0.1979	5266
3	0.1480	0.0109	0.1589	4228
4	0.1315	0.0096	0.1411	3610

Table 2-5. Description of Fuel Rods tested in NPR-1 and NPR-2

HFIR zone	Max End cap (mm)	Matrix					Fuel[f] Homogeneity	Burn-Leach[c] U Fraction	Exposed Heavy Metal[c,g] U Fraction	Fission Gas Release
		filler[b] (wt %)	macroporosity[c,d] (%)			coke content[e] (%)				
			top	middle	bottom					
1	6.7 ± 0.8	39.70 ± 0.59	32.0 ±4.9	24.9 ±6.9	24.7 ±6.9	29.9 ± 0.8	1.01 ± 0.18	0.0018 1.8×10^{-5}	4.6×10^{-7} ± 3.3×10^{-7}	
2	7.1 ± 0.6	38.46	36.5 ± 5.6	27.6 ± 7.7	27.9 ± 3.9	29.5 ± 0.5	1.01 ± 0.02	2.2×10^{-6}		
3	8.4 ± 0.8	38.10	29.5 ± 3.1	25.3 ± 6.6	27.8 ± 9.6	30.1 ± 0.4	1.00 ± 0.02	5.1×10^{-6}		
4	8.9 ± 1.0	37.88 ± 0.06	31.6 ± 4.7	26.4 ± 7.2	23.6 ± 6.5	29.0 ± 0.7	1.02 ± 0.04	1.9×10^{-6}		

(a) All compacts are approximately 12.43 mm in diameter by 49.42 mm long
(b) Measurement made on companion green rod
(c) Measurement made on companion fired rod
(d) Determined from metallographic cross section
(e) Calculated by dividing the coke weight by the initial pitch plus filler weight
(f) Determined by gamma counting both ends of the rod and calculating the ratio of the maximum to the mean values for the compact lot
(g) Determined by HCL leach; 9 lots containing 7 HFIR region 1 and 4 compacts with 3 HFIR region 2 and 4 compact

2.2.3 Piggyback Samples

The piggyback specimens consisted of niobium tubes containing coated particles held individually in holes bored in graphite inserts. The coated particles consisted of either standard fuel particles or unfueled coated particles with carbon kernels. The samples were sealed in the niobium tubes by welding caps on the ends. An argon-helium atmosphere at a pressure of about 0.5 atm was trapped in the tubes at the time of welding. The welded containment was leak-checked to assure a leak rate $\leq 10^{-8}$cc He/s. The graphite inserts were significantly shorter than the niobium tubes to prevent damage during welding of the end or in the opening process during PIE.

Standard Fuel Particles: The purpose of the unbonded standard fuel particle samples was to obtain information on fuel particle performance statistics for particles having the eight-layer TRISO configuration without the influence of the compact matrix. Results obtained from these particles will be compared with results from particles irradiated in compacts in NPR-1 and NPR-2 where matrix effects may exist. The results will also be compared with the performance of bonded and unbonded particles irradiated in other irradiation experiments. These irradiated standard fuel particles will also serve as a specimen source for benchmark post irradiation heating tests as well as for tests to determine the effect of thermal cycling on particle performance.

Full length niobium tubes, 2.2 mm diameter and 29 mm in length were manufactured and loaded with a graphite insert holding loose particles as shown in Figure 2.2.3.1. Each insert holds sixteen standard fueled particles, each contained in a separate hold, 1.02 mm in diameter and 1.02 mm deep with centers spaced 1.27 mm apart. The graphite insert has a Grafoil cover to isolate the individual particles from each other and from the niobium tube. The niobium tube was filled with a He/Ar gas mixture at a pressure between 0.25 and 0.50 atm and sealed by welding on niobium end caps. NPR-1 graphite body 1 and 2 and NPR-2 graphite body 2 each contained 6 full-length niobium tubes each containing 16 standard fuel particles (a total of 288 particles). NPR-2 graphite body 1 contained 10 full-length niobium tubes each containing 16 standard fuel particles (a total of 160 particles). The NPR 1A capsule did not contain piggyback samples.

Unfueled Particles: These specimens represent the first attempt to provide characterization of fission product element solubility and transport rate under a neutron flux and are intended to produce fundamental information related to the transport of fission products in SiC. The use of unfueled TRISO particles (Batch 6351-060100) and carefully selected elements representing fission products will maintain a relatively low radioactivity level for post irradiation examination. The low radioactivity level is necessary to permit the use of quantitative analytical methods, such as SEM and TEM, to establish quantitative profiles of fission product elements across the thickness of the SiC. The use of these particles will provide data on a representative microstructure. The fission product elements Pd, Ag, Cs, Sr, I, Na, K and Rb were prepared in solutions convenient for handling and doped into graphite crucibles. While the dopants may not exactly simulate the chemical form of the fission products produced in the fuel kernel during irradiation, it is expected that the diffusion of the elemental forms into the particles will provide a reasonable simulation of the behavior without compromising the results.

The elements sodium, potassium, and rubidium were included in the test matrix because they should exhibit chemical properties similar to cesium but because of their much smaller atomic size they may show more mobility in the SiC at the lower temperature of NPR 2 where Cs is expected to be immobile. Comparison of the solubility and transport rate of these four elements in SiC under a neutron flux as a function of temperature will provide a better fundamental understanding of the important parameters controlling transport in SiC and reduced uncertainty in fission product transport models. The elements are included singly and in combination with others to provide data on several effects which may exist.

Since the TRISO particles are unfueled, a necessary compromise is to have the fission product elements diffuse inward rather than outward. This reversal of the normal diffusion direction is not expected to influence the applicability of the results to standard fueled particles as long as the concentration of elements is maintained at the levels specified. At the size scale of the migrating atom, the SiC surface approximates a plane surface very well and the direction of transport through the plane is not important.

Half-length niobium tubes, 2.2 mm diameter and 14 mm in length, were loaded, as shown in Figure 2.2.3.1, with graphite inserts holding particles chosen to match the type of experiment. One design allows for a maximum of five particles and the other allows for single particles. In each case, the graphite insert was closed with a graphite cap and the entire

insert was sealed into a niobium tube filled with a He/Ar gas mixture at a pressure between 0.25 and 0.50 atm by welding. The assembly was then leak-tested using a helium leak detector. A number of the experiments were doped with various concentration levels of fission products. There are two types of experiments requiring different concentration levels. The two types are (1) diffusion (D type) and (2) structure (S type). In the former, the analysis will be by gamma counting, using the Irradiated Microsphere Gamma Analyzer (IMGA). In the latter, techniques such as optical microscopy, scanning electron microscopy (SEM) and transmission electron microscopy (TEM) were used for characterizing the microstructure. The TEM and SEM techniques will also be used for elemental analysis. Measurements of the mechanical properties of the SiC coatings will be made. The criteria for selecting the inventory were as follows:

1. The inventory was determined by three factors in order of importance:
   (a) detectability (maximum consistent with criterion [c]);
   (b) representative of normal particle inventory over a range of burnup; and
   (c) minimization of radioactivity for ease in handling.

2. In D-type experiments, the radioactivity expected in the SiC layer and the identity of the diffusing metals should be measurable by gamma spectroscopy, using IMGA.

3. In S-Type experiments, the radioactivity should be as low as possible, consistent with detectability ($<3 \times 10^{-4}$ Ci), to allow analysis by techniques, such as SEM, outside the hot cells.

4. Only stable fission product elements are to be added to the piggyback samples before irradiation.

In D-type experiments, the number of atoms of the fission product element that had to be added to obtain a detectable number of atoms in the SiC layer spanned the number of atoms generated in a particle under NP-MHTGR conditions from very low to beyond maximum burnup, 75% FIMA. In S-type experiments, the concentration level of added fission products was chosen as a compromise between criterion (a) and (c) above. In some

cases, this will lead to a small amount of radioactivity which could limit the techniques planned to be used in the postirradiation microstructural examination.

The present effort is the first attempt at such experiments designed to provide information on the solubility and transport of fission products in SiC and will assist in the planning of future experiments. Definitions of the types of experiments, the abbreviated notation for each type, and more descriptive detail are given below.

Standard, unfueled TRISO particles, IS (structure): Six half-length tubes containing 5 unfueled TRISO particles each were irradiated in NPR-1 to provide information on the effect of irradiation on SiC coating microstructure and properties. This data will provide baseline information on the behavior of SiC coatings.

Doped unfueled TRISO particles, ID_1 (structure): Twelve half-length tubes containing 5 unfueled TRISO particles were irradiated in NPR-1 to provide information on the distribution of fission products in SiC coatings and the effect of these fission products on the microstructure and mechanical properties of SiC coatings. "Doped" refers to the presence of fission product elements (non-activated where possible), sorbed onto the graphite insert, which will enter the OPyC layer and diffuse into the particle and SiC coatings. The experiments will include several isotopes and combinations of isotopes. Particles were exposed to individual isotopes of ^{104}Pd, ^{133}Cs, ^{107}Ag, and a mixture of ^{104}Pd, ^{133}Cs, ^{107}Ag, ^{86}Sr, and ^{127}I. In the case of Cs and I the sources were composed of the normal distribution of naturally occurring isotopes. Comparable out-of-reactor studies are planned to evaluate the effects of neutron fluence on microstructure and properties.

Doped unfueled TRISO particles, ID_2 (diffusion): Thirty-two half-length tubes containing single unfueled TRISO particles were irradiated in NPR 1 and NPR 2 to provide information on the diffusion of fission products into SiC coatings. "Doped" refers to the presence of fission product elements, sorbed onto the graphite insert, which will enter the OPyC layer and diffuse into the particle and SiC coatings. Except for ^{84}Sr, the isotopes were composed of the normal distribution of naturally occurring isotopes. These isotopes become activated during irradiation. The use of single particles allows quantitative measurement of the amount of fission product which diffuses into the particles. After irradiation, gamma counting and sectioning techniques should permit determinations of the extent of transport into the SiC coating. Some particles were exposed to individual isotopes and some were to be exposed to mixtures of isotopes. In NPR-1, the individual isotopes used are Pd, Cs, Ag,

^{84}Sr, I, and a mixture of Pd, Ag, and Cs. In NPR-2 the individual isotopes used are Pd, Cs, Ag, ^{84}Sr, I, Na, K, Rb, and a mixture of Pd, Cs, and Ag. Comparable out-of-reactor diffusion studies are planned to evaluate the effects of neutron fluence on fission product transport.

Doped unfueled TRISO particles with cracked SiC layers, IC (diffusion): Four half-length tubes, each containing one unfueled TRISO particle with the OPyC burned off were irradiated in NPR 1 and NPR 2, respectively (eight tubes total). Oxidative burning of the OPyC layer should provide an SiO_2 layer 1-10 nm thick on the exposed SiC surface. One half of these particles were treated in HF acid to remove the oxide layer. The diffusion of fission products into both oxidized and unoxidized SiC layers were studied for silver and for a mixture of palladium, silver, and cesium

Loading of specimens: The graphite crucibles (POCO graphite) were machined in different lengths according to the experiment and type of specimen. After fabrication the crucibles were engraved with markings appropriate to the experiment (these markings match those of the niobium tubes), heat treated in argon at 1350°C for one hour, and doped with simulated fission elements where appropriate (the details of the doping procedure are presented below). Graphite spacers and end plugs were also machined and heat treated.

Appropriate unfueled particles were placed in the graphite crucibles with the use of vacuum tweezers. A specially prepared check list was used as part of the loading procedure. The check list was used to verify the crucible identification markings, the dopant, the concentration level of the dopant, and the number and type of particle(s). As each crucible was loaded, the check list was initialed by two individuals. After the end cap was inserted, graphite spacers were inserted where necessary and the crucible was inserted into the matching niobium tubes prior to welding of the second cap following procedure MET-WM-SOP-40. As a final check of the integrity of the welds, the tubes were checked for leaks following procedure NDE 71 by members of the ORNL Quality Department. For piggyback experiments containing standard fuel, single fuel particles were placed into each of the sixteen holes in the graphite crucible with the use of vacuum tweezers. A Grafoil cover sheet (21 mm x 0.9 mm x 3.2 mm thick) was aligned along the top of the crucible covering all of the holes. The crucible and Grafoil cover were carefully inserted into the matching niobium tube and slid into the tube until the crucible was flush with the end of the tube. A graphite rod was used to push the crucible-Grafoil assembly into the niobium tube until it seated on the bottom. A graphite spacer was inserted into the remaining space prior to welding the

second niobium end cap in place following procedure MET-WM-SOP-40. After welding, the tubes are checked for leaks following procedure NDE 71.

In addition to the piggyback specimens to be included in the NPR 1 and NPR 2 irradiation capsules, a series of laboratory experiments was planned to provide comparative data on unfueled TRISO particles heated in the absence of irradiation. The information to be obtained includes determination of structural changes in SiC, SiC decomposition effects, and fission product transport. Three identical sets of specimens were to be subjected to laboratory tests conducted at three different temperatures, one temperature to be equivalent to the highest irradiation temperature achieved in the NPR 1 experiment and two higher temperatures chosen based on the results of the experiments carried out at the first temperature. The higher temperatures will be chosen to allow reasonable diffusion distances of the fission products during times readily achievable in laboratory tests. A number of the specimens were doped with stable fission product elements according to the procedure described below. The doping was conducted at the same time as the doping for the in-reactor experiments and made up of the same solutions. The preparation of unfueled particles followed the same procedures as were used for the irradiation experiments. The graphite crucibles were fabricated, engraved, heat treated, and doped; the graphite end plugs and spacers fabricated and heat treated; and the niobium tubes were cut to appropriate lengths. The samples were stored in ORNL Building 3525 for heating at a future time.

Doping of graphite crucibles with various concentrations of fission product elements was carried out by members of the Analytical Chemistry Division following procedure AC-OP-104-0603. The procedure varies slightly depending on the initial form of the fission product elements. The general steps are as follows. For those elements which are initially in metallic form (isotopic ^{104}Pd, and isotopic ^{107}Ag), a measured weight of the metal was first dissolved in a nitric acid solution. A volume of a solution was produced containing the highest concentration of fission product element desired in atoms/ml. Precautions were taken to ensure that the resulting solution contained only dilute acid (< 0.1 N) by diluting with double distilled water. Using a micropipette, the appropriate volume of solution was deposited into the hole of an engraved graphite crucible. After doping, the crucible was dried in air. To achieve lower concentration levels, the initial solution was diluted with double distilled water to reach the appropriate concentration. The procedure for preparing the solution of the other fission products was similar. However, the starting materials were in the form of

soluble compounds. The compounds used in the doping were: strontium carbonate (isotopic forms prepared with ^{84}Sr, and ^{86}Sr), rubidium iodide, potassium nitrate, silver nitrate, sodium nitrate, potassium iodide, cesium oxalate, and silicon dioxide (in this case the SiO_2 was dissolved in nitric acid before being diluted with double distilled water). A measured weight of each compound (with the exception of the SiO_2- see note above) was dissolved in double distilled water to produce a known volume of the desired concentration. The doping was conducted as specified above and lower concentrations were produced by diluting the starting solutions appropriately. For those cases requiring a mix of fission products, equal volumes of the required fission product solutions were mixed together and a micropipette was used to deposit the appropriate volume of solution into the hole in the graphite crucible. A specially prepared doping check list was prepared for the doping procedure. The check list was used to verify the identification marking of the crucible, the dopant, and the concentration of the dopant. After doping, the check list was initialed by two individuals. Variations in the doping plan were indicated with notes on the check list and initialed.

The piggyback samples included in the NPR 1 and NPR 2 irradiation experiments are all contained in sealed niobium tubes. Each tube, as well as the graphite insert inside the tube, is engraved with a marking which positively identifies the specimen. The location of the various piggyback specimens and the spacers in the irradiation experiments are shown in Tables 2.2.3.1 and 2.2.3.2. The three to five character designation of the specimen is an indicator of the location and the type of specimen. Since there were several different types of experiments, each with its own objective, tables 2.2.3.3, 2.2.3.4, and 2.2.3.5 are provided to clarify the experiments, and the identification markings engraved for the laboratory heating experiments is also included for completeness. The lists are broken down in terms of location. The concentrations of the dopants are in units of atoms.

Table 2.2.3.1. Markings on the Nb tubes in the NPR-1 capsule piggyback samples.

Axial Location	NPR-1 Piggyback ID Numbers			
	Graphite Body	Hole 1	Hole 2	Hole 3
Top of Capsule	1	11C1	11C2	11C3
	1	11S	11C4	11S
	1	15mm spacer	15mm spacer	15mm spacer
	1	11GA	11UA	11GA
	1	15mm spacer	15mm spacer	15mm spacer
	1	11S	11P2	11S
	1	11V	11A2	11A3
	1	15mm spacer	15mm spacer	15mm spacer
	1	11UB	11GB	11UB
	1	15mm spacer	15mm spacer	15mm spacer
	1	11S	11M	11S
	1	11C1	11C2	11C
HFIR Midplane				
	2	12C4	12A5	12I5
	2	12Y	12T5	12X
	2	15mm spacer	15mm spacer	15mm spacer
	2	12GA	12UA	12GA
	2	15mm spacer	15mm spacer	15mm spacer
	2	12FC4	12F15	12M
	2	12P5	12DP3	12P6
	2	15mm spacer	15mm spacer	15mm spacer
	2	12UB	12GB	12UB
	2	15mm spacer	15mm spacer	15mm spacer
Bottom of Capsule	2	120A5	12T6	12WA5
	2	12C5	12A6	12I6

Table 2.2.3.2. Markings on the Nb tubes in the NPR-2 capsule piggyback samples

Axial Location	NPR-2 Piggyback ID Numbers			
	Graphite Body	Hole 1	Hole 2	Hole 3
Top of Capsule	1	21N5	15mm spacer	21K6
	1	21R6	21GA	21C5
	1	30mm spacer	21UB	30mm spacer
	1	21GA	21GC	21UA
	1	30mm spacer	21UD	30mm spacer
	1	21UB	21GE	21GB
	1	30mm spacer	21UF	30mm spacer
	1	21N6	15mm spacer	15mm spacer
	1	15mm spacer		21C6
HFIR Midplane				
	2	22C4	22A5	22I5
	2	22Y	22T5	22X
	2	15mm spacer	15mm spacer	15mm spacer
	2	22GA	22UA	22GA
	2	15mm spacer	15mm spacer	15mm spacer
	2	22FC4	22FI5	22M
	2	22P5	22C3	22P6
	2	15mm spacer	15mm spacer	15mm spacer
	2	22UB	22GB	22UB
	2	15mm spacer	15mm spacer	15mm spacer
	2	22OA5	22T6	22WA5
Bottom of capsule	2	22C5	22A6	22I6

Table 2.2.3.3. Unfueled TRISO Particles
NPR-1, Graphite Body 1:

Tube Identification	Type of Experiment	Contents (total atoms)
11C1	Structural	5 unfueled particles, 1 X 10^7 Cs, stable
11C2	"	5 unfueled particles, 1 X 10^9 Cs, stable
11C3	"	" 1 X 10^{11} Cs, stable
11S	"	" undoped
11C4	"	" 1 X 10^{13} Cs, stable
11S	"	" undoped
11S	"	" undoped
11P2	"	" 1 X 10^9 ^{104}Pd, stable
11S	"	" undoped
11V	"	" 1 X 10^{11} ea. ^{104}Pd, ^{107}Ag,Cs,I ^{86}Sr
11A2	"	" 1 X 10^{107}Ag, stable
11A3	"	" 1 X 10^{11} ^{107}Ag, stable
11S	"	" undoped
11M	"	1 unfueled particle, 1 X 10^5 ea. ^{108}Pd, Ag, Cs, stable
11S	Diffusion	5 unfueled particles, undoped
11C1	Structural	" 1 X 10^7 Cs, stable
11C2	"	" 1 X 10^9 Cs, stable
11C3	"	" 1 X 10^{11} Cs, stable

Table 2.2.3.3. Unfueled TRISO Particles
NPR-1, Graphite Body 2

Tube Identification	Type of Experiment	Contents (total atoms)
12C4	Diffusion	1 unfueled particle, 1 X 10^{13} Cs, activated
12A5	"	" 1 X 10^{15} Ag, active
12I5	"	" 1 X 10^{15} I, activated
12Y	"	1 unfueled particle, 1 X 10^{13} ea., ^{104}Pd, no OPyC, oxidized Ag, Cs, active
12T5	"	" 1 X 10^{9} ^{84}Sr, active
12X	"	1 unfueled particle, 1 X 10^{13} ea., ^{104}Pd, no OPyC Ag, Cs, active
12FC4	"	1 unfueled particle, 1 X 10^{13} Cs, active with cracked SiC
12FI5	"	1 unfueled particle, 1 X 10^{15} I, activated with cracked SiC
12M	"	1 unfueled particle, 1 X 10^{15} ea. ^{104}Pd, Ag, Cs, activated
12P5	"	" 1 X 10^{15} ^{104}Pd, active
12DP3	Structural	5 unfueled particles, 1 X 10^{11} ^{104}Pd, stable
12P6	Diffusion	1 unfueled particle, 1 X 10^{17} ^{104}Pd, active
12OA5	"	1 unfueled particle, 1 X 10^{15} Ag, active no OPyC, oxidized
12T6	"	1 unfueled particle, 1 X 10^{11} ^{84}Sr, active
12WA5	"	1 unfueled particle, 1 X 10^{15} Ag, active no OPyC
12C5	"	1 unfueled particle, 1 X 10^{15} Cs,active
12A6	"	" 1 X 10^{17} Ag, active
12I6	"	" 1 X 10^{17} I, active

Table 2.2.3.3 Unfueled TRISO Particles (continued)
NPR-2, Graphite Body 1:

Tube Identification	Type of Experiment	Contents (total atoms)
21N5	Diffusion	1 unfueled particle 1 X 10^{15} Na, active
21K6	"	" 1 X 10^{17} K, active
21R6	"	" 1 X 10^{17} Rb, active
21C5	"	" 1 X 10^{15} Cs, active
21N6	"	" 1 X 10^{17} Na, active
21K7 (not inserted)	"	" 1 X 10^{19} K, active
21R7 (not inserted)	"	" 1 X 10^{19} Rb, active
21C6	"	" 1 X 10^{17} Cs, active
22C4	Diffusion	1 unfueled particle, 1 X 10^{13} Cs, activated
22A5	"	" 1 X 10^{15} Ag, active
22I5	"	" 1 X 10^{15} I, activated
22Y	"	1 unfueled particle, 1 X 10^{13} ea., ^{104}Pd, no OPyC, oxidized Ag, Cs, active
22T5	"	" 1 X 10^{9} ^{84}Sr, active
22X	"	1 unfueled particle, 1 X 10^{13} ea., ^{104}Pd, no OPyC Ag, Cs, active
22FC4	"	1 unfueled particle, 1 X 10^{13} Cs, active with cracked SiC
22FI5	"	1 unfueled particle, 1 X 10^{15} I, activated with cracked SiC
22M	"	1 unfueled particle, 1 X 10^{15} ea. ^{104}Pd, Ag, Cs, activated
22P5	"	" 1 X 10^{15} ^{104}Pd, active
22C3	"	" 1 X 10^{11} Cs, active
22P6	"	1 unfueled particle, 1 X 10^{17} ^{104}Pd,active

Table 2.2.3.3 Unfueled TRISO Particles (continued)
NPR-2, Graphite Body 1:

Tube Identification	Type of Experiment	Contents (total atoms)
22OA5	"	1 unfueled particle, 1 X 10^{15} Ag, active no OPyC, oxidized
22T6	"	1 unfueled particle, 1 X 10^{11} ^{84}Sr, active
22WA5	"	1 unfueled particle, 1 X 10^{15} Ag, active no OPyC
22C5	"	1 unfueled particle, 1 X 10^{15} Cs, active
22A6	"	" 1 X 10^{17} Ag, active
22I6	"	" 1 X 10^{17} I, active

Table 2.2.3.4. Standard Fuel Particles

The fueled piggyback experiments all contain identical standard fueled particles. Each engraved niobium tube contains 16 identical particles contained in individual wells in engraved graphite inserts. The markings serve only to indicate the location of the tubes in the irradiation experiments.

Location	Engraved Marking on Sample
NPR-1, Graphite Body 1	11GA, 11UA, 11GA, 11UB, 11GB, 11UB
NPR-1, Graphite Body 2	12GA, 12UA, 12GA, 12UB, 12GB, 12UB
NPR-2, Graphite Body 1	21GA, 21UA, 21GA, 21UB, 21UB, 21GC, 21UD, 21GE, 21UF
NRP-2, Graphite Body 2	22GA, 22UA, 22GA, 22UB, 22UB

Table 2.2.3.5. Laboratory Experiments

The three sets of laboratory experiments are exact duplicates except for temperature. Only one set will be listed. The other two will be identical except for the second identifier (1,2 or 3) in the marking sequence. All particles in these tests are unfueled TRISO.

Tube Identification	Type of Experiment	Contents (total atoms)
L1H	SiC Structure	10 particles, no F.P.
L1J	SiC Decomposition	1 particle, no F.P.
L1J	"	"
L1J	"	"
L1J	"	"
L1BA2	SiC Structure	10 particles, 10^9 Ag
L1BP2	"	" 10^9 ^{104}Pd
L1BA3	"	" 10^{11} Ag
L2BP3	"	" 10^{11} ^{104}Pd
L1BC1	"	" 10^7 Cs
L1BC2	"	" 10^9 Cs
L1BC3	"	" 10^{11} Cs
L1BC4	"	" 10^{13} Cs
L1BV	"	" 10^{11} ea. Pd, Ag, Cs, Sr, I
L1EC4	F.P. Diffusion	2 particles, 10^{13} Cs
L1EA4	"	" 10^{13} Ag
L1EP5	"	" 10^{15} Pd
L1ET5	"	" 10^9 Sr, could not get 10^{15}
L1EZ6	"	" 10^{17} Si
L1EI5	"	" 10^{15} I

Table 2.2.3.5. Laboratory Experiments (Continued)

Tube Identification	Type of Experiment	Contents (total atoms)
L1EC5	"	" 10^{15} Cs
L1EA5	"	" 10^{15} Ag
L1EP6	"	" 10^{17} Pd
L1ET6	"	" 10^{11} Sr, could not get 10^{17}
L1EZ7	F.P. Diffusion	" 10^{19} Si
L1EI6	"	" 10^{17} I
L1EN5	"	" 10^{15} Na
L1ER6	"	" 10^{17} Rb
L1EK6	"	" 10^{17} K
L1EC5	"	" 10^{15} Cs
L1EN6	"	" 10^{17} Na
L1ER7	"	"10^{19} Rb, not doped-could not get 10^{19}
L1EK7	"	" "
L1EC6	"	10^{17} Cs

2.3 Capsule Design

The irradiation capsules NPR-1 and NPR-2 each consist of a doubly contained, single purged cell with 16 fuel compacts surrounded by H-451 graphite fuel holders. Figure 2.3.1 is a schematic cross section of the capsule internal design, and Fig. 2.3.2 is a longitudal view of a graphite fuel body illustrating the physical placement of the compacts. Figures 2.3.3 and 2.3.4 show the as loaded fuel compact configuration for NPR-1 and NPR-2, respectively. Pure helium gas sealed between the primary and secondary containment vessels (Inconel-718) serves as a containment integrity monitor during irradiation. A helium-neon (He-Ne) gas mixture flows between the graphite fuel holder and the primary containment wall, providing active temperature control. By adjusting the helium and neon concentrations, the thermal conductivity of the sweep gas can be varied to control the radial heat flow to the HFIR cooling water. The flow rate and the gas mixture are adjustable for fine tuning of the fuel compact temperatures, which can be monitored by thermocouples inserted into the fuel holder. The thermocouple junctions are located in the same horizontal plane as the axial midpoints of the fuel compacts. For these experiments, there are no thermocouples in the fuel compacts. The fuel holder is held concentric with the primary containment wall by six alumina centering pins recessed in the outer wall of the graphite fuel holder (three at either end).

The graphite holders contain the fuel compacts, flux monitors, thermocouples, and encapsulated, unbonded fuel particles known as piggyback samples. The fuel compacts are contained within the fuel holders in two 1.260-cm-diameter holes on a 1.448-cm-diameter bolt circle. The fuel compacts are about 49.3 mm long and about 12.5 mm in diameter. The holder design, with the compacts stacked one upon the other as in a typical MHTGR, was driven by the desire to maximize the number of fuel particles in the experiment by obtaining uniform irradiation conditions for all the compacts. This was accomplished by minimizing the axial separation of the compacts. The limiting parameter in maintaining uniform irradiation conditions is the axial flux distribution in the HFIR (see Appendix A), as a function of cycle time and test burnup.

In NPR-1 all thermocouples were nisil-nicrosil (ANSI type N) but in NPR-2 two of the TCATs contained type N while the other two contained chromel-alumel (ANSI type K) thermocouples. The radial locations the TCATs are shown in Fig. 2.3.5. The axial location

of the thermocouple measuring junctions corresponded with the axial midplane of the fuel compacts as shown in Figs. 2.3.6 and 2.3.7 for NPR-1 and NPR-2, respectively. The Inconel 600 sheathed TCAT assemblies were brazed into the primary and secondary containment bulkheads and continued to a junction box located immediately above the HFIR pressure vessel top lid. From there flexible compensating lead wire carried the signals to another junction box at poolside, and then on to the capsule-dedicated instrumentation facility.

2.3.1 Description Of Test Articles

2.3.2 Fuel Compacts

The fuel compacts tested consisted of coated fuel particles and shim particles bonded in a carbonaceous matrix material. The fuel compacts are right circular cylinders with a typical diameter of about 12.43 mm and a typical length of about 49.42 mm. The loadings of the compacts are found in Table 2.3.1. Details of the UCO kernels, coated particles, compact matrix materials and fuel compacts are documented elsewhere.

Table 2.3.1. Loading per Compact in NPR-1 and NPR-2.

Region	235U (g)	238U (g)	Total U (g)	Approximate Number of Particles
1	0.2144	0.0518	0.2302	6126
2	0.1844	0.0135	0.1979	5266
3	0.1480	0.0109	0.1589	4228
4	0.1315	0.0096	0.1411	3755
5	0.1315	0.0096	0.1411	3755
6	0.1480	0.0109	0.1589	4228
7	0.1844	0.0135	0.1979	5266
8	0.2144	0.0158	0.2302	6126

Note that two compacts are located in each region, thus the total number of particles per capsule is about 77,500. These compacts have been designated 1A and 1B for region 1, 2A and 2B for region 2, etc. The pair of regions located at the same distance from the HFIR midplane are said to make up a zone, such that zone 1 consists of compacts 1A, 1B, 8A, and 8B, etc., through zone 4 consisting of compacts 4A, 4B, 5A, and 5B.

2.4 IRRADIATION FACILITY

2.4.1 BRIEF DESCRIPTION OF THE HFIR

The High Flux Isotope Reactor (HFIR) is a beryllium-reflected, light water-cooled and moderated flux-trap type reactor which uses highly enriched ^{235}U as the fuel. Figure 2.4.1 shows the various irradiation positions in the HFIR, with those utilized by NPR-1 and NPR-2 labeled.

The HFIR is a versatile isotope production and test reactor with the capability and facilities for performing a wide variety of irradiation experiments. The HFFR is a pressurized light water-cooled and moderated thermal nuclear reactor, designed to operate at 100 MW(t) steady-state power. Current operation is limited to 85 MW(t) to preserve the reactor vessel service life.

The HFIR was designed and built in the early sixties. Initial criticality and commencement of low power physics testing began in 1965. Full power was first achieved on September 9, 1966. The HFIR is unique in the sense that it provides the highest neutron fluxes available in any of the world's reactors, and neutron currents from the four horizontal beam tubes are among the highest available. A brief summary of the primary characteristics is as follows:

CHARACTERISTICS OF THE HIGH FLUX ISOTOPE REACTOR

Design Power.....100 MW(t)

Current Operation.....85 MW(t)

NOTE: Current operation limited to 85 MW to extend reactor vessel life.

Coolant/Moderator.....Pressurized Light Water

Reflector.....Beryllium

Typical Neutron Fluxes (unperturbed):

	Thermal	(>.183 MeV)
Target Region	$\sim 2 \times 10^{15}$	$\sim 1 \times 10^{15}$ [a]
Experiments	$2 - 1 \times 10^{15}$	$.01 - .8 \times 10^{15}$ [a]

[a] To convert to equivalent graphite damage flux for the HTGR multiply ty 0.93 (Refs. 2.4.1 and 2.4.2)

A fuel cycle for the HFIR normally consists of full power operation for a period of from 21 to 23 days (depending on the experiment and radioisotope load in the reactor) followed by an end-of-cycle shutdown for refueling and changeout of targets and tests. This corresponds to ~1800-2000 MWD per cycle at 85 MW thermal power.

HFIR cycles 299 through 307 irradiated the NPR-1 and NPR-2 tests. The reactor data has undergone detailed review as part of the data validation process. The data exhibited no unusual or inexplicable characteristics.

2.4.2 Materials Irradiation Facility (MIF)

Instrument and control functions for each experiment is provided by the Material Irradiation Facility (MIF). Each MIF consists of an integrated set of instruments, recorders, controllers, plus associated piping, wiring and power supplies, and an automated data acquisition system (DAS).

The system is designed to be connected directly with an in-reactor experiment assembly to provide test monitoring, gas flow and temperature control, and data collection. The test can be located in any HFIR irradiation position. The MIF also serves as the data interface

between the test specimens, the reactor control room and the Test Sponsor. Figure 2.4.2 is a functional schematic which shows the basic MIF instrumentation and control features. Instruments that are key to proper test control provide a local MIF panel alarm and a remote common alarm in the reactor control room. The reactor control system is designed to permit selected direct inputs from the MIF to the reactor power control system, to provide automatic power reduction, if required.

Currently, there are five operational MIFs in the HFIR facility Experiment Control Room (ECR). Capsules NPR 1 and NPR 2 utilized MIF 2 and MIF 5, respectively.

A schematic instrument application diagram for the facility used to support the operation of NPR 1 and NPR 2 is shown in Fig. 2.4.3. Most of the experiments which utilize the MIFs have similar control and monitoring needs; therefore, a significant amount of equipment common to the operation of five similar facilities, i.e., electrical power source, gas bottle stations, molecular sieve and titanium sponge gas cleanup systems, sweep gas sampling system, etc., is installed in the HFIR Experiment Room.

2.4.2.1 NPR 1 and NPR 2 Monitoring

Operating temperatures in each capsule were measured by 27 thermocouples incorporated into four discrete Thermocouple Array Tubes (TCATs). The locations of the TCATs and the individual TC jucntions are discussed in section 4.1.

The gas pressure between the primary and secondary containment vessels (nominally 575 psig) was monitored continuously by three strain-gage-type pressure transducers. The outputs of these transducers are connected to an automated power reduction system such that a loss of pressure, through a leak in either the primary or secondary containments, would reduce the reactor power to 10% of full power.

The helium and neon sweep gas (secondary gas system) flows were measured by three mass flowmeters, two on the inlet side measuring the individual gas flows and one on the outlet side measuring the combined flows. The pressure of the sweep gas system was also monitored, through the use of two pressure transducers, one on the inlet and one on the outlet lines.

In addition to flow and pressure, the sweep gas outlet lines were monitored for radioactivity through the use of two ionization chambers for NPR-1 and two Geiger-Muller

monitors for NPR-2. In each case, about 15 feet of the 1/8-in OF outlet-line tubing is coiled around the monitors. This system is sensitive enough to discern single particle failures through the burst of activity released by such failures. The output of all four monitors was continuously recorded on strip-chart recorders and the analysis of these data is discussed in section 6 of this report.

2.4.2.2 Data Acquisition

Thermocouple outputs, primary and secondary gas pressures, and sweep gas flow rates were recorded every six seconds on a hard disk using Kayeview software on a PC connected to a Kaye Digi-4 combination strip-chart recorder and data acquisition system. During steady-state operation these data were also printed out once per hour on hard copy. During reactor startups the hard copy data were printed at five minute intervals. All of the hard disk data has been transferred to 5.25-in Bernoulli disks for storage. The data was managed and evaluated in accordance with the Fuel Material Testing Group Data Management Guideline as outlined in the operating guideline "Fuel Materials Testing Group Mission Statement and Responsibility Matrix" (document No. MET-NFM-GP-001).

2.5 References

2.2.1 M. L. Russell, "NPR 1 and NPR 2 Test Article Preirradiation Report," EG&G Idaho (INEL) NPR-MHTGR-0494, 8/6/92 (DRAFT).

2.2.2 NPR-MHTGR Performance Test Fuel, Uranium Oxycarbide Fuel Kernels Composite Lot Number: B10-K-91381, EG&G Contract Number C90-102940 add. #2, DE-AC07-76ID-51570.

2.2.3 QC Data Package, NPR-MHTGR Performance Test Fuel, Test Capsules NPR 1, 1a, and 2, Coated Particles - Composite FM19-00001, General Atomics, June, 1991.

2.2.4 QC Data Package, NPR-MHTGR Performance Test Fuel, Test Capsules NPR 1, and 1a, FM23-00001, General Atomics, June 1992.

2.4.1 Kerr, H. T. et al., "Lattice Displacement Calculations and Compilations for Different Irradiation Facilities," ORNL/TM-5269, 1976.

2.4.2 Myers, B. F., "Compilation of Data on Reactor Experiment for Use in Fission Product Transport Calculations," HBK-IB-05184, Kernfornschungsanlage, Jülich Gmbh, 1984.

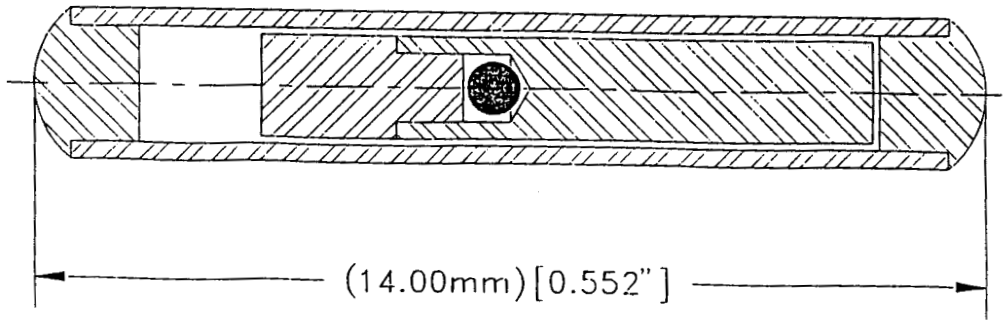

ASSEMBLY "A"
ONE PARTICLE HOLDER

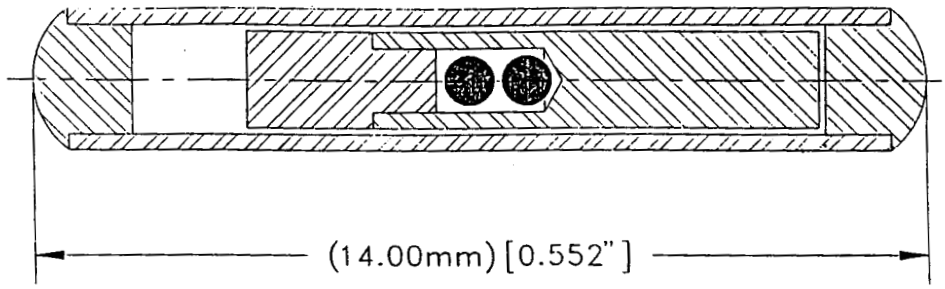

ASSEMBLY "B"
TWO PARTICLE HOLDER
DIFFUSION STUDIES

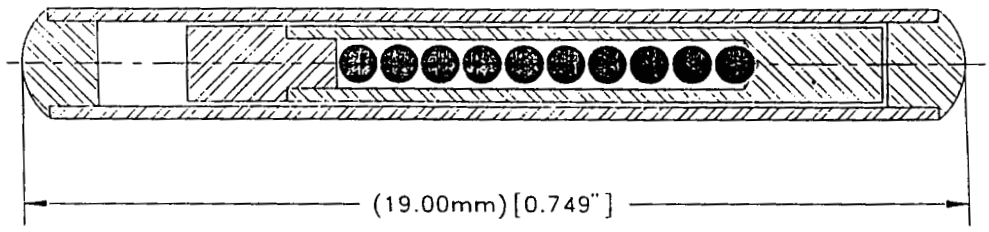

ASSEMBLY "D"
TEN PARTICLE HOLDER
STRUCTURAL STUDIES

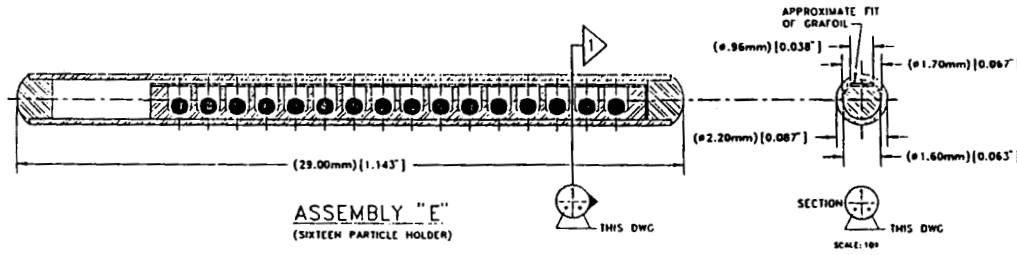

ASSEMBLY "E"
SIXTEEN PARTICLE HOLDER

Figure 2.2.3.1 Schematic of piggyback samples

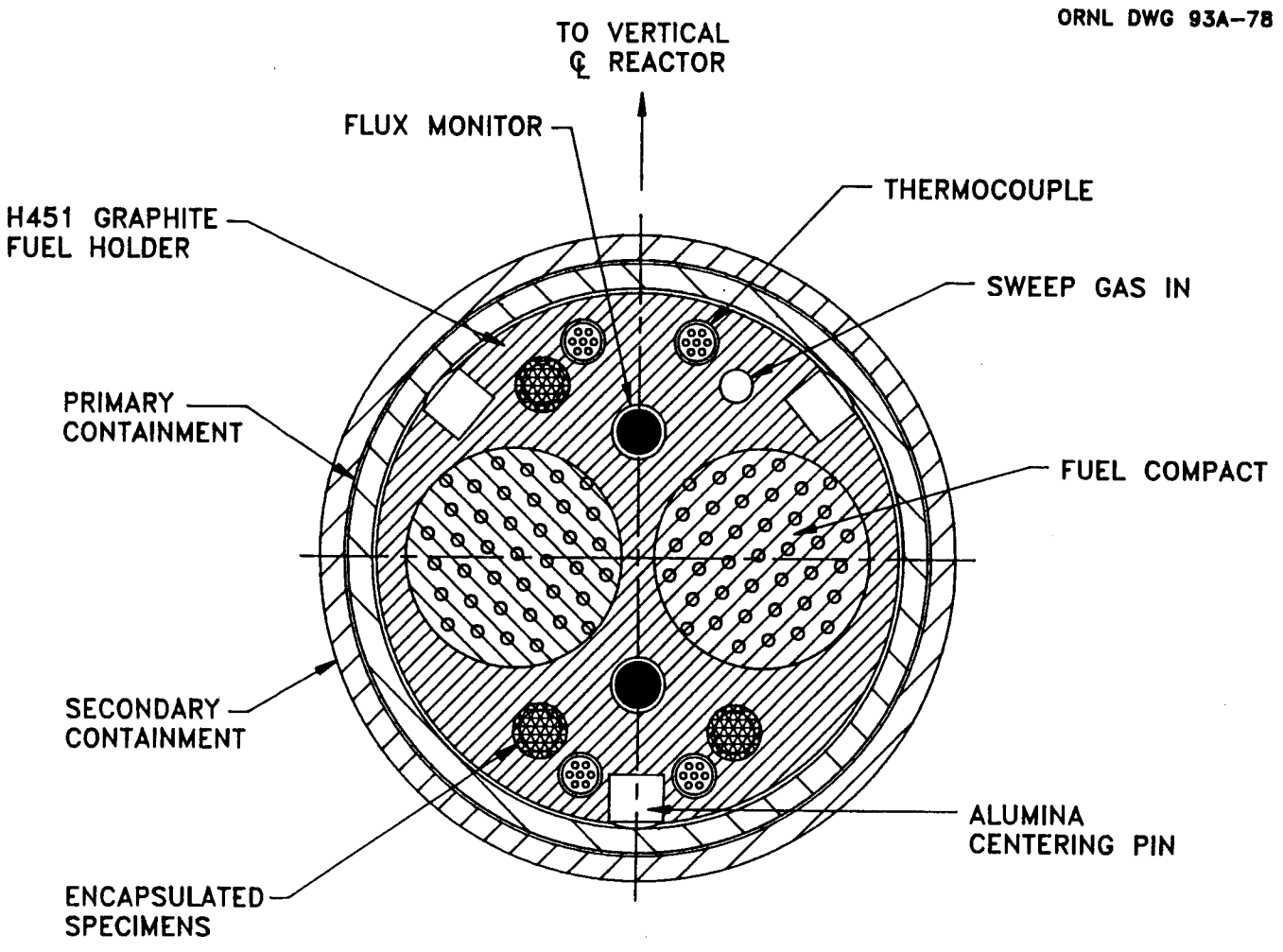

Figure 2.3.1 Schematic cross section of the NPR 1/2 irradiation capsule
(Shows fuel compacts, thermocouple bundles, flux monitors and encapsulated specimen cavities and sweep gas feed. Gas returns through the gap between the graphite and the Inconel-718 containment. The HFIR cooling water is in contact with the outer wall of the secondary containment.)

ORNL-DWG 90-17187

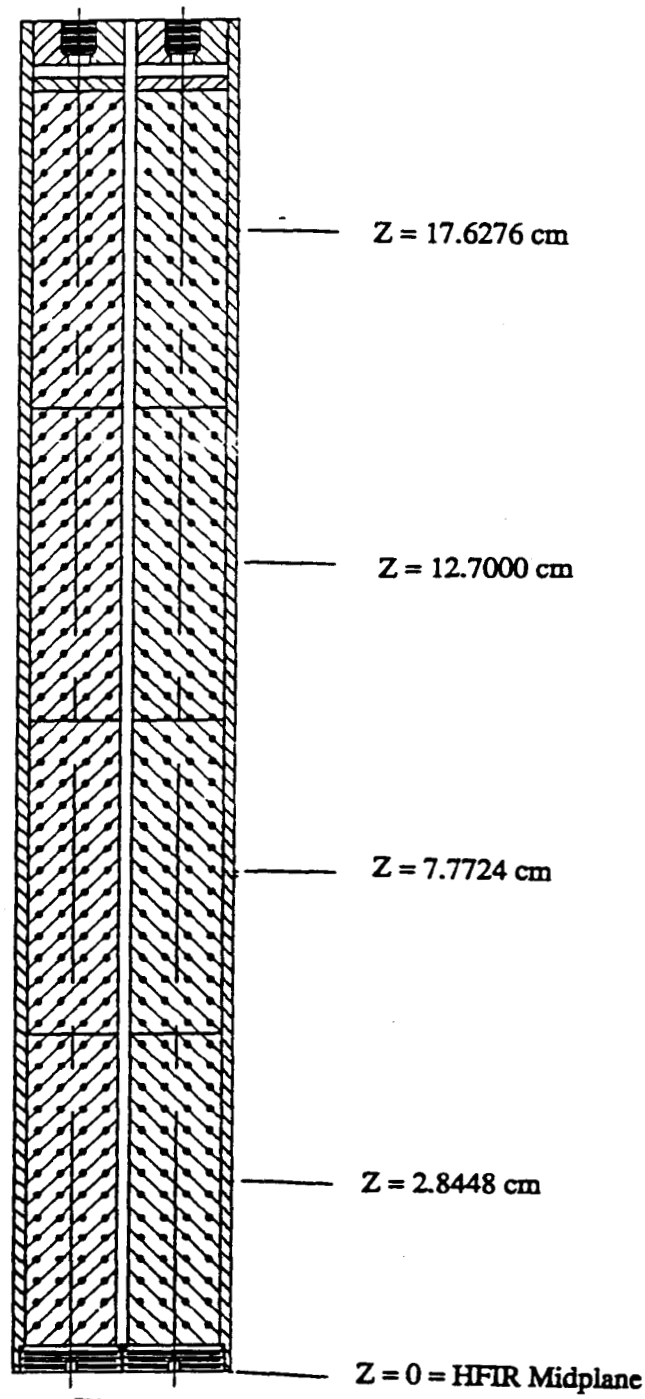

Figure 2.3.2 Longitudinal view of the NPR 1/2 graphite holder

(Shows placement of the fuel compacts. The HFIR midplane defines Z = 0. The two fuel holders are positioned symmetrically about the HFIR midplane.)

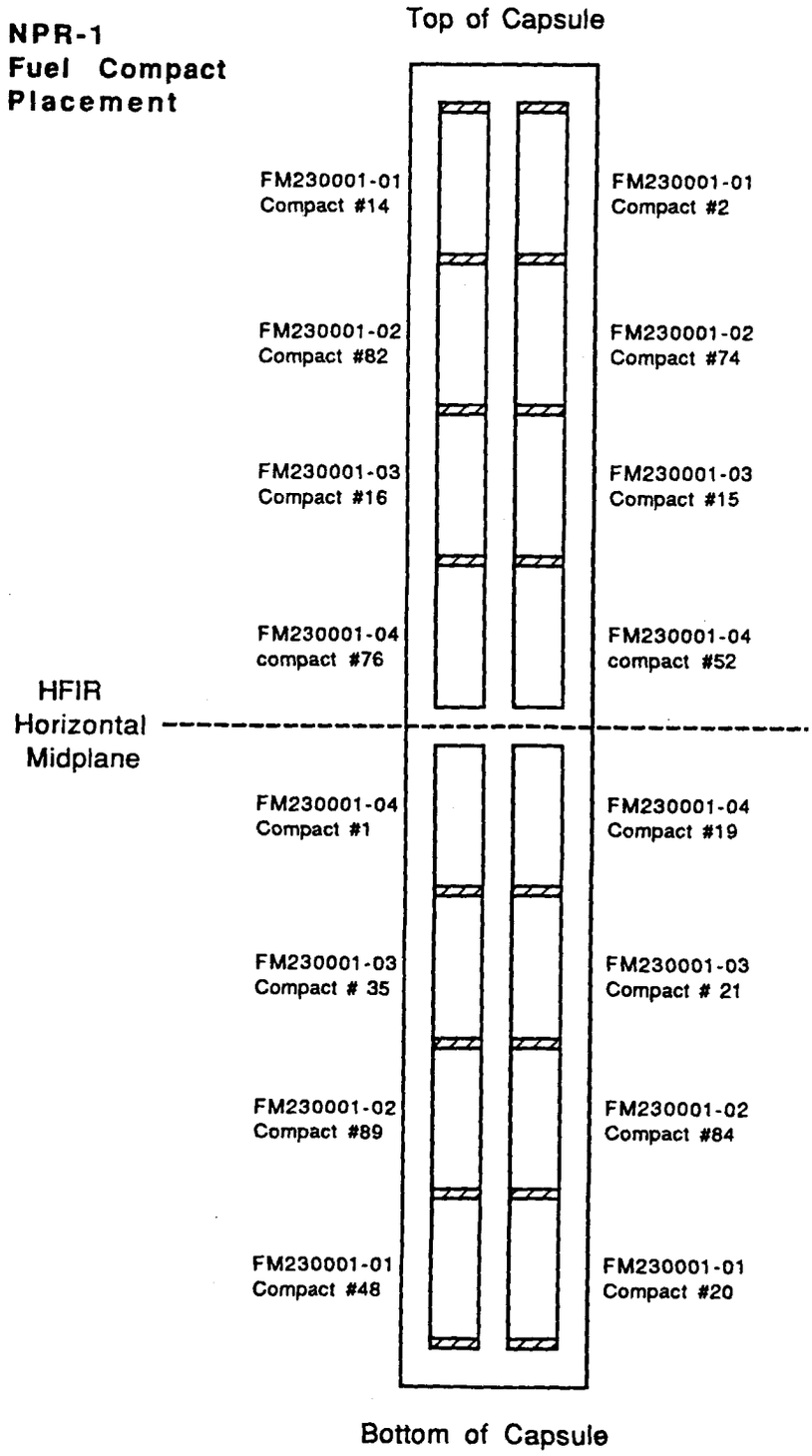

Figure 2.3.3 NPR 1 Fuel compact loading scheme
(compact end cap shown cross hatched)

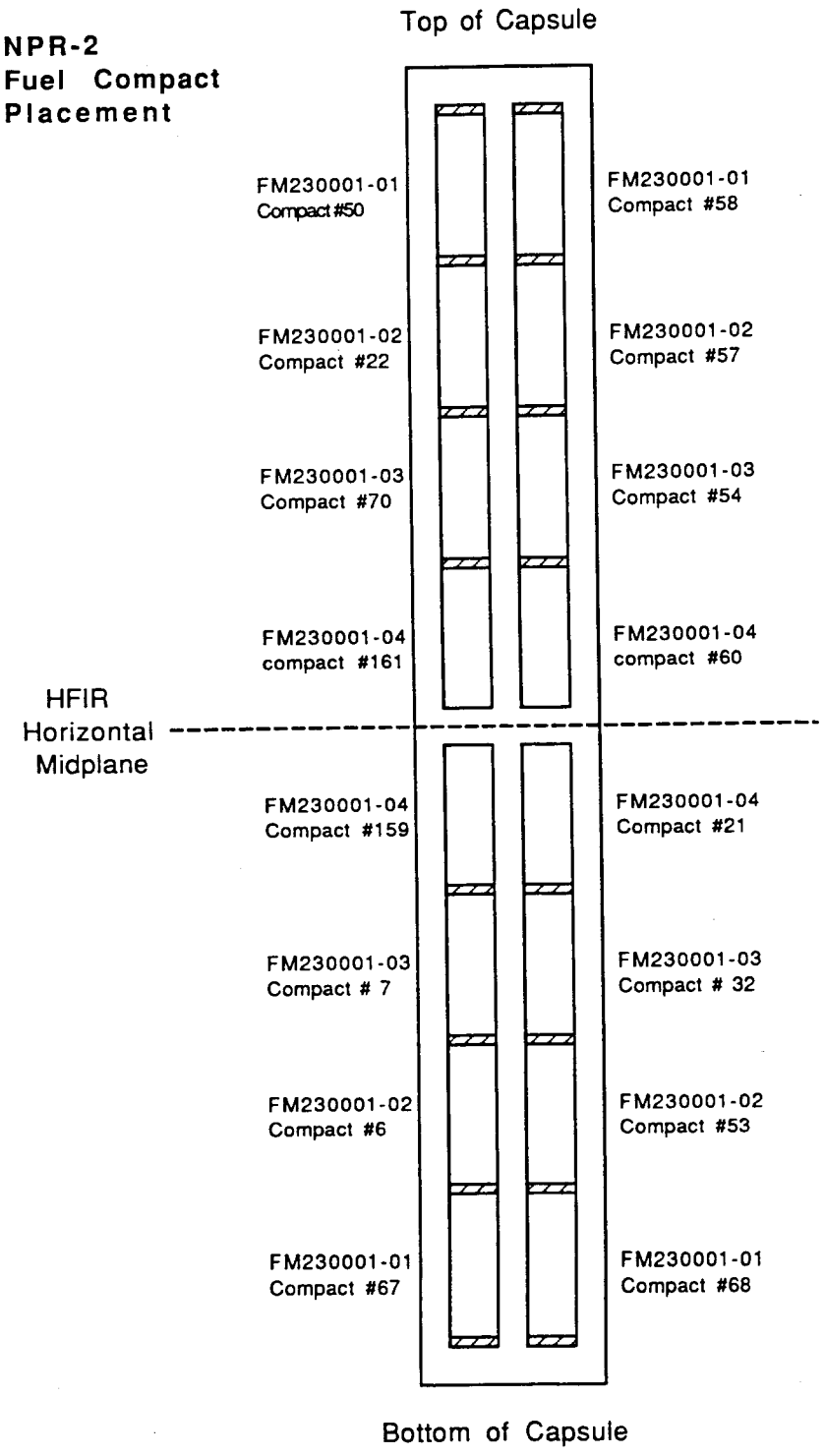

Figure 2.3.4 NPR 2 Fuel compact loading scheme
(compact end cap shown cross hatched)

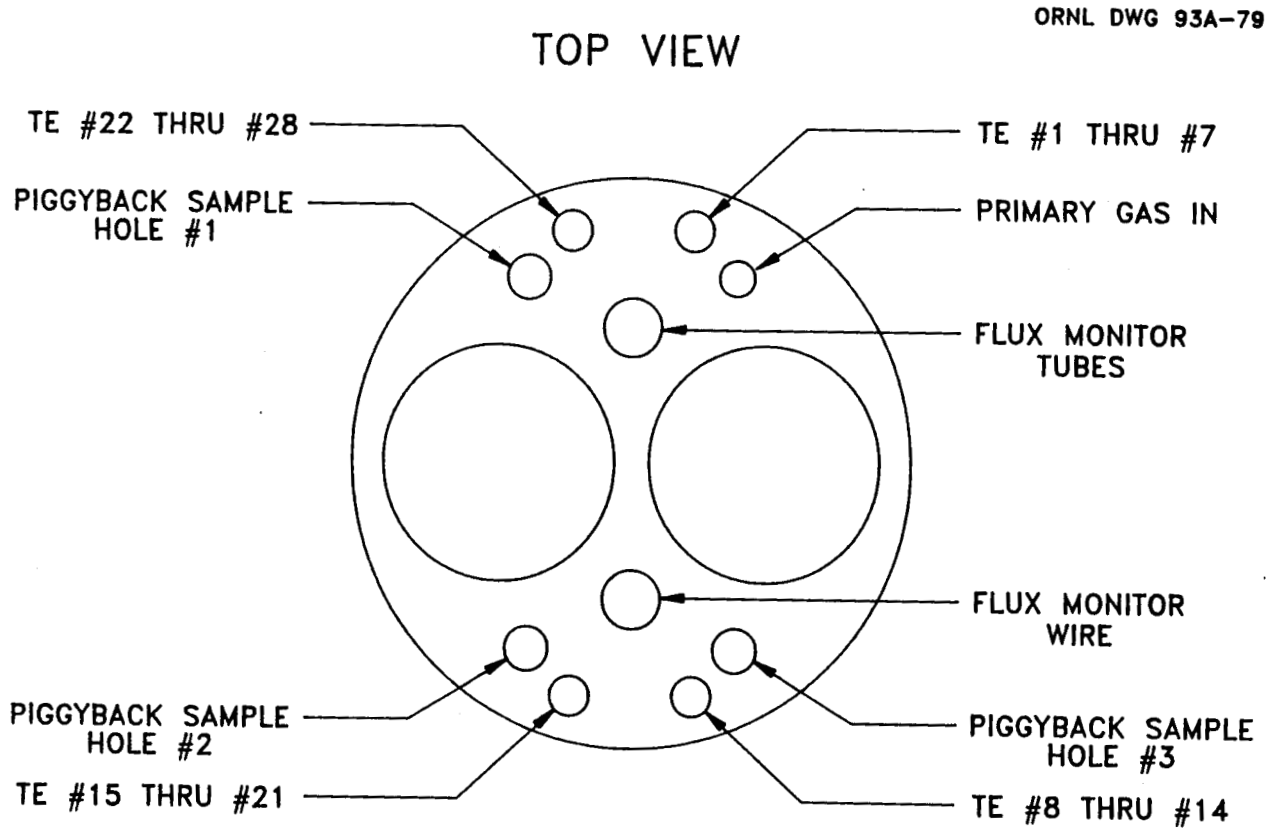

Figure 2.3.5 Radial locations of the thermocouple array tubes, piggyback specimen holes and flux monitor locations

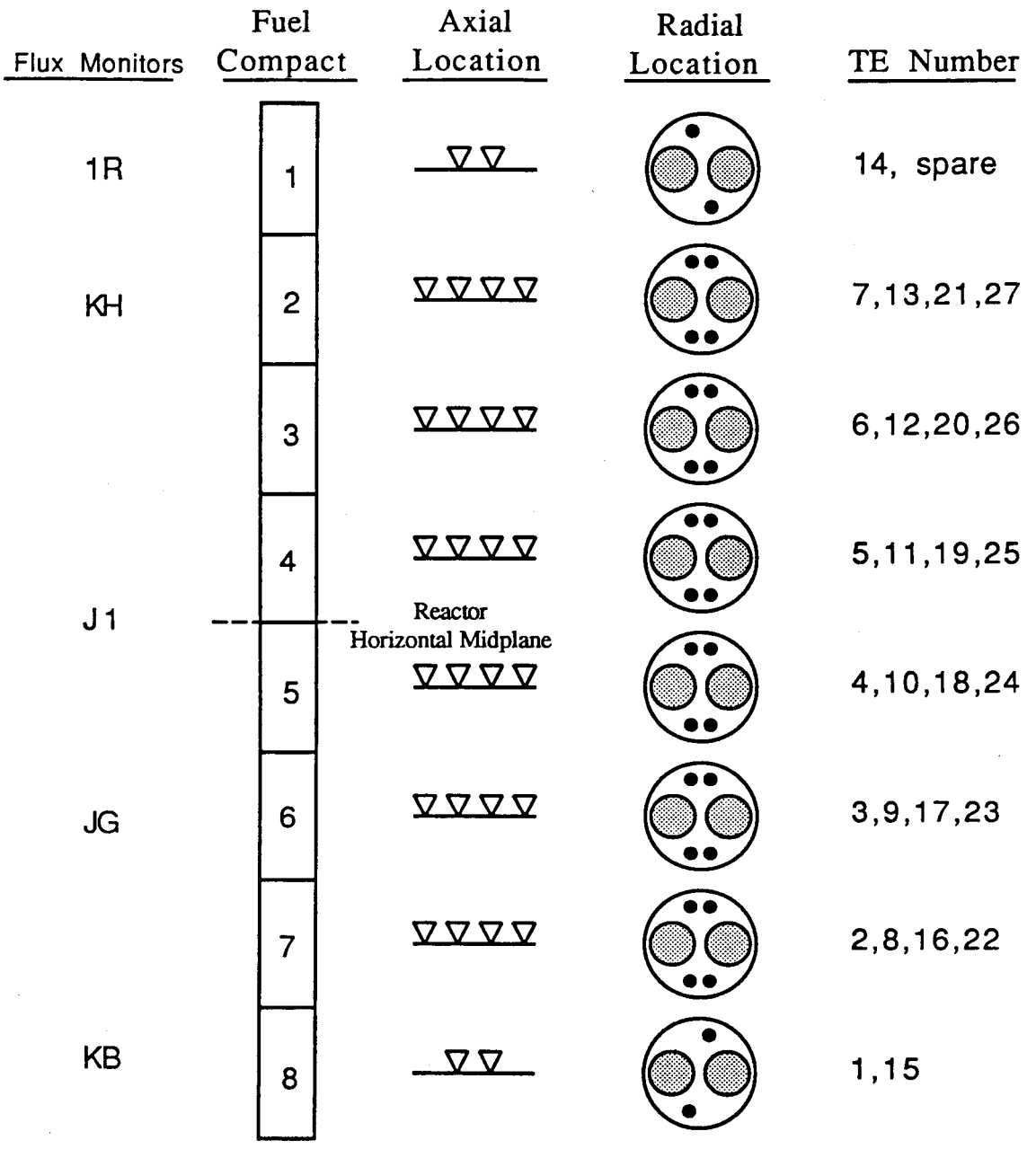

Figure 2.3.6 Axial location of the thermocouple junctions and flux monitors in the NPR 1 graphite fuel holders. All thermocouple junctions were nisil-nicrosil

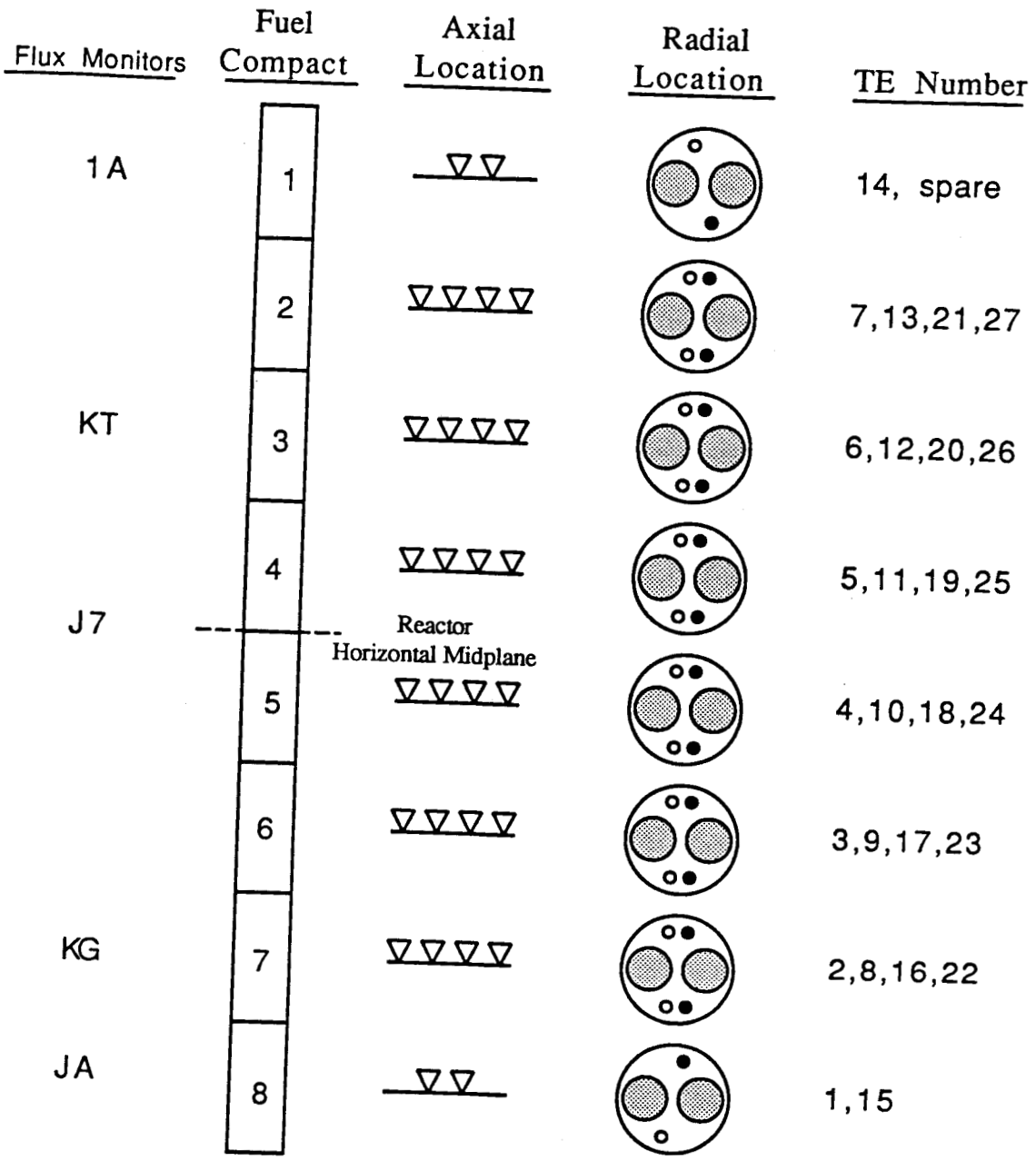

Figure 2.3.7 Axial location of the thermocouple junctions and flux monitors in the NPR 2 graphite fuel holders. Thermocouples 1-14 are nisil-nicrosil junctions (black dots) and thermocouples 15-27 are chromel-alumel junctions (white dots)

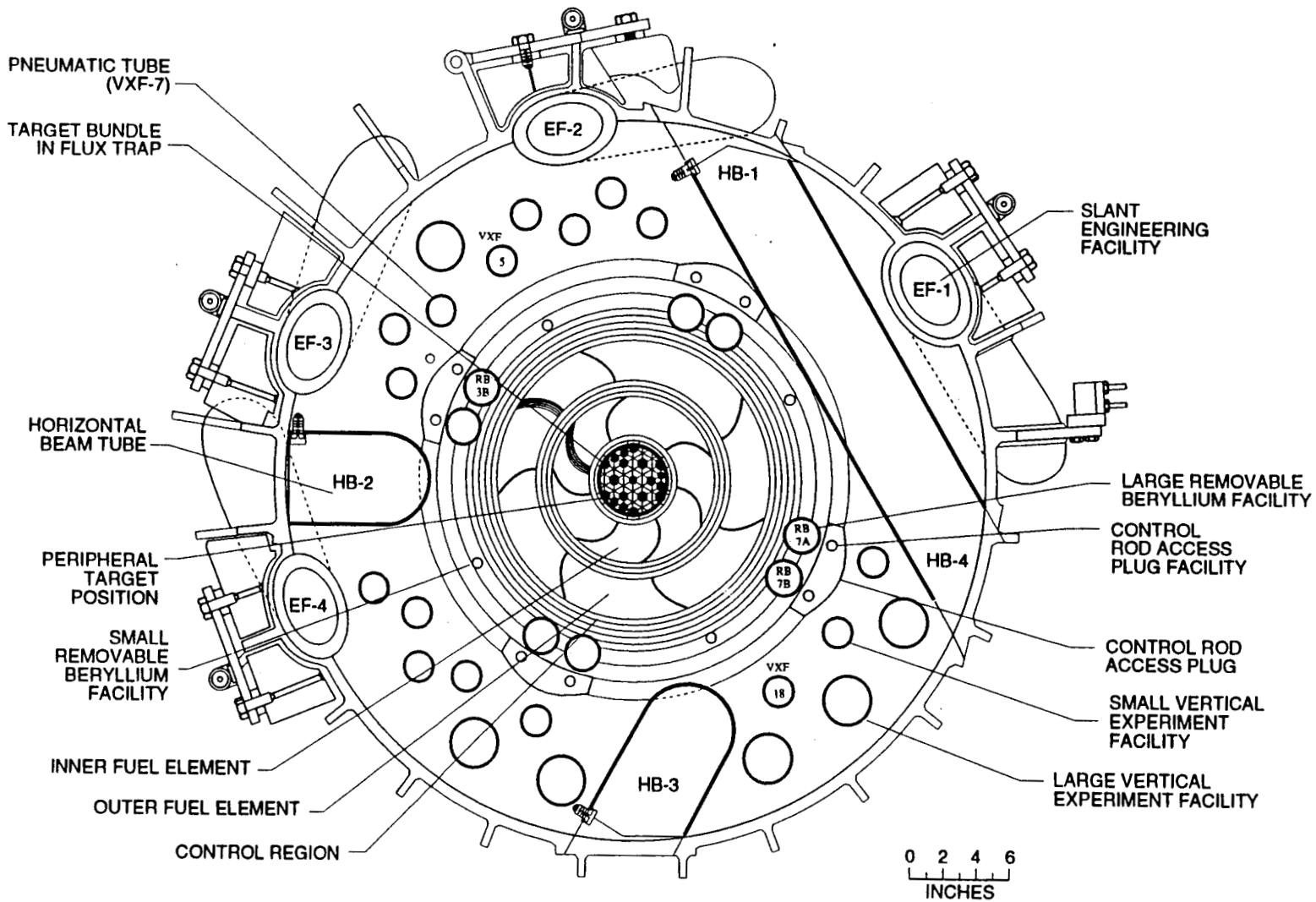

Figure 2.4.1 A cross section of the HFIR core at the horizontal midplane
NPR 1 was irradiated in VXF-5 for 3 cycles, RB-7A for 4 cycles, and RB-7B for one cycle.
NPR 2 was irradiated in VXF-18 for 3 cycles, and RB-3A for 5 cycles

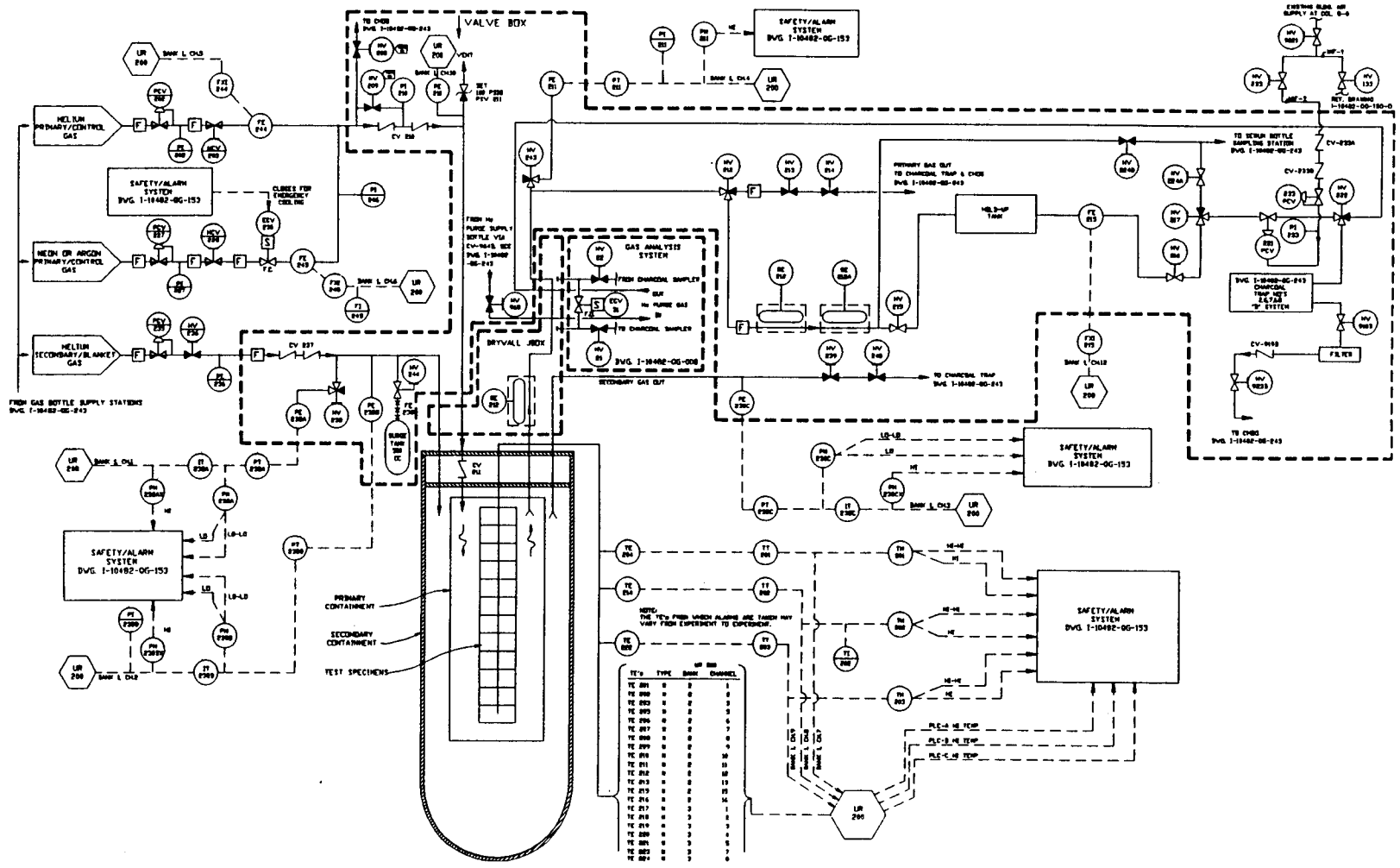

Figure 2.4.2 Schematic instrument application diagram for the facility (MIF-2) used to support the operation of NPR 1 Test

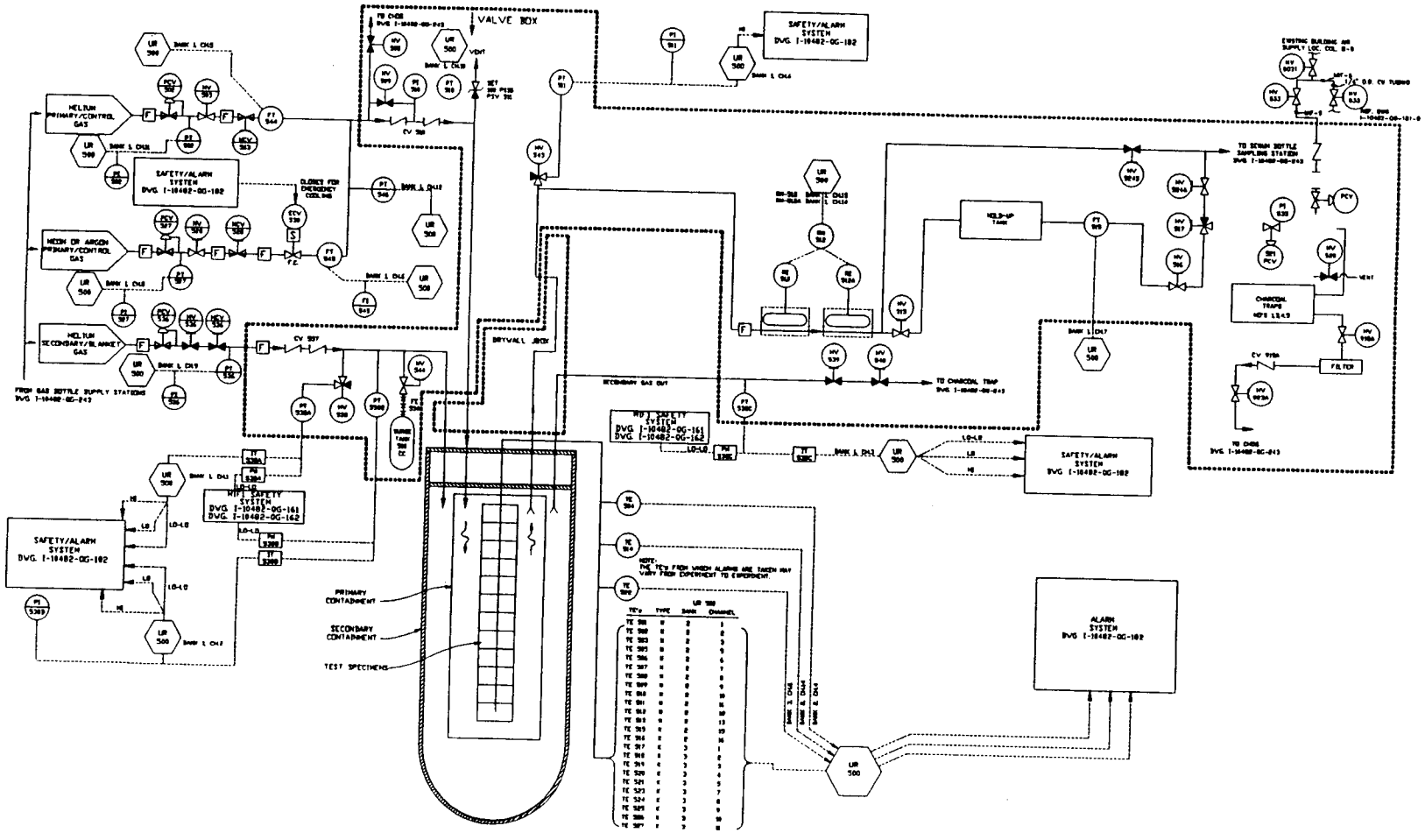

Figure 2.4.3 Schematic instrument application diagram for the facility (MIF-5) used to support the operation of NPR 2 Test

3.0 Capsule Operation and Evaluation

3.1 Operating History

The NPR 1 and NPR 2 capsules were irradiated in the HFIR for a total of eight reactor cycles. The irradiation was started in the permanent beryllium (PB) facility. The capsules were moved to the removable beryllium (RB) facility once the test fuel had achieved sufficient burnup such that the maximum linear fission heat rate in the RB facility did not exceed 65.6 kW/m (20 kW/ft). This requirement was based on the need to maintain the maximum primary wall temperature below 400°C. Consequently, each capsule was irradiated for 3 cycles in a PB facility before being moved to a higher flux RB facility. In the RB facility, the capsules were irradiated for five additional cycles.

Table 3.1.1 contains the NPR 1 HFIR cycle numbers, irradiation facility occupied, irradiation dates, elapsed time, cycle time at full power and total time at full power. Table 3.1.2 presents the same data for the NPR 2 test. The startup time is taken to be the time at which the reactor reaches full power operation [85 MW(t)].

Table 3.1.1. NPR 1 Irradiation Dates, with time elapsed since first HFIR full power exposure, cycle time at full power and total time at full power.

HFIR cycle	Position	date	elapsed time (days)	cycle time at full power (days)	total time at full power (days)
299	VXF-5	07/25/91 22:10	0	0	0
299	VXF-5	08/15/91 08:55	20.448	20.448	20.448
300	VXF-5	08/28/91 11:48	33.568	0	20.448
300	VXF-5	09/17/91 17:44	53.815	20.247	40.695
301	VXF-5	09/27/91 21:18	63.964	0	40.695
301	VXF-5	10/19/91 17:35	85.809	21.845	62.540
302	RB-7A	10/30/91 12:00	96.618	0	62.540
302	RB-7A	11/21/91 02:18	118.214	21.596	84.316

Table 3.1.1 (continued)

303	RB-7A	12/01/91 12:00	128.618	0	84.136
303	RB-7A	12/22/91 21:40	150.021	21.403	105.539
304	RB-7A	12/31/91 15:20	158.757	0	105.539
304	RB-7A	01/16/92 00:08	174.124	15.367	120.906
304	RB-7A	01/18/92 16:35	176.809	15.367	120.906
304	RB-7A	01/24/92 18:45	182.899	21.457	126.996
305	poolside	01/30/92 22:42	-	0	126.996
305	poolside	02/06/92 13:34	-	6.619	-
305	poolside	02/06/92 13:57	-	6.619	-
305	poolside	02/16/92 11:35	-	16.521	-
305	poolside	02/21/92 20:30	-	16.521	-
305	poolside	02/27/92 08:28	-	22.019	126.996
306	RB-7A	03/31/92 13:22	249.675	0	126.996
306	RB-7A	04/11/92 21:01	260.952	11.277	138.273
306	RB-7A	04/14/92 11:55	263.573	11.277	138.273
306	RB-7A	04/19/92 08:40	268.438	16.142	143.138
306	RB-7A	04/21/92 24:00	271.076	16.142	143.138
306	RB-7A	04/27/92 12:34	276.600	21.666	148.662
307	RB-7B	05/01/92 23:16	281.046	0	148.662
307	RB-7B	05/15/92 19:15	294.878	13.832	162.494
307	RB-7B	05/18/92 16:15	297.753	13.832	162.494
307	RB-7B	05/21/92 23:23	301.051	17.130	165.792
307	RB-7B	05/24/92 16:52	303.779	17.130	165.792
307	RB-7B	05/29/92 04:45	308.274	21.625	170.287

Table 3.1.2. NPR 2 Irradiation Dates, with time elapsed since first HFIR full power exposure, cycle time at full power and total time at full power.

HFIR cycle	Position	date	elapsed time (days)	cycle time at full power (days)	total time at full power (days)
300	VXF-18	08/28/92 11:48	0	0	0
300	VXF-18	09/17/91 17:44	20.247	20.247	20.247
301	VXF-18	09/27/91 21:18	30.396	0	20.247
301	VXF-18	10/19/91 17:35	52.241	21.845	42.092
302	VXF-18	10/30/91 12:00	63.050	0	42.092
302	VXF-18	11/21/92 02:18	84.646	21.596	63.688
303	RB-3B	12/01/91 12:00	95.050	0	63.688
303	RB-3B	12/22/92 21:40	116.453	21.403	85.091
304	RB-3B	12/31/91 15:20	125.189	0	85.091
304	RB-3B	01/16/92 00:08	140.556	15.367	100.458
304	RB-3B	01/18/92 16:35	143.241	15.367	100.458
304	RB-3B	01/24/92 18:45	149.331	21.457	106.548
305	RB-3B	01/30/92 22:42	155.496	0	106.548
305	RB-3B	02/06/92 13:34	162.115	6.619	113.167
305	RB-3B	02/06/92 13:57	162.131	6.619	113.167
305	RB-3B	02/16/92 11:35	172.033	16.521	123.069
305	RB-3B	02/21/92 20:30	177.404	16.521	123.069
305	RB-3B	02/27/92 8:28	182.903	20.019	128.567
306	RB-3B	03/31/92 13:22	216.107	0	128.567
306	RB-3B	04/11/92 21:01	227.384	11.277	139.844
306	RB-3B	04/14/92 11:55	230.005	11.277	139.844
306	RB-3B	04/19/92 08:40	234.869	16.142	144.709
306	RB-3B	04/21/92 24:00	237.508	16.142	144.709
306	RB-3B	04/27/92 12:34	243.032	21.666	150.233
307	RB-3B	05/01/92 23:16	247.478	0	150.233

Table 3.1.2 (continued)

HFIR Cycle	Position	Date	Elapsed time (days)	Cycle time at full power (days)	Total time at full power (days)
307	RB-3B	05/15/92 19:15	261.310	13.833	164.065
307	RB-3B	05/18/92 16:15	264.185	13.833	164.065
307	RB-3B	05/21/92 23:23	267.483	17.130	167.363
307	RB-3B	05/24/92 16:52	270.211	17.130	167.363
307	RB-3B	05/29/92 04:45	274.706	21.625	171.858

A detailed description of the operation of the capsules and the thermal analysis methodology can be found in Ref. 3.1.1.

3.1.1 Operating Temperatures

The NPR capsules did not have thermocouples in direct contact with the fuel compacts. Thermocouples were installed at positions corresponding to the axial midplane of each fuel compact in the graphite fuel body. The temperature of the fuel compacts was calculated or predicted based on measurements of the graphite fuel body temperatures and properties of the graphite and fuel compacts.

The calculated fuel temperatures are a function of several variables, including the measured graphite body temperature, the thermal conductivities of the graphite body and the fuel compact, the gas gap between the fuel compact and the graphite body, and the gas composition in the gap between the Inconel primary containment and the graphite fuel body. Irradiation, i.e., fast neutron damage, causes shrinkage of both graphite body and the fuel compact. The fast neutron damage is a function of time. The calculations to obtain an estimate of the fuel compact average temperature takes into account the time variations of these variables. The fundamental materials property data was obtained from the fuel and graphite design data manuals (Refs. 3.1.2, 3.1.3). The method used in the analysis to predict the operating temperature history of the fuel compacts is as follows.

The thermal analysis was performed using a three dimensional thermal analysis code HEATING 7.0. This computer code can be used to compute the temperature profiles in the fuel and the graphite body for a given time point during the irradiation. It is not capable of following time dependent variables, such as thermal conductivity, fuel-compact gaps, etc., throughout the irradiation phase. It was used to compute the temperature field in the fuel compacts and the graphite fuel body for a given set of parameters. These parameters are:

Pv - the power generation rate in the compact,

K_g - the thermal conductivity of graphite,

K_f - the thermal conductivity of the fuel,

f_g - radial gas gap between the fuel and the graphite,

g_inc - radial gap between the primary containment and the graphite fuel body

and

%He - percentage of helium in the sweep gas (in the gas gaps)

During the irradiation, all of these parameters change as a function of time due to fuel burnup, irradiation induced thermal conductivity change and irradiation induced dimensional change of the graphite fuel body and the fuel compacts. The irradiation induced dimensional change is caused by fast neutron damage. Even the thermal conductivities of the fuel compacts and the graphite fuel bodies are functions of the fast fluence and temperature. A new simplified computer code named NPR1AVEx.f, where x denotes a pair of compacts in a given axial location in the irradiation capsule, was used to account for the time dependent variables. The collection of eight programs, NPR1AVE1.f, - NPR1AVE8.f are referred to as MAPPING, because they map the average thermocouple temperature to the volume average fuel temperature. The MAPPING code was extensively used to compute the time history of the fuel compact temperatures predicted in this report.

The actual values of flux and fast fluence were not available for performing detailed thermal analysis. Hence an estimate of the fast fluence as a function time was used. Recall that the two graphite fuel bodies containing the fuel compacts were positioned symmetrically about the HFIR midplane, with compacts 1A, 1B, 8A and 8B having the same fuel loading and located the same distance from the HFIR midplane. These compacts undergo irradiation

under identical conditions and make up region 1. Similarly, compacts 2A, 2B, 7A and 7B make up region 2, compacts 3A, 3B, 6A and 6B make up region 3 etc. This nomenclature will be adhered to throughout this section. Keep in mind that compacts in a given zone have the same fuel loading and are assumed to experience the same fast flux owing to assumed flux symmetry about the HFIR midplane.

The fast neutron flux used in the calculation of material properties is given by the expression

$$Flux(z) = \alpha \sum_{i=1}^{5} a_i z^i \qquad (1)$$

where

$a_0 = 1.551390 \times 10^{18}$

$a_1 = 0.357201 \times 10^{18}$

$a_2 = 3.22098 \times 10^{16}$

$a_3 = -4.89680 \times 10^{15}$

$a_4 = 1.06604 \times 10^{14}$

$a_5 = 6.60525 \times 10^{11}$.

z is the distance in inches from the top of the 55.88 cm long core

α = 0.85*0.93 for RB position

and α = 0.85*0.93*0.507/4.98 for PB position

The coefficients, a_i, were developed to describe the fast flux for the old HFIR operating power of 100 MW. The 0.85 is an approximation to adjust for the current operating level of 85 MW.

To follow the changing environment during the irradiation, a set of HEATING 7.0 runs were made wherein one of the above parameters was varied over its expected range, while holding all other parameters constant. The fuel compact average temperature predictions from these runs were then used to define a set of scaling equations for each of the parameters. These scaling equations were incorporated into the NPR1AVEx.f code such

that by providing the graphite temperatures as a function of time and the known reactor operating conditions as input, an estimate of the average temperature of the fuel compacts could be computed.

The measured thermocouple temperatures (graphite body) as a function of time are shown in Fig 3.1.1a for the NPR 1 capsule and Fig. 3.1.1b for the NPR 2 capsule. These are the averages for the thermocouples at each compact position.

The fuel compact operating temperatures (volume average and local maximum) computed by the mapping code are shown in figures 3.1.2 through 3.1.5. The plots show the temperatures as a function of a) elapsed time (Fig 3.1.2), b) effective full power days of operation of the HFIR (Fig. 3.1.3), c) fast neutron fluence (Fig 3.1.4), and d) burnup (Fig. 3.1.5). Each of these plots display a different feature of the irradiation. For example, Figure 3.1.4 and Figure 3.1.5 show that the compacts undergo greater than 60% of the burnup prior to accumulating significant fraction of fast fluence. Figure 3.1.6 shows fuel burnup as function of fast neutron fluence. The fast fluence was calculated using equation 1. The burnup (FIMA) was calculated using the CACA-2 computer program (Ref. 3.2.5).

The average fuel particle power for each region can be estimated by dividing the total power per compact by the number of particles in the compact. Fig 3.1-7 is a plot of average power per particle as a function of fast neutron fluence for each region. Figure 3.1-8 shows the average fuel particle power as a function of average particle burnup.

Tables 3.1.3 and 3.1.4 present the time integrated fuel temperature for each HFIR cycle.

Table 3.1.3 NPR 1 capsule time integrated average fuel temperatures

Cycles	Compact 1	Compact 2	Compact 3	Compact 4	Compact 5	Compact 6	Compact 7	Compact 8	Average
1	913	1104	1109	1086	1099	1110	1102	892	1052
2	919	1100	1086	1050	1055	1081	1088	904	1035
3	927	1100	1072	1028	1028	1061	1083	917	1027
4	844	1052	1047	1021	1027	1022	1023	832	984
5	885	1086	1060	1009	1002	1004	1011	861	990
6	869	1029	1002	945	935	945	952	815	937
7	840	991	977	913	899	915	915	809	907
8	790	936	934	892	852	870	854	735	858
Average	874	1050	1036	993	987	1001	1003	845	974

Table 3.1.4 NPR 2 capsule time integrated average fuel temperatures

Cycles	Compact 1	Compact 2	Compact 3	Compact 4	Compact 5	Compact 6	Compact 7	Compact 8	Average
1	835	932	916	891	905	896	904	787	883
2	771	846	814	798	795	799	821	737	798
3	757	815	775	752	747	756	788	718	764
4	787	831	783	754	762	755	769	698	767
5	709	734	685	662	665	665	679	708	688
6	822	841	790	757	757	757	787	823	792
7	736	737	705	699	668	664	690	665	696
8	661	669	651	657	622	609	622	592	635
Average	760	800	765	746	740	738	757	716	753

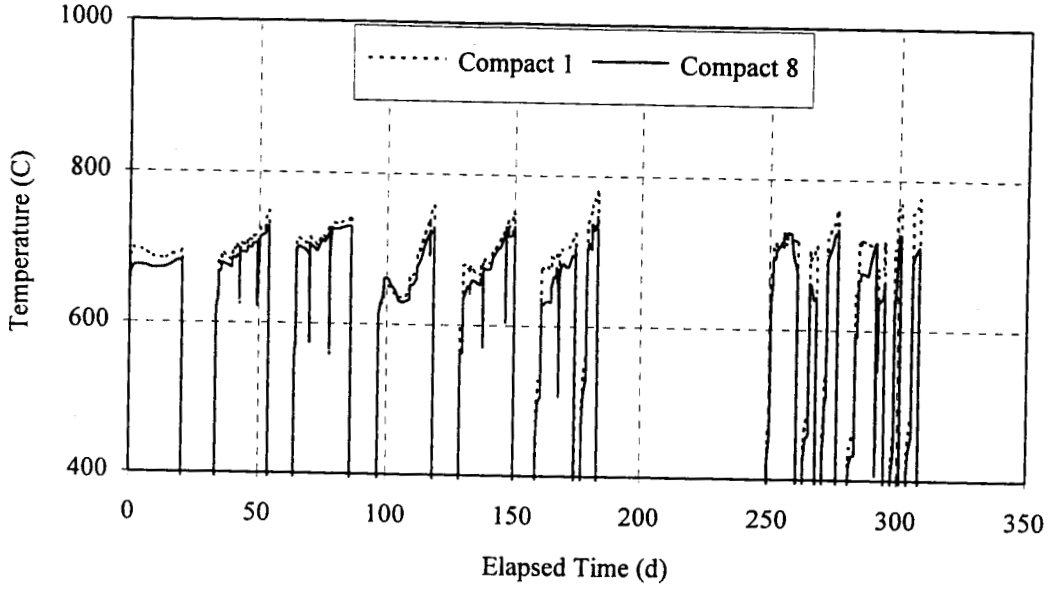

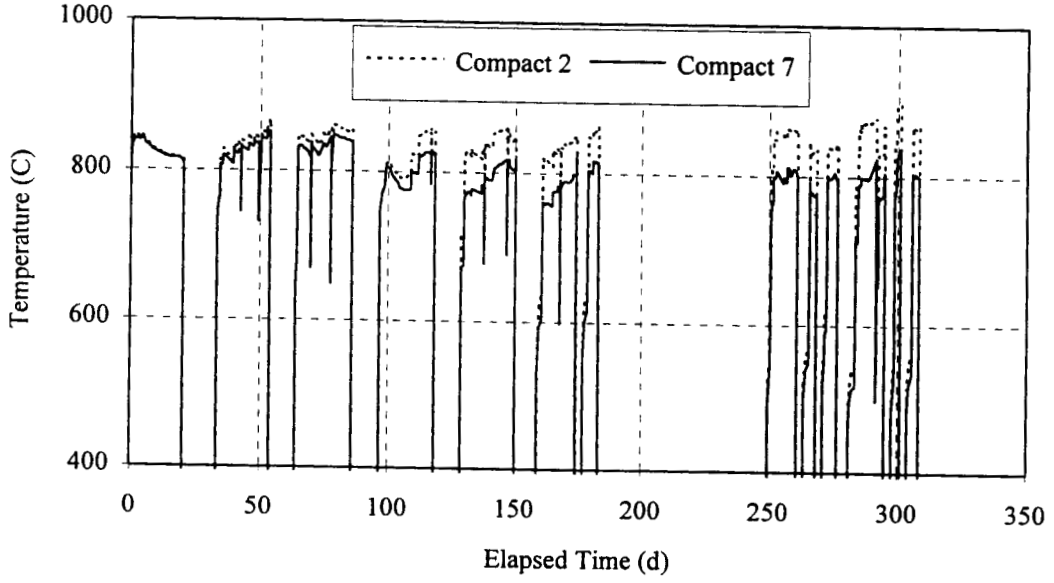

Figure 3.1-1a NPR 1 capsule regions 1 & 2 average of the measured temperatures in the graphite body

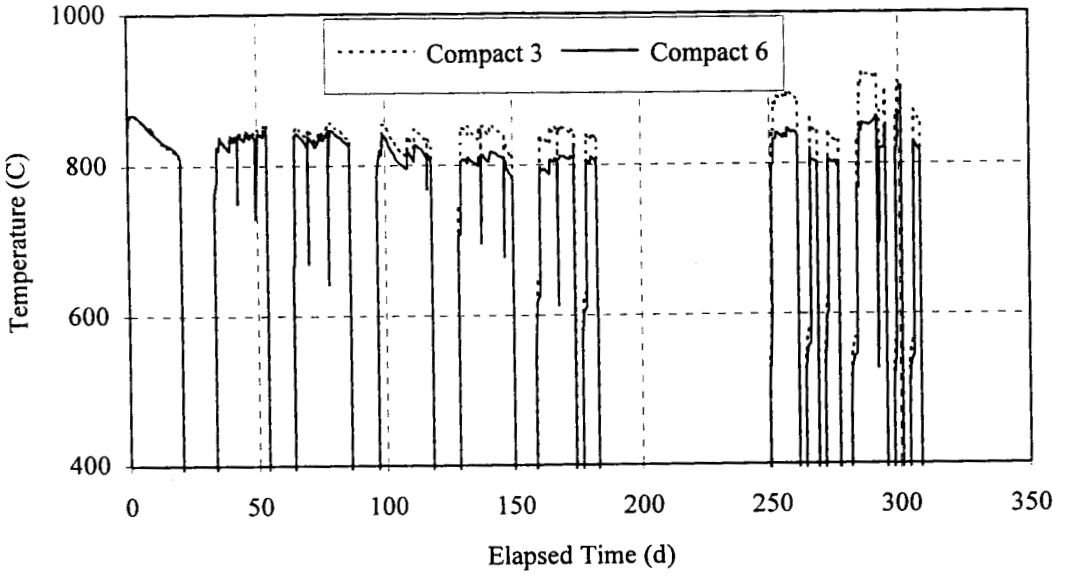

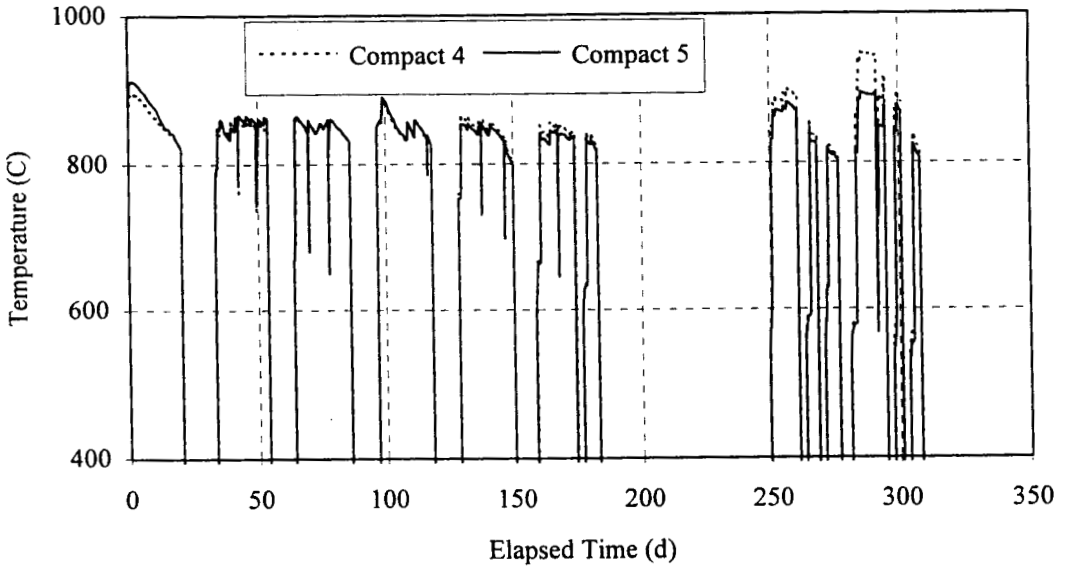

Figure 3.1-1a NPR 1 capsule regions 3 & 4 average of the measured temperatures in the graphite body

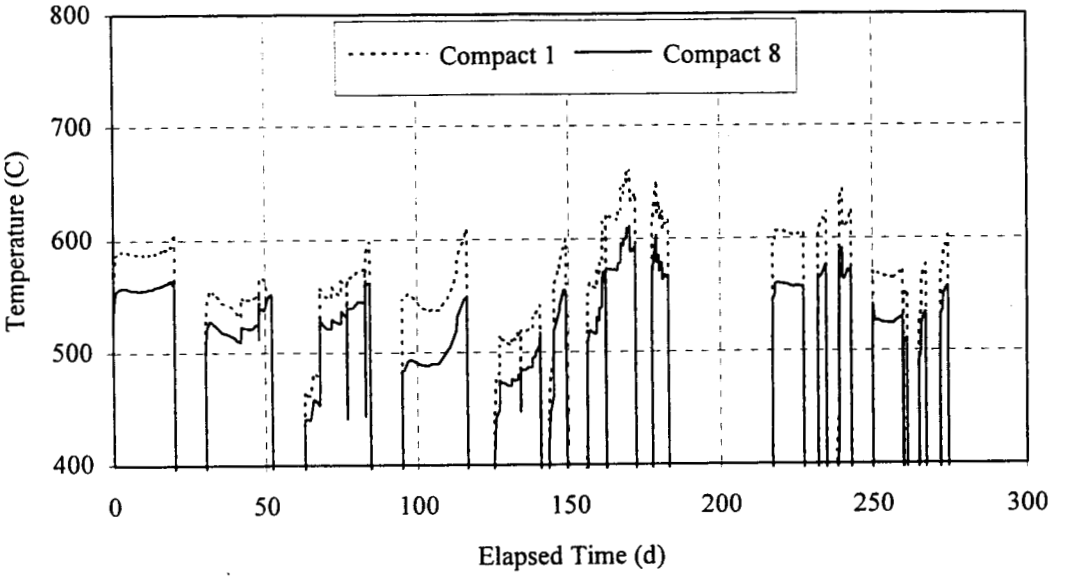

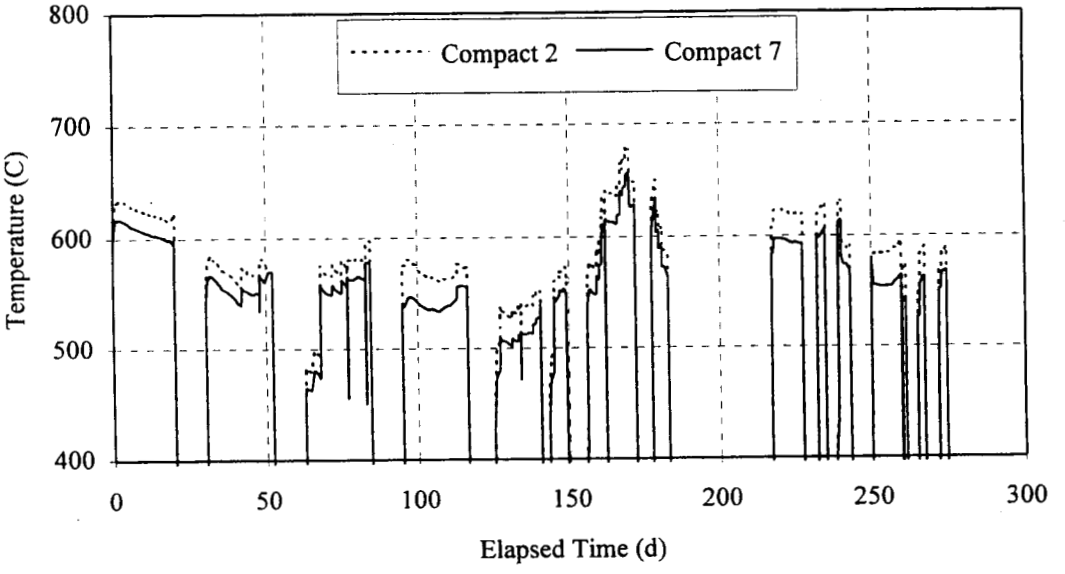

Figure 3.1-1b NPR 2 capsule regions 1 & 2 average of the measured temperatures in the graphite body

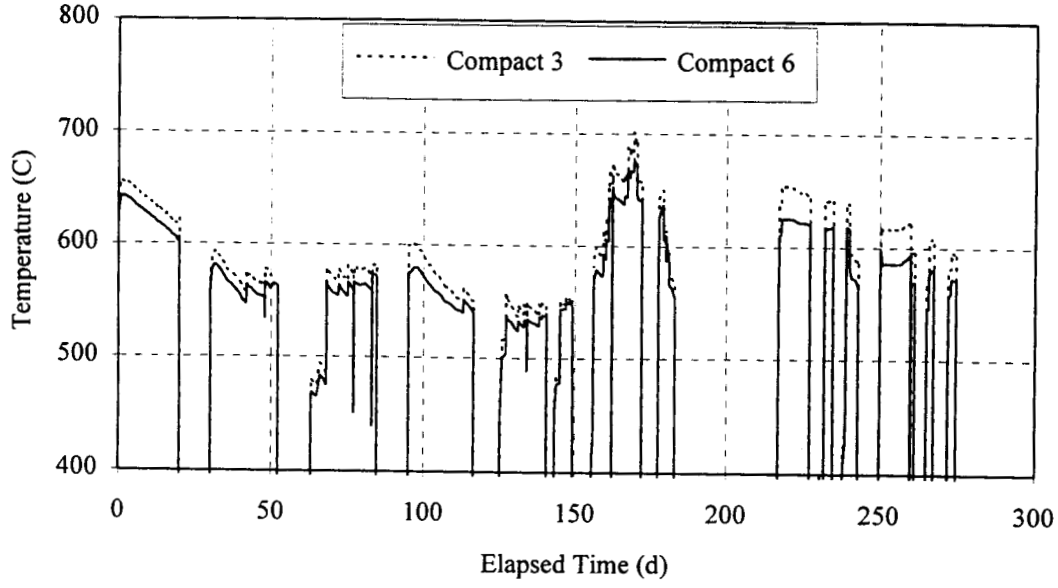

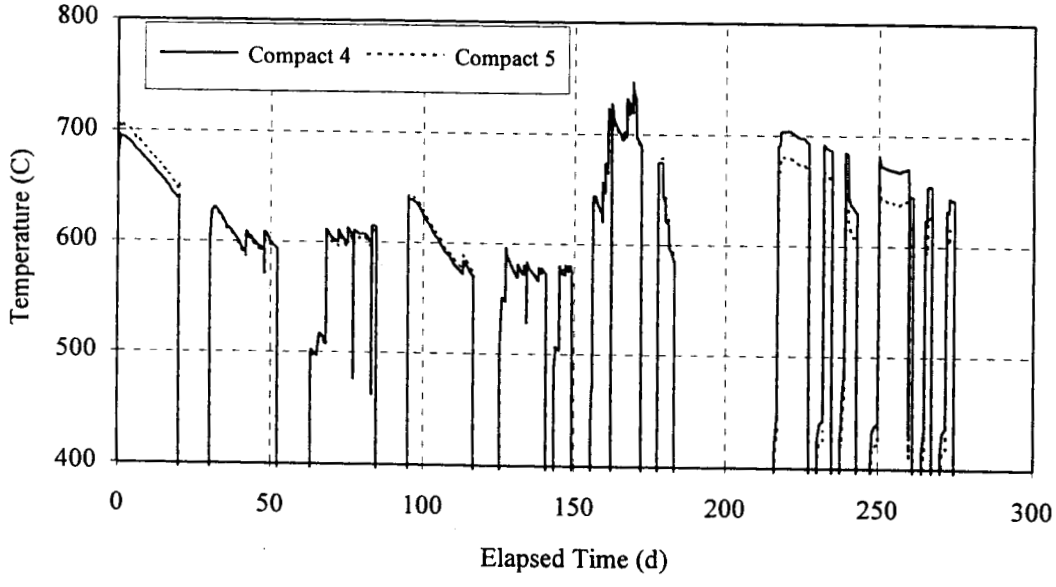

Figure 3.1-1b NPR 2 capsule regions 3 & 4 average of the measured temperatures in the graphite body

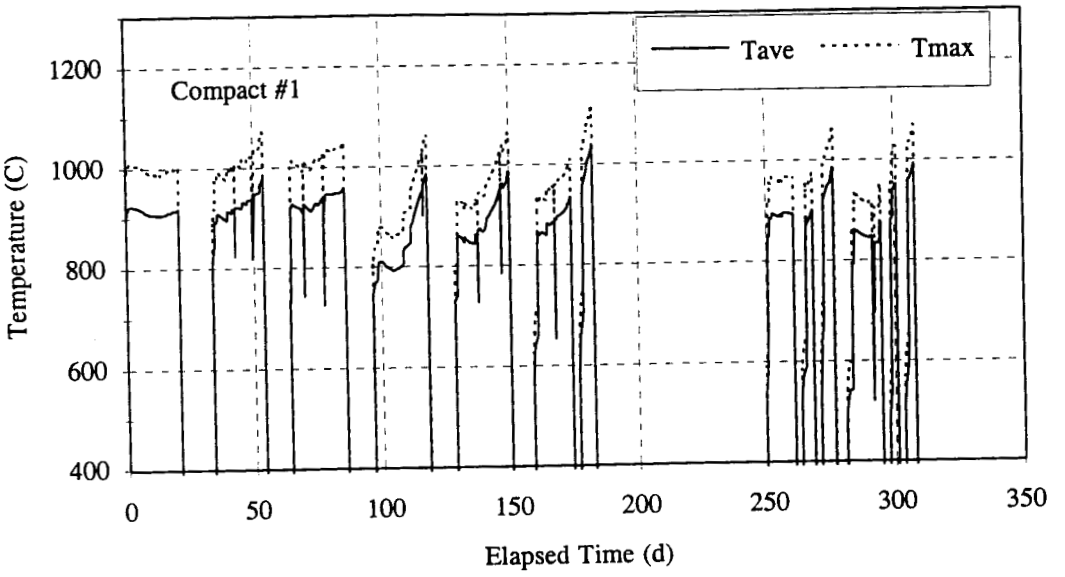

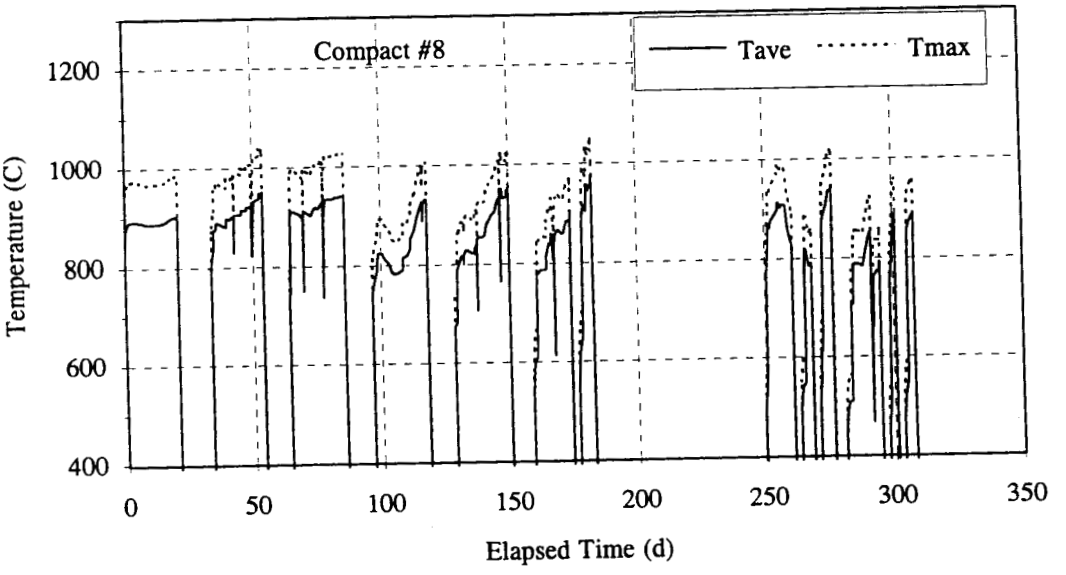

Figure 3.1-2a NPR 1 capsule region 1 volume average fuel temperature and local maximum fuel temperature

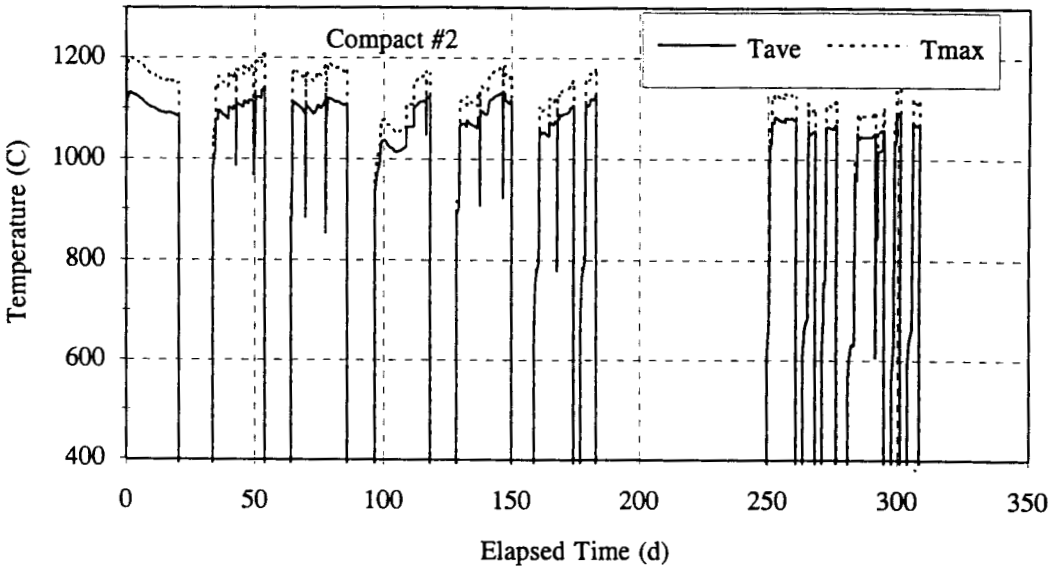

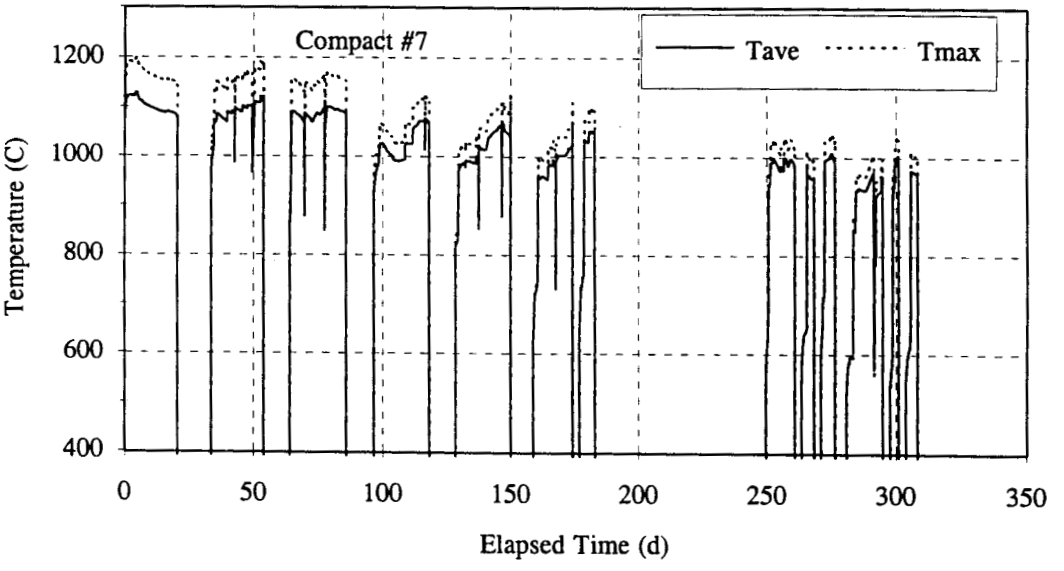

Figure 3.1-2a NPR 1 capsule region 2 volume average fuel temperature and local maximum fuel temperature

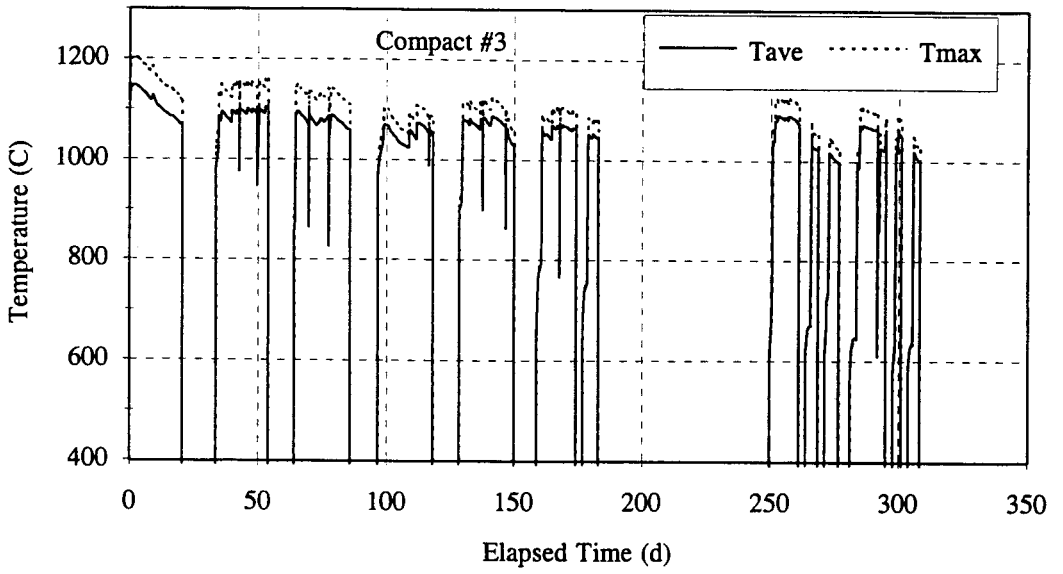

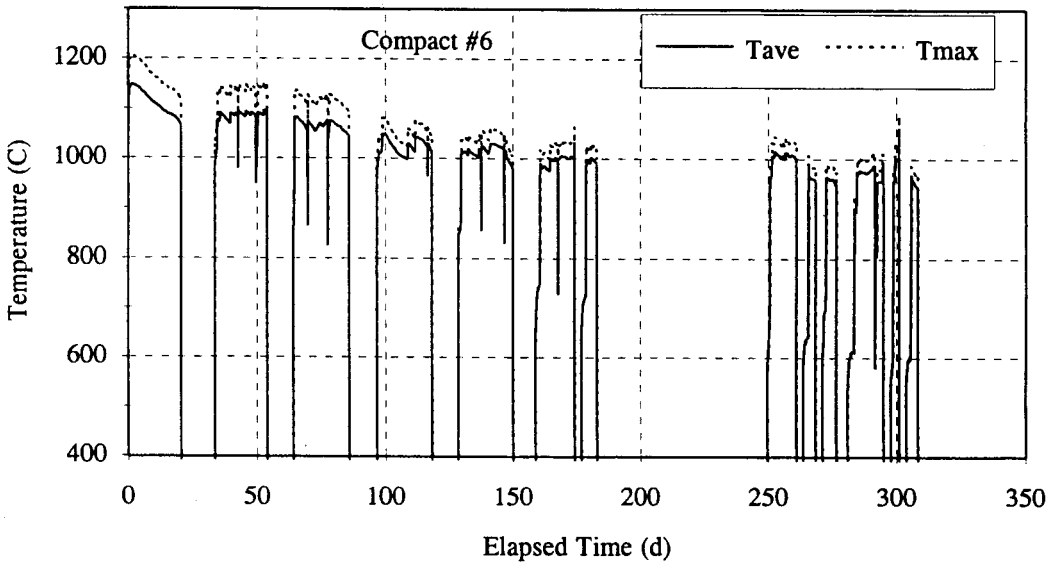

Figure 3.1-2a NPR 1 capsule region 3 volume average fuel temperature and local maximum fuel temperature

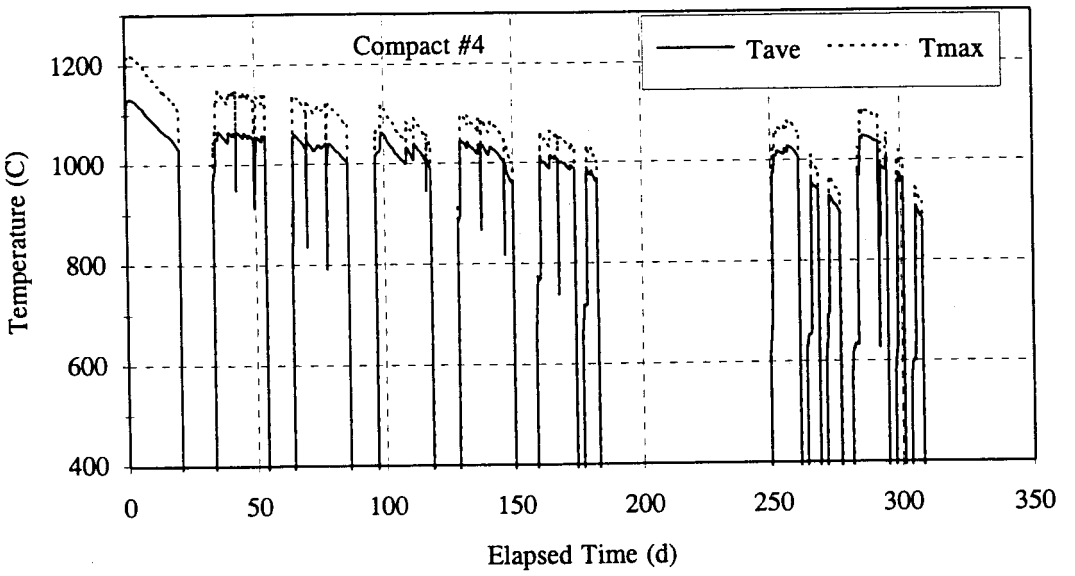

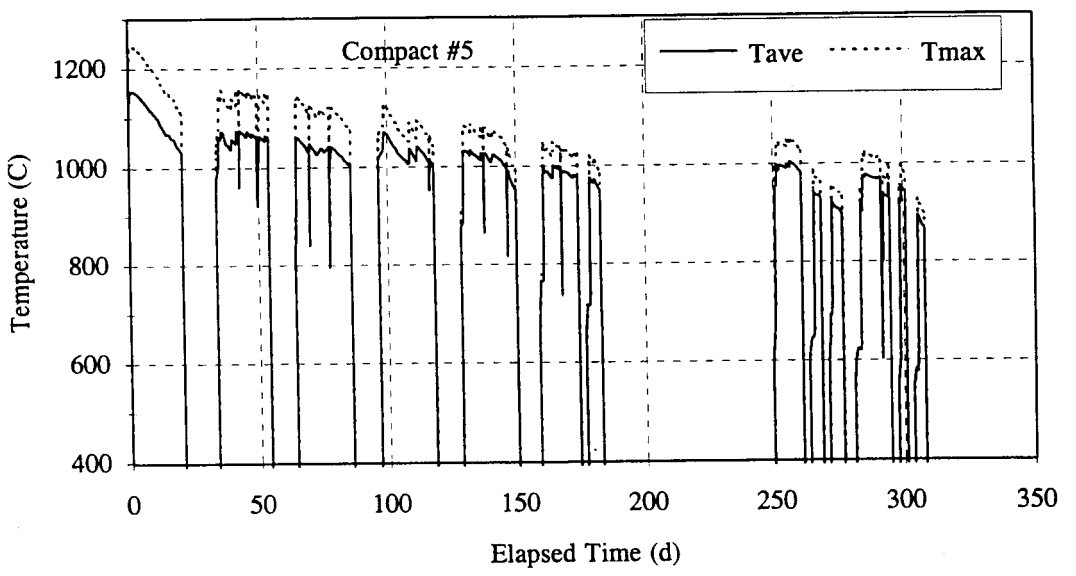

Figure 3.1-2a NPR 1 capsule region 4 volume average fuel temperature and local maximum fuel temperature

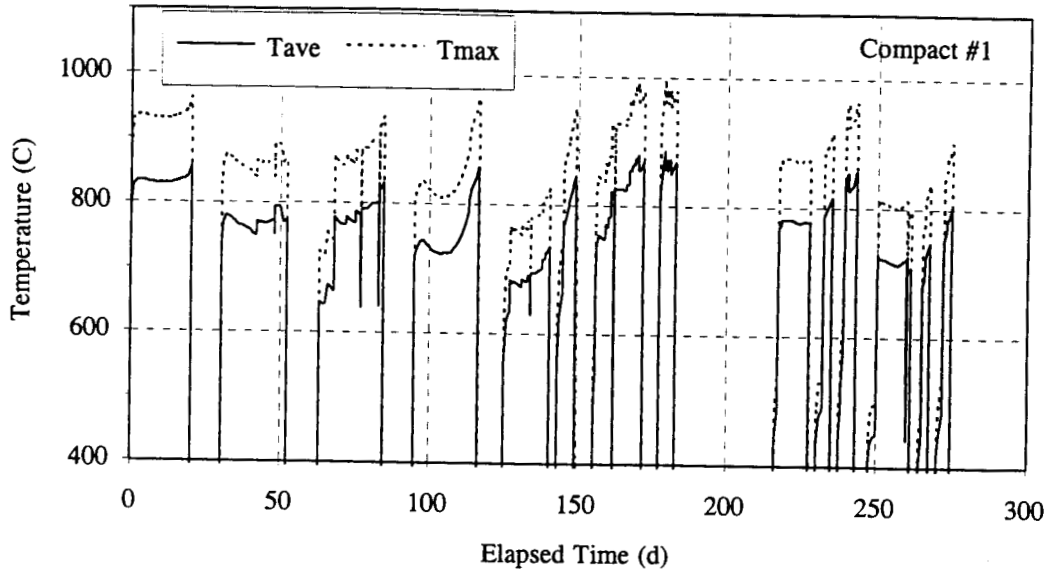

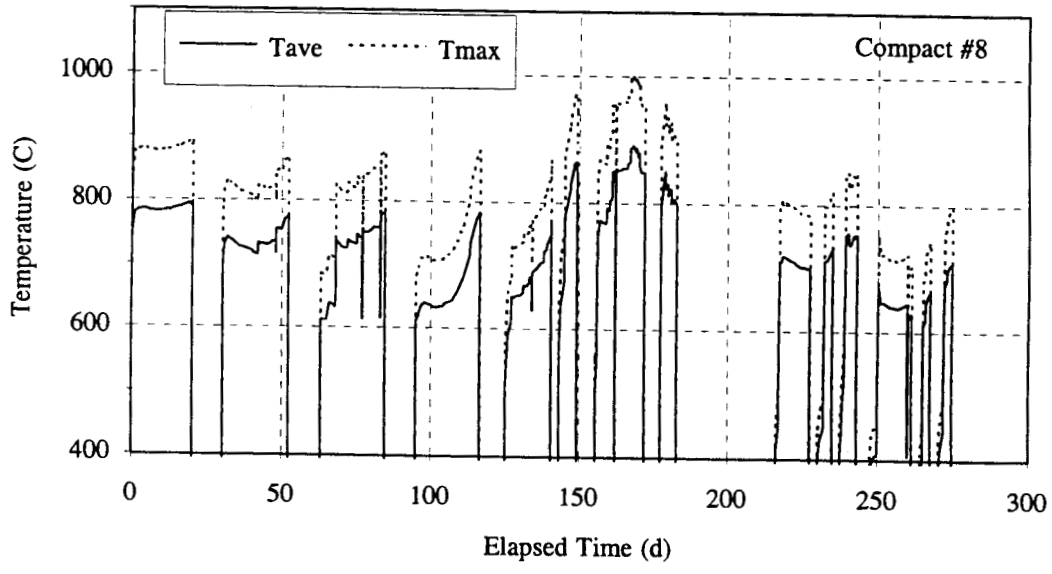

Figure 3.1-2b NPR 2 capsule region 1 volume average fuel temperature and local maximum fuel temperature

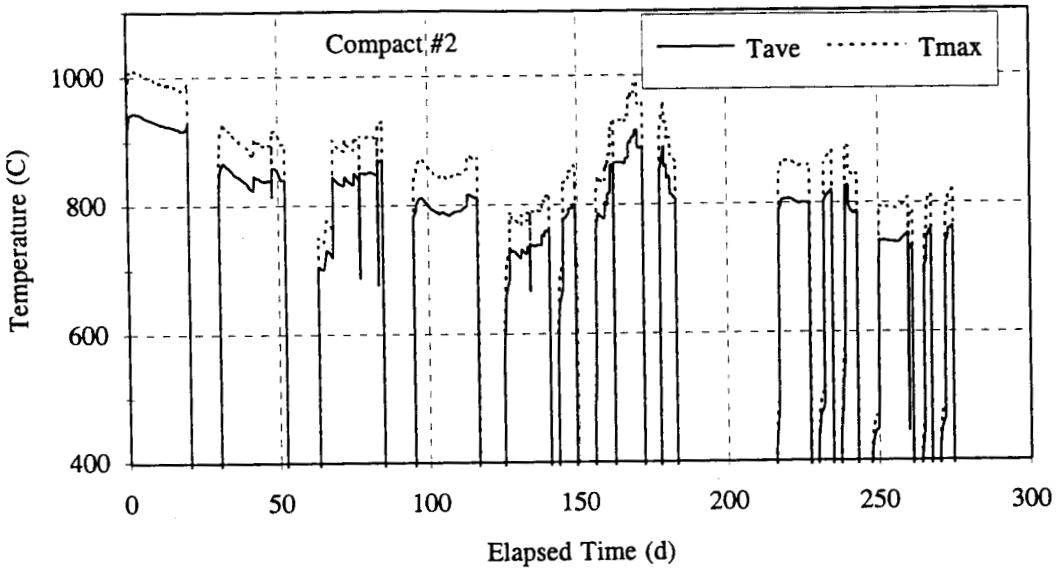

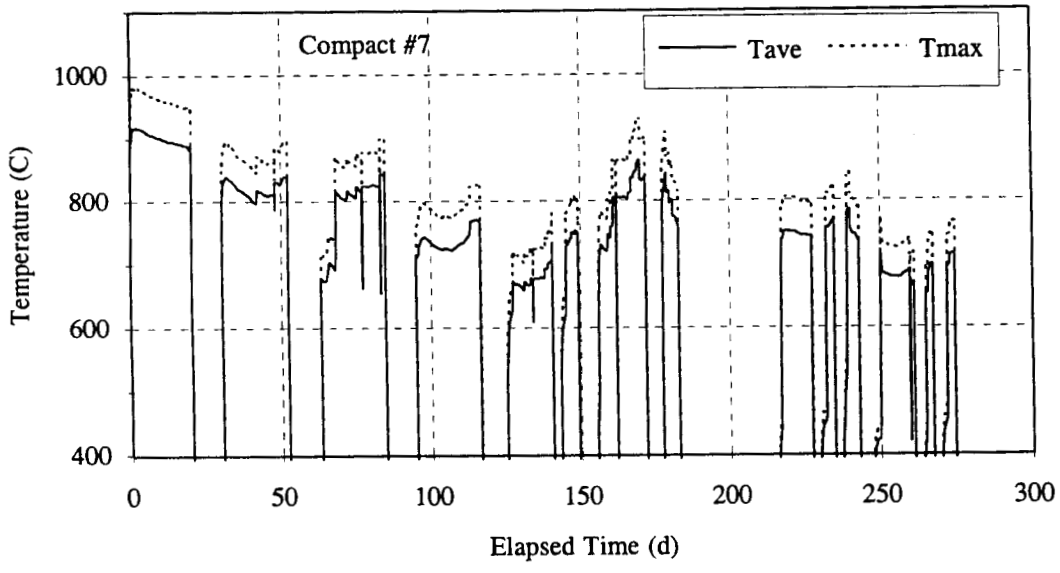

Figure 3.1-2b NPR 2 capsule region 2 volume average fuel temperature and local maximum fuel temperature

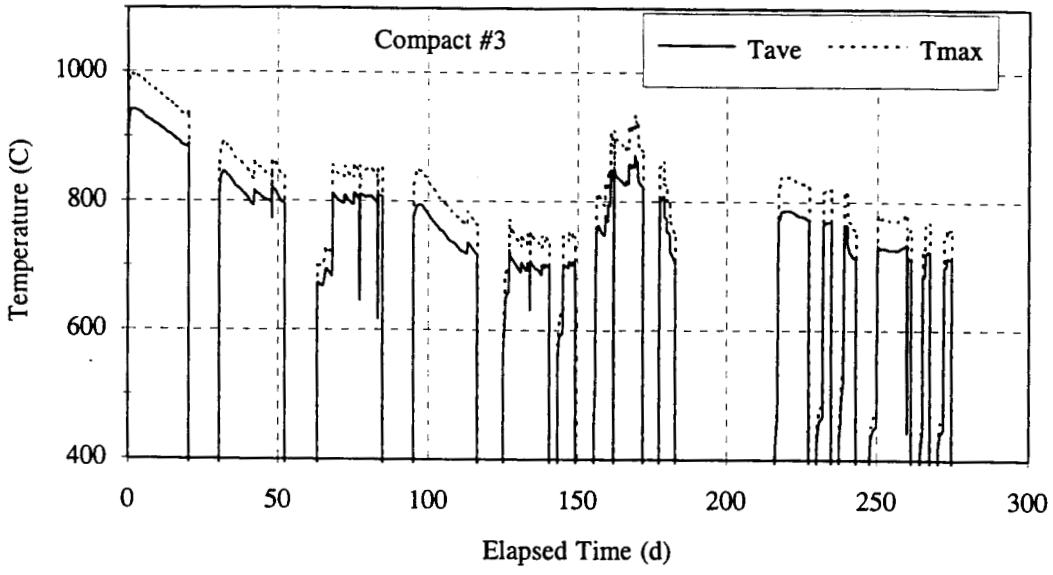

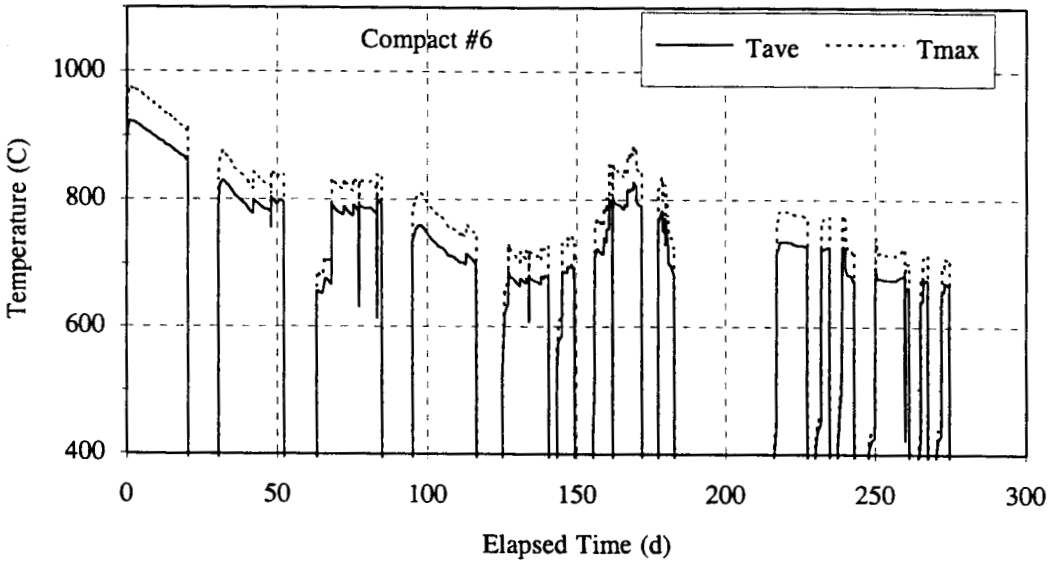

Figure 3.1-2b NPR 2 capsule region 3 volume average fuel temperature and local maximum fuel temperature

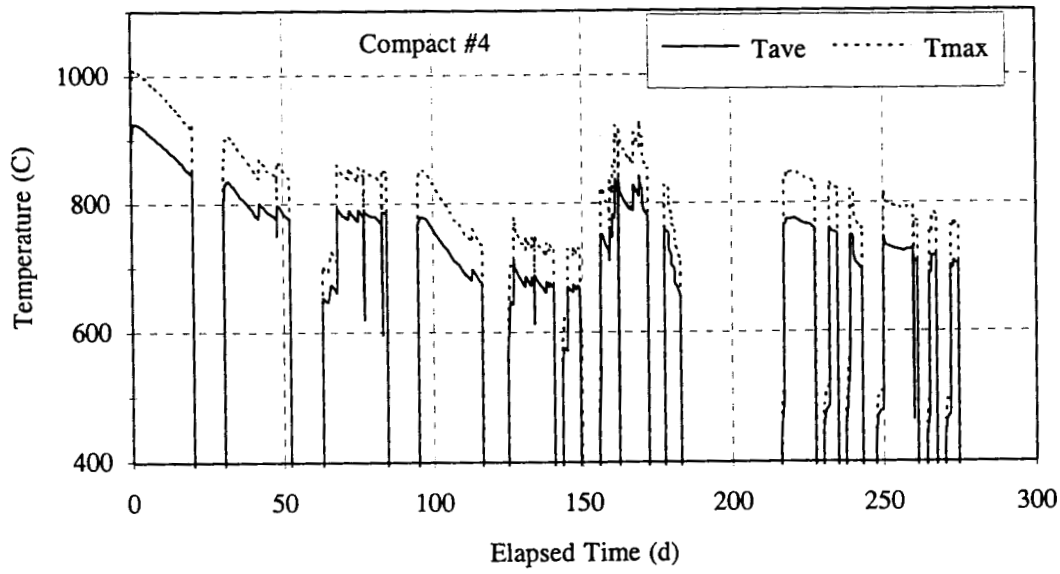

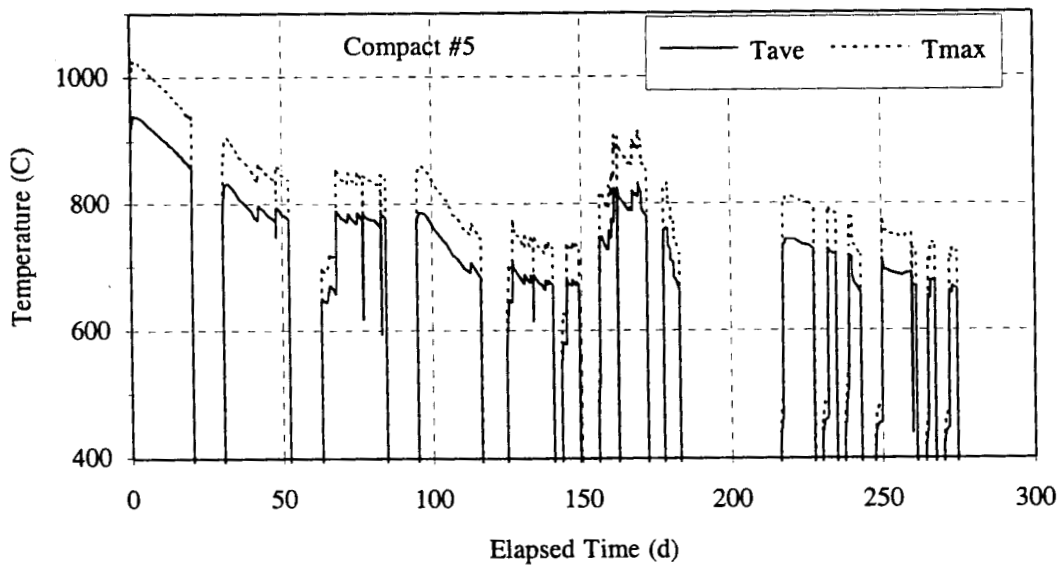

Figure 3.1-2b NPR 2 capsule region 4 volume average fuel temperature and local maximum fuel temperature

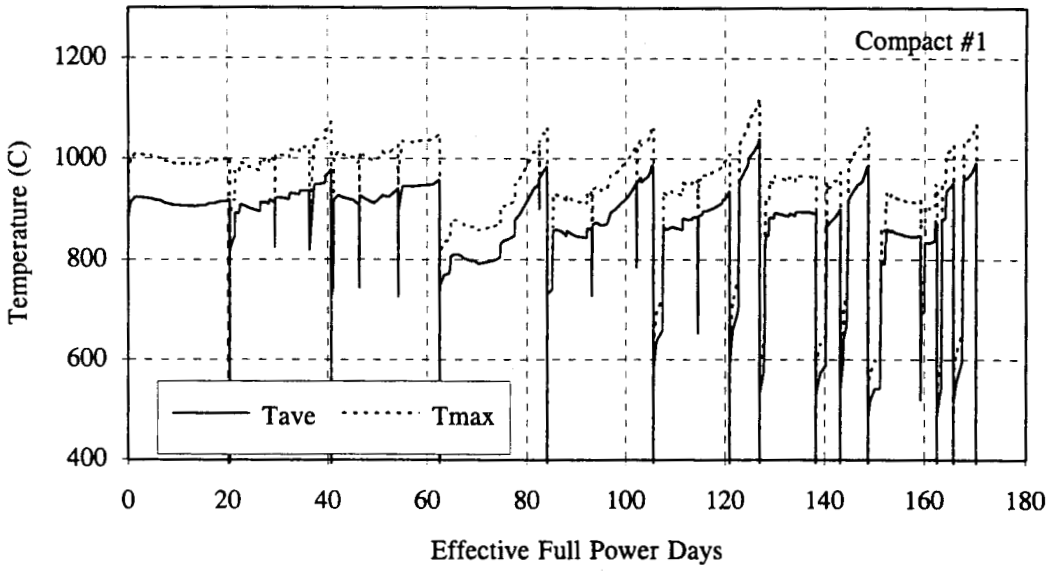

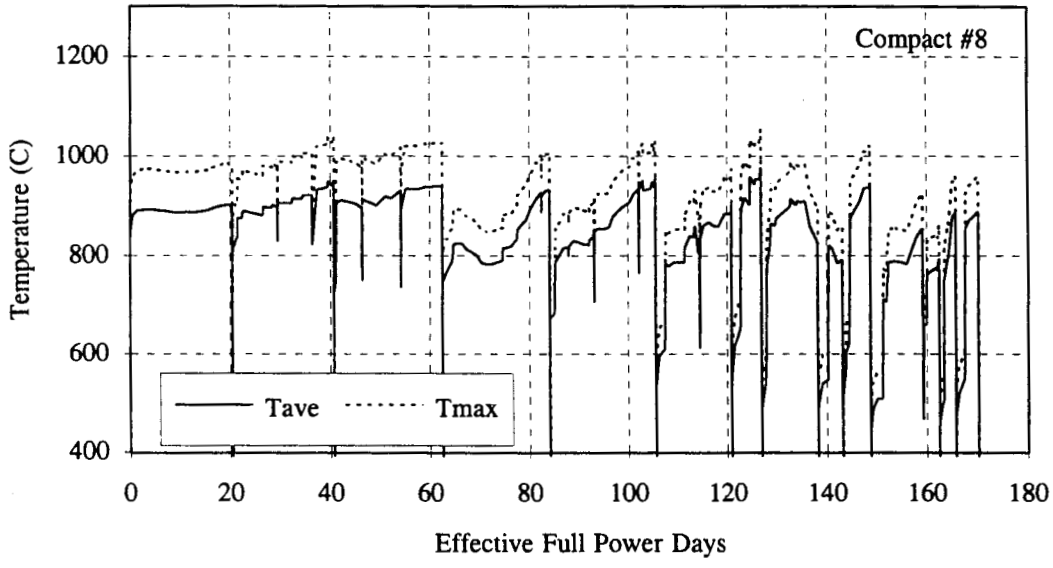

Figure 3.1-3a NPR 1 capsule region 1 volume average fuel temperature and local maximum fuel temperature

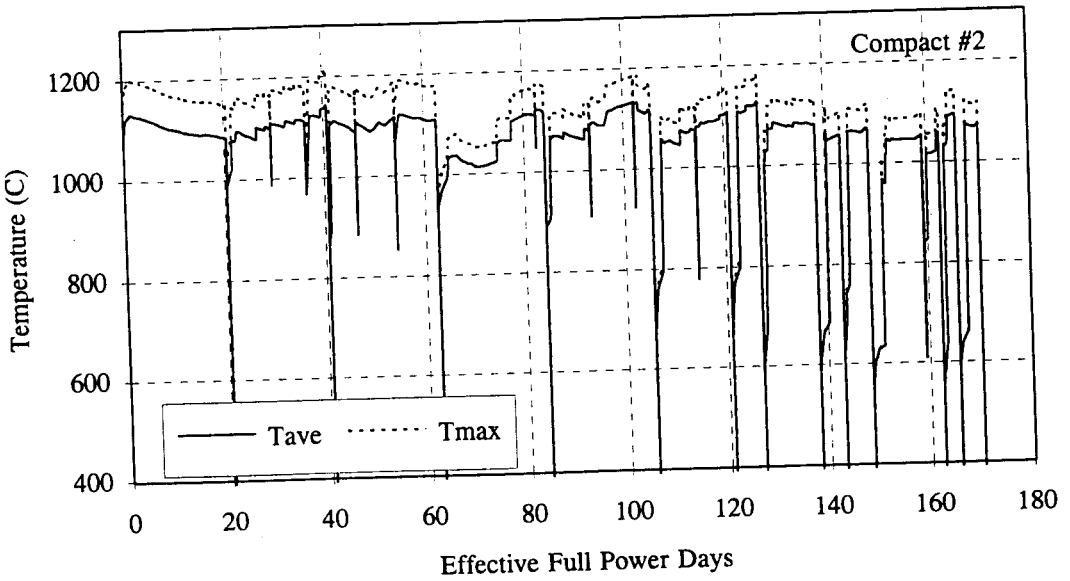

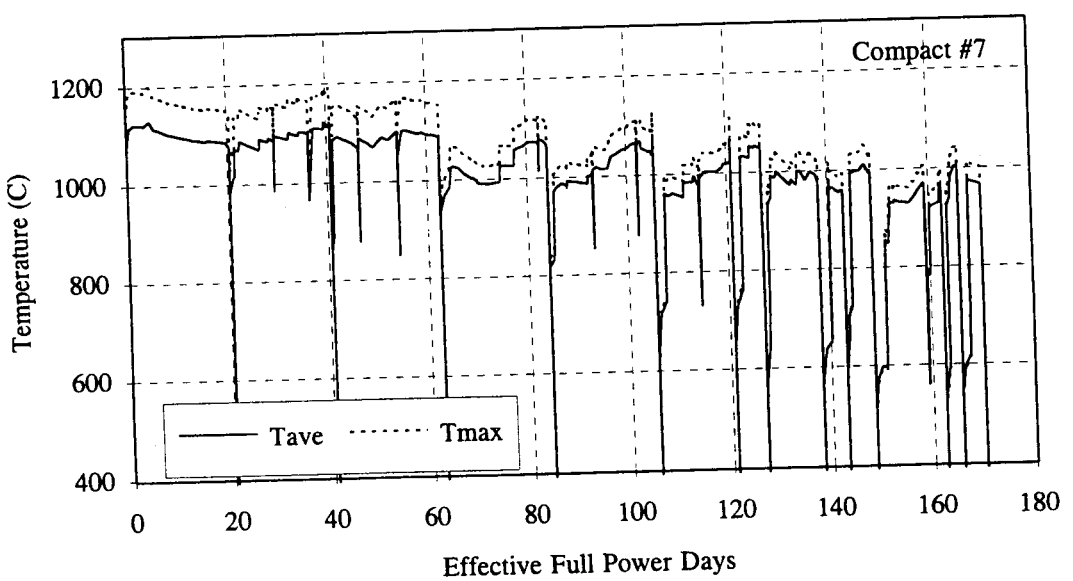

Figure 3.1-3a NPR 1 capsule region 2 volume average fuel temperature and local maximum fuel temperature

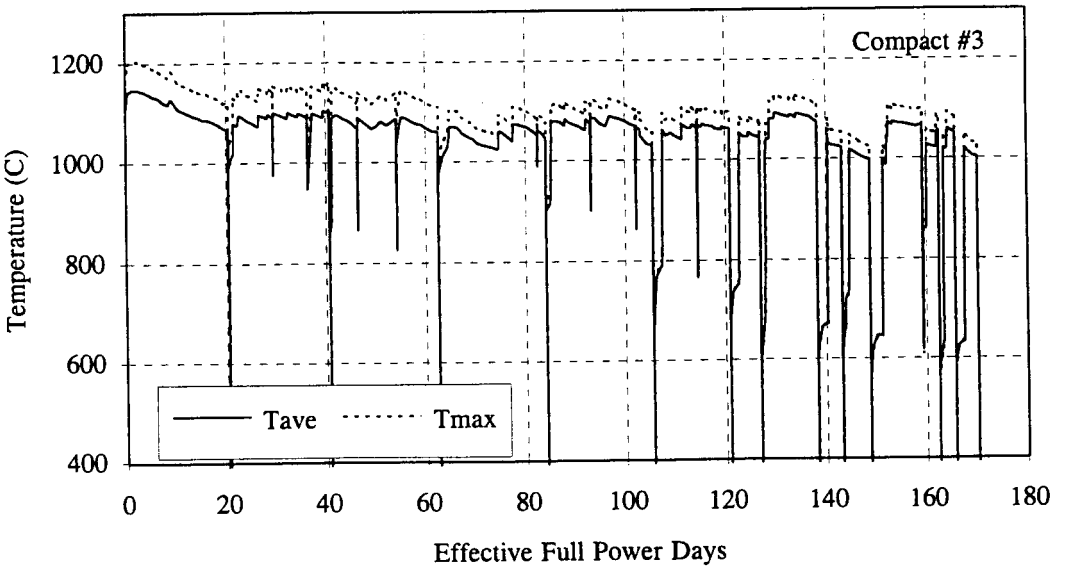

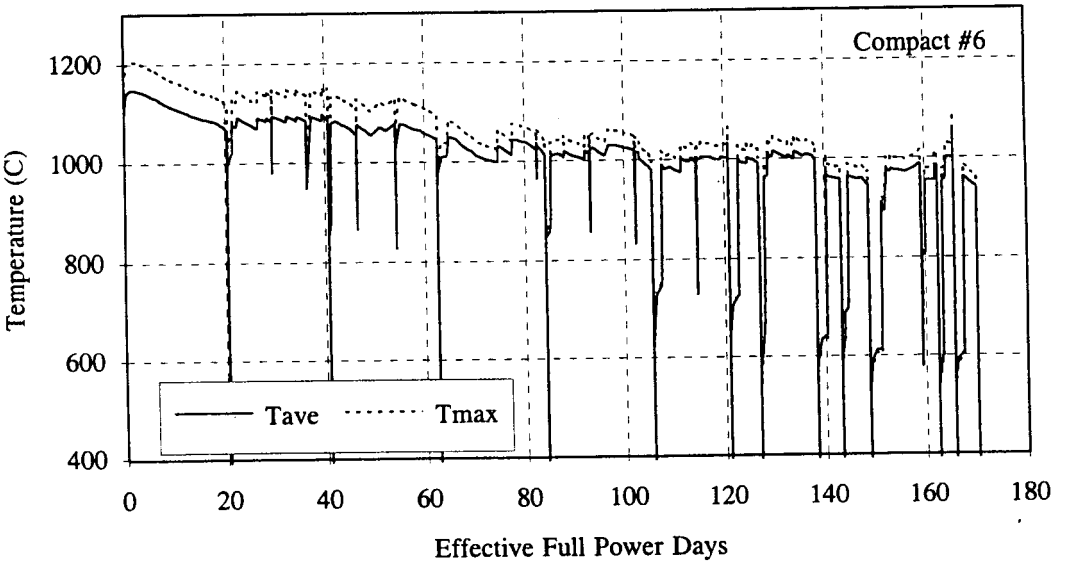

Figure 3.1-3a NPR 1 capsule region 3 volume average fuel temperature and local maximum fuel temperature

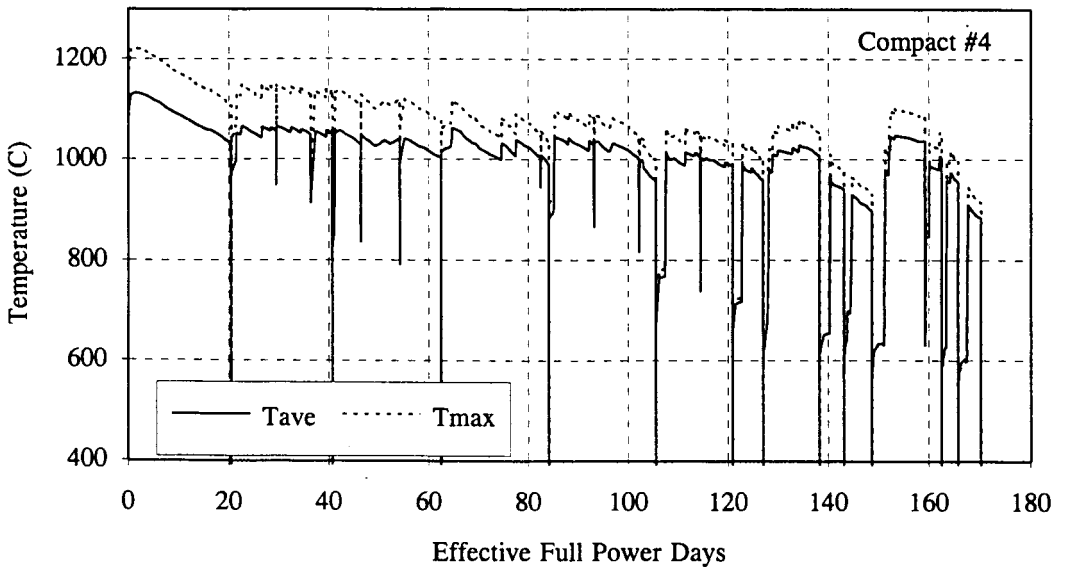

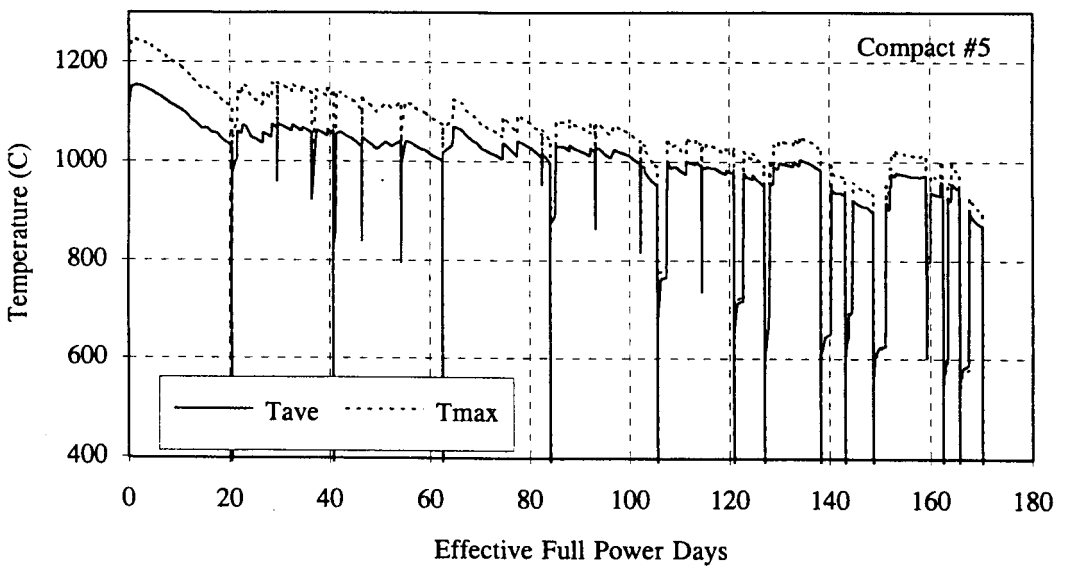

Figure 3.1-3a NPR 1 capsule region 4 volume average fuel temperature and local maximum fuel temperature

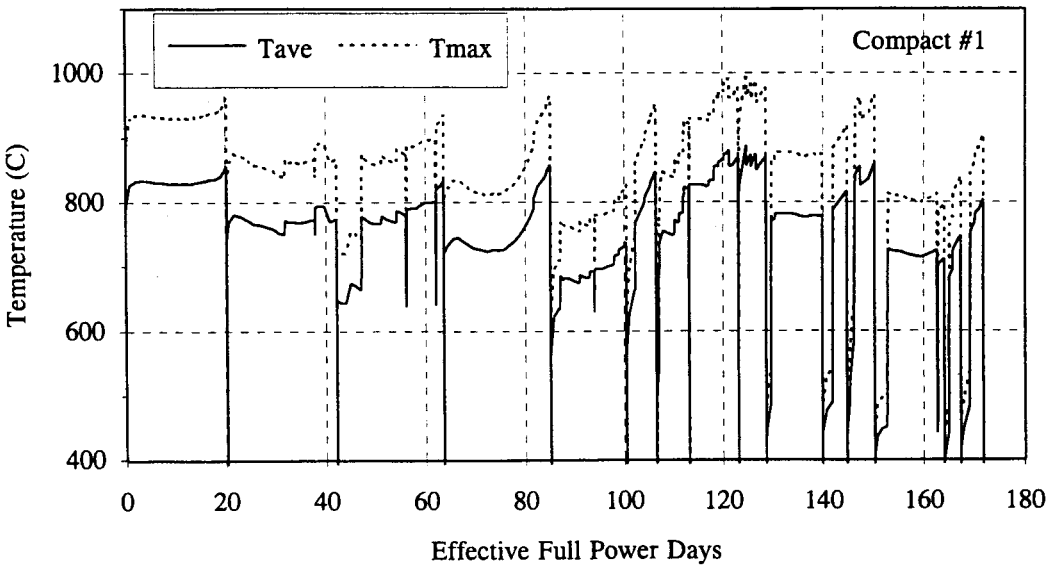

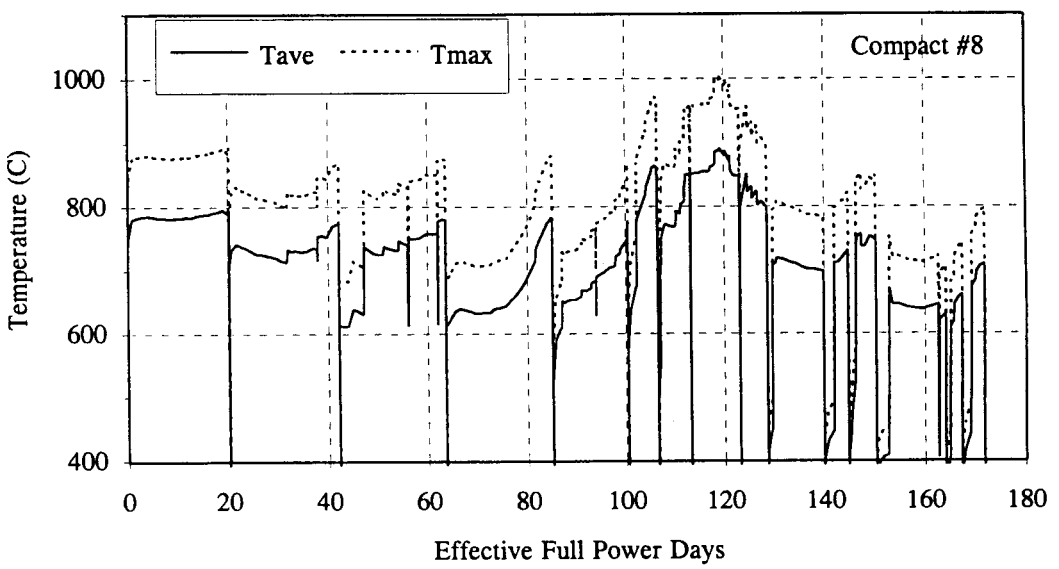

Figure 3.1-3b NPR 2 capsule region 1 volume average fuel temperature and local maximum fuel temperature

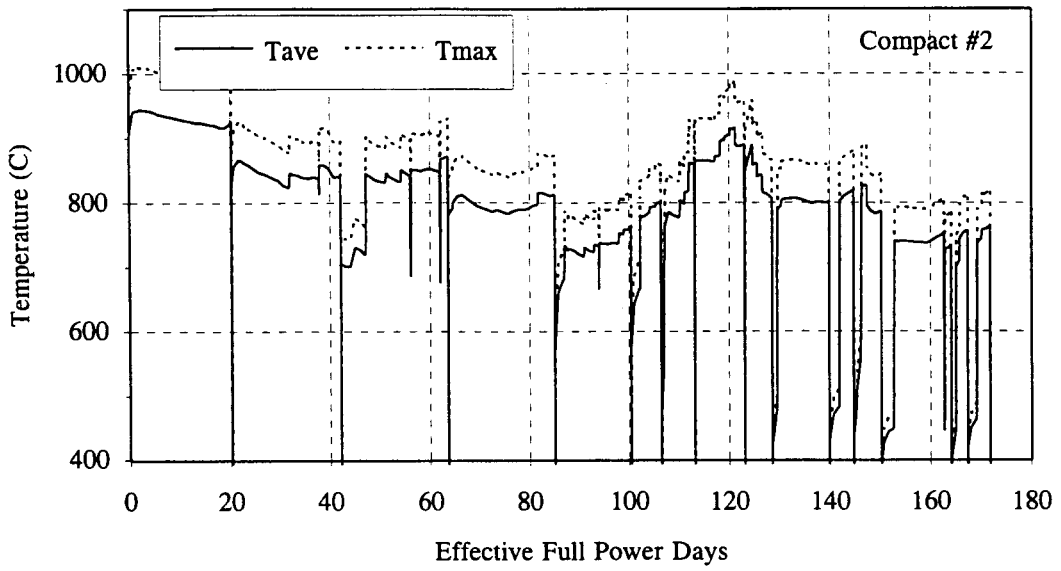

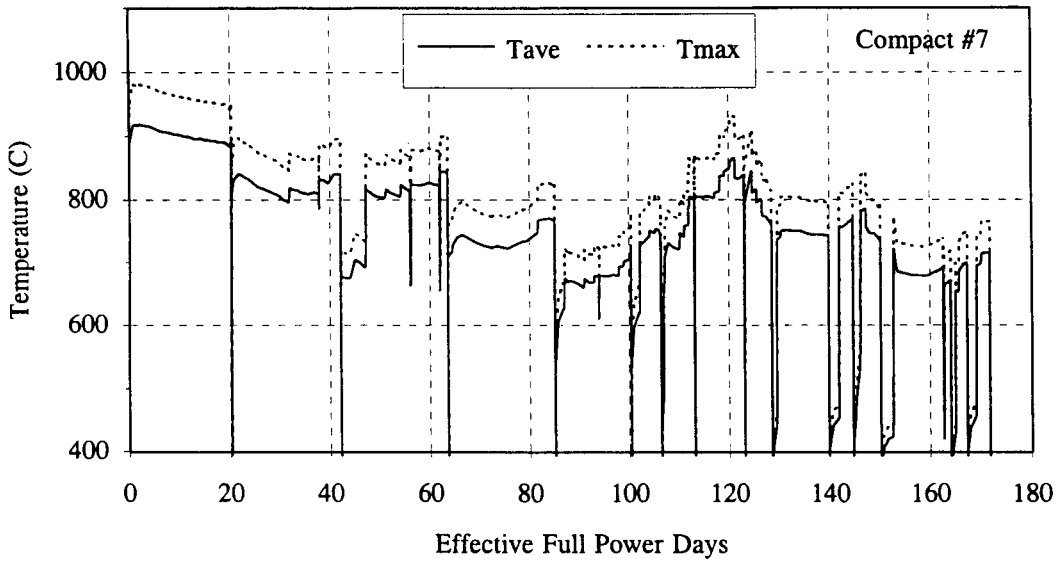

Figure 3.1-3b NPR 2 capsule region 2 volume average fuel temperature and local maximum fuel temperature

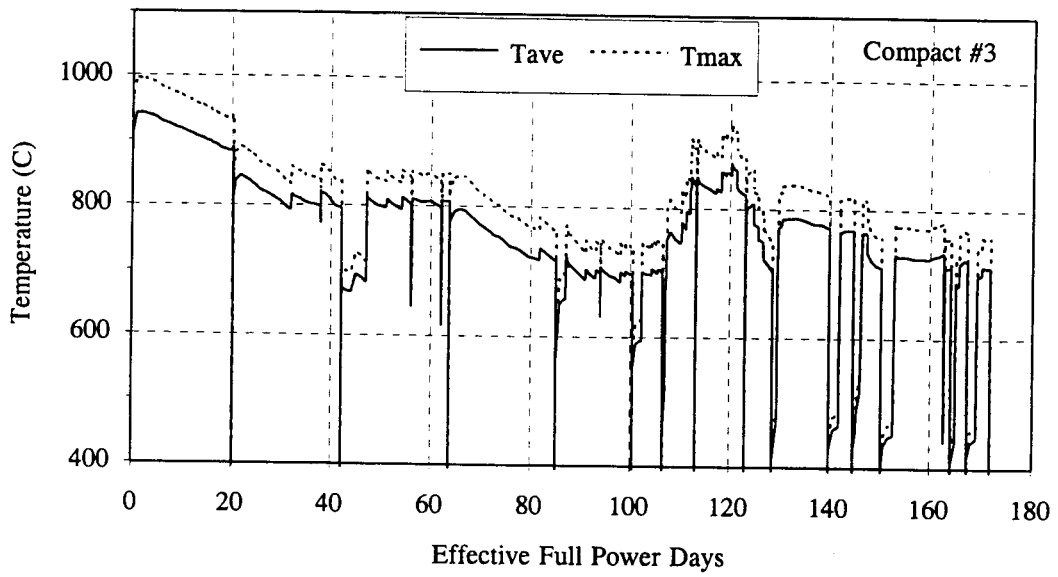

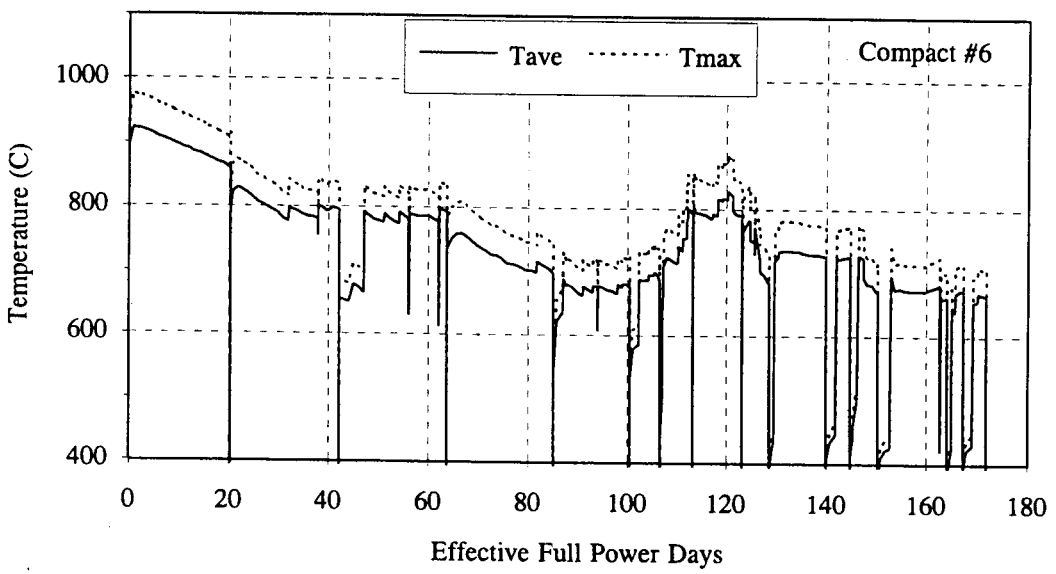

Figure 3.1-3b NPR 2 capsule region 3 volume average fuel temperature and local maximum fuel temperature

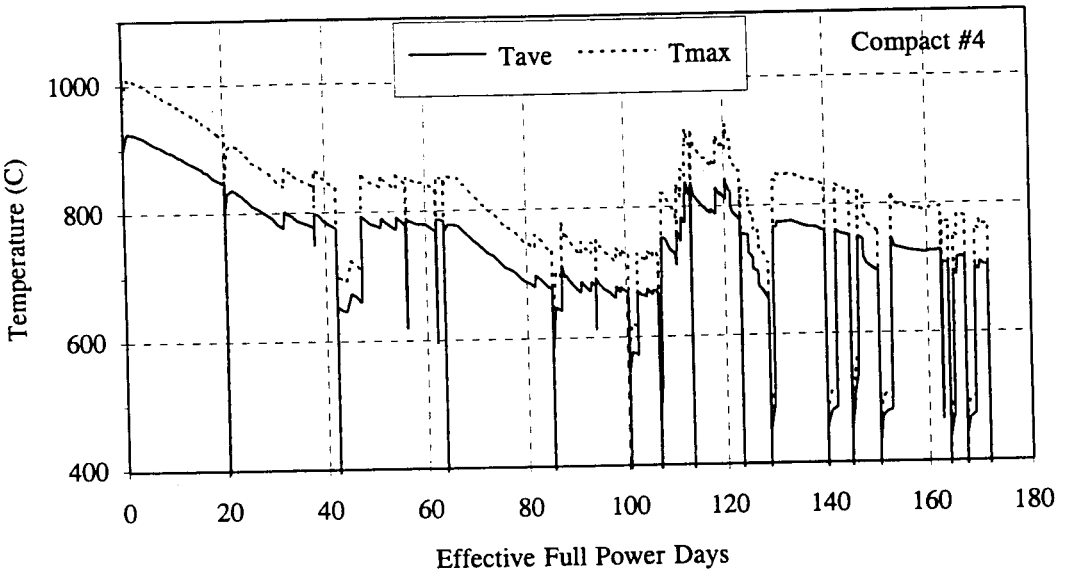

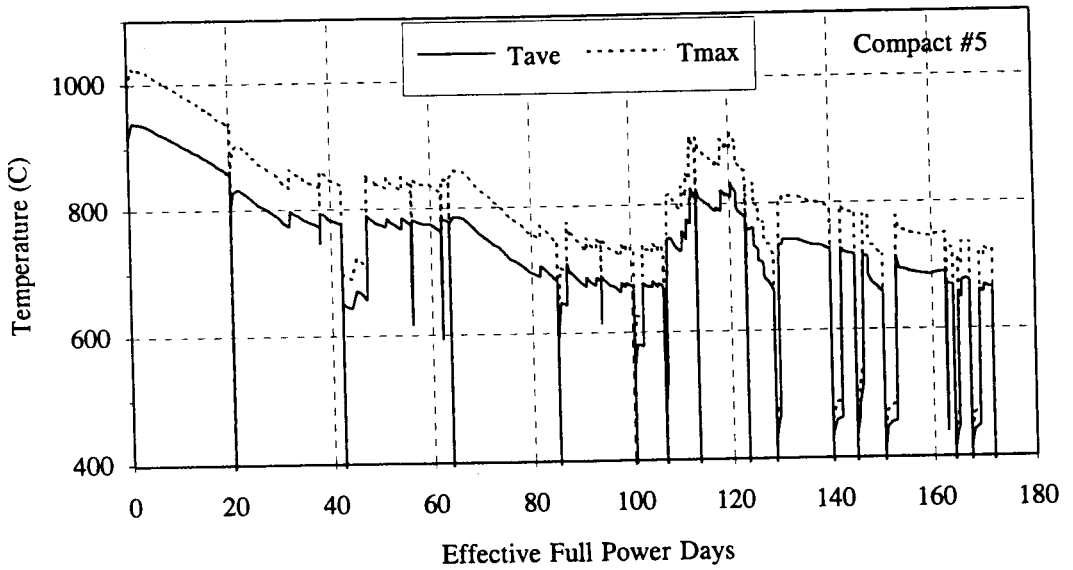

Figure 3.1-3b NPR 2 capsule region 4 volume average fuel temperature and local maximum fuel temperature

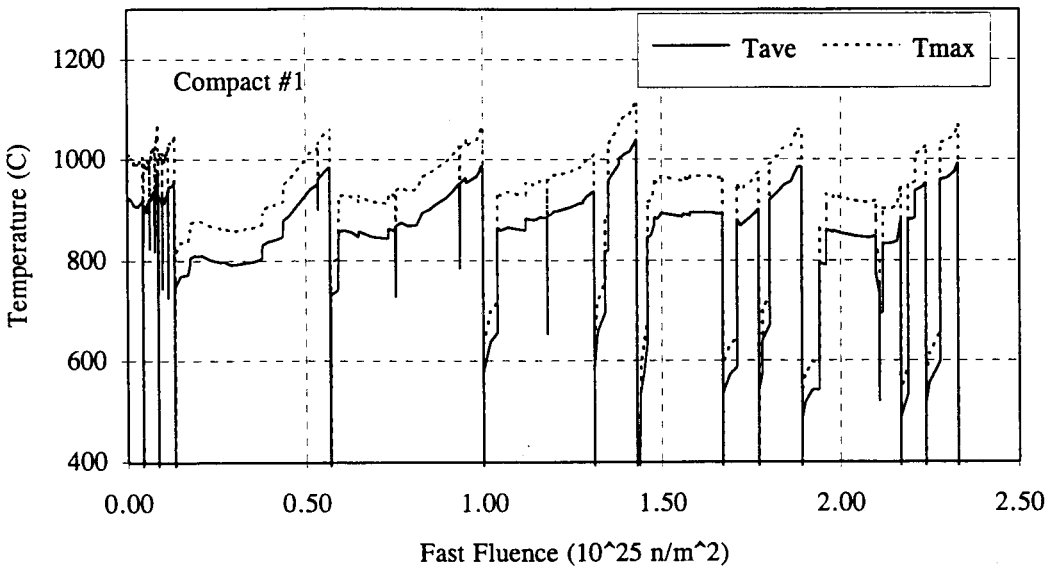

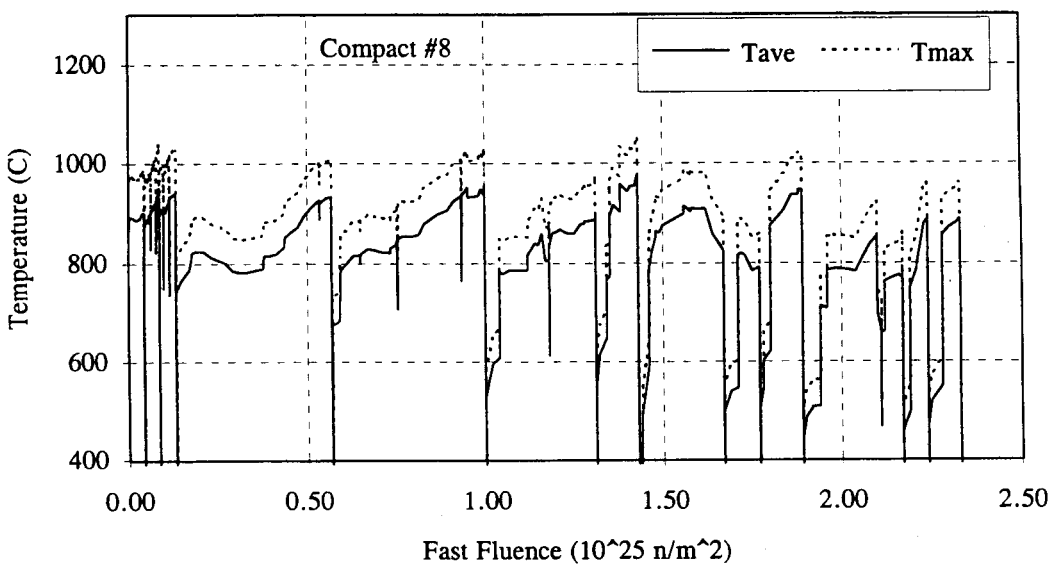

Figure 3.1-4a NPR 1 capsule region 1 volume average fuel temperature and local maximum fuel temperature

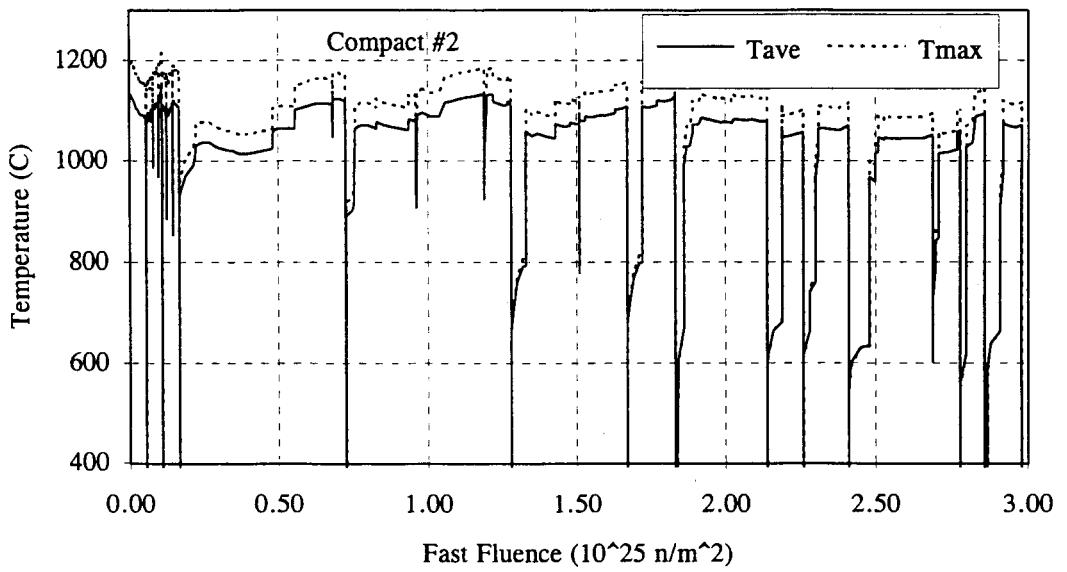

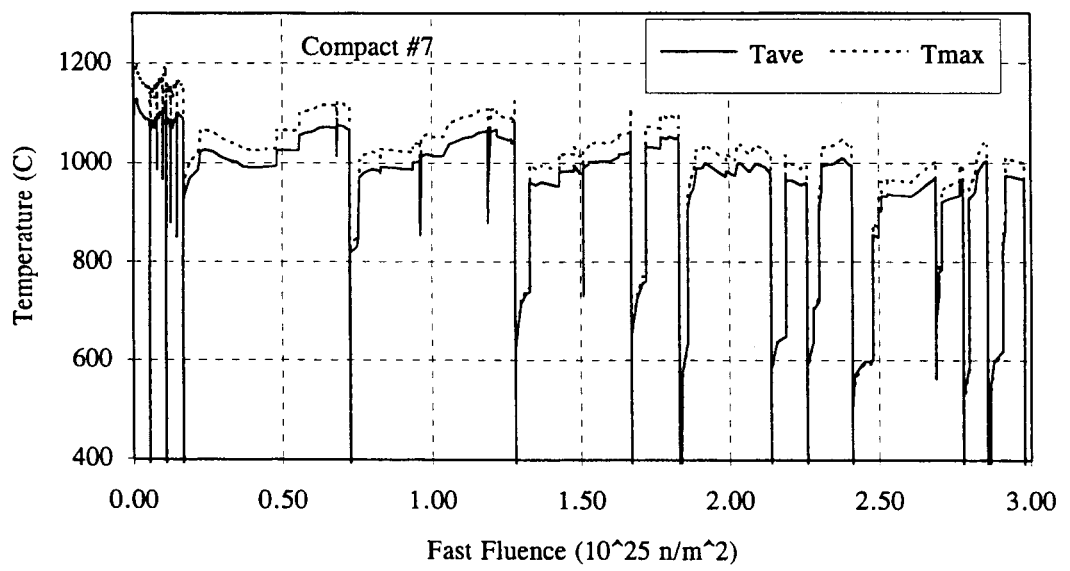

Figure 3.1-4a NPR 1 capsule region 2 volume average fuel temperature and local maximum fuel temperature

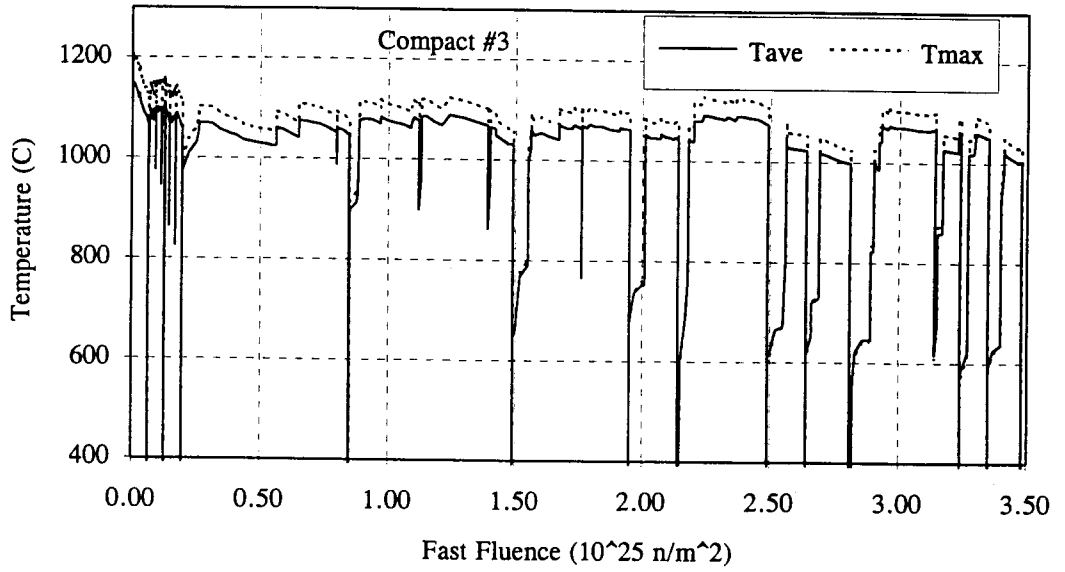

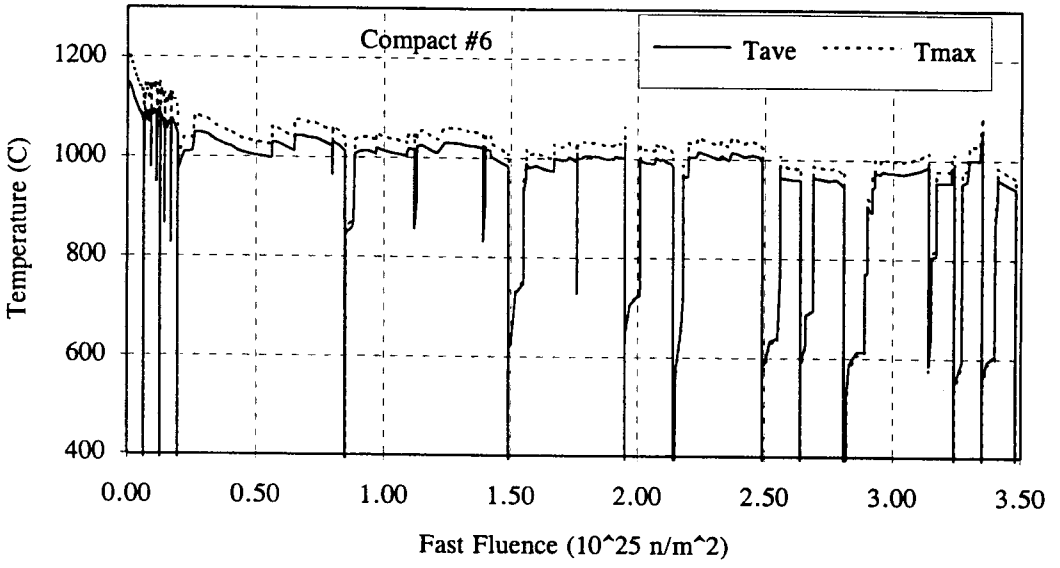

Figure 3.1-4a NPR 1 capsule region 3 volume average fuel temperature and local maximum fuel temperature

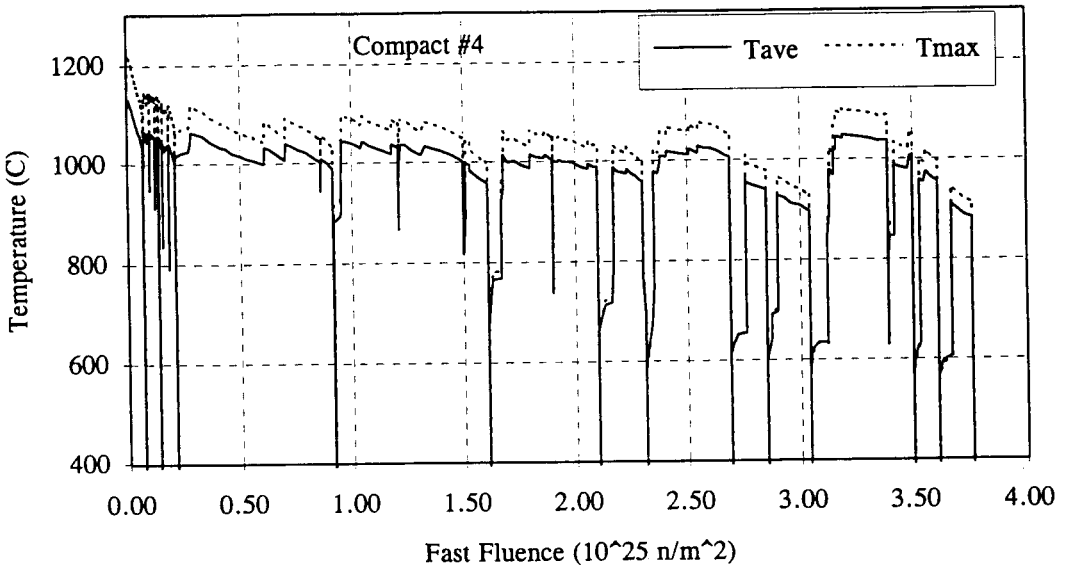

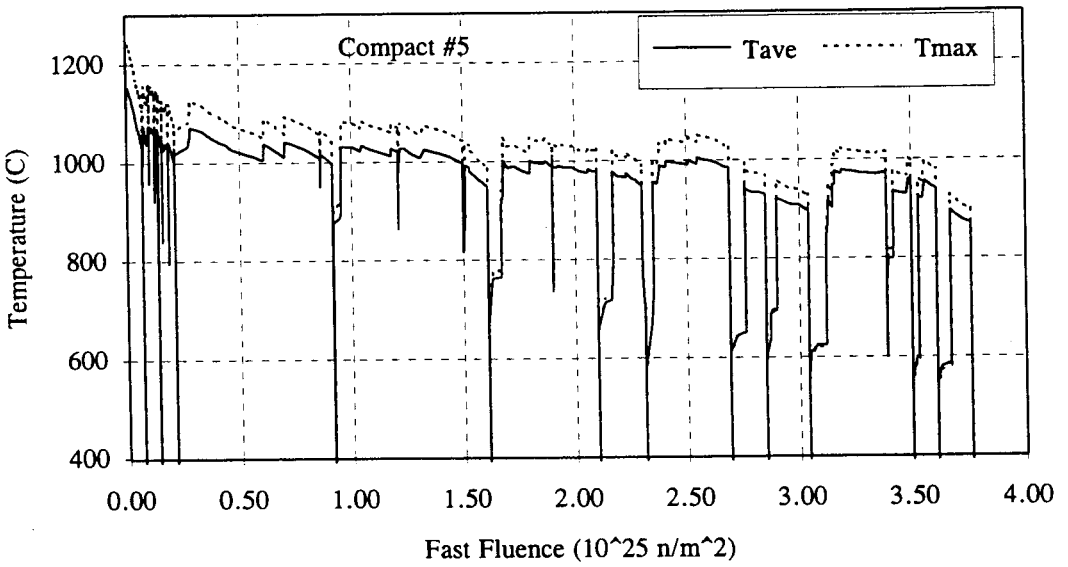

Figure 3.1-4a NPR 1 capsule region 4 volume average fuel temperature and local maximum fuel temperature

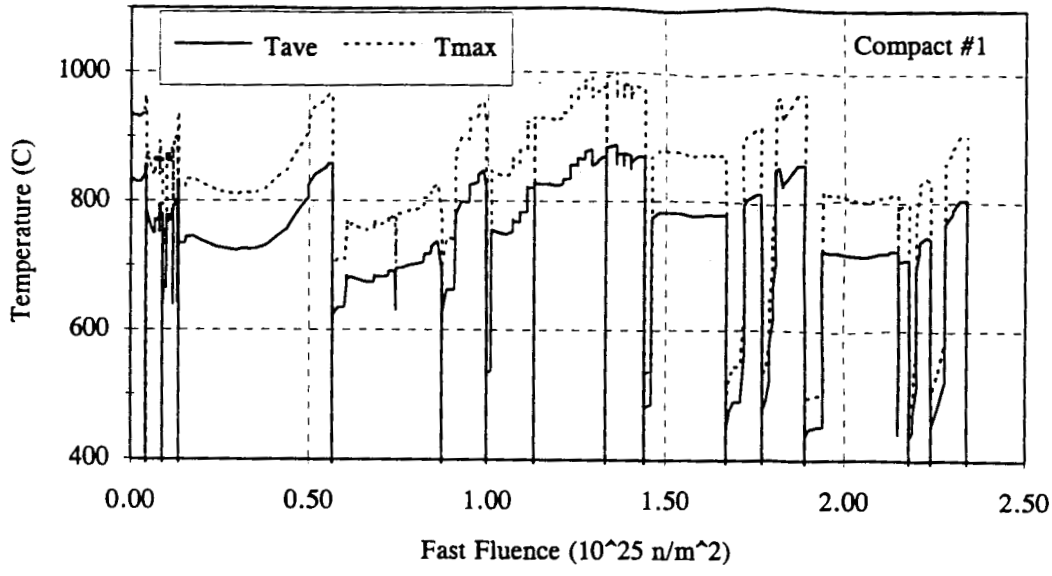

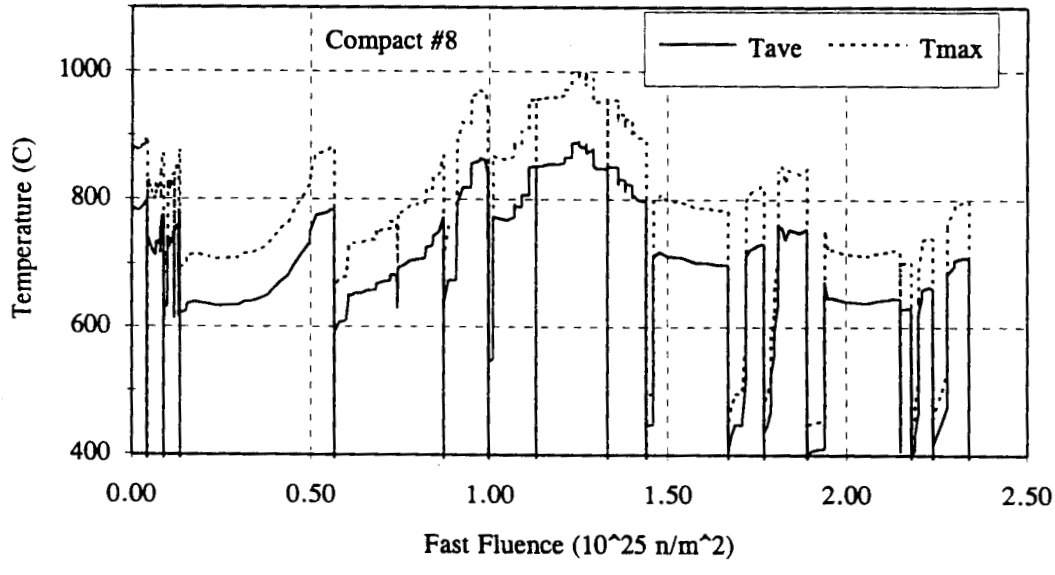

Figure 3.1-4b NPR 2 capsule region 1 volume average fuel temperature and local maximum fuel temperature

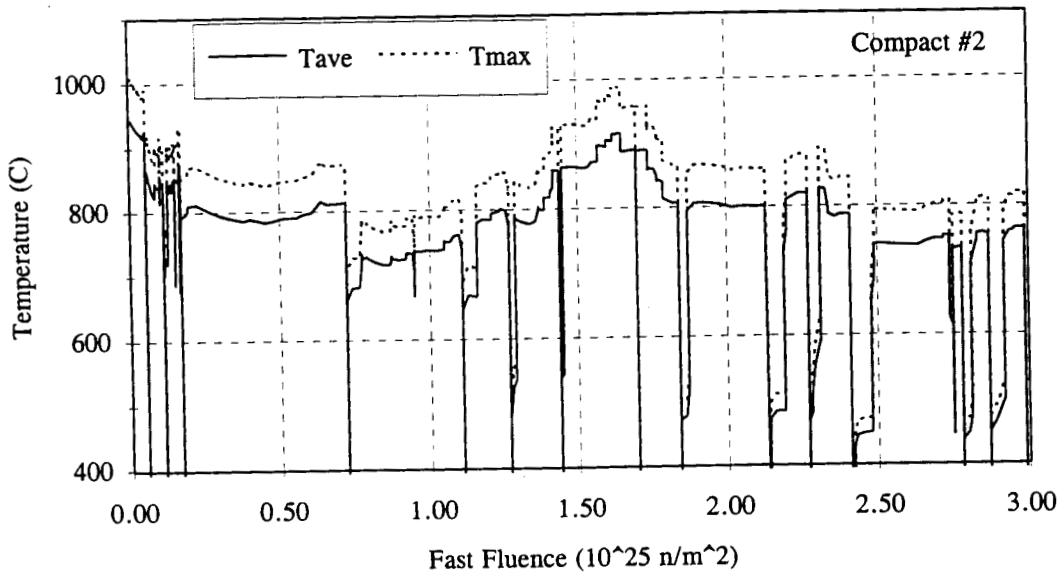

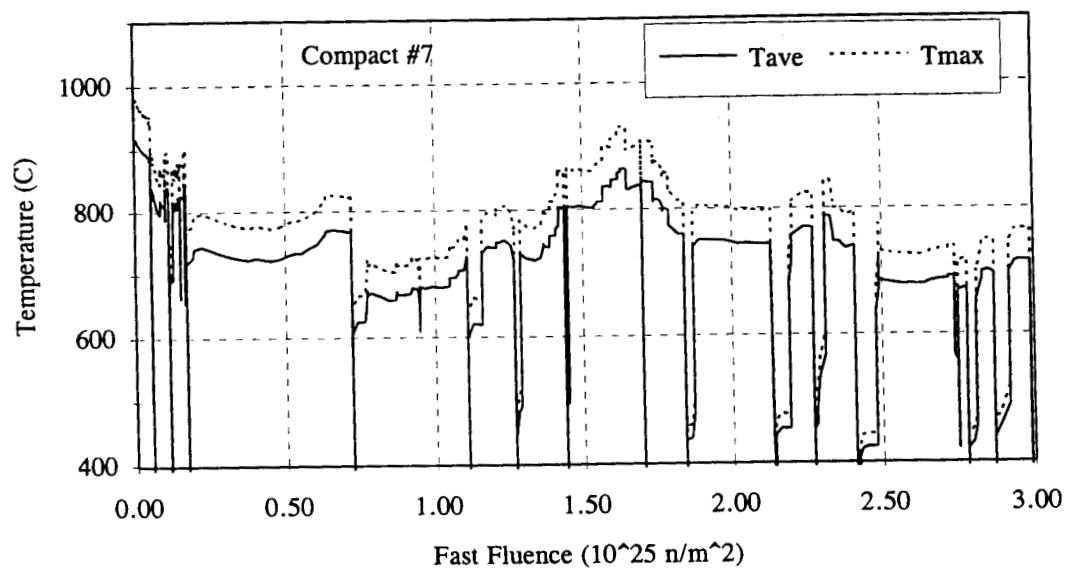

Figure 3.1-4b NPR 2 capsule region 2 volume average fuel temperature and local maximum fuel temperature

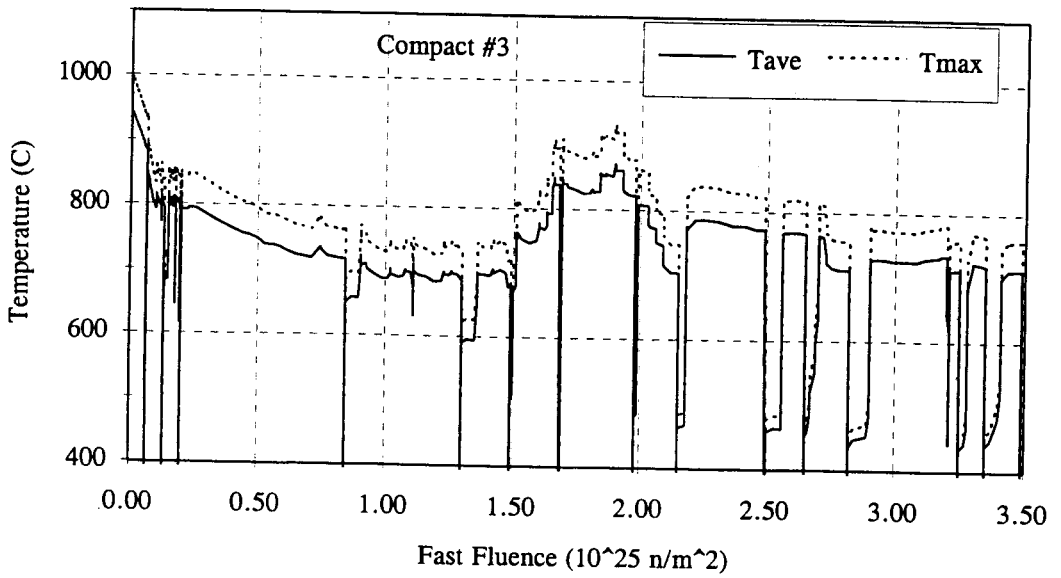

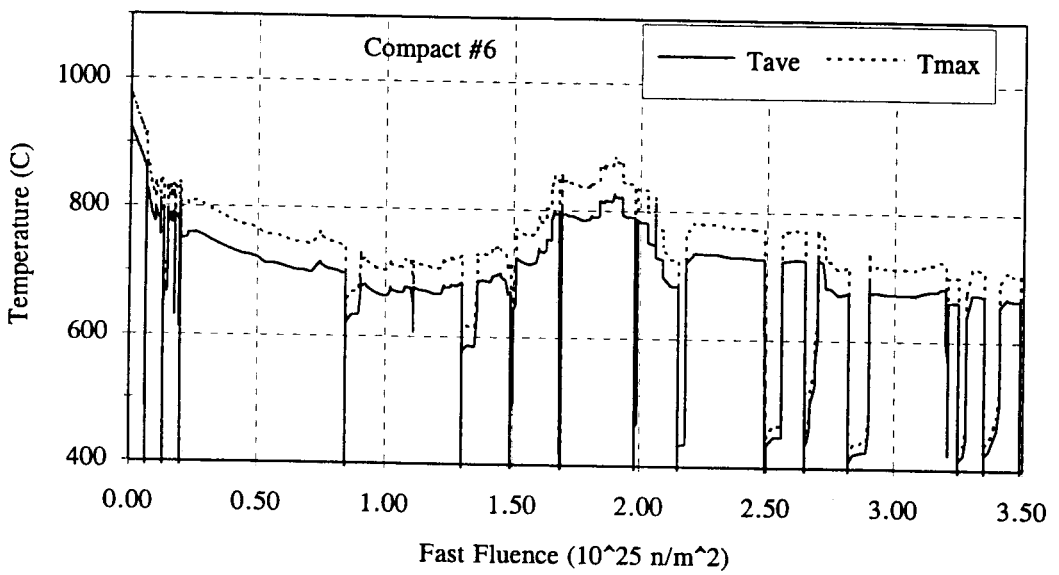

Figure 3.1-4b NPR 2 capsule region 3 volume average fuel temperature and local maximum fuel temperature

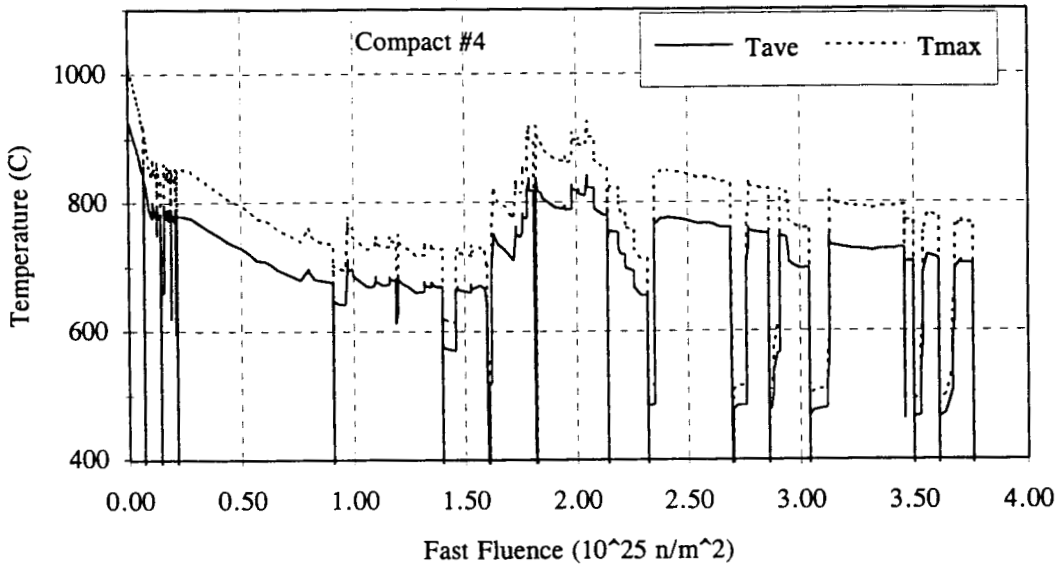

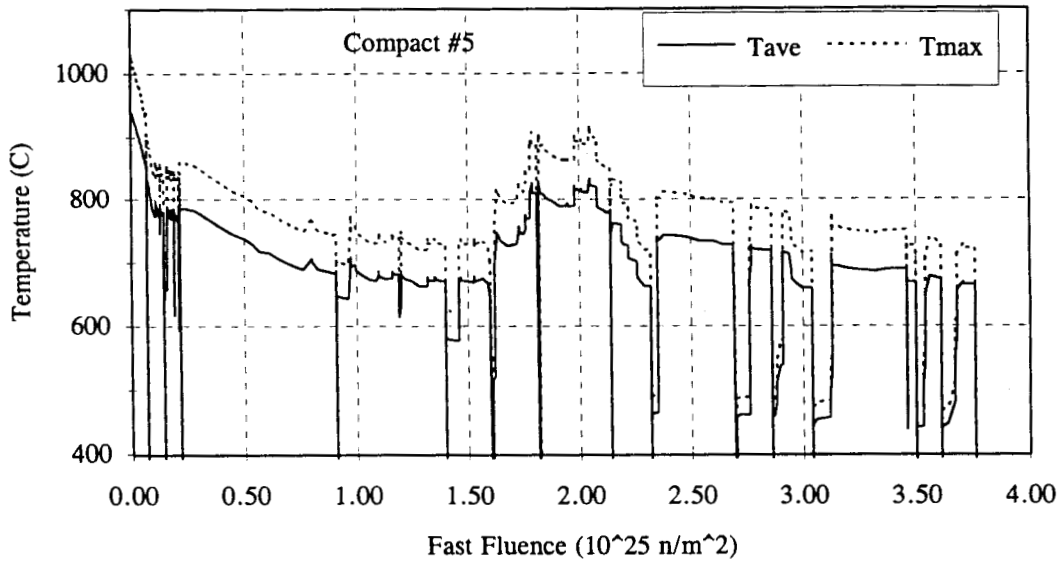

Figure 3.1-4b NPR 2 capsule region 4 volume average fuel temperature and local maximum fuel temperature

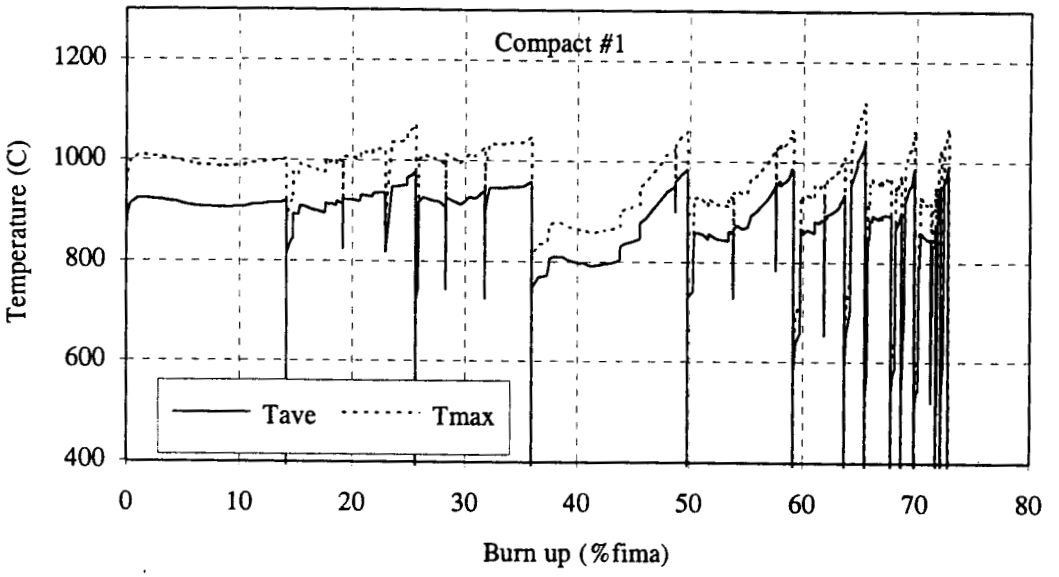

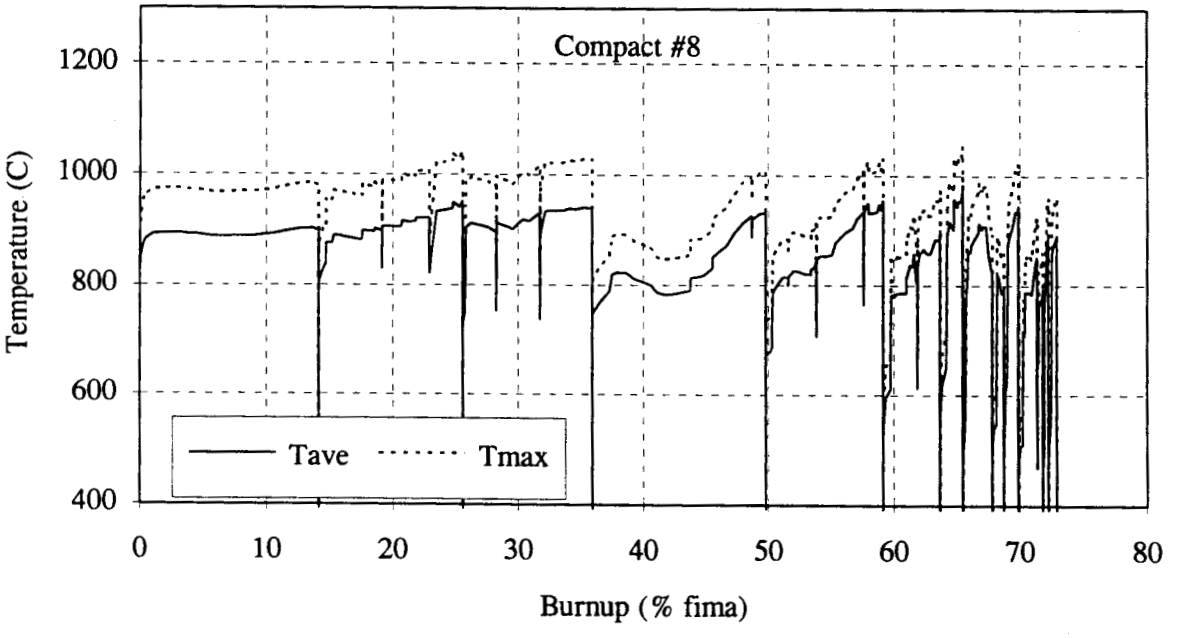

Figure 3.1-5a NPR 1 capsule region 1 volume average fuel temperature and local maximum fuel temperature

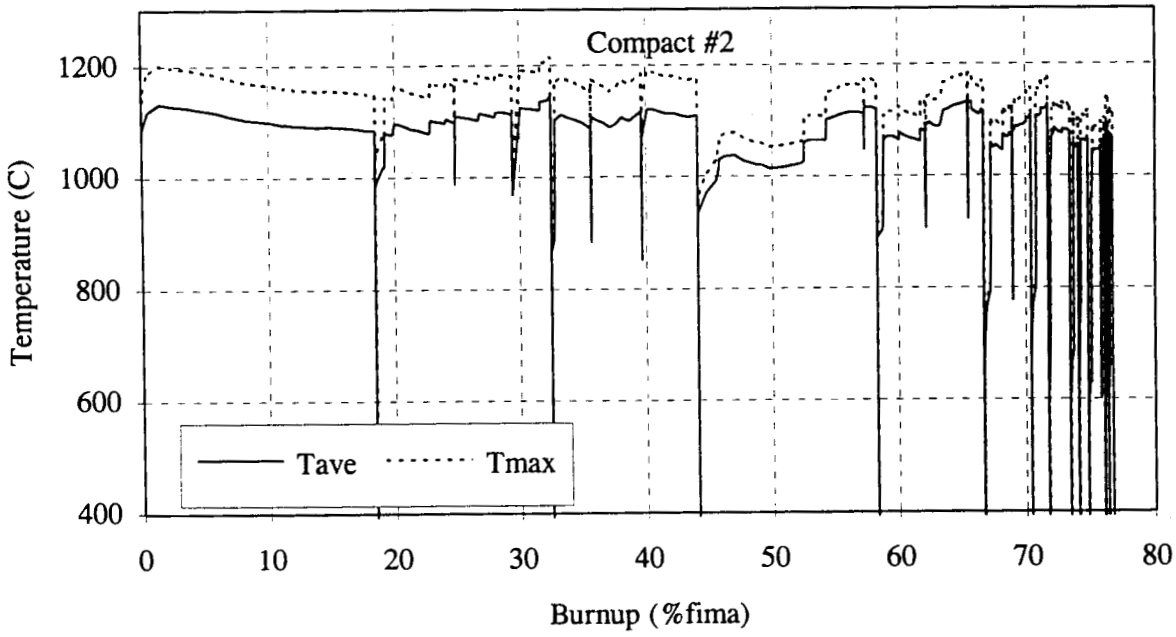

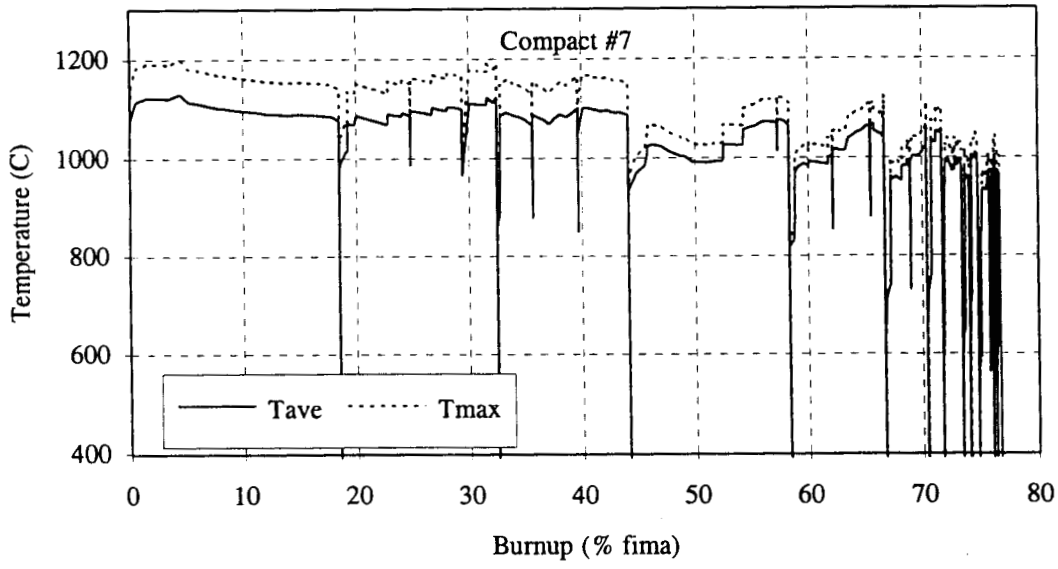

Figure 3.1-5a NPR 1 capsule region 2 volume average fuel temperature and local maximum fuel temperature

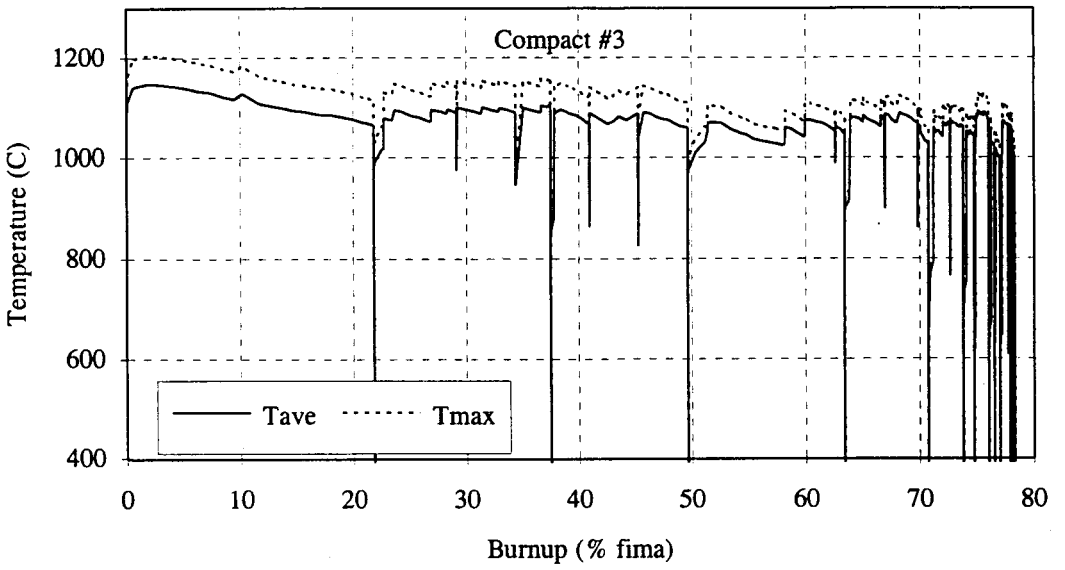

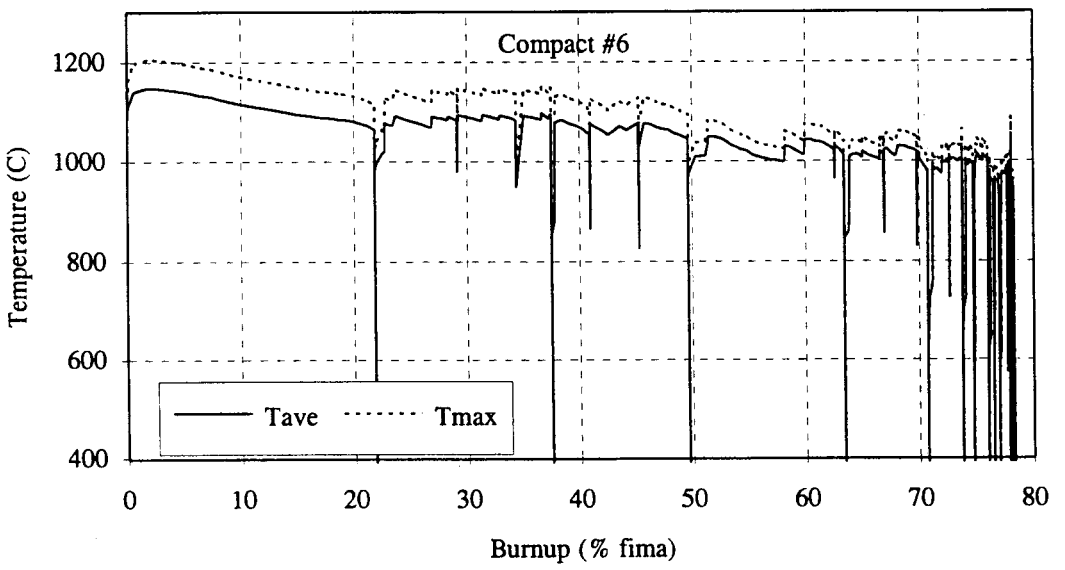

Figure 3.1-5a NPR 1 capsule region 3 volume average fuel temperature and local maximum fuel temperature

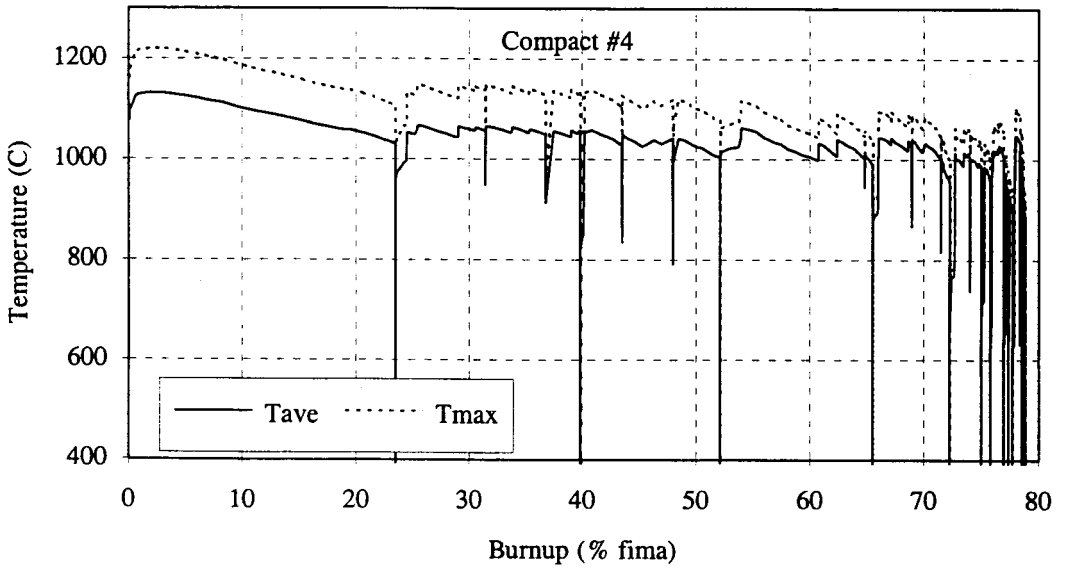

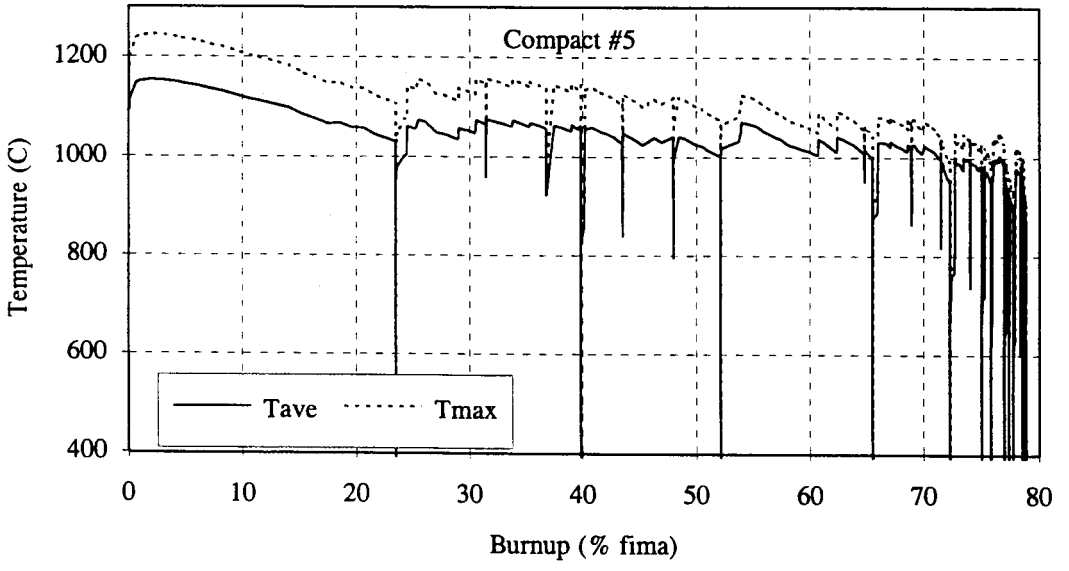

Figure 3.1.5a NPR 1 capsule region 4 volume average fuel temperature and local maximum fuel temperature

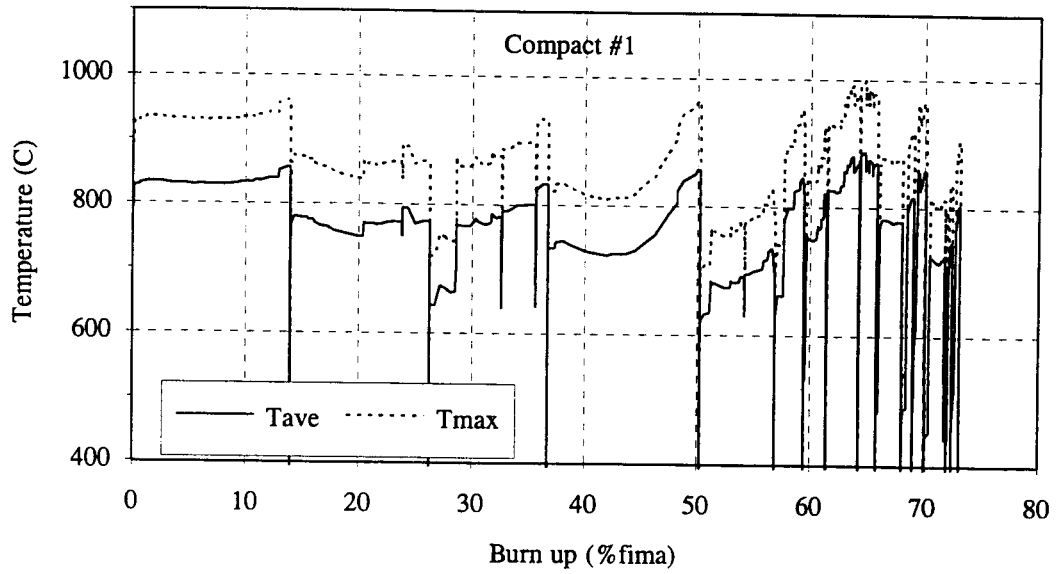

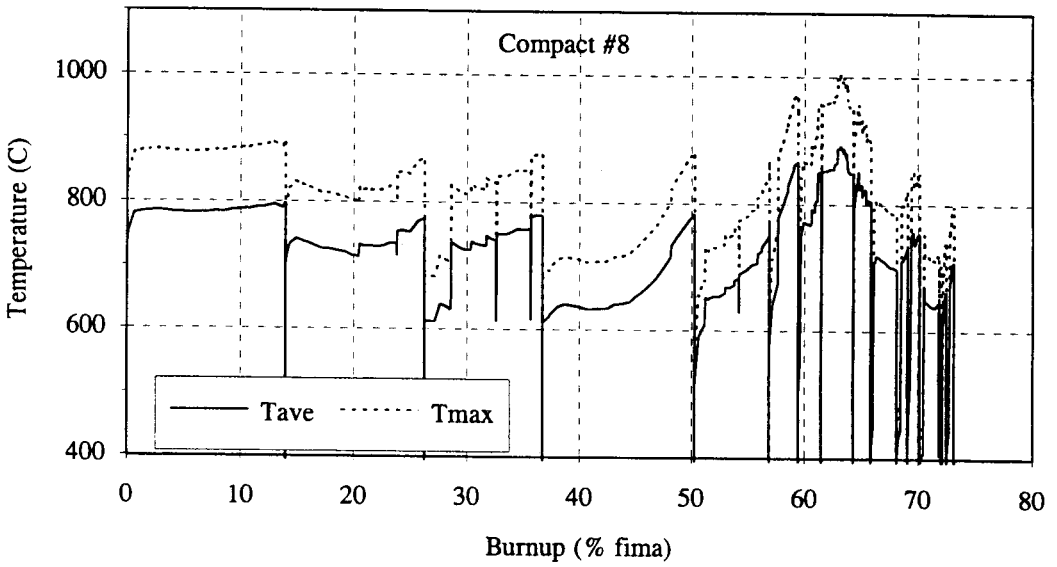

Figure 3.1-5b NPR 2 capsule region 1 volume average fuel temperature and local maximum fuel temperature

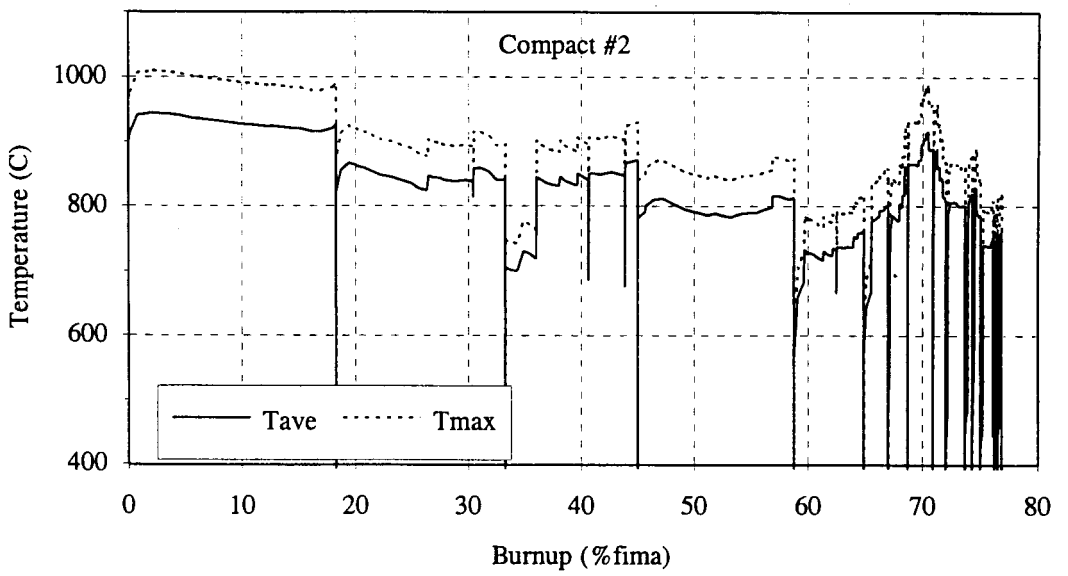

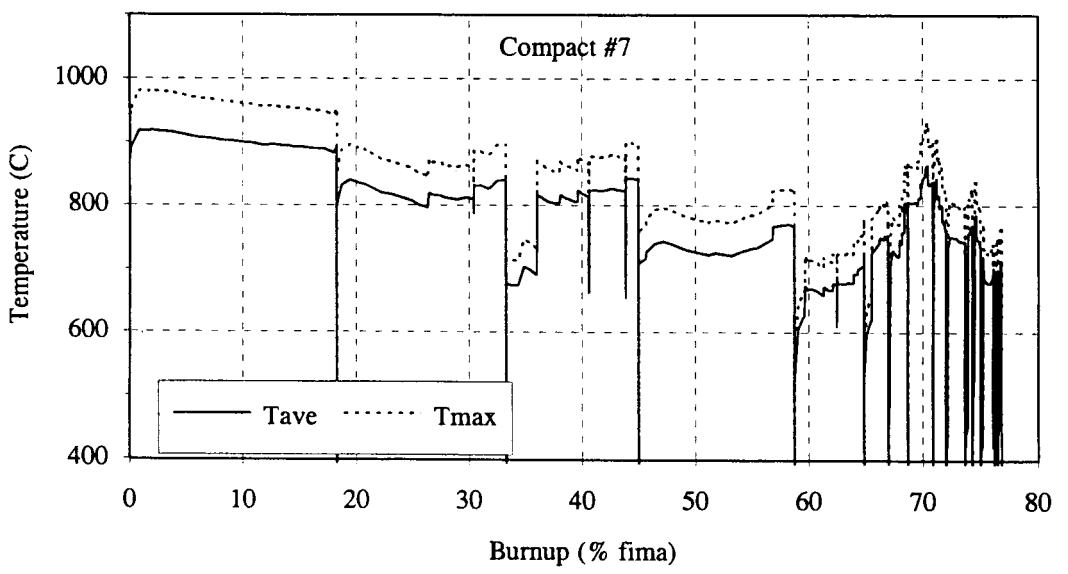

Figure 3.1-5b NPR 2 capsule region 2 volume average fuel temperature and local maximum fuel temperature

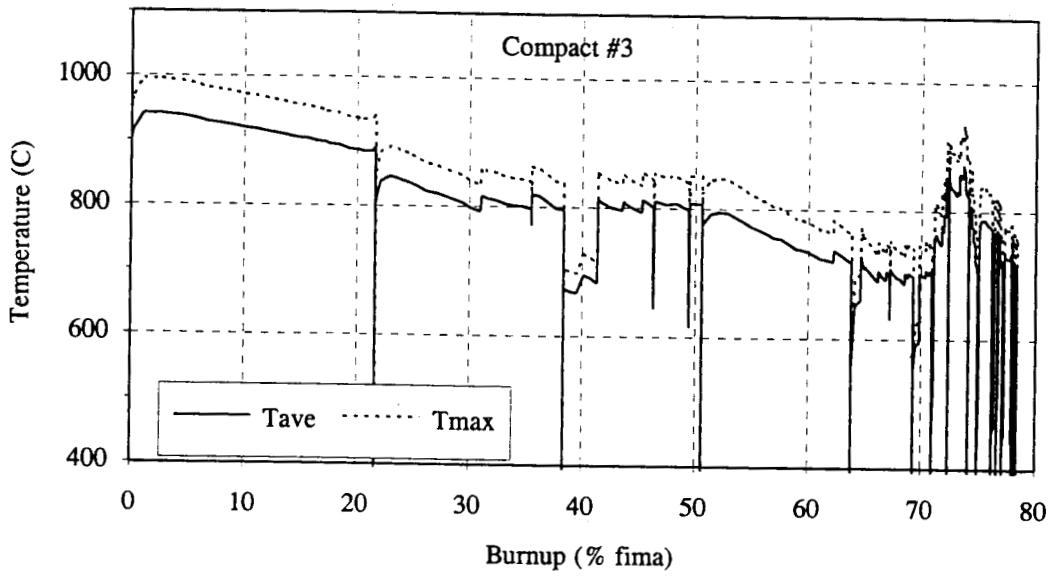

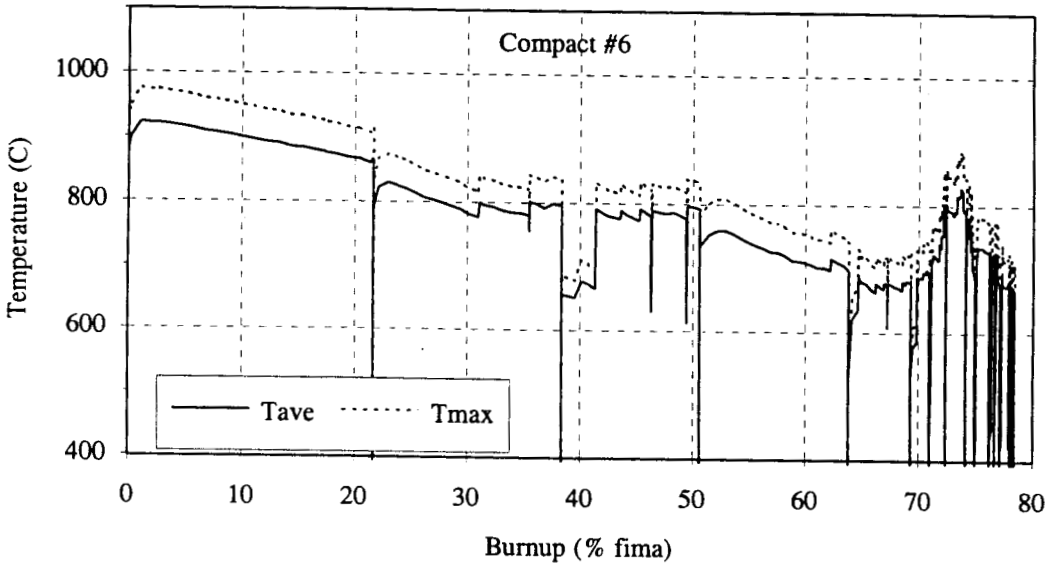

Figure 3.1-5b NPR 2 capsule region 3 volume average fuel temperature and local maximum fuel temperature

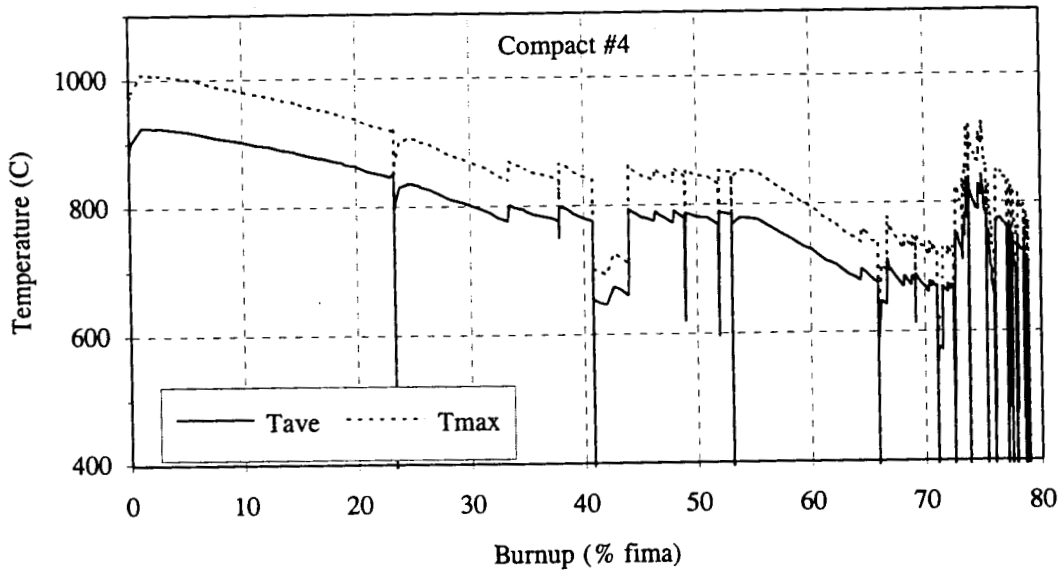

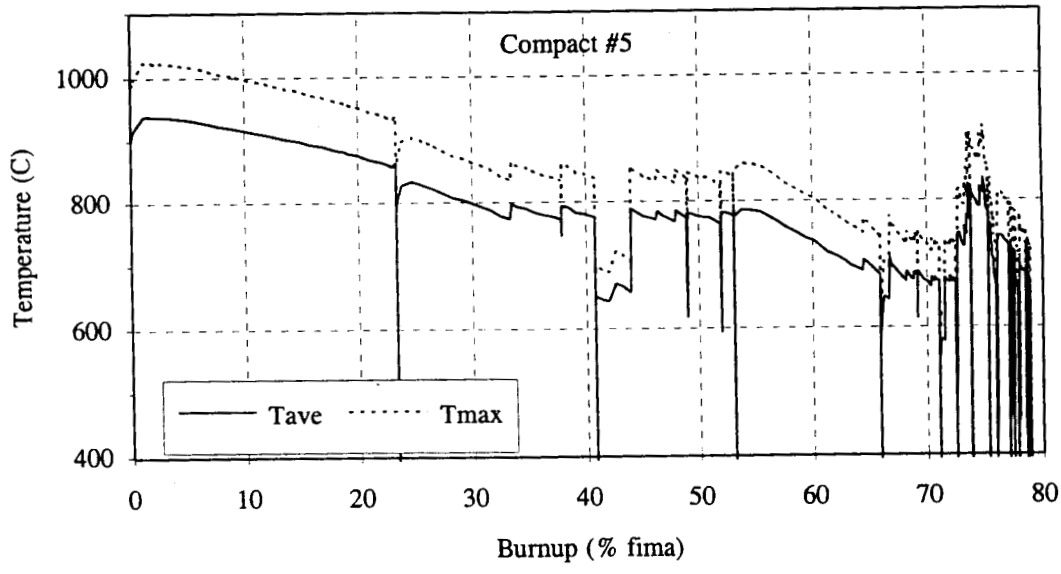

Figure 3.1-5b NPR 2 capsule region 4 volume average fuel temperature and local maximum fuel temperature

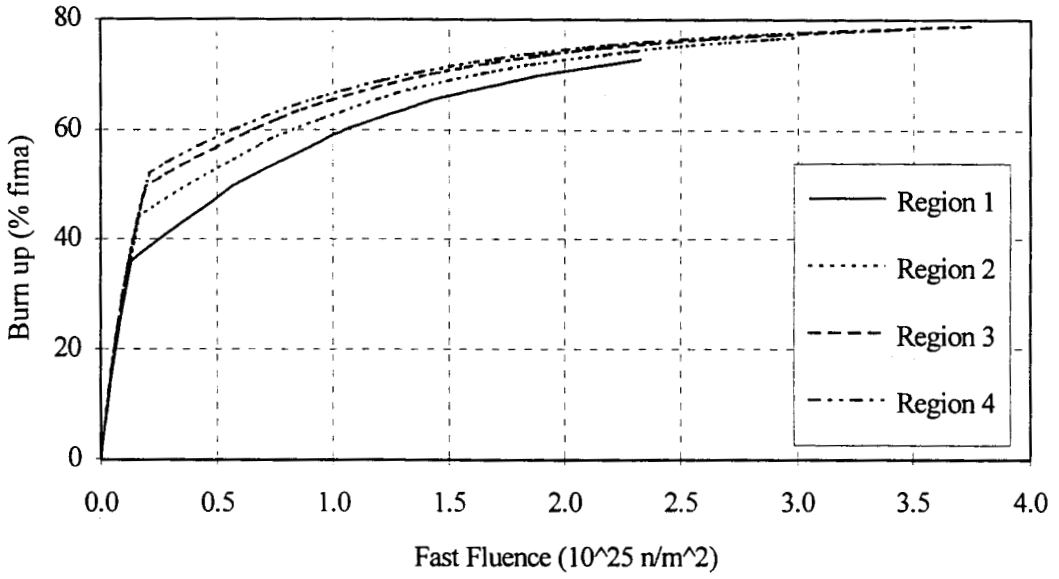

Figure 3.1-6a NPR 1 capsule fast neutron fluence versus burnup (% fima)

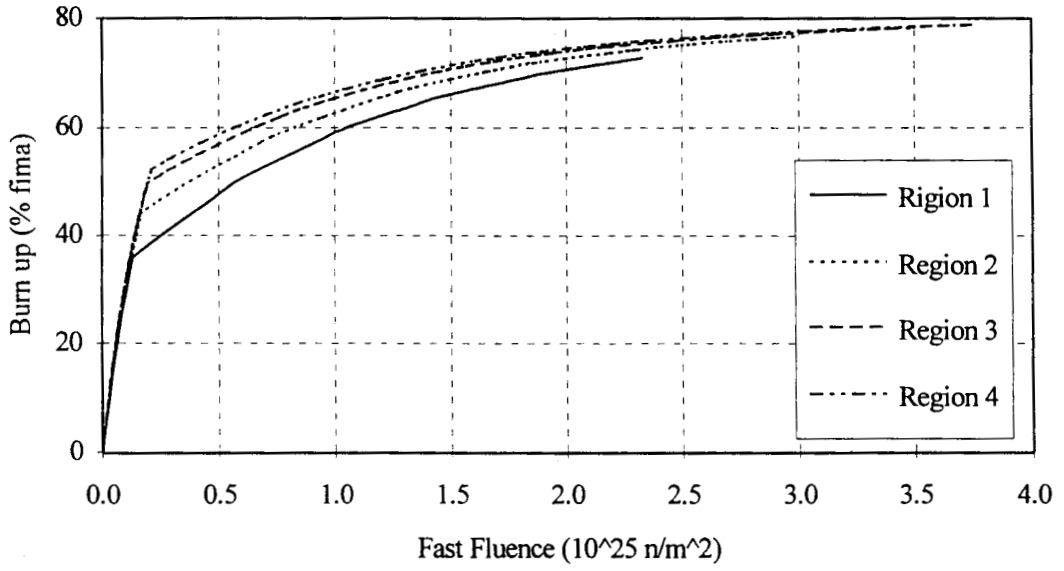

Figure 3.1-6b NPR 2 capsule fast neutron fluence versus burnup (% fima)

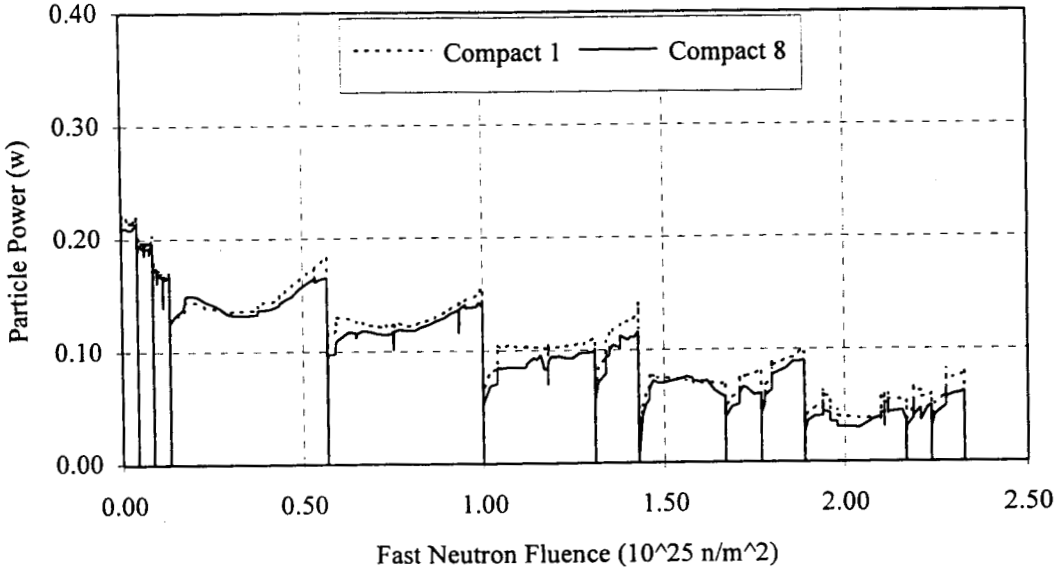

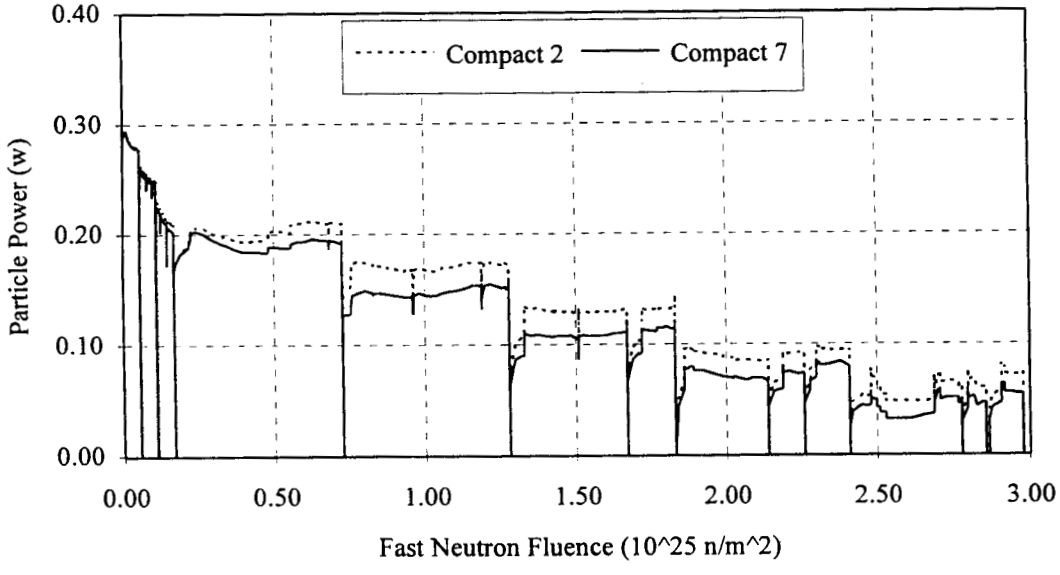

Figure 3.1-7a NPR 1 capsule regions 1 & 2 fuel particle power as a function of fast neutron fluence

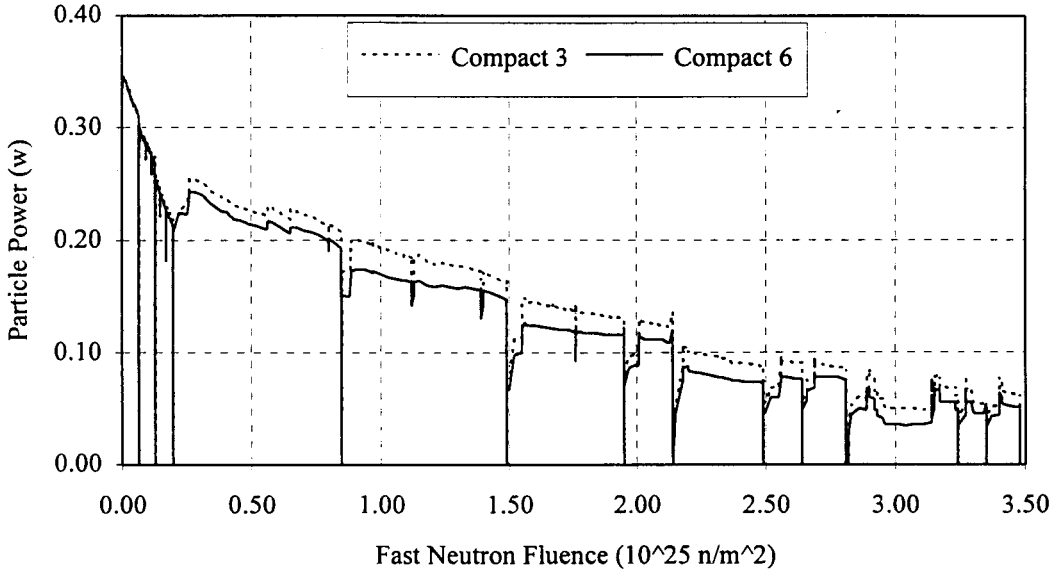

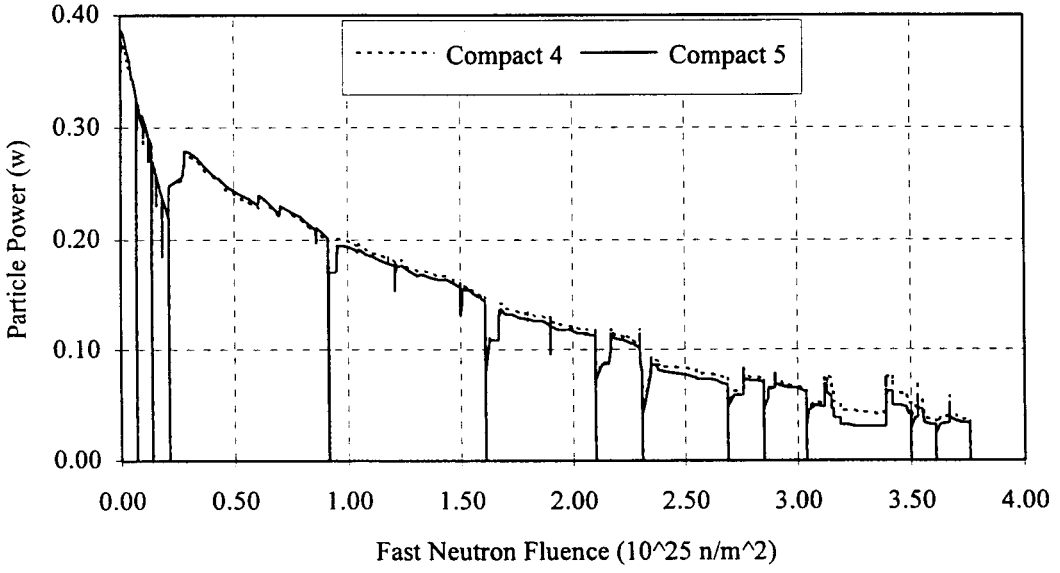

Figure 3.1-7a NPR 1 capsule regions 3 & 4 fuel particle power as function of fast neutron fluence

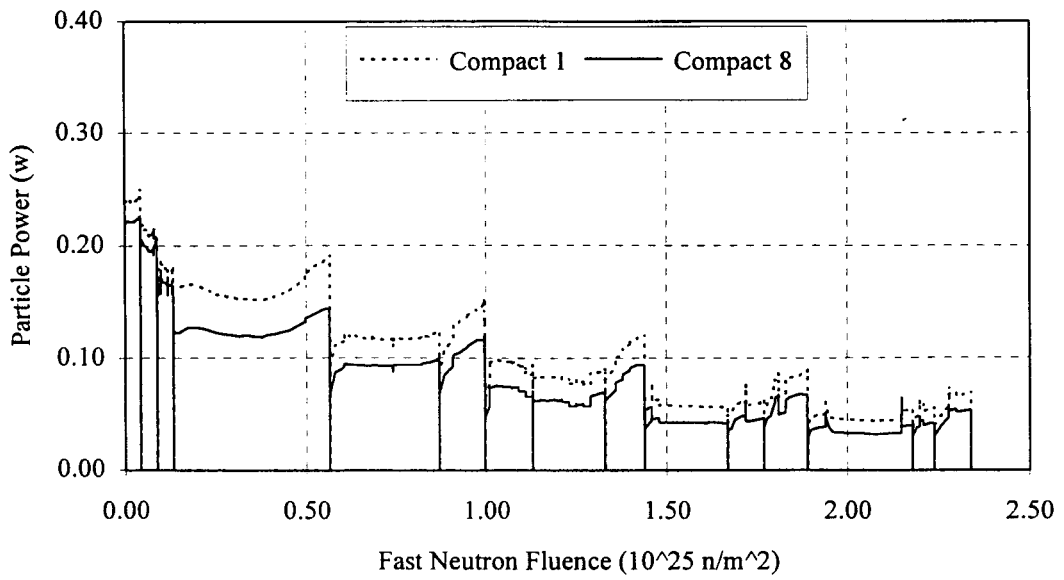

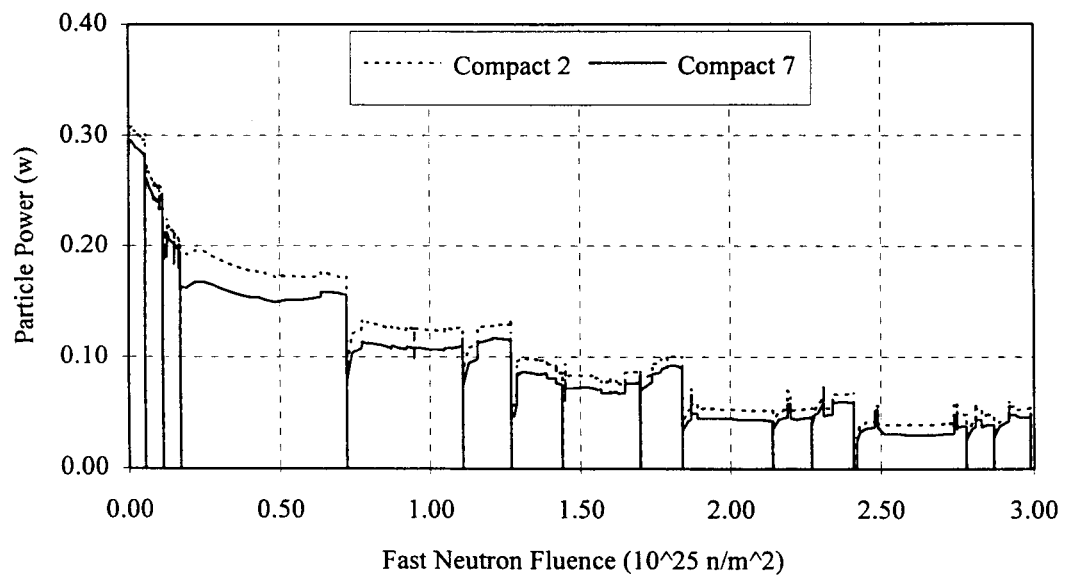

Figure 3.1-7b NPR 2 capsule regions 1 & 2 fuel particle power versus fast neutron fluence

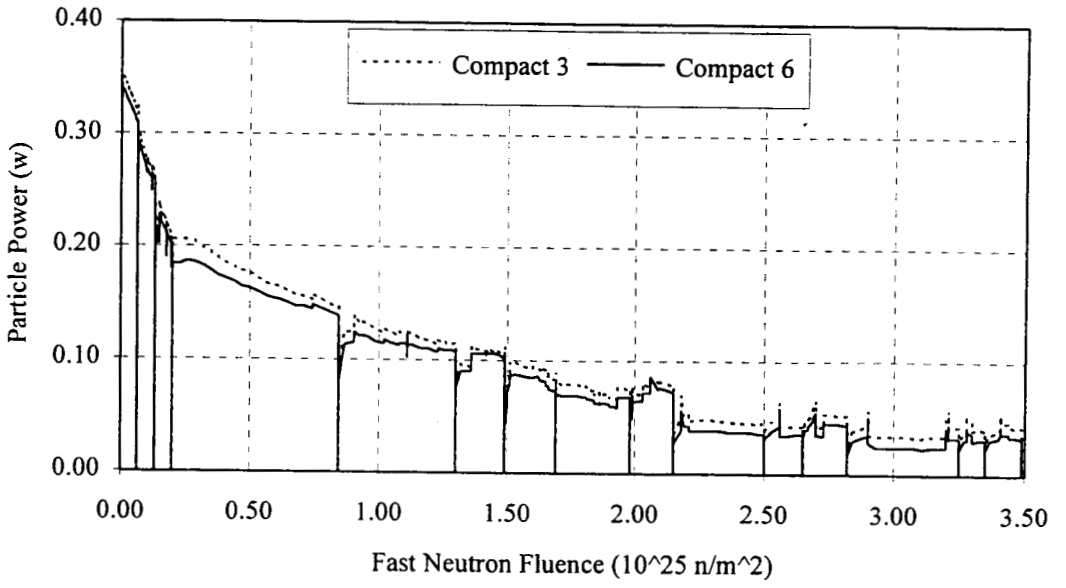

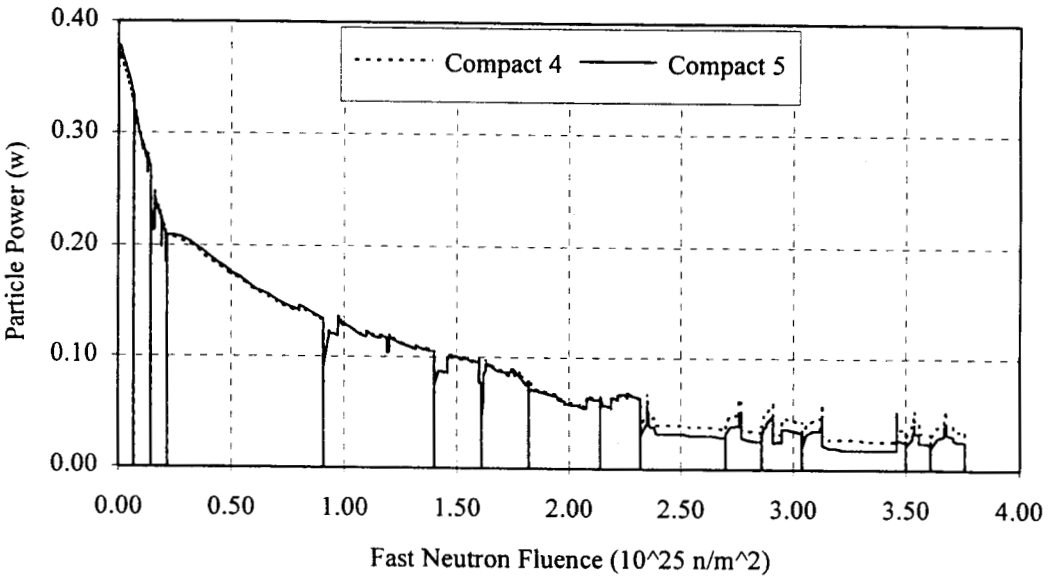

Figure 3.1-7b NPR 2 capsule regions 3 & 4 fuel particle power versus fast neutron fluence

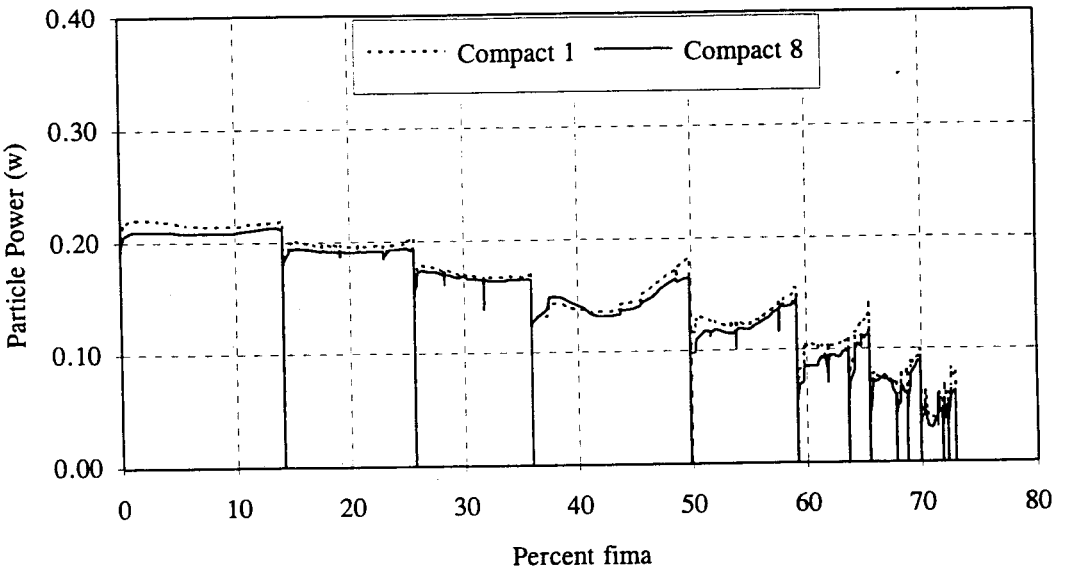

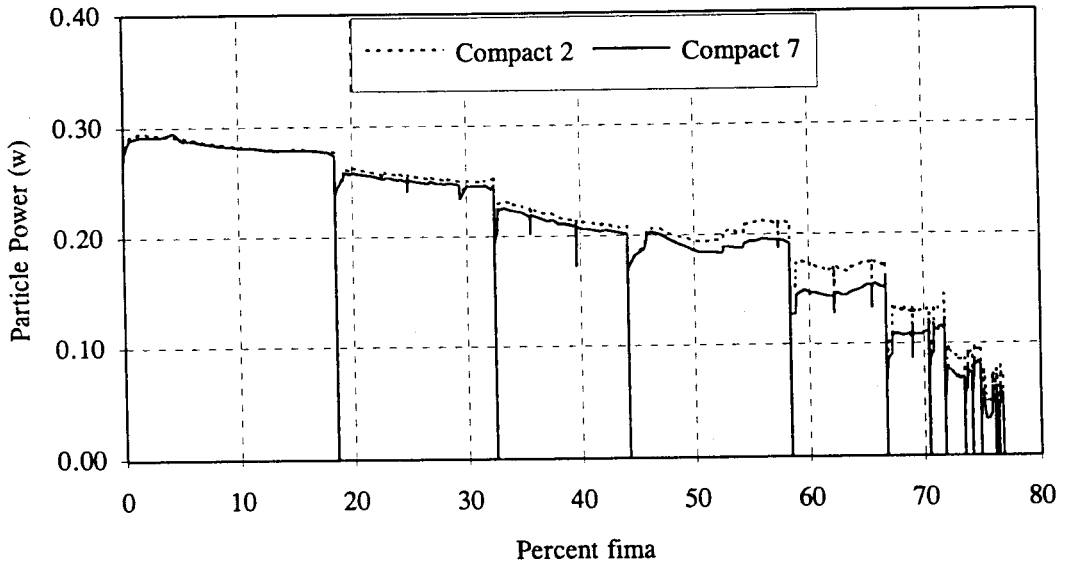

Figure 3.1-8a NPR 1 capsule regions 1 & 2 average particle power in fuel compacts as a function of burnup

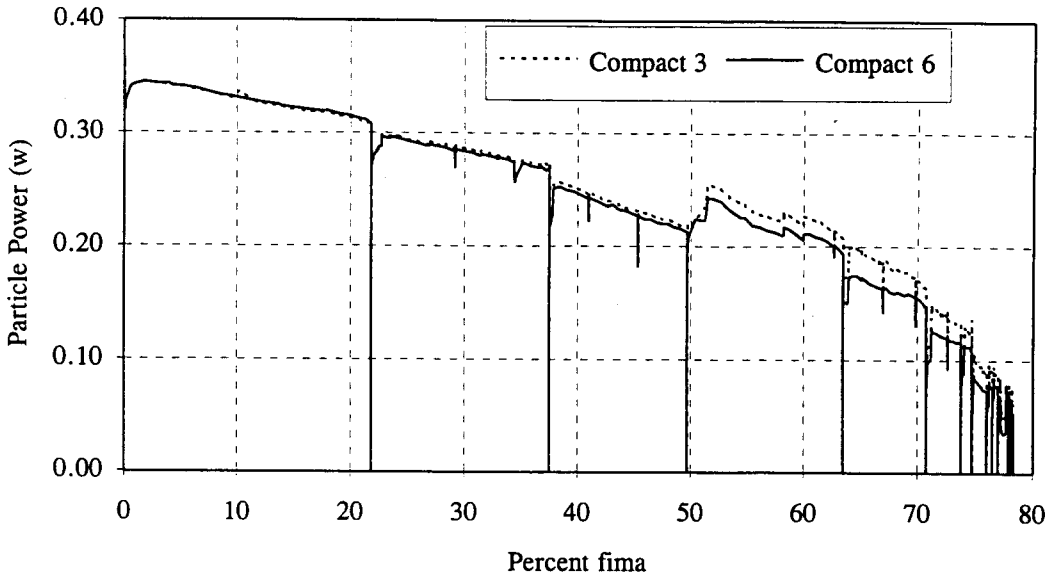

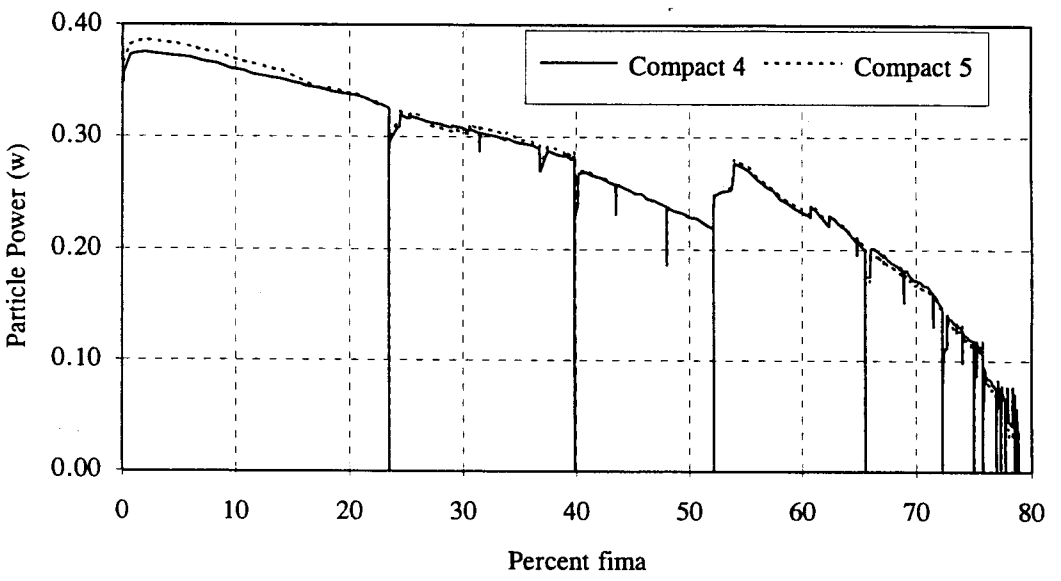

Figure 3.1-8a NPR 1 capsule regions 3 & 4 average particle power in fuel compacts as a function of burnup

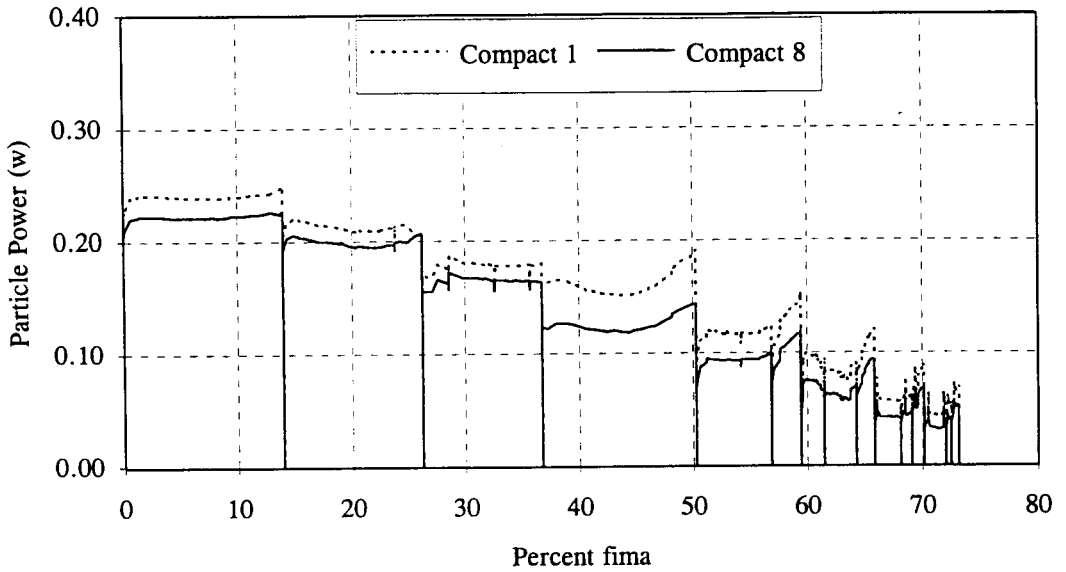

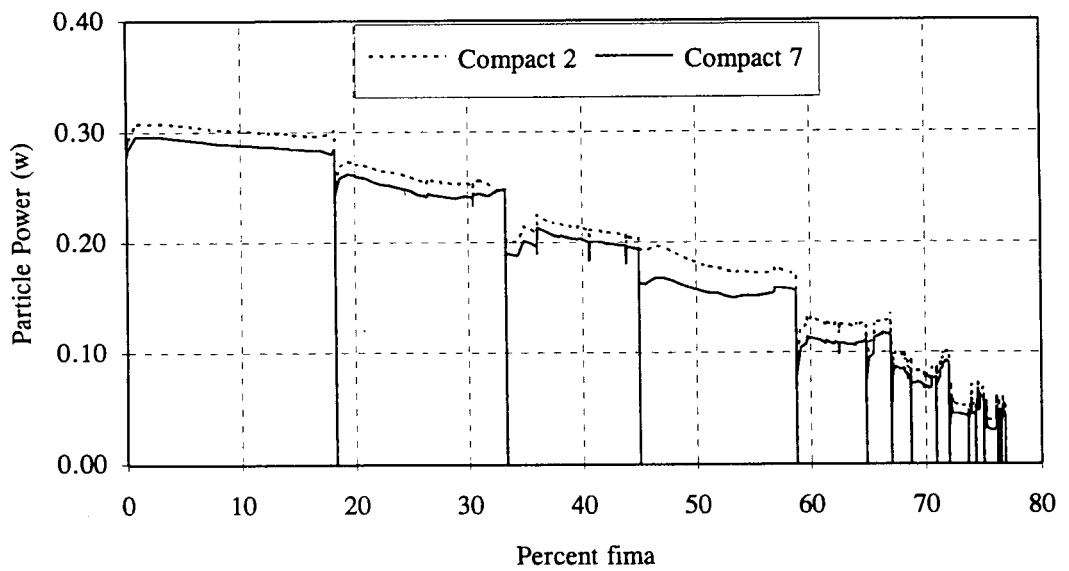

Figure 3.1-8b NPR 1 capsule regions 1 & 2 average particle power in fuel compacts as a function of burnup

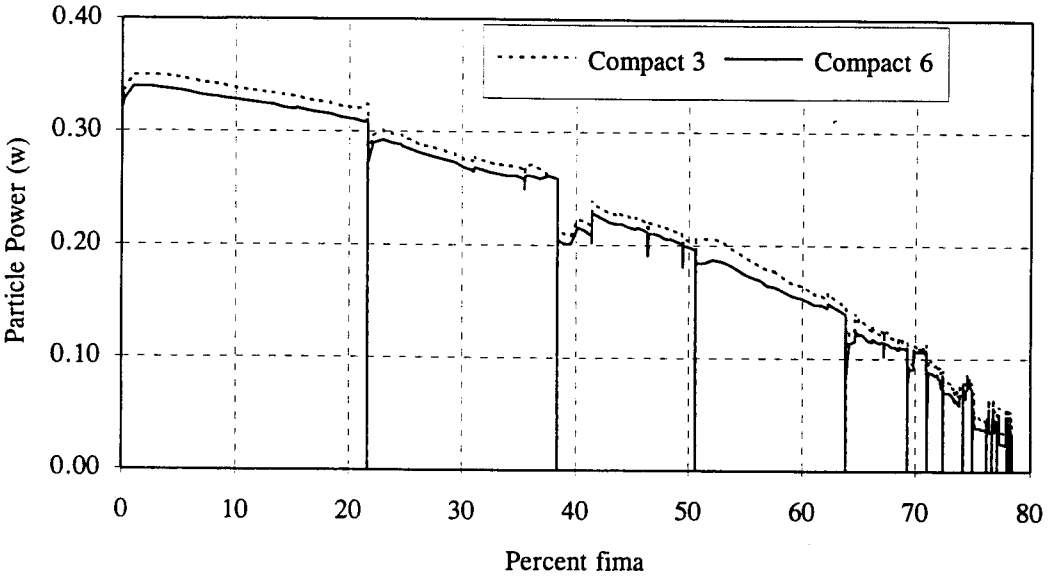

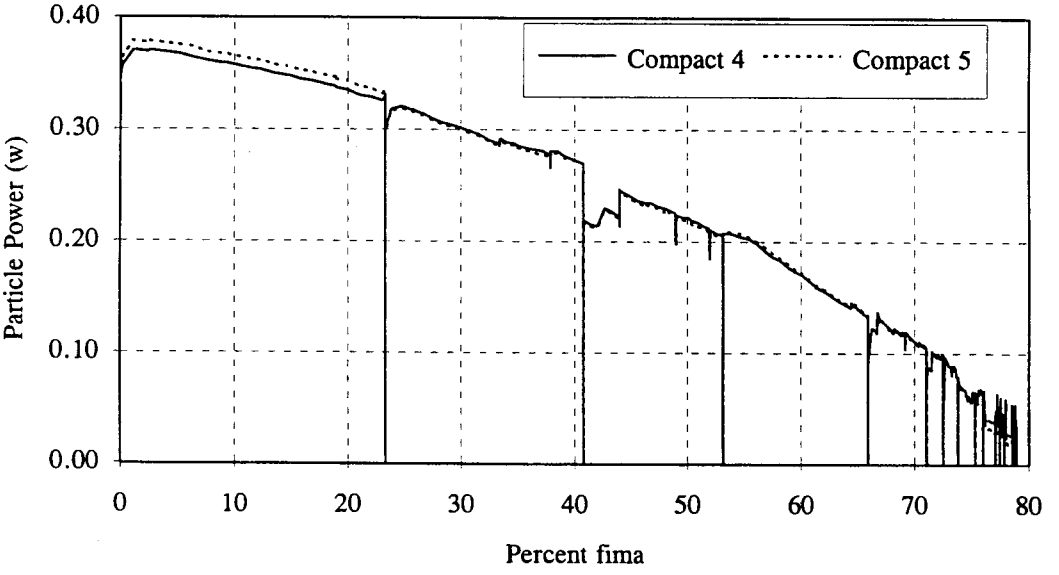

Figure 3.1-8b NPR 1 capsule regions 3 & 4 average particle power in fuel compacts as function of burnup

3.2 Determination of the Fission Gas Release Rate to Birth Rate Ratios (R/B)

The release rate to birth rate ratios were determined from direct measurements of the fission gases present in the sweep gas mixture and the birth rate using standard techniques. The measurements were carried out using the "grab sample" technique for sampling the sweep gas as required. Standard medical serum bottles were used to collect samples of the sweep gas exiting the fuel capsule assembly as shown in Figure 3.2.1 (Refs. 3.2.2 and 3.2.3). These gas samples were then transported in shielded containers to the Irradiated Fuels Examination Facility (IFEL) where they were immediately analyzed for fission gas inventory using a high-efficiency germanium gamma ray spectroscopy system. (Ref. 3.2.4). The birth rates were calculated with the CACA-2 fuel depletion code (Ref. 3.2.5) using the initial fuel loadings and one-group neutron-flux and cross-section data.

The reactor startup sequence was modified for these tests to minimize possible particle failures due to the rapid increases in the power generated in the fuel particles. Short hold times were incorporated in the sequence at reactor power levels of 10, 30, 50, 70 and 90 percent of full power. The sweep gas was sampled at each startup, and two samples per day were taken for the first five days of operation. For the remainder of each cycle each capsule was sampled three times per week.

3.3 Analysis of Flux Dosimeters

The NPR 1 and NPR 2 fuel assemblies each contained two sets of flux monitors during the eight cycle HFIR irradiation. One of the sets consisted of five sealed vanadium tubes each containing five individual monitors of titanium, nickel, iron, cobalt/vanadium, copper/manganese, and niobium. The useful threshold neutron energies for each of these monitors is presented in Table 3.3.1. The second monitor of each set consisted of a single 16 inch length of iron wire. Both vanadium capsules and the iron wire were contained within a 16 inch long platinum tube with an outer diameter of 0.090". The axial location of each vanadium capsule is shown in Figure 3.3.2. Following the in-cell removal of the monitor sets from the capsule assembly the two platinum tubes from each experiment were stored in IFEL hot cells in capped steel pipes until ready for processing.

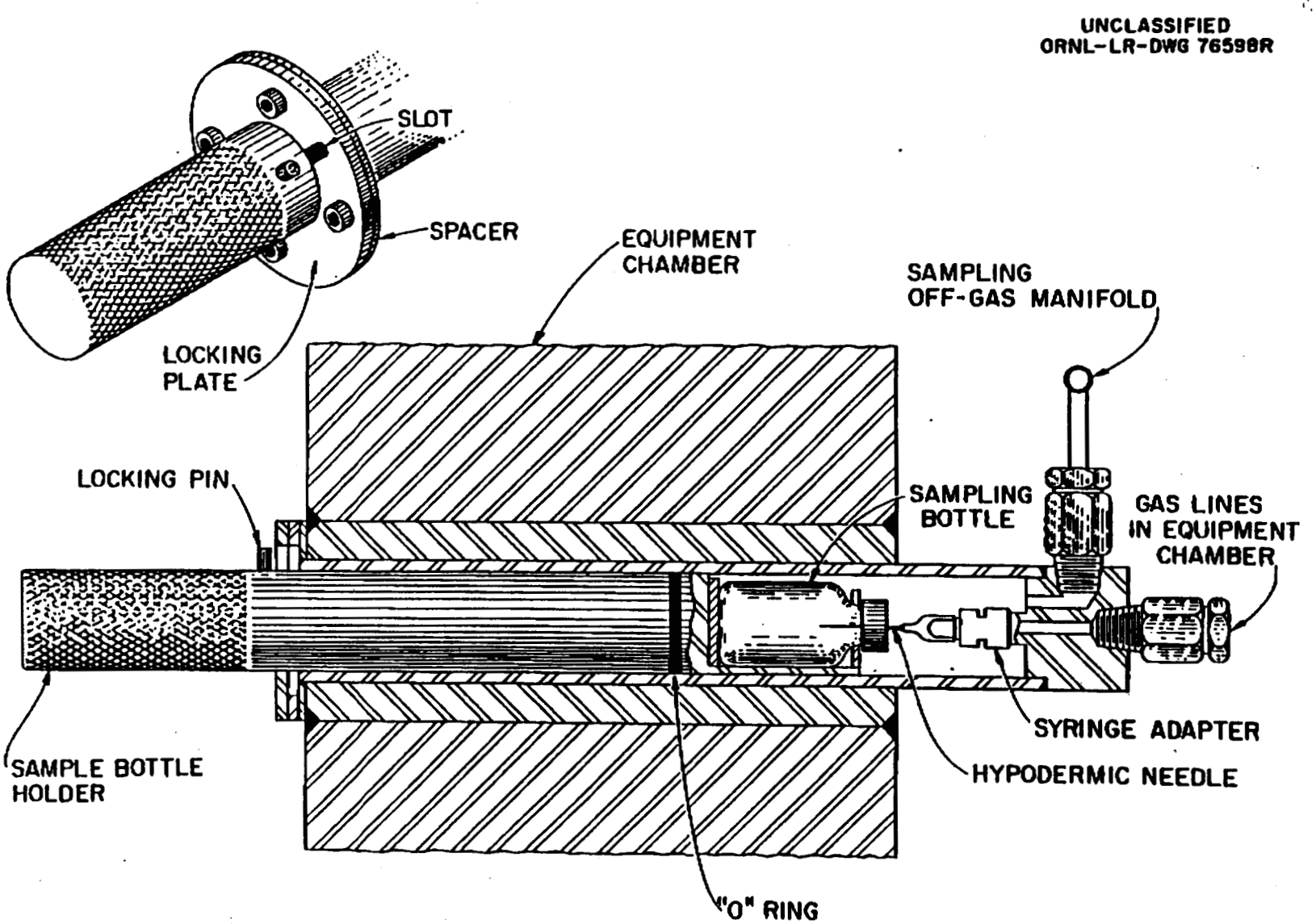

Figure 3.2.1 ORR poolside gas sampling station

Table 3.3.1 Flux monitor reactions and useful threshold energies

Flux Monitor	Reaction	Useful Threshold Energy
0.5Co/V	$Co(n,\gamma)Co^{60}$	Thermal
Nb	$Nb(n,n)Nb^{93m}$	0.5 MeV
Ni	$Ni(n,p)Co^{60}$	2.1 MeV
Fe	$Fe(n,p)Mn^{54}$	2.2 MeV
Ti	$Ti(n,p)Sc^{46}$	4.4 MeV
80.2Mn/Cu	$Cu(n,\alpha)Co^{60}$	5.0 MeV

3.3.1 Description

Ten vanadium dosimetry capsules, each containing six individual flux monitors, were prepared by the Analytical Chemistry Laboratory at Battelle Pacific Northwest Laboratories (PNL) for use in the NPR 1 and NPR 2 experiments. Each dosimetry capsule was approximately 8 mm in length and 2 mm in diameter and contained individual monitors made of iron, titanium, nickel, niobium, 80.2% manganese-copper, and 0.5% cobalt-vanadium. These monitors were in the form of small disks varying in length from 1 to 3 mm and in diameter from 1 to 1.5 mm, and were stacked inside the outer vanadium tubular capsule. The capsules were sealed by inert gas welding and then leak tested in boiling water. Following this each capsule was laser etched with an identification code.

Five of the vanadium capsules were then inserted into each of two 6.5 cm long by 2.3 mm diameter thin wall platinum tubes along with stainless steel spaces to position each capsules at prescribed distances along the length of the stack of fuel compacts. The ends of the platinum tube were closed by crimping to lock each capsule into place and to prevent any movement during the course of the irradiation experiment. One of the platinum tubes was then inserted into both the NPR 1 and NPR 2 fuel assemblies. The exact placement of each capsule within the platinum tube is shown in Fig. 3.3.1.

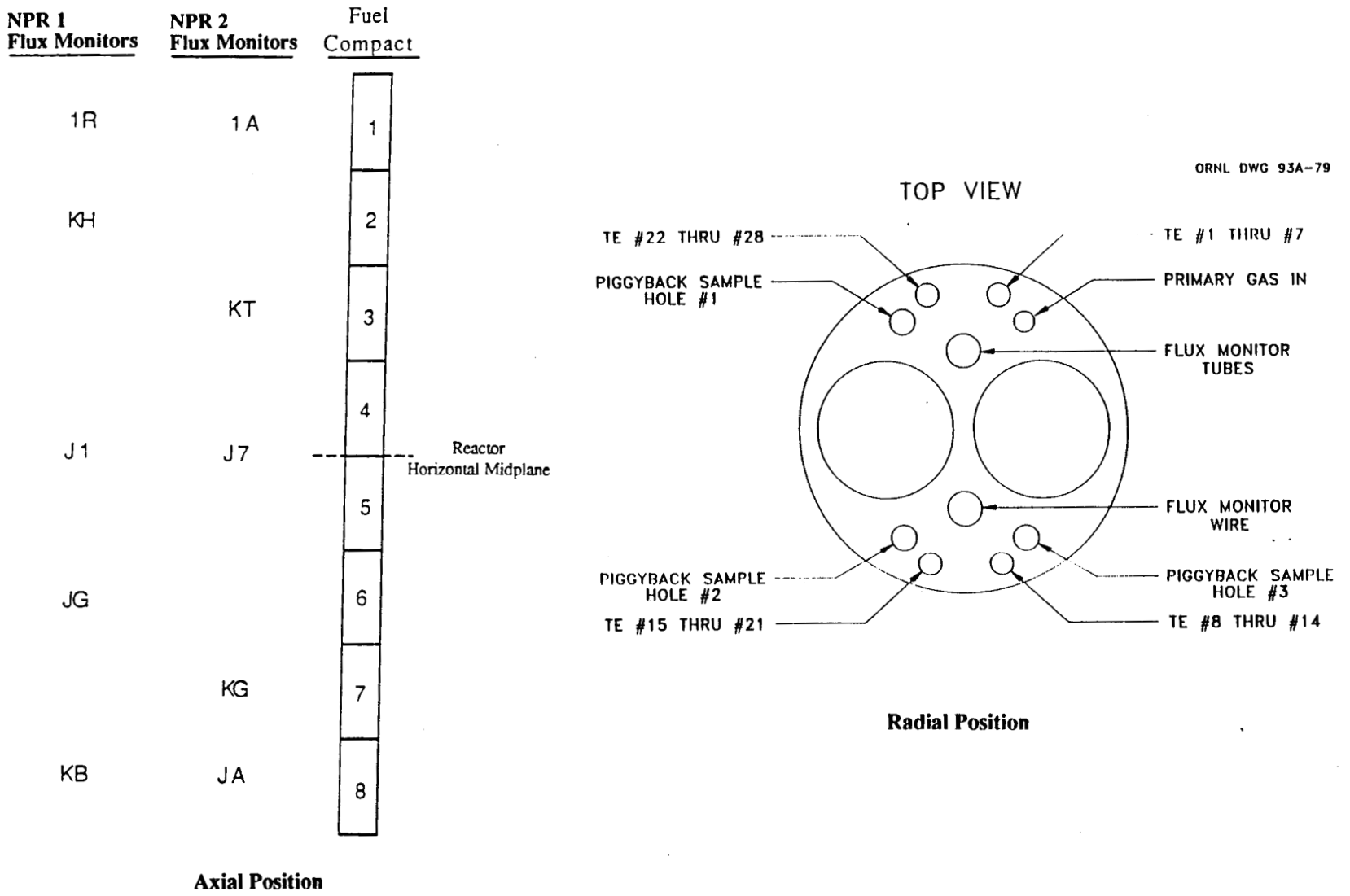

Figure 3.3.1 Location of platinum sheathed flux monitor tubes and iron wire in experiments NPR 1 and NPR 2

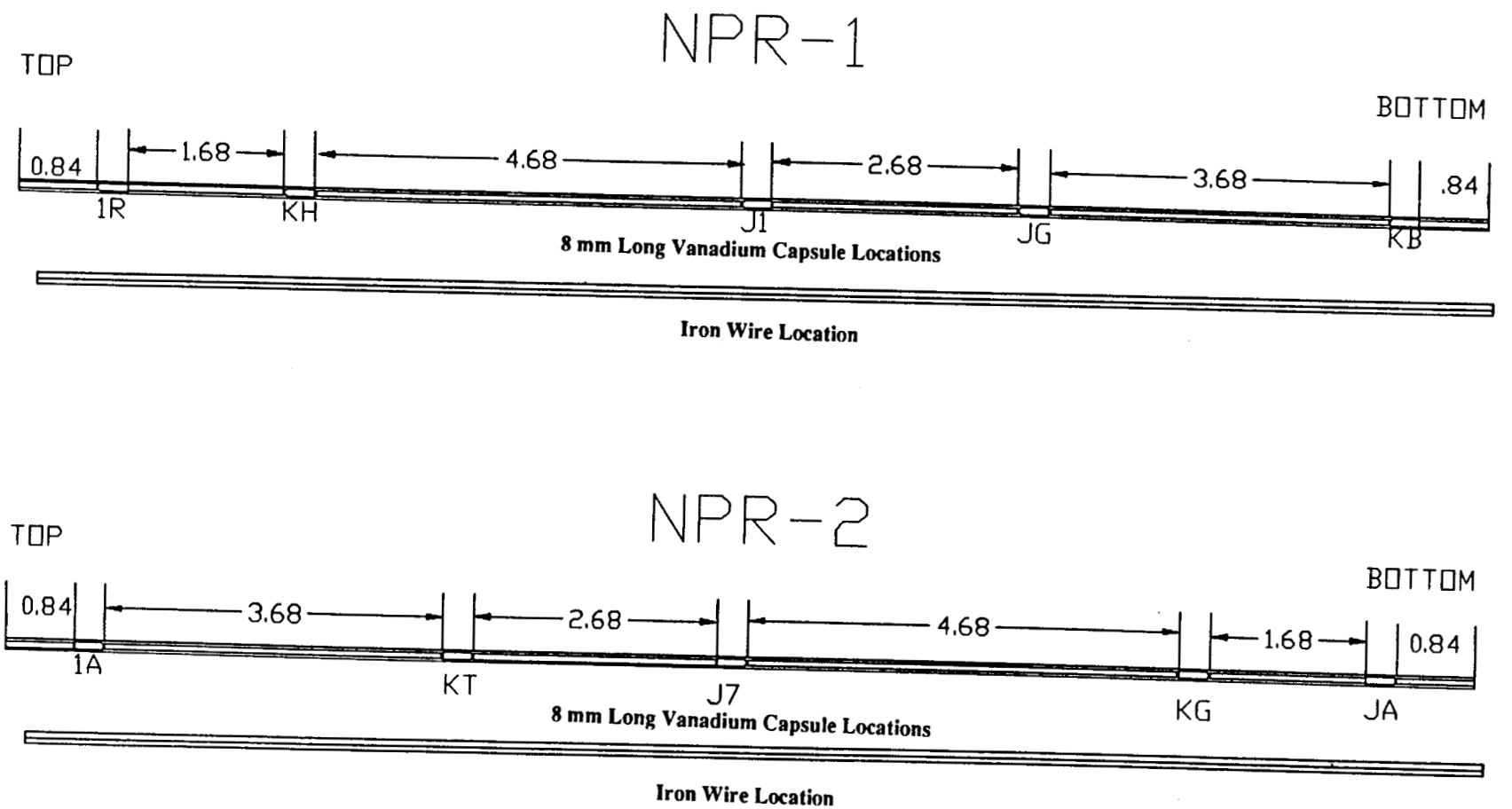

Figure 3.3.2 Location of vanadium dosimetry capsules and iron dosimetry wire in platinum tubes in experiments NPR 1 and NPR 2

Two additional platinum tubes with identical dimensions, but containing a 6.3 cm long by 0.5 mm diameter iron wire were also prepared. These additional flux monitors were also positioned within the two fuel assemblies. The location of both of the platinum tubes in NPR 1 and NPR 2 are shown in Fig. 3.3.2.

3.3.2 Disassembly

Following irradiation, the four platinum tubes containing the various monitors were removed from the fuel assemblies by remote operations in the building 3525 hot cell complex. Some difficulty was experienced with the mechanical removal of the tubes which resulted in considerable flexing and bending of the tubes. The mechanical distortion effectively obviated the use of the in-cell gamma ray scanner to inspect the longitudinal activity distribution. The scanner utilized an extremely small aperture to view the specimen and the bowing and deformation of the tubes made it impossible to maintain the specimen in the center of the aperture window.

Visual inspection revealed that the iron wire from the NPR 1 experiment was protruding slightly through the crimped end of its platinum tube. This was carefully removed and was found to be only the end segment of the wire monitor approximately six cm in length. Three other shorter pieces were removed in a like manner. Attempts to open the tube at each end using a small metal saw were unsuccessful due to the thin and pliable nature of the wall.

Following the unsuccessful attempts to remove the iron wire, a special jig was fabricated to hold the platinum tube during the cutting operation. Using the new holding jig, attempts were made to remove the vanadium capsules from the NPR 1 monitor tube. The two capsules were removed (labeled 1R and KB in Fig. 3.3.1), but in this operation one of the capsules was cut into near one end. A section of the remaining outer tube was cut, but it has been impossible to remove the vanadium capsule from the distorted tube. Attempts to remove the remaining two capsules are continuing. It is anticipated that most of the radioactivity that would make outside handling difficult is associated with the stainless steel spacers. If these can be removed either by mechanical disassembly or by cutting it may make it possible to remove the remaining platinum tubes, along with the contained vanadium capsules, to the outside where disassembly can continue.

NPR 1 Flux Monitors

When NPR 1 flux monitor sets were removed from the storage pit it was noted that both of the platinum tubes were considerably distorted, probably caused by the handling during the original removal from the fuel capsule. The platinum tube was thin walled (0.005" dia.) and could have been easily damaged by the manipulator grips. On of the crimped ends of the tube containing the iron wire was observed to be so damaged that a portion of the iron wire was found to be protruding from the tube. The wire proved to be quite brittle and the operator was able to recover only sections of the wire in pieces of various lengths. Because the wire was removed in short pieces, all registration was lost and it was not possible to determine the position of the removed portions within the platinum tube during the irradiation phase of the experiment. .

The arrangement of the five vanadium capsules and the separating spacers is shown in Fig. 3.3.2. All of the individual capsules were recovered, but the KH capsule was lost during the in-cell handling. These tubes are only 0.080" dia and 5/16" long and represent a challenge to the operator in handling with manipulator grips designed for mare massive objects. Because of this small size, it was necessary to perform all operations using the smallest available tweezers fitted with manipulator grips. The small size also necessitated that virtually all handling operations be carried out by the operator while observing with high power lens of the Kollmorgen viewing device.

The four capsules that were successfully recovered were opened by mounting the tubes in a motorized drill chuck turning at low speeds and filling off the end using a thin blade file. While all four of the recovered capsules were successfully opened three of the six individual wires from the center monitor capsule (J1) were lost. The individual monitor wires are so small that it is difficult to see them through the cell window with the unaided eye.

In many cases the wires were found to be partially welded together and it was necessary to use mechanical means to separate them. Counting has been completed on all monitor wires from the NPR 1 fuel assembly. With one exception the activity levels resulted in good counting statistics. The single exception were the cobalt/vanadium wires which were too radioactive to count with any degree of assurance in the results. A gain shift was observed in the analyzing amplifier at the extremely high counting rate which casts some

doubt on the results. Because of this problem only one of the cobalt/vanadium wires was analyzed. This was the monitor from the J1 set and the results, along with the others from the NPR 1 monitor sets is shown in Table 3.2.2.

There is considerable ambiguity in the identification of certain of the monitors as several of the wires exhibit activities not normally attributable to that particular monitor composition. If there had been no melding or blending of the individual wires an accurate determination of the weights and then comparing that with the weights recorded at the time the capsules were sealed would be sufficient to uniquely identify each of the six wires. With the exception of the cobalt/vanadium monitors all of the remaining monitors were accurately weighed on a calibrated microbalance. These post irradiation weights are also listed in Table 3.3.2. However, because of the melding problem among the NPR 1 flux monitors this weight determination was not sufficient to determine the identity of the individual monitor wires. For those monitors for which an identification is shown in Table 3.3.2, the determination was based on the predominant spectral lines.

All of the spectral analysis was carried out using the vertical counting system in the IFEL. This system was calibrated using a NIST-traceable standard point source of mixed isotopes in the same geometry in which the wires were analyzed. The results are listed in Table 3.3.2.

It is obvious that there is a problem with the Mn/Cu monitor as Mn-54 appears in the spectrum of most of the monitors. It is interesting to note that PNL reported considerable melting of this type monitor in their analysis of the HRB-21 flux monitors. Evidence of both Co-60 and Nb-93m also appear on each sample, however there may be some doubt about the ubiquitous appearance of niobium. The presence of metastable state of Nb-93 is determined by strength of the 16 keV X-ray line. This low energy is not only difficult to measure accurately, but is in the region populated by many other X-ray lines as well as high background due to the Compton scattered photons.

A number of wires exhibited impurity activities, notably Zn-65, Ag-110m, Sb-124, and Ta-182. The tantalum is always associated with the niobium as a minor impurity.

NPR 2 Flux Monitors

The problem with melding of the individual monitors from the NPR 2 experiment was

not as severe as was observed with the NPR 1 monitor sets. This can be explained by the fact that the NPR 2 capsule was operated at a lower temperature. All five of the vanadium capsules were successfully recovered and opened. Only one of the individual monitors was lost during the in-cell handling. This was the nickel monitor from the JA capsule.

The results are listed in Table 3.3.3 which includes the identification of the monitors. This identification is based on post-irradiation weights as well as the observed spectral lines.

Table 3.3.2 NPR 1 Flux monitor data

Monitor Wire	Net Weight	Tentative Assignment	Isotope	Activity
1R-1	Activity Level too High to Analyze			
1R-2	2.898 mg	Unknown	Sc-46	0.014 μCi
			Mn-54	0.275
			Co-57	0.291
			Co-58	4.025
			Co-60	4.381
			Zn-65	2.397
			Nb-93m	0.105
1R-3	3.965 mg	Unknown	Mn-54	2.209 μCi
			Co-57	0.002
			Co-58	0.012
			Fe-59	0.035
			Co-60	0.644
			Zn-65	0.749
			Nb-93m	0.073
			Ag-110m	0.026
1R-4	2.200 mg	Niobium	Sc-46	0.002 μCi
			Mn-54	0.025
			Co-58	0.004
			Co-60	0.011
			Nb-93m	38.24
			Nb-94	1.168
			Nb-95	0.774
			Ta-182	0.037

Table 3.3.2 NPR 1 Flux monitor data (continued)

Monitor Wire	Net Weight	Tentative Assignment	Isotope	Activity
1R-5	1.818 mg	Unknown	Sc-46	0.016 μCi
			Mn-54	9.559
			Fe-59	0.217
			Co-60	3.208
			Zn-65	0.043
			Nb-93m	0.252
1R-6	2.142 mg	Unknown	Sc-46	0.008 μCi
			Mn-54	5.441
			Fe-59	0.106
			Co-60	0.836
			Zn-65	0.076
			Nb-93m	0.128
KH	Entire Capsule Lost during In-Cell Handling			
J1-1	4.792 mg	Unknown	Mn-54	0.572 μCi
			Co-60	93.02
			Nb-93m	1.387
			Nb-94	0.943
			Nb-95	1.136
J1-2	Activity Level too High to Analyze			
J1-3	3.262 mg	Unknown	Sc-46	0.040 μCi
			Mn-54	9.559
			Co-57	0.441
			Co-58	4.100
			Co-60	8.958
			Zn-65	9.706
			Nb-93m	0.231
J1-4	Sample lost during in-cell handling			
J1-5	Sample lost during in-cell handling			
J1-6	'Sample lost during in-cell handling			
JG-1	Activity Level too High to Analyze			

Table 3.3.2 NPR 1 Flux monitor data (continued)

Monitor Wire	Net Weight	Tentative Assignment	Isotope	Activity
JG-2	1.234 mg	Unknown	Sc-46	0.075 μCi
			Mn-54	0.446
			Co-57	0.246
			Co-58	2.793
			Co-60	49.78
			Zn-65	1.076
			Nb-93m	0.745
JG-3	3.033 mg	Niobium	Sc-46	0.005
			Mn-54	0.089
			Co-57	0.021
			Co-58	0.217
			Co-60	0.427
			Zn-65	0.041
			Nb-93m	46.43
			Nb-94	1.451
			Nb-95	1.429
			Ta-182	0.041
JG-4	1.966 mg	Unknown	Mn-54	1.105
			Co-57	0.184
			Co-58	1.941
			Co-60	34.69
			Zn-65	3.201
			Nb-93m	0.422
JG-5	3.947 mg	Unknown	Sc-46	0.040 μCi
			Mn-54	9.035
			Co-58	0.012
			Fe-59	0.257
			Co-60	4.199
			Zn-65	0.238
			Nb-93m	0.230
JG-6	1.451 mg	Unknown	Mn-54	0.962 μCi
			Co-57	0.361
			Co-58	3.656
			Co-60	5.698
			Zn-65	9.883
			Nb-93m	0.228
			Sb-124	0.015

Table 3.3.2 NPR 1 Flux monitor data (continued)

Monitor Wire	Net Weight	Tentative Assignment	Isotope	Activity
KB-1	2.155 mg	Titanium	Sm-46	0.903 μCi
			Mn-54	0.039
			Co-60	0.074
			Zn-65	0.232
			Nb-93m	0.159
			Ag-110m	0.012
KB-2	1.765 mg	Nickel	Mn-54	0.165 μCi
			Co-57	0.513
			Co-58	8.53
			Co-60	3.56
			Zn-65	6.215
			Nb-93m	0.178
			Sb-124	0.003
KB-3	1.039 mg (PNL)	Cobalt/Vanadium	Co-60	1.109 mCi
KB-4	1.290 mg	Niobium	Mn-54	0.006 μCi
			Co-60	0.007
			Nb-93m	31.46
			Nb-94	1.244
			Nb-95	1.062
			Ta-182	0.047
KB-5	1.410 mg	Iron	Mn-54	12.85 μCi
			Fe-59	0.374
			Co-60	0.912
			Nb-93m	0.137
KB-6	4.620 mg	Manganese/Copper	Mn-54	1.918 μCi
			Co-57	0.002
			Co-58	0.046
			Co-60	2.492
			Zn-65	1.678
			Nb-93m	0.080
			Ag-110m	0.087
			Sb-124	0.016

Table 3.3.3 NPR 2 Flux monitor data

Monitor Capsule	Net Weight	Tentative Assignment	Isotope	Activity
1A-1	Activity level too high to handle			
1A-2	3.744 mg	Iron	Mn-54	10.51 μCi
			Fe-59	0.198
			Co-60	0.775
1A-3	2.711 mg	Nickel	Co-57	0.344 μCi
			Co-58	4.168
			Co-60	3.076
			Zn-65	3.923
			Nb-93m	0.244
1A-4	2.461 mg	Niobium	Mn-54	0.004 μCi
			Co-60	0.007
			Nb-93m	39.98
			Nb-94	1.176
			Nb-95	0.603
			Ta-182	0.032
1A-5	2.138 mg	Titanium	Sc-46	0.402 μCi
			Mn-54	0.100
			Co-60	0.047
			Zn-65	0.072
			Nb-93m	0.019
			Ag-110m	0.007
1A-6	6.205 mg	Manganese/Copper	Mn-54	0.488 μCi
			Co-58	0.005
			Co-60	0.619
			Zn-65	0.456
			Nb-93m	0.024
			Ag-110m	0.021
			Sb-124	0.004
KT-1	Activity level too high to handle			
KT-2	3.202 mg	Nickel	Mn-54	0.040 μCi
			Co-57	0.430
			Co-58	3.705
			Co-60	8.290
			Zn-65	7.309

Table 3.3.3 NPR 2 Flux monitor data (continued)

Monitor Wire	Net Weight	Tentative Assignment	Isotope	Activity
KT-3	2.803 mg	Niobium	Sc-46	0.002 μCi
			Mn-54	0.009
			Co-60	0.025
			Nb-93m	5.738
			Nb-94	1.757
			Nb-95	1.336
			Ta-182	0.028
KT-4	1.975 mg	Titanium	Sc-46	0.535 μCi
			Mn-54	0.089
			Co-57	0.001
			Co-58	0.008
			Co-60	0.153
			Zn-65	0.464
			Nb-93m	0.013
			Ag-110m	0.009
			Sb-124	0.001
KT-5	4.006 mg	Iron	Mn-54	1.183 μCi
			Fe-59	0.255
			Co-60	2.749
			Zn-65	0.085
KT-6	5.788 mg	Manganese/Copper	Mn-54	2.102 μCi
			Co-58	0.010
			Fe-59	0.031
			Co-60	2.022
			Zn-65	1.494
			Ag-110m	0.024
J7-1	5.736 mg	Manganese/Copper	Mn-54	1.221 μCi
			Co-57	0.001
			Co-58	0.008
			Fe-59	0.012
			Co-60	1.080
			Zn-65	1.812
			Nb-93m	0.060
			Ag-110m	0.026
			Sb-124	0.005
J7-2	Activity level too high to handle			

Table 3.3.3 NPR 2 Flux monitor data (continued)

Monitor Wire	Net Weight	Tentative Assignment	Isotope	Activity
J7-3	3.833 mg	Iron	Mn-54	1.459 μCi
			Fe-59	0.348
			Co-60	1.933
			Zn-65	0.035
			Nb-93m	0.216
J7-4	3.054 mg	Nickel	Mn-54	0.031 μCi
			Co-57	0.461
			Co-58	3.836
			Co-60	10.53
			Zn-65	9.224
			Nb-93m	0.251
J7-5	2.085 mg	Titanium	Sc-46	0.593 μCi
			Mn-54	0.222
			Fe-59	0.002
			Co-60	0.141
			Zn-65	0.403
			Nb-93m	0.020
			Ag-110m	0.008
J7-6	2.495 mg	Niobium	Mn-54	0.005 μCi
			Co-58	0.002
			Co-60	0.011
			Nb-93m	6.709
			Nb-94	1.920
			Nb-95	1.729
			Ta-182	0.024
KG-1	Activity level too high to handle			
KG-2	4.627 mg	Manganese/Copper	Mn-54	1.903 μCi
			Co-57	0.004
			Co-58	0.042
			Fe-59	0.034
			Co-60	0.924
			Zn-65	1.418
			Nb-93m	0.051
			Ag-110m	0.026
KG-3	2.184 mg	Niobium	Mn-54	0.004 μCi
			Co-60	0.006
			Nb-93m	47.60
		Nb-94		1.512
			Nb-95	0.928
			Ta-182	0.033

Table 3.3.3 NPR 2 Flux monitor data (continued)

Monitor Wire	Net Weight	Tentative Assignment	Isotope	Activity
KG-4	3.922 mg	Nickel	Mn-54	0.124 μCi
			Co-57	0.380
			Co-58	3.591
			Co-60	5.629
			Zn-65	3.287
KG-5	3.995 mg	Iron	Mn-54	9.918 μCi
			Co-57	0.004
			Co-58	0.021
			Fe-59	0.196
			Co-60	1.172
			Zn-65	0.051
			Nb-93m	0.104
KG-6	2.050 mg	Titanium	Sc-46	0.459 μCi
			Mn-54	0.056
			Co-58	0.002
			Co-60	0.056
			Zn-65	0.232
			Nb-93m	0.018
			Ag-110m	0.007
			Sb-124	0.001
JA-1	Activity level too high to handle			
JA-2	6.555 mg	Manganese/Copper	Mn-54	0.748 μCi
			Co-58	0.005
			Fe-59	0.006
			Co-60	0.731
			Zn-65	0.649
			Ag-110m	0.021
			Sb-124	0.003
JA-3	2.899 mg	Niobium	Mn-54	0.001 μCi
			Co-60	0.019
			Nb-93m	33.39
			Nb-94	1.176
			Nb-95	0.545
			Ta-182	0.031

Table 3.3.3 NPR 2 Flux monitor data (continued)

Monitor Wire	Net Weight	Tentative Assignment	Isotope	Activity
JA-4	2.246 mg	Titanium	Sc-46	0.361 μCi
			Co-57	0.005
			Co-58	0.065
			Co-60	0.093
			Zn-65	0.167
			Nb-93m	0.022
			Ag-110m	0.009
JA-5	4.143 mg	Iron	Mn-54	8.946 μCi
			Co-58	0.007
			Fe-59	0.162
			Co-60	1.015
			Zn-65	0.022
JA-6	Sample lost during handling			

3.4 Burnup Determination

Determination of the burnup of MHTGR fissile and fertile particles by radiochemical methods can be an expensive and laborious process that creates a significant amount of hazardous waste if more than a few particles are to be analyzed. One way of avoiding the radiochemical method is by measuring the inventory of several gamma emitting fission products in the particle. Once the inventory of several key isotopes is known, the burnup can be determined by making use of the radionuclides' decay constant fission yield. Since the measurement of the particle's inventory is already part of the PIE program, this method makes economical use of the collected data.

Rapid determination of a particle's inventory of several gamma emitting fission products was accomplished by using the Irradiated-Microsphere Gamma Analyzer (IMGA) device. Typically, a particle's inventory of ^{95}Zr, ^{103}Ru, ^{106}Ru, ^{137}Cs, ^{141}Ce, and ^{144}Ce was determined in several minutes using this device. The averaging of a large number of particle measurements provided a good mean value for the burnup calculation.

A single group neutronics model was used to determine a set of equations that relates the end of irradiation radionuclide inventory to the number of fissions that have taken place

during the course of the irradiation (Ref. 3.4.1). The fission rate is modelled by a set of test functions with adjustable parameters. A least squares minimization technique is used to find the best values for the parameters in the fission rate that leads to the least error between the measured and calculated end-of-irradiation inventories for the above radionuclides. Typically, the errors between the calculated and measured values for radionuclides were less than a few percent. A major strength of this technique is that it made use of all the collected data- both the radionuclide inventory and its standard deviation. This fact reduced the error introduced by the measurement of any one radionuclide and can point out possible losses of radionuclides. Finally, the standard deviation of the burnup was estimated. The technique can also determine the burnup as a function of time during the irradiation, subject to the limitations of the model.

3.5 Thermal Analysis

3.5.1 Fuel Compact Radial Temperature Distribution

The NPR capsules were modeled numerically using the HEATING 7.0 Thermal Transport Code. Results from the 3-dimensional analysis are presented for selected times during the irradiation of NPR-1 and NPR-2. Radial temperatures profiles in the compacts were extracted for various points in the irradiation. The axial location of the profiles corresponds to the horizontal midplane of each compact. The profiles represent beginning of cycle and end of cycle in both the PB and RB positions. These profiles are shown along the diameter of the fuel compact in each region. These are shown in Figures 3.5.1-1. Figures 3.5.1-2 is a sample histogram showing the fuel compact temperature-volume distribution (volume fraction) per temperature range at elapsed time = 101.517 d, corresponding to the beginning of the fourth HFIR cycle (cycle 302), the first cycle in the RB facility.

3.5.2 Piggyback specimen Temperatures

Estimates of the temperature at the surface of a piggyback particle have been made based on a r-z model developed for analysis by the HEATING 7.0 code. The intent of this

effort is to provide an estimate of the temperature drop between the piggyback particle surface and the graphite fuel body temperature (a measured quantity). This will contribute to any comparisons of fuel compact particle temperatures and piggyback particle temperatures that may be made. Note that the fuel compact temperatures presented in this report were generated using a model which assumes a uniform heat generation rate and thermal conductivity for the fuel compact. While the comparison may not be a clean one, the results of this piggyback model provide a starting point for estimating the piggyback kernel temperature during the test.

A representation of the geometric model is shown in Figure 3.5.2-1. In this model the fuel particle was taken to be a small cylinder as an approximation to take advantage of the available geometries in HEATING 7.0. It was assumed that the internal structure of the particle was sufficiently well behaved that the particle could be represented as a slug of heat generating material surrounded by a layer of H-451 graphite. The dependence of the surface temperature on sweep gas composition and internal particle power was determined assuming a fixed temperature (850 C) boundary condition. The temperature drop (ΔT) between the particle outer surface and the (graphite) boundary was determined as a function of particle power and sweep gas mix (see Table 3.5.2.1).

Table 3.5.2.1.
Temperature difference between the particle surface and the graphite fuel body for several particle powers and several sweep gas compositions.

	Particle Power	$\Delta T = T_{particle\ surface} - T_{graphite\ body}$ (°C)		
	(W)	100% He	50% He	0% He
RB gamma heating	0.5	70	81	112
	0.3	48	56	82
	0.2	37	44	67
	0.1	25	32	52
PB gamma heating	0.5	60	67	87
	0.3	38	42	56
	0.2	26	30	41
	0.1	15	17	25

The data in Table 3.5.2.1 is plotted in Figure 3.5.2-1 (PB) and 3.5.2-2 (RB).

An estimate of the operating temperatures of the surface of the piggyback particles may be made using the ΔTs listed in Table 3.5.2.1 and the time dependent measured temperatures of the graphite body. The locations in the graphite body where the temperatures were measured represent the axial midpoint of the individual fuel compacts. The location of the piggyback particles do not correspond to the thermocouple locations. In order to estimate the measured temperatures at the location of the piggyback particles required some amount of interpolation. A detailed time dependent interpolation was not attempted here. Instead the time averaged temperature of the graphite body for each irradiation cycle was calculated. These time averaged measured graphite temperatures at the axial locations of the compacts were then used to obtain the time averaged temperatures at the location of the piggyback samples by interpolation. Examining the table above, a minimum ΔT of approximately 20 C can be assumed to represent the particles during the entire irradiation. This value of ΔT was then added to the time averaged temperature computed for the location of the piggyback samples. The estimated particle surface temperatures are given in Tables 3.5.2.2 and 3.5.2.3.

Table 3.5.2.2 NPR 1 Capsule piggyback particle surface temperature estimates (C)

	Hole 1 Sample ID	Hole 2 Sample ID	Hole 3 Sample ID	Distance from Midplane (mm)	Cycle 1	Cycle 2	Cycle 3	Cycle 4	Cycle 5	Cycle 6	Cycle 7	Cycle 8	Test Ave temperature (C)
Top of capsule	11C1	11C2	11C3	193	664	678	694	640	640	665	660	651	662
	11S	11C4	11S	179	703	715	730	682	682	705	693	685	699
	11GA	11UA	11GA	150	783	791	804	768	787	763	755	737	774
	11S	11P2	11S	107	852	853	862	842	853	820	818	807	838
Graphite body 1	11V	11A2	11A3	93	856	854	860	846	853	821	823	814	841
	11UB	11GB	11UB	64	864	858	861	855	855	824	828	826	846
	11S	11M	11S	21	883	867	865	868	858	824	825	831	853
	11C1	11C2	11C3	7	886	868	865	868	857	823	823	823	851
HFIR Midplane													
	12C4	12A5	12I5	-7	888	868	865	869	855	821	820	815	850
	12Y	12T5	12X	- 21	890	869	865	870	854	819	818	807	849
	12GA	12UA	12GA	-64	870	841	855	844	829	797	797	785	827
Graphite body 2	12FC4	12F15	12M	-93	856	849	851	829	816	783	781	767	817
	12P5	12DP3	12P6	-107	852	847	851	824	812	779	774	756	812
	12UB	12GB	12UB	-150	775	782	794	755	755	723	721	691	749
	12A5	12T6	12WA5	-179	686	703	722	675	691	660	666	628	679
Bottom of capsule	12C5	12A6	12I6	-193	643	666	688	637	659	630	639	598	645

Note: The temperatures listed in table above are the minimum estimated cycle average particle surface temperatures
The maximum cycle average surface temperatures are approximately 40 degrees greater than the minimum.

Table 3.5.2.3 NPR 2 Capsule piggyback particle surface temperature estimates (C)

	Hole 1 Sample ID	Hole 2 Sample ID	Hole 3 Sample ID	Distance from Midplane (mm)	Cycle 1	Cycle 2	Cycle 3	Cycle 4	Cycle 5	Cycle 6	Cycle 7	Cycle 8	Test Ave Temperature
Top of capsule	21N5	Spacer	21K6	196	575	540	537	569	569	515	599	557	558
	21R6	21GA	21C5	182	585	547	541	574	574	519	603	559	563
	Spacer	21UB	Spacer	168	596	554	545	579	579	523	606	561	568
	21GA	21GC	21UA	138	618	568	554	590	531	613	565	523	570
Graphite body 1	Spacer	21UD	Spacer	110	631	574	556	596	535	6 21	573	534	578
	21UB	21GE	21GB	80	639	575	555	599	537	630	585	549	584
	Spacer	21UF	Spacer	52	647	593	570	615	553	651	611	576	602
	21N6	Spacer	Spacer	22	655	614	588	634	572	675	639	607	623
	11V	11A2	11A3	7	676	609	583	632	568	669	625	590	619
HFIR Midplane													
	22C4	22A5	22I5	-7	679	608	583	633	568	669	619	584	618
	12Y	12T5	12X	- 21	681	608	582	634	568	668	614	578	617
	22GA	22UA	22GA	-64	642	524	554	598	538	629	577	540	575
Graphite body 2	22FC4	22FI5	22M	-93	621	563	542	578	521	607	558	519	564
	22P5	22C3	22P6	-107	616	561	541	572	517	602	553	513	559
	22UB	22GB	22UB	-150	585	542	529	545	498	577	533	492	538
	22OA5	22T6	22WA5	-179	555	523	515	519	483	557	516	477	518
Bottom of capsule	22C5	22A6	22I6	-193	540	514	508	507	475	548	508	469	509

Note: The temperatures listed in table above are the minimum estimated cycle average particle surface temperatures The maximum cycle average surface temperatures are approximately 40 degrees greater than the minimum.

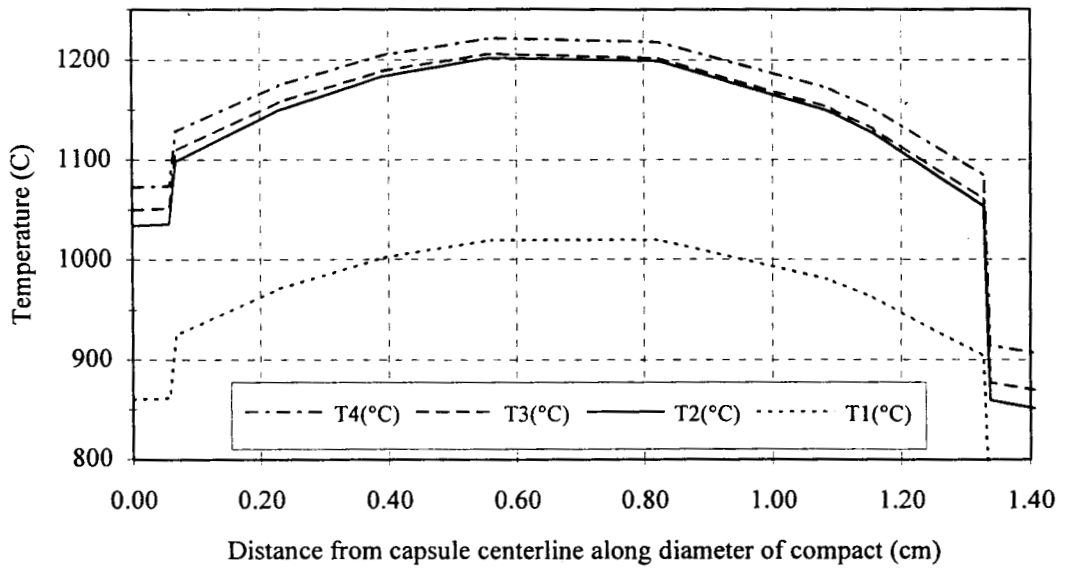

Figure 3.5.1-1a NPR-1 Radial temperature profiles in compacts 1-4 at 1.49 days of irradiation (start of cycle 1 in the PB position)

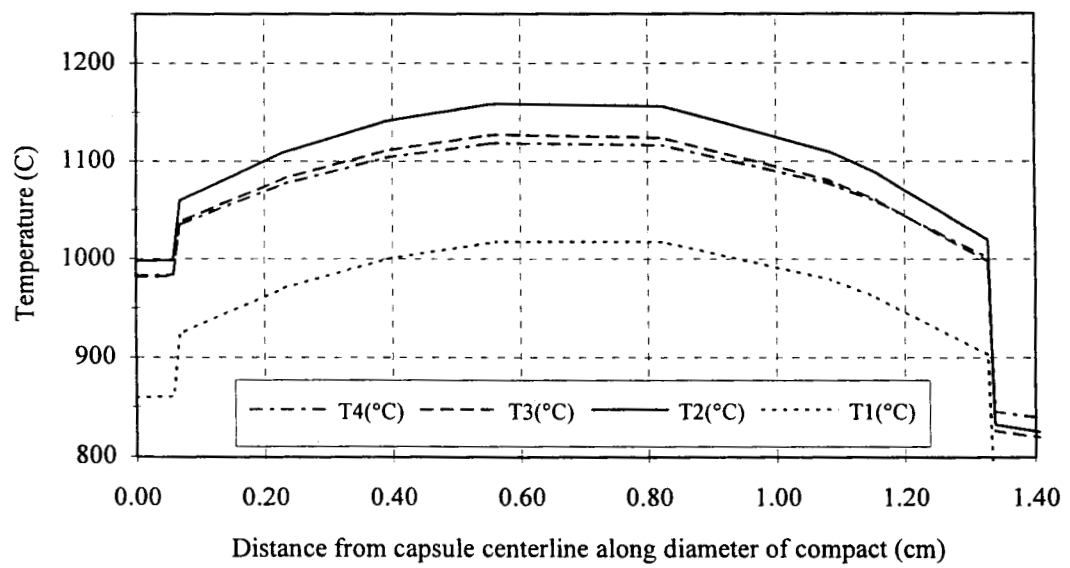

Figure 3.5.1-1b NPR-1 Radial temperature profiles in compacts 1-4 at 20.48 days of irradiation (end of cycle 1 in PB position)

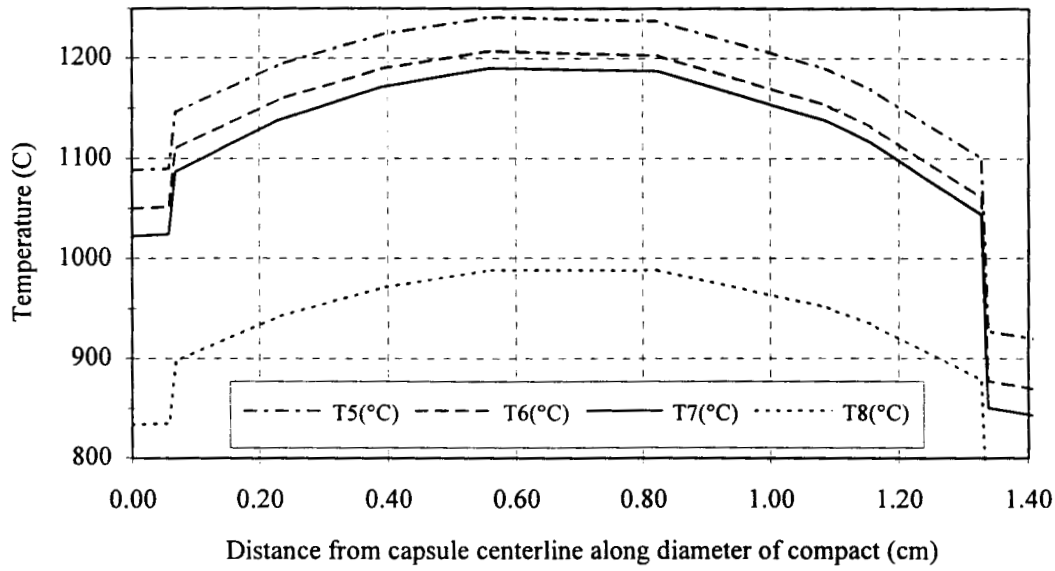

Figure 3.5.1-1c NPR-1 Radial temperature profiles in compacts 5-8 at 1.49 days of irradiation (start of cycle 1 in PB position)

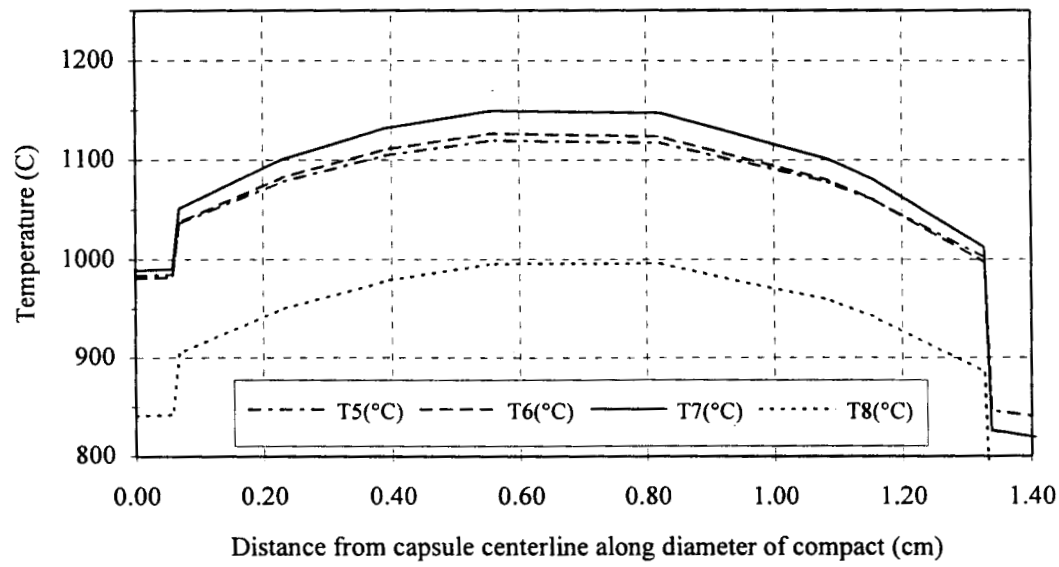

Figure 3.5.1-1d NPR-1 Radial temperature profiles in compacts 5-8 at 20.48 days of irradiation (end of cycle 1 in PB position)

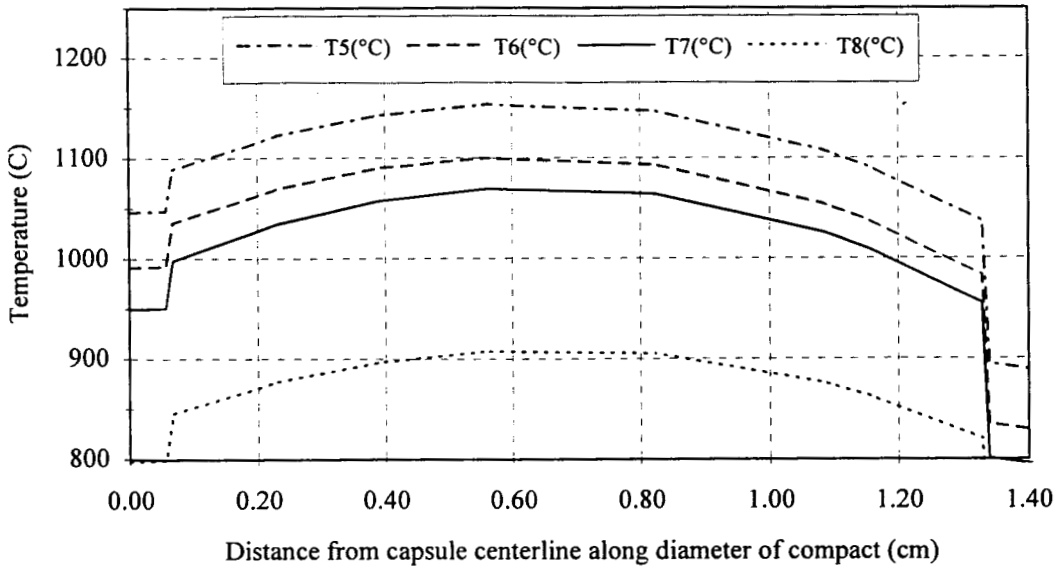

Figure 3.5.1-1e NPR-1 Radial temperature profiles in compacts 5-8 at 99.47 days of irradiation (start of cycle 1 in RB position)

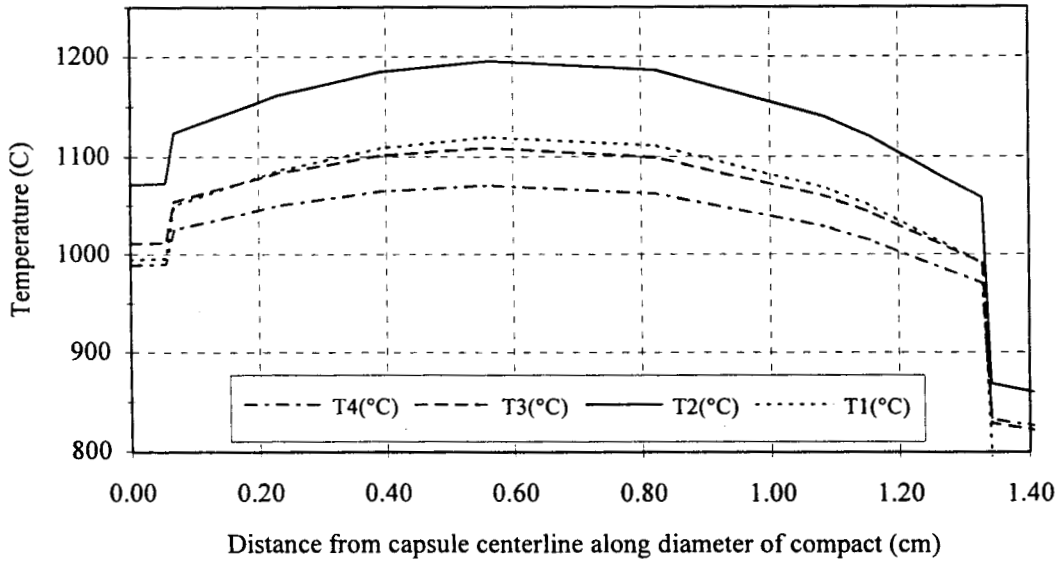

Figure 3.5.1-1f NPR-1 Radial temperature profiles in compacts 1-4 at 118.21 days of irradiation (end of cycle 1 in RB position)

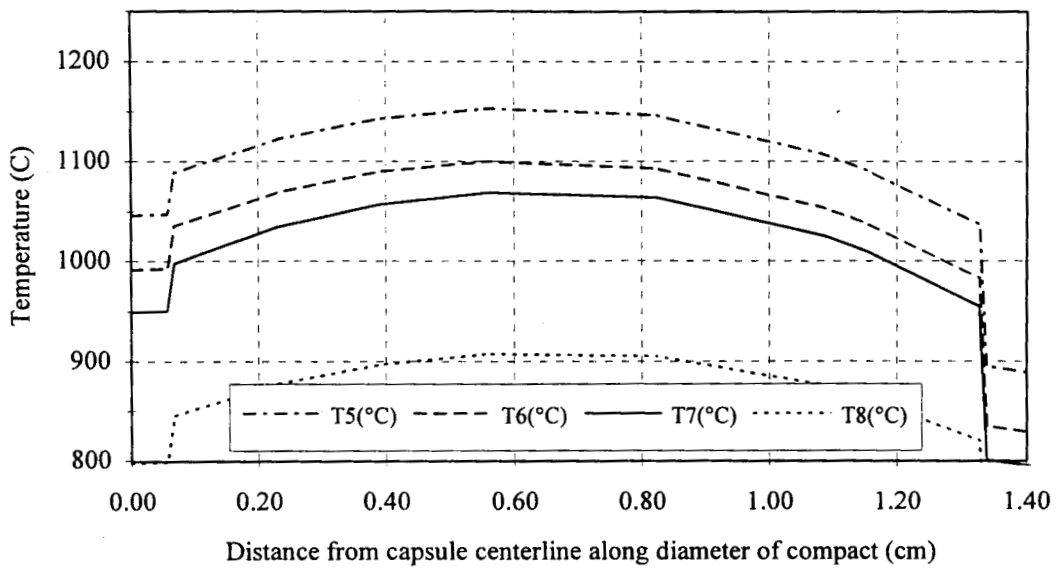

Figure 3.5.1-1g NPR-1 Radial temperature profiles in compacts 5-8 at 99.47 days of irradiation (start of cycle 1 in RB position)

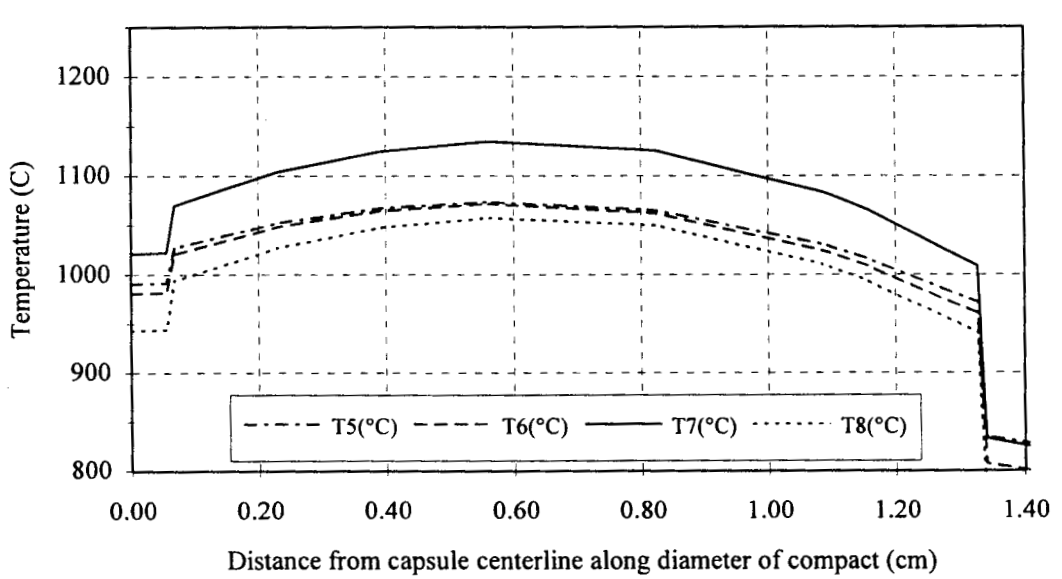

Figure 3.5.1-1h NPR-1 Radial temperature profiles in compacts 5-8 at 118.21 days of irradiation (end of cycle 1 in RB position)

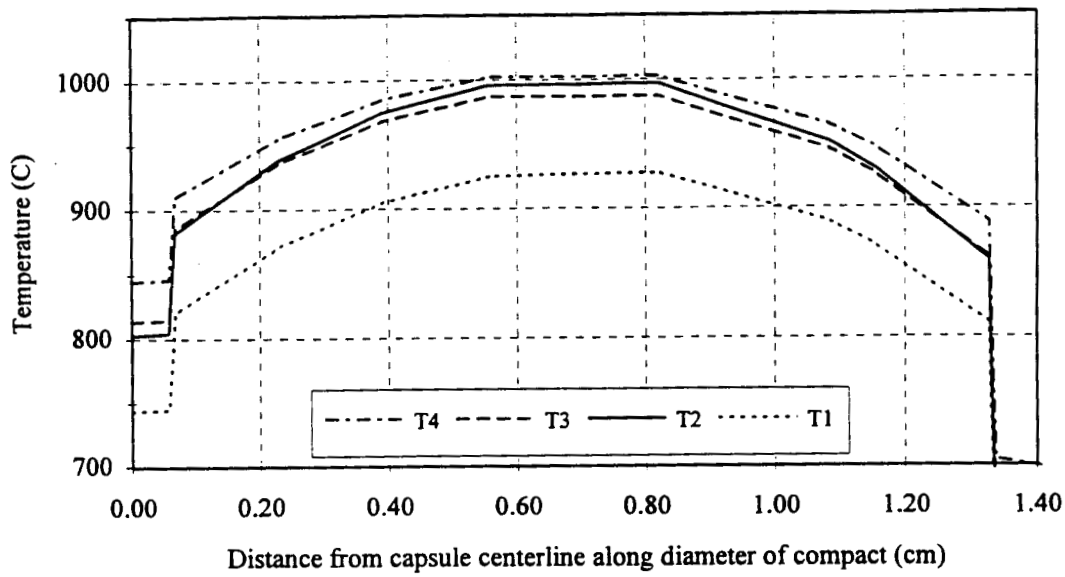

Figure 3.5.1-2a NPR-2 Radial temperature profiles in compacts 1-4 at 1.962 days of irradiation (start of cycle 1 in PB position)

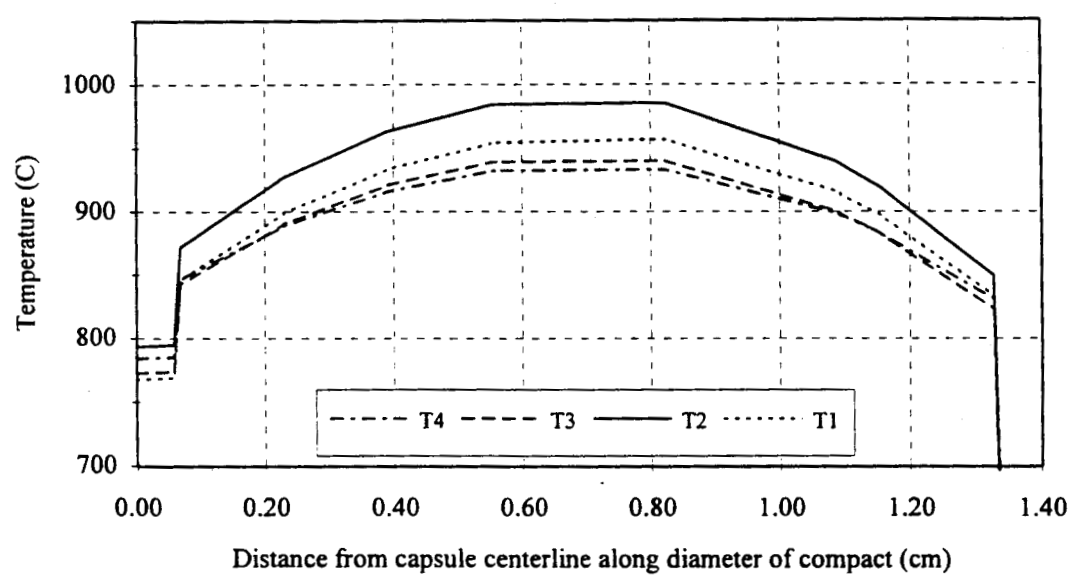

Figure 3.5.1-2b NPR-2 Radial temperature profiles in compacts 1-4 at 20.247 days of irradiation (end of cycle 1 in PB position)

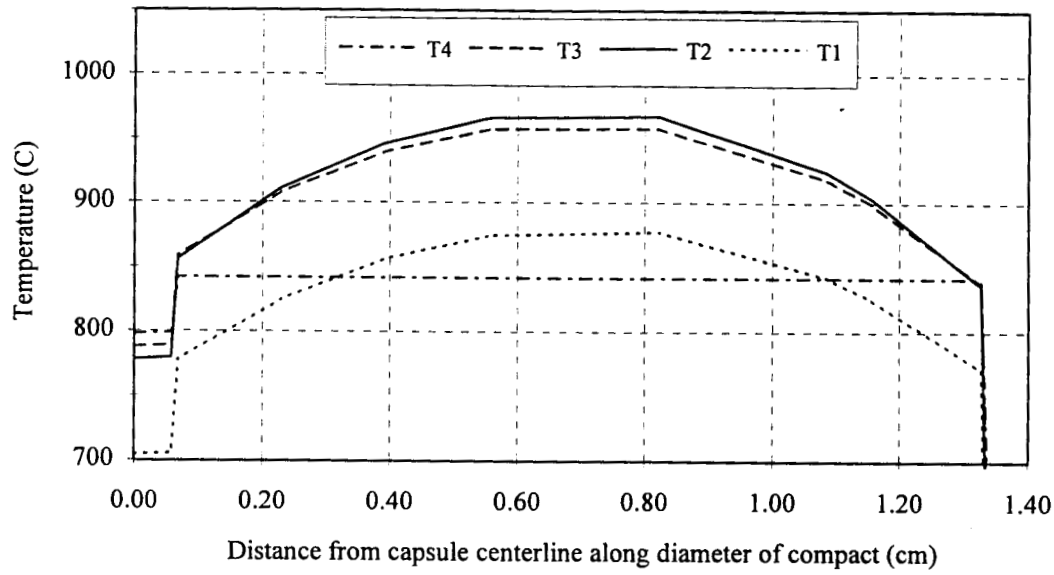

Figure 3.5.1-2c NPR-2 Radial temperature profiles in compacts 5-8 at 1.962 days of irradiation (start of cycle 1 in PB position)

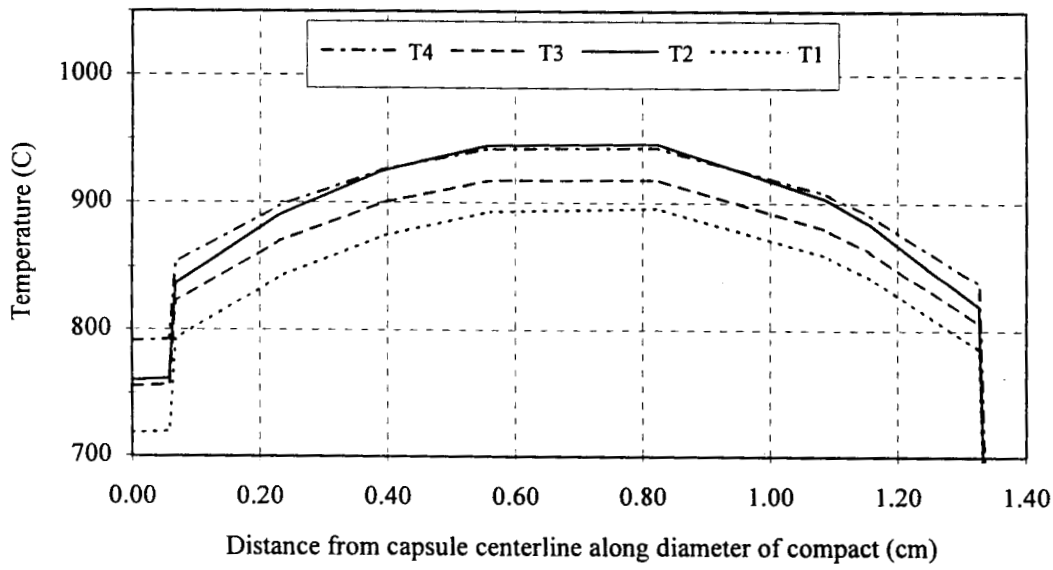

Figure 3.5.1-2d NPR-2 Radial temperature profiles in compacts 5-8 at 20.247 days of irradiation (end of cycle 1 in PB position)

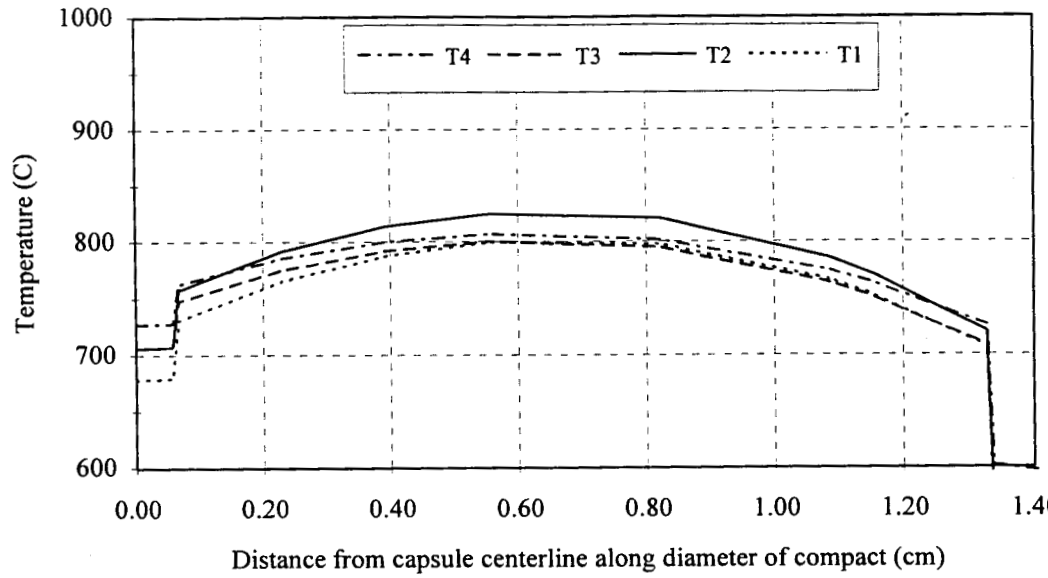

Figure 3.5.1-2e Radial temperature profiles in compacts 1-4 at 99.963 days of irradiation (start of cycle 1 in RB position)

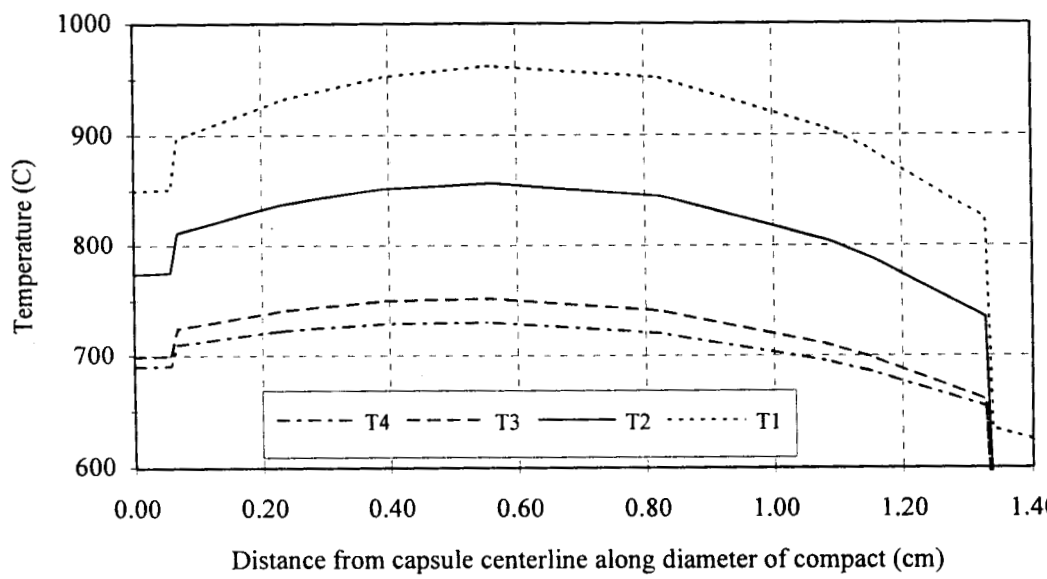

Figure 3.5.1-2f NPR-2 Radial temperature profiles in compacts 1-4 at 116.453 days of irradiation (end of cycle 1 in RB position)

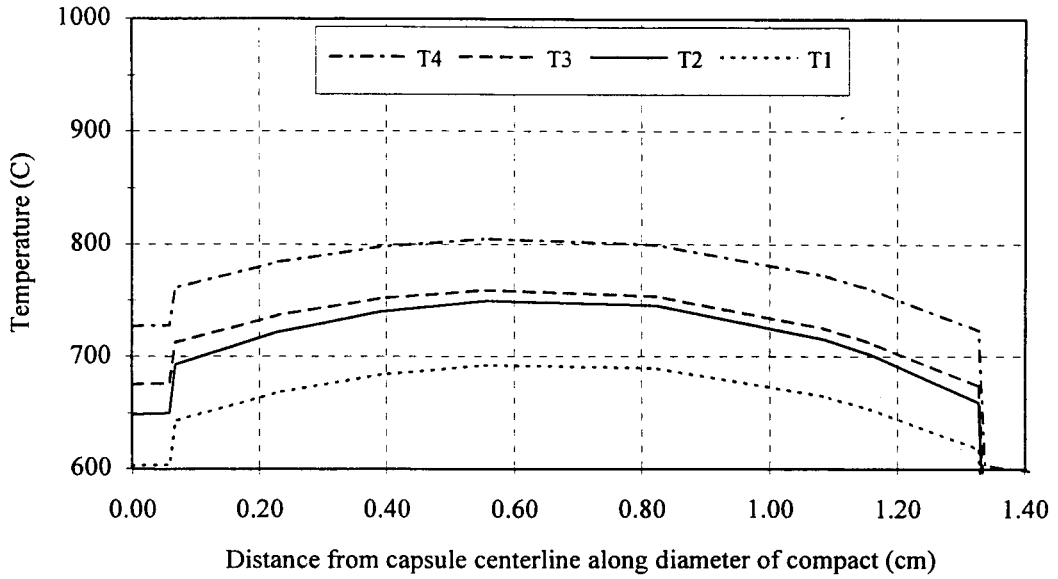

Figure 3.5.1-2g NPR-2 Radial temperature profiles in compacts 5-8 at 97.963 days of irradiation (start of cycle 1 in RB position)

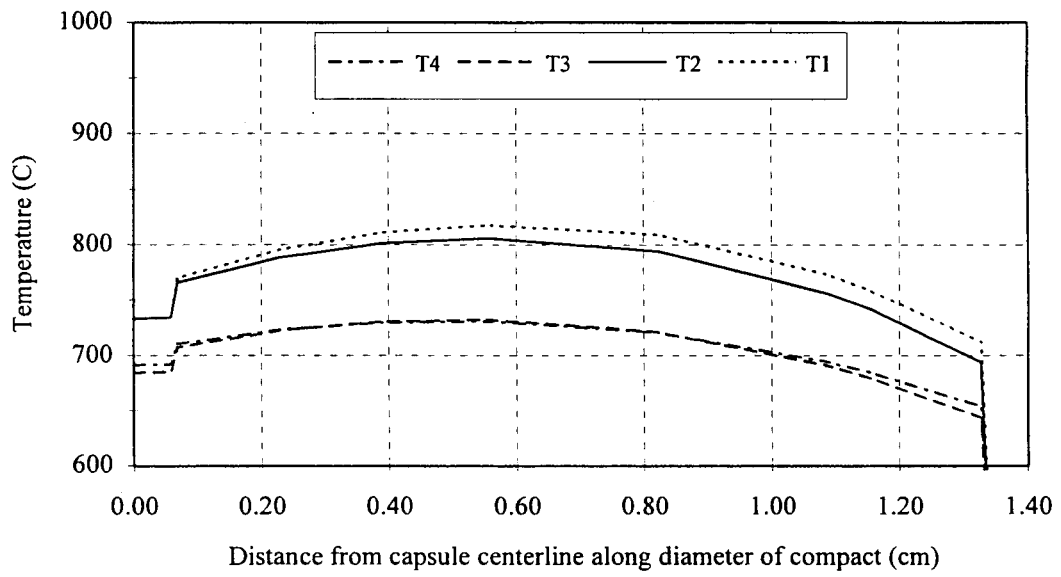

Figure 3.5.1-2h NPR-2 Radial temperature profiles in compacts 5-8 at 116.453 days of irradiation (end of cycle 1 in RB position)

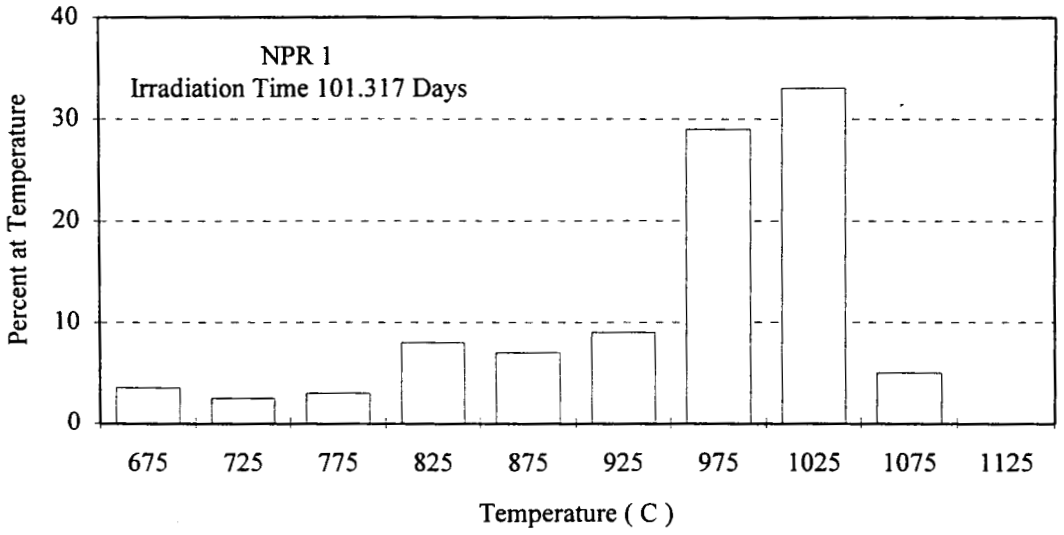

Figure 3.5.1.1 Fuel compact temperature distribution

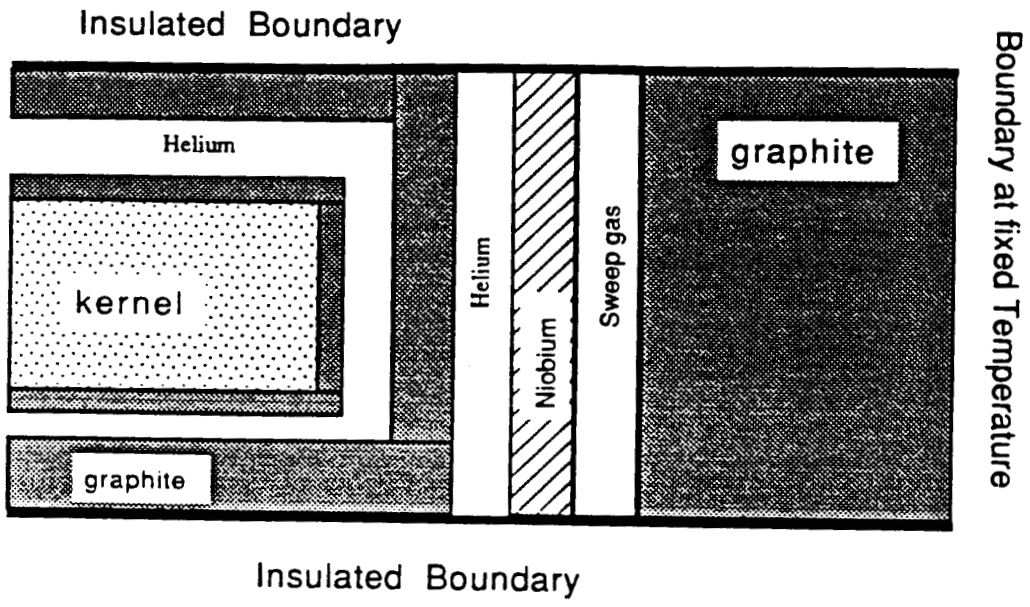

Figure 3.5.2.1 Representation of piggyback particle, thermal model (not to scale)

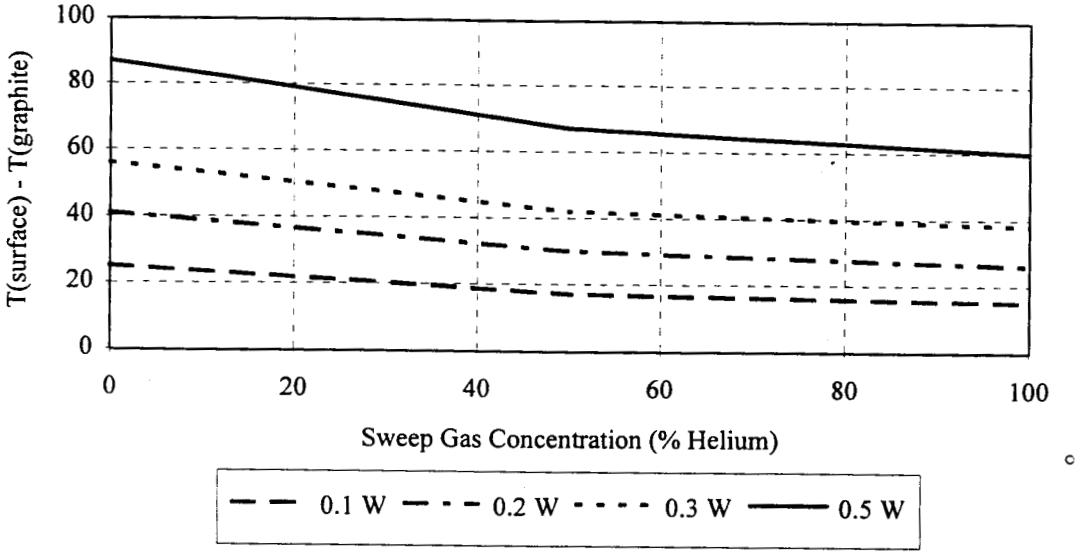

Figure 3.5.2.2 Piggyback Particle surface temperature estimate for PB irradiation

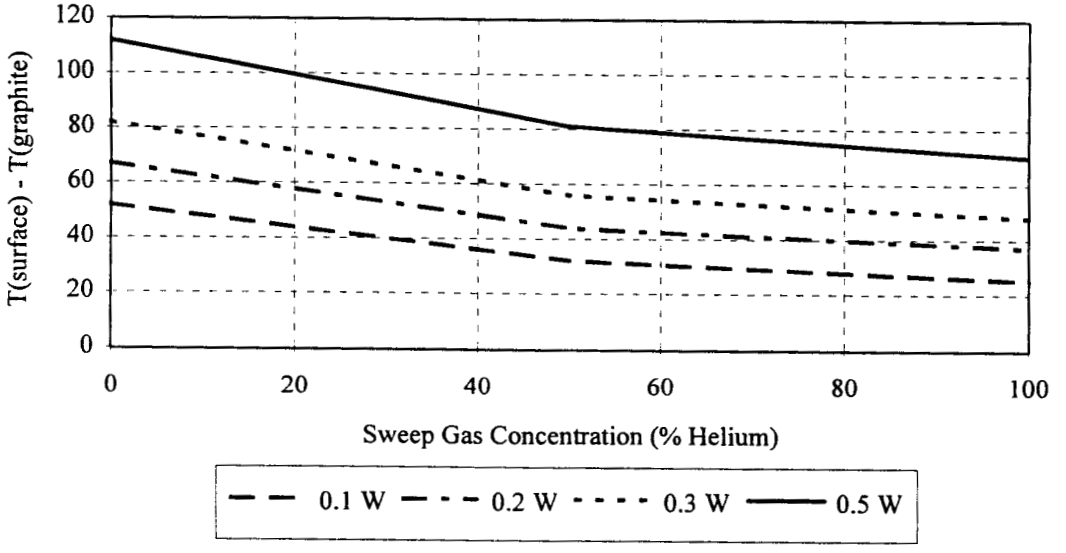

Figure 3.5.2.3 Piggyback particle surface temperature estimate for RB irradiation

3.5.3 Fuel Temperature Uncertainty

Section 3.1.1 describes the technique used to estimate fuel compact volume averaged temperatures. The method uses the measured graphite fuel body temperatures and design equations describing the thermal and physical properties of the capsule components to calculate the average fuel temperatures. Thermal properties of graphite and fuel are a function of temperature and fast fluence. The time dependent average fuel and local maximum fuel temperatures calculated using this technique are also described in Section 3.1.1. Reference 3.1.1 gives a general detailed description of the technique.

The NPR capsules were irradiated for the first three cycles in the PB position and for the next five cycles in the RB position in the HFIR. There is a significant difference between the irradiation conditions in the PB and RB positions. The fast fluence during the irradiation in the PB position (first three cycles) of HFIR is small. The corresponding changes in the parameters (i.e., thermal conductivities of fuel and graphite, and the dimensions of the fuel compacts and graphite) are small. Based on this, the thermal analysis of the capsules during the first three cycles uses average values for all the parameters. Therefore, the calculated average fuel compact temperature is a direct function of the measured graphite temperature and the sweep gas concentration.

Based on this consideration, the thermal analysis uses a few 3-D HEATING 7 runs followed by a simple MAPPING code (see Section 3.1.1)to determine average and maximum fuel temperatures as a function of time. (The thermocouple to fuel temperature mapping program, i.e., a collection of eight programs, one for each region, is collectively called MAPPING code.) Since this method masks the independent effects of each parameter, a Monte-Carlo technique to statistically combine the effect of uncertainties in each parameter is not feasible.

Essentially all the fast fluence is accumulated during the last 5 cycles of irradiation in the RB position of HFIR. Due to the increasing fast fluence as a function of time, the

parameters (i.e., thermal conductivity, dimensions of the fuel and graphite) change significantly and affect the thermal performance of the capsule. The methodology used, i.e., a comprehensive set of HEATING 7 runs, followed by a series of MAPPING code runs, is specifically designed to follow these time dependent changes. In this case the MAPPING code considers the effect of changes in all of the parameters. Thus, the use of a Monte-Carlo technique is feasible to determine the uncertainty in the average fuel temperature during the last five cycles of irradiation.

Two different methods to perform the uncertainty analysis were developed. The details of these methods for the uncertainty analysis of the NPR capsules in the PB and RB positions are briefly described below.

3.5.3.1 Analysis Methodology for the Irradiation in the PB Position

A set of 3-D HEATING 7 runs, i.e.,a run with nominal values for all the parameters followed by multiple runs where each parameter was varied by $\pm 2\sigma$, were performed. The effect of change in each parameter on the average fuel temperature, $<T>$ was then combined using propagation of error methodology given in Reference 3.5.1. Uncertainties in the a) graphite inconel gap, (g_inc), b) fuel graphite gap, (f_g), c) fuel thermal conductivity, (K_f), d) graphite thermal conductivity, (K_g), and e) measured graphite temperature, (TC), are included in this analysis. The resulting value of the standard deviation (σ) of the calculated average fuel temperature is typical for the entire irradiation period in the PB position of HFIR.

3.5.3.2 Analysis Methodology for the Irradiation in the RB Position

A bound on the uncertainty in the average fuel temperature, $<T>$ can be estimated by propagating the uncertainties introduced from several sources through the programs used to calculate the fuel compact temperature. If we view the thermocouple to fuel temperature mapping program (MAPPING Code) as an input/output box, then we can readily calculate the uncertainty in $<T>$ (or the variation in $<T>$) introduced from the uncertainty in the input parameters. A distribution of $<T>$ values can be generated by providing a set of input

parameters x_i (K_g, K_f, TC, g_inc, f_g, %He) to the program and recording the value of <T> returned for each input set. The members of the input set are selected independently using a Monte Carlo sampling from a distribution of values for each parameter.

The input parameter x_i is assumed to be characterized by the Gaussian or normal density distribution:

$$f(x) = \frac{1}{\sqrt{2\pi} * \sigma} * \exp\left(\frac{-(x-\mu)^2}{(2\sigma^2)}\right)$$

where μ is the mean value and σ is the standard deviation. Recall that for the normal density distribution, 50 percent of the area under the curve (probability) falls between $\pm$ 0.67 standard deviations from the mean, 95.5 percent of all values fall between $\pm$ 2 standard deviations from the mean and 99.7 percent of the values will be within $\pm$ 3 standard deviations from the mean. Using a random number generator, random values of the input parameter, x_i, can be selected from the Gaussian distribution (characterized by μ_i and σ_i) for input into the MAPPING routines. The output <T> distribution can then be fit with a Gaussian to provide the mean value and standard deviation for the average fuel temperature.

The mean value in the Gaussian distribution used to describe the potential value of the given parameter in the input set {K_g, K_f, TC, g_inc, f_g, %He} is taken to be the nominal value measured or calculated at that point in time during the irradiation.

3.5.3.3 Estimates of the Uncertainty in the Input Parameters

The calculation of the fuel temperatures depends on the following input parameters;

a) thermal conductivity of the fuel,

b) thermal conductivity of graphite,

c) fuel graphite gas gap,

d) graphite inconel gap,

e) inconel-inconel gap,

f) the measured graphite fuel body temperatures and

g) the sweep gas composition.

The time dependent fuel temperature is influenced by the dimensional changes of the fuel and graphite bodies. Dimensional changes are caused by accumulation of neutron fluence during the irradiation. The uncertainties in the seven parameters listed above may be considered using an estimate of the standard deviation of each parameter. The total uncertainty on the fuel average temperature may be computed using either a Monte-Carlo technique previously discussed or an error propagation technique (Ref. 3.5.1). The uncertainties in the individual parameters are discussed below. There is lack of reliable data on the uncertainties. The discussion below shows the source of data if any and where data does not exist, the best estimate of the uncertainty.

Thermal conductivity of the fuel

The uncertainty in the thermal conductivity of the fuel is defined by a standard deviation of 12.5% (General Atomics, private communication). The uncertainty used in the analysis (σ value of 15% of nominal, shown in Table 3.5.3.1)includes the uncertainty in the calculated nominal thermal conductivity of the fuel (12.5%) and the additional uncertainty relating to the uncertainty in the neutron fluence. The uncertainty in the neutron fluence is not a random variable. The fast fluence used in the analysis may be either low or high. To obtain its effect, the MAPPING code was used with fluence modified by $\pm$ 10% to calculate the time history of the thermal conductivity and other parameters. The time dependent thermal conductivity of the fuel for the low and high fluence cases was compared to the nominal value. This comparison showed that the thermal conductivity for either case is within $\pm$ 4% of the nominal fluence value. This uncertainty is then added to initial uncertainty to obtain the final value of $\sim$15%.

Thermal conductivity of graphite

The uncertainty in the thermal conductivity of graphite is given in the Graphite Design Manual (Ref. 3.1.1). This is defined by a standard deviation of 10% of the nominal value. An additional contribution from the uncertainty of the fluence is added to obtain the

overall uncertainty of 15% of the nominal value (see Table 3.5.3.1).

Graphite inconel gap

The uncertainty in the gap between the graphite fuel body and the inconel primary containment arises from the measurement uncertainties, changes in the dimensions during irradiation, uncertainties in the coefficients of thermal expansion and eccentricity in the positioning of the graphite body in the primary containment. Again, this uncertainty is estimated to be represented by a standard deviation of 15% of the gap nominal dimension.

Table 3.5.3.1
Nominal values at elapsed time = 101.517, and estimated uncertainty

Parameter Name	Parameter Symbol	Nominal values for NPR 1 @ t=101.517	Standard Deviation
Graphite Temperature	TC	868°C	2% for NPR 1 6% for NPR 2
Fast fluence $(E \geq f)_{MHTGR}$	fast fluence	0.371×10^{25} neutrons/cm^2	10%
Thermal conductivity of graphite	Kg	0.5399 W/cm.K	15%
Thermal conductivity of fuel compact	K_f	0.1541 W/cm_K	15%
Gas filled gap between graphite and inconel	g_inc	14.74×10^{-3} in	15%
Gas filled gap between fuel compact and graphite	f_g	4.48×10^{-3} in	15%
Percent helium in sweep gas	%He	100%	1.2%
Volume average fuel compact temperature (Region 4) (Tap)	<T>	1034 °C	
Fuel compact power density	Pv	154.9 W/cc	5%

Fuel graphite gas gap

The initial uncertainty in the gap between the fuel rod and the graphite body arises from the uncertainty in the initial dimensional measurements. Additionally, the dimensions of both fuel compacts and graphite change due to fast fluence effects during the irradiation. The MAPPING code with fluence values equal to $\pm$ 10% of the nominal value was used to calculate the changes in the gap size as a function of fluence. The resulting uncertainty to account for the fluence was found to be small (< 3%). An overall uncertainty equal to a standard deviation of 15% of the nominal value of the gap dimensions is assumed in the analysis. This assumption accounts for the uncertainty in the initial measurements, uncertainties in the coefficients of thermal expansion of the fuel rods and the graphite, any eccentricity in the positioning of the fuel rod in the graphite fuel holder and the irradiation induced dimensional changes occurring during the irradiation.

Inconel-inconel gap

The gap between the primary inconel containment and the secondary inconel containment was assumed to be 2 mils in the thermal analysis of the NPR 1 capsule during the irradiation in the RB position. (Please note that the gap assumed for the thermal analysis for the PB portion of the irradiation is 1.0 mil.) A peer review of this assumption revealed that a 1.0 mil gap was more representative of the capsule. An analysis using the 3 dimensional HEATING 7 code was performed to determine the effect of this assumption. Three runs with inconel-inconel gaps of 0.5, 1.0 and 2.0 mils were performed and the results are shown in Table 3.5.3.2.

The results show that the effect of the change in the gap dimension from 2.0 mils to 1 mil is to reduce the calculated fuel average temperature by 25 C. This is a bias on the reported average fuel operating temperatures during the irradiation in the RB position of the NPR 1 capsule, i.e., during irradiation cycles 4 through 8.

Table 3.5.3.2.
Results of HEATING 7.0 runs for several inc_inc gas gaps. Heat rates and conductivities of graphite and fuel remain constant.

Region	Parameter	0.5 mil gap	1.0 mil gap	2.0 mil gap	Value(2) - value(0.5)
1	inc_inc gap ΔT	38	74	142	104
1	g_inc ΔT	739	720	686	-52
1	Thermocouple	1006	1022	1055	49
1	<T>	1321	1336	1363	42
2	inc_inc gap ΔT	43	79	151	110
2	g_inc ΔT	863	842	804	-60
2	Thermocouple	1145	1161	1191	46
2	<T>	1470	1483	1510	40
3	inc_inc gap ΔT	42	81	155	113
3	g_inc ΔT	865	844	805	-60
3	Thermocouple	1157	1172	1200	43
3	<T>	1443	1456	1481	38
4	inc_inc gap ΔT	41	79	150	109
4	g_inc ΔT	926	905	866	-60
4	Thermocouple	1195	1208	1233	38
4	<T>	1418	1430	1453	35

Measured graphite fuel body temperatures

Significant uncertainty in the measured temperatures of the graphite body exists. Multiple measurements at the compact axial midplane location were made during irradiation. These measurements (four thermocouples in most locations) were averaged to obtain the measured value of the graphite temperatures used in the thermal analysis with the MAPPING code.

A standard deviation of the four measured values at various time points in the irradiation was computed. On the average the standard deviation of the measured temperatures in the NPR 1 capsule was less that 2% of the nominal value. Similarly the standard deviation of the measured temperature in the NPR 2 capsule on the average was 6% of the nominal value. This standard deviation is assumed to represent all uncertainties arising from measurement, thermocouple calibrations, effect of eccentricities in the positioning of the graphite body in the capsule and any degradation of the thermocouple during the irradiation.

Sweep gas composition

The uncertainty in the sweep gas composition arises from the flow measurement accuracies. This was evaluated to be equal to a standard deviation of 1.2% of the nominal value.

Other

Table 3.5.3.1includes uncertainties in the estimated fast fluence (standard deviation of 10%) and compact power density (standard deviation of 5%). The methodology used in the analysis makes it difficult to account of the uncertainty in the fast fluence. Instead, the mapping code was used to obtain a time dependent graphite-inconel gap, fuel-graphite gap, graphite thermal conductivity and fuel thermal conductivity for a) nominal fast fluence, b) lower limit of 90% of the fast fluence and c) an upper limit of 110% of the fast fluence. The variation of the gaps, the graphite thermal conductivity and the fuel thermal conductivity between the two limits of fast fluence was estimated from these calculations. For a 10% change in the nominal fluence, the gaps, and the thermal conductivities change by less than 4%. An additional uncertainty was then added to the estimated uncertainty of the gas gaps and the thermal conductivities. The values in the Table 3.5.3.1represent the uncertainty in the parameters as well as the uncertainties in the fast fluence that effect these parameters.

Even after accounting for the uncertainties described above, it is felt that the power density estimates made by the MAPPING code may have an additional uncertainty. This

uncertainty may be the result of uncertainties in the analysis models and methodology. To account for this, the power density obtained from the correlation in the MAPPING code (power density for a given time as a function of the measured graphite temperature) was assigned an uncertainty represented by a standard deviation of 5%.

AGNAIL has performed additional supporting analysis to obtain the effect of eccentricity on the graphite and fuel temperatures. These are discussed in Reference 3.5.2.

A detailed discussion on the development of the thermal model, associated assumptions and possible impact on the calculated fuel temperatures are discussed in Reference 3.5.3.

3.5.3.4 Results of the Uncertainty analysis for the first 3 cycles of irradiation (PB Position)

The results of the uncertainty analysis for the first three cycles of irradiation is listed table below in terms of the standard deviation of the average fuel temperature. The higher temperatures of operation of capsule NPR 1 required larger graphite inconel gap than that of capsule NPR 2, resulting in greater contribution to the uncertainty. The uncertainty of the measured temperature, TC for region 4 (~44 C) resulted in the larger uncertainty in NPR 2 capsule.

Table 3.5.3.3
Predictions for the first 3 cycles of irradiation in PB position

Capsule	Zone 1	Zone 2	Zone 3	Zone 4
NPR 1 T average σ (C)	56	49	50	50
NPR 2 T average σ (C)	32	36	52	73

Of interest is the average fuel compact temperature at the upper 95% confidence level. This can be obtained by adding 2σ to the calculated average temperatures given in Section 3.1.1.

3.5.3.5 Results of the Uncertainty analysis for the last 5 cycles of irradiation (RB position)

The predictions of the cumulative uncertainty of the average fuel temperature during the irradiation in the RB position using the Monte-Carlo technique is given in Table 3.5.3.4. These uncertainty values are lower than those computed for the irradiation in the PB position. Typically, a rigorous Monte-Carlo technique results in lower cumulative uncertainty. These uncertainty predictions are for one time point early in the irradiation at the RB position. At that point in time the compact powers were the highest for the RB position. For all other times in the irradiation the uncertainty is somewhat lower. Time dependent upper and lower confidence intervals for the average fuel temperature were computed but are not included in this report. Many plots will be needed to display these values and are not included in this report. The values shown in Table 3.5.3.4are typical.

The uncertainties in the NPR 2 capsule average fuel temperatures are greater due to the greater uncertainty in the measured graphite temperature.

Table 3.5.3.4
Uncertainty Predictions for the last 5 cycles of irradiation in RB position

Capsule	Zone 1	Zone 2	Zone 3	Zone 4
NPR 1 T average σ (C)	38	45	40	38
NPR 2 T average σ (C)	63	67	64	61

3.5.3.5 Uncertainties not considered in the analysis

The following uncertainties were not considered in the analysis:

1. heat transfer coefficient at the inconel secondary containment vessel and HFIR water coolant interface,
2. effect of possible oxide layer on the outside surface of secondary inconel containment,
3. eccentricity of the graphite fuel body in the primary inconel containment, and

4. uncertainty in the helium/neon concentration during the irradiation in the PB position.

It is estimated that these uncertainties are of second order importance.

3.5.3.6 Comparison of Measured and Calculated Dimensions of the Compacts

After the irradiation was completed, the capsule was disassembled and the dimensions (diameters and lengths) of the compacts were measured. These diameter measurements are compared to the predictions. The prediction are based on the operating temperature history of each compact as predicted by the mapping code (NPR1AVEx.f). The mapping code uses the physical property correlations from the Fuel Design Data Manual, Issue F and Graphite Design Data Manual. The correlation for the volumetric change in the fuel compact provided in the design manual is a function of fluence and temperature and includes the thermal expansion component. Another correlation in the design manual provides the thermal expansion as a function of fluence. Using these correlations, the time evolution of the fuel compact diameter was computed. Table 3.5.3.5and 3.5.3.6provide a comparison of the measured and computed dimensional changes.

The dimensional change prediction for the NPR 1 compacts matches reasonably well with the measurements. On the other hand the NPR 2 compact dimensional change predictions and measurements are significantly different. Similarly, a comparison of the measurements of dimensional change of compacts from NPR 1 and NPR 2 capsules indicates no significant difference. Both capsules were irradiated to similar final fuel burnup and fast fluence. But they differed only in the average fuel operating temperature. NPR 2 fuel operated at considerably lower average temperature but exhibits almost the same dimensional change. This indicates that the temperature dependence of the dimensional change is less than predicted by the correlations in the Fuel Design Data Manual (Ref. 3.1.3).

The dimensional changes of the graphite fuel body was also measured after the irradiation was completed. These are shown in Table 3.5.3.6.These changes are fairly well predicted.

Table 3.5.3.5 NPR 1 and NPR 2 Fuel Compact Dimensional Change

Capsule	Pos.	GA Compact No.	Pre-Ira (1) diameters Do (in)	Post-Ira Spec Dia D (in.)	Input to Mapping Code(2)	Mapping Code (3) Prediction	% change diameter Predicted	% change diameter Measured	Difference (%)
NPR 1	A1	1-14	0.4900	0.4827	0.49005	0.48364	1.31	1.48	13
	A2	2-82	0.4894	0.4828	0.48965	0.48192	1.58	1.35	16
	A3	3-16	0.4906	0.4845	0.49060	0.48328	1.49	1.23	19
	A4	4-76	0.4907	0.4851	0.49065	0.48462	1.23	1.14	8
	A5	4-01	0.4902	0.4843	0.49025	0.48440	1.19	1.20	1
	A6	3-35	0.4905	0.4827	0.49060	0.48398	1.35	1.58	16
	A7	2-89	0.4896	0.4830	0.48970	0.48302	1.36	1.35	1
	A8	1-48	0.4899	0.4815	0.49010	0.48462	1.12	1.72	42
	B1	1-2	0.4901	0.4830	0.49005	0.48364	1.31	1.45	11
	B2	2-74	0.4899	0.4855	0.48965	0.48192	1.58	0.91	54
	B3	3-15	0.4906	0.4842	0.49060	0.48328	1.49	1.30	14
	B4	4-52	0.4906	0.4835	0.49065	0.48462	1.23	1.45	17
	B5	4-19	0.4903	0.4826	0.49025	0.48440	1.19	1.56	27
	B6	3-21	0.4907	0.4833	0.49060	0.48398	1.35	1.51	11
	B7	2-84	0.4898	0.4816	0.48970	0.48302	1.36	1.68	21
	B8	1-20	0.4903	0.4814	0.49010	0.48462	1.12	1.81	47
NPR 2	A1	1-50	0.4892	0.4821	0.48915	0.48448	0.95	1.44	41
	A2	2-22	0.4898	0.4821	0.48975	0.48514	0.94	1.56	50
	A3	3-70	0.4898	0.4822	0.48975	0.48572	0.82	1.55	61
	A4	4-161	0.4904	0.4823	0.49065	0.48672	0.80	1.65	69
	A5	4-159	0.4902	0.4830	0.49035	0.48690	0.70	1.47	71
	A6	3-07	0.4899	0.4831	0.48980	0.48630	0.71	1.40	65
	A7	2-06	0.4901	0.4831	0.49020	0.48612	0.83	1.44	53
	A8	1-67	0.4899	0.4825	0.48980	0.48594	0.79	1.51	63
	B1	1-58	0.4891	0.4817	0.48915	0.48448	0.95	1.51	45
	B2	2-57	0.4897	0.4812	0.48975	0.48514	0.94	1.73	59
	B3	3-54	0.4897	0.4831	0.48975	0.48572	0.82	1.36	49
	B4	4-60	0.4909	0.4833	0.49065	0.48672	0.80	1.55	64
	B5	4-21	0.4905	0.4817	0.49035	0.48690	0.70	1.80	88
	B6	3-32	0.4897	0.4838	0.48980	0.48630	0.71	1.20	51
	B7	2-53	0.4903	0.4821	0.49020	0.48612	0.83	1.66	67
	B8	1-68	0.4897	0.4828	0.48980	0.48594	0.79	1.41	56

Notes:

(1) Pre-Irradiation diameters of the fuel rods were measured at the axial center of the compacts at two orientations and then averaged

(2) Diameter input to the mapping code is the average of the diameters at the axial center in capsule positions A and B

(3) Diameter change prediction is based on correlations given in the Fuel Design Data Manual, Issue F

Table 3.5.3.6 NPR 1 and NPR 2 Graphite Body Dimensional Change

Capsule	body No.	graphite body	diameters Do (in)	Post-Irr Spec Dia D (in.)	Mapping Code(2) Prediction	%change diameter Predicted	%change diameter Measured	Difference (%)
NPR 1	U	Zone 1	1.2024	1.1998	1.20055	-0.15	-0.22	34
		Zone 2	1.1985	1.1951	1.19449	-0.33	-0.28	16
		Zone 3	1.1975	1.1932	1.19205	-0.46	-0.36	24
		Zone 4	1.1915	1.1863	1.18520	-0.53	-0.44	19
	L	Zone 4	1.1913	1.1865	1.18504	-0.53	-0.40	26
		Zone 3	1.1973	1.1934	1.19205	-0.44	-0.33	30
		Zone 2	1.1986	1.1963	1.19465	-0.33	-0.19	53
		Zone 1	1.2025	1.2006	1.20087	-0.14	-0.16	15
NPR 2	U	Zone 1	1.2105	1.2086	1.20819	-0.19	-0.16	19
		Zone 2	1.2128	1.2090	1.20976	-0.25	-0.31	22
		Zone 3	1.2102	1.2058	1.20685	-0.28	-0.36	27
		Zone 4	1.2046	1.1996	1.20118	-0.28	-0.42	38
	L	Zone 4	1.2045	1.2001	1.19772	-0.56	-0.37	43
		Zone 3	1.2103	1.2053	1.20654	-0.31	-0.41	28
		Zone 2	1.2127	1.2087	1.20937	-0.27	-0.33	18
		Zone 1	1.2108	1.2078	1.20819	-0.22	-0.25	14

Notes:

(1) Pre-Irradiation diameters of the graphite were measured at two orientations and then averaged

(2) Diameter change prediction is based on correlations given in the Fuel Design Data Manual, Issue F

3.6 References

3.1.1 Bell, G. L. et.al. "The New Production Reactor Fuel Irradiation Experiments NPR 1 and NPR 2 Irradiation Phase Report, ORNL/M-2663, Feb. 12, 1993.

3.1.2 Graphite Design Handbook, DOE-HTGR-8811, Rev 0, General Atomics, September 1988.

3.1.3 Fuel Design Data Manual, Issue F, General Atomics Design Document 90866, August 26, 1987.

3.1.4 Morris, R. N., "MHTGR Fissile and Fertile Particle Burnup Determination by Gamma Spectroscopy," ORNL-TM-12310 (to be published)

3.2.1 N.H. Packan, et al., "Operating Plan for Capsule HRB-21 Irradiation," DOE-HTGR-88370, ORNL/TM-11403, Martin Marietta Energy Systems, Inc., Oak Ridge National Laboratory, December 1989.

3.2.2 Martin Marietta Energy Systems, Inc., Oak Ridge National Laboratory, Drawing I-10482-QG-243-E

3.2.3 E.D. Clemmer, "Sweep Gas Sampling," ORNL Engineering Technology Division Procedure ETD-IE-SOP-005, Martin Marietta Energy Systems, Inc., Oak Ridge National Laboratory, December 1988.

3.2.4 L.C Emerson, "HFIR Sweep,Gas Counting and Analysis,"Metals and Ceramics Division Quality Assurance Document MET-FMT-OG-002, Martin Marietta Energy Systems, Inc., Oak Ridge National Laboratory, June 1991.

3.2.5 E.J. Allen, "CACA-2: Revised Version of CACA-A Heavy Isotope and Fission Product Concentration Calculational Code for Experimental Irradiation Capsules," ORNL/TM-5266, Union Carbide Corporation, Nuclear Division, Oak Ridge National Laboratory, February 1976.

3.5.1 Yardley Beers, "Introduction to the Theory of Error," Addison Wesley Publishing Company Inc, 1962.

3.5.2 G. Hawkes, "Thermal Analysis of HFIR NPR 1 Test Assembly," EDF NPR-MHTGR-0689, September 16, 1993.

3.5.3 G. L. Bell to J. T. Parks, "Discussion of NPR Irradiation Capsules Thermal Modelling," September 15, 1993.

4.0 POSTIRRADIATION EXAMINATION RESULTS

4.1 Capsule Disassembly

Disassembly and associated tasks on Capsules NPR 1 and NPR 2 were carried out in accordance with Reference 4.1.1.

4.1.1 Post Irradiation Handling & Shipping

At the end of the desired irradiation period, during the End-of-Cycle 307 Planned Outage, both capsules were transferred from the reactor tank to a poolside storage location. The tests remained in the storage location until preparations began for the shipment to the Hot Cells in early December.

All test instrumentation remained active until shortly before the shipment. A constant helium purge was maintained for several days following the end-of-Cycle 307 and the gas was sampled for radioactivity.

In order to eliminate the need for two separate radioactive shipments, the normal procedure for the Loop Transport Cask was revised to permit the simultaneous shipment of both NPR 1 and NPR 2 tests. The cask was loaded in the following basic steps, in accordance with Refs 4.1.1, 4.1.2, 4.1.3, and 4.1.4 as follows:

1. The NPR 1 test was placed in the open cask and the first cut of the instrumentation leadouts completed, as indicated in Figure 4.1.1.1.

2. The cask, with NPR 1 inside, was raised to the pool surface and the second cut of the lead tubes, closest to the test capsule, was made and the lead tubes closed and sealed, as shown in Figure 4.1.1.2.

3. The cask was again lowered to the pool bottom and the NPR 2 test placed inside the cask, alongside the NPR 1 test, as shown in Figure 4.1.1.3, and the first cut made on the NPR 2 leadout tubing.

4. The cask was again raised to the pool surface and the second cut sealing completed on the NPR 2 leads, as shown in Figure 4.1.1.4.

5. The cask was again lowered to the pool bottom and the shield-closure plug installed.

6. The loaded cask was then raised above the pool, drained and loaded onto the truck for final shipment preparations.

The cask was transferred to Bldg. 3525 and both tests successfully discharged into the North Cell Bank in accordance with Ref. 4.1.3. From the North Bank, the tests were transferred to the East Bank for gamma scans and photography, in accordance with Ref. 4.1.1.

4.1.2 Visual Examination of Capsules

Each capsule was examined visually through the cell window and with the Kollmorgen periscope. The capsules appeared to be in good condition with no obvious deformation or damage (other than some very light longitudinal scratches and some radial scratches on the bottom face). There was a white film or scale on generally the lower half of each capsule. A clearly visible broad notch in the uppermost portion ("adapter" component) of each capsule containment is defined as the "0°" reference for all subsequent PIE activities; this notch aligned with a lug on the junction box above and can be related to the direction either directly toward or away from HFIR core (reactor records specify which direction for each irradiation cycle).

4.1.3 Gamma Scanning of Capsules

The intact capsules were each hung vertically (by a hose clamp with flexible wire bail) for gamma scanning to give indication that all components were in place. Gamma scanning was accomplished according to the generic gamma scanning procedure; the output is an analog trace on a chart recorder of integrated gamma intensity. The region of interest (ROI) was set at 550 to 800 KeV (in order to exclude most gammas from the Inconel cladding

activation) and longitudinal scans were made with a 1/16-in-diameter collimator. Scans were made with a lateral shift to align with fuel columns A or B, respectively. These scans showed that the graphite fuel bodies and compacts were in the expected positions (see Fig. 4.1.3.1 for an example). The above pertains to both capsules, NPR 1 and NPR 2.

4.1.4 Removing Contents of Capsule NPR-1

The capsule was placed in the rotating chuck on the milling machine for cutting through the containment tubes. A ledge was milled through both containments at the 0° location as a reference for orientation of the containment tubes. The first circumferential cut ("Cut #1" in Fig. 4.1.4.1) was made using a 3/8-in. carbide end mill bit. The secondary (outer) containment was cut through; with a fresh bit the primary containment was then penetrated. Pulling on the upper assembly opened a gap of about 3/4-in with the lower part of the capsule. A dovetail-shaped cutter was installed and used to remove the inner burr on the primary containment.

At this point the assembly was moved to the pushout fixture and set against the U-shaped "gate" block designed to restrain the outer containments while allowing pass-through of the contents (visible at the left end in Fig. 4.1.4.2). Grasping the upper assembly, one continuous pull yielded the emergence of the Upper Insulator and both Upper and Lower Graphite Bodies, all still connected by the TCAT (Thermocouple Central Array Tube) assembly. All components appeared to be in good condition. The Lower Insulator remained at the bottom of the containment tubes.

Attempts were then made to clamp down the lower body and pull out the upper assembly/TCAT tubes, but prolonged tugging only yielded an eventual ~0.75 in. gap between the upper and lower bodies. It was decided to cut through the linking thermocouple (TC) tubes using a hacksaw, one by one, and in fact all four had to be severed this way. Then pulling was finally able to isolate the lower body from the components above it, but the two full-length platinum-sheathed flux monitor tubes stayed with the lower body. These tubes were then individually pulled out of the lower body. Removal of the upper body also required saw-severing of two TC tubes, the other two emerging intact with the pull. Reference "0°" scratch marks were made at the upper end of each graphite body corresponding to the 0° ledge milled into the outer containment.

4.1.5 Removing Contents of Capsule NPR 2

The upper-end cut through containment (Cut #1 in Fig 4.1.4.1) was made and deburred in the same manner as with capsule NPR 1. Pulling on the upper assembly was able to bring out only the upper insulator in a "crumbly" condition, after which the TCAT leads emerged leaving both graphite bodies still within the containment tubes.

The capsule was turned around and remounted in the rotary chuck for the ("Cut #2") circumferential cut at the bottom. The inner edge of the lower end of the primary tube was then deburred and bevelled. Pushout from the top finally produced the Lower Insulator, Support Disk, and the Lower and Upper Graphite Bodies, all in good condition.

4.1.6 Removal of Components from Graphite Bodies

Following visual examination and gamma scanning of the graphite bodies (see below), removal of the fuel compacts was initiated. A fixture was used to align a screwdriver blade above any screw slot so that the blade could be turned with the in-cell manipulator with no downward or misalignment force on the graphite cap. This system worked well and all of the screw-caps were loosened easily -- final removal was done with the graphite body horizontal.

Compacts were removed in accordance with section 14 of procedure MET-FME-ESP-12, Rev. 1, and the removal sequences were videotaped using a VHS camcorder with 10:1 zoom lens lashed to the camera platform and eyepiece of the Cell #1 Kollmorgen periscope. Live observation on an adjacent high quality monitor was possible with surprisingly detailed, magnified views (given sufficient light from a photoflood and after making accommodation for the top/bottom, left/right inverted image).

The general method used to remove the compacts was to push them out with only very light "hand force" using a 0.37 in. diam wood dowel pushout rod through one end hole against the opposite end of the fuel compact stack. Based on experience with the PIE of capsule HRB-21, the "pushout plugs" provided were removed and not used because of the likelihood of their becoming cocked and jammed in the bore (see Fig. 4.1.6.1). Initial pushing was in the horizontal position and subsequently, if necessary, with gradually increasing amounts of tilt. The impediments to smooth removal were accumulations of a few loose particles in the screw-threaded end cap regions which tended to bind the compact from sliding

past -- tilting and tapping helped to eject these particles. Switching push directions and effecting removal of another compact from the opposite end also helped. Pushout was halted after each individual compact emerged into the height-aligned receiver trough; it was immediately stored (see below).

The first fuel compacts to be removed were from the hole B of the Lower Graphite Body of NPR 1. [Hole A is defined as having "X" marks on the end caps; hole B lacked them.] The initial handling method was to pick up each compact from the trough very carefully using the rubber-padded manipulator tips and allow it to slide down into the corresponding marked, aluminum container held nearby. However, when compact NPR-1-FC-A8 was brought to the mouth of its container, one half of it broke off and fell away, showing the very delicate condition of the as-irradiated compacts. The method was then changed to unclamping and removing the graphite body temporarily, substituting the aluminum storage container so that the compact could be pushed laterally from the trough into the container without any pickup, and then replacing the graphite body for the next pushout. No further compacts were broken in the unloading of either capsule, and none were found broken upon emergence. All fuel compacts were stored in marked, 60mm x 20mm diameter screw-top aluminum containers. All loose particles (as many as ~35) and debris from each four-compact fuel hole were stored, together with that hole's top and bottom graphite end caps, pushout disk, and any thin Grafoil spacer disks, in one small aluminum container coded "NPR-x-FCP-xx" (fuel compact parts).

The piggyback specimens were removed from each graphite body by first removing the small top and bottom graphite screw plugs retaining them in the full-length hole and attempting to pour them out. A 1/16-in metal rod was then used to push those specimens that did not slide out. All the small screw plugs were removed with no trouble. Asymmetrical or overhanging welds on certain specimens were apparently the cause of any sticking. None of the piggyback specimens appeared to be harmed by the removal process. All piggyback specimens were stored in marked small screw-top aluminum containers.

4.2 Visual Examination

4.2.1 Visual Examination of Graphite Bodies

The graphite fuel bodies of Capsule NPR-2 appeared to be in very good condition -- essentially the same as when they were loaded into the experiment. Some scratches were evident and also some small cracks and grain separations. The graphite bodies of Capsule NPR 1 exhibited numerous signs of the trauma incurred in being separated from the TCAT assembly, as discussed above. Typical photographs of the graphite bodies and other components are in Figs. 4.2.1.1 through 4.2.1.7

4.2.2 Gamma Scanning of Graphite Bodies with Fuel Compacts

An aluminum holder was fabricated for gamma scanning the graphite fuel bodies. The holder could be translated so that individual fuel compact columns were placed in front of the collimator. The 1/16-in diameter collimator was used and longitudinal scans were made in a manner to view each fuel compact column individually. Four separate scans were made for each graphite body with the ROI's set for 720 to 775 KeV to detect ^{95}Zr, 655 to 670 KeV for ^{137}Cs, 600 to 610 KeV for ^{134}Cs, and 127 to 141 KeV to detect ^{144}Ce. These data are to be used later in the analysis of the experiment to correlate burnup, fission power, etc. for the various fuel compact positions.

4.2.3 Visual Examination of Fuel Compacts

As noted above, all sixteen fuel compacts in each experimental capsule (NPR 1 and NPR 2) were intact upon unloading. However, the compacts were obviously very delicate since one (NPR-1-A8) broke in initial handling and four others (A5, A6, A7, and B8 from NPR 1; none from NPR-2) were found broken upon receipt back from TRIGA reirradiation. Macrophotographs were taken of both sides and both ends of every fuel compact; Figs 4.2.3.1a through 4.2.3.9 illustrate typical compact appearance. [Compacts were loaded in the capsule with the end cap regions facing away from capsule midplane: upward in the upper graphite bodies and down in the lower bodies.] There was generally some extent of

circumferential cracking between the end cap material and the particle-containing remainder of each compact (in a few cases the end caps looked ready to fall off). There were also variable amounts of particle loss from the non-end-cap ends. Some exposed particles appeared to have breaks in the outer low density protective pyrocarbon (PPyC) coating and/or the outer PyC coating); Fig. 4.2.3.8 appears to show one instance of even deeper particle degradation. A macrophotograph of the fracture surface of compact NPR-1-A8 which broke during handling is given in Fig. 4.2.3.9

4.2.4 Piggyback Specimen Capsules

Eight piggyback capsules were chosen for initial opening: those containing standard fuel particles located in high fluence positions in Capsule NPR 1, as well as one low-fluence NPR 1 and one high-fluence NPR-2 capsule to go first as practice units. As shown in Fig. 4.2.4.1, each piggyback capsule was a sealed 1.1-in-long Nb tube containing one POCO graphite holder or "boat" with individual holes for 16 particles. Also shown in the figure is a thin and narrow (0.96 mm) full-length strip of Grafoil aligned with the flat top of the holder to cover the particle holes and prevent particle/outer tube contact.

Disassembly of a Nb capsule was carried in accordance with procedure MET-FME-ESP-13, Rev. 0, "NPR 1 and NPR 2 Piggyback Capsule Disassembly" (Ref 4.2.1). Opening commenced with the cutoff of each end using a slow-speed Isomet saw fitted with a 0.015-in-thick diamond abrasive blade. The capsule body was then inserted into a special pushout holder designed to retain the outer tubing segment and allow the graphite boat contents to descend into a separate collector well. Pushing with a 0.062 in. diam. push rod with handle did accomplish the ejection of capsule contents, unlike the previous experience with Experiment HRB-21 piggyback capsules (where the Nb tubing ultimately had to be slit and peeled from the graphite holders). Pushing forces ranged from very light to "moderate", and tapping of the manipulator holding the push rod was generally beneficial. After the first several capsules were unloaded in this way, it was discovered that a few particles had been crushed and some graphite boats had sustained damage on one end. Close examination revealed that at least one severed end of the containment tubing tended to be deformed into a "D" shape, and it was hypothesized that some of the pushout resistance might be coming from forcing the contents to open up this constriction. The remedy adopted was to clamp

the ductile tubing especially gently in carrying out the end cut-off operation; no further damage to contents was sustained. Particles and capsule remnants were transferred using a metal funnel from the pushout receptacle to storage in screw-top aluminum containers.

The total recovered yield from each of the eight capsules (out of 16 particles initially loaded per capsule, listed by order of unloading) was: 16 intact particles from capsule 22GA, 15 from 11GA, 11 intact and two damaged from 11UB, 15 intact and one damaged from 11GB, 16 (intact) each from 11UB' and 12GA, 15 intact from 12UA and 16 intact from 12GA'. Particles with high exposure of 3.7 x 10^{25} n/m^2 but low exposure temperature of ~600°C did not show surface cracking. However, particles with both high temperature (~800°C) and high fast neutron exposure exhibited external-surface cracking of the PyC seal coat and perhaps the PPyC. Particles were notably non-spherical, with flat spots or facetting. A summary of observations is given in Table 4.2.4.1. Photographs of the piggy back particles are shown in Figures 4.2.4.2 through 4.2.4.09.

The irradiation induced dimensional change of piggyback particles from NPR-2 sample 22GA was determined by comparison with two steel spheres with precisely known diameter of 457μm and 711μm. The steel spheres were placed with the 16 unbonded particles from holder 22GA of NPR 2 and photographed. The ratio of the true diameter of the steel spheres divided by the diameter measured on the photographic image calibrated the magnification of the photograph. The diameter of the particle image was then measured at two to four different places to obtain an estimate of the average diameter of the particle photographic image. The average particle diameter as measured on the photograph was then multiplied by the ratio described above to obtain the actual average particle diameter. The measured particle diameter varied from 672μm to 758μm with an average of 722μm. The diameter of these specific piggyback particles had not been measured prior to irradiation so the diameter measured after irradiation was compared with the nominal diameter of particles in the coated particle composite (FM19-00001). The Unirradiated particles had an average diameter of 758μm ± 4μm. Relative to the average particle unirradiated diameter, the average unbonded piggyback particle decreased in diameter 36μm.

The 36μm diameter decrease exhibited by the piggyback particles represented about 5% of the total diameter. However, the actual decrease in diameter was expected to be limited to the PPyC and OPyC layers shrinking down over an unyielding SiC substrate. A reasonable estimate of OPyC shrinkage in the radial direction would be 5% of the 39μm

Table 4.2.4.1

NPR 1 and NPR 2 Unbonded Piggyback Fuel Particle Observations

Capsule Number	Sample Number	Irrad. Temp. (°C)	Fast Neutron Exposure ($x10^{25}$ n/m^2) (E>0.18MeV)	Heavy Metal Burnup (%FIMA)	Particles Observed (a) Intact	Broken	Observations
NPR 1	11GA	775	2.7	75	15	0	No surface cracks
	11GB	850	3.7	78	15	1	10 particles with fine surface cracks in PyC seal coat
	11UB	850	3.7	78	11	2	All intact particles with fine surface cracks in PyC seal and perhaps in PPyC
	11UB*	850	3.7	78	16	0	14 particles with fine surface cracks in PyC seal coat
	12GA	825	3.7	78	16	0	9 particles with fine surface cracks in PyC seal coat
	12GA*	825	3.7	78	16	0	11 particles with fine surface cracks in PyC seal coat
	12UA	825	3.7	78	15	0	8 particles with fine surface cracks in PyC seal coat
NPR 2	22GA	575	3.7	78	16	0	No surface cracks. Diameter shrinkage ~35 um about 40% of PPyC thickness across the diameter

(a) The total irradiated in each sample was 16 particles, some were lost in opening the sealed containers after irradiation

thickness. This shrinkage would amount to about 2μm radial shrinkage and 4μm diametral shrinkage. If 4μm of the 36μm diameter shrinkage was acccounted for by the OPyC, then 32μm shrinkage took place in the PPyC. The PPyC, which was 47μm thick, would have shrunk 16μm (32/2) or 34% radially to produce the observed results. Such a large amount of shrinkage is probable with the approximately 50% dense PPyC (1.06 Mg/m^3). Similarly, large amounts of radial shrinkage were observed in the buffer PyC which had a similar low density.

4.3 Dimensional Change Analysis

4.3.1 Metrology of Fuel Compacts

The compacts were measured for diameter and length according to procedure MET-FME-SOP-09, Rev. 1, "Determination of Diameters and Lengths of Cylindrical Objects Using Comparator Stand, Dial Gage and V-Block" (Ref. 4.3.1). Diameters were measured at the top, middle, and bottom at two orientations (0° and 90°). The values reported are averages of the measurements at the different orientations. Reference was made to certified standard cylinders before and after taking measurements of each compact. Obviously, the broken compacts could not be measured for length. The results of the dimensional measurements are in Tables 4.3.1.1 to 4.3.1.3, including calculated changes from the preirradiation measurements (Ref. 4.3.2). All the compacts in both capsules underwent a general shrinkage (1 to 2%) with increasing fast neutron exposure in diameter as shown in Figures 4.3.1.1 and 4.3.1.2. The lengths underwent a similar dimensional change.

TABLE 4.3.1.1

DIAMETER CHANGES OF FUEL COMPACTS (NPR-1)

Capsule	Pos.	Zone-GA #	Loc. on compact	Preirr Dp (in)	Preirr Dp (mm)	Spec Dia D (in.)	Spec Dia D (mm)	D - Dp (in.)	D - Dp (mm)	(D-Dp)/Dp (%)
NPR-1	A1	1-14	top	0.4873	12.3774	0.4806	12.2067	-0.0067	-0.1707	-1.3791
			middle	0.4900	12.4460	0.4827	12.2613	-0.0073	-0.1847	-1.4840
			bottom	0.4904	12.4562	0.4826	12.2592	-0.0078	-0.1970	-1.5812
	A2	2-82	top	0.4873	12.3774	0.4789	12.1647	-0.0084	-0.2127	-1.7183
			middle	0.4894	12.4308	0.4828	12.2634	-0.0066	-0.1674	-1.3464
			bottom	0.4908	12.4663	0.4838	12.2886	-0.0070	-0.1777	-1.4257
	A3	3-16	top	0.4887	12.4130	0.4814	12.2277	-0.0073	-0.1853	-1.4925
			middle	0.4906	12.4612	0.4845	12.3075	-0.0061	-0.1538	-1.2339
			bottom	0.4910	12.4714	0.4852	12.3243	-0.0058	-0.1471	-1.1797
	A4	4-76	top	0.4883	12.4028	0.4807	12.2109	-0.0076	-0.1919	-1.5472
			middle	0.4907	12.4638	0.4851	12.3222	-0.0056	-0.1416	-1.1362
			bottom	0.4904	12.4562	0.4852	12.3243	-0.0052	-0.1319	-1.0588
	B1	1-2	top	0.4875	12.3825	0.4791	12.1689	-0.0084	-0.2136	-1.7247
			middle	0.4901	12.4485	0.4830	12.2676	-0.0071	-0.1809	-1.4535
			bottom	0.4906	12.4612	0.4839	12.2907	-0.0067	-0.1706	-1.3687
	B2	2-74	top	0.4881	12.3977	0.4823	12.2508	-0.0058	-0.1469	-1.1852
			middle	0.4899	12.4435	0.4855	12.3306	-0.0044	-0.1129	-0.9073
			bottom	0.4906	12.4612	0.4847	12.3117	-0.0059	-0.1496	-1.2002
	B3	3-15	top	0.4881	12.3977	0.4808	12.2130	-0.0073	-0.1847	-1.4900
			middle	0.4906	12.4612	0.4842	12.2991	-0.0064	-0.1622	-1.3013
			bottom	0.4913	12.4790	0.4842	12.2991	-0.0071	-0.1799	-1.4419
	B4	4-52	top	0.4882	12.4003	0.4818	12.2382	-0.0064	-0.1621	-1.3070
			middle	0.4906	12.4612	0.4835	12.2802	-0.0071	-0.1811	-1.4529
			bottom	0.4909	12.4689	0.4841	12.2970	-0.0068	-0.1719	-1.3785

TABLE 4.3.1.1, continued

DIAMETER CHANGES OF FUEL COMPACTS (NPR-1)

Capsule	Pos.	Zone-GA #	Loc. on compact	Preirr Dp (in)	Preirr Dp (mm)	Spec Dia D (in.)	Spec Dia D (mm)	D - Dp (in.)	D - Dp (mm)	(D-Dp)/Dp (%)
NPR-1	A5	4-01	top	0.4911	12.4739	0.4837	12.2865	-0.0074	-0.1875	-1.5028
			middle	0.4902	12.4511	0.4843	12.3012	-0.0059	-0.1499	-1.2039
			bottom	0.4882	12.4003	0.4812	12.2214	-0.0070	-0.1789	-1.4424
	A6	3-35	top	0.4912	12.4765	0.4847	12.3117	-0.0065	-0.1648	-1.3209
			middle	0.4905	12.4587	0.4827	12.2613	-0.0078	-0.1974	-1.5845
			bottom	0.4884	12.4054	0.4779	12.1375	-0.0105	-0.2679	-2.1596
	A7	2-89	top	0.4900	12.4460	0.4837	12.2865	-0.0063	-0.1595	-1.2816
			middle	0.4896	12.4358	0.4830	12.2676	-0.0066	-0.1682	-1.3529
			bottom	0.4880	12.3952	0.4790	12.1668	-0.0090	-0.2284	-1.8423
	A8	1-48	top	0.4902	12.4511	0.4836	12.2844	-0.0066	-0.1667	-1.3388
			middle	0.4889	12.4181	0.4815	12.2298	-0.0074	-0.1882	-1.5159
			bottom	0.4877	12.3876	0.4790	12.1668	-0.0087	-0.2207	-1.7819
	B5	4-19	top	0.4907	12.4638	0.4841	12.2949	-0.0066	-0.1689	-1.3551
			middle	0.4903	12.4536	0.4826	12.2592	-0.0077	-0.1944	-1.5612
			bottom	0.4883	12.4028	0.4787	12.1584	-0.0096	-0.2444	-1.9703
	B6	3-21	top	0.4914	12.4816	0.4847	12.3117	-0.0067	-0.1699	-1.3611
			middle	0.4907	12.4638	0.4833	12.2760	-0.0074	-0.1878	-1.5067
			bottom	0.4881	12.3977	0.4783	12.1500	-0.0098	-0.2477	-1.9979
	B7	2-84	top	0.4904	12.4562	0.4829	12.2655	-0.0075	-0.1907	-1.5307
			middle	0.4898	12.4409	0.4816	12.2319	-0.0082	-0.2090	-1.6800
			bottom	0.4874	12.3800	0.4793	12.1752	-0.0081	-0.2047	-1.6537
	B8	1-20	top	0.4905	12.4587	0.4836	12.2823	-0.0069	-0.1764	-1.4160
			middle	0.4903	12.4536	0.4814	12.2277	-0.0089	-0.2259	-1.8140
			bottom	0.4870	12.3698	0.4804	12.2025	-0.0066	-0.1673	-1.3523

TABLE 4.3.1.2

DIAMETER CHANGES OF FUEL COMPACTS (NPR-2)

Capsule	Pos.	Zone-GA #	Loc. on compact	Preirr Dp (in)	Preirr Dp (mm)	Spec Dia D (in.)	Spec Dia D (mm)	D - Dp (in.)	D - Dp (mm)	(D-Dp)/Dp (%)
NPR-2	A1	1-50	top	0.4874	12.3800	0.4808	12.2130	-0.0066	-0.1669	-1.3485
			middle	0.4882	12.4003	0.4821	12.2466	-0.0061	-0.1537	-1.2393
			bottom	0.4906	12.4612	0.4841	12.2970	-0.0065	-0.1643	-1.3182
	A2	2-22	top	0.4876	12.3850	0.4788	12.1626	-0.0088	-0.2224	-1.7957
			middle	0.4898	12.4409	0.4821	12.2466	-0.0077	-0.1943	-1.5619
			bottom	0.4907	12.4638	0.4836	12.2844	-0.0071	-0.1794	-1.4393
	A3	3-70	top	0.4878	12.3901	0.4788	12.1605	-0.0090	-0.2296	-1.8529
			middle	0.4898	12.4409	0.4822	12.2487	-0.0076	-0.1922	-1.5450
			bottom	0.4905	12.4587	0.4839	12.2907	-0.0066	-0.1680	-1.3486
	A4	4-161	top	0.4879	12.3927	0.4793	12.1752	-0.0086	-0.2174	-1.7545
			middle	0.4904	12.4562	0.4823	12.2508	-0.0081	-0.2054	-1.6486
			bottom	0.4912	12.4765	0.4853	12.3264	-0.0059	-0.1501	-1.2032
	B1	1-58	top	0.4873	12.3774	0.4799	12.1899	-0.0074	-0.1875	-1.5148
			middle	0.4891	12.4231	0.4817	12.2361	-0.0074	-0.1870	-1.5055
			bottom	0.4899	12.4435	0.4831	12.2718	-0.0068	-0.1717	-1.3796
	B2	2-57	top	0.4875	12.3825	0.4786	12.1563	-0.0089	-0.2262	-1.8264
			middle	0.4897	12.4384	0.4812	12.2235	-0.0085	-0.2149	-1.7274
			bottom	0.4907	12.4638	0.4839	12.2907	-0.0068	-0.1731	-1.3888
	B3	3-54	top	0.4876	12.3850	0.4798	12.1857	-0.0078	-0.1993	-1.6093
			middle	0.4897	12.4384	0.4831	12.2697	-0.0066	-0.1687	-1.3562
			bottom	0.4909	12.4689	0.4845	12.3054	-0.0064	-0.1635	-1.3111
	B4	4-60	top	0.4887	12.4130	0.4795	12.1794	-0.0092	-0.2335	-1.8815
			middle	0.4909	12.4689	0.4833	12.2760	-0.0076	-0.1929	-1.5468
			bottom	0.4907	12.4638	0.4841	12.2970	-0.0066	-0.1668	-1.3383

TABLE 4.3.1.2, continued

DIAMETER CHANGES OF FUEL COMPACTS (NPR-2)

Capsule	Pos.	Zone-GA #	Loc. on compact	Preirr Dp (in)	Preirr Dp (mm)	Spec Dia D (in.)	Spec Dia D (mm)	D - Dp (in.)	D - Dp (mm)	(D-Dp)/Dp (%)
NPR-2	A5	4-159	top	0.4911	12.4739	0.4850	12.3180	-0.0061	-0.1560	-1.2504
			middle	0.4902	12.4511	0.4830	12.2676	-0.0072	-0.1835	-1.4737
			bottom	0.4886	12.4104	0.4795	12.1794	-0.0091	-0.2310	-1.8614
	A6	3-07	top	0.4908	12.4663	0.4845	12.3054	-0.0063	-0.1609	-1.2910
			middle	0.4899	12.4435	0.4831	12.2697	-0.0068	-0.1738	-1.3964
			bottom	0.4881	12.3977	0.4792	12.1710	-0.0089	-0.2267	-1.8286
	A7	2-06	top	0.4910	12.4714	0.4850	12.3180	-0.0060	-0.1534	-1.2302
			middle	0.4901	12.4485	0.4831	12.2697	-0.0070	-0.1788	-1.4367
			bottom	0.4881	12.3977	0.4789	12.1647	-0.0092	-0.2330	-1.8794
	A8	1-67	top	0.4910	12.4714	0.4845	12.3054	-0.0065	-0.1660	-1.3312
			middle	0.4899	12.4435	0.4825	12.2550	-0.0074	-0.1885	-1.5145
			bottom	0.4872	12.3749	0.4798	12.1878	-0.0074	-0.1870	-1.5115
	B5	4-21	top	0.4907	12.4638	0.4841	12.2949	-0.0066	-0.1689	-1.3551
			middle	0.4905	12.4587	0.4817	12.2340	-0.0088	-0.2247	-1.8035
			bottom	0.4886	12.4104	0.4791	12.1689	-0.0095	-0.2415	-1.9460
	B6	3-32	top	0.4907	12.4638	0.4844	12.3033	-0.0063	-0.1605	-1.2877
			middle	0.4897	12.4384	0.4838	12.2886	-0.0059	-0.1498	-1.2043
			bottom	0.4879	12.3927	0.4795	12.1794	-0.0084	-0.2132	-1.7206
	B7	2-53	top	0.4908	12.4663	0.4847	12.3117	-0.0061	-0.1546	-1.2405
			middle	0.4903	12.4536	0.4821	12.2466	-0.0082	-0.2070	-1.6623
			bottom	0.4881	12.3977	0.4799	12.1899	-0.0082	-0.2078	-1.6762
	B8	1-68	top	0.4908	12.4663	0.4839	12.2907	-0.0069	-0.1756	-1.4089
			middle	0.4897	12.4384	0.4828	12.2634	-0.0069	-0.1750	-1.4068
			bottom	0.4875	12.3825	0.4800	12.1920	-0.0075	-0.1905	-1.5382

TABLE 4.3.1.3

LENGTH CHANGES OF FUEL COMPACTS (NPR-1)

Capsule	Pos.	Zone-GA #	Preirr Lp (in)	Preirr Lp (mm)	Spec avg L (in.)	Spec avg L (mm)	L - Lp (in.)	L - Lp (mm)	(L-Lp)/Lp (%)
NPR-1	A1	1-14	1.9450	49.4030	1.9140	48.6156	-0.0310	-0.7874	-1.5938
	A2	2-82	1.9420	49.3268	1.9202	48.7731	-0.0218	-0.5537	-1.1226
	A3	3-16	1.9490	49.5046	1.9219	48.8163	-0.0271	-0.6883	-1.3905
	A4	4-76	1.9460	49.4284	1.9209	48.7896	-0.0252	-0.6388	-1.2924
	B1	1-2	1.9420	49.3268	1.9198	48.7616	-0.0222	-0.5652	-1.1457
	B2	2-74	1.9460	49.4284	1.9218	48.8137	-0.0242	-0.6147	-1.2436
	B3	3-15	1.9480	49.4792	1.9195	48.7553	-0.0285	-0.7239	-1.4630
	B4	4-52	1.9460	49.4284	1.9226	48.8328	-0.0234	-0.5956	-1.2050
NPR-1	A5	4-01	1.9500	49.5300	broken	n.a.	n.a.	n.a.	n.a.
	A6	3-35	1.9450	49.4030	broken	n.a.	n.a.	n.a.	n.a.
	A7	2-89	1.9410	49.3014	broken	n.a.	n.a.	n.a.	n.a.
	A8	1-48	1.9500	49.5300	broken	n.a.	n.a.	n.a.	n.a.
	B5	4-19	1.9470	49.4538	1.9212	48.7985	-0.0258	-0.6553	-1.3251
	B6	3-21	1.9500	49.5300	1.9257	48.9115	-0.0243	-0.6185	-1.2487
	B7	2-84	1.9420	49.3268	1.9154	48.6512	-0.0266	-0.6756	-1.3697
	B8	1-20	1.9410	49.3014	broken	n.a.	n.a.	n.a.	n.a.

TABLE 4.3.1.3, continued

LENGTH CHANGES OF FUEL COMPACTS (NPR-2)

Capsule	Pos.	Zone-GA #	Preirr Lp (in)	Preirr Lp (mm)	Spec avg L (in.)	Spec avg L (mm)	L - Lp (in.)	L - Lp (mm)	(L-Lp)/Lp (%)
NPR-2	A1	1-50	1.9490	49.5046	1.9195	48.7540	-0.0295	-0.7506	-1.5162
	A2	2-22	1.9430	49.3522	1.9128	48.5851	-0.0302	-0.7671	-1.5543
	A3	3-70	1.9390	49.2506	1.9159	48.6639	-0.0231	-0.5867	-1.1913
	A4	4-161	1.9400	49.2760	1.9121	48.5673	-0.0279	-0.7087	-1.4381
	B1	1-58	1.9380	49.2252	1.9129	48.5864	-0.0251	-0.6388	-1.2977
	B2	2-57	1.9400	49.2760	1.9099	48.5102	-0.0301	-0.7658	-1.5541
	B3	3-54	1.9460	49.4284	1.9160	48.6651	-0.0300	-0.7633	-1.5442
	B4	4-60	1.9460	49.4284	1.9160	48.6664	-0.0300	-0.7620	-1.5416
NPR-2	A5	4-159	1.9450	49.4030	1.9184	48.7274	-0.0266	-0.6756	-1.3676
	A6	3-07	1.9480	49.4792	1.9166	48.6816	-0.0314	-0.7976	-1.6119
	A7	2-06	1.9390	49.2506	1.9079	48.4607	-0.0311	-0.7899	-1.6039
	A8	1-67	1.9490	49.5046	1.9159	48.6626	-0.0331	-0.8420	-1.7009
	B5	4-21	1.9460	49.4284	1.9131	48.5915	-0.0330	-0.8369	-1.6932
	B6	3-32	1.9370	49.1998	1.9110	48.5381	-0.0261	-0.6617	-1.3449
	B7	2-53	1.9450	49.4030	1.9148	48.6359	-0.0302	-0.7671	-1.5527
	B8	1-68	1.9480	49.4792	1.9250	48.8950	-0.0230	-0.5842	-1.1807

4.3.2 Metrology of Graphite Bodies

The dimensions of the graphite fuel bodies are needed for calculating the gas gaps for the postirradiation thermal analysis. The diameters were measured for this purpose using the same procedure as described for compacts above (Ref. 4.3.1). The external diameter measurements were made for two orientations (0° and 90°) at the mid-length location of each stepped portion or "zone" of each graphite body. Reference was made to a cylindrical calibration standard of diameter 1.1903 ± 0.00005 in. before and after each measurement series.

Fuel compact bore hole inside diameters were measured using a Dyer-Subito 10-in. capacity bore gage. Multiple readings (0° and 90°) were made of the I.D. of each fuel compact hole (A and B) of each graphite body at five axial locations: the one-quarter, one-half, and three-quarter points and at a distance 0.625 inches in from each end (to avoid the end cap threaded region). Comparison was made with a Class "X" precision ring gage, 0.4900 in. I.D., before and after each series of hole measurements.

The graphite body external dimensions are in Table 4.3.2.1. It can be seen from the data that the bodies have contracted in outside diameter by amounts ranging from about 0.2 % (those zones on the ends of the capsule) to 0.4 % (those in the middle). The fuel compact bore diameters, given in Table 4.3.2.2, are all less (0.1 to 0.3 %) than initially, with the greatest shrinkage in the center of the test.

TABLE 4.3.2.1

DIAMETER CHANGES OF GRAPHITE BODIES

Capsule	Bdy No.	Loc. on gr.body	Preirr Dp (in)	Preirr Dp (mm)	Spec Dia D (in.)	Spec Dia D (mm)	D - Dp (in.)	D - Dp (mm)	D-Dp/Dp (%)
NPR-1	U	zone 1	1.2024	30.5410	1.1998	30.4761	-0.0026	-0.0649	-0.2125
		zone 2	1.1985	30.4419	1.1951	30.3554	-0.0034	-0.0865	-0.2843
		zone 3	1.1975	30.4165	1.1932	30.3081	-0.0043	-0.1084	-0.3563
		zone 4	1.1915	30.2641	1.1863	30.1308	-0.0052	-0.1333	-0.4406
	L	zone 4	1.1913	30.2590	1.1865	30.1377	-0.0048	-0.1213	-0.4010
		zone 3	1.1973	30.4114	1.1934	30.3128	-0.0039	-0.0987	-0.3244
		zone 2	1.1986	30.4444	1.1963	30.3854	-0.0023	-0.0591	-0.1940
		zone 1	1.2025	30.5435	1.2006	30.4960	-0.0019	-0.0475	-0.1555
NPR-2	U	zone 1	1.2105	30.7467	1.2086	30.6996	-0.0019	-0.0471	-0.1532
		zone 2	1.2128	30.8051	1.2090	30.7091	-0.0038	-0.0961	-0.3118
		zone 3	1.2102	30.7391	1.2058	30.6261	-0.0044	-0.1129	-0.3674
		zone 4	1.2046	30.5968	1.1996	30.4698	-0.0050	-0.1271	-0.4153
	L	zone 4	1.2045	30.5943	1.2001	30.4824	-0.0044	-0.1119	-0.3659
		zone 3	1.2103	30.7416	1.2053	30.6135	-0.0050	-0.1281	-0.4166
		zone 2	1.2127	30.8026	1.2087	30.7007	-0.0040	-0.1019	-0.3309
		zone 1	1.2108	30.7543	1.2078	30.6786	-0.0030	-0.0757	-0.2461

TABLE 4.3.2.2

INSIDE DIAMETER CHANGES OF GRAPHITE BODY FUEL HOLES

Capsule	Bdy- Hole	Loc. in hole	Preirr Dp (in)	Preirr Dp (mm)	Meas Dia D (in.)	Meas Dia D (mm)	D - Dp (in.)	D - Dp (mm)	(D-Dp)/Dp (%)
NPR-1	U-A	top	0.4965	12.6111	0.4961	12.6009	-0.0004	-0.0102	-0.0806
		1/4	0.4965	12.6111	0.4959	12.5959	-0.0006	-0.0152	-0.1208
		middle	0.4965	12.6111	0.4960	12.5984	-0.0005	-0.0127	-0.1007
		3/4	0.4965	12.6111	0.4951	12.5743	-0.0014	-0.0368	-0.2920
		bottom	0.4965	12.6111	0.4950	12.5717	-0.0015	-0.0394	-0.3122
	U-B	top	0.4965	12.6111	0.4963	12.6048	-0.0002	-0.0063	-0.0504
		1/4	0.4965	12.6111	0.4960	12.5984	-0.0005	-0.0127	-0.1007
		middle	0.4965	12.6111	0.4959	12.5959	-0.0006	-0.0152	-0.1208
		3/4	0.4965	12.6111	0.4951	12.5755	-0.0014	-0.0356	-0.2820
		bottom	0.4965	12.6111	0.4947	12.5641	-0.0018	-0.0470	-0.3726
	L-A	top	0.4965	12.6111	0.4949	12.5705	-0.0016	-0.0406	-0.3223
		1/4	0.4965	12.6111	0.4952	12.5768	-0.0013	-0.0343	-0.2719
		middle	0.4965	12.6111	0.4956	12.5870	-0.0009	-0.0241	-0.1913
		3/4	0.4965	12.6111	0.4960	12.5971	-0.0005	-0.0140	-0.1108
		bottom	0.4965	12.6111	0.4959	12.5959	-0.0006	-0.0152	-0.1208
	L-B	top	0.4965	12.6111	0.4951	12.5755	-0.0014	-0.0356	-0.2820
		1/4	0.4965	12.6111	0.4953	12.5806	-0.0012	-0.0305	-0.2417
		middle	0.4965	12.6111	0.4961	12.5997	-0.0005	-0.0114	-0.0906
		3/4	0.4965	12.6111	0.4960	12.5971	-0.0005	-0.0140	-0.1108
		bottom	0.4965	12.6111	0.4960	12.5971	-0.0005	-0.0140	-0.1108

TABLE 4.3.2.2, continued

INSIDE DIAMETER CHANGES OF GRAPHITE BODY FUEL HOLES

Capsule	Bdy-Hole	Loc. in hole	Preirr Dp (in)	Preirr Dp (mm)	Meas Dia D (in.)	Meas Dia D (mm)	D - Dp (in.)	D - Dp (mm)	(D-Dp)/Dp (%)
NPR-2	U-A	top	0.4965	12.6111	0.4957	12.5908	-0.0008	-0.0203	-0.1611
		1/4	0.4965	12.6111	0.4955	12.5857	-0.0010	-0.0254	-0.2014
		middle	0.4965	12.6111	0.4952	12.5768	-0.0013	-0.0343	-0.2719
		3/4	0.4965	12.6111	0.4947	12.5641	-0.0018	-0.0470	-0.3726
		bottom	0.4965	12.6111	0.4947	12.5641	-0.0018	-0.0470	-0.3726
	U-B	top	0.4965	12.6111	0.4961	12.5997	-0.0005	-0.0114	-0.0906
		1/4	0.4965	12.6111	0.4958	12.5933	-0.0007	-0.0178	-0.1410
		middle	0.4965	12.6111	0.4956	12.5870	-0.0010	-0.0241	-0.1913
		3/4	0.4965	12.6111	0.4950	12.5730	-0.0015	-0.0381	-0.3021
		bottom	0.4965	12.6111	0.4951	12.5755	-0.0014	-0.0356	-0.2820
	L-A	top	0.4965	12.6111	0.4948	12.5667	-0.0017	-0.0444	-0.3525
		1/4	0.4965	12.6111	0.4950	12.5730	-0.0015	-0.0381	-0.3021
		middle	0.4965	12.6111	0.4954	12.5819	-0.0011	-0.0292	-0.2316
		3/4	0.4965	12.6111	0.4959	12.5946	-0.0006	-0.0165	-0.1309
		bottom	0.4965	12.6111	0.4962	12.6022	-0.0003	-0.0089	-0.0705
	L-B	top	0.4965	12.6111	0.4949	12.5692	-0.0016	-0.0419	-0.3323
		1/4	0.4965	12.6111	0.4948	12.5679	-0.0017	-0.0432	-0.3424
		middle	0.4965	12.6111	0.4953	12.5806	-0.0012	-0.0305	-0.2417
		3/4	0.4965	12.6111	0.4957	12.5908	-0.0008	-0.0203	-0.1611
		bottom	0.4965	12.6111	0.4960	12.5984	-0.0005	-0.0127	-0.1007

4.4 Fission Gas Release

To obtain one measure of the irradiation performance of the fuel compacts in experiments NPR 1 and NPR 2, three methods of monitoring fission gas release were employed. The results were used to estimate the fraction of coated fuel particles embedded in compacts which failed to retain fission gases under the irradiation conditions. The coatings of the releasing particles had to have a connected pore system through which the fission gases released from the kernels could escape from the particles. Contributing to this pore system presumably were cracks developing under the effects of irradiation, gas pressure buildup, chemical interactions and the permeabilities of the coatings as manufactured and through changes in service. Aside from cracks and permeabilities, the measurement of fission gas release was not an indicator of fuel particle performance in terms of the sequence of events leading to failure of the particle to retain fission gases.

4.4.1 Methods of Monitoring Fission Gas Release

The three methods of monitoring fission gas release involved: (1) the concentration of fission gas in a series of samples of the capsule sweep gas during irradiation in the HFIR, (2) monitoring of the ionization chamber signal resulting from radiodecay of fission products in the HFIR effluent sweep gas and (3) determination of the ratio of released fission gas to that from a sample of uranium stearate in TRIGA experiments on compacts irradiated in HFIR .

4.4.1.1 Gas Release in HFIR Experiments

4.4.1.1.1 Grab Samples

In the first method (Refs. 4.4-1, 4.4-2) a small volume of the effluent sweep gas was taken periodically and the number density of atoms of each isotope determined. The release rate, R, was calculated using equation (4.4-1):

$$R_i = N_i f_r \tag{4.4-1}$$

where

R_i = release rate (atom/s) for isotope i

N_i = number density of atoms (atom/cm^3) for isotope i

f_r = flow rate (cm^3/s)

The number density of atoms was determined by measuring the fission gas inventory collected in a serum bottle using a gamma spectrometer fitted with a high-efficiency germanium detector. The efficiency of the gamma spectrometer at various photon energies was measured using a simulated gas source placed inside a serum bottle.

The flow rate through the capsule was determined by a mass flowmeter in the exit tubing of the capsule and by flowmeters measuring the inlet flows of helium and neon. The exit flowmeter reading was used for the calculations and generally was within $\pm 10\%$ of the combined inlet flows.

In order to account for decay during the transit of the gas from the outlet of the capsule to the gas sampling station, gamma counting data was back-corrected to an effective sampling time. This time was calculated using the measured flow rate and assuming slug flow in the tubing:

$$Sample\ Time_{eff} = Clock\ time - \frac{V_{tube}}{60\, f_r} \tag{4.4-2}$$

where

$Sample\ Time_{eff}$ = the time the sample exited the capsule (hr)

$Clock\ time$ = actual time the sample was obtained (hr)

V_{tube} = volume of tubing between the capsule and the sampling station (cm^3)

f_r = flow rate (cm^3/min)

In many cases, the time between obtaining the grab sample and the gamma analysis was sufficiently long that ^{89}Kr (with a 3.18 min. half-life) had decayed so that its concentration was below the detectable limit of the spectrometer. In these instances, the initial ^{89}Kr in the grab sample was estimated from the concentration of its daughter, ^{89}Rb, using the growth and decay equation:

$$N_{kr} = \frac{N_{rb}\,(\lambda_{rb} - \lambda_{kr})}{\lambda_{kr}\,(e^{-\lambda_{kr} t} - e^{-\lambda_{rb} t})} \qquad (4.4\text{-}3)$$

where

N_{kr} = the number density of ^{89}Kr (atoms/cm^3) at the capsule sample time

N_{rb} = the number density of ^{89}Rb (atoms/cm^3) at the start of gamma counting

λ_i = the decay constant for nuclide i (1/sec)

t = delay time between sampling and gamma counting (s)

The release rate, R, was normalized to the birth rate, B, to obtain the release rate to birth rate ratio, R_i/B_i. The birth rate, B_i, of fission gas nuclides which are produced by decay of precursor nuclides with much shorter half lives than the fission gas (^{85m}Kr, ^{87}Kr, ^{88}Kr, ^{89}Kr, ^{138}Xe) was calculated using the CACA computer code (Ref. 4.4-3) from

$$B_i = \Phi \sum_j \sigma_j N_j Y_i \qquad (4.4\text{-}4)$$

where

B_i = birth rate of isotope i (atom/s)

ϕ = neutron flux (n/m^2-s)

σ_j = fission cross section for neutron capture of U or Pu isotopes (m^2)

N_j = number of atoms of ^{235}U, ^{239}Pu and ^{241}Pu (dimensionless)

Y_i = cumulative fission yield of isotope i

The birth rate for fission gases that have a precursor nuclide with a similar or longer half-life than the gas depends on the decay rate of the precursor. Thus, for ^{133}Xe, ^{135m}Xe, and ^{135}Xe, the birth rate was calculated using the CACA computer code via equation (4.4-5):

$$B_i = N_{i-1}\lambda_{i-1}f_i + \Phi\sum \sigma_j N_j DY_i \qquad (4.4\text{-}5)$$

where

N_{i-1} = number of atoms of the precursor nuclide in the capsule

λ_{i-1} = decay constant of the precursor nuclide (1/s)

f_i = branching ratio (fraction of precursor disintegrations that yield the fission gas)

DY_i = Direct fission yield of the fission gas i

and the remaining symbols have been defined in the preceding equations.

The R/B values thus determined, $(R_i/B_i)_{capsule,t}$, represent the average release rate to birth rate ratio at time t in an irradiation capsule throughout which the temperature, burnup, fission rate density and fast fluence varied. Normally, R/B represents the steady-state, fractional fission gas release and therefore would apply to constant values of R/B. To encompass the variation in the deduced R/B, the assumption is normally made that the release is always close to the steady state and that recovery of R/B from a perturbation in the steady-state or a change in gas release is sufficiently rapid.

To determine the fraction of particles with a connected pore system, *i.e.* the fraction of particles "failed", using the measured values of $(R_i/B_i)_{capsule,t}$, the following relation is required:

$$\left(\frac{R_i}{B_i}\right)_{capsule,t} = \frac{\sum_{volumes,k=1}^{n} f_{f,k} \left(\frac{R}{B}\right)_{particle,k} B_k}{\sum_{k=1}^{n} B_k} \qquad (4.4\text{-}6)$$

where

$f_{f,k}$ = the fraction of particles "failed"

$(R/B)_{particle,k}$ = the R/B for an individual failed particle averaged over the temperatures, burnups, fission rate densities and fast fluences of the capsule at time t in the manner implicit in the measurement of $(R_i/B_i)_{capsule,t}$.

In lieu of measurements of $(R_i/B_i)_{particle,t}$, it is necessary to calculate this quantity at selected times in determining the fractional particle failure. To do so requires a model for failed particles and a correlation between the occurrence, or at least the beginning, of failure and the reactor parameters. With the aid of the correlation, the range of parameters entered into the fission gas release model can be restricted to more closely approach the distribution implicit in the measured values of $(R_i/B_i)_{capsule,t}$.

A complication in the above approach to determining the fraction of particles "failed" is the release of stored-fission gas from bubbles. This type of release may occur in the process of particle failure and from failed particles following increases in temperature for temperatures above 1100°C or addition of oxidants to the system. The release is greater than

normal and is transient. As a consequence, the release declines with time after the onset and the number of contributing failed particles is difficult to assess.

In the process of the coatings of a particle becoming permeable to gases, developing complete radial cracks or fragmenting, a connected pore system can be established provided all coatings undergo one or more of these changes; then fission gas released from the kernel can escape from the particle. The gas release is clearly not an indicator of the sequence in which the coatings undergo these changes.

4.4.1.1.2 Transient Fission Gas Release

Transient fission gas release occurs when the kernels of intact particles are exposed, when exposed kernels are subject to rapid increases in temperature and when oxidants or other chemical species that readily diffuse in the fuel kernels are added to the particle system. The transients are monitored by the response of an ionization chamber to the pulses of radioactivity in the effluent gas flowing through a tube helically wound around the wall of an ionization chamber. Under conditions of constant temperature and gas composition (He gas), pluses such as are shown in Figure 4.4-1 are observed. For particles with UCO kernels surrounded only by a 23 μm thick pyrocarbon layer, the pulses of Figure 4.4-1 occurred when the pyrocarbon cracked from the accumulated damage within the first 50 h of irradiation in HFIR (Ref. 4.4-4). In the case of normally configured fuel particles and changing temperatures and gas compositions, the ionization chamber signals are more difficult to interpret.

The sweep gas is initially helium; when temperatures above those reached with He flowing are desired, neon is added to the sweep gas to reduce the thermal conductivity. The consequences of this addition are: (1) The ionization chamber signal is increased as a result of the decay following the excitation of neon to ^{23}Ne. The latter decays by emitting a photon at 440 KeV and an electron at 4.38 MeV. (2) The increased temperature following neon addition induces the release of stored fission gas (see section 4.4.1.1). (3) The initial transient after neon addition is observed to occur after a constant decay time; this is in contrast to the random timing expected of failure processes. (4) In the presence of only helium, a preponderant number of the transient peaks have small heights whereas in the presence of a mixture of helium and neon, the distribution clearly shifts to larger peak heights. (5) The

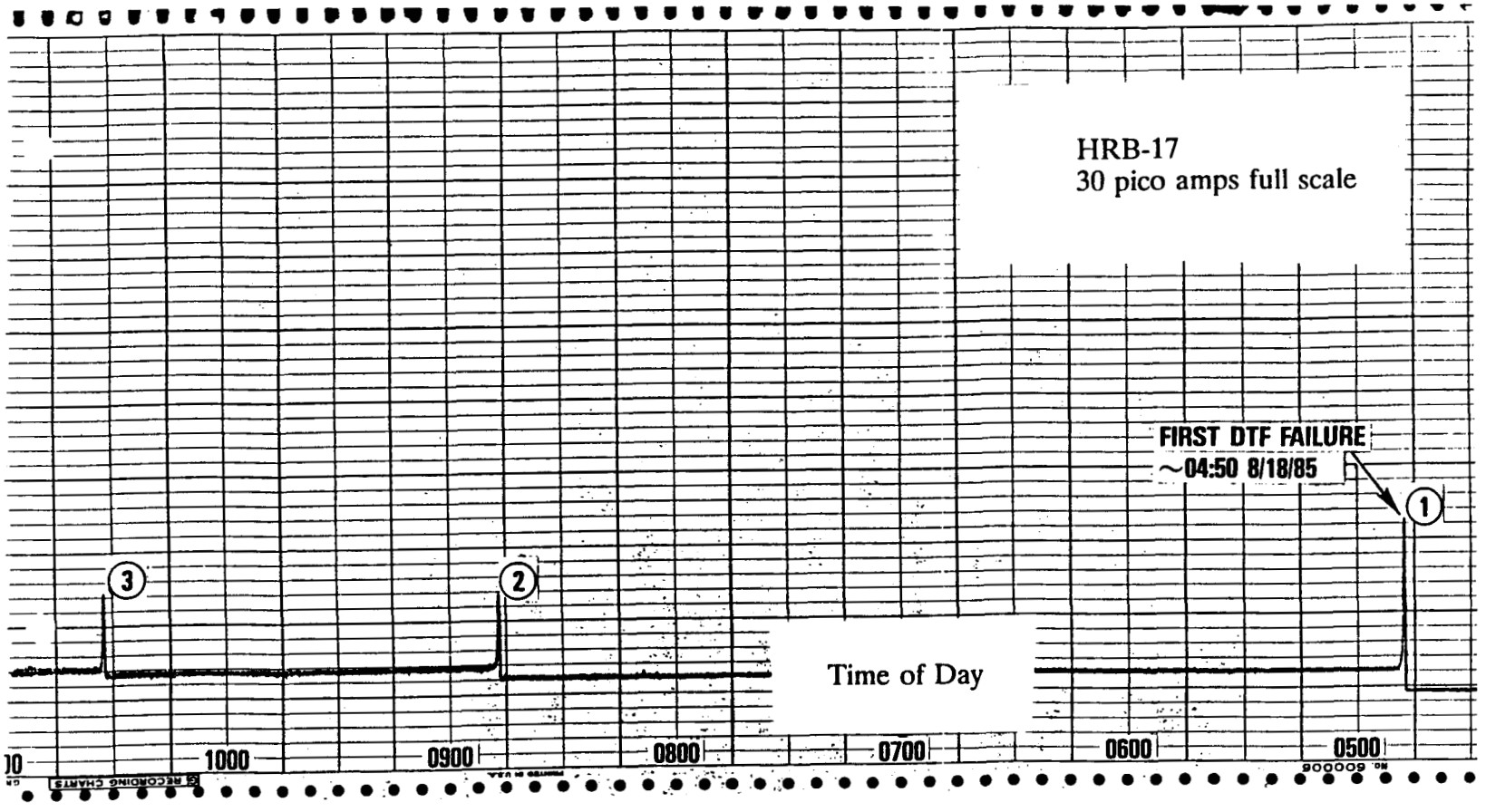

Figure 4.4-1.Transient fission gas release detected as a pulse on a sweep gas ionization chamber.

possibility exists that particles having exposed kernels could emit fission gas transiently inresponse to a rapid increase in temperature as in neon addition. Thus, two or more transients could represent pulsed fission gas release from a single particle.

In the analysis of transients, the resulting spikes are classified into four categories which are based on the gas composition and mode of operation: (1) 100% He; (2) Ne being added; (3) a constant sweep gas mixture of He and Ne and (4) shutdown. In the latter class, the ionization chamber signal is quite different from all other signals, occurs only at shutdown, and has the same form in all cases.

4.4.1.2 Gas Release in TRIGA Experiments

4.4.1.2.1 The calibration method

Fuel compacts were irradiated in the TRIGA Mark I reactor at temperatures of 900, 1100 and 1300°C and the released fission gases were collected in a cooled charcoal trap and gamma counted (Ref. 4.4-5). To provide a calibration factor representing a known fractional release of fission gases generated, this procedure was repeated but at room temperature with uranyl stearate (assumed to be 100% releasing). The irradiations were conducted for 30 min. and gas was collected for an additional 15 min. In one case, the irradiation and sampling continued for 20 h.

The measurement of the fission gas released from the compact is reported in the Gamma Spectrum Analyses as (Ref. 4.4-6) "activity" of the compact according to the relation

$$A' = \frac{C}{(t_c \; b \; \alpha)} \qquad (4.4\text{-}7)$$

where

C = counts (dimensionless)

t_c = counting time (s)

b = branching ratio (fraction of the gammas that result in the measured gamma peak)

α = a constant = 3.7E+04 $dis/(s \cdot \mu C_i)$

dis = disintegration (dimensionless)

A' = "activity" (μC_i)

The comparable term for radiodecay during collecting fission gas in the trap is not explicitly included as the same factor occurs in the calibration factor which is a divisor to A'. A companion measurement under the same conditions but without a compact was made to evaluate the background contribution to A'; this contribution was then subtracted from A'; let

$$\Delta A' = A_{sample} - A_{background} \tag{4.4-8}$$

where

$\Delta A'$ = the true sample "activity" for compact or stearate

If the detector efficiency is known, then $\Delta A'$ can be converted to a "pure" number of μC_i, thus

$$A = \frac{\Delta A'}{\epsilon} \tag{4.4-9}$$

where

A = activity (μC_i)

ϵ = detector efficiency representing the ratio of the number of counts to the number of disintegrations (dimensionless)

The R/B from measurements with the compact and the uranyl stearate can be determined using a version of $\Delta A'$ in which the common factors b and α are omitted and by correcting for the differences in the quantities of fissionable isotopes in the compact and uranyl stearate, provided the counting geometry is the same for compact and stearate. Thus,

$$\frac{R}{B} = \frac{\Delta A'_{compact}}{\Delta A'_{stearate}} \times \frac{U^{235}_{stearate}}{U^{235}_{eq,compact}} \tag{4.4-10}$$

The compacts contain not only ^{235}U but also ^{239}Pu and ^{241}Pu; the equivalent ^{235}U content of the compacts is obtained as

$$U^{235}_{eq,compact} = \sum_{i=1}^{n} m_i \left(\frac{\sigma_i}{\sigma}\right) \left(\frac{Y_i}{Y}\right) \tag{4.4-11}$$

where

m_i = mass of fissionable isotope i

σ_i = cross section for fissionable isotope i

σ = cross section for ^{235}U

Y_i = fission yield for fissionable isotope i

Y = fission yield for ^{235}U

The R/B derived with the calibration method requires a correction for steady state. There are three considerations: (1) a model of fission gas release must be adopted from which the ratio of R/B at times large compared with λt to the R/B at 30 min. can be determined; (2) for the TRIGA data, the release at the end of 30 min. of irradiation must be derived from the measured release after 30 min. of irradiation and 15 min. of postirradiation collection; (3) the observation of an apparently large relative release in the first 0.5 h of irradiation compared with that measured in a second 0.5 h of irradiation, when the irradiation is continued for at least 1 h, has to be resolved. Of possible relevance to the third consideration is the effect of the deposition of energy by slowing fission fragments on the low melting stearate.

The fraction of the generated fission gas which escapes from the uranyl stearate samples must be determined. The fraction is not one as was assumed in the preliminary analysis but is smaller. This is not surprising when the terminal stopping sites of the recoiling fission fragments are considered.

4.4.1.2.2 The absolute method

The TRIGA data can also be used to calculate the R/B without relying on relative measurements. Thus the release rate, R, can be calculated as follows:

$$R_i = \frac{C_i}{t_c \cdot \epsilon \cdot b \cdot \lambda \cdot t \cdot f_i} \tag{4.4-12}$$

where

R_i = release rate of isotope i (atom/s)

C_i = counts for isotope i (dimensionless)

t_c = counting time (s)

ϵ = detector efficiency representing the ratio of the number of counts to the number of disintegrations (dimensionless)

b = branching ratio (dimensionless)

λ = radiodecay constant (1/s)

t = collection time (s)

f_i = $\{(1-e^{-\lambda t})/\lambda t\}$ = fractional reduction in counts from radiodecay during collection of isotope i

The birth rate is given by equations (4.4-4) or (4.4-5), above.

If the absolute method is applied to the results of the standard TRIGA method (i.e., fission gas collection during 30 min. of irradiation and 15 min. of postirradiation conditions), then steady state considerations (1) and (2) presented above apply; however, consideration (3) is not relevant. With the absolute method applied to TRIGA data, there is no aberration in the derived R/B values for a set of first and second 0.5 h irradiation periods.

4.4.2 The Results of Monitoring Fission Gas Release

4.4.2.1 Gas Release in HFIR Experiments

4.4.2.1.1 R/B Measurements

Measurements of the fission gas release rates were carried out using the grab sample technique for sampling the sweep gas after exiting from the fuel capsule. The initial results, as reported in the Irradiation Phase report (Ref. 4.4-7), have been updated to reflect small changes in the capsule sweep gas flow rates and refinements in the CACA code calculation of the fission gas birth rate. In addition, the release of ^{89}Kr has been calculated based on the amount of ^{89}Rb using equation (4.4-3). Thus, a table of the NPR 1 results is included in Appendix A and Appendix B includes the NPR 2 results. The appendixes report the

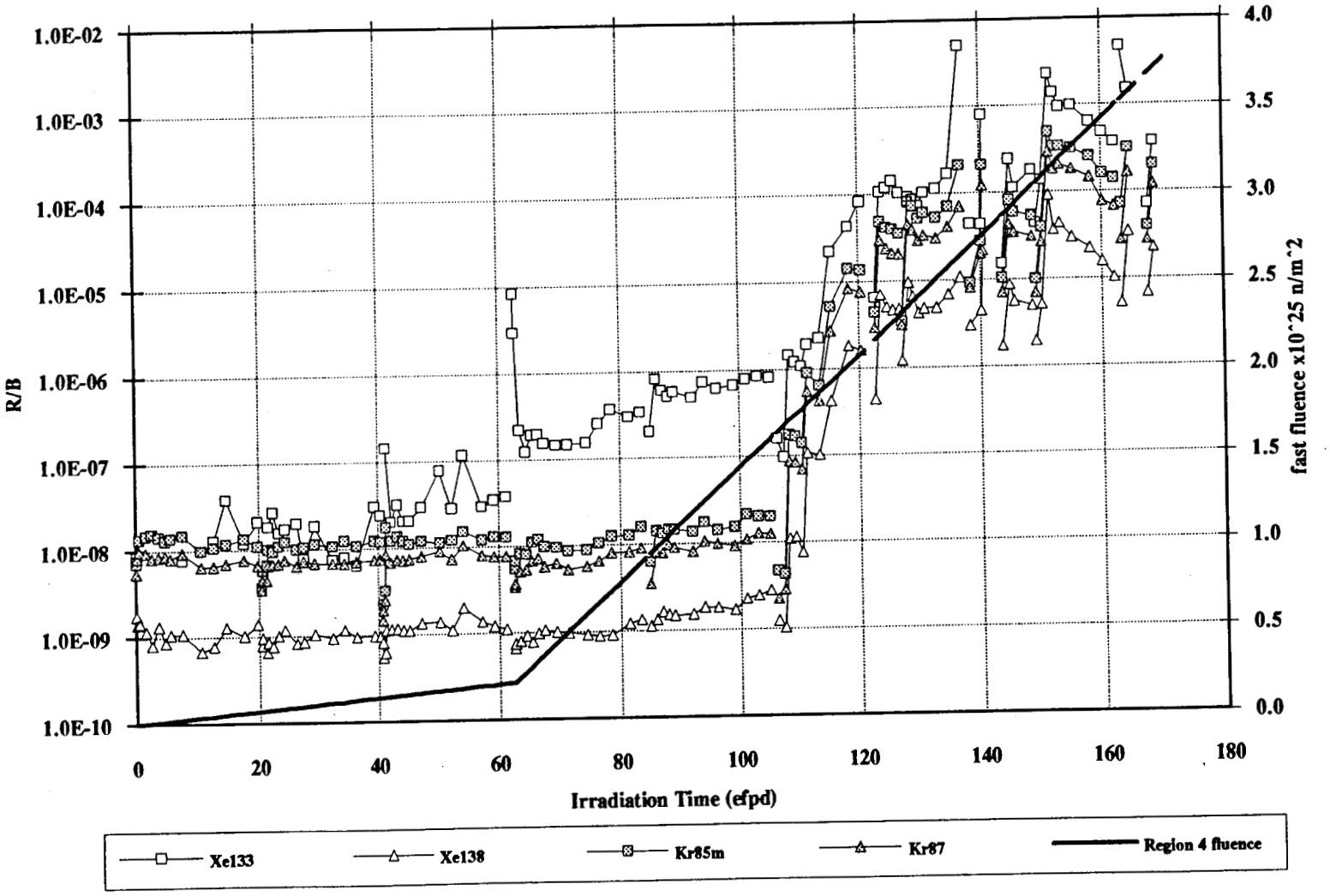

Figure 4.4-2. NPR 1 R/B of selected fission gases and estimated region 4 compact fast fluence as a function of efpd.

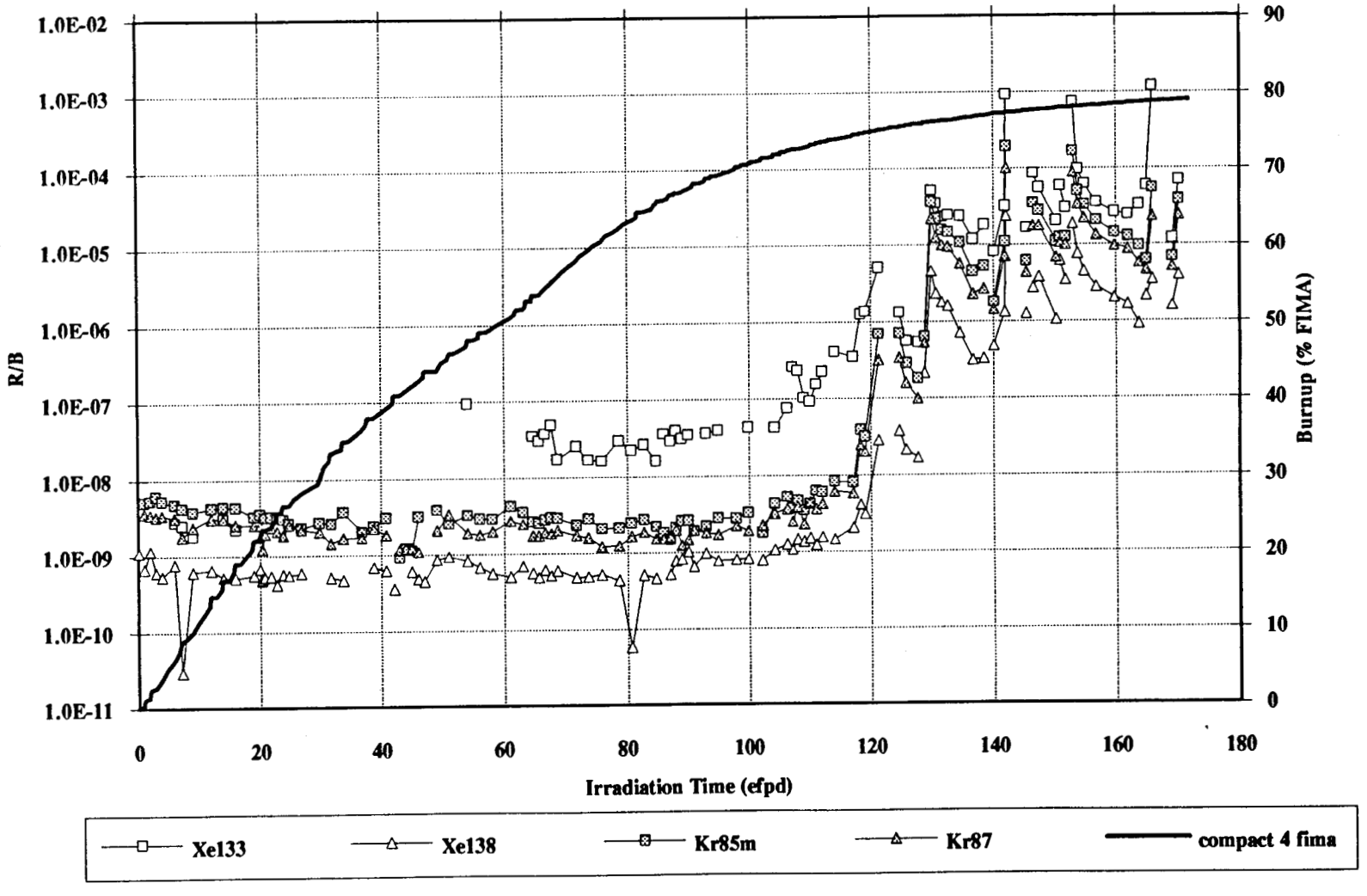

Figure 4.4-3. NPR 2 R/B of selected fission gases and estimated burnup for compacts irradiated in HFIR region 4 as a function of efpd.

R/B value, the measured specific activity of the sweep gas, and some estimated fuel conditions at the time the samples were obtained. The Release rate to Birth rate ratio (R/B) for selected isotopes (^{133}Xe, ^{138}Xe, ^{85m}Kr, and ^{87}Kr) is plotted as a function of the effective full power days (efpds) in Figure 4.4-2 for NPR 1 and in Figure 4.4-3 for NPR 2. Initial R/B ratios were very low ($<10^{-8}$), which shows that the as-manufactured fuel compacts had only a very small amount of uranium contamination, and that the coatings on the fuel particles in the compacts were intact. The R/B ratios remained low for over 100 efpds after which the R/B increased rapidly. Close examination of the data shows that the R/B for each of the nuclides with a half-life of greater than about 15 min remained constant for a period of time and then gradually increased up to the time of the sudden, large increase. For example, as shown in Figure 4.4-2, the R/B for ^{133}Xe in the NPR 1 capsule began to increase after about 40 efpds. The time at which xenon and krypton isotopes break through the coatings prior to the sudden increase was dependent upon the half-life of the fission gas as shown in Figure 4.4-4. This early release of ^{133}Xe has been analyzed at GA and is considered to be the result of diffusional release from a small fraction ($\sim 10^{-4}$) of particles that have porous SiC layers after the outer PyC layers fail because of irradiation induced stress (Ref. 4.4-8). The

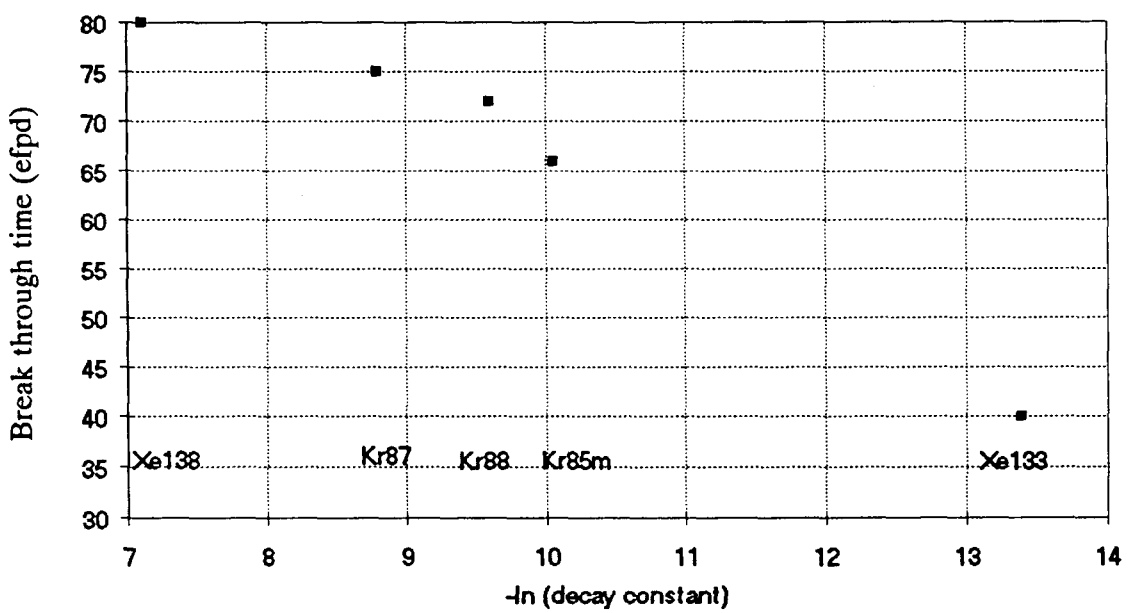

Figure 4.4-4. Fission gas break through times for NPR 1 as a function of the decay constant.

release profile for both the ^{133}Xe and the ^{85m}Kr can be predicted using a simple model that includes pore sizes of around 10 nm with only 50 pores per particle.

During HFIR shutdowns for refueling, which usually takes 6 to 10 days, ^{133}Xe accumulates in the NPR fuel because of ^{133}I decay. The accumulated ^{133}Xe is released upon HFIR startup and the associated increase in temperature. This is seen clearly in Figure 4.4-2 after the restarts at 40 and 60 efpd. The subsequent decline in the ^{133}Xe R/B is caused when the stored ^{133}Xe is released and is removed from the capsule by the sweep gas. This may have occurred after most startups but was not detected in the majority of instances because the first R/B sample after startup was not obtained until after the capsule had been purged with helium for several hours.

The R/B of ^{135m}Xe is about a factor of 3 greater than the R/B for the ^{138}Xe in NPR 1. Since both of these isotopes have similar half lives (15.3 min and 14.2 min, respectively), the difference in R/B is not a half-life effect. Most likely, the difference is due to the mobility of the iodine precursor. ^{135m}Xe is formed in greater than 99% yield by decay of ^{135m}I, whereas only 26% of the ^{138}Xe is formed by decay of ^{138}I (Ref. 4.4-9). Furthermore, ^{135m}I has a 6.5 hr half-life and ^{138}I has only a 6.5 sec half-life. The longer half-life of ^{135m}I results in transport of ^{135m}I to locations in which the daughter ^{135m}Xe has an accessible path to the void space in the capsule.

During the first two irradiation cycles of the NPR 2 capsule, ^{135m}Xe was not detected, even though ^{138}Xe was observed in almost every grab sample. Since ^{135m}Xe was observed in the NPR 1 grab samples, and the gamma counting was conducted using the same procedure, ^{135m}Xe should have been detected if it had been present in the grab samples. Thus, the ^{135m}I generated in NPR 2 was not transported as easily as in the NPR 1. This can be explained by the approximately 200 °C higher temperature in NPR 1.

Significant release of the krypton isotopes did not occur until the maximum fuel burnup (Figure 4.4-5) was greater than 72% and the fast fluence was greater than 1.6×10^{25} n/m^2 (Figure 4.4-6). These figures also show that the increase in release from the NPR 2 capsule occurred after a greater irradiation exposure than the NPR 1 capsule. Since NPR 2 operated at a lower temperature than did NPR 1, this result suggests that the compact temperature has a influence on the onset of coating failure.

As discussed in section 4.4.1, R/B is generally reported after reaching a steady-state value. The approach to steady-state is seen in the krypton data shown in Figure 4.4-2 after

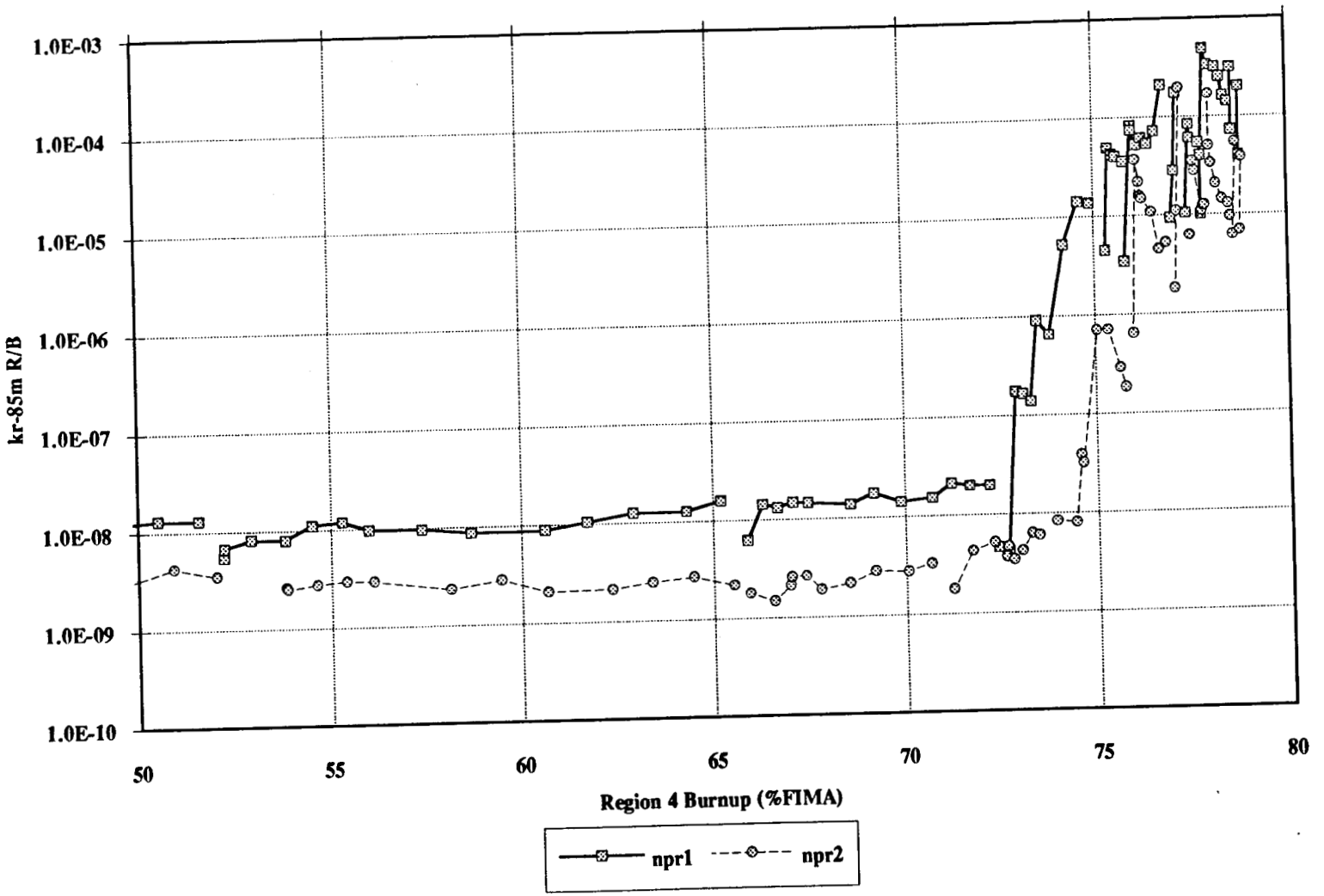

Figure 4.4-5. ^{85m}Kr R/B as a function of region 4 compact burnup for NPR 1 and NPR 2.

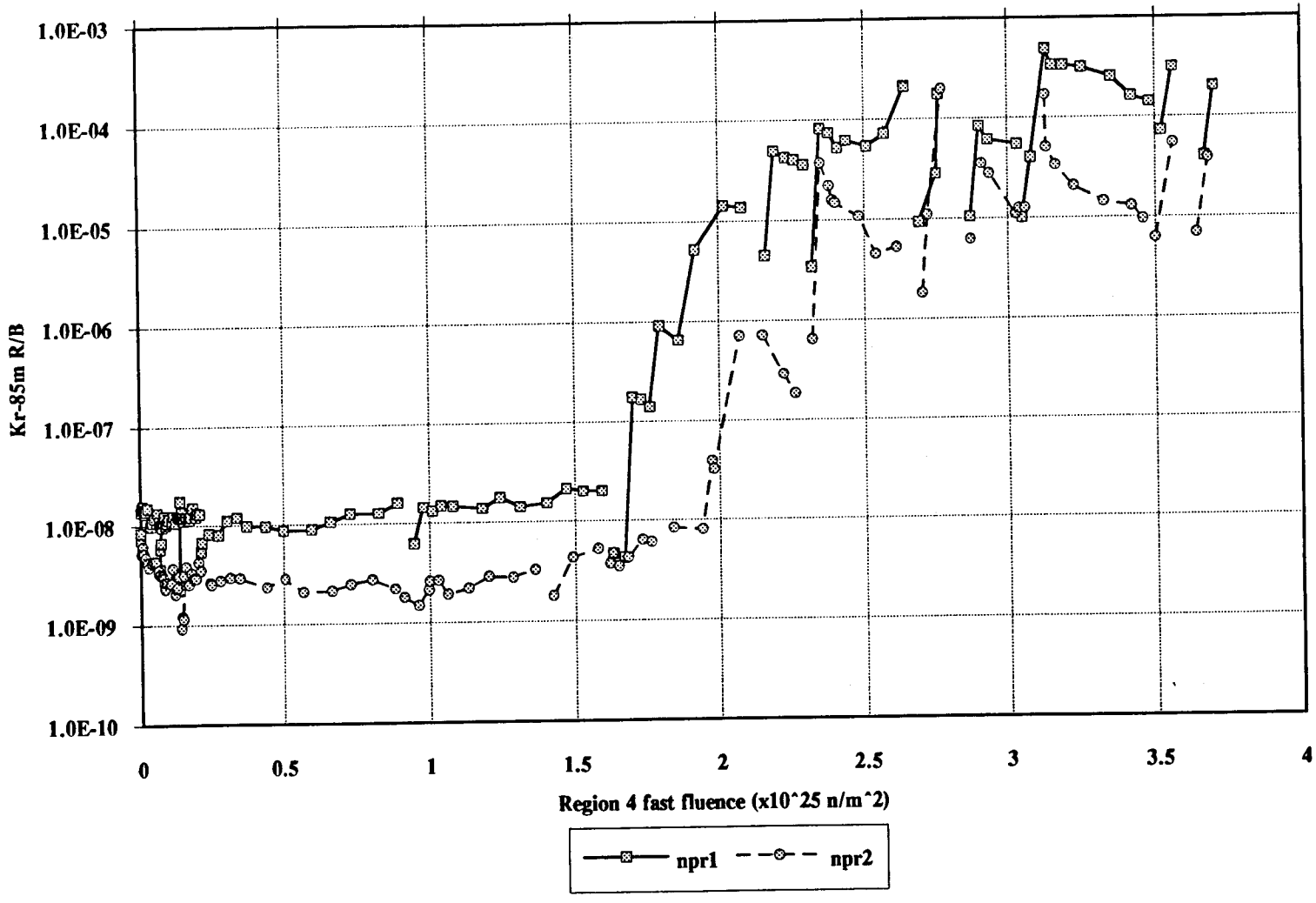

Figure 4.4-6. ^{85m}Kr R/B as a function of region 4 compact fast fluence for NPR 1 and NPR 2.

the restart of HFIR at about 40 efpds. The approach to steady-state results from a release mechanism in which a diffusional process is the controlling step. Provided that the release rate from the particle is small when compared to the radiodecay constant, the concentration of fission gas in the particle reaches a steady-state value when the production rate is balanced by the decay rate. The approach to steady-state is given by

$$N_i = \frac{B_i}{\lambda_i} (1 - e^{-\lambda_i t}) \tag{4.4-13}$$

where the terms have been defined in the previous equations.

The R/B of a failed particle is known to depend on the mechanism controlling the release. At temperatures below about 600 °C, an athermal mechanism (Ref. 4.4-10) often prevails for dense kernel materials, and the R/B remains relatively constant as the temperature decreases. With an increase in temperature, bulk diffusional processes become important. Since the bulk diffusion constant increases with temperature, the R/B increases. Shown in Figure 4.4-7 for NPR 1 and in Figure 4.4-8 for NPR 2 is the ^{85m}Kr R/B plotted as a function of the efpds with an overplot of the estimated volume-averaged fuel temperature for the compacts in HFIR region 2 (see Figures 2.3.3 and 2.3.4 for the compact loading scheme). Region 2 temperatures were plotted because the thermal analysis indicated that the highest temperatures in the capsules were in this region. The large temperature decreases are caused by reactor shutdowns, during which the temperature of the compacts decreased to less than 100 °C. The smaller temperature changes are caused when neon is added or removed from the capsule sweep gas. An analysis of the effects that temperature had on the R/B measured in NPR 1 and NPR 2 is complicated by the fact that both the axial and the radial temperature profiles varied widely during the test. In addition to altering the temperature of the fuel, neon can also influence the capsule averaged R/B by changing the rate at which gas is transported from the fuel compact, across the graphite fuel body, to the sweep gas. This effect results from a change in the effective gas-phase diffusion coefficient which is inversely dependent on the reduced mass of the system (Ref. 11)

$$D_{eff} = \frac{\epsilon}{q} \frac{C_i T^{n_i}}{p \sqrt{\mu}} \tag{4.4-14}$$

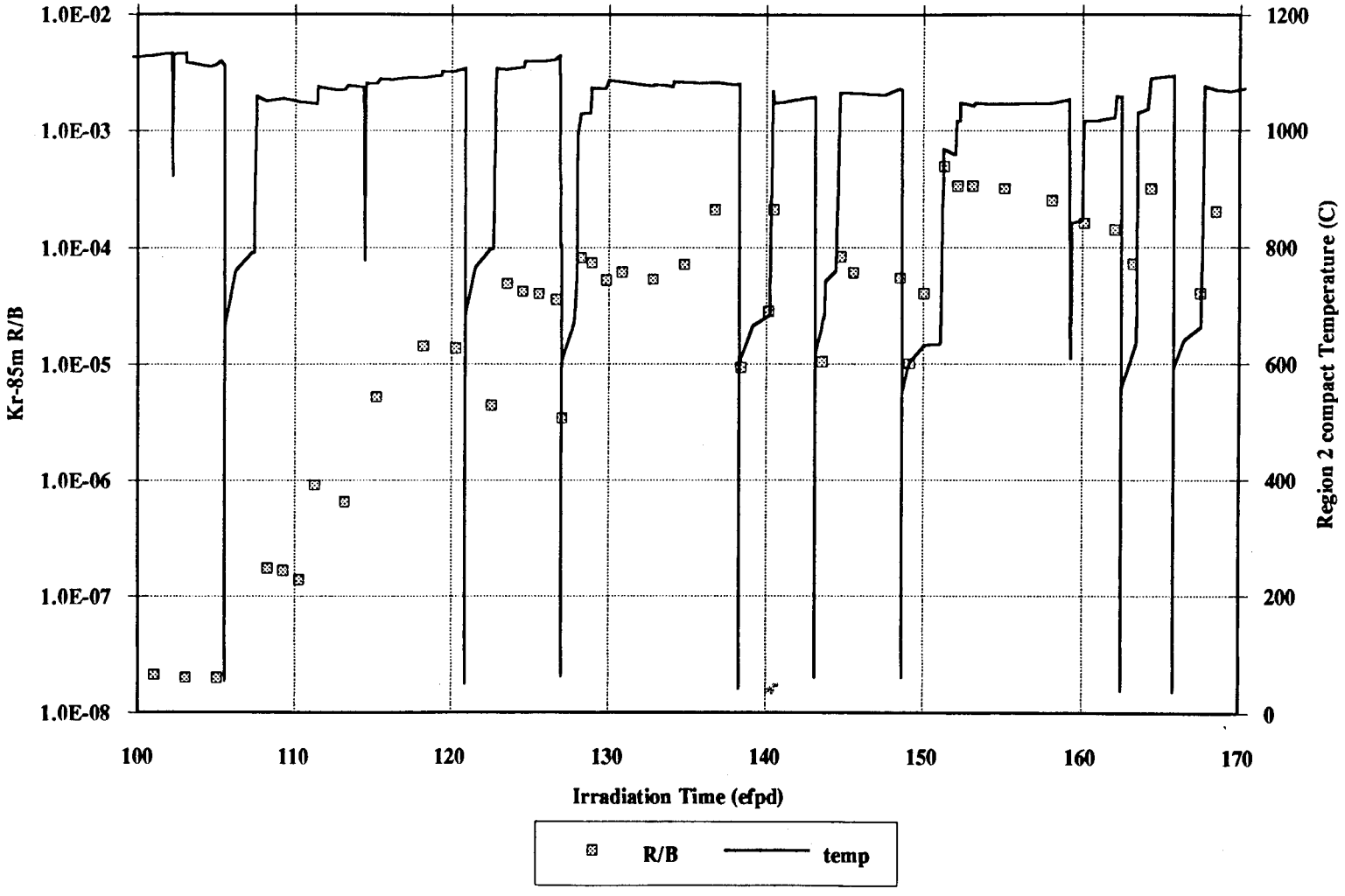

Figure 4.4-7. NPR 1 ^{85m}Kr R/B and estimated region 2 compact temperature versus efpd.

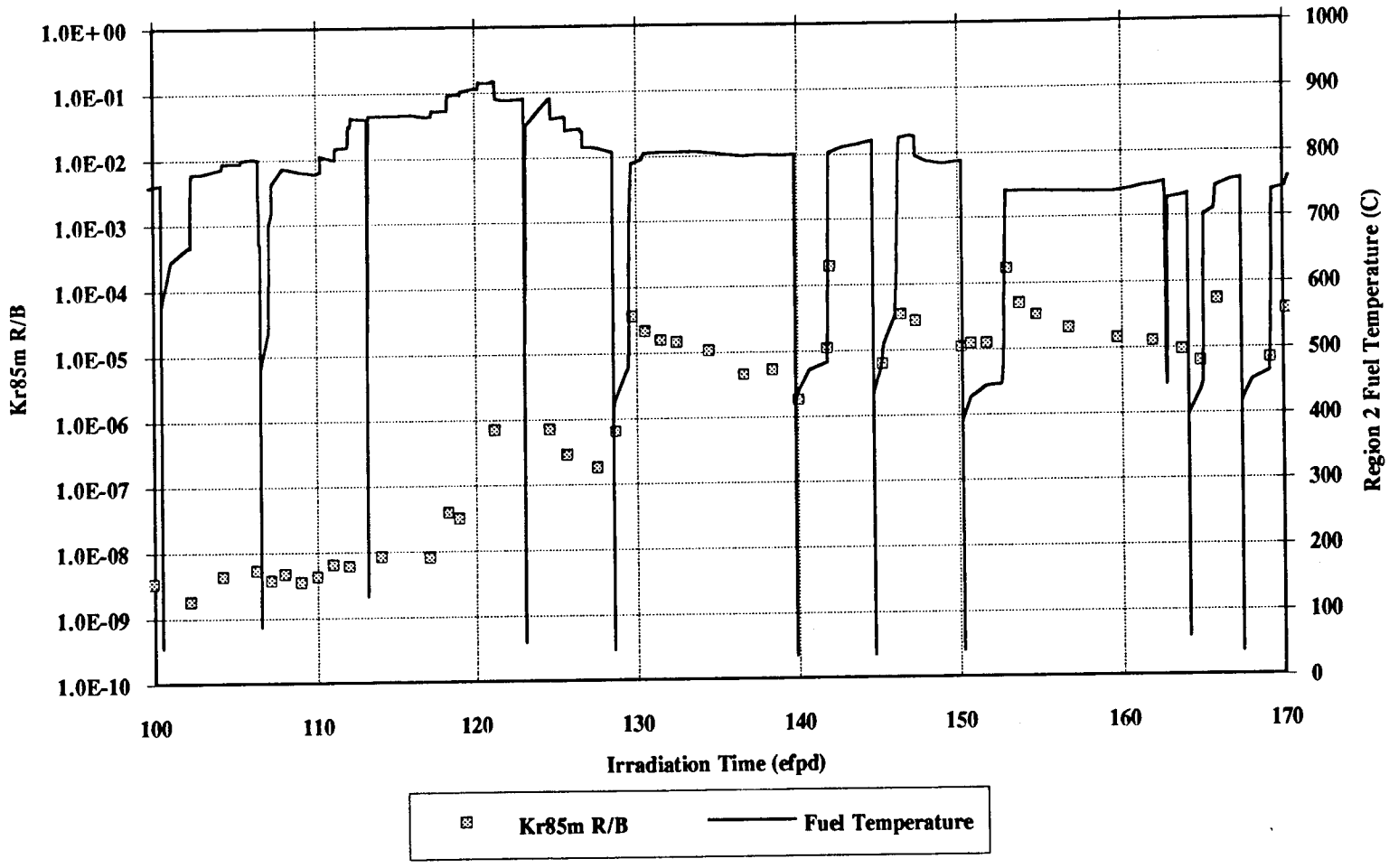

Figure 4.4-8. NPR 2 ^{85m}Kr R/B and estimated region 2 compact temperature versus efpd.

where

D_{eff} = gas-phase diffusion coefficient for species i (m^2/s)

ϵ = void fraction in the porous solid

q = factor to allow for tortuosity and varying pore cross section

C_i, n = constants which depend on the nuclide species

T = temperature (K)

μ = reduced mass = sqrt[$m_1 m_2/(m_1+m_2)$]; m_i= atomic weight of species i (gm/mole)

p = total absolute pressure (Mpa)

During the final cycle of NPR 1, 100% neon addition increased the region 2 fuel temperature from about 550°C to 950°C. With n_i=1.65 (Ref. 4.4-11), equation (4.4-14) predicts that the neon addition decreases the effective gas-phase diffusion coefficient for ^{89}Kr by less than 10%. Thus, gas-phase diffusion is not important for low pressure capsule tests and the resistance from bulk diffusion must be much larger than gas-phase diffusion.

No analysis of the flow dynamics inside the NPR 1 and NPR 2 capsules has been done. R/B data is corrected for decay in the line from the capsule to the sampling station using equation (4.4-2). Inside the capsule, the sweep gas flows in the small gap between the fuel bodies and the primary containment wall; it is assumed that the delay in the capsule has a negligible effect on the R/B results.

Insight into the release mechanism of fission gases may often be obtained by the dependence of R/B on the decay constant. This dependence, n, can be obtained from the value of $-\partial \ln(R/B)/\partial \ln\lambda$. Shown in Figure 4.4-9 and in Figure 4.4-10 are the n-values calculated using the R/B for ^{85m}Kr, ^{87}Kr, and ^{88}Kr for NPR 1 and NPR 2, respectively. Also plotted on the figures are the ^{85m}Kr R/B values. The normal range of the n-value when the NPR 1 capsule was at steady-state conditions for the Kr isotopes was 0.28 to 0.5. The values below 0.2 were usually caused when the data was obtained before the capsule had reached steady-state after a reactor startup.

The n-values for the NPR 2 capsule displayed more scatter than the data for NPR 1. The normal range for NPR 2 was 0.2 to 0.5, but the majority of the values were below 0.4.

The ^{85m}Kr R/B values toward the end of irradiation of both capsules show a dramatic rise. This is attributed to failure of the SiC layer in particles which already have the PyC broken or to failure of all coatings. Close examination of the NPR 2 data shows that after

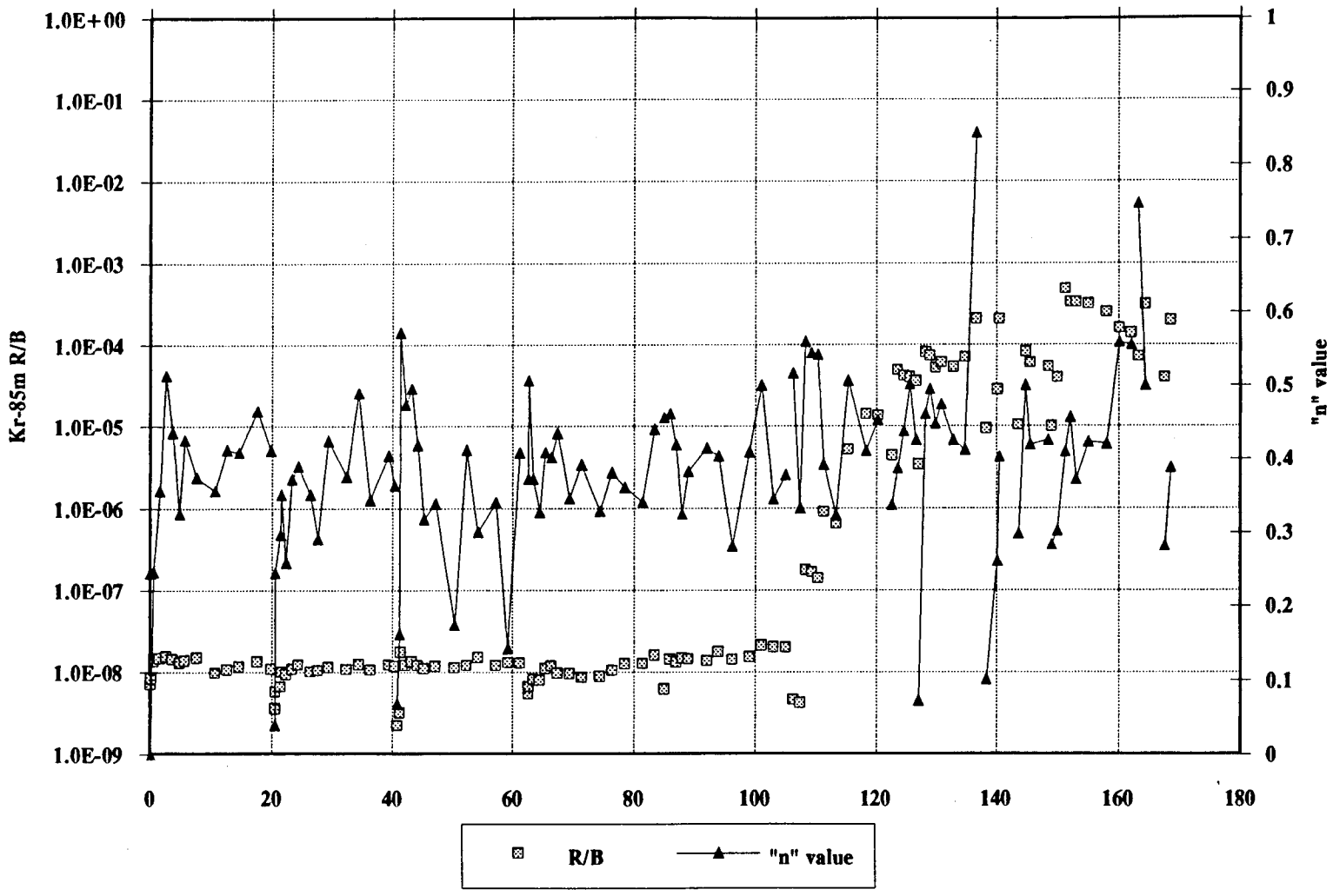

Figure 4.4-9. Dependence of R/B on half-life ("n"-value) and ^{85m}Kr R/B vs efpd for NPR 1.

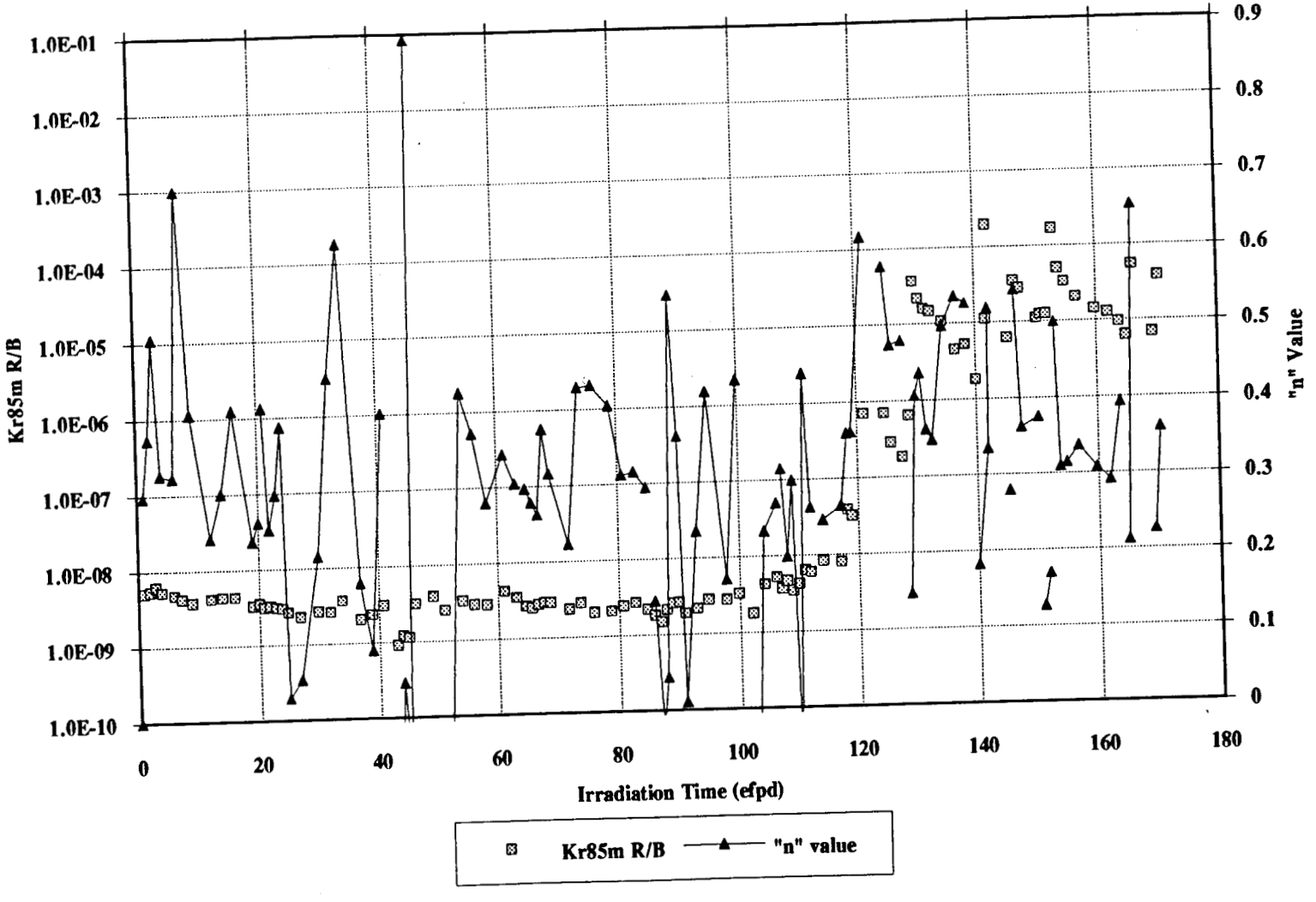

Figure 4.4-10. Dependence of R/B on half-life ("n"-value) and ^{85m}Kr R/B vs efpd for NPR 2.

the initial increase, the ^{85m}Kr R/B declines steadily over about 10 days to a value that is at least 1/10 that of the maximum value. Since the n-value for the maximum R/B does not increase significantly, it seems likely that the increase is not associated with the release of stored fission gas. Conversely, the decrease is not caused by the depletion of stored fission gas. Thus, the decrease in the capsule R/B must be associated with a decrease in the release from a failed particle, $(R/B)_{particle,k}$, in equation (4.4-6). One explanation for this decrease in $(R/B)_{particle,k}$ is that the kernel structure is changing with time.

The influence of the kernel structure on R/B from uncoated UO_2 spheres has been studied and it is found that the release rate fraction increases with porosity or surface area (Ref. 4.4-12). Continued irradiation of hydrolyzed UC_2 while heating at 1100°C results in a decrease in the R/B (Ref. 4.4-13). This effect has been attributed to densification or grain growth which decreases the porosity of the releasing material. In general, isothermal grain growth in polycrystalline materials follows a power law of the type (Ref. 4.4-14)

$$G(t)^m = G(0)^m + kt \tag{4.4-15}$$

where

$G(t)$ = grain size at time t

$G(0)$ = grain size at zero time

t = time after initiating grain growth

k,m = constants

The R/B of the samples should be inversely related to the average particle size if the fission gas is rapidly released once it intersects the particle free surface. Then, the time dependence of R/B would conform to $1/G(t)^m$ or

$$R/B = \frac{1}{[G(o)^m + kt]^m} \tag{4.4-16}$$

Equation (4.4-16) was fit to the declining R/B data for the NPR 2 capsule which occurred after the increase at 153 efpd. The R/B spike was caused when the temperature was increased by the change from helium to 100% neon in the sweep gas. During the period after the temperature increase, six measurements were taken without changing the sweep gas or the reactor power. The fit using the constants in Table 4.4-1 is shown in Figure 4.4-11. The best fit was obtained with m = 0.61. Using this value for m, the other two R/B increase-

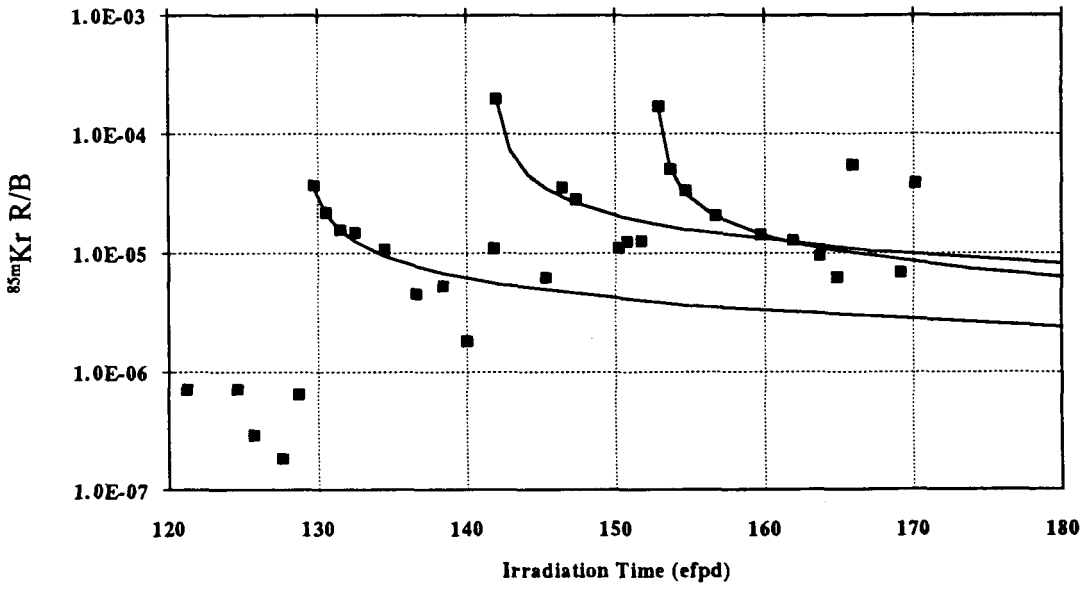

Figure 4.4-11. Declining R/B in NPR 2 with a fit to equation (4.4-16).

decline cycles for NPR 2 also fit equation (4.4-16). However, as Table 4.4-1 shows, different fitting constants were required. A difficulty in interpreting the data in this manner is that the time, t, is relative to the time at which the maximum R/B occurred. This time could not be determined because the R/B data was not taken on a frequent enough basis. However, the analysis indicates that the NPR 2 capsule average ^{85m}Kr R/B at end of life was no greater than 0.001%.

Table 4.4-1.Constants used to fit equation (4.4-16) to NPR 2 R/B data

irradiation efpd	fitting constants	
	G(0)	k
129.7 to 138.4	1.84E+07	1.33E+06
142 to 150	1.16E+06	2.40E+05
152.9 to 163.6	1.46E+06	5.22E+05

The R/B values from NPR 1 also showed the same behavior, although not as distinctly as NPR 2. The NPR 1 data for the decline between 152 - 162 efpds could not be fit using equation (4.4-16) with m = 0.61. During this time, however, the capsule temperature was continuously being increased, so the fuel did not reach a steady-state condition.

To determine the fraction of particles with a connected pore system using equation (4.4-6), the release from a single particle under identical irradiation conditions must be known. The latter quantity has not been measured; measurement would have required a capsule design in which the fission gas release from small isolated groups of laser-failed particles homogeneously distributed could have been measured independently of the gas release from fuel compacts. A crude estimate of the number of failed particles may be obtained from reported data on the release from failed particles irradiated in TRIGA tests.

The release from laser-failed UCO particles has been measured in TRIGA experiments after irradiation in HFIR capsules (Ref. 4.4-15). Particles with an initial enrichment of about 20% ^{235}U irradiated to 18.5% FIMA, have a ^{85m}Kr R/B at 850 °C of 0.3% as measured in the GA TRIGA reactor. However, the burnup influences the R/B, and particles irradiated to 24% FIMA have a TRIGA R/B of approximately 0.8%. The enrichment in the particles used in NPR 1 and NPR 2 was 92%, and the final burnup was around 80%. Hydrolysis of the 24% FIMA particles increases the TRIGA R/B to 3%-5%. If we use 0.8 to 3% as a range for the R/B value from a failed NPR-1 particle (to account for difference in enrichment and burnup), the NPR 1 capsule average particle failure at the end of the HFIR irradiation is in the range of 0.3 to 1.3%. The time integrated average fuel temperature was lower in NPR 2 than in NPR 1. For the last HFIR cycle, this temperature was 635 °C in NPR 2 and 858 °C in NPR 1. The lower temperature in NPR 2 results in a smaller release from a failed particle, but by less than 20%. Thus, the NPR 2 capsule average particle failure is between 0.03 to 0.13%. Since there were about 77,500 particles in each capsule, the number of failed particles is in the range of 230-1000 for NPR-1 and 23-100 for NPR 2. The disparate failure fractions in NPR 1 and NPR 2 based on the HFIR in-pile R/B disagrees with the results of the TRIGA R/B values (section 4.4.2.2) in which the failure fractions were found to be the same.

4.4.2.1.2 Transient Fission Gas Release

Transient fission gas release is monitored by the response of a radiation detector to pulses of radioactivity in the capsule effluent gas. The radiation level of the sweep gas exiting the NPR-1 capsule was continuously monitored by two independent ionization chambers (IC) connected to strip chart recorders. Because of an insufficient number of ionization chambers, the radiation level of the NPR 2 capsule sweep gas was monitored by two independent Geiger-Müller (GM) tubes for irradiation cycles 299 - 306 and, after purchase of an additional IC, with a GM tube and a separate ionization chamber for the last cycle. The chart records for the ionization chambers and the GM tube were examined and a compilation of the pulse heights, time of occurrence, and the full width of the spikes at half maximum was reported in the irradiation phase report (Ref.7). Transient spikes are characterized by a very rapid increase in radiation level of only 1-2 minutes duration at half-height, followed by slower return to a level somewhat higher than before the spike.

Transient fission gas release spikes were first detected after the irradiations had continued for about 110 efpd. Figure 4.4-12 and Figure 4.4-13 show the heights of the transient fission gas spikes detected by the sweep gas monitors on NPR 1 and NPR 2. Overlayed on the figures is the R/B for ^{85m}Kr. In both cases, the sharp increase in R/B coincided with a high activity of transient gas release. The onset of the NPR 1 transient spikes corresponded to a burnup in the region 4 compacts of about 72% FIMA and a fluence of 1.7×10^{25} N/m^2. Once transient spikes were observed the total number of spikes increased for the duration of the irradiation (Figure 4.4-14). Details of transient gas release are seen in Figure 4.4-15 which shows the cumulative number of spikes that occurred between 138 and 158 efpd after the start of the NPR 1 irradiation. Also shown is the calculated temperature of the region 4 compacts. In order to display shut-down times, the abscissa is the elapsed real time from the start of irradiation. No spikes are observed when the reactor is shut down and the temperature is <100 °C. Spikes are detected 6 to 8 hours after the reactor power is increased to 85Mw. In the presence of only helium (region 4 compact temperature of 600 - 700 °C) a preponderant number of the transient peaks have small heights. Furthermore, when neon is being added, and the temperature is being increased, the spikes have a higher amplitude. This is shown in Figure 4.4-16 in which the cumulative spike heights are plotted for the same time period. Note that the cumulative spike height increases slower when the

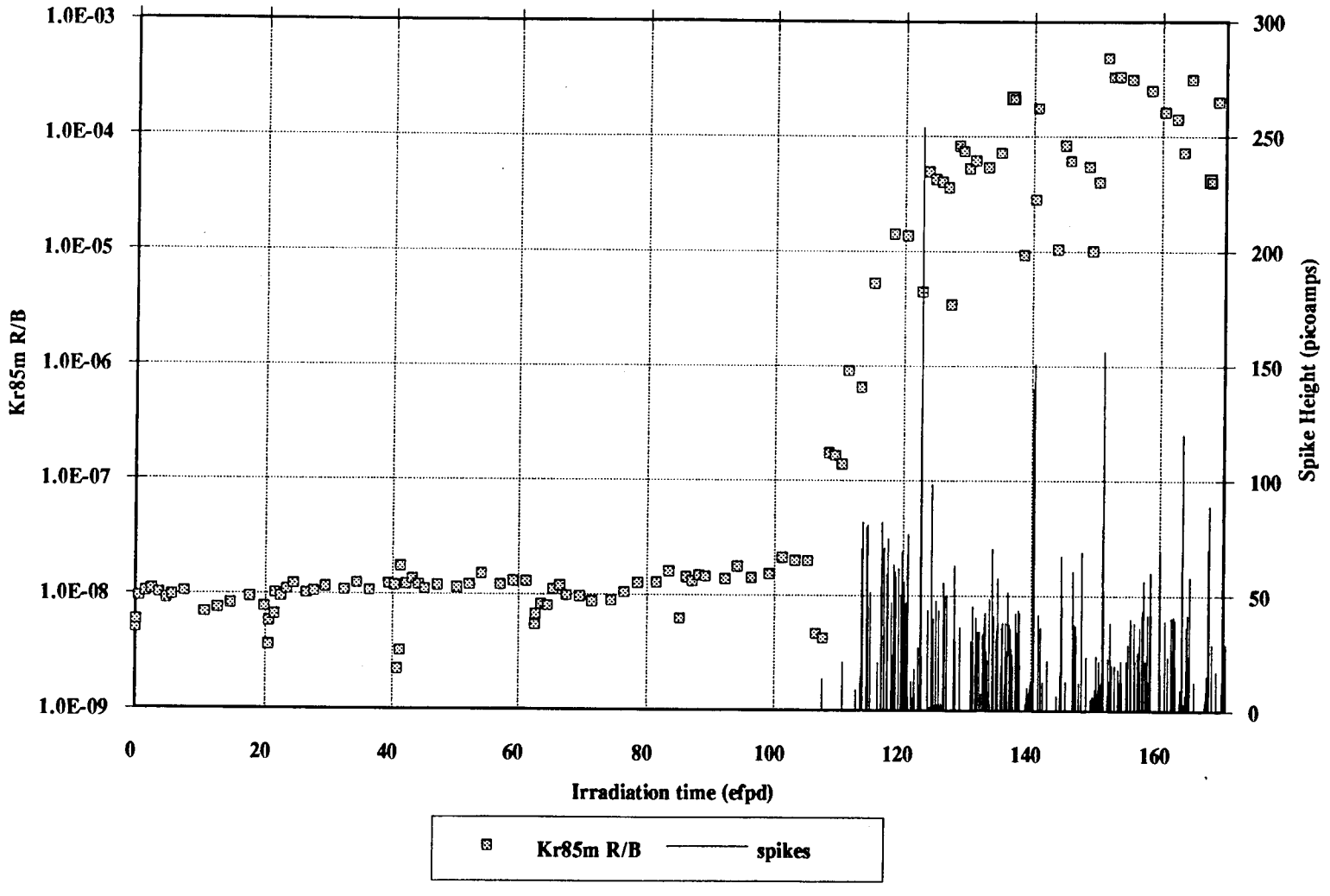

Figure 4.4-12. NPR 1 transient fission gas release spikes versus efpd.

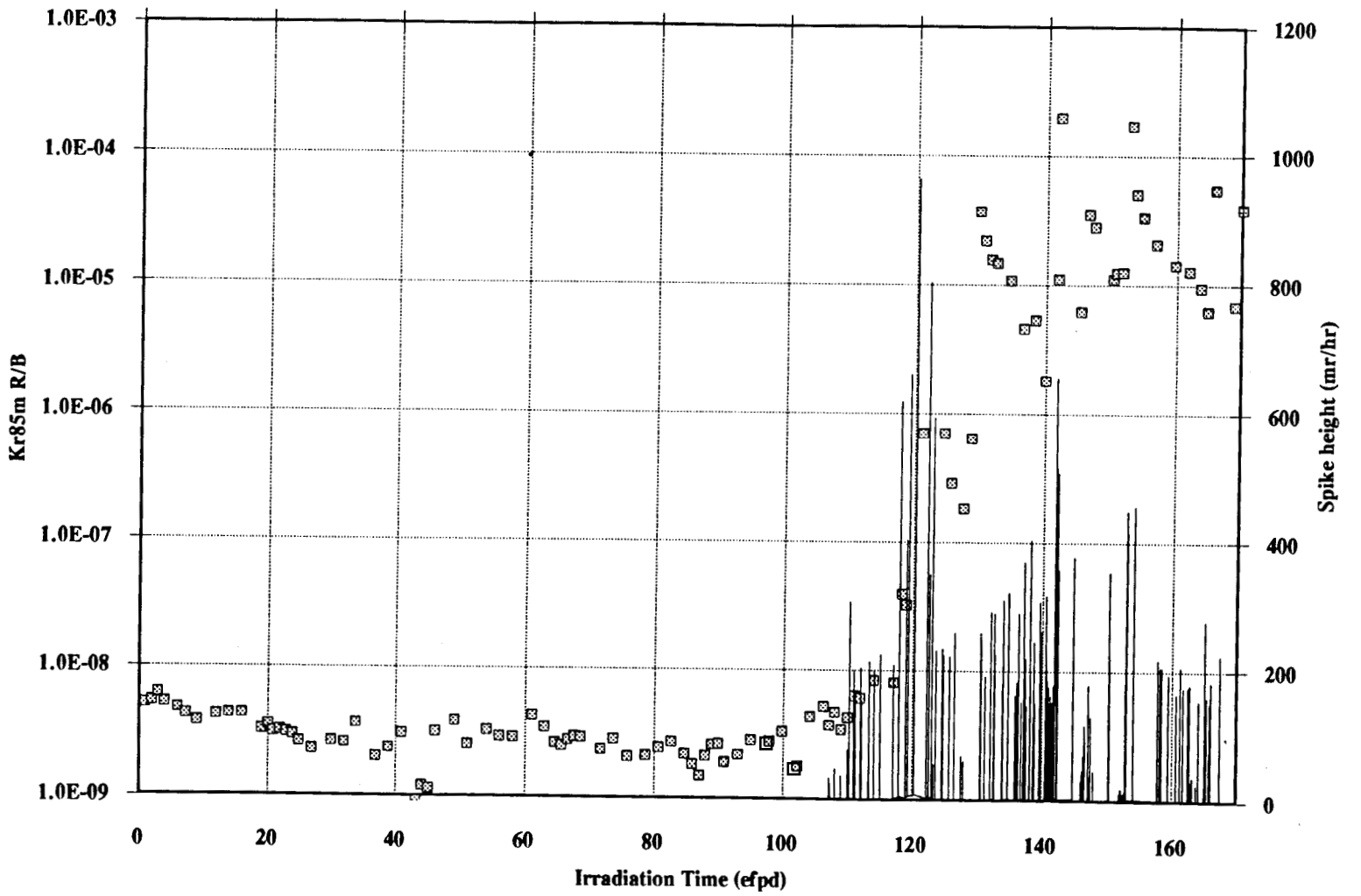

Figure 4.4-13. NPR 2 transient fission gas release spikes versus efpd.

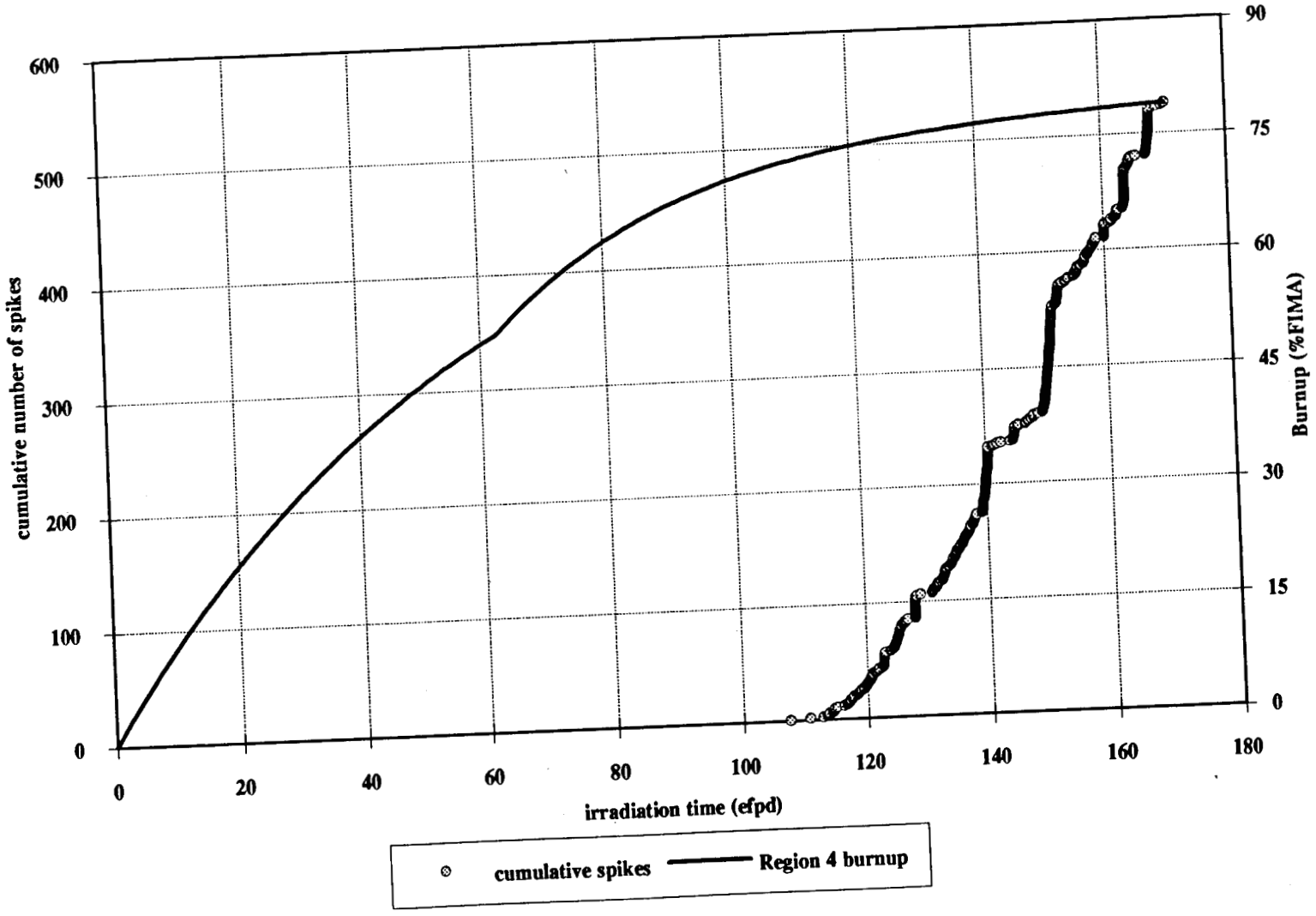

Figure 4.4-14. NPR 1 cumulative number of fission gas release spikes and estimated burnup of the region 4 compacts.

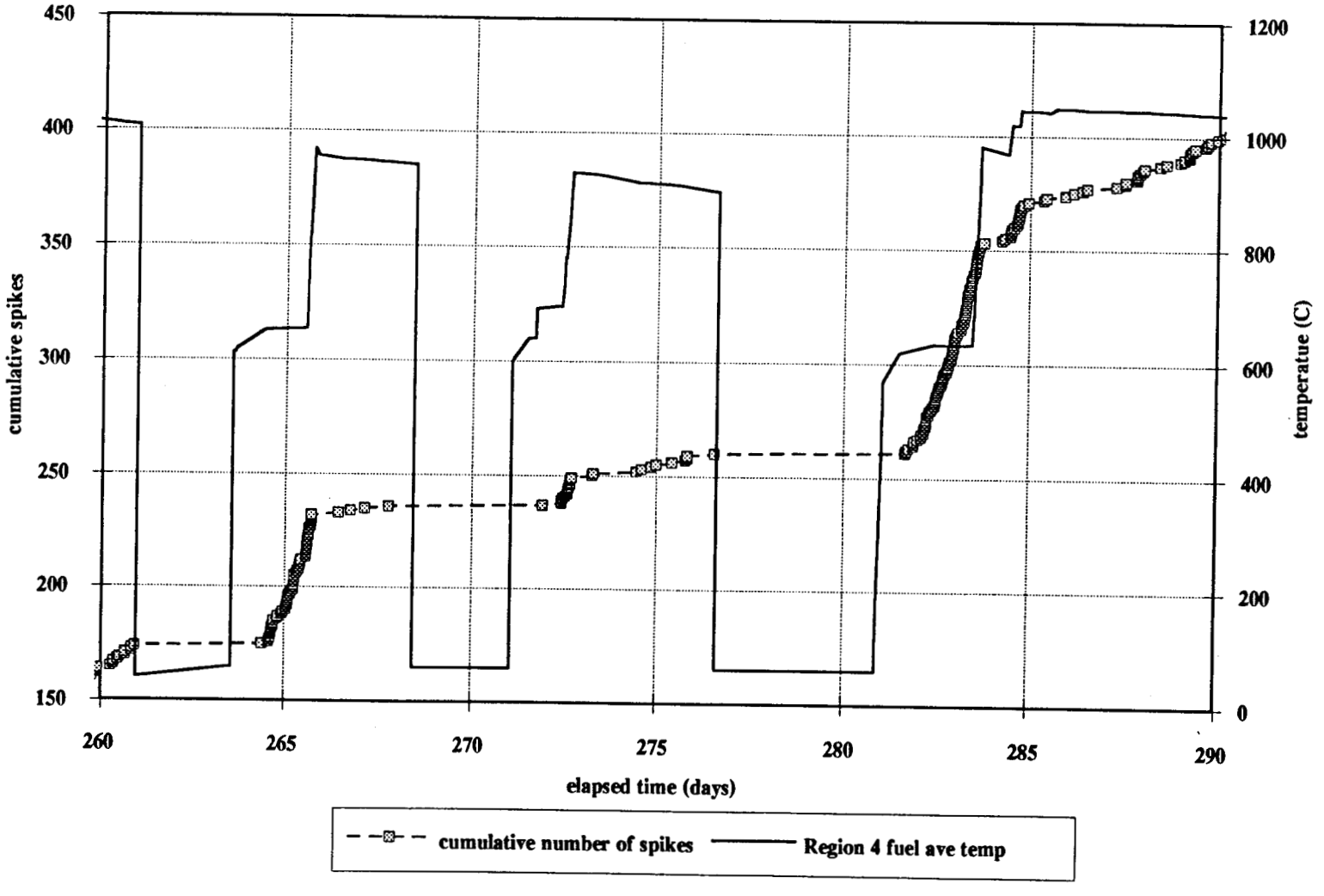

Figure 4.4-15. NPR 1 cumulative number of transient gas spikes and region 4 compact temperature vs elapsed time.

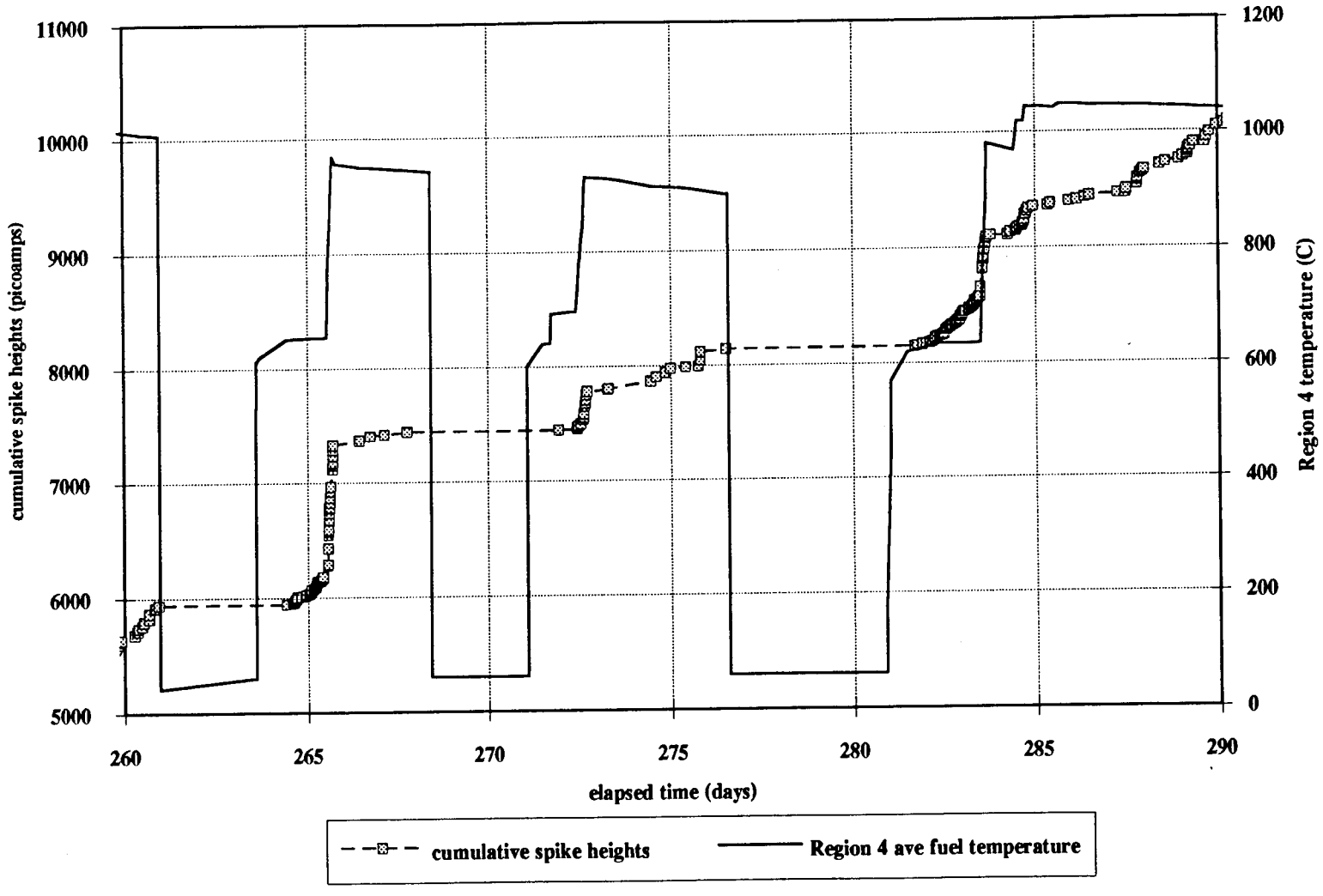

Figure 4.4-16. Cumulative spike heights and region 4 temperature versus elapsed time for NPR 1.

capsule is being purged by helium and operating at 600 - 700 °C than when neon is being added.

The total number of particle failures is hard to assess based on the transient gas release spikes. Since the amplitude of the spikes vary by over a factor of 100, it is not known what amplitude represents a particle failure. The largest spikes must be caused by ruptureof the SiC in particles with the PyC layers already failed. Small spikes may be due to failure of other layers, or may be due to fission gas bubbles being vented to open porosity in particles with failed coatings. A lower bound on the fraction of failed particles can be computed if we make the assumption that each gas spike is the result of a single particle failure. Ionization chamber RR-212A detected 526 spikes originating from the NPR 1 capsule. The GM tube, RE-512, monitoring NPR 2 detected 135 spikes. A comparison between the GM tube and the ionization chamber showed that the GM tube was significantly less sensitive than the chamber, so it is possible that transient spikes might have been missed in NPR 2. Dividing the number of spikes by the number of fuel particles gives the failed fraction: 0.7% for NPR 1 and 0.2% as a lower limit for NPR 2.

Transient fission gas release was also observed 7 to 8 minutes after the reactor was shut down. In this case the pulse height was larger than the spikes obtained at full power and the full-width at half maximum was at least 3 minutes. Fission gas released at shutdown of UO_2 fuel elements which had operated at 1400 °C is known to occur. This gas is believed to have been stored in the center of the element after migrating up the thermal gradient (Ref. 4.4-16). Because the hot center portion is plastic and uncracked, the gas collected in this region is sealed off from the pore volume that intersects the free surface. When the reactor is shut down, the rapid cooling results in cracks which open to the free volume. Metallographic post-irradiation examination of NPR fuel particles, shows that the fuel kernel has many void spaces. These probably were formed by the accumulation of fission gas. Thus, it seems plausible that the transient gas release observed at reactor shut down is caused by release from fission gas bubbles in failed particles in a manner similar to that explained above.

4.4.2.2 TRIGA R/B Measurements

After the irradiation, fuel compacts were removed from the capsule and transported to General Atomics for measurements of the R/B of individual compacts. The R/B of

compacts from each HFIR region was measured in a TRIGA King Furnace (Ref. 4.4-17) at 900 °C and 1100 °C using the procedure described in section 4.4.1.2. The results are reproduced in Appendix C (Ref. 4.4-18).

The TRIGA ^{85m}Kr R/B, shown in Figure 4.4-17, was dependent on the fast fluence. The fluence dependence was analyzed at General Atomics (Ref. 4.4-19). The NPR 1, NPR 2, and NPR 1A TRIGA data could be fit by

$$\frac{R}{B} = A(1-e^{-fluence\,/\,f_o})^n + B \qquad (4.4\text{-}17)$$

where

R/B is the ^{85m}Kr R/B

A, f_o n and B are fitting constants

The R/B values measured in the TRIGA tests are too high to predict the capsule-averaged values measured at the end of the HFIR irradiations. This discrepancy could be caused by (1) fission rate density difference between HFIR irradiation and TRIGA;

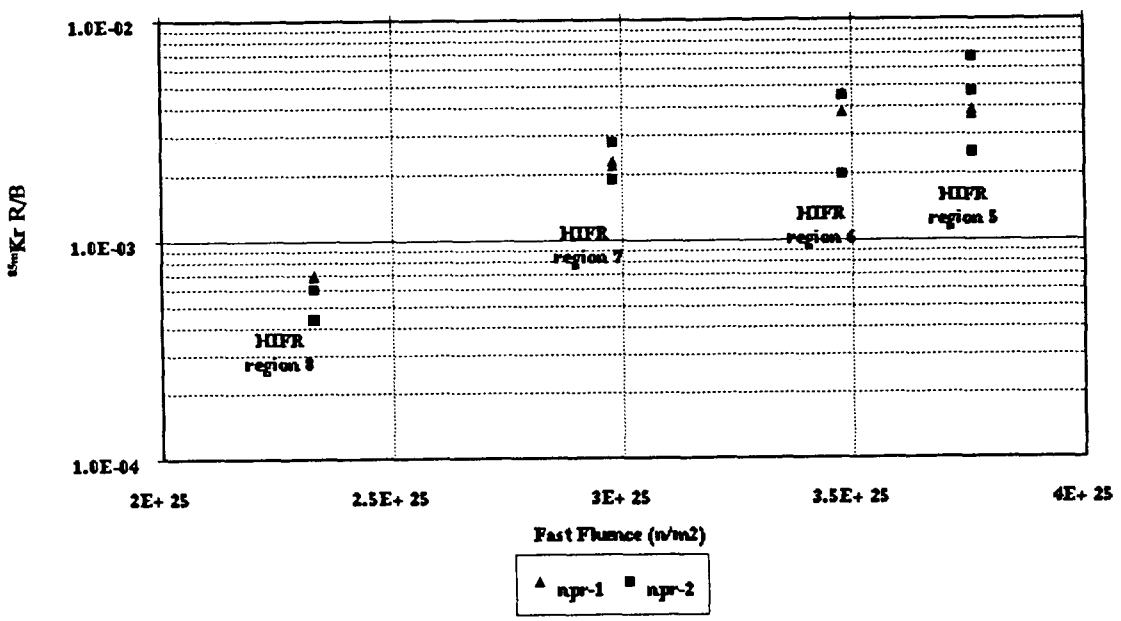

Figure 4.4-17.Triga ^{85m}Kr R/B as a function of fluence for NPR 1 and NPR 2 compacts.

(2) particle damage after the HFIR test was completed; or (3) chemical reactions in failed particles which increase the release rate.

A major difference between HFIR and TRIGA is the high neutron flux in HFIR resulting in a higher fission rate density. The density of fissioning within a kernel can affect the release rate in a complicated manner. Carroll, Sisman and Perez have shown that in dense UO_2 the fractional release rate can decrease as the fission density increases from (1.8 to 9)x10^{12} fissions/(cm^3 sec)(Ref. 4.4-20). After a burnup of 9x10^{20} fissions/cm^3, the release rates are accelerated (Ref. 4.4-21) due to cracking of the UO_2. In addition, fission rate densities greater than 10^{13} result in accelerated release. During the HFIR capsule irradiation, the fission rate density exceeded 10^{13}, and a burnup of 9x10^{20} fissions/cm^3 was surpassed early in the irradiation. Thus, the difference in fission rate density can not explain the increased R/B in the TRIGA experiments.

During the post-irradiation examination (PIE), the compacts are removed from the capsule. This process required significant remote handling procedures. In order to increase the R/B by a factor of 10, several hundred particles would have to have been broken. But, the removal of the compacts proceeded easily, and no visible damage was reported. Thus, the increased TRIGA R/B was not caused by damage during PIE.

The TRIGA R/B test is conducted at 1100 °C, which is higher than the temperature of irradiation for most of the compacts. Although we believe that the increased temperature did not fail any particles in the compacts, this possibility can not be ruled out.

Another possible cause of the increased TRIGA R/B is that the release rate was enhanced by oxidation or hydrolysis of the exposed kernels in the failed particles. The effect of air oxidation of irradiated laser-failed $UC_{0.3}O_{0.7}$ particles has been studied. Oxidation can occur at 185 °C, and after 16 hr the R/B increases by a factor of 2 to 3 (Ref. 4.4-22). Hydrolysis at 800 °C can increase the R/B by a factor of 5 (Ref. 15.). The compacts were not stored in an inert gas. The effect of long exposure to moist air may cause surface oxidation of the kernels in the failed, irradiated particles. In addition, oxidation may occur during the heatup prior to the TRIGA R/B measurement. Although the TRIGA procedure uses a evacuation/backfill method to remove air from the furnace after it is loaded with the sample, substantial amounts of water vapor are adsorbed to the carbonaceous surfaces in the compact and the sample crucible which may be desorbed during the heatup.

Additional work will be necessary to determine the cause of the difference between HFIR R/B values and TRIGA values.

4.5 Particle Fission Product Inventory by IMGA

The Irradiated Microsphere Gamma Analyzer (IMGA) system is a unique research tool located in the Irradiated Fuels Examination Laboratory at ORNL (Refs. 4.5.1 and 4.5.2). The primary function of the IMGA system is to accurately measure radioisotopic inventories of individual coated particles used in MHTGR applications. This is accomplished by detecting the gamma radiation given off by the fuel particles as various fission products decay. The system consists of three major components: (1) a high-resolution gamma-ray spectrometer, (2) a computer-based multichannel analyzer, and (3) an automated particle-handling system. These three components have been integrated into a sophisticated system capable of automatic operation.

The automated particle handler is the unique component in the IMGA system. It is composed of a singularizer, a sample changer, and a sample collector which are all synchronized and controlled by the computer. The singularizer isolates an individual microsphere from a given sample and transfers it to the sample changer. The sample changer moves the microsphere from the loading position below the singularizer to the counting position in front of the spectrometer. After the microsphere is counted, the sample changer moves the particle to the unloading position above the sample collector which contains 20 bin locations. Bin-selection criteria are based on the measured photopeak intensities, so, it is possible to physically separate particles as a function of their ability to retain key radioisotopes. As part of the examination process, the measured photopeak intensities for each particle are recorded in a disk file for later off-line detailed evaluation.

Fuel particles from the NPR 1, NPR 2, and NPR 1A experiment capsules examined by the IMGA system fall into two categories, those deconsolidated from fuel compacts and a small number of unbonded particles contained in piggyback containers. The following sections present the results of the IMGA examination of these particles and discusses the performance of the fuel based on the measurements.

4.5.1 Particles unbonded from fuel compacts

Three fuel compacts from NPR 1, one fuel compact from NPR 2, and one fuel compact from NPR 1A have been deconsolidated and a portion of their fuel particles examined by the IMGA system. Compact NPR 1/B8 was irradiated in the lower region of its experiment capsule and compacts NPR 1/B4, NPR 1/B5, NPR 2/B4, and NPR 1A/13 were irradiated near the axial center-lines of their respective capsules. All the compacts were composed of HEU UCO TRISO coated fuel particles. Nominal compact loadings and estimated irradiation parameters for the five compacts are given in Table 4.5.1 Temperature, fluence, and compact loading parameters were taken from pre-irradiation and preliminary irradiation reports and the particle burnups were estimated from IMGA activity measurements using the methodology described in Ref. 4.5.3.

Table 4.5.1. Nominal compact loadings and estimated irradiation parameters for NPR-1, NPR-2 and NPR-1A compacts.

Compact	Operating temp. °C	Fast[a] fluence n/m^2	Particles per compact	Heavy Metal burnup %FIMA
NPR-1/B4	902 to 1087	3.8×10^{25}	3610	77.6
NPR-1/B5	889 to 1099	3.8×10^{25}	3610	78.4
NPR-1/B8	814 to 926	2.5×10^{25}	6126	69.9
NPR-2/B4	634 to 849	3.8×10^{25}	3610	80.4
NPR-1A/13	1034 to 1153	1.9×10^{25}	3610	50.5

[a] ($E \geq 0.18$ Mev fJ).

Particles for IMGA examination from the NPR 1 and NPR 2 compacts were obtained by electrolytic deconsolidation of the compacts while particles from the NPR-1A compact were

obtained by burning the compact. The electrolytic procedure produces a mixture of unbonded fuel particles, graphite debris, and sections of intact compact material. The graphite debris and undeconsolidated portions of the compact would quickly clog the IMGA particle handler so it was necessary to sieve and table the material prior to the IMGA examination to separate the unbonded particles. Particles obtained by burning the compact were free of all graphite matrix material and their outer pyrocarbon layers. Additional details of the deconsolidation of the 5 compacts will be discussed later in Section 4.5.2.

Difficulties were encountered during initial attempts to examine NPR particles with the IMGA system in the fully automatic mode. It was discovered that some particles were being damaged in the singularizer mechanism. Efforts to solve the problem involved replacing the singularizer hopper feed-plate and adjusting the feed-plate with special tools made specifically for the purpose. These efforts met with some success, but, were not 100% effective in eliminating all damaged particles. An observation was made that graphite denuded NPR particles are considerably smaller in diameter than any material previously examined with the IMGA particle handler. Several attempts to automatically examine these bare SiC particles met with failure, so, it appears that with the present singularizer the bare SiC particles have reached a minimum diameter limit which can no longer be safely handled. Due to the limited amount of time available to gather data, it was decided to examine smaller numbers of particles from each compact using a manual loading technique which by-passes the singularizer mechanism. This reduced through put, but, was deemed acceptable because of the relatively high fraction failure of releasing particles encountered and the necessity to avoid data compromise by damage to particles.

At the time the particles from the compacts were counted, the predominate gamma-rays in the spectrum were produced by the decay of ^{95}Zr, ^{106}Ru, ^{134}Cs, ^{137}Cs, and ^{144}Ce. The absolute activities for these isotopes were determined for each particle from the photopeak data and corrected for decay back to the end-of-irradiation. The particles in each distribution were then analyzed to determine maximum and minimum values, means, and standard deviations. The resulting activity parameters for the distributions are summarized in Tables 4.5.2 through 4.5.6 for compacts NPR 1/B4, NPR 1/B5, NPR 1/B8, NPR 2/B4, and NPR 1A/13, respectively. The two isotopes of cesium and the isotope of cerium are of particular interest in evaluating individual particle performance. At the temperatures encountered during irradiation, cesium, with a

Table 4.5.2. Activity distribution parameters for particles from compact NPR-1/B4.

Isotope	Maximum particle activity (Bq)	Minimum particle activity (Bq)	Mean particle activity (Bq)	Std. Dev. mean (%)
^{95}Zr	1.00E+08	5.33E+07	7.39E+07	8.28
^{106}Ru	7.62E+06	3.32E+06	5.54E+06	8.71
^{134}Cs	1.23E+07	5.82E+06	9.00E+06	7.77
^{137}Cs	4.75E+06	2.47E+06	3.48E+06	7.58
^{144}Ce	9.53E+07	4.84E+07	7.05E+07	7.63

[a] Activities corrected to May 29, 1992.
[b] Based on measurements from the 562 retentive particles.

Table 4.5.3. Activity distribution parameters for particles from compact NPR-1/B5.

Isotope	Maximum particle activity (Bq)	Minimum particle activity (Bq)	Mean particle activity (Bq)	Std. Dev. mean (%)
^{95}Zr	9.99E+07	5.86E+07	7.73E+07	7.99
^{106}Ru	7.46E+06	4.00E+06	5.61E+06	8.05
^{134}Cs	1.16E+07	6.67E+06	8.92E+06	7.71
^{137}Cs	4.62E+06	2.65E+06	3.52E+06	7.57
^{144}Ce	9.20E+07	5.40E+07	7.17E+07	7.30

[a] Activities corrected to May 29, 1992.
[b] Based on measurements from the 953 retentive particles.

Table 4.5.4. Activity distribution parameters for particles from compact NPR-1/B8.

Isotope	Maximum particle activity (Bq)[a]	Minimum particle activity (Bq)[a]	Mean particle activity (Bq)[a]	Std. Dev. mean (%)
^{95}Zr	1.23E+08	6.05E+07	9.39E+07	7.67
^{106}Ru	6.83E+06	2.94E+06	4.86E+06	8.16
^{134}Cs	7.84E+06	2.98E+06	5.31E+06	12.21
^{137}Cs	4.18E+06	1.85E+06	3.11E+06	7.58
^{144}Ce	8.81E+07	4.16E+07	6.69E+07	7.11

[a] Activities corrected to May 29, 1992.
[b] Based on measurements from the 499 retentive particles.

Table 4.5.5. Activity distribution parameters for particles from compact NPR-2/B4.

Isotope	Maximum particle activity (Bq)[a]	Minimum particle activity (Bq)[a]	Mean particle activity (Bq)[a]	Std. Dev. mean (%)
^{95}Zr	1.15E+08	6.50E+07	9.16E+07	7.97
^{106}Ru	7.36E+06	4.22E+06	5.87E+06	7.89
^{134}Cs	1.12E+07	6.50E+06	9.13E+06	7.24
^{137}Cs	4.34E+06	2.53E+06	3.50E+06	7.18
^{144}Ce	9.51E+07	5.59E+07	7.66E+07	7.06

[a] Activities corrected to May 29, 1992.
[b] Based on measurements from the 423 retentive particles.

Table 4.5.6. Activity distribution parameters for particles from compact NPR-1A/13.

Isotope	Maximum particle activity (Bq)	Minimum particle activity (Bq)	Mean particle activity (Bq)	Std. Dev. mean (%)
^{95}Zr	3.17E+08	1.96E+08	2.52E+08	8.01
^{106}Ru	5.77E+06	3.58E+06	4.55E+06	7.93
^{134}Cs	2.36E+06	1.31E+06	1.89E+06	8.29
^{137}Cs	2.81E+06	1.73E+06	2.27E+06	7.48
^{144}Ce	8.51E+07	5.17E+07	6.84E+07	7.17

[a] Activities corrected to January 3, 1992.
[b] Based on measurements from the 449 retentive particles.

relatively low boiling point of 690 °C, is known to be mobile and readily escapes defective coatings. Cerium, on the other hand, with a relatively high boiling point of 3468 °C, forms chemically stable compounds in oxide and oxy-carbide fuel which tend to remain in the kernel. The ratio of ^{137}Cs to ^{144}Ce, therefore, can provide a measure of the retention of the metallic fission product cesium within the particle.

The isotope ^{134}Cs is formed primarily by the activation reaction $^{133}Cs(n,\gamma)^{134}Cs$; direct production from fission is negligible. The stable isotope ^{133}Cs is produced for the most part from the decay of ^{133}Xe, a fission gas with a relatively high cumulative fission yield. Because of its short half-life of 5.2 days, it is generally not possible to directly measure the amount of ^{133}Xe in a particle months after the end-of-irradiation when post-irradiation examination begins. Measuring the amount of ^{134}Cs, however, with a half-life of 2.07 years is possible and directly relates to the amount of ^{133}Xe retained by the particle during irradiation. Therefore, the ratio of ^{134}Cs to ^{137}Cs can provide an indirect measure of a particle's ability to retain fission gases during irradiation.

Based on the preceding logic, it should be possible to distinguish individual particles responsible for fission product release from a distribution of non-releasing particles. To that end, a simple histogram method was employed to analyze the individual particle data obtained from the IMGA examinations. First, the activity ratios ^{137}Cs:^{144}Ce and ^{134}Cs:^{137}Cs were computed for each particle and the resulting activity ratio distributions examined to determine the retentive and non-retentive particles. Generally, the non-retentive particles were well separated from the distribution of retentive particles making them easy to identify. Next, the non-retentive particle records were removed from each data set and the distributions re-analyzed to determine mean values and standard deviations for the retentive particles alone. The ^{137}Cs:^{144}Ce and ^{134}Cs:^{137}Cs activity ratio distributions for each compact were subsequently recomputed and normalized to the mean value of the retentive particles to provide a consistent basis for comparison. A final histogram representation of the particle data was obtained by defining intervals 1% wide and counting the number of normalized ratios which fell within each interval. The resulting ^{137}Cs:^{144}Ce ratio histograms for the particles from compacts NPR-1/B4, NPR-1/B5, NPR-1/B8, NPR-2/B4 and NPR-1A/13 are shown in Figs. 4.5.1 through 4.5.5, respectively. In the figures, the particle data (vertical bars) have been superimposed over a theoretical normal distribution (gray) that was calculated using the standard deviation of the retentive particles in each group. Figures 4.5.6 through 4.5.10 illustrate the corresponding information for the ^{134}Cs:^{137}Cs ratios.

As can be seen in Figs. 4.5.1 to 4.5.5, release of ^{137}Cs from individual non-retentive particles was generally in excess of 40% of a normal particle inventory. Most of these non-retentive particles appeared to have intact SiC coatings when examined under low (10X) magnification. The remaining retentive particles in each compact have ratio distributions which appear to be somewhat biased toward higher values than the theoretical normal distribution.

Figures 4.5.6 and 4.5.7 show clear evidence of fission gas release in the two high fluence, high temperature, and high burnup compacts, NPR-1/B4 and NPR-1/B5. The non-retentive particles revealed by these histograms have ^{134}Cs inventories that range from 5% to 35% less than that of a normal particle. Although it is not evident from the histogram data, particles identified as having low ^{134}Cs:^{137}Cs ratios are a subset of the particles with low ^{137}Cs inventories.

Figure 4.5.8 shows the ^{134}Cs:^{137}Cs ratio distribution for compact NPR-1/B8. The distribution is complicated and does not conform to a normal like distribution nor does it appear bi-modal as one would expect if there were overlapping distributions of retentive and non-retentive particles. At present the cause of the irregular variation in this ratio is not known. It has been suggested that since this compact occupied the lowest position in the irradiation capsule, perturbations in the neutron flux common to end locations may be responsible. For now, without a more complete understanding of this distribution, no attempt will be made to draw conclusions about fission gas release from the data.

Since release of ^{137}Cs was found to be the most conservative indicator of individual particle performance, estimates of overall fuel performance will be based on ^{137}Cs:^{144}Ce ratio data. Table 4.5.7 summarizes the fuel performance results for the particles from compacts NPR-1/B4, NPR-1/B5, NPR-1/B8, NPR-2/B4 and NPR-1A/13. As one would expect, the high fluence, high temperature and high burnup compacts, NPR-1/B4 and NPR-1/B5, experienced the greatest percentage of particles releasing cesium. For these two compacts, it was found that approximately 2% to 4% of the particles examined were deficient in ^{137}Cs. The two lower temperature compacts, NPR-1/B8 and NPR-2/B4, experienced fewer particles releasing cesium by factors of 10 to 20 even though compact NPR-2/B4's fluence and burnup were comparable to those for compacts NPR-1/B4 and NPR-1/B5. The final compact, NPR-1A/13, had a similar percentage of particles releasing cesium as the two low temperature compacts even though its operating temperature was reported to be the highest of the 5 compacts examined. This apparent contradiction appears to be caused by compact NPR-1A/13's significantly lower fast fluence and heavy metal burnup.

Table 4.5.7. Fuel performance based on cesium release for compacts NPR-1/B4, NPR-1/B5, NPR-1/B8, NPR-2/B4, and NPR-1A/13.

Compact	Particle type	Particles releasing cesium	Total particles examined	Percent releasing
NPR-1/B4	UCO	22	582	3.8
NPR-1/B5	UCO	19	972	2.0
NPR-1/B8	UCO	1	500	0.2
NPR-2/B4	UCO	1	424	0.2
NPR-1A/13	UCO	1	450	0.2

4.5.2 Compact Deconsolidation Debris and Electrolyte

To obtain unbonded particles for IMGA examination it was necessary to decompose the irradiated compacts into their constituent fuel particles and graphite shim material. One method of performing this task was to electrolytically deconsolidate the compacts in a nitric acid solution at room temperature. The process was carried out for compacts NPR-1/B4, NPR-1/B5, NPR-1/B8 and NPR-2/B4 following standard operating procedure MET-FME-SOP-18, Rev.1. Briefly, a compact is loaded into the deconsolidation apparatus as shown in Fig. 4.5.11. Next, a current is applied across the compact with the compact acting as the anode and the wire mesh basket acting as the cathode. Anodic oxidation of the compact occurs causing the carbonaceous matrix material holding the compact together to disintegrate into a fine powder releasing the particles and graphite shim material. As the particles fall away from the compact the circuit is broken thus halting further oxidation of the outer pyrocarbon layer of the particle. The particles and matrix debris were collected in a wire mesh basket below the compact and are later retrieved and washed. The mixture is then dried and poured through a series of sieves to grade the material by size. The material from the intermediate sieve was processed one step further to separate the round unbonded particles from the randomly shaped pieces of graphite shim material. The shape separation was accomplished with a vibrating table that produced particle and non-particle fractions. Figures 4.5.12 and 4.5.13 illustrate representative samples of the material obtained from the electrolytic deconsolidation of compacts NPR-1/B5 and NPR-1/B8.

While leaching of some material from exposed kernels during deconsolidation may take place to a limited degree, the low temperature and relative short exposure time (~ 0.5 h) of the process is expected to keep the leaching to an insignificant level. For compact NPR-1A/13 the unbonded particles were obtained by burning the compact in air at a temperature of 750°C for 48 hours following standard operating procedure MET-FME-SOP-27, Rev. 0. Figure 4.5.14 shows the resulting graphite denuded particles as received for IMGA examination.

The majority of particles from the NPR-1 and NPR-2 compacts had visible cracks in the PPyC/OPyC coatings. The cracks were more severe in the higher fluence compacts, NPR-1/B4, NPR-1/B5 and NPR-2/B4, which exhibit crevices which extend down to the SiC

layer as predetermined by ceramography. In approximately 20-30% of the particles from the high fluence compacts the PPyC/OPyC coatings had broken away entirely leaving particles with bare SiC coatings. In the lower fluence compact, NPR-1/B8, the PPyC/OPYC coatings retained their structural integrity and only a few scattered particles with bare SiC coatings were observed.

4.5.3 Piggyback particles (IMGA)

Included in the NPR experiment capsules were several containers filled with unbonded fuel particles identical to those used to fabricate the fuel compacts. These piggyback particles were initially loaded into graphite holders and sealed inside niobium tubes. After irradiation the containers were recovered along with the fuel compacts. To analyze the piggyback particles with IMGA it was necessary to remove them from their niobium containers. Section 4.4 contains a description of the recovery process for the first 8 piggyback containers chosen for examination. Particles removed from the piggyback containers were examined by the IMGA system in batches. The batches varied from 11 to 16 particles depending on how many were recovered intact from each container.

After examination, the individual particle data was processed to determine activities at end-of-irradiation for several isotopes of interest. Activity data from each particle batch was then analyzed to determine mean values and standard deviations for use in calculating burnup estimates. The methodology described in Ref. 4.5.3. was used estimate the burnup and the results are summarized in Table 4.5.8 for the 8 piggyback samples examined.

Because of the very limited number of particles associated with each batch, only a qualitative analysis of ^{137}Cs:^{144}Ce activity ratios was attempted to identify particles deficient in cesium. The activity ratio distributions for each batch were analyzed and the means and standard deviations determined. For the ^{137}Cs:^{144}Ce activity ratio distributions, the standard deviations were all less than 1.5% and none of the individual particles appeared to have low ratios.

Table 4.5.8. Summary of IMGA measurements and burnup determinations for NPR-1 and NPR-2 piggyback particles.

Particle batch	^{95}Zr mean activity (Bq)	^{106}Ru mean activity (Bq)	^{137}Cs mean activity (Bq)	^{144}Ce mean activity (Bq)	Burnup %FIMA
NPR-1/11GA	9.38E+07	4.41E+06	3.20E+06	6.89E+07	72.14
NPR-1/11UB	8.11E+07	4.85E+06	3.42E+06	6.94E+07	76.00
NPR-1/11GB	7.77E+07	4.80E+06	3.36E+06	6.87E+07	75.05
NPR-1/11UB'	7.68E+07	5.13E+06	3.44E+06	7.04E+07	77.14
NPR-1/12GA	8.34E+07	5.08E+06	3.46E+06	7.20E+07	77.78
NPR-1/12UA	7.85E+07	5.01E+06	3.37E+06	6.96E+07	75.51
NPR-1/12GA'	7.76E+07	5.10E+06	3.47E+06	7.12E+07	77.94
NPR-2/22GA	1.00E+08	5.47E+06	3.51E+06	7.74E+07	79.64

4.6 Ceramographic Examination

Ceramography, in which polished surfaces of fuel materials are prepared and examined at high magnification, provides valuable data regarding material microstructure and mechanical condition of the fuel. The work described here was carried out on fuel specimens with different levels of irradiation exposure in a systematic attempt to gain a better understanding of fuel material and design features which could be used to improve performance.

4.6.1 Unirradiated Fuel

Compact Ceramography:

In order to provide for a measure of changes which may take place in fuel during irradiation, ceramographic examination of an unirradiated fuel compact was carried out. A compact was selected from reference NPR 1 and NPR 2 fuel compacts in storage at ORNL. The compacts were provided by General Atomics and they were from the same compact lot as the capsule NPR 1 and NPR 2 compacts which were irradiated. The compact (No. FM23-00001-02-2) was manufactured with a particle packing fraction of about 10 volume percent which produced a metal loading of 0.1844g U-235. This was the lowest metal loading of those manufactured for NPR 1 and NPR 2.

The compact was mounted and sectioned to produce a circular cross section of the compact. The examination showed the eight layer TRISO particles dispersed along with H-451 graphite shim in the graphite powder and carbonized petroleum pitch matrix. The compact components appeared to be well bonded and no evidence of matrix intrusion into the PPyC or detrimental coating-matrix interaction was observed. Many particles were in contact with each other but no damage to structural coatings as a result of the contact was evident. Examples of the appearance of the unirradiated fuel cross section are shown in Figures 4.6.1.1 and 4.6.1.2.

The UCO fuel kernel microstructure clearly showed the UO_2 and UC_2 phases. The UC_2 phase tended to be located in a thin (<10 micron thick) layer on the surface of the kernel and also dispersed at the center of the kernel. Prior work has shown that the UC_2

phase appears white in bright field illumination while the UO_2 appears as dark gray. Typical microstructures are shown in Figures 4.6.1.1 and 4.6.1.2.

SiC Characterization:

Examination of the SiC coating was carried out at high magnification. The cross sections of the SiC were featureless in both bright field and polarized light which was consistent with the response expected for high density SiC. No etching procedures were imposed so that SiC grain features were not revealed. Examples of the appearance of the SiC cross section is shown in Figures 4.6.1.1 and 4.6.1.2.

An extensive characterization of the SiC coating structure of fuel made for the NPR1 and NPR 2 capsules was carried out at the B&W company (Ref 4.6.1.1). Scanning electron microscopy of fracture surfaces revealed traces of impurities including Cr, Ni, Fe, Cu, and U. Columnar SiC grains oriented with the long axis in the radial direction were observed. The grains were typically 10 to 20 microns in length so that the 35 micron thickness of the coating could be spanned by two or three SiC grains.

4.6.2 Irradiated Fuel

4.6.2.1 Examination Procedure:

Compacts were selected from Capsule NPR 1, which operated with estimated time integrated average fuel temperatures of 858 C to 1052 C, and from NPR 2 which operated with fuel temperatures of 635 to 883 C. Both capsules exposed fuel to the same range of fast neutron fluence and heavy metal burnup.

Two compacts, NPR 1 A5, and NPR 1 A8 were selected for examination to provide information on the condition of fuel after maximum and minimum fast neutron exposure and heavy metal burnup respectively. Since these compacts were irradiated in NPR 1 they were exposed to the highest irradiation temperatures. A third compact, number A4 from capsule NPR 2, was selected to characterize fuel condition after maximum fast neutron exposure and burnup similar to capsule NPR 1 compact A5 conditions but at a temperature about 200 C lower.

The compacts were very fragile so the first step in ceramographic preparation was to impregnate the compact with an epoxy resin. This was accomplished by enclosure of the compact in a metal tube which was then filled with resin. After the resin cured, transverse cuts were made through the compact with a low speed diamond impregnated circular saw. The cuts through the compact were made about 15mm from each end and the two end pieces were mounted in resin for grinding and polishing. The specimen were mounted so that grinding was in the axial direction in the compact and a circular cross section was obtained. A typical compact cross section is shown in Figure 4.6.2.1.1.

Compacts, such as A8, at the ends of the irradiation capsules had up to 30% difference in fast neutron exposure from one end of the 50mm long compact to the other. Therefore, careful attention was given to maintaining the identity of the two mounts obtained from each compact so that condition of the fuel could be correlated with the actual fast neutron fluence experienced by the specific specimen.

In the following sections the observations which were made are organized in terms of fuel components, starting with the kernel and proceeding outward. In most cases there is interaction of components so more than one must be discussed at one time but an attempt has been made in each section to focus on the primary fuel material affected.

4.6.2.2 Irradiation Effects in HEU UCO Kernels

The majority of UCO kernels were contained by the buffer coating during irradiation and retained a spherical shape. There was development of large gas voids within the kernel. An example of the appearance of a typical kernel cross section is shown in Figure 4.6.2.2.1.

Although accurate kernel dimensions could not be determined from ceramography of the kernel microsphere, and the initial dimensions of the specific kernel under examination was not known, it is reasonable to assume that kernel swelling took place as a result of fission and the development of gas bubbles within the kernel. Based on results from LEU UCO, the amount of kernel swelling was estimated to decrease with increasing burnup and for these experiments, be on the order of 36 vol % (Ref. 4.6.2.1). This volume change would result in a diameter increase of about 11%.

The gas voids within the kernels usually appeared to be empty. However, in some kernels the voids were filled with a material which appeared to be the same as the densified

buffer material which surrounded each kernel. Examples of the deposits are shown in Figures 4.6.2.2.2 and 4.6.2.2.3. Similar deposits were observed in UCO previously and no correlation with coating performance has been identified (Ref. 4.6.2.2)

It is hypothesized that the material in the voids was carbon transported to the voids from the buffer by either solid state or gas phase mechanisms. The driving force could have been the higher temperatures which existed in the kernel voids relative to temperature in the buffer region, but usually carbon transport in coated particle fuel is in the direction of lower temperatures.

The presence or absence of the deposits may have been a function of the relative amount of UC_2 in the initial kernel and the resulting CO gas pressure which developed during irradiation. Further examination of the fuel by microprobe would be necessary to gain an better understanding of the deposits. There was no evidence that the material in the kernel voids contributed to detrimental interaction of kernels with the structural coatings so further characterization was not performed on the deposits.

The kernel material normally contained a continuous matrix of dark grey material with a dispersion of a white second phase. The kernels of all the fuel observed had very high heavy metal burnup of at least 70% FIMA. At such a high burnup no UC_2 phase should have remained, having either been fissioned or converted to UO_2 by excess oxygen from fission in the UO_2 phase. The dark grey phase was probably UO_2 and the white phase fission products in either oxide, carbide, or metallic phase. An example of the distribution is shown in Figure 4.6.2.2.2.

Not all kernels showed the abundance of the white phase illustrated in Figure 4.6.2.2.2. In these latter kernels there was a white phase but it was limited to the surface of some voids. The differences in microstructures observed were probably related to variations in the original UC_2 and UO_2 content of the kernels. An example of this second type of phase distribution is shown in Figure 4.6.2.2.3.

There was no evidence of kernel displacement as a result of the amoeba effect. In the amoeba effect the kernel moves up the thermal gradient as carbon is deposited on the cool side of the kernel (Ref 4.6.2.3). The phenomenon takes place in pure UO2 and UC2 coated particles and the UCO kernel composition was designed to eliminate the effect. From the evidence presented here the UCO design was effective in preventing kernel displacement by the amoeba effect.

Although the amoeba effect did not result in kernel migration, there was extensive displacement of kernel material by a swelling mechanism. The generation of fission gas and solid fission products produced a force for expansion of the UCO kernels. While in most cases the buffer restrained the kernel and did not fracture, there were examples of kernel swelling into cracks in the buffer. Usually cracks in the buffer did not penetrate completely through the coating thickness so that the kernel merely filled the void produced by the crack in the buffer. An illustration of this effect is shown in Figure 4.6.2.2.4.

When there was a complete fracture across the buffer coating the kernel could swell through the crack into the void created by the buffer shrinking away from the IPyC. The tendency of the cracked buffer to continue shrinking down around the kernel as a result of fast neutron exposure may have amplified the apparent swelling of the kernel by extruding it out of the original position within the buffer. An example of a kernel swelling through a breach in the buffer coating is shown in Figure 4.6.2.2.5.

The extreme kernel swelling shown in Figure 4.6.2.2.5 was observed only in fuel exposed to the high temperatures of Compact A5 from NPR 1. The white phase adjacent to the kernel material in Figure 4.6.2.2.5 was presumed to be densified PyC from the buffer containing fission fragments recoiled from the kernel. No detrimental effects on structural coatings were associated with the kernel swelling. The IPyC coating remained intact and apparently prevented significant amounts of fission products from reaching the SiC coating even when the kernel was in contact with the inner IPyC surface.

There was a tendency toward less retention of kernels in ceramographic mounts which had been exposed to air and then heated in the TRIGA fission gas release tests. Compact NPR 1 A4, which had been exposed to air but not heated, retained 29% of kernels while the heated compacts retained only 15% to 24% even at lower burnup as shown in Figure 4.6.2.2.6.

The evidence for greater loss of kernels during grinding and polishing, after heating in TRIGA may result from reaction of exposed kernels with moisture and air sorbed on compact matrix which was released upon heating. In order for this reaction to take place, 70 to 85% of the coatings would have to be permeable to gases during heating. While this conjecture is only weakly supported by the data in Figure 4.6.2.2.6, it is consistent with the following observations. The TRIGA Fission gas release rates were systematically higher than observed during irradiation in HFIR and ATR. This observation may have resulted from oxidation of

exposed kernels in TRIGA. Secondly, the burning of compact NPR 1A number 13, which had a relatively high TRIGA fission gas release, did not reveal obvious cracks in any of the SiC coatings. This observation is not inconsistent with gas release from permeable coatings in a large fraction of the population. However, the IMGA examination indicated that SiC permeability was high in only percent level portions of the particle population and those results are consistent with ceramographic observation of SiC cracks. Until more conclusive evidence for permeability in 70 to 85% of SiC is obtained, the conclusion that the SiC permeable coating fraction was about 1% is most credible.

4.6.2.3 Irradiation Effects in TRISO Coatings

After a cross section of the compact was adequately polished it was examined in detail and the condition of coatings with regard to cracks or other unusual feature recorded. During the grinding and polishing process about 75% of the kernels and many buffer layers fell from the center of the particles and were lost. In order to keep the data base as uniform as possible the decision was made to collect data for all coating only from those particles which had a kernel. In those particles where the kernel had been lost, a separate record was kept describing the condition of the SiC coating only.

In order to obtain an adequate number of observations of particles with kernels it was necessary to prepare two or three polished surfaces for each ceramographic mount. Each surface was more than 1mm further into the mount so under normal circumstances the same particles were not examined twice. Using this approach a total of 176 particles with kernels were examined in the three compacts and 715 without kernels were examined. The results for each compact are summarized in Tables 4.6.2.1 and 4.6.2.2. The results are discussed for each coating layer in the following sections.

Buffer/IPyC:

The buffer underwent irradiation induced shrinkage which resulted in about a 50% reduction in the thickness of the layer. The buffer material exhibited a large capacity to accommodate the shrinkage with only 5% of the particles with kernels developing cracks across the layer thickness. Since the shrinkage took place against the kernel which was non yielding, the density of the buffer increased to accommodate the shrinkage. The increased

density of the buffer can be illustrated by comparison of the unirradiated microstructure in Figure 4.6.1.2 and the irradiated particle in Figure 4.6.2.2.4.

Around each kernel was about a 10 to 20 micron thick layer of buffer PyC which was densified more than the rest of the buffer as a result of fission fragment recoil from the kernel. In some cases the shrinkage of the layer adjacent to the kernel surface was sufficient to result in the initiation of a crack in the buffer. The crack width decreased as it proceeded into the buffer and had the appearance of the "spearhead" attack from fission fragment recoil damage reported for dense PyC deposited on fuel kernels (Ref 4.6.2.4).

Typically when the buffer shrunk away from the IPyC the highly anisotropic PyC seal coating deposited on the buffer during manufacture remained bonded to the IPyC. The seal coating was deposited to provide a smooth surface on the buffer layer so that the IPyC could be easily separated from the buffer for characterization during manufacturing quality control measurements. The fact that during irradiation the seal coating was torn from the buffer layer rather than parting as expected at the seal-IPyC interface indicates that the bond at the IPyC interface was relatively strong. The observation also indicates that the IPyC had higher strength than the buffer layer, an expected result. The PyC seal coat can be seen adhering to the IPyC in the high magnification photos of Figures 4.6.2.2.1 and 4.6.2.2.4.

Cracks which developed in the IPyC did not propagate into the SiC layer. However, there was a tendency for cracked SiC and cracked IPyC to appear in the same particle. No microstructure features were observed which conclusively connected between the IPyC crack and development of a crack in SiC or a crack in the SiC which caused the IPyC to fail. Examples of typical IPyC and SiC cracks appearing in the same particle are shown in Figure 4.6.2.3.1.

The IPyC remained in contact with the SiC coating in all particles except those in which the IPyC was cracked. When the IPyC was cracked it appeared that irradiation induced shrinkage caused the IPyC to pull away from the SiC and curl toward the particle center. This action left a gap between the IPyC and the SiC at the location of the IPyC crack. The phenomenon described here may have resulted in complex interaction between IPyC and SiC in the vicinity of the IPyC crack where there was contact between SiC and IPyC. If the interaction resulted in tensile stress in the SiC it may have contributed to the observation of cracked SiC near cracks in the IPyC. The development of a gap between cracked IPyC and the SiC coating as well as the nearby crack in the SiC is illustrated in Figure 4.6.2.3.1.

The IPyC effectively protected the SiC from the swelling kernel. In about 5% of the particles the buffer layer was broken and the UCO kernel swelled into the void left by the shrinking buffer. In some cases the kernel swelled up against the IPyC layer. Under the irradiation conditions of these tests the IPyC was not attacked by the kernel and no evidence of SiC attack by fission products from the kernel was observed. An example of kernel material in contact with IPyC and no SiC attack evident is shown in Figure 4.6.2.2.5.

The frequency of particles with cracked IPyC increased with fast neutron exposure. At the lowest exposure of 1.8×10^{25} n/m^2 in compact NPR 1 A8 failure of the IPyC was 6% but at the maximum exposure of 3.8×10^{25} n/m^2 in compact NPR 1 A5 the IPyC failure fraction was 30%. In compact NPR 2 A4 which had the same exposure as NPR 1 A5 but at about 250C lower temperature the IPyC failure fraction was 65%. This result was not expected because normally the failure fraction of PyC coatings increases with increasing temperature as a result of increased irradiation induced dimensional change. The cause of the higher IPyC failure at lower temperatures of NPR 2 is not apparent. The summary of observations made on the ceramographic sections is shown in Table 4.6.2.1.

SiC:

The SiC coating is the primary barrier to fission product release in the TRISO coated particle. The ceramographic sections of compacts were examined at high magnification to characterize cracks or other flaws which might give rise to fission product release. The results for particles which retained their kernels in the metallographic mounts are shown in Table 4.6.2.1.

The data in Table 4.6.2.1 was collected only for particles with kernels in order to create a uniform data set where preparation conditions were as similar as possible. A second set of data for SiC condition was collected for particles which had lost the kernel and inner coatings but had retained the SiC. In these latter particles the condition of the SiC was recorded and if the SiC was cracked a photograph was taken of the particle. The frequency of cracks in the total population whether or not the kernel was present is presented in Table 4.6.2.2.

Two types of fracture were observed in the SiC. The most frequent was a relatively straight radial crack across the thickness of the SiC layer. An example of the radial crack in SiC is shown in Figure 4.6.2.3.2.

Table 4.6.2.1
Ceramography of NPR 1, NPr2, and NPR1A Compacts (Particles with Kernels)

Fuel Compact	Compact End (a)	No. of Particles with Kernels	Coating Condition Observations Cracked Coatings Observed						Comments
			buffer.	IPyC	SiC (b)	SiC (c)	OPyC	PPyC	
NPR 2 A4	1	40	0	26	2	4	31	34	3.8 x 10^{25}n/m^2, 730 °C, 79% FIMA
	2	44	0	29	3	0	24	43	
	Total No.	84	0	55	5	4	56	77	
	Total %		0	65	6	5	67	92	
NPR 1 A5	1	19	8	1	1	0	16	19	3.8 x 10^{25}n/m^2, 975°C, 79% FIMA
	2	20	0	11	0	0	19	20	3.7x10^{25}n/m^2
	Total No.	39	8	12	1	0	35	39	
	Total %		20	30	3	0	90	100	
NPR 1 A8	1	34	0	3	0	1	24	29	2.4x10^{25}n/m^2, 850°C, 72% FIMA
	2	19	0	0	0	0	1	3	1.8x10^{25}n/m^2
	Total No.	53	0	3	0	1	25	32	
	Total %		0	6	0	2	47	60	
NPR 1 A9	1	17	0	3	1	0	8	17	2.1x10^{25}n/m^2, 1075°C, 64% FIMA
	Total No.	17	0	3	1	0	8	17	
	Total %		0	18	6	0	47	100	

Note: (a) End #1 Irradiated nearest reacor core midplane (highest exposure)
End #2 Opposite end #1
(b) Through radial cracks
(c) Circumferential cracks, not through coating

Table 4.6.2.2
Ceramography of NPR 1, NPr2, and NPR1A Compacts (All Particles with and without Kernels)

Fuel Compact	Compact End (a)		No. of Particles examined with and without kernels	Coating Conditions Observations Cracked SiC Coating Observed		Comments
				(b)	(c)	
NPR 2 A4	1		135	3	5	3.8 x 10^{25}n/m^2, 730 °C, 79% FIMA
	2		152	5	1	
		Total No.	287	8	6	
		Total %		3	2	
NPR 1 A5	1		96	1	0	3.8 x 10^{25}n/m^2, 975°C, 79% FIMA
	2		82	0	1	3.7x10^{25}n/m^2
		Total No.	178	1	1	
		Total %		0.6	0.6	
NPR 1 A8	1		139	0	3	2.4x10^{25}n/m^2, 850°C, 72% FIMA
	2		121	0	0	1.8x10^{25}n/m^2
		Total No.	260	0	3	
		Total %		0	1	
NPR 1 A9	1		83	1	0	2.1x10^{25}n/m^2, 1075°C, 64% FIMA
		Total No.	83	1	0	
		Total %		1	0	

Note: (a) End #1 Irradiated nearest reacor core midplane (highest exposure)
End #2 Opposite end #1
(b) Through radial cracks
(c) Circumferential cracks, not through coating

The second type of SiC crack was circumferential and did not propagate through the coating. There were several forms of the circumferential cracks. Some circumferential cracks were only 10 to 30 microns in length and proceeded at a shallow angle from the SiC outer or inner surface and into the SiC. Examples of these cracks are shown in Figures 4.6.2.3.3 and 4.6.2.3.4.

Circumferential cracks which extended for a 100 microns or more were observed in compact NPR 1 A8 which had a relatively low fast neutron exposure of 2.3 x 1025 n/m2. This extensive crack system was only observed in one particle and the relatively long circumferential SiC cracks observed are shown in Figure 4.6.2.3.5.

In the preparation of ceramographic TRISO fuel specimen there is always uncertainty regarding whether the brittle coating layers were cracked in the grinding and polishing procedure or during irradiation exposure. In the case of the extensive circumferential cracks shown in Figure 4.6.2.3.5 it seems likely that they result from the polishing procedure since samples at 50% higher exposure did not show the same effect. The radial SiC cracks shown in the other figures are less likely to be polishing artifacts.

Confidence that the grinding a polishing procedure was not a major source of the SiC cracks was provided by preparing multiple surfaces in the same coated particle. If the number of observed cracks did not increase with each new surface, the conclusion was that the grinding and polishing procedure did not introduce cracks in the SiC. Several particle samples were prepared in this way. Particles which did not show cracks in the initial SiC polished surface did not develop cracks when the particle was subjected to further grinding and polishing. Alternately, particles which had cracks in the first SiC polished surface prepared, did not develop additional cracks when the particle was ground and polished further. An example of a particle with a distinctive radial crack pattern illustrating that the number of radial cracks did not change during the second grind and polish procedure is shown in Figure 4.6.2.3.6.

Ceramographic mounts prepared with particles identified by IMGA as releasing and non-releasing of cesium provided further confidence that the ceramographic preparation was not introducing significant SiC cracks. In that work the particles which had released cesium during irradiation all were shown to have cracks or porosity in the SiC while the particles which had been retentive showed less than 5% with minor cracks which did not penetrate the SiC. Even particles with "gold spot" inclusions in the SiC did not show SiC cracks and were

found among the retentive particle population. The results of the ceramographic examination of particles characterized by IMGA are shown in Table 4.6.2.3.

Lenticular flaws oriented parallel to the deposition plane were detected in the SiC of several particles. These flaws had the appearance of a feature known as "Gold Spots". The gold spot term was derived from the fact that when the OPyC is burned from the particle the flaw appears gold in color when observed through the thin outer layer of SiC. Analysis of the contents of the flaw has shown it to be Si and C. It is formed during SiC coating in a spouting fluidized bed when the particle is momentarily ejected and touches the coater wall above the bed. Some Si and carbon soot is picked up on the surface of the particle which then falls back into the bed where the SiC coating process is completed. Although the gold spot represents a discontinuity in the SiC it has not been associated with cracks in the SiC coating. Examples of gold spots are shown in Figures 4.6.2.3.7 and 4.6.2.3.8.

Consideration of the coated particle as a pressure vessel would favor perfect spheres for the maximum pressure containment capability. However, many particles deviate from perfect sphericity. The SiC coating elastic modulus is much higher than the PyC coatings so that eventually most of the load for gas pressure containment is borne by the SiC and overpressure conditions cause failure of the SiC. In the case where greater than expected SiC failure takes place, as in capsules NPR 1 and NPR 2, the particles which deviate most from spherical geometry would appear to be probable sources of failure. However, examination of particles over the range of shapes showed no correlation of SiC failure and the degree of sphericity. An example of a relatively spherical SiC coating which cracked is shown in Figure 4.6.2.3.6 while the non spherical particle shown in Figure 4.6.2.3.8 did not crack.

The SiC coatings were carefully examined to determine if any reactions had taken place. No second phases, indicative of fission metal attack, or missing Si, indicative of CO/CO_2 or Cl_2 attack was observed. The UCO kernel had effectively retained the rare earth fission products and even the release of Pd was low enough that no SiC attack was observed. However, examination by scanning electron microscopy, discussed in section 4.8, revealed that Pd and Ag had penetrated the SiC at very low concentrations.

Table 4.6.2.3

Ceramography of Debonded Particles Characterized by IMGA Supports the Assumption that Observation of Cracked or Partially Cracked SiC is a Good Indication that the Particle is not Retentive

Source of Particle Mount	IMGA Identified Particles Releasing Cesium		IMGA Identified Particles Retaining Cesium	
	No. Particles Exam./Mount	%SiC Cracked Through or (Partial)	No. Particles Exam./Mount	% SiC Cracked Through or (Partial)
NPR 1 B4 (P3)	1	100 (0)		
NPR 2 B4 (P7)			1	0 (0)
NPR 1 B4 (Multi Hole)	7	43 (57)	143	0 (0)
NPR 1 B5 (Multi Hole)	7	86 (14)	116	7 (1)
Total	15	67 (a)(33) (b)	260	3.5(c)(0.1)(d)

(a) 9 out of 10 particles with through radial SiC crack had failed IPyC
(b) 4 out of 5 particles with part through SiC crack had failed IPyC

Conclusion: Consistent with Compact Data

(c) Only 1 out of 8 particles with through radial SiC crack had failed IPyC
(d) The 1 particle with part through SiC crack did not have failed IPyC

Conclusion: Not consistent with Compact Data; SiC Damage in PIE

PPyC/OPyC:

Failure of the PPyC coating resulted from tensile stress which developed as a result of irradiation induced shrinkage of the low density PyC material around the unyielding substrate of OPyC and SiC. Cracks initiated in the PPyC which failed and continued to shrink in a circumferential direction. The cracks in the PPyC expanded as irradiation progressed. The contraction of the PPyC was transmitted to the OPyC across the PyC seal coat. In this way the PPyC contributed to an already high tensile stress component developing in the OPyC as a result of irradiation induced shrinkage in that coating. Through the combination of PPyC shrinkage and shrinkage in the OPyC the tensile stress in the OPyC became large enough to result in radial cracking of the OPyC coating. The cracks normally propagated from the PPyC through the seal coating and OPyC as shown in Figure 4.6.2.3.9 The failure of the PPyC and OPyC was highly dependent on the fast neutron fluence. As the fluence increased above 1.8×10^{25} n/m^2 (E>0.18Mev) the frequency of failure increased rapidly. The failure of the retentive OPyC coating as fluence increased correlates well with the rapid increase in fission gas release observed in capsules NPR 1, NPR 2, and NPR 1A at about the same fluence. It is apparent that the failure of the OPyC either contributed to the SiC failure or revealed a previously failed SiC releasing stored fission gas and allowing the steady state fission gas release rate to increase. The relationship between OPyC failure observed in ceramographic sections and fission gas release observed in the capsules is shown in Figure 4.6.2.3.10

High magnification examination of the seal coats was carried out at the OPyC outer and inner surfaces. Examination under polarized light was useful in characterizing the seal coats which exhibit optical anisotropy and are bright while the OPyC and PPyC are isotropic and dark. The seal coats were cracked in many locations as a result of circumferential shrinkage of the highly anisotropic PyC. It appeared that the seal coat had cracked without introducing cracks in the PPyC or OPyC coatings. An example of the cracked condition of the PyC seal coat is shown in the polarized light photograph shown in Figure 4.6.2.3.9.

There was no evidence that cracks which developed in the PPyC and OPyC propagated directly into the SiC. Because of the high failure fraction of OPyC it was not unusual for a crack in the OPyC to be near a crack in the SiC. However, the OPyC has a much lower elastic modulus than SiC and was not strongly bonded to the SiC as indicated by the fact that the OPyC spalled off the SiC when the OPyC was severely cracked. Therefore, propagation of cracks from the OPyC into the SiC is unlikely.

Compact Matrix:

The matrix at the time of manufacture was about 50% of theoretical density. During irradiation shrinkage took place which resulted in reduction of compact length and diameter as discussed earlier (see section 4.3.1). The irradiation induced shrinkage of the matrix around the relatively stable coated particles and H-451 graphite shim particles results in cracks in the matrix to accommodate the contraction.

The compacts were very fragile and particles were easily debonded from the surface by contact with containers and handling equipment. Ceramographic sections of the compacts showed that the compact matrix was very porous and laced with cracks. Bonding was maintained between matrix and particles but the high porosity and cracks which ran through the matrix resulted in a friable compact body.

The matrix was bonded to the particles, many of which had broken outer coatings. However, there was no obvious detrimental interaction between the matrix and particles. Detrimental interaction has been observed in prior irradiation tests where the shrinking matrix pulls the OPyC coatings away from the SiC substrate. Such dislocation was not observed in this fuel. An example of the matrix microstructure is illustrated in Figure 4.6.2.3.11.

4.6.3 Summary Discussion

The failure of the PPyC/OPyC coatings was a strong function of fast neutron exposure. At a temperature of about 900C the onset of OPyC failure was at about 1.8×10^{25} n/m^2 and nearly about 70% OPyC failure was observed at 2.4×10^{25} n/m^2. The OPyC failure onset was delayed and rate of increase was less at lower temperatures where the rate of irradiation induced dimensional change of PyC was reduced. Fuel samples with the lowest fast neutron exposure had significantly less OPyC failure than the fuel with maximum exposure.

The SiC coating failure fraction showed no strong correlation with either fast neutron exposure, or burnup. The SiC failure fraction observed in the compact irradiated at the lowest temperature (730C) was about 2 times the fraction failed at 975C and the same fast neutron fluence. This observation is contrary to expected effects of temperature and probably reflects a lack of significant temperature dependence coupled with large uncertainty because of the relatively small sample size. The IMGA data on more than 400 particle shows ten times higher failure fraction at 975° C versus 730° C at 3.7×10^{25} n/m^2 fast neutron exposure.

Burnup of heavy metal increased in the fuel along with fast neutron exposure so increased coating failure had an apparent dependence on burnup. However, because of the relatively narrow range of burnup (64% to 79%) in the fuel examined by ceramography, and lack of evidence that kernel or fission product attack contributed to mechanical failure of the SiC coating it was concluded that burnup had no detectable effect on coating failure within the burnup range of these experiments.

Particle shape and the existence of the lenticular SiC flaw known as a "gold spot" did not contribute to the observed failure of SiC or OPyC. Non spherical particles performed as well as spherical particles. Cracks in the SiC were never seen to connect with or be associated with a gold spot discontinuity in the SiC. The source of stress causing SiC failure acted independent of these shape and flaw features. However, these features should be removed because they can be expected to become limiting when the source of failure in these particles is identified and eliminated.

The fact that the cracks in the SiC were associated with a crack in the IPyC suggests that the mechanism of failure involves both coatings. From 10% to 30% of the particles with failed IPyC also had cracked SiC. Since the IPyC crack was not observed to be aligned with the SiC crack and the IPyC was typically debonded from the SiC in the vicinity of the crack the conclusion was drawn that cracks in one coating did not propagate into the other. While this conclusion seems likely, the data are not conclusive since only a two dimensional view of the particle was observed. Perhaps in a plane of the particle not observed, the IPyC and SiC crack were aligned at the point where the crack was initiated. The data obtained here does not provide the required evidence to resolve this issue.

4.7 Characterization by Burning and Leaching

4.7.1 Leach-Burn-Leach

Leach-Burn-Leach measurements were conducted to determine the fraction of high burnup HEU UCO kernels completely exposed by failed coatings and those with failed SiC but intact OPyC or 1PyC. Such measurements have been conducted in prior experiments (Ref. 4.7.1, 4.7.2, and 4.7.3).

In this work the entire irradiated compact was first leached by boiling in a concentrated nitric acid (14M) plus a hydrofluoric acid (0.03M) solution for 24 hours to remove kernels which were exposed by failure of all coating layers. Radio-chemical analysis of the leach solution and knowledge of the radionuclide inventory and uranium content of compact permits an estimate of the fraction of kernels leached out through failed coatings.

A subsequent burning at 750° C in air for 48 h removed all compact matrix and PyC from the surface of particles in the leached compact. The SiC coating was oxidation resistant and not damaged by this procedure. However, SiC coatings which had cracks or porosity large enough to permit gas diffusion were expected to permit oxidation of the underlying IPyC and buffer layers to expose the kernel. Subsequent leaching in boiling concentrated (14M) nitric and hydrofluoric acid (0.03M) for 72 hours then removed the kernels exposed in this manner. Analysis of the leach solution provided the data needed to determine the fraction of particles with permeable SiC which were exposed by burning. The procedures used in this work were documented in references 4.7.4 and 4.7.5.

The results of leach-burn-leach measurements enhance the value of TRIGA fission gas release measurements because the first leach provides a measure of fraction exposed kernels which could release fission gas. The second leach coupled with results of the first leach provided an independent measure of SiC failure fractions which can be compared with gamma spectrometry results to improve the characterizations of SiC retentivity. Leach-burn-leach procedures were carried out on NPR 1 compact B6 and NPR 1A compact 17. Results for NPR 1A compact 17 were not available at the time the project ended. Results from the first 24 hours of leaching prior to burning and 48 hours of leaching after burning NPR 1 compact B6 were available, and they are discussed below.

Uranium Analysis: The lower limit of detection for uranium in the leach solutions submitted for radiochemistry analysis was 0.02mg/ml. The analyses showed that in every

sample the amount of uranium present was <0.02mg/ml of leach solution. The volume of leach solution obtained for each of the two 12 hour leach prior to burning was 250ml. The leach solution volume at each step after burning the compact were 100ml in volume. From the results of the radiochemical analysis indicated that the amount of uranium leached in the first two leach steps was less than 10mg and during the subsequent 4 leach steps less than 8mg uranium was removed. Therefore, the total uranium leached from exposed kernels was less than 18mg.

An estimate of the uranium inventory of the NPR 1 B6 compact after irradiation was 12mg (Ref. 4.7.6). Because of the relatively high uranium detection limit in the radiochemistry method, the amount of uranium which could have been undetected in the leach solutions was larger than the total amount in the compact. Therefore, the results of the uranium analysis were not useful.

Fission Product Analysis: To determine the fraction of fission and activation products leached from Compact NPR 1 B6, an estimate of the inventory of each radionuclide of interest in the compact was required. The radionuclide inventory for 95Zr, 106Ru, 134Cs, 137Cs, and 144Ce was determined for an individual particle by interpolation from IMGA measurements of activities (Bq) for each isotope in particles from compacts NPR 1 B5 and NPR1 B8. The activities were corrected for the approximate time of the radiochemical analysis (8/30/93). The activity for each particle was then multiplied by the number of particles in the compact (4090) to obtain the total compact activity. The results are shown in Table 4.7.1.1

Work on the project was terminated after radiochemical analysis was obtained for only the first 6 leaching steps which represented 72 total hours of leaching (24h prior to burning + 48h after burning). However, the full 72 hours of leaching was carried out after burning.

After the first 24 h leach and the burning step, a white material covered about 1.7% of the particles. The amount of broken SiC shells visible was < 0.2%. After subsequent leaching, the white material was no longer present and a large number of broken SiC shells were visible. The white material was probably fission product oxide from the burning of PyC on particles with failed SiC where the OPyC was exposed to fission products.

The activity for each isotope in the leach solution was divided by the total activity of that isotope in the compact to determine the fraction leached for each 12 hour increment

Table 4.7.1.1

Estimated Fission Product Inventory in Compact NPR 1 B6 Prior to Leach

Isotope	Bq/particle @EOI (a)	Bq/Particle @ 8/30/93	Bq/compact @8/30/93 4090 part/comp.
95Zr	8.25E+7	5.984E+5	2.447E+9
106Ru	5.40E+6	2.316E+6	9.473E+9
134Cs	7.70E+6	5.069E+6	2.073E+10
137Cs	3.40E+6	3.304E+6	1.351E+10
144Ce	7.00E+7	2.311E+7	9.451E+10

(a) Interpolation from IMGA data Section 4.5

of leaching. The results are given in Table 4.7.1.2 and the cumulative fraction of each isotope extracted from the fuel is shown as a function of leaching time in Figure 4.7.1.1.

The first two 12 h extractions for compact NPR 1 B6 took place prior to burning the compact. Those two acid solutions contained 80% to 98% of total fission products removed in the total of 6 leaching steps. After the first two leaching steps, burning of the compact (750C, 72h, in air) removed the PPyC/OPyC coatings. In those particles with cracked or permeable SiC, the IPyC was also expected to be removed.

The rate of radionuclide extraction slowed significantly after the first 24 h of leaching for all isotopes. The reduction in extraction rate after an initial rapid removal rate indicated that all the readily accessible material had been removed. This condition was interpreted as complete removal of all the subject fission products from kernels with coatings which failed and had exposed the kernel. Therefore, the fraction of fission product removed was considered to be equivalent to the fraction of particles with failed coatings.

It was expected that some failed SiC layers were covered by intact OPyC or they contained an intact IPyC coating so that the initial leach would not have removed the kernel material from those particles. In order to measure the portion of the fuel particles having failed SiC layers but intact PyC layers, the PyC coatings were removed by burning 72 h at 750 C in air.

The leaching operations that were carried out after burning removed a relatively small amount of radionuclides. Because there was no significant increase in leaching rate after removing the PyC coatings it was not possible to separate the two distinct fuel fractions consisting of particles with completely exposed kernels and those with failed SiC but intact PyC. This point is illustrated in Figure 4.7.1.1 where the cumulative fraction leached from the compact rises smoothly and a decreasing rate of leaching when passing from the second to the third and subsequent leaching steps.

The above observations indicated that the particles with cracked or permeable SiC also had failed or permeable PyC at the time the irradiation ended. The UCO fuel kernels were completely exposed and fission gases were released into the capsule purge gas stream. The fact that the PPyC/OPyC and IPyC coatings were failed on particles with failed SiC suggests the failure mechanism involves all three coatings.

The fraction of leached material fell into two groups. The Zr and Ce leach results indicated about 1.5% coating failure. The Cs and Ru results indicated about 0.5% failure of

Table 4.7.1.2

Fraction Fission Products Leached from Compact NPR 1 B6 at Each Leach Increment

95Zr

Isotope	Cumulative Leach Time (h)	Leachant Concentration (Bq/ml)	Total Leached (Bq)	Fraction of Compact Inventory	Cumulative Fraction Leached
95Zr	12	1.2E+5	3.0E+7	1.2E-2	0.0120
	24	7.5E+3	1.9E+6	7.8E-4	0.0128
		Burning of Compact 72h, 750 C, in air			
	36	1.3E+4	1.3E+6	5.3E-4	0.0133
	48	1.5E+3	1.5E+5	6.1E-5	0.0134
	60	6.7E+3	6.7E+5	2.7E-4	0.0136
	72	2.0E+3	2.0E+5	8.2E-5	0.0137

106Ru

Isotope	Cumulative Leach Time (h)	Leachant Concentration (Bq/ml)	Total Leached (Bq)	Fraction of Compact Inventory	Cumulative Fraction Leached
106Ru	12	1.2E+5	3.0E+7	3.2E-3	0.00320
	24	2.5E+4	6.2E+6	6.5E-4	0.00385
		Burning of Compact 72h, 750 C, in air			
	36	4.5E+4	4.5E+6	4.7E-4	0.00432
	48	2.9E+3	2.9E+5	3.1E-6	0.00432
	60	1.6E+3	1.6E+5	1.7E-5	0.00434
	72	1.7E+3	1.7E+5	1.8E-5	0.00436

134Cs

Isotope	Cumulative Leach Time (h)	Leachant Concentration (Bq/ml)	Total Leached (Bq)	Fraction of Compact Inventory	Cumulative Fraction Leached
134Cs	12	3.4E+5	8.5E+7	4.1E-3	0.00410
	24	1.0E+5	2.5E+7	1.2E-3	0.00530
		Burning of Compact 72h, 750 C, in air			
	36	2.6E+4	2.6E+6	1.2E-4	0.00542
	48	6.1E+3	6.1E+5	2.9E-5	0.00545
	60	2.1E+3	2.1E+5	1.0E-5	0.00546
	72	4.6E+4	4.6E+6	2.2E-4	0.00568

Table 4.7.1.2 (cont.)
Fraction Fission Products Leached from Compact NPR 1 B6 at Each Leach Increment

137Cs

Isotope	Cumulative Leach Time (h)	Leachant Concentration (Bq/ml)	Total Leached (Bq)	Fraction of Compact Inventory	Cumulative Fraction Leached
137Cs	12	2.3E+5	5.7E+7	4.2E-3	0.00420
	24	6.5E+4	1.6E+7	1.2E-3	0.00540
		Burning of Compact 72h, 750 C, in air			
	36	1.9E+4	1.9E+6	1.4E-4	0.00554
	48	4.1E+3	4.1E+5	3.0E-5	0.00557
	60	1.4E+3	1.4E+5	1.0E-5	0.00558
	72	3.0E+4	3.0E+6	2.2E-4	0.00580

144Ce

Isotope	Cumulative Leach Time (h)	Leachant Concentration (Bq/ml)	Total Leached (Bq)	Fraction of Compact Inventory	Cumulative Fraction Leached
144Ce	12	5.3E+6	1.3E+9	1.4E-2	0.01397
	24	3.7E+5	9.2E+7	9.7E-4	0.01406
		Burning of Compact 72h, 750 C, in air			
	36	1.8E+6	1.8E+8	1.9E-3	0.01515
	48	2.7E+4	2.7E+6	2.8E-5	0.01518
	60	3.4E+4	3.4E+6	3.6E-5	0.01521
	72	7.4E+4	7.4E+6	7.8E-5	0.01529

in this manner. Analysis of the leach solution provided the data needed to determine the fraction of particles with permeable SiC which were exposed by burning. The procedures used in this work were documented in references 4.7.4 and 4.7.5.

The results of leach-burn-leach measurements enhance the value of TRIGA fission gas release measurements because the first leach provides a measure of fraction exposed kernels which could release fission gas. The second leach coupled with results of the first leach provided an independent measure of SiC failure fractions which can be compared with gamma spectrometry results to improve the characterizations of SiC retentivity. Leach-burn-leach procedures were carried out on NPR 1 compact B6 and NPR 1A compact 17. Results for NPR 1A compact 17 were not available at the time the project ended. Results from the first 24 hours of leaching prior to burning and 48 hours of leaching after burning NPR 1 compact B6 were available, and they are discussed below.

Uranium Analysis: The lower limit of detection for uranium in the leach solutions submitted for radiochemistry analysis was 0.02mg/ml. The analyses showed that in every sample the amount of uranium present was <0.02mg/ml of leach solution. The volume of leach solution obtained for each of the two 12 hour leach prior to burning was 250ml. The leach solution volume at each step after burning the compact were 100ml in volume. From the results of the radiochemical analysis indicated that the amount of uranium leached in the first two leach steps was less than 10mg and during the subsequent 4 leach steps less than 8mg uranium was removed. Therefore, the total uranium leached from exposed kernels was less than 18mg.

An estimate of the uranium inventory of the NPR 1 B6 compact after irradiation was 12mg (Ref. 4.7.6). Because of the relatively high uranium detection limit in the radiochemistry method, the amount of uranium which could have been undetected in the leach solutions was larger than the total amount in the compact. Therefore, the results of the uranium analysis were not useful.

Fission Product Analysis: To determine the fraction of fission and activation products leached from Compact NPR 1 B6, an estimate of the inventory of each radionuclide of interest in the compact was required. The radionuclide inventory for 95Zr, 106Ru, 134Cs, 137Cs, and 144Ce was determined for an individual particle by interpolation from IMGA measurements of activities (Bq) for each isotope in particles from compacts NPR 1 B5 and NPR1 B8. The activities were corrected for the approximate time of the radiochemical analysis (8/30/93). The activity for each particle was then multiplied by the number of

particles in the compact (4090) to obtain the total compact activity. The results are shown in Table 4.7.1.1

Work on the project was terminated after radiochemical analysis was obtained for only the first 6 leaching steps which represented 72 total hours of leaching (24h prior to burning + 48h after burning). However, the full 72 hours of leaching was carried out after burning.

After the first 24 h leach and the burning step, a white material covered about 1.7% of the particles. The amount of broken SiC shells visible was < 0.2%. After subsequent leaching, the white material was no longer present and a large number of broken SiC shells were visible. The white material was probably fission product oxide from the burning of PyC on particles with failed SiC where the OPyC was exposed to fission products.

The activity for each isotope in the leach solution was divided by the total activity of that isotope in the compact to determine the fraction leached for each 12 hour increment of leaching. The results are given in Table 4.7.1.2 and the cumulative fraction of each isotope extracted from the fuel is shown as a function of leaching time in Figure 4.7.1.1.

The first two 12 h extractions for compact NPR 1 B6 took place prior to burning the compact. Those two acid solutions contained 80% to 98% of total fission products removed in the total of 6 leaching steps. After the first two leaching steps, burning of the compact (750C, 72h, in air) removed the PPyC/OPyC coatings. In those particles with cracked or permeable SiC, the IPyC was also expected to be removed.

The rate of radionuclide extraction slowed significantly after the first 24 h of leaching for all isotopes. The reduction in extraction rate after an initial rapid removal rate indicated that all the readily accessible material had been removed. This condition was interpreted as complete removal of all the subject fission products from kernels with coatings which failed and had exposed the kernel. Therefore, the fraction of fission product removed was considered to be equivalent to the fraction of particles with failed coatings.

It was expected that some failed SiC layers were covered by intact OPyC or they contained an intact IPyC coating so that the initial leach would not have removed the kernel material from those particles. In order to measure the portion of the fuel particles having failed SiC layers but intact PyC layers, the PyC coatings were removed by burning 72 h at 750 C in air.

The leaching operations that were carried out after burning removed a relatively small amount of radionuclides. Because there was no significant increase in leaching rate after

of leaching. The results are given in Table 4.7.1.2 and the cumulative fraction of each isotope extracted from the fuel is shown as a function of leaching time in Figure 4.7.1.1.

The first two 12 h extractions for compact NPR 1 B6 took place prior to burning the compact. Those two acid solutions contained 80% to 98% of total fission products removed in the total of 6 leaching steps. After the first two leaching steps, burning of the compact (750C, 72h, in air) removed the PPyC/OPyC coatings. In those particles with cracked or permeable SiC, the IPyC was also expected to be removed.

The rate of radionuclide extraction slowed significantly after the first 24 h of leaching for all isotopes. The reduction in extraction rate after an initial rapid removal rate indicated that all the readily accessible material had been removed. This condition was interpreted as complete removal of all the subject fission products from kernels with coatings which failed and had exposed the kernel. Therefore, the fraction of fission product removed was considered to be equivalent to the fraction of particles with failed coatings.

It was expected that some failed SiC layers were covered by intact OPyC or they contained an intact IPyC coating so that the initial leach would not have removed the kernel material from those particles. In order to measure the portion of the fuel particles having failed SiC layers but intact PyC layers, the PyC coatings were removed by burning 72 h at 750 C in air.

The leaching operations that were carried out after burning removed a relatively small amount of radionuclides. Because there was no significant increase in leaching rate after removing the PyC coatings it was not possible to separate the two distinct fuel fractions consisting of particles with completely exposed kernels and those with failed SiC but intact PyC. This point is illustrated in Figure 4.7.1.1 where the cumulative fraction leached from the compact rises smoothly and a decreasing rate of leaching when passing from the second to the third and subsequent leaching steps.

The above observations indicated that the particles with cracked or permeable SiC also had failed or permeable PyC at the time the irradiation ended. The UCO fuel kernels were completely exposed and fission gases were released into the capsule purge gas stream. The fact that the PPyC/OPyC and IPyC coatings were failed on particles with failed SiC suggests the failure mechanism involves all three coatings.

The fraction of leached material fell into two groups. The Zr and Ce leach results indicated about 1.5% coating failure. The Cs and Ru results indicated about 0.5% failure of

coatings. The reason for the difference in failure indication from the different isotopes is not known with certainty.

A possible explanation for the difference in leached radionuclide fraction draws on the fact that both Zr and Ce form very refractory oxides and carbides and they would be expected to exist in one of those forms in the exposed kernel. On the other hand, neither Cs nor Ru form refractory oxides or carbides. Cesium is very mobile as a metal and Ru forms a volatile oxide so that both could have migrated out of failed particles and the compact prior to the end of irradiation. They would not be available for leaching and the low failure fraction indications would result.

The Zr and Ce was expected to remain in the kernel after coating failure and, assuming complete removal by leaching, the cumulative fraction of Zr and Ce removed represented the best estimate of coating failure fraction. Based on this argument, the coating failure fraction determined by Leach-Burn-Leach was 1.5%. In addition, since there was no significant affect of PyC removal on leaching results, particles with failed SiC did not have intact or impermeable PyC coating. Under these conditions all particles with failed SiC could release fission gases.

Coating Failure Estimate: The results of this work (1.5% failure) show about a factor of 3 less SiC failure than the highest fraction indicated from cracked SiC observed in ceramography. Since the ceramography can sometimes result in systematically high SiC failure estimates because of polishing damage, the ceramography results may be taken as an upper limit of SiC failure.

Better agreement with leach results was obtained with gamma spectroscopy data. During the IMGA examinations of fission product inventory of individual particles, about 2% SiC failure was indicated at high exposure. The agreement with leach results is also good when compared with the maximum estimated capsule average coating failure of 1.3% predicted from fission gas release at the end of irradiation in HFIR. The best estimate of coating failure, where most techniques are in agreement, is in the range 1% to 2%.

The results from this work can be applied to the TRIGA fission gas release measurements to deduce the gas release rate per HEU failed particle. For compact NPR 1 B6 the Kr85m fission gas release rate at 1100°C in TRIGA was 2.0x10-3 (R/B Kr85m). If the gas release came from a compact with coating failure of 1.5%, then the release per failed particle in TRIGA was 13% R/B Kr85m. This estimate of release rate per exposed kernel is significantly higher than deduced from laser failed LEU UCO particles as discussed in

Section 4.4. However, for the reasons discussed in section 4.4 a higher release fraction from the high burnup UCO is possible.

The fact that ^{134}Cs and ^{137}Cs fraction leached was nearly identical indicated that significant retention of ^{133}Xe in the failed particle. If the ^{133Xe} had been released, then the ^{134}Cs fraction retained would have been much lower than the ^{137}Cs fraction retained.

A key assumption in the interpretation of the Leach-Burn-Leach data was that the fission products in failed particles were completely leached out. It is assumed that 1.5% of the particles lost all the cerium in the exposed kernel rather than all the particles losing 1.5% of their cerium. The rapid decrease in leaching rate with time provides the best evidence that the assumption of depletion of only failed particles is correct. If material was being leached from each particle the rate of leaching would be expected to remain constant until nearly 100% of the activity was removed. Gamma spectrometry results from IMGA examination of the leached particle population would be desirable to provide empirical verification of the assumption by measuring the fission product inventory of each particle.

4.7.2 Burn-Visual Examination

In addition to the complete Leach-Burn-Leach procedure discussed above, simple application of the burning operation is also useful for characterizing correlation of the irradiated particles. The burning exposed the SiC coatings so that gross flaws and other features which may influence performance can be revealed. As described below, burn visual examination was carried out on fuel from NPR 1 compact B4 and NPR-1A compact number 13.

The particles of NPR-1 B4 were obtained for IMGA examination by electrolytic deconsolidation of the compact. After the particles destined for IMGA examination were were separated from the shim and matrix debris, it was observed that many particles remained in the debris because they did not completely debond from the matrix and shim. In an attempt to examine those particles which were not submitted to IMGA the deconsolidation debris was burned in air at 750° C for 12 hours. An aluminum oxide lid was placed over the aluminum oxide crucible to prevent loss of particles which might burst during heating.

During burning, all the shim and matrix material was removed as well as the PPyC and OPyC on the TRISO particles. If a particle were broken open the IPyC and buffer was also burned away. The following is a description of what remained after burning:

Item	Sample Description	Observation
1.	Individual particles which had not completely debonded from matrix.	3 to 6 particles still bonded together; about 5 SiC shards At least one bare kernel; 1 particle failed
2.	Deconsolidation debris >350μm <841μm	Intact particles and debris from alumina lid,
3.	Deconsolidation debris <350μm	About 10 black shards, probably SiC with incompletely burned OPyC/PPyC (~ 5 particles failed)
4.	Deconsolidation debris >841μm	Intact particles covered with debris from lid.

Most of the graphite shim particles, OPyC and PPYC was removed by burning but a decision was made to return the samples to the furnace for an additional 12 hour exposure so that a total of 24 hours were spent at 750°C. In subsequent work, a quartz cloth cover was used to cover the crucibles containing the specimen to avoid the debris from the crucible lid.

Compact NPR-1A number 13 was burned and the particles examined. This compact was selected for burning because it had a relatively high TRIGA fission gas release rate of 3.3×10^{-4} R/B Kr-85m and observation of several broken particles in the burned product was expected. After burning 24 hours at 750°C in air, the specimen was carefully examined by microscope at about 25X. The particles had been burned back to the SiC and no PyC coating remained. No broken particles or SiC shards were observed in visual examination at about 25x. From this observation, the gas release detected by TRIGA for this compact appears to have taken place through SiC coatings which have connected porosity or extremely small cracks not detected by these methods.

4.7.3 Burn-Dimensional Change Analysis

In the interest of ruling out the possibility that the SiC coating had resulted from unexpected failure irradiation induced dimensional change, measurement was made of the particle outside diameter at the SiC coating stage. Unirradiated samples were prepared by burning NPR capsule archive TRISO UCO particles deconsolidated from unirradiated compact (FM-23-00001-04-2). Irradiated samples were obtained by taking particles from the

remains of compacts NPR 1 B4 and NPR 1A number 13 which were previously burned for visual examination as discussed in the previous section.

Small groups of NPR-type fuel particles, burned-back to cleanly exposed SiC coatings were photographed at the IMGA facility with accurately known (to ± 1 μm) size reference balls in the pictures. Enlargements of about 50X (which raise a particle's image on the print to about one inch diameter) were measured using a millimeter scale. With the exact photo magnification being determined each time from the reference balls, the diameters of particles were obtained. Generally two to four different-direction diameters were measured (to 0.1 mm) and averaged for each of the particles, most of which were conspicuously non-round. The results of the measurements are shown in Table 4.7.3.1.

Table 4.7.3.1

Results of the Diameter measurements on Irradiated and Unirradiated NPR 1, NPR 2, and NPR 1A particles at the SiC stage.

	NPR-1 Archive (Unirr ad.) --burned	NPR-1A-13 --burned	NPR-1A-13 --burned (additional group)	NPR-1-B4 --burned
No. of particles n	25	25	17	33
Particle mean diam. d	562.6 μm	569.8 μm	567.1 μm	565.7 μm
Population std. dev. σ_n	20.5 μm	20.1 μm	18.4 μm	16.5 μm
Sample std. dev. σ_{n-1}	20.9 μm	20.5 μm	18.9 μm	16.8 μm
Min. observ. diam. d_{min}	532 μm	528 μm	545 μm	517 μm
Max. observ. diam. d_{min}	606 μm	602 μm	603 μm	597 μm

The results of this work show that the mean diameter of the particles at the SiC stage did not change significantly as a result of irradiation. The SiC is expected to expand about 0.5%, or 3 μm, (Fef. 4.7.7) as a result of irradiation. The observed change in diameter is consistent with an increase of 3 μm. Such a change in dimension has not previously been considered a source of SiC failure.

4.8 Analytical Scanning Electron Microscopy on Coated Fuel Particles

4.8.1 Introduction

A total of four particles from NPR-1, compacts B4 and B5 were examined. The particles were labeled B4-P4, B4-P7, B5-P1, and B5-P3. In order to reduce the readiation level to permit examination in an unshielded microscope the particles were remotely ground and polished to a level below the kernel. Difficulties in monitoring remote polishing resulted in different layers remaining. In one case, a portion of the kernel remained resulting in a high radiation level but, nonetheless, one at which the particle could be safely handled.

Prior to polishing, the particles were examined by gamma spectral analysis in the Irradiated Microsphere Gamma Analyzer (IMGA) in order to determine fission product retention. The ratio of Cs to Ce, is indicative of the particle's ability to retain fission products. The tests showed that particles BR-P7 and B5-P3 were fission product retentive whereas particles B4-P4 and B5-P1 were non-retentive particles.

4.8.2 Electron Microprobe Analysis

The scanning electron microscope (SEM) uses a very sharply focused beam which is scanned over the specimen. A CRT is then scanned in synchronism with the beam, and the ratio of the distance covered on the CRT to that covered on the specimen is the magnification. The signal supplied to the CRT is determined by the analysis desired. An electron beam causes several effects upon interacting with a metal surface. The most common is the release of electrons from the specimen. These electrons are of low energy, and their emission rate is very sensitive to the distance from the surface at which they originate and thus to the surface topography. Secondary electrons are the most common signal used for scanning electron microscopy. Excitation of the specimen atoms by the electron beam also results in characteristic x-ray radiation. Since the energy of the emitted x-rays is characteristic of the atom that emits the photon, the x-ray photon can be used to produce a map of a particular element. This is the mode that was primarily used in the analysis of the fuel particles.

Two analytical methods were used to examine the particles. The first was Energy Dispersive Spectroscopy (EDS) which employs a scintillation detector which produces an electrical pulse proportional to the energy of the absorbed x-ray photon. This method was used to make a general determination of the elements present. The method of Wavelength Dispersive Analysis (WDS) was used to determine the distribution of elements within the fuel particle. This method uses a crystal to diffract x-rays of specific wave length so that only the desired wavelength x-rays reach the detector. This method is not susceptible to saturation by background radiation form radioactive samples and generally gives a higher signal to noise ratio than Energy Dispersive Analysis. Since in both cases the electron beam is scanned over the surface of the specimen, both methods of analysis can produce an image.

4.8.3 Fission Product Distribution Analysis

The primary emphasis was placed on the integrity of the SiC layer. Particular emphasis was placed upon examination of cracks in the SiC and of any surface features present. Most of the SEM photographs that follow were taken in a mode to optimize the x-ray signal resulting in a lower resolution than can normally be obtained with an SEM. An EDS spectrum can show any element present at a particular position on the specimen in a short time. This method was, therefore, the first that was used for examination of a particle. A typical spectrum appears in Fig. 4.8.1 from particle B4-P4. Common products appear as well as the large Si peak. In some casies, Ci, a remnant from the CVD process, was detected in the SiC. The elements Fe, Cr, Ni, Cu, and Zn sometimes appeared probably the result of stainless steel and brass either in the process line for manufacture of the particles or from the SEM itself. Careful attention was paid to elements Ba, Ce, Cs, and Pd often produced strong signals from which elemental distributions could be determined.

It must be remembered that only a signle plane through the particles was examined. A particle could have a large breach in the SiC that would not appear in the polished plane of the speciment. The cracks observed in the polished plane are believed to originate mostly from the polishing operation. Since it is possible that such cracks could have started from existing microcracks or regions of sission product interaction, they were examined nonetheless.

Table 4.8.1 shows the primary results of the x-ray WDS examination of the four specimens. The specimens were categorized into retentive and non-retentive particles. The

Table 4.8.1. Distribution of Fission Products

	Non-Retentive		Retentive	
	B4-P4 SiC-OPyC-PPyC	B5-P1 Kernel-Buffer-IPyC-SiC	B4-P7 IPyC-SiC-OPyC-PPyC	B5-P3 IPyC-SiC-OPyC
Ba	Partly through SiC ≈5 µm	Concentrated at kernel/buffer interface	Does not penetrate SiC at interface of SiC/IPyC	Mostly in IPyC Slightly in SiC
Pd	~20% into SiC non-uniform at interface of SiC/IPyC	Only trace outside kernel	Weak signal	Slightly in IPyC at SiC/IPyC interface precipitate.
	Through SiC	Through SiC	In IPyC not SiC	At interface in 1PyC not in SiC
Cs	Concentrated at interface partly through SiC ~5 µm	Through SiC	Penetrates SiC? Weak signal	Concentrated at inner surface of IPyC.
Ag				Through SiC
La				At 1PyC/SiC interface -with Pd
Sr		Kernel only		

first row of the table indicates the layers that remained with the particle, the others being lost in the polishing process. As expected, the missing layers differ from one particle to another.

Barium appears to partially penetrate the SiC in both retentive and non-retentive In the cases where it was detected in the SiC, penetration was slight as can be seen from Fig. 4.8.1 (546, 543) (Photo numbers appear in parentheses following figure numbers.)of non-retentive B4-P4, where penetration was only about 5 μm. A low magnification view of particle B5-P1 is seen in Fig. 4.8.2 (559, 562) where a portion of the kernel is shown. A corresponding Ba scan is also shown where the Ba signal is seen to extend through the IPyC but perhaps not into the SiC. Cracks that opened between layers became filled with epoxy during the grinding process where epoxy was added in order to keep the particle from falling apart. This is the reason for bands devoid of Ba between layers. A higher concentration of Ba in the IPyC than in the SiC can be seen in Fig. 4.8.3 (569, 567) which shows a portion of particle B5-P1 at higher magnification. Retentive particle B4-P7 shows similar behavior shown in Fig. 4.8.4 (206, 212) at low magnification and in Fig. 4.8.5 (204, 205) where the Ba signal is lower in the SiC than in the IPyC. Since much of the noise is bremstrallung radiation produced from deceleration of the electrons in the beam, the noise is expected to increase as the square of the atomic number of the target. Therefore, greater noise is expected in the SiC than in the pyrocarbon layers. A decrease in signal in the SiC is, therefore, an indication of a decrease in the element. A slight increase would be an ambiguous result. Non-retentive particle B5-P3 again shows an absence of Ba in the SiC. Figure 4.8.6 (272, 274) shows the Ba signal to decrease significantly upon entering the SiC, and Fig. 4.8.7 (530, 531) shows the same phenomenon at a higher magnification. The strong Ba signal at the lower right in Fig. 4.8.6 is the result of angular dependence of the spectrometer that appears at low magnifications; it is not a real effect.

The behavior of palladium was different for all four particles examined and did not appear to correlate with the retention ability of the particle. In non-retentive B4-P4, Pd was observed to penetrate about 20% into the SiC and was found in a non-uniform distribution on the inside surface of the SiC which can be seen in Fig. 4.8.8 (542, 539). The upper portion of Fig. 4.8.8 is the inside of the SiC since the IPyC has fallen out. A feature of interest in this specimen is a linear decohesion commonly called a "gold spot" shown in Fig. 4.8.9 (534). Neither Pd nor any other element could be found associated with the defect even though significant effort was placed upon detecting elemental segregation at the gold spot. In non-retentive particle B5-P1, only trace concentrations of Pd could be found outside

the kernel. No segregation of the element could be found. In retentive particle B4-P1, only a weak signal for Pd could be found; no segregation was found in any layer. This behavior contrasts with that found in retentive particle B5-P3 where Pd was concentrated at the SiC/IPyC interface, Fig. 4.8.10 (521, 522). The effect is shown at higher magnification in Fig. 4.8.11 (523, 524) and in Fig. 4.8.12 (519, 520). In Fig. 4.8.12, a concentration of Pd appears to correlate with a precipitate particle as seen approximately in the center of the view on the SiC/IPyC interface. This is the only place in the present study where a concentration of a fission product could be correlated with a particle.

Cesium is of particular interest since the ratio of Cs/Ce is used to distinguish between retentive and non-retentive particles. Cesium was found in all four particles with differing behavior. In the retentive particles, Cs was not found to penetrate the SiC layer. In the non-retentive particles, Cs was found to completely penetrate the SiC layer. An example of penetration is shown in Fig. 4.8.13 (555, 556) for non-retentive particle B5-P1 in the region of a crack. The entire particle is shown in Fig. 4.8.14 (557, 559) where the Cs signal can also been seen in all layers. Where mounting material covers the SiC layer from the 1 o'clock to the 4 o'clock positions, the Cs signal is seen to be diminished, providing further evidence that a real signal is being imaged in the SiC. Particle B4-P4 exhibited similar penetration, but the Cs signal was significantly weaker, Fig. 4.8.15 (525, 526). Figures 4.8.16 (197, 198) and 4.8.17 (207, 208) show the lack of penetration in a retentive particle. Both figures show a portion of SiC and IPyC with a very abrupt change in concentration as the interface is traversed. This phenomenon is shown for the entire particle in Fig. 4.8.18 (195, 196) where a relatively high concentration of Cs was found in the IPyC. Similar behavior was observed in particle B5-P3, Fig. 4.8.19 (525, 526) where a very sharply defined change in concentration appears between the SiC and the IPyC. It could not be determined if there were an absence of Cs in the SiC, but it is believed that the signal in the SiC was mostly background noise.

Cerium behavior is somewhat confusing based upon previous results. Previous experience has shown that Ce is not likely to be released from a fuel particle. However, all four particles showed complete or partial penetration of the SiC by Ce. Since the signals in the SiC layer and the layers beyond it are very weak, the evidence of partial penetration of Ce are somewhat in doubt. Threrefore, the data may not really be inconsistent. Further work is need to clarify this issue. Figure 4.8.20 (566, 568) shows particle B5-P1 which exhibits Ce in the IPyC with a lower but nonetheless significant concentration in the SiC layer. The proximity of an L-β Ba peak in the region of the Ce L-α peak used for the analysis raises the

question of an interference; however, the Ce signal is stronger than the L-α Ba signal obtained from the same specimen. This supports the view that the image in Fig. 4.8.20 is in fact that of Ce. Figure 4.8.21 (559, 561) shows Ce to be present in all layers of particle B5-P1 with a very strong signal coming from the kernel, as expected. Cerium is shown in Fig. 4.8.22 (529, 530) for particle B5-P3 where a higher concentration of Ce is seen in the IPyC than in the SiC. A non-uniform distribution of Ce also appears on the inside surface of the IPyC in the same figure. Particle B4-P4 shows the presence of Ce on the inside surface of the SiC layer and about 5 μm penetration into the SiC, Fig. 4.8.23 (542, 545). It might also be concluded from the segregation of Ce on the inner surface of the SiC that the SiC is providing an impediment to diffusion of Ce. Low magnification views shown in Fig. 4.8.24 (572, 573, 574, 575) offer a comparison between fission products in specimen B5-P3.

The particles were examined for other fission products such as Sr, La, I, and Ag. Most scans were inconclusive because of the low concentrations of these elements encountered. Particle B5-P3 had Ag which appeared to be associated with Pd. In fact, the second phase particle that was found rich in Pd was also rich in Ag. This is not surprising because of the complete miscibility of these alloys. The Ag scan is shown in Fig. 4.8.25 (538, 539).

4.8.4 Fracture of the SiC layer

As described in 4.8.1, various layers fell out during the polishing process. In other cases, the layers remained, but cracks were initiated. An effort was made to examine the cracks, not only in terms of segregation of fission products but in terms of crack morphology. The seal coat of the OPyC of specimen B4-P4, a non-retentive particle, was examined to locate cracks and imperfections. Figure 4.8.26 (549) shows what appears to be a small pore or a crack in the seal coat. No fission products were found concentrated at this imperfection, and no evidence of corrosion was found near the imperfection. It may also be observed that the crack or imperfection does not propagate into surrounding material.

Compact B4 had some SiC shards remaining after its decompaction. The fracture surfaces of a few of these shards were examined by SEM. One such shard positioned with its inner surface upward is shown in Fig. 4.8.27 (554). Higher magnification views appear if Fig. 4.8.28 (551, 552, 553). The columnar nature of the grains appears in this fractograph. The mechanism of the fracture appears to be nearly entirely transgranular cleavage, perhaps with very small areas of intergranular separation. No fission products could be found to

concentrate on the fracture surface, and the initiation site of the fracture could not be determined. As with the mounted particles, the shards may have fractured in the handling process following irradiation. Further work is needed on analysis of crack tips and fracture surfaces to attempt to determine the mechanism of crack initiation.

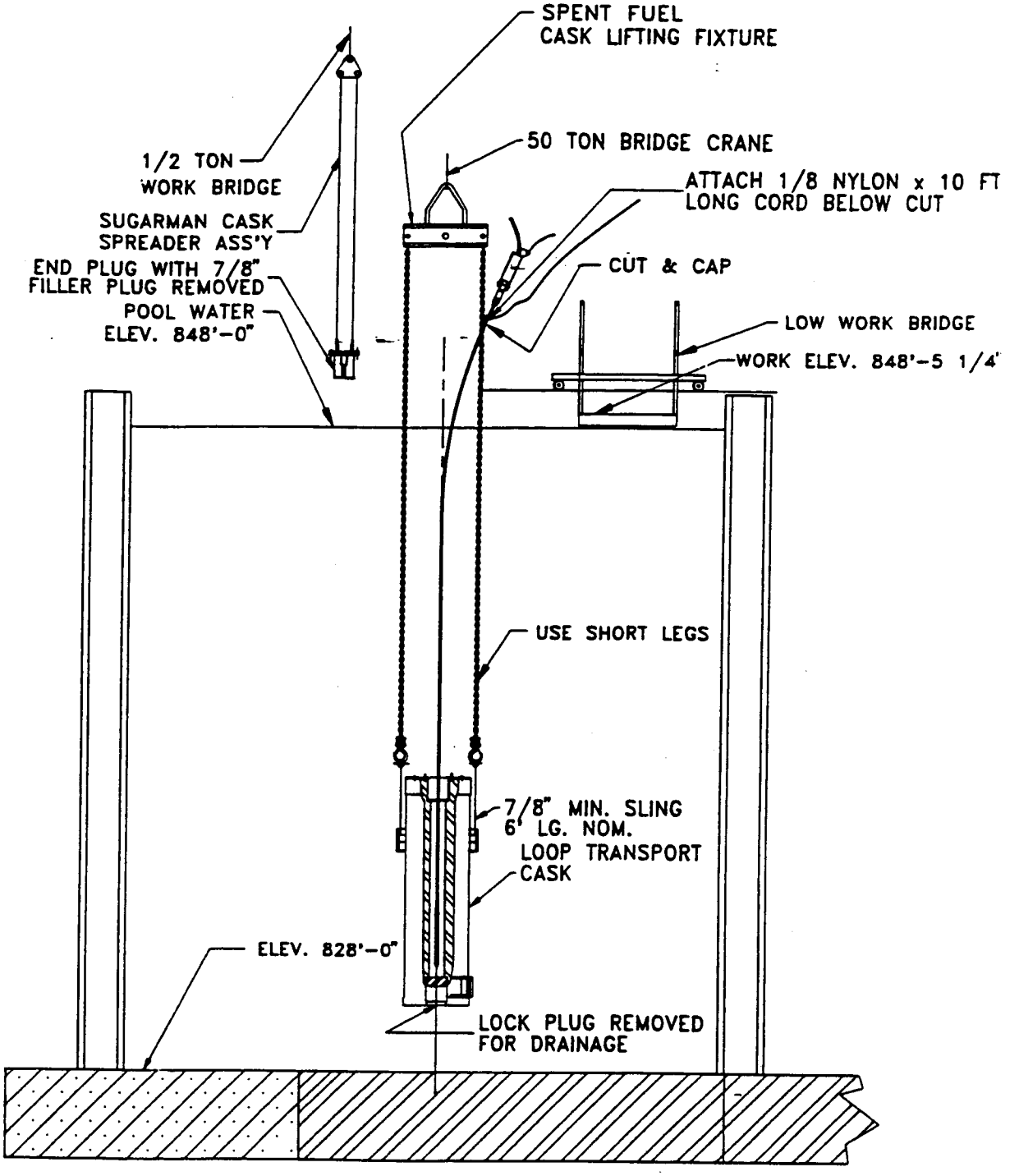

Figure 4.1.1.1 Instrumented capsule, First cut of leads (one capsule)

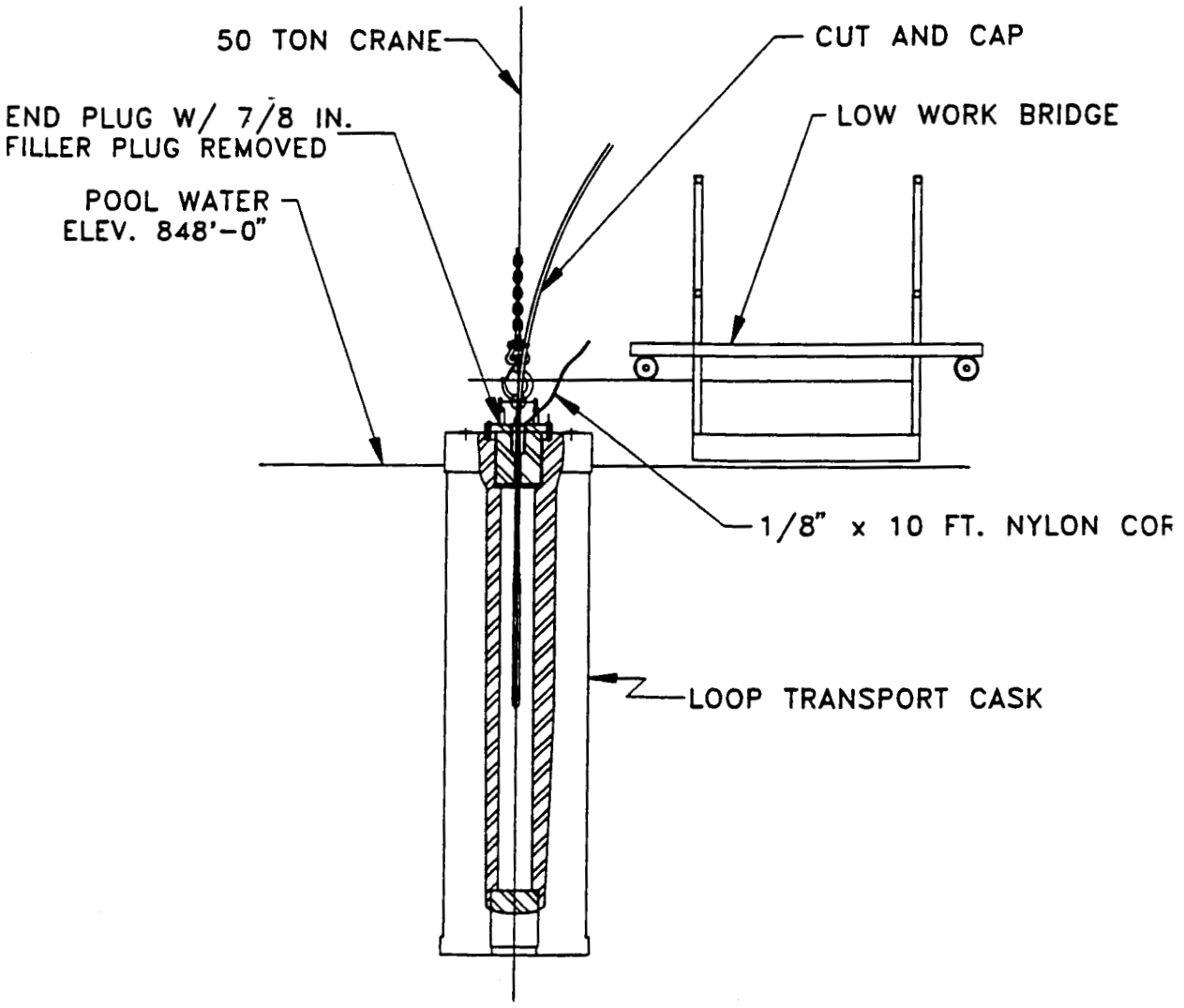

Figure 4.1.1.2 Instrumented capsule, Second cut of leads (one capsule)

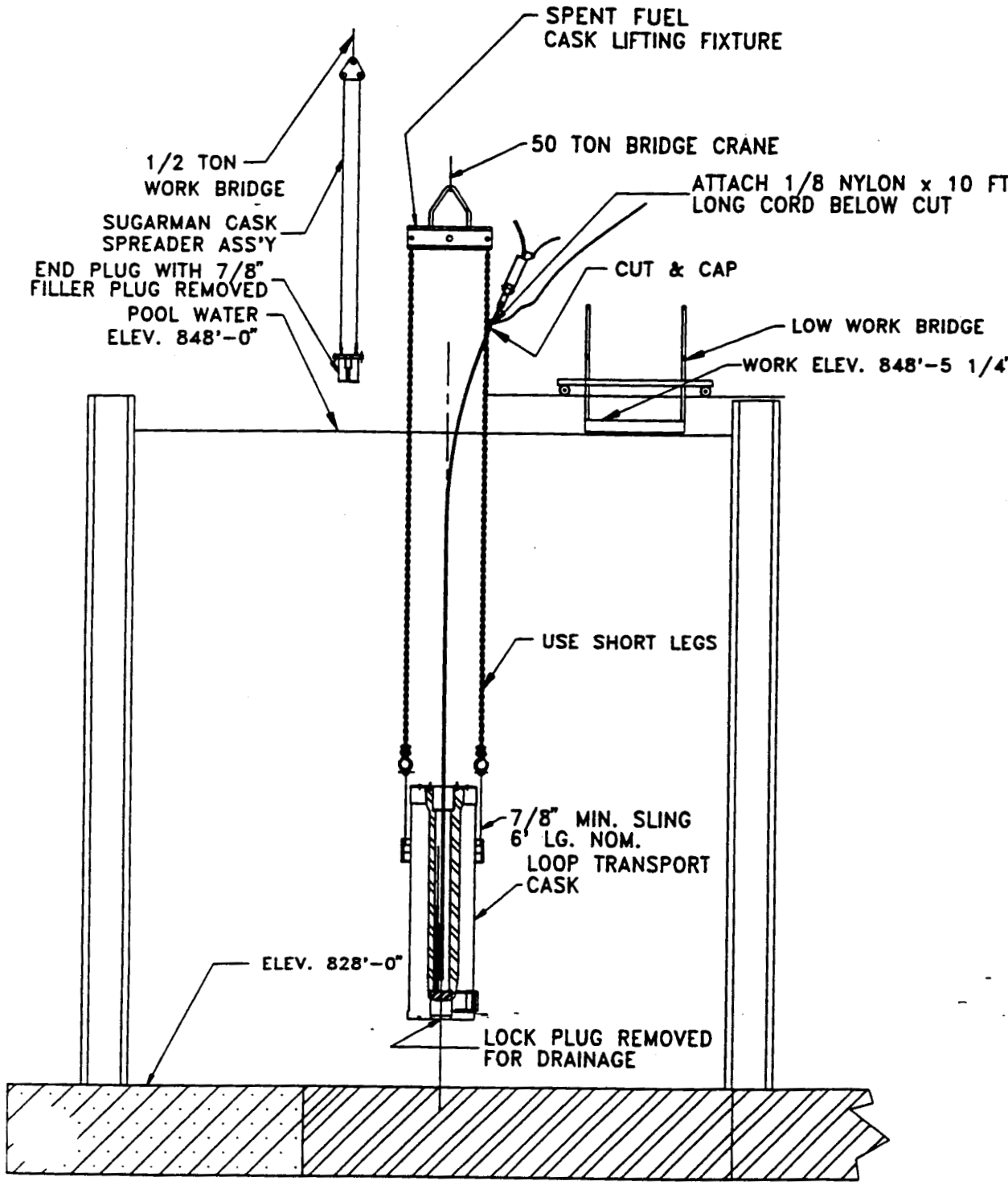

Figure 4.1.1.3 Instrumented capsule, First cut of leads (second capsule)

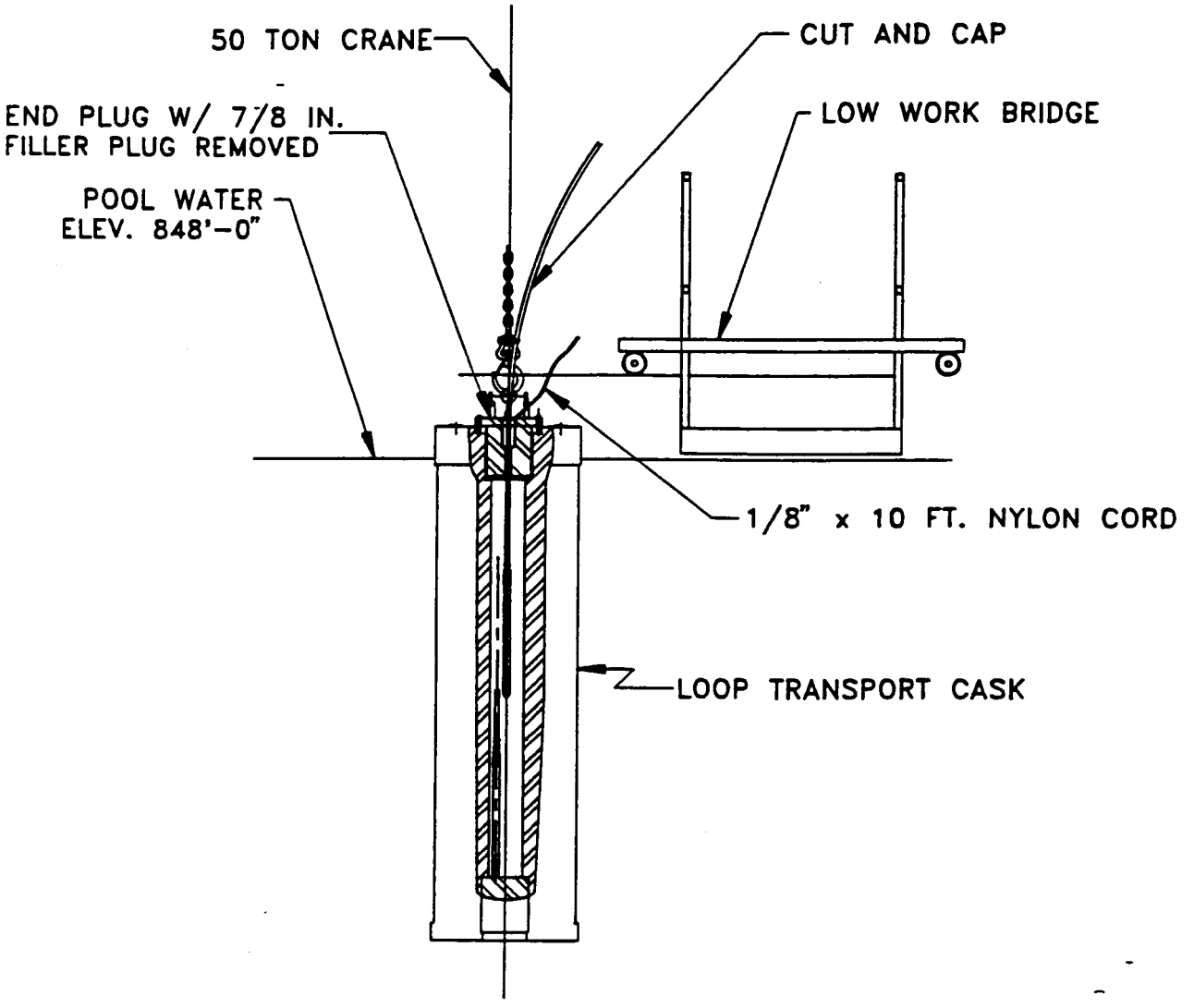

Figure 4.1.1.4 Instrumented capsule, Second cut of leads (Second capsule)

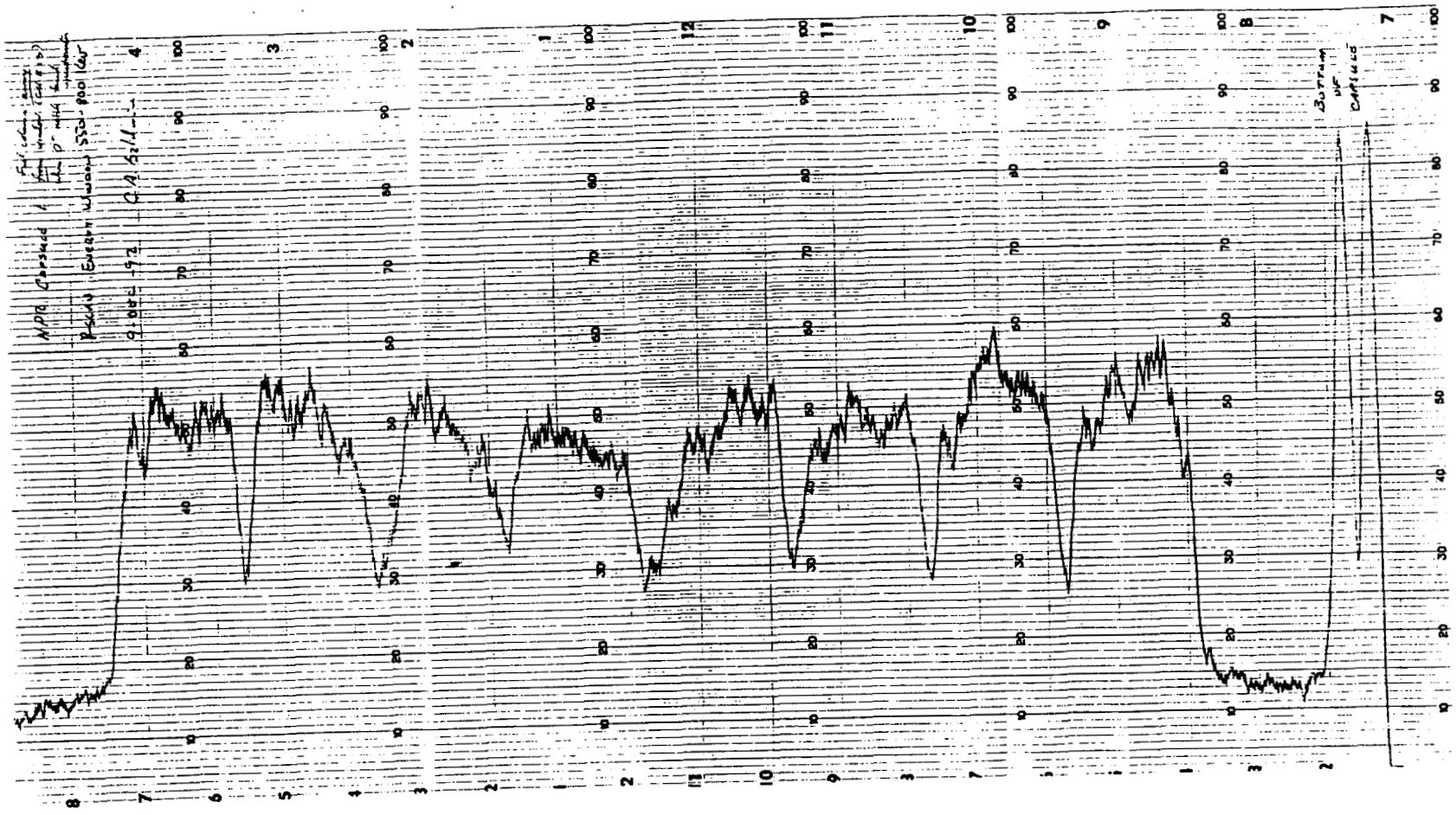

Figure 4.1.3.1 Gamma scan of fuel column "B" of capsule NPR 1 prior to opening, with compact positions (reading L to R) of 1 to 8

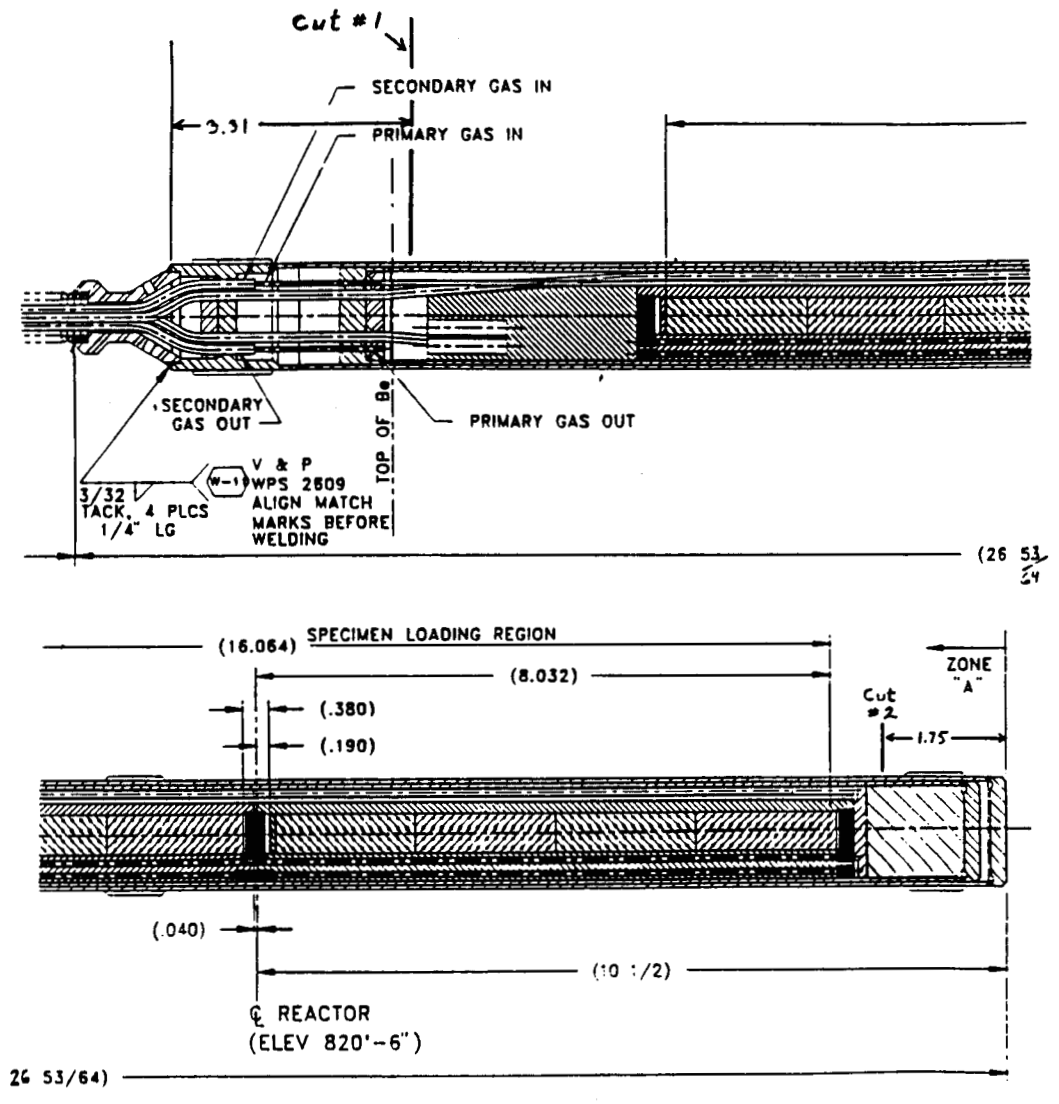

Figure 4.1.4.1 Section views of NPR 1 or NPR 2 capsule (dimensions in inches)

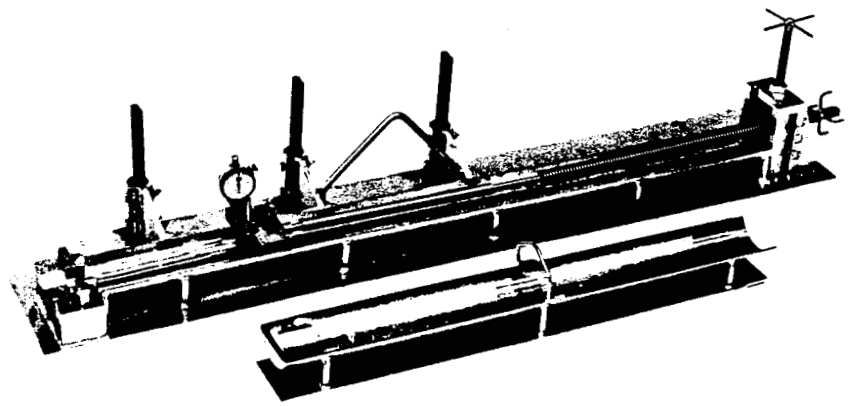

Figure 4.1.4.2 Pushout fixture, including (detached) receiving tray in foreground and installed force gage R-80186

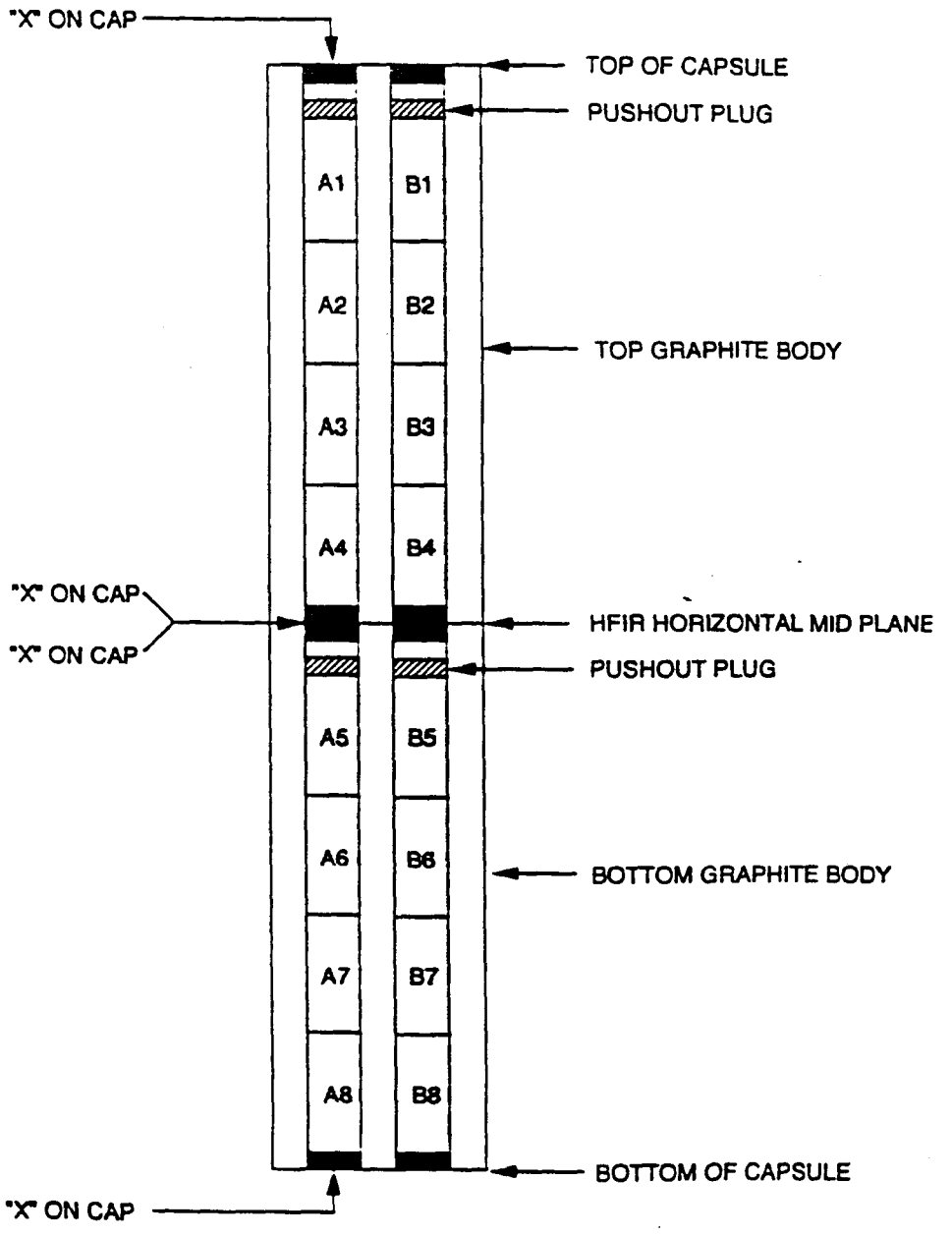

Figure 4.1.6.1 Placement of fuel compacts withinh capsules NPR 1 and NPR 2

Figure 4.2.1.1a Upper insulator from NPR 1 R-08642

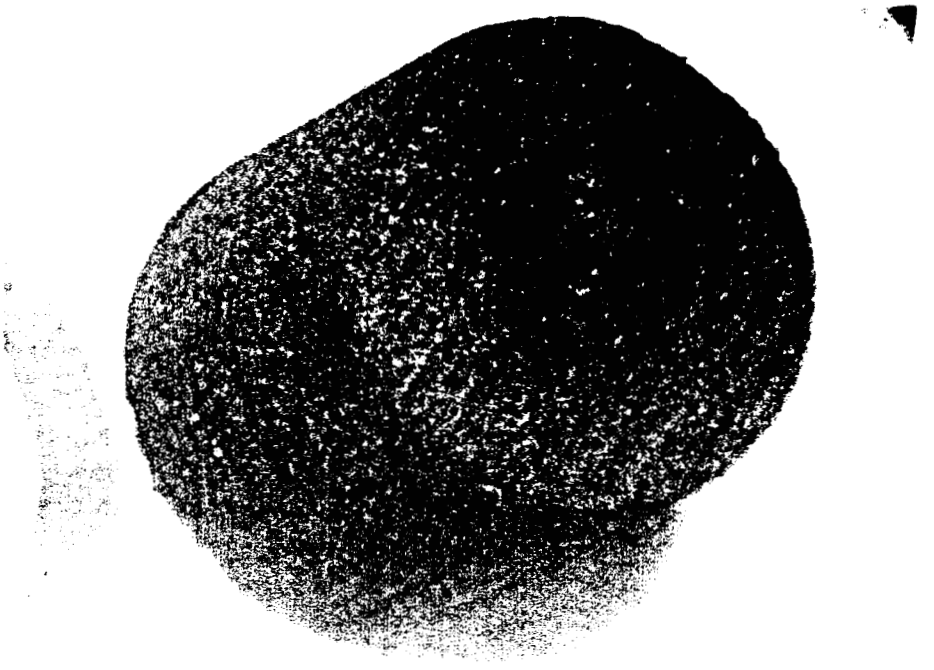

Figure 4.2.1.1b Lower insulator from NPR 1 R-08713

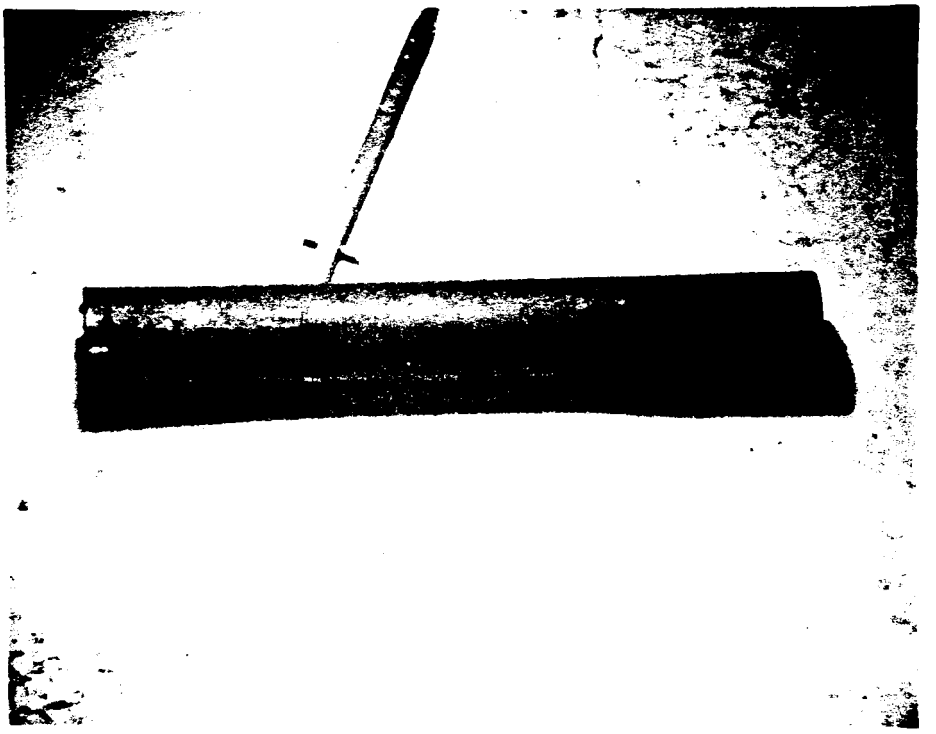

Figure 4.2.1.2a Upper graphite body (GB-U) of NPR 1, side. R-80708

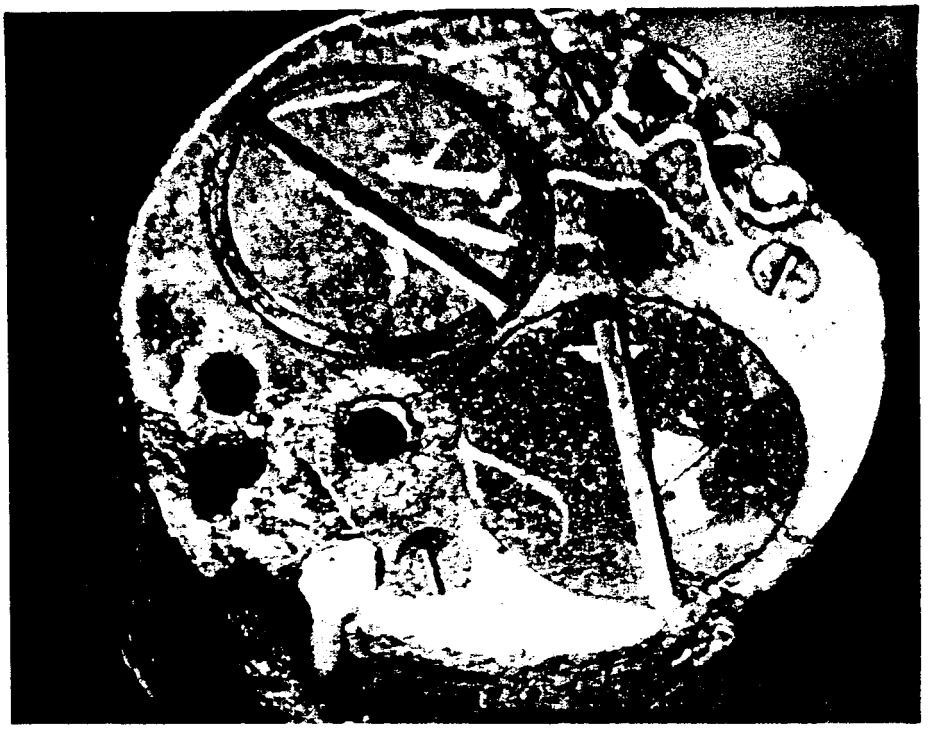

Figure 4.2.1.2b GB-U of NPR 1, upper end R-80710

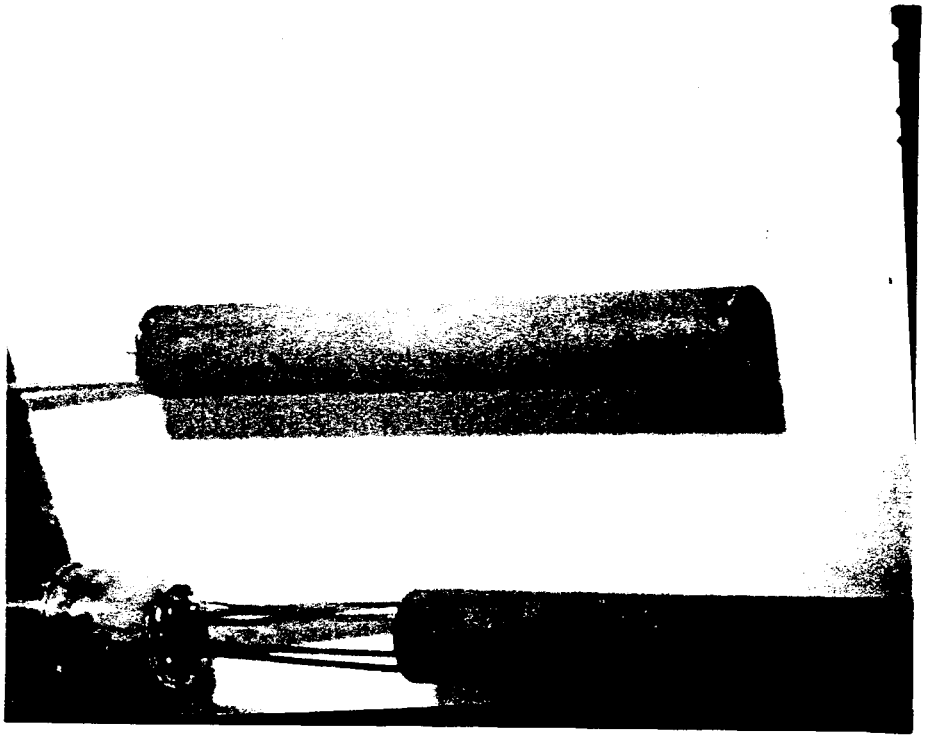

Figure 4.2.1.3a Lower Graphite body (GB-L) of NPR 1 side R-08614

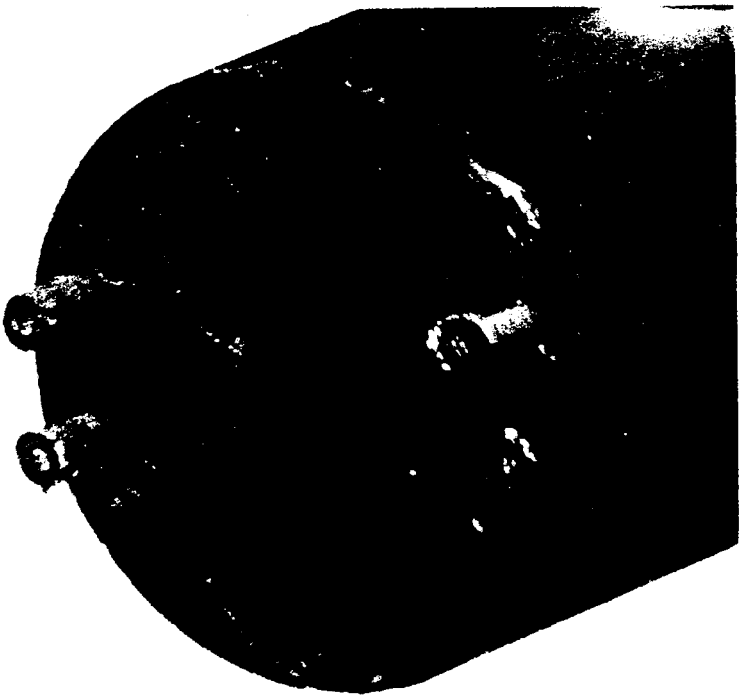

Figure 4.2.1.3b GB-L of NPR 1, upper end R-80610

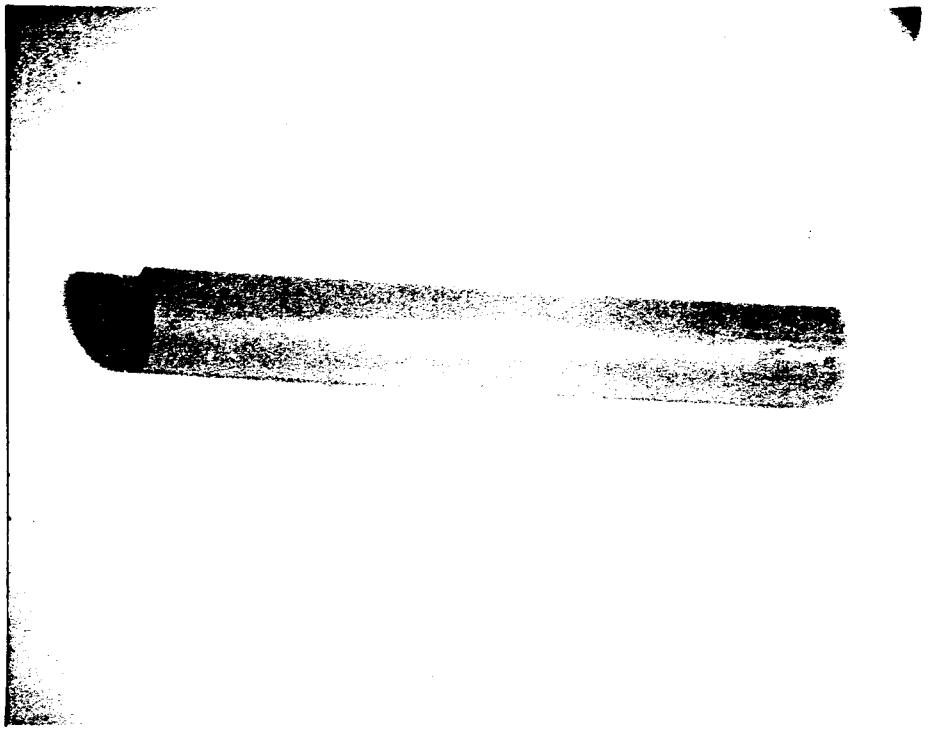

Figure 4.2.1.4a GB-U of NPR 2 side view R-80753

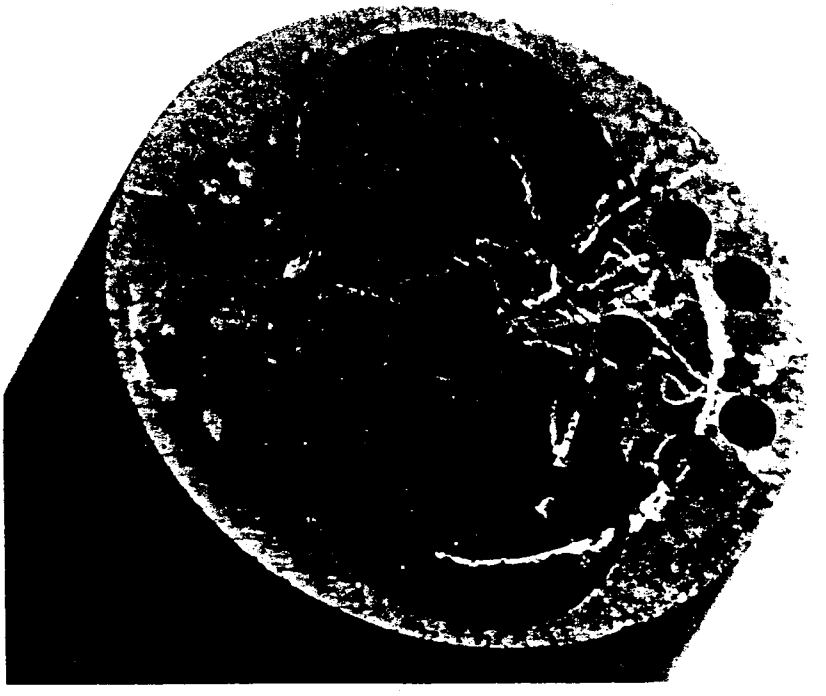

Figure 4.2.1.4b GB-U of NPR 2 lower end R-80754

Figure 4.2.1.5a GB-L of NPR 2, side view R-80615

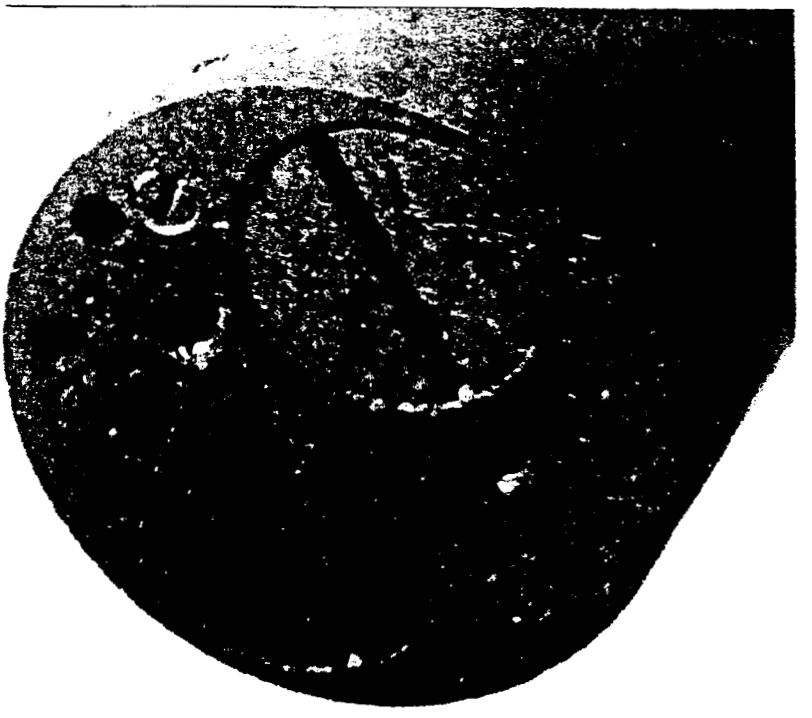

Figure 4.2.1.5b GB-L of NPR 2, lower end R-80609

Figure 4.2.1.6 Flux monitor tubes of NPR 2 R-80685

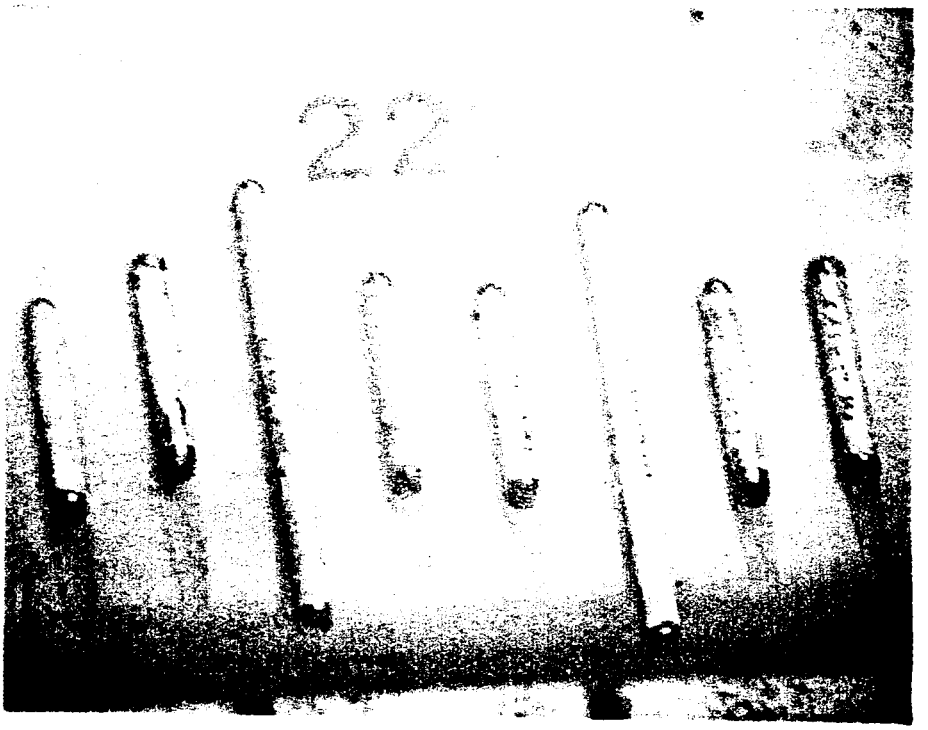

Figure 4.2.1.7 Piggyback specimens recovered from NPR 2, GB 2, Hole 2 ("222") R-80831

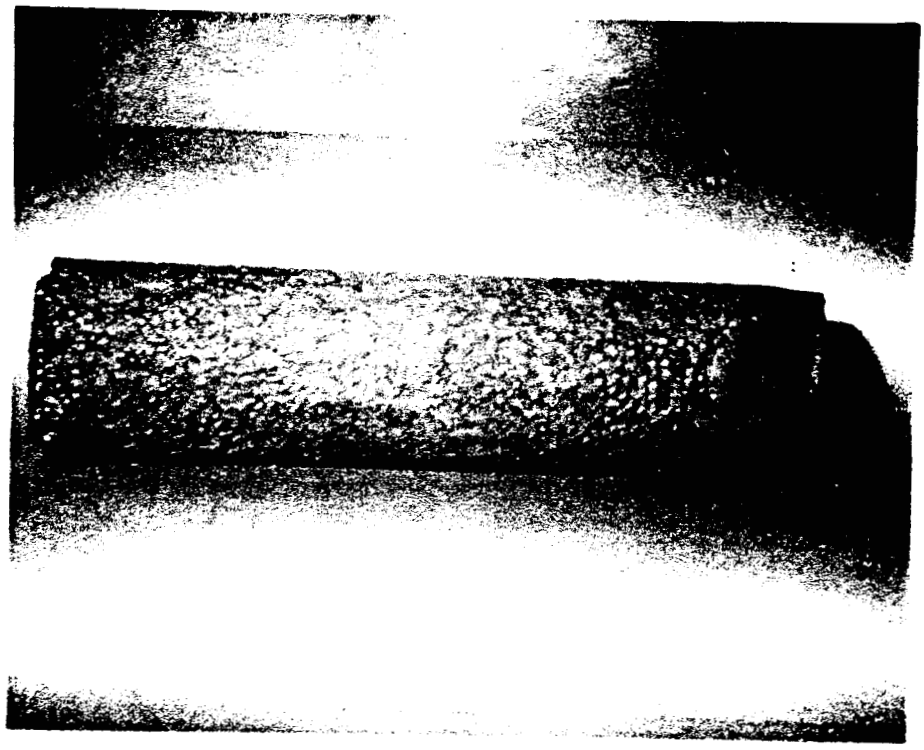

Figure 4.2.3.1a Fuel compact NPR 1 A1, side view R-80758

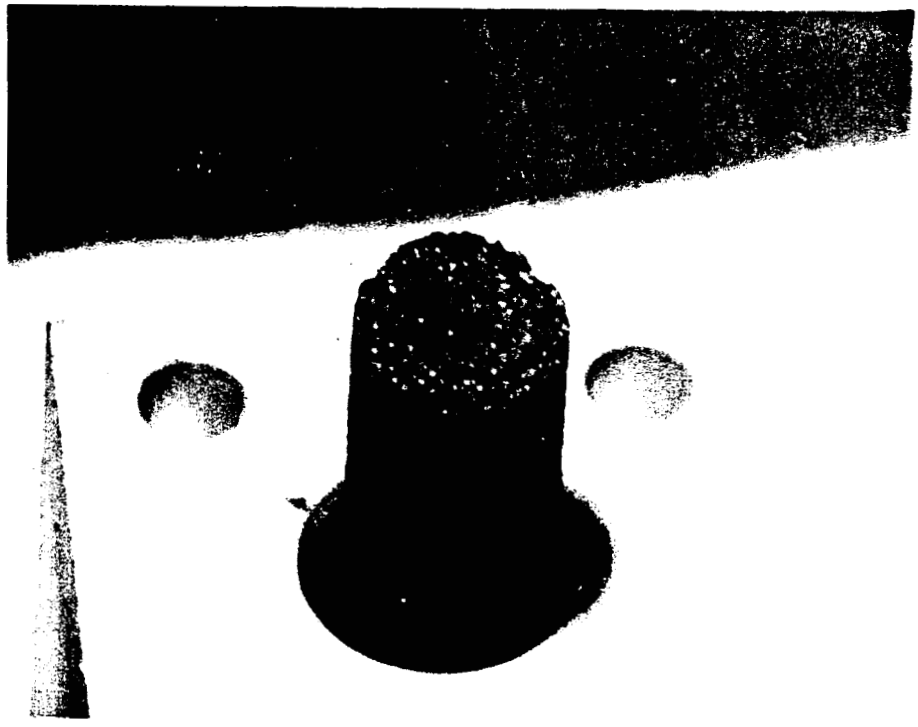

Figure 4.2.3.1b Compact NPR 1 A1, bottom end R-80760

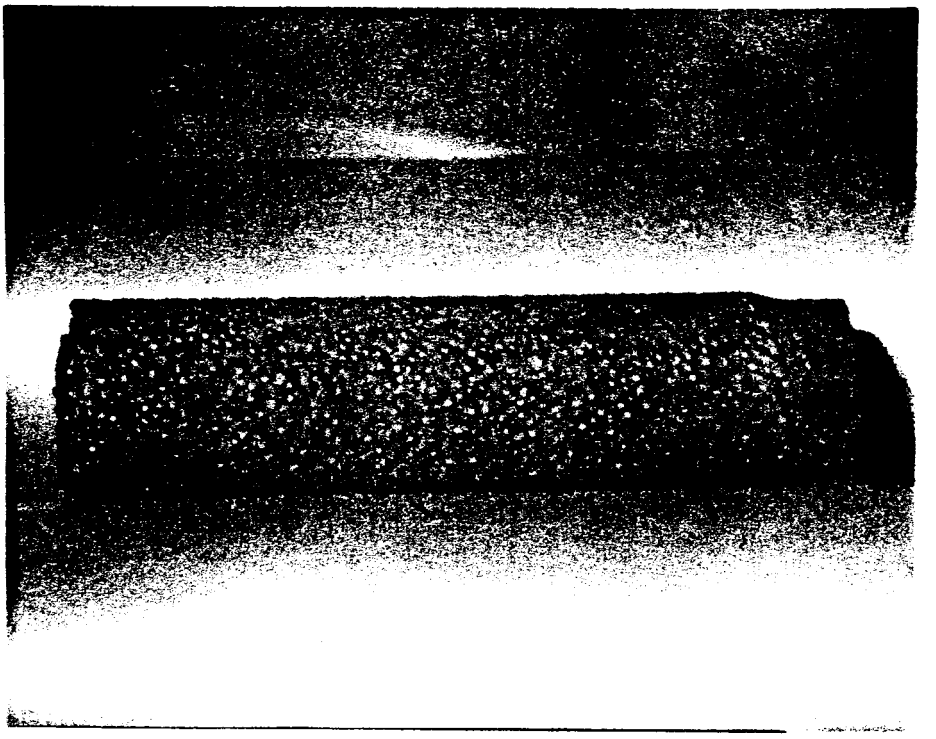

Figure 4.2.3.2a Fuel compact NPR 1 A2, side view R-80780

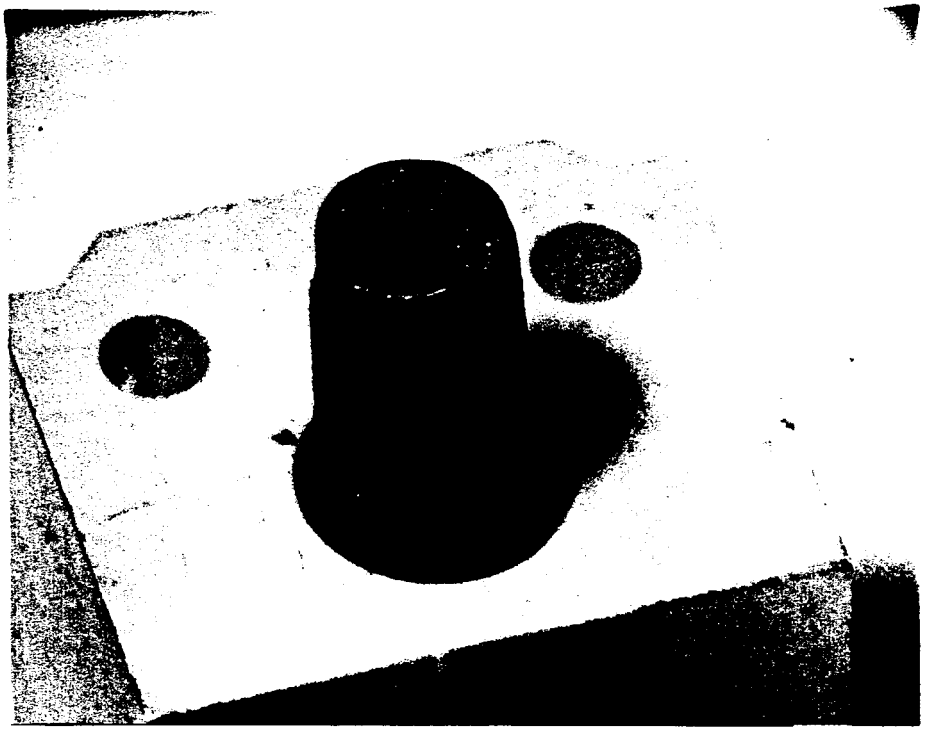

Figure 4.2.3.2b Compact NPR 1 A2, upper end R-80779

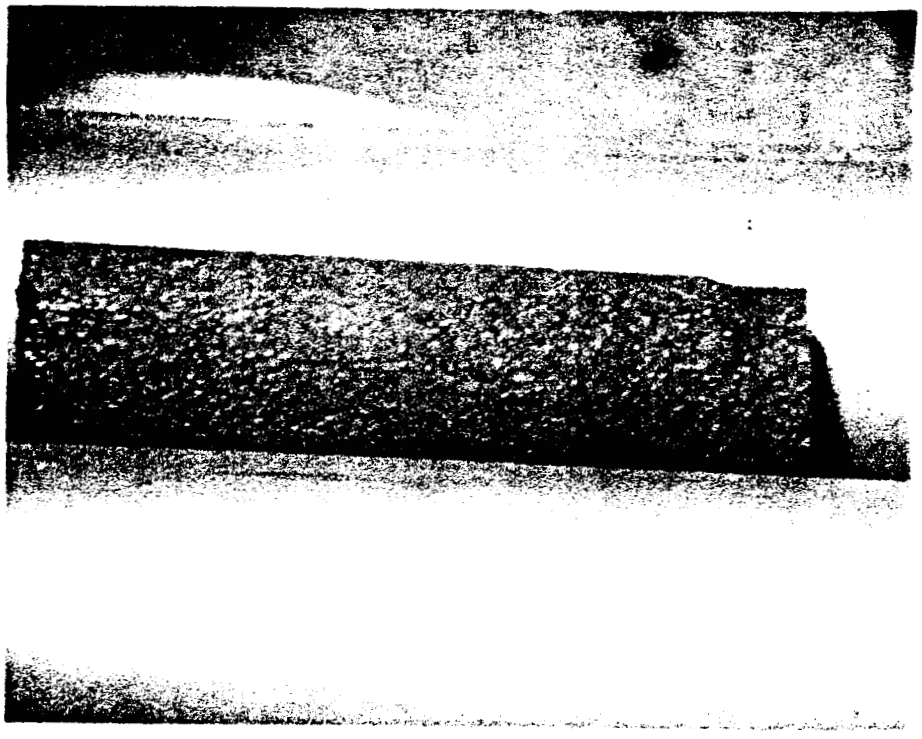

Figure 4.2.3.3a Fuel compact NPR 1 B3, side view R-80785

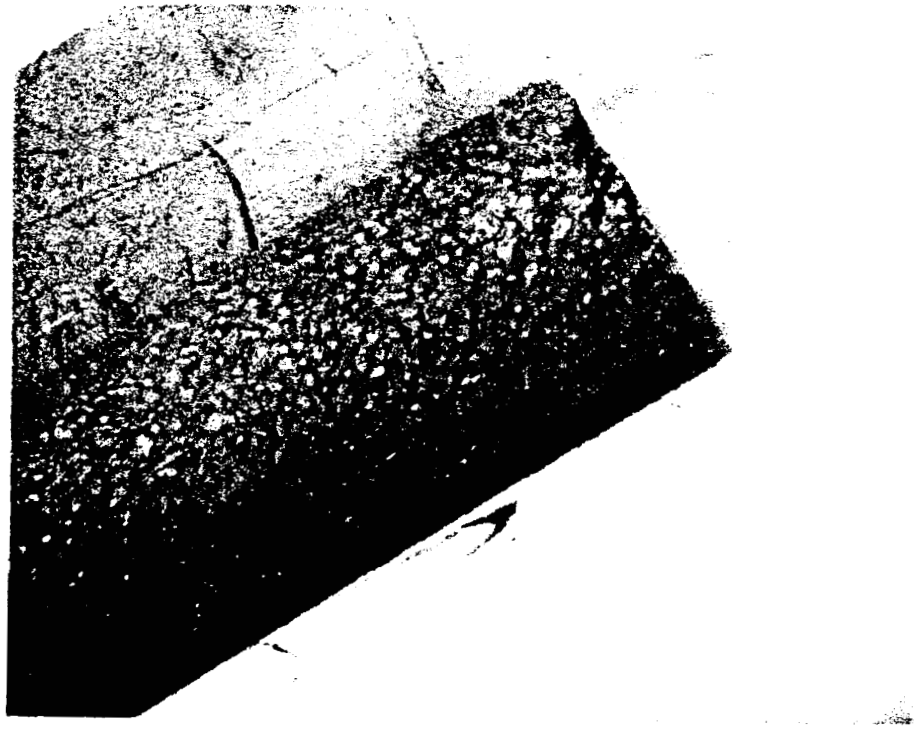

Figure 4.2.3.3b Compact NPR 1 B3, side surface cracking R-90787

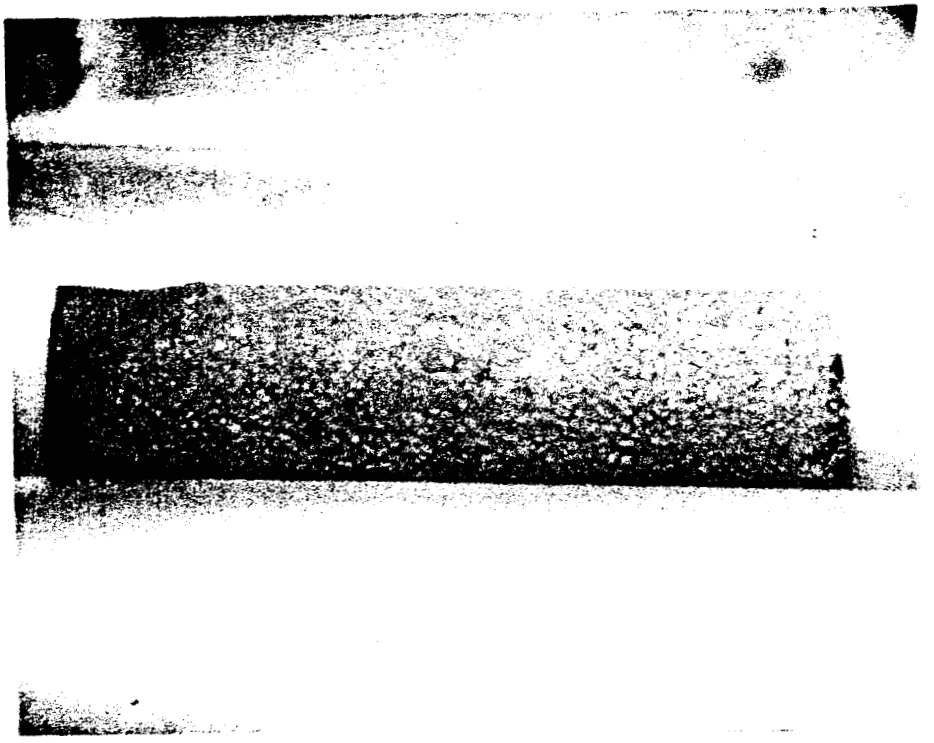

Figure 4.2.3.4a NPR 1 B4, side view at 0° R-80782

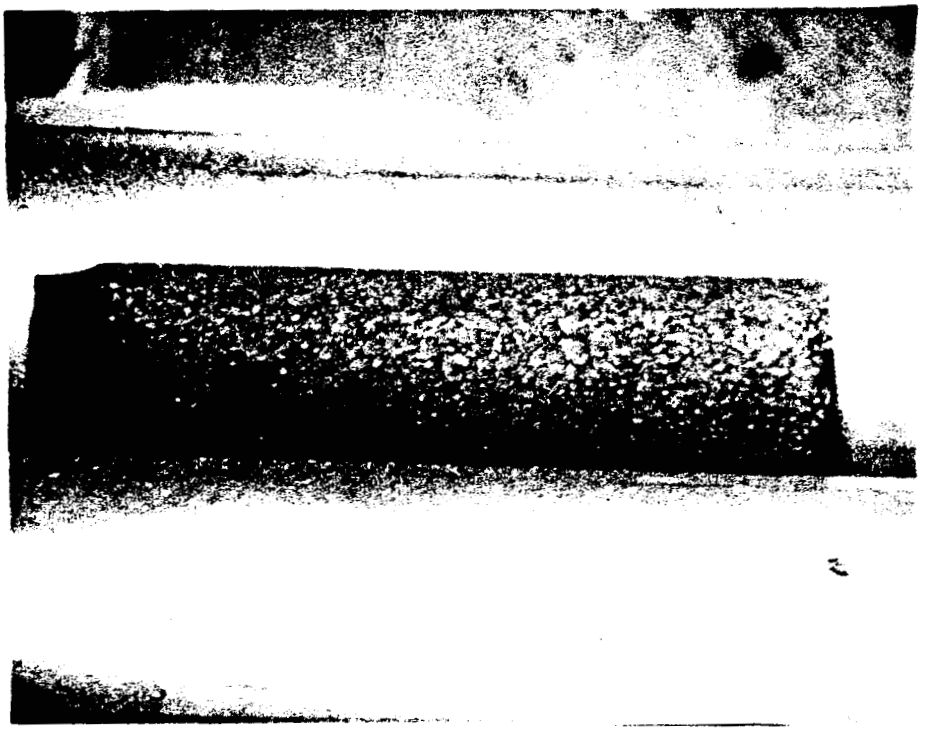

Figure 4.2.3.4b Compact NPR 1 B4, side view at 180° R-80790

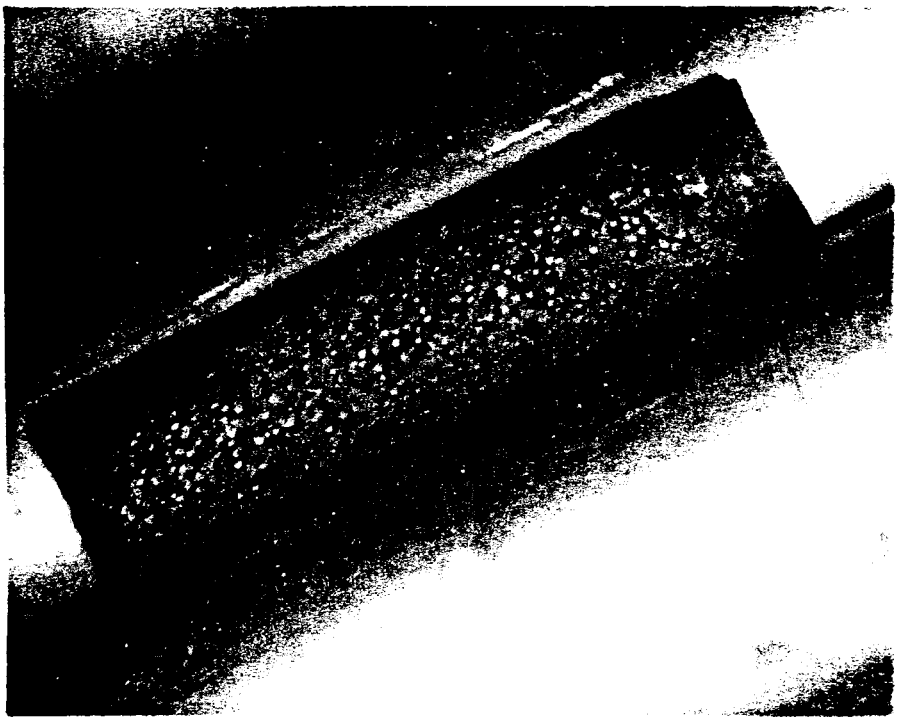

Figure 4.2.3.5a Fuel compact NPR 2 B5, side view R-81117

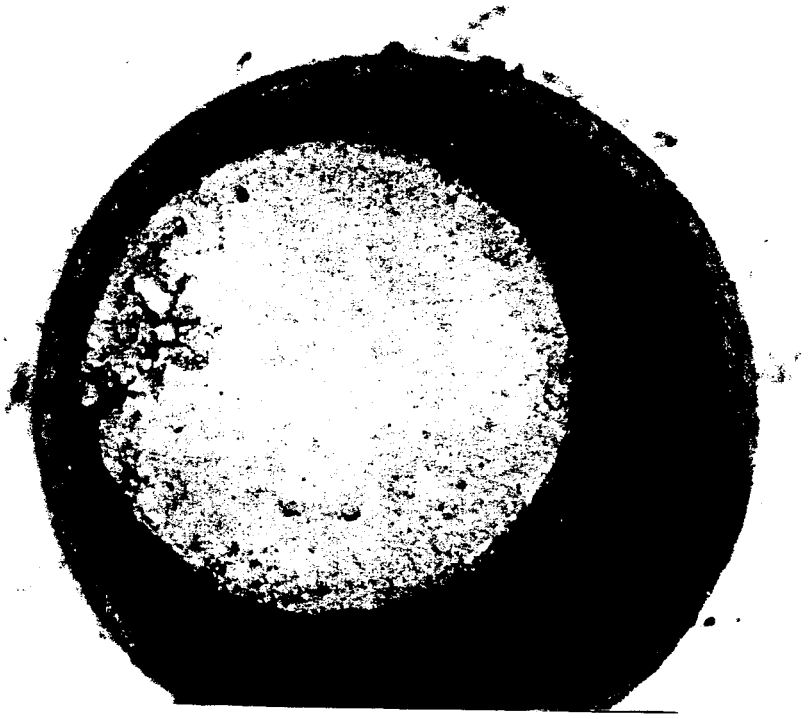

Figure 4.2.3.5b Compact NPR 2 B5, lower end R-81132

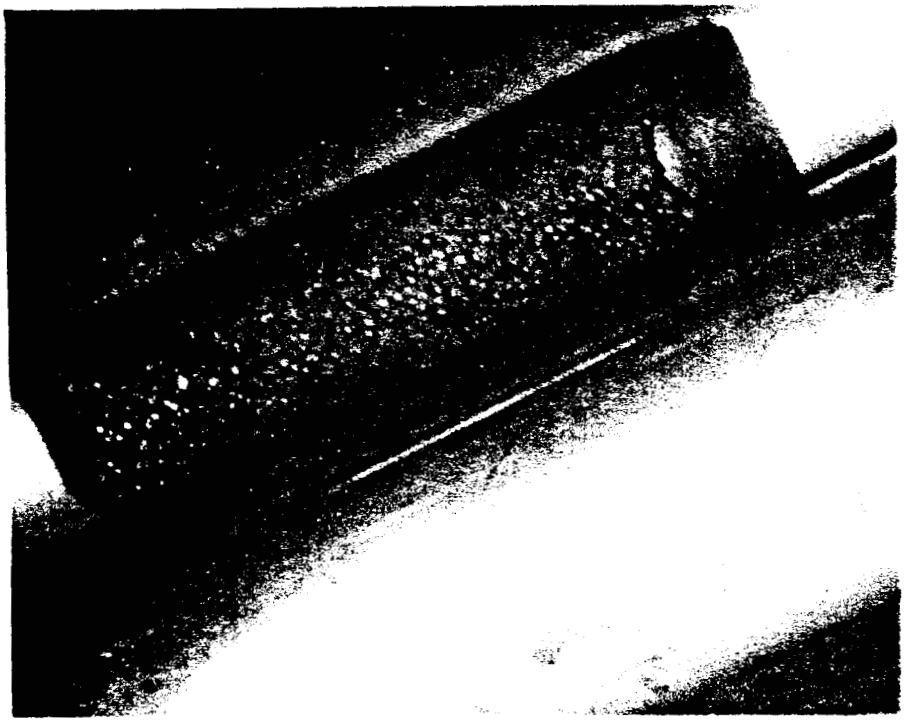

Figure 4.2.3.6a Fuel compact NPR 2 A6, side view R-81110

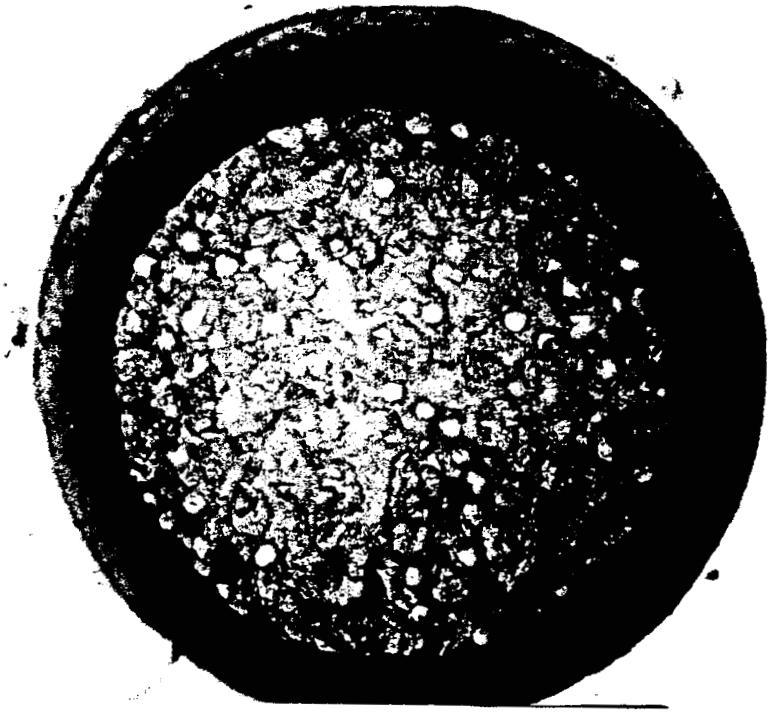

Figure 4.2.3.6b Compact NPR 2 A6, upper end R-81143

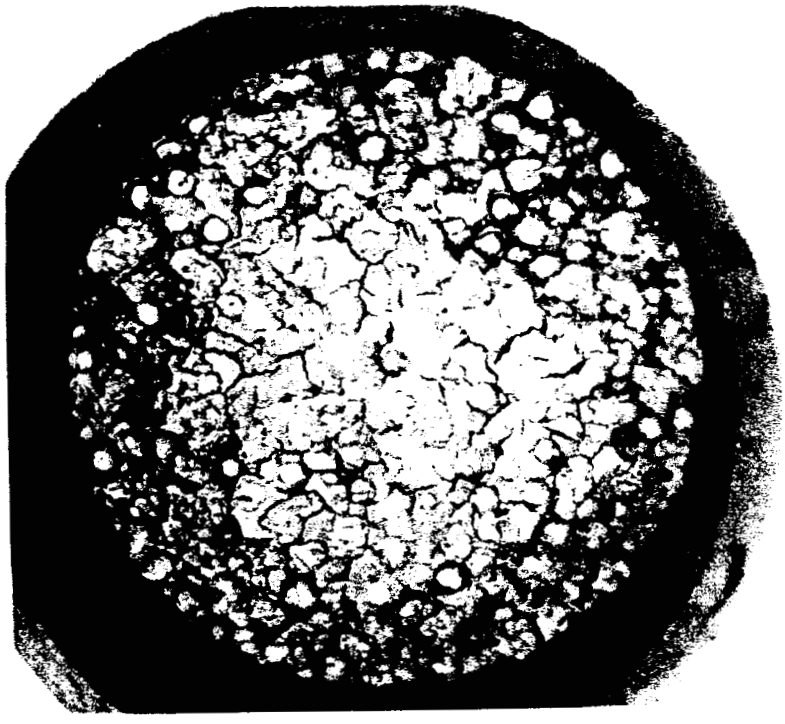

Figure 4.2.3.7a Fuel compact NPR 1 B7, upper end R-81074

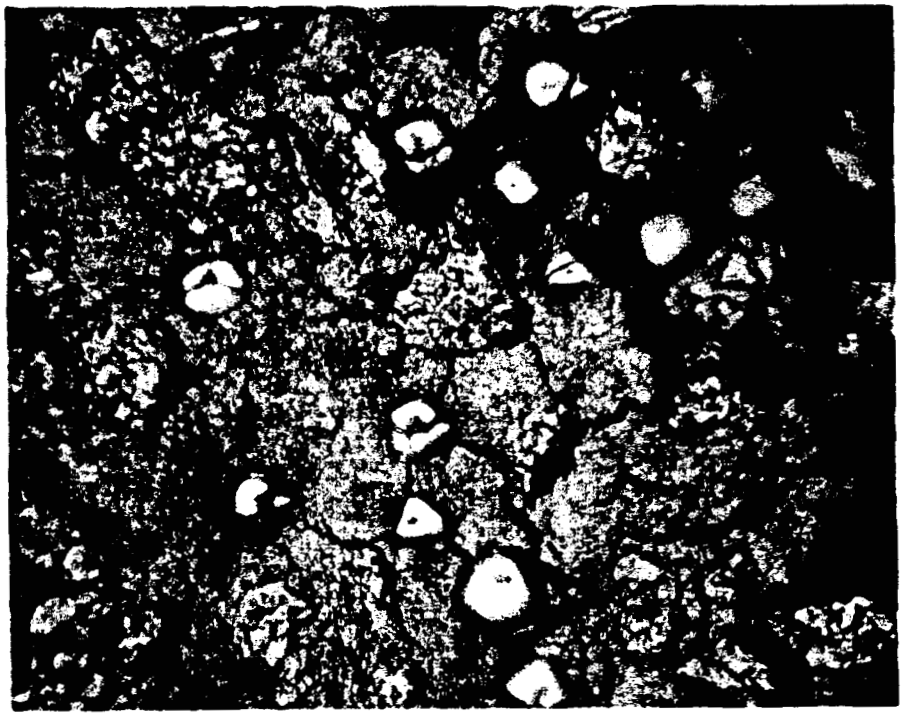

Figure 4.2.3.7b Compact NPR 1 B7, upper end (detail view) R-81073

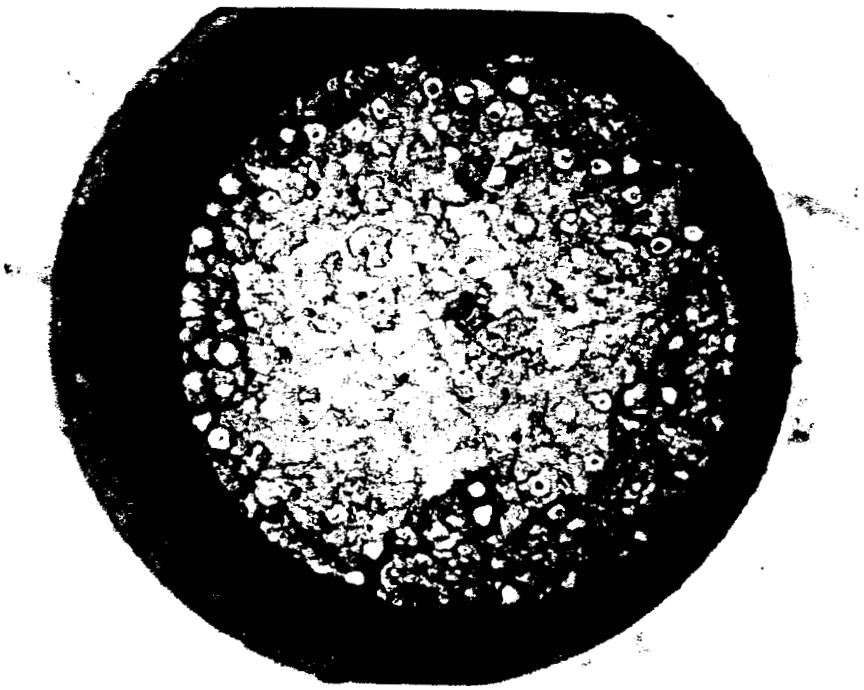

Figure 4.2.3.8a Fuel compact NPR 2 A8, upper end R-81101

Figure 4.2.3.8b Compact NPR 2 A8, upper end (detail view) R-81145

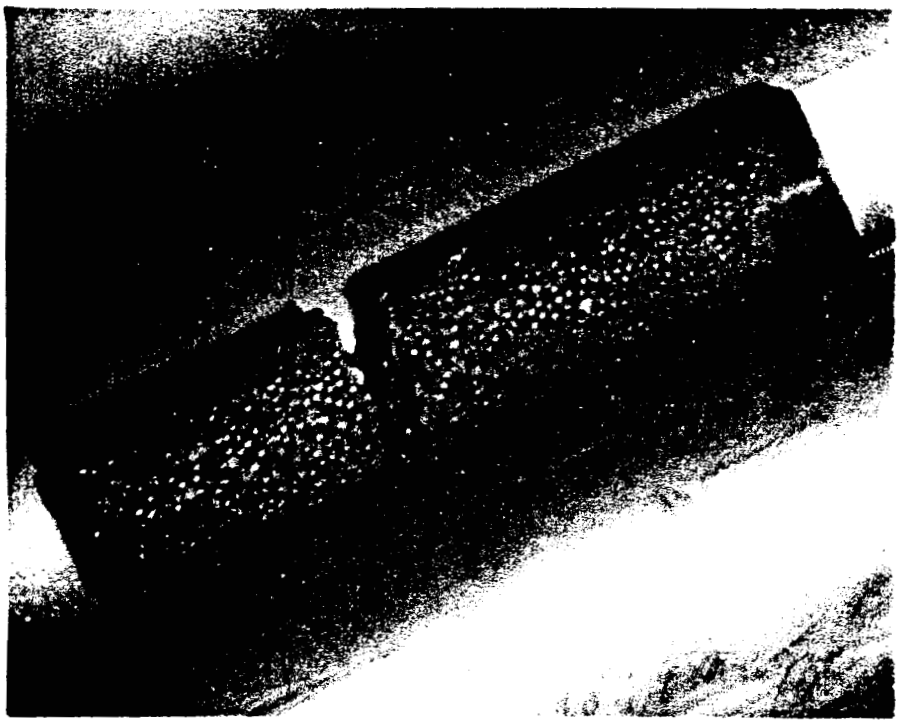

Figure 4.2.3.9a Fuel compact NPR 1 A8, side view R-80189

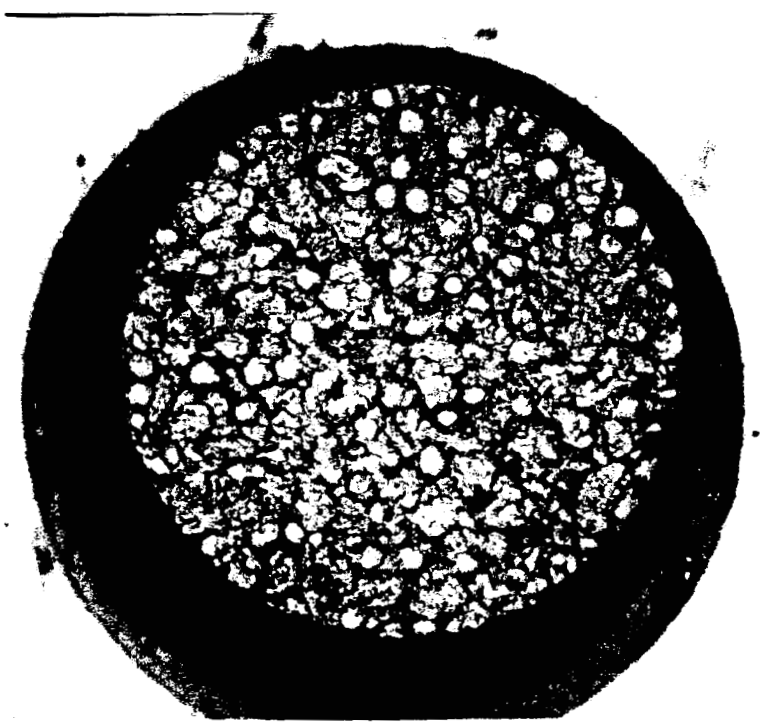

Figure 4.2.3.9b Compact NPR 1 A8, fracture surface of large segment R-81125

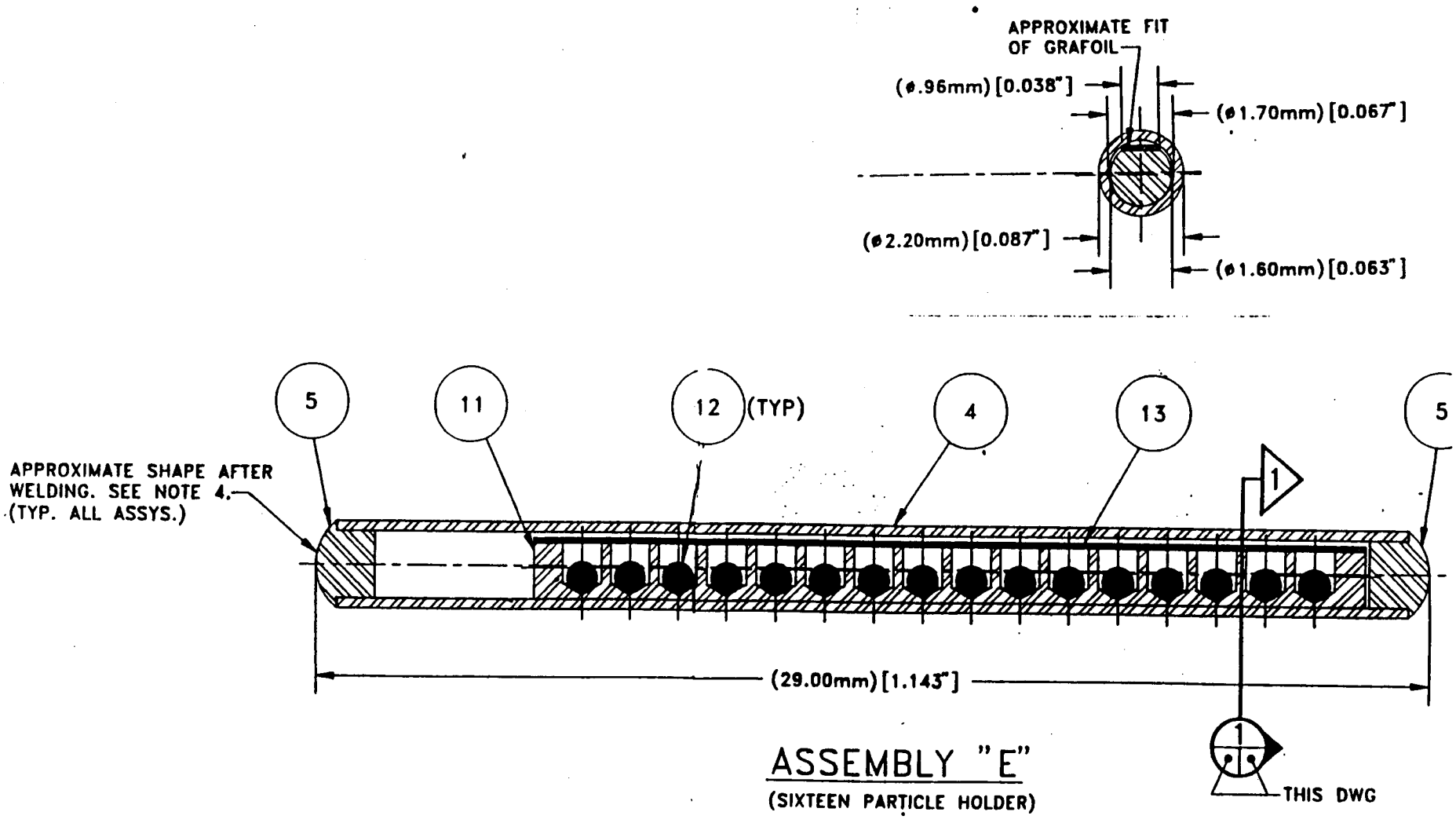

Figure 4.2.4.1 Unbonded fuel particle (piggyback specimen) holder used in NPR 1 and NPR 2

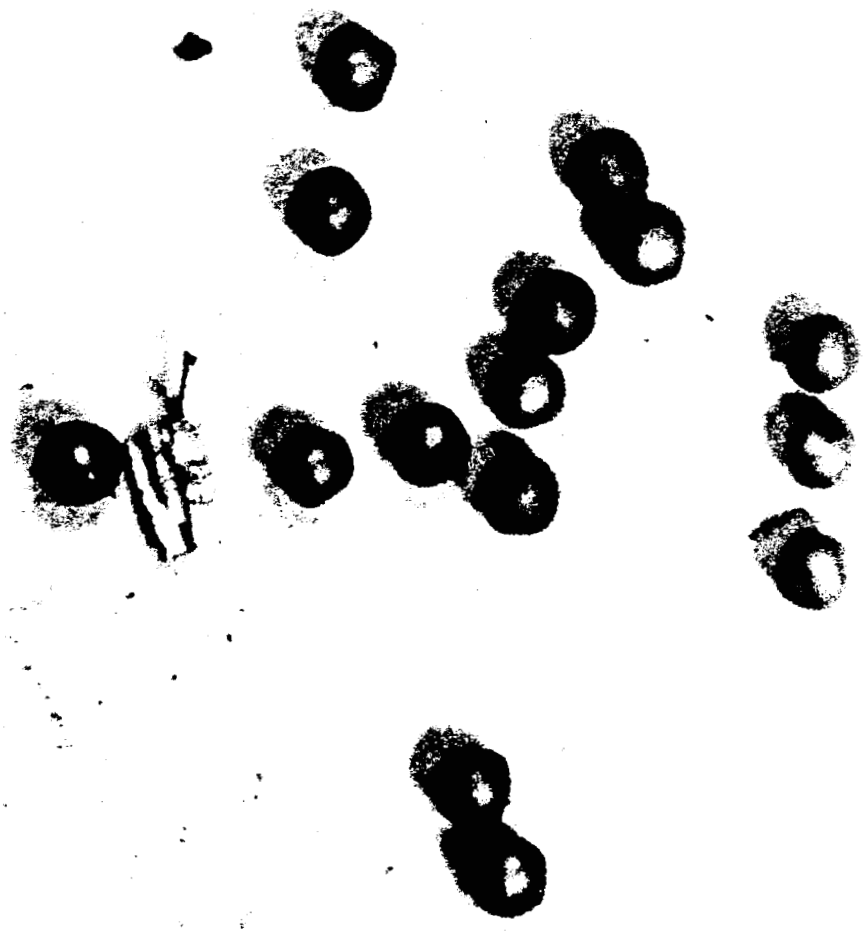

R80950

Figure 4.2.4.2 Irradiated unbonded HEU UCO TRISO particles from capsule NPR 1, piggyback sample 11GA

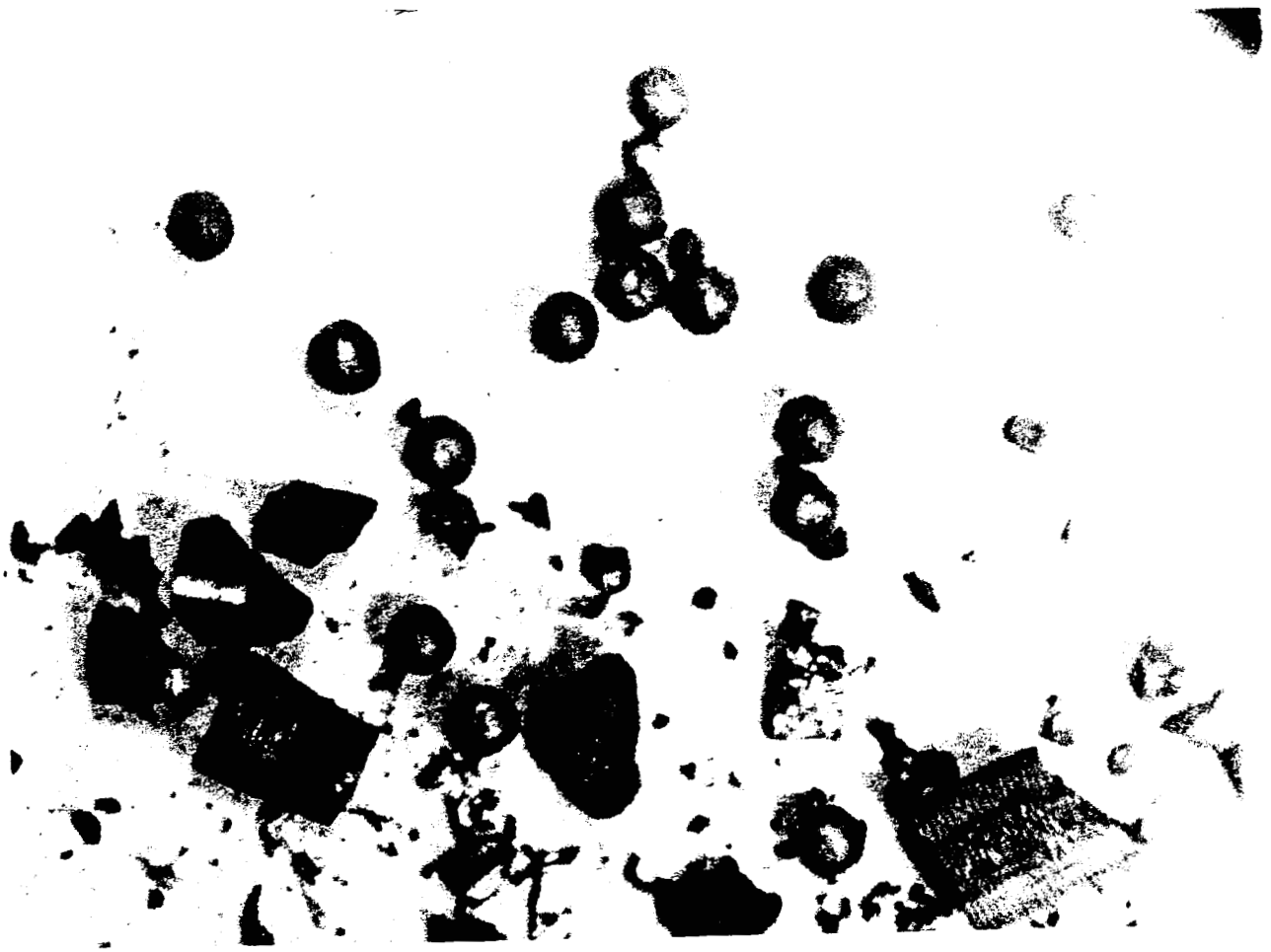

R80949

Figure 4.2.4.3 Irradiated unbonded HEU UCO TRISO particles from capsule NPR 1, piggyback sample 11GB

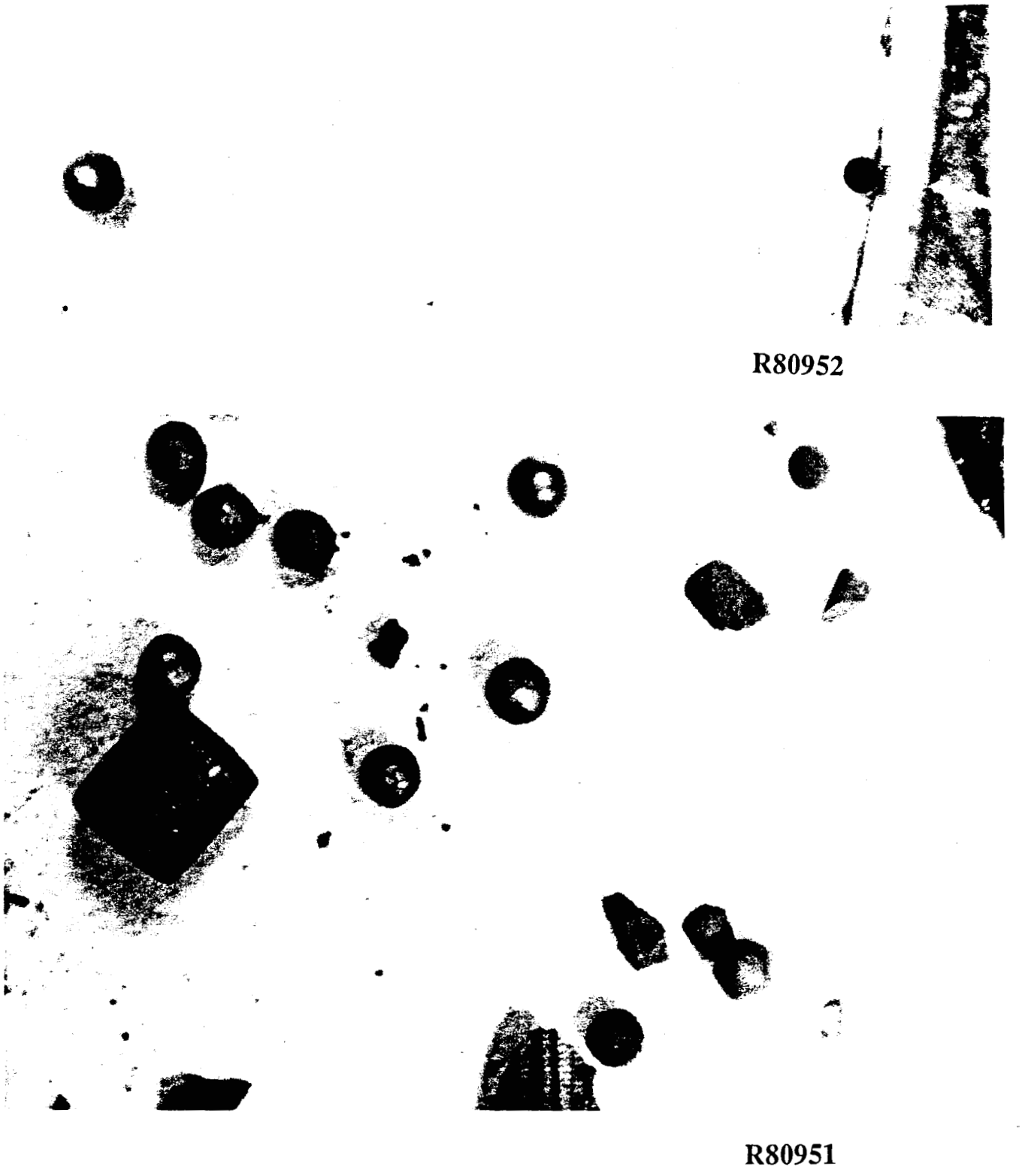

Figure 4.2.4.4 Irradiated unbonded HEU UCO TRISO particles from capsule NPR 1, piggyback sample 11UB

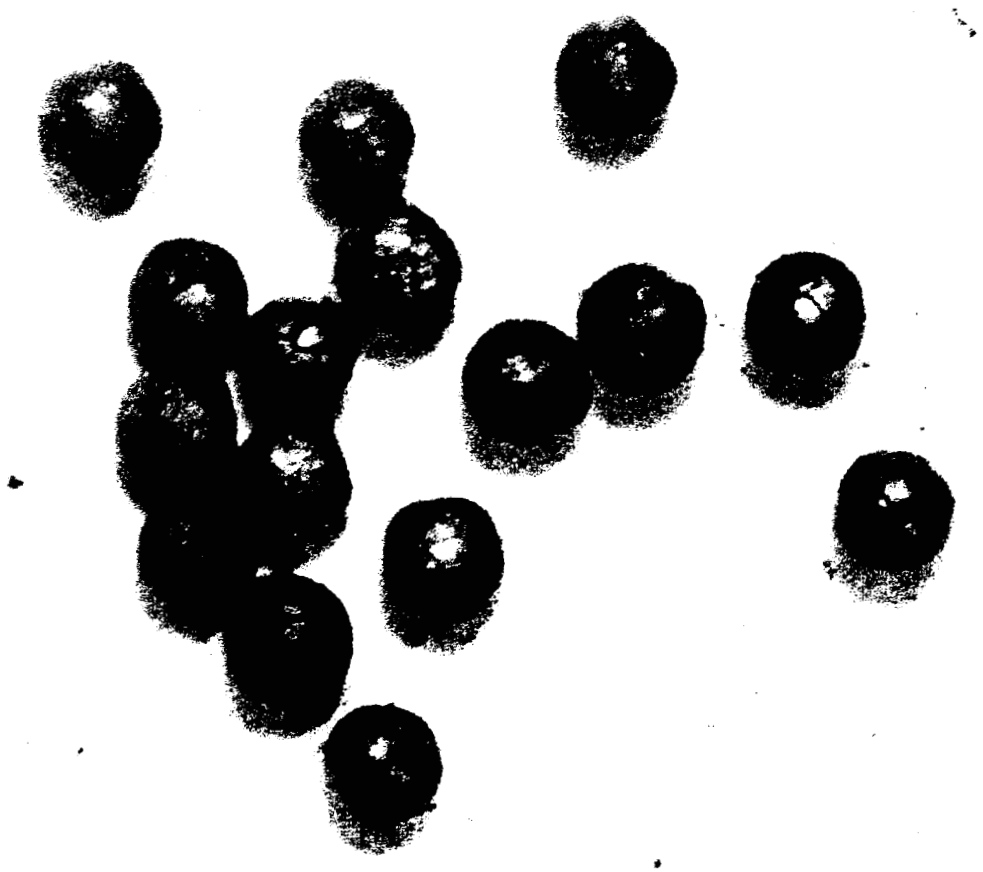

R80954

Figure 4.2.4.5 Irradiated unbonded HEU UCO TRISO particles from capsule NPR 1, piggyback sample 11UB*

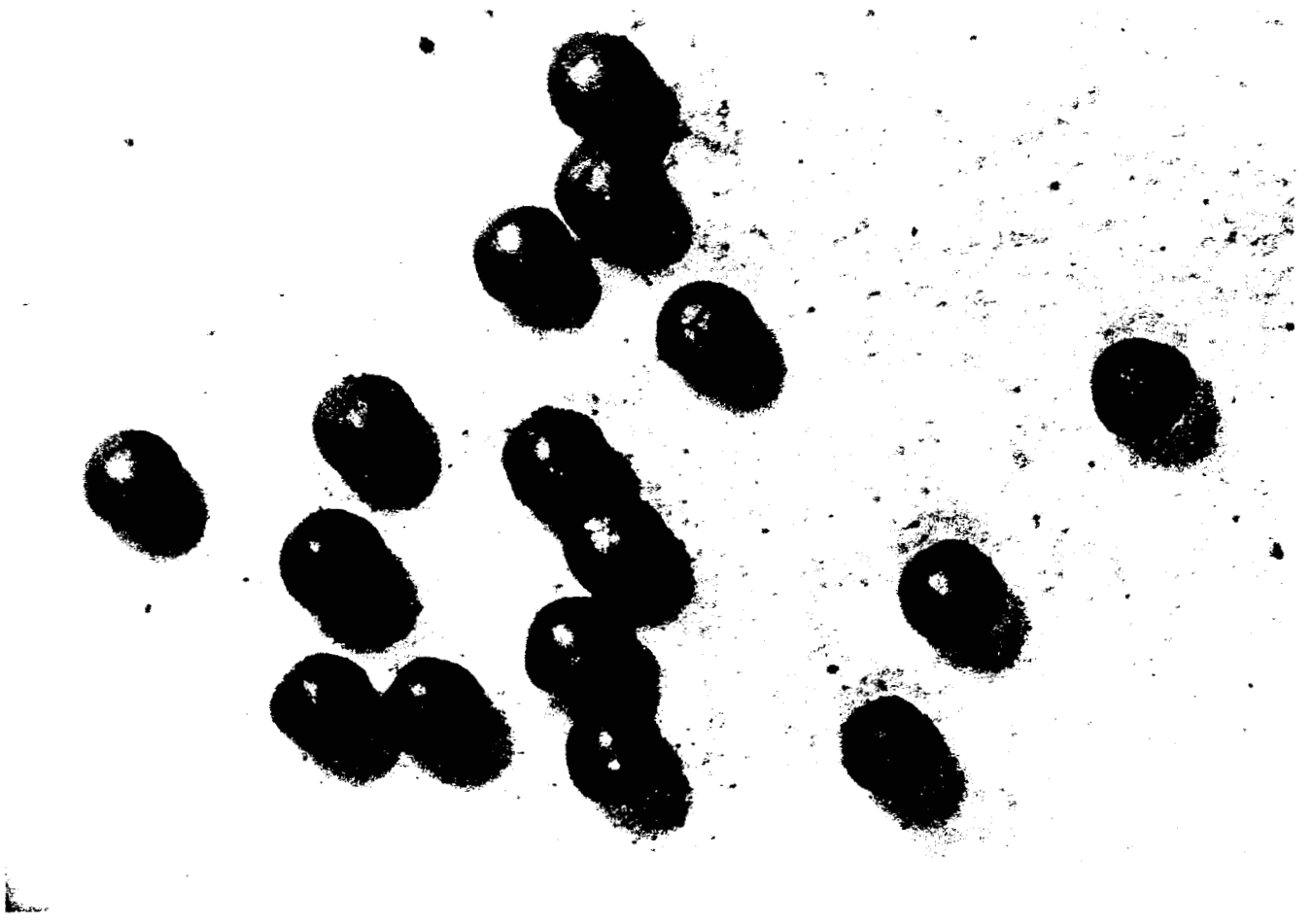

R80957

Figure 4.2.4.6 Irradiated unbonded HEU UCO TRISO particles from capsule NPR 1, piggyback sample 12GA

R80961

Figure 4.2.4.7 Irradiated unbonded HEU UCO TRISO particles from capsule NPR 1, piggyback sample 12GA*

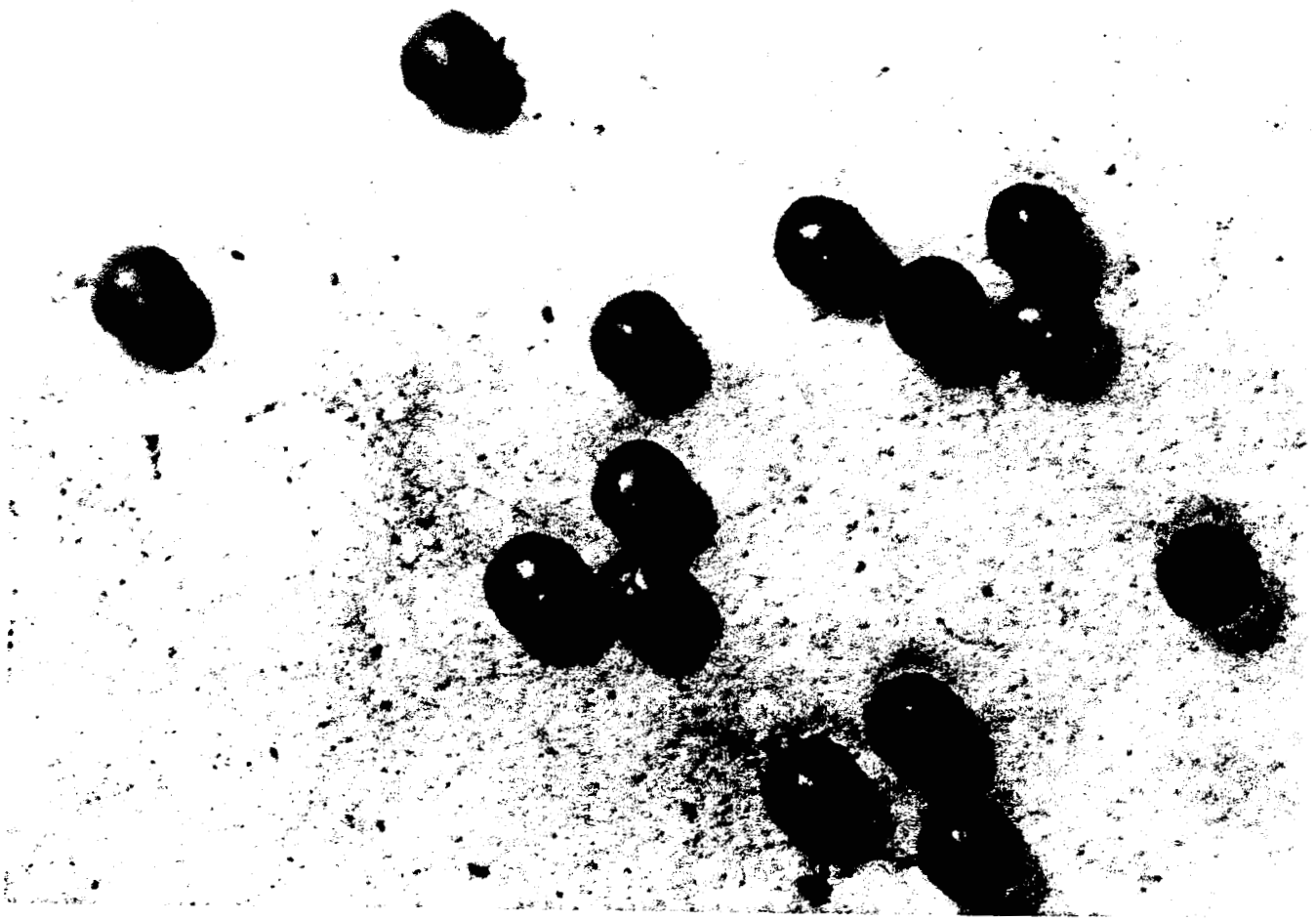

R80959

Figure 4.2.4.8 Irradiated unbonded HEU UCO TRISO particles from capsule NPR 1, piggyback sample 12UA

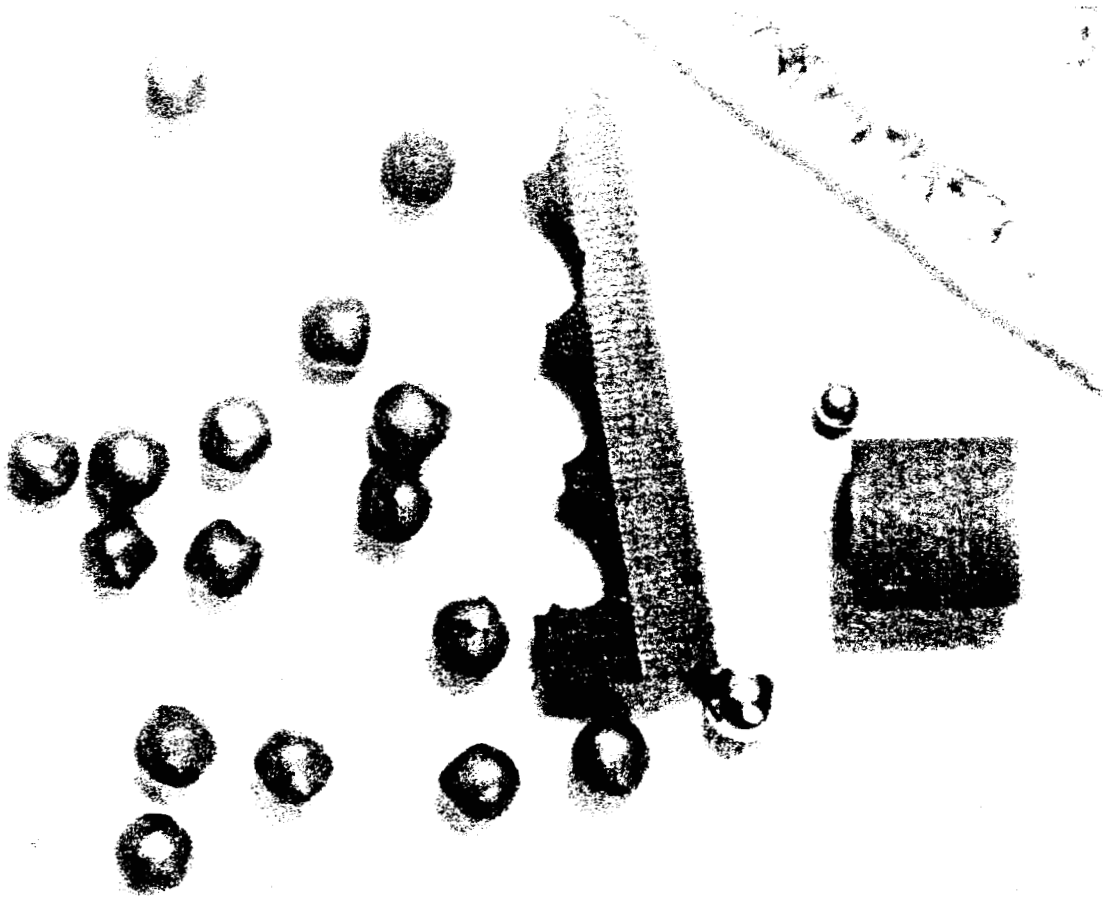

R80965

Figure 4.2.4.9 Irradiated unbonded HEU UCO TRISO particles from capsule NPR 1, piggyback sample 12GA. The two spheres on the extreme right side are microspheres with known diameter (0.711 mm & 0.457 mm)

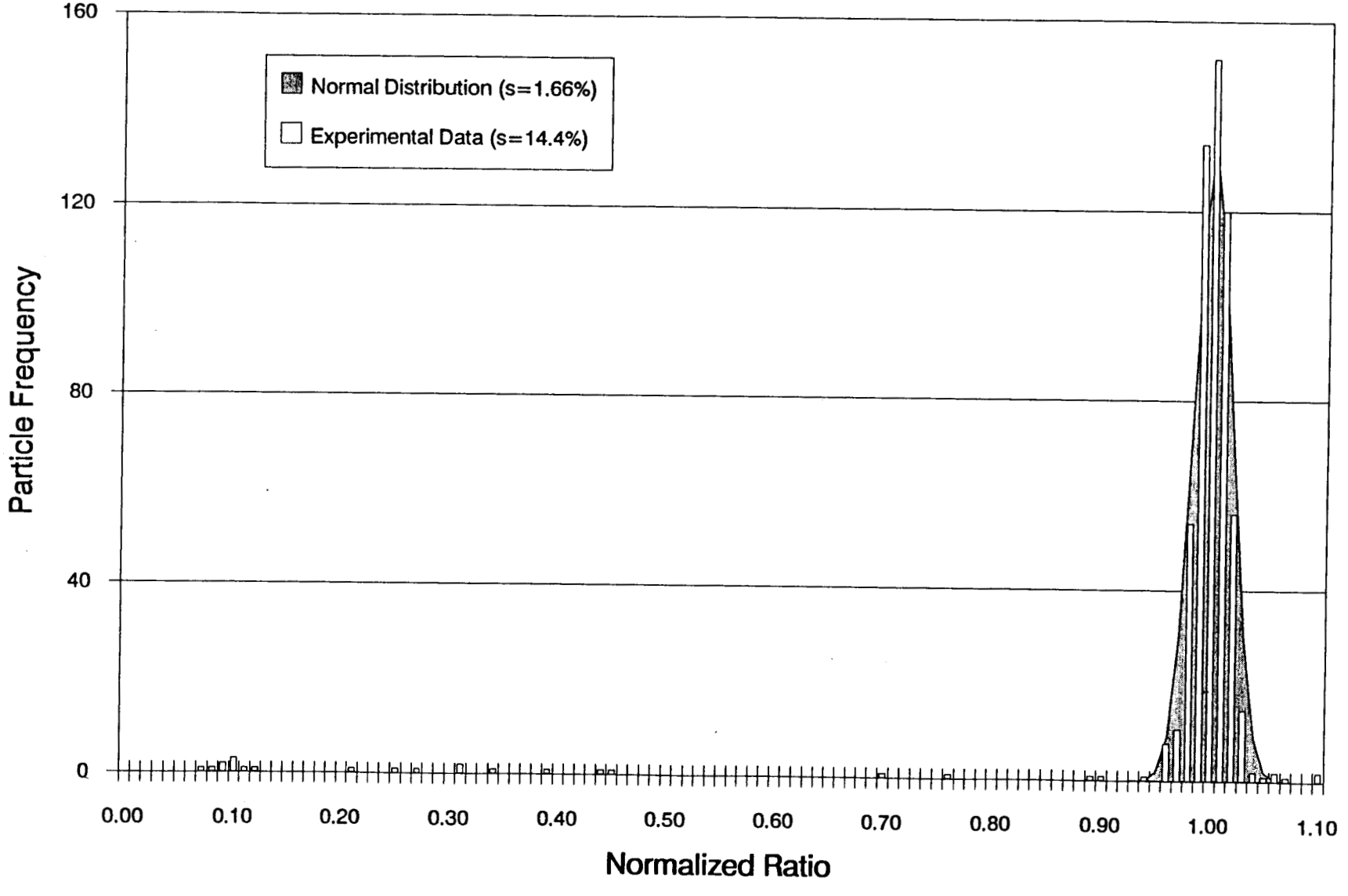

Figure 4.5.1 Compact NPR 1 B4 distribution of ^{137}Cs:^{144}Ce ratios in 582 particles

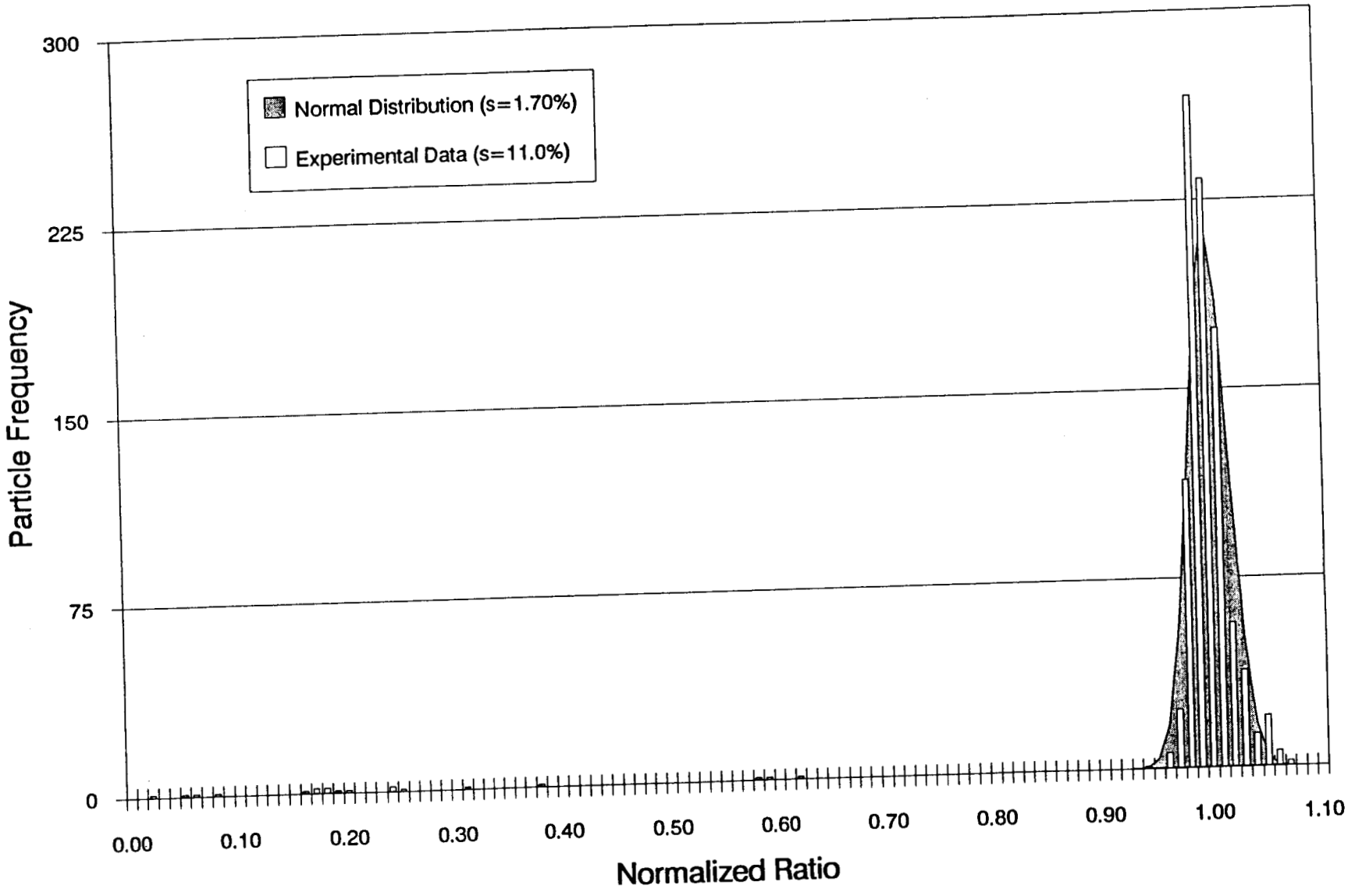

Figure 4.5.2 Compact NPR 1 B5 distribution of ^{137}Cs:^{144}Ce ratios in 972 particles

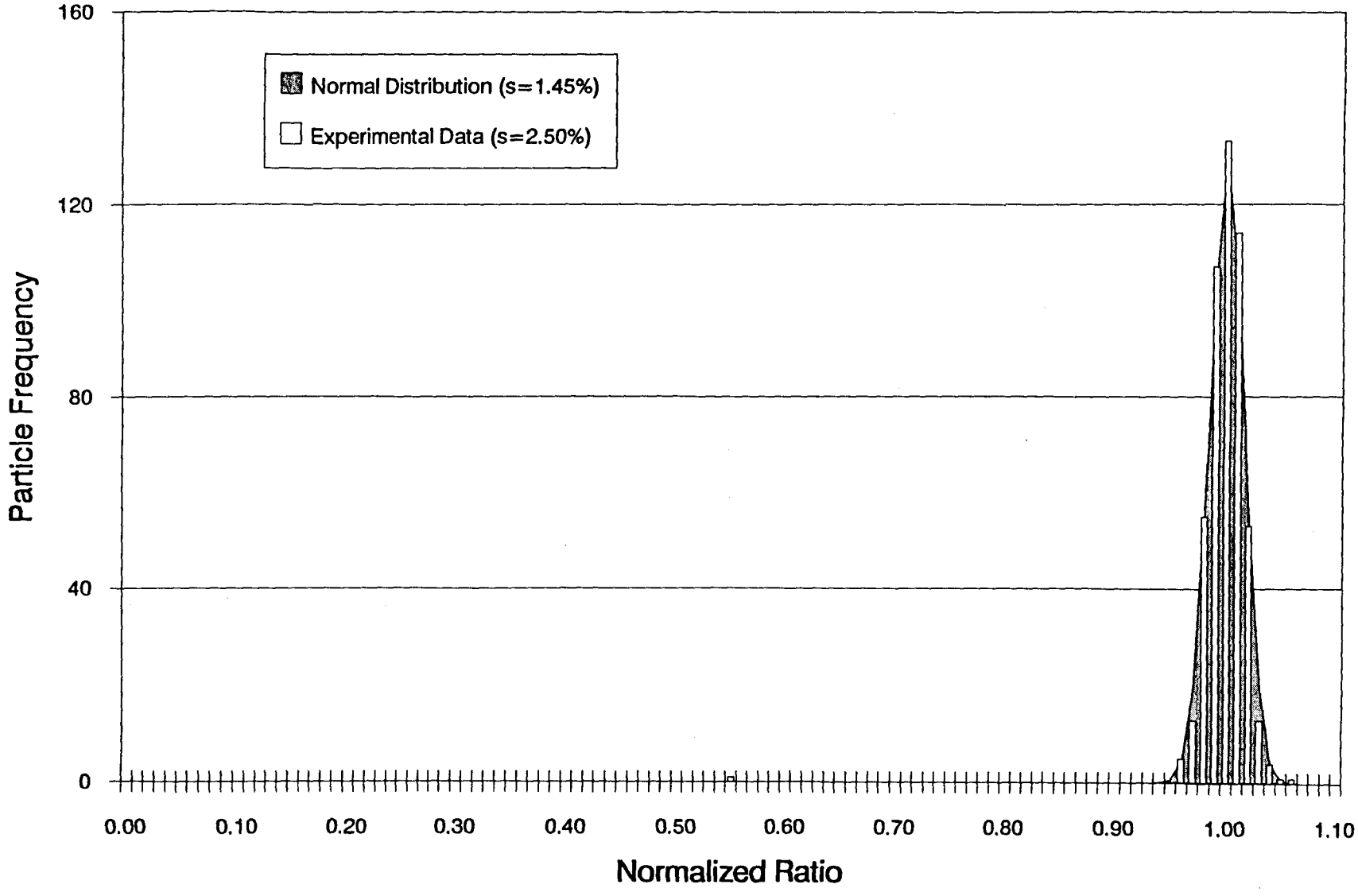

Figure 4.5.3 Compact NPR 1 B8 distribution of ^{137}Cs:^{144}Ce ratios in 500 particles

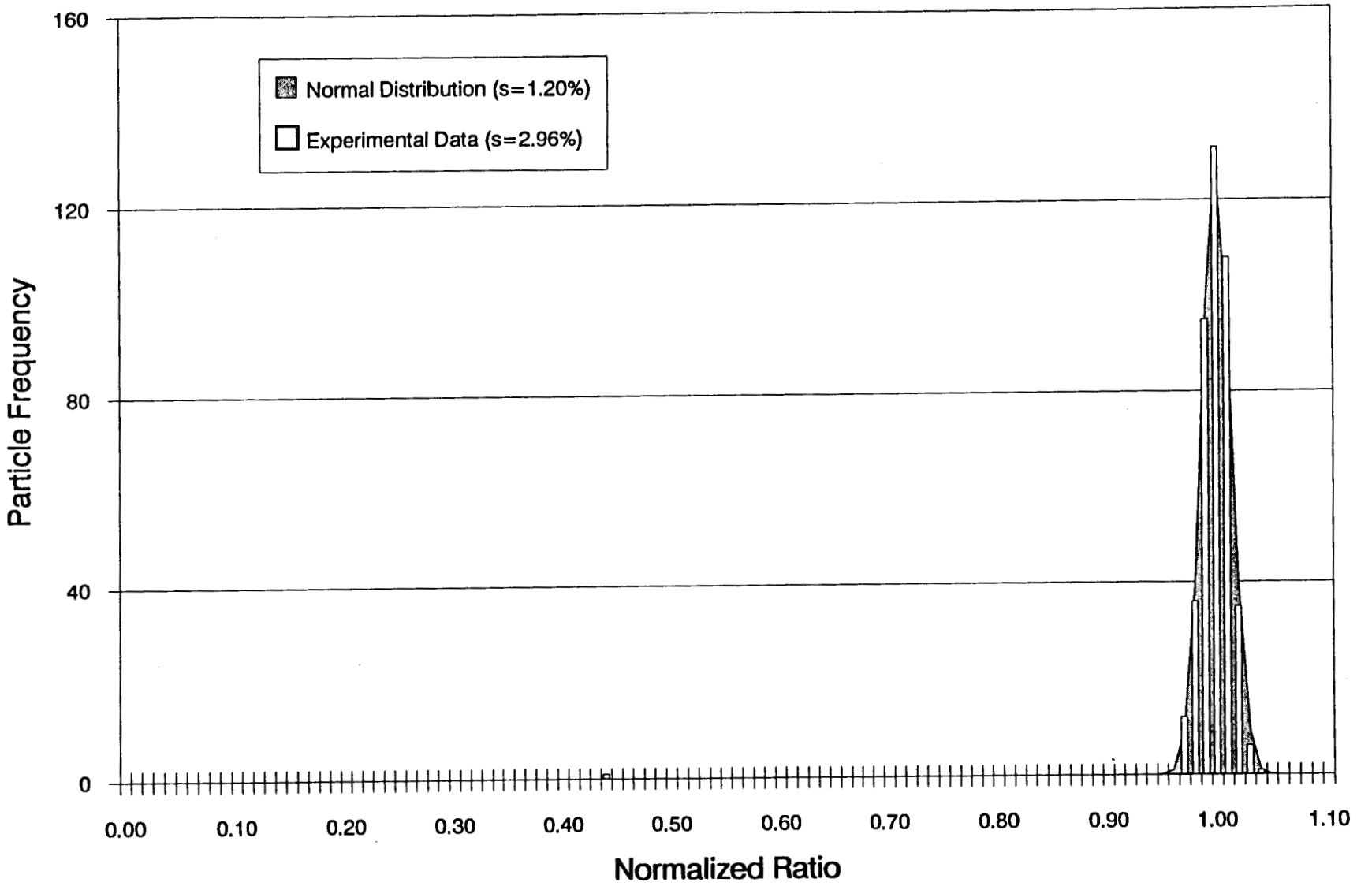

Figure 4.5.4 Compact NPR 2 B4 distribution of ^{137}Cs:^{144}Ce ratios in 424 particles

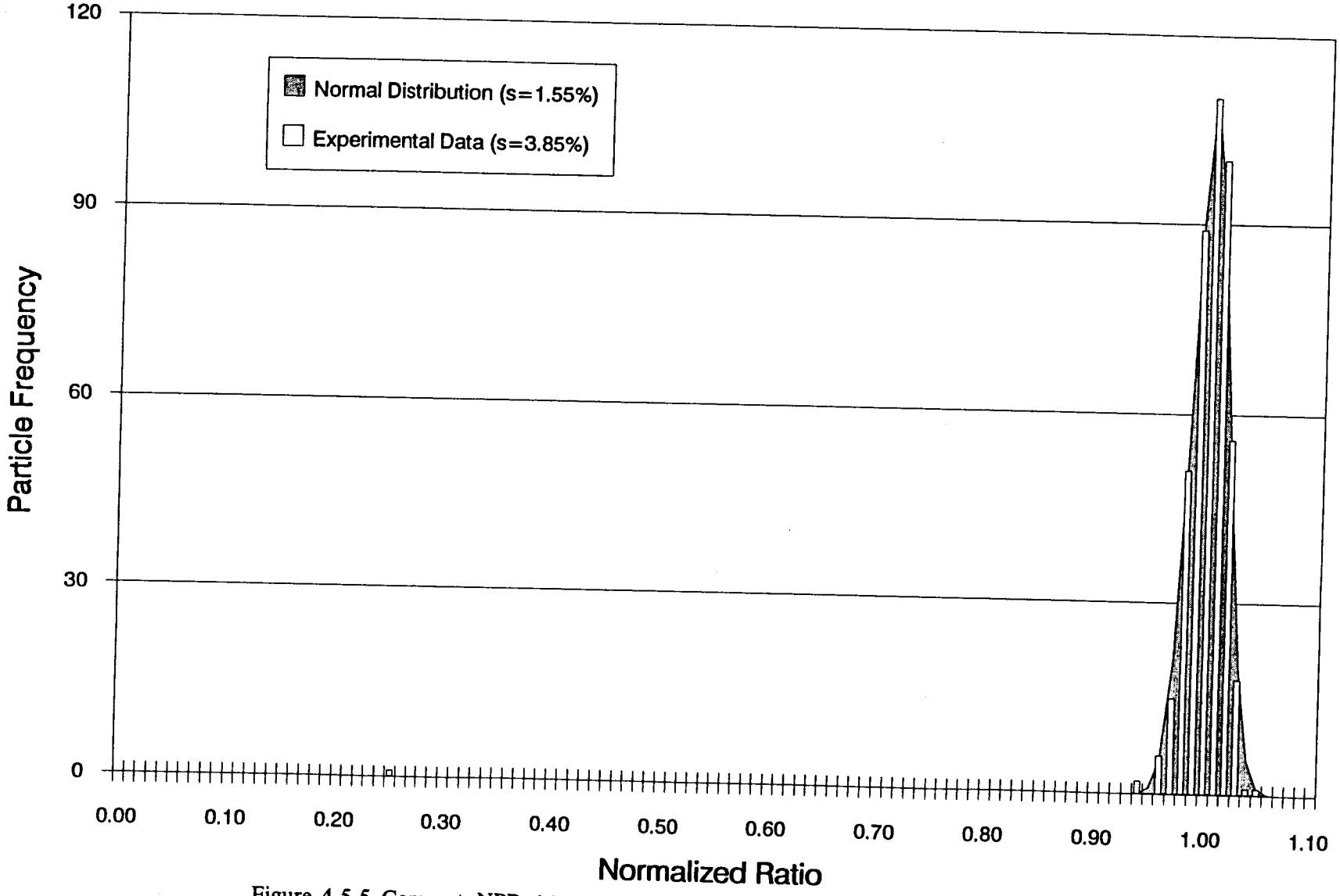

Figure 4.5.5 Compact NPR 1A A13 distribution of ^{137}Cs:^{144}Ce ratios in 450 particles

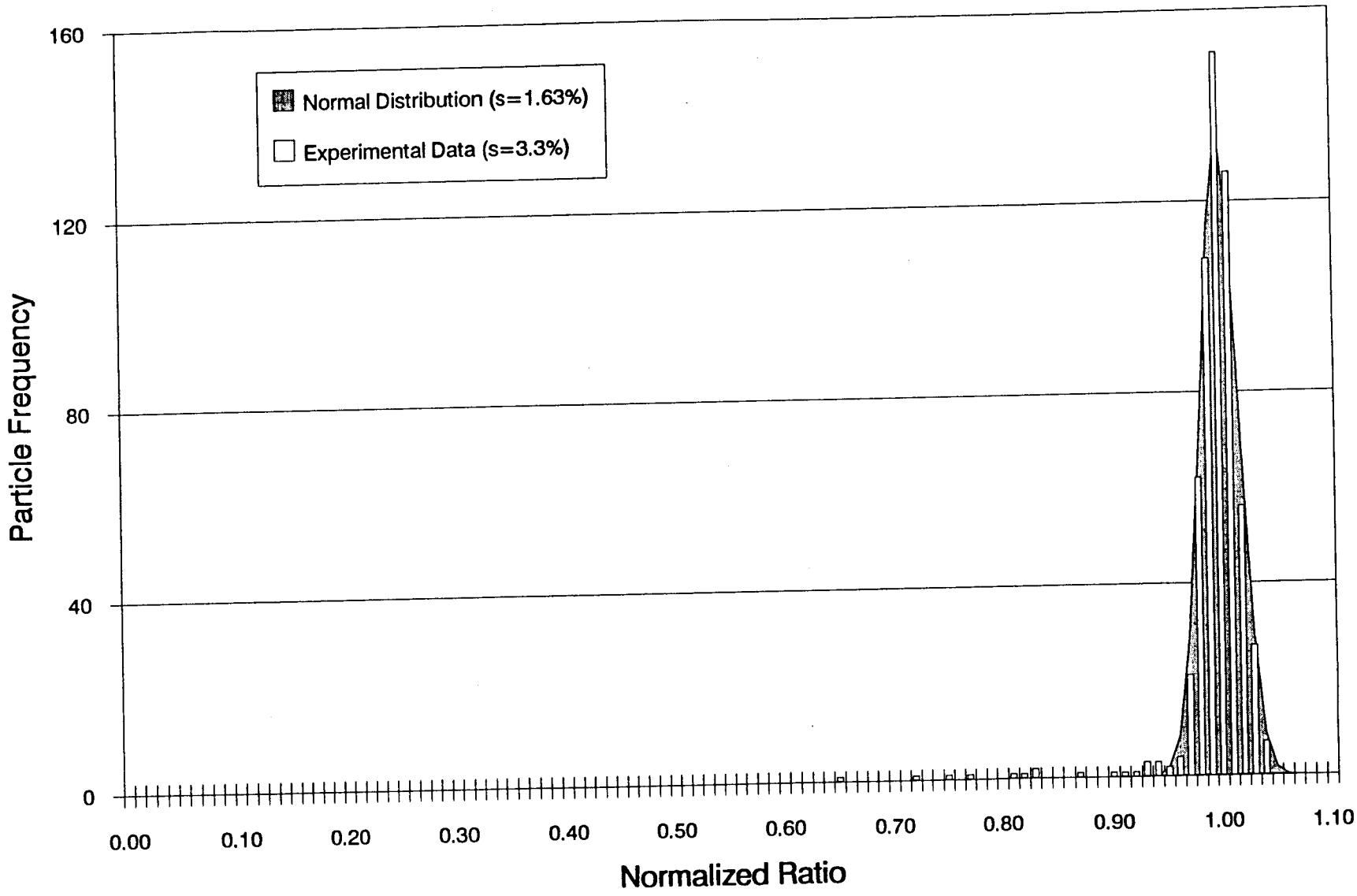

Figure 4.5.6 Compact NPR 1 B4 distribution of ^{134}Cs:^{137}Cs ratios in 582 particles

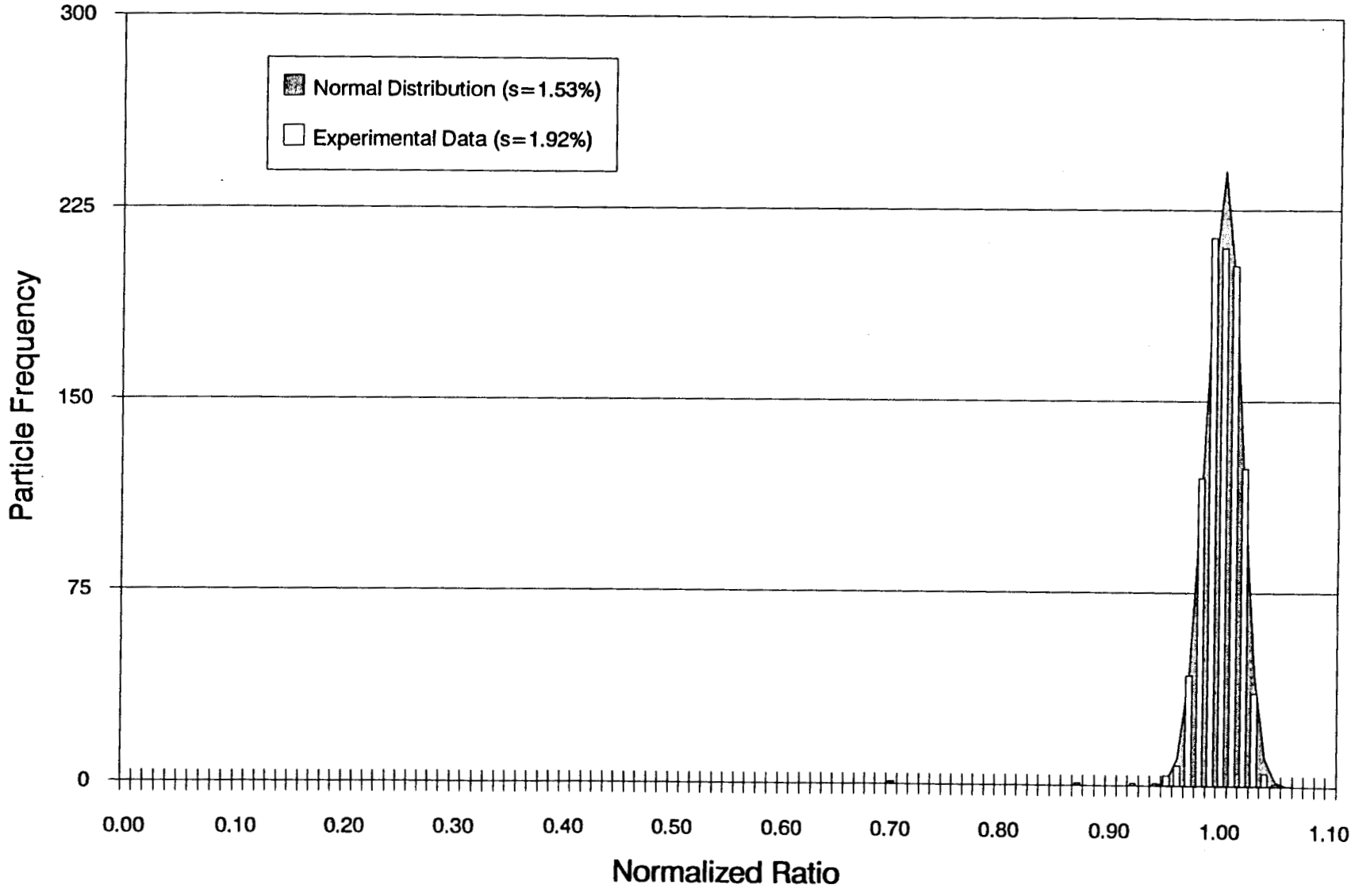

Figure 4.5.7 Compact NPR 1 B5 distribution of ^{134}Cs:^{137}CS ratios in 972 particles

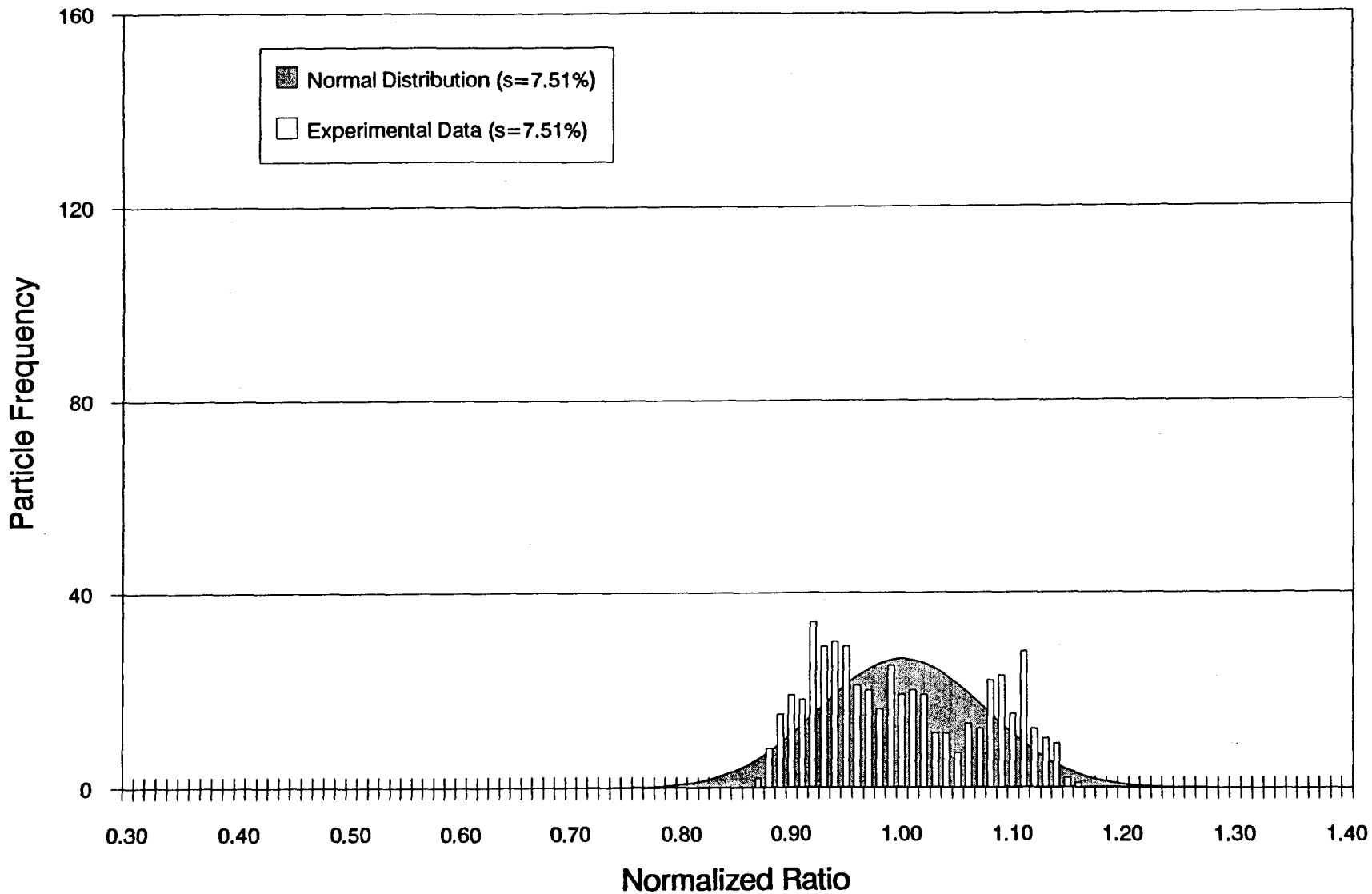

Figure 4.5.8 Compact NPR 1 B8 distribution of ^{134}Cs:^{137}Cs ratios in 500 particles

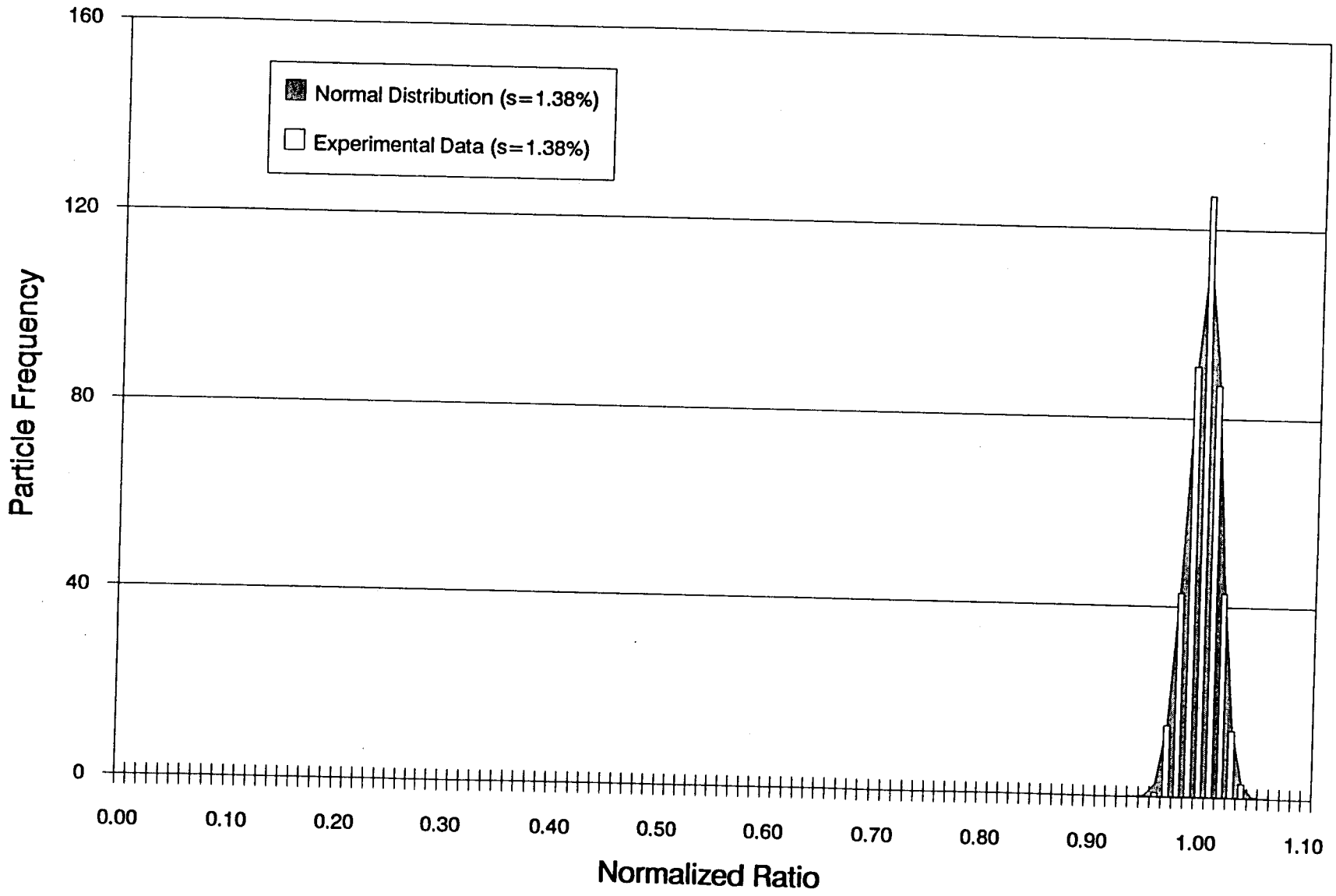

Figure 4.5.9 Compact NPR 2 B4 distribution of ^{134}Cs:^{137}Cs ratios in 424 particles

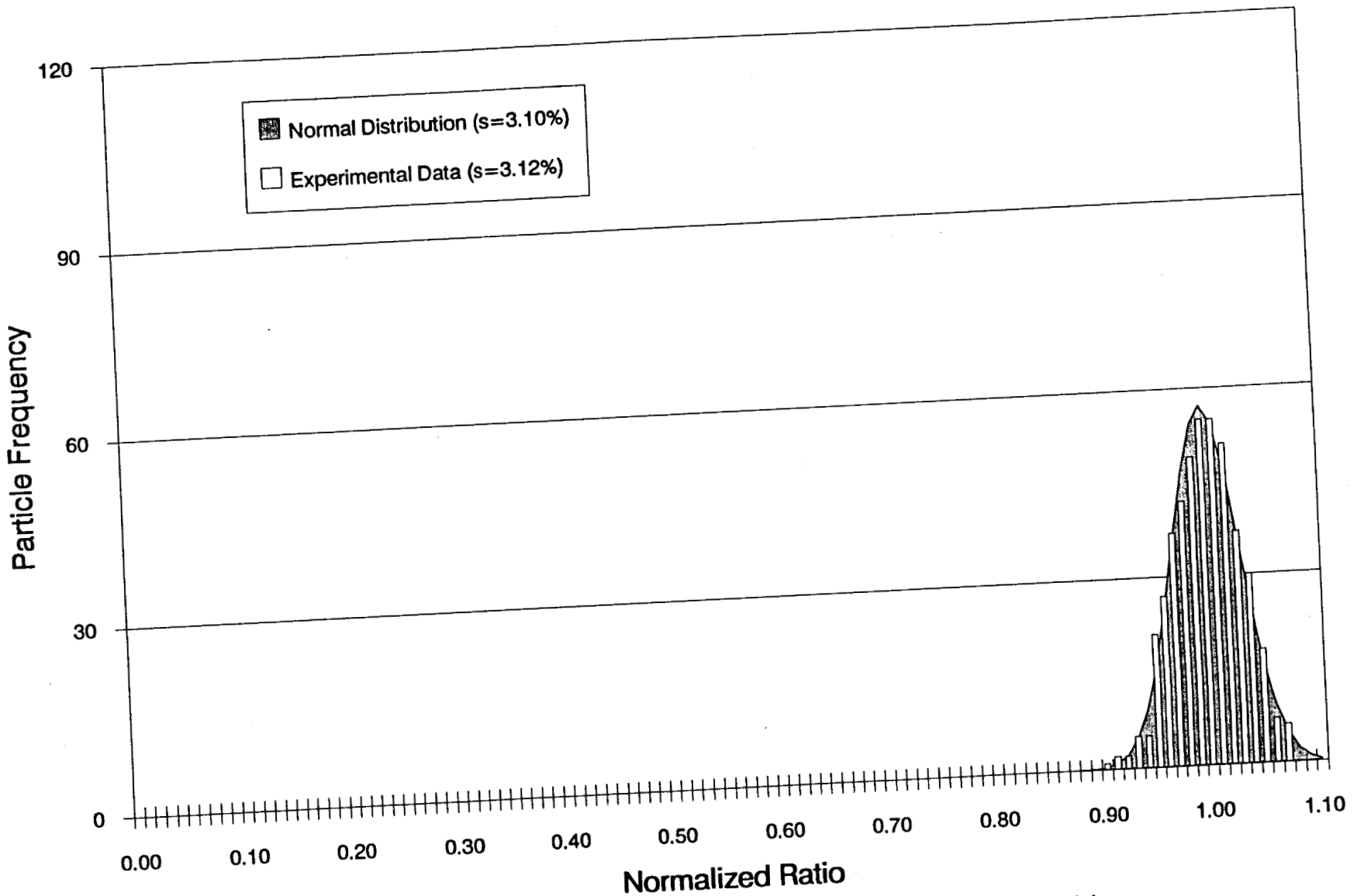

Figure 4.5.10 Compact NPR 1A A13 distribution of ^{134}Cs:^{137}Cs ratios in 450 particles

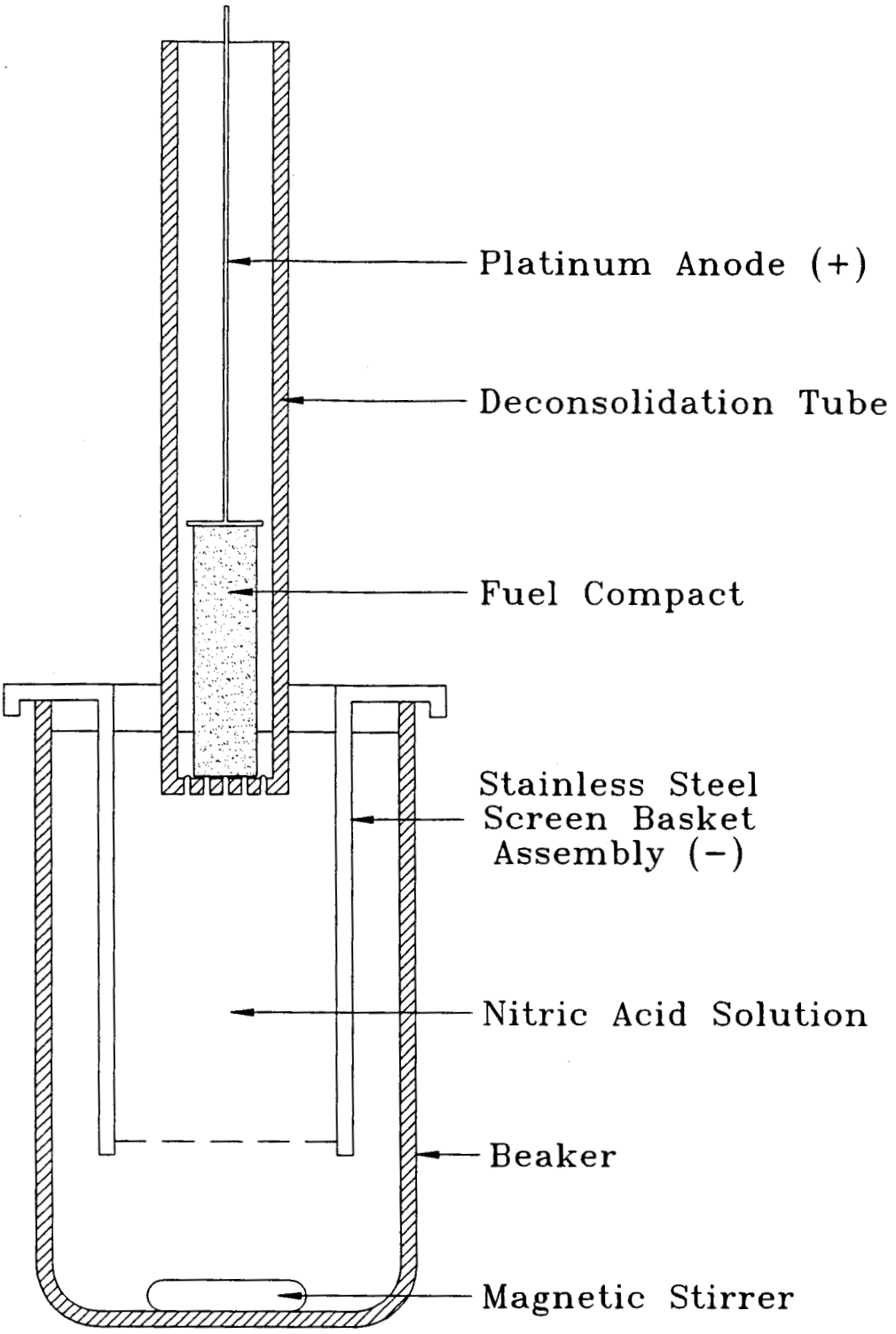

Fig. 4.5.11 Fuel compact deconsolidation apparatus.

(a) R81306

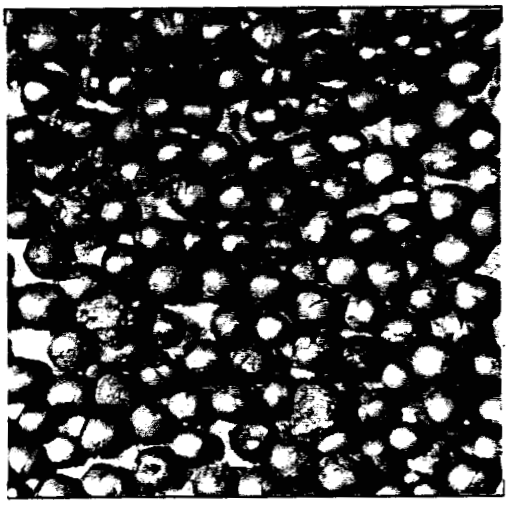

(b) R81307

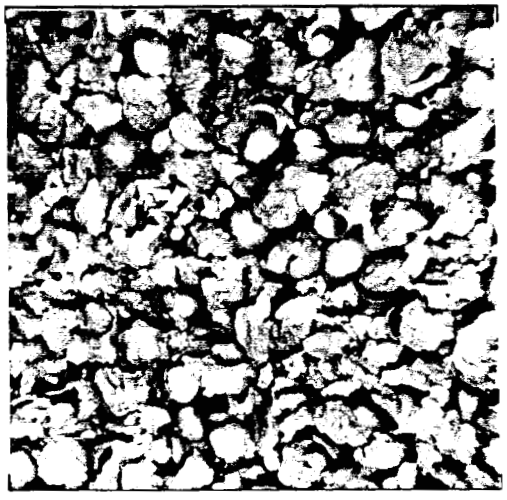

(c) R81309

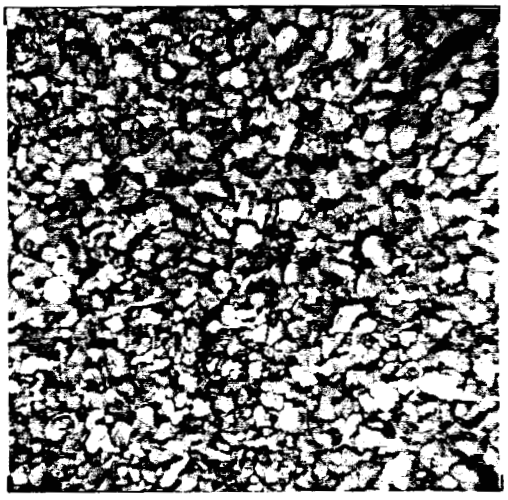

(d) R81308

Fig. 4.5.12 Deconsolidation fractions for compact NPR-1/B5 (a) large graphite shim material, (b) unbonded fuel particles from shape separation, (c) non-particle fraction from shape separation, and (d) small shim material and coating fragments.

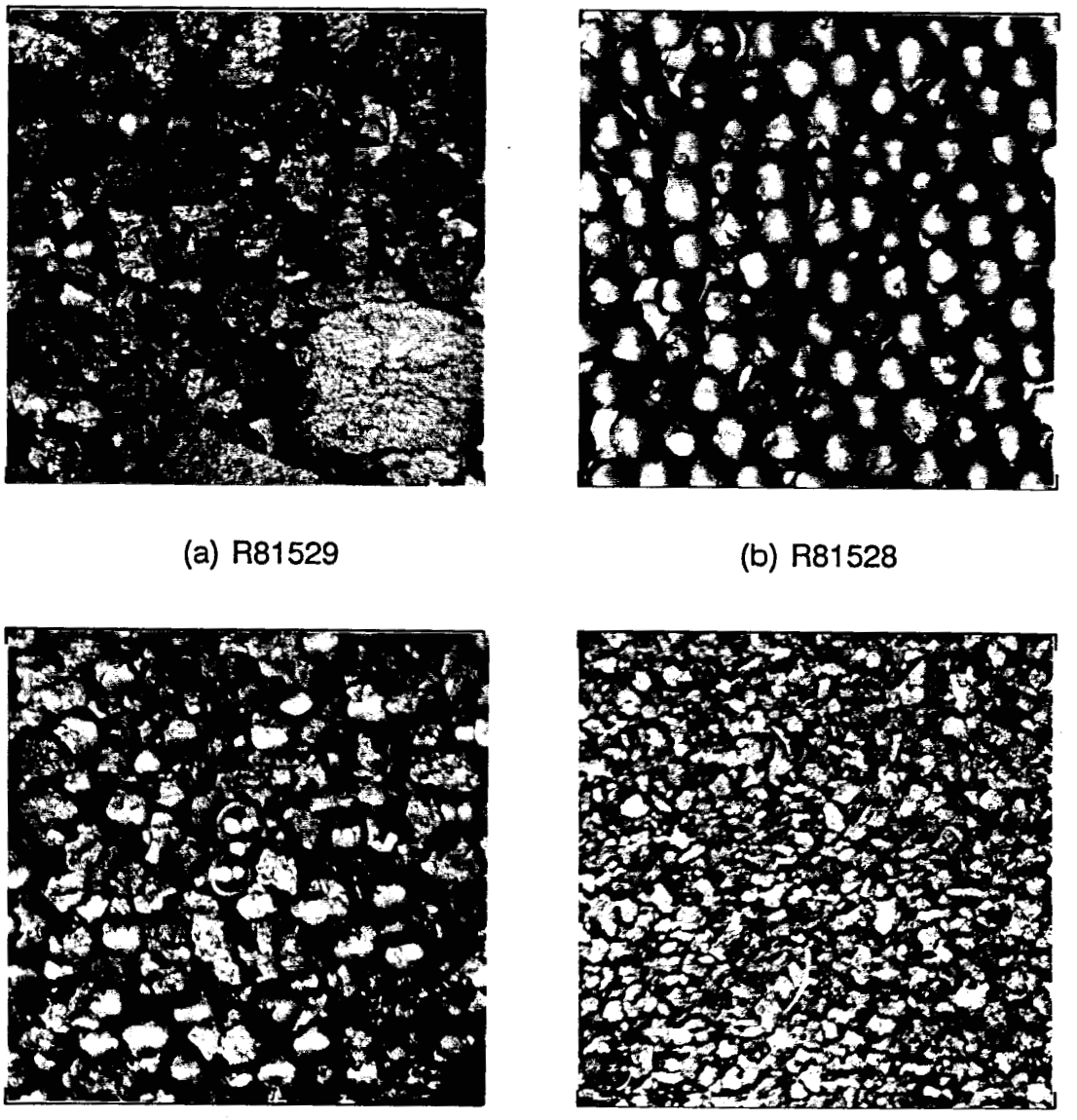

(a) R81529 (b) R81528

(c) R81530 (d) R81527

Fig. 4.5.13 Deconsolidation fractions for compact NPR-1/B8 (a) large graphite shim material, (b) unbonded fuel particles from shape separation, (c) non-particle fraction from shape separation, and (d) small shim material and coating fragments.

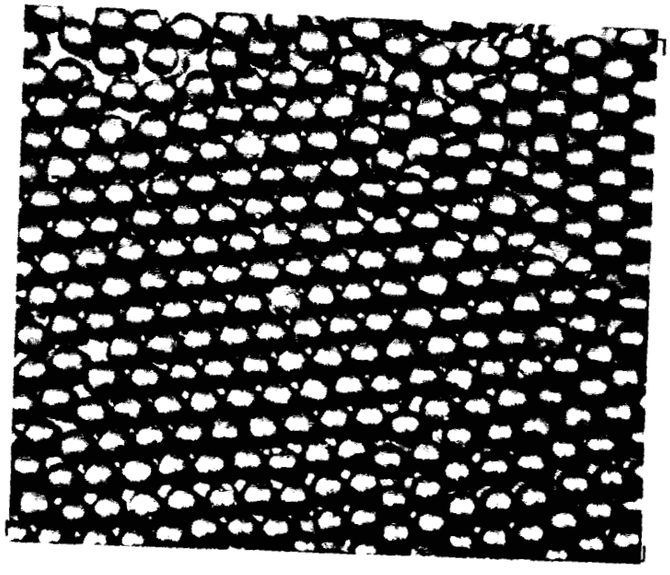

R81565

Fig. 4.5.14 Graphite denuded particles from compact NPR-1A/13.

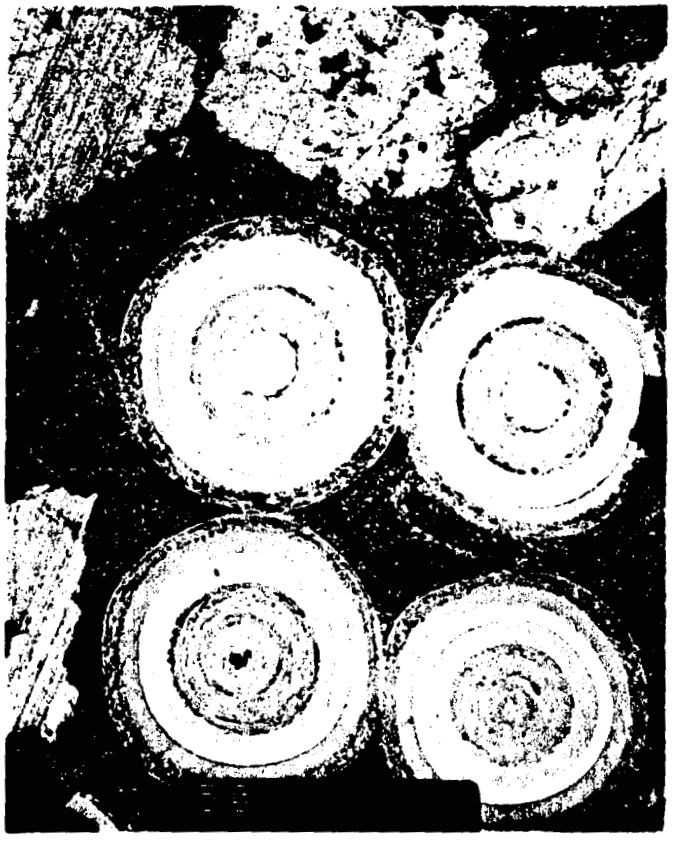

YP16874 100um

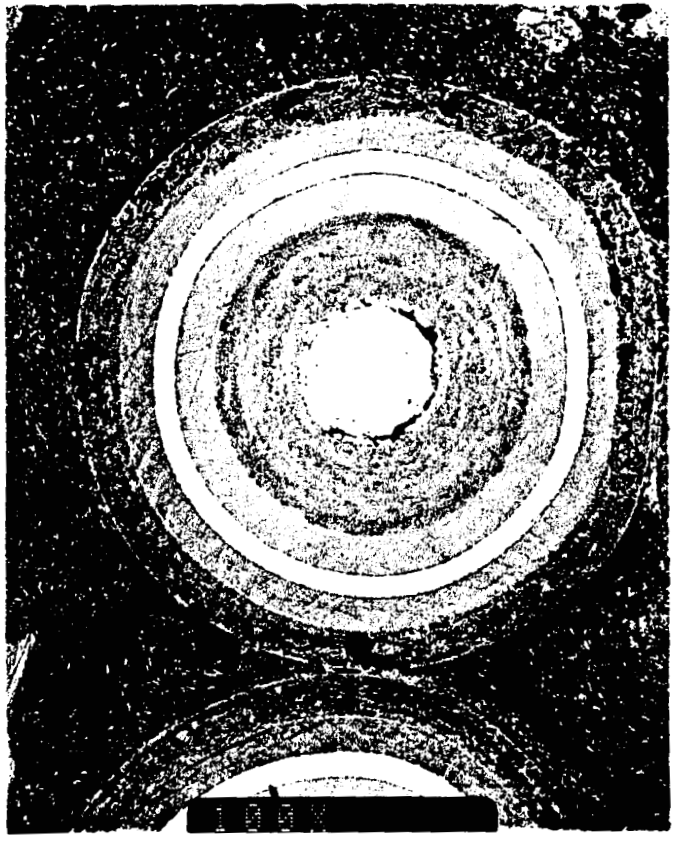

YP 16870 50um

Figure 4.6.1.1. Unirradiated NP-MHTGR Archive Compact 01-18, 20 Vol % UCO. Remarks: the compact consisted of TRISO particles and H-451 graphite shim particles bonded with a matrix of graphite flour and carbonized petroleum pitch.

YP16869 100um

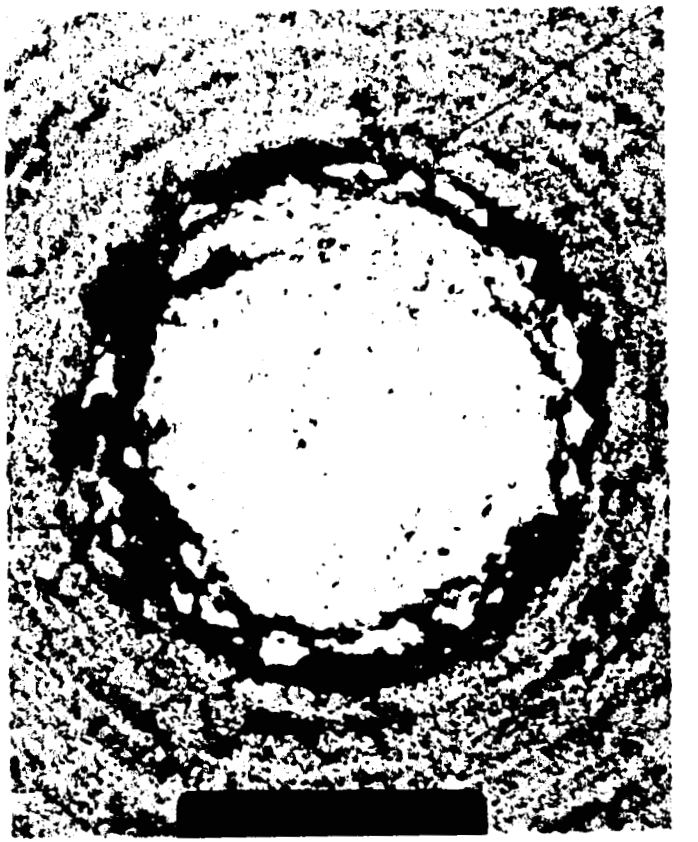

YP16873 50um

Figure 4.6.1.2. Unirradiated NP-MHTGR Fuel Archive Compact 01-18, 20 Vol % Fissile UCO. Remarks: No coating-matrix interaction was observed in the unirradiated fuel compacts. The UO_2 (gray) and UC_2 (white) phases in the kernel were dispersed throughout the kernel.

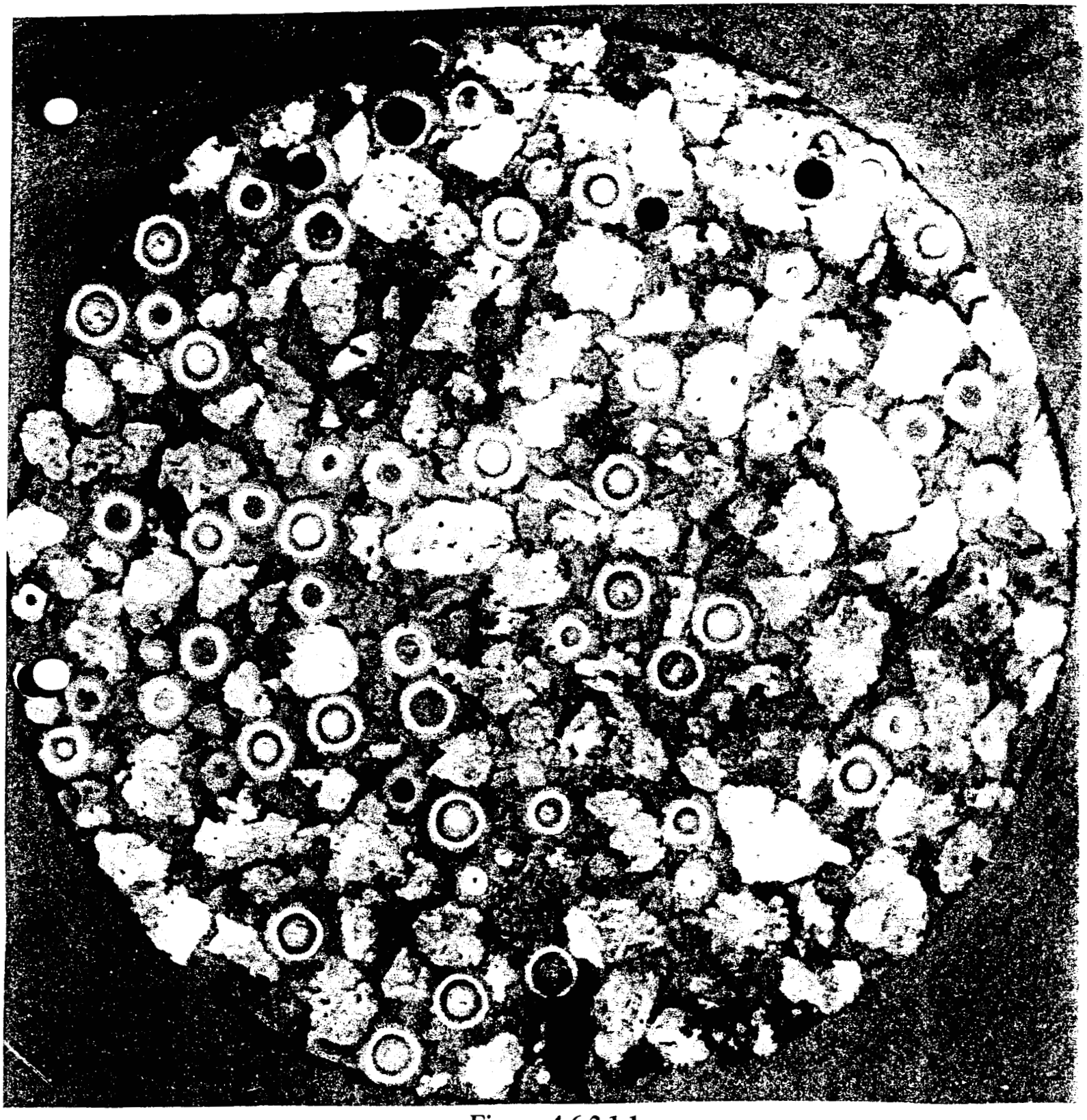

Figure 4.6.2.1.1

Ceramographic Crossection of NPR 2 Compact A4 about 13 mm from the End Cap. Particles are Dispersed among H-451 Graphite Shim Particles and Matrix Material. This Compact Contained 12 Volume Percent Coated Particles which was the minimum for Capsules NPR 1 and NPR 2. The Maximum Particle Loading was 18 Volume Percent at the Capsule Ends.

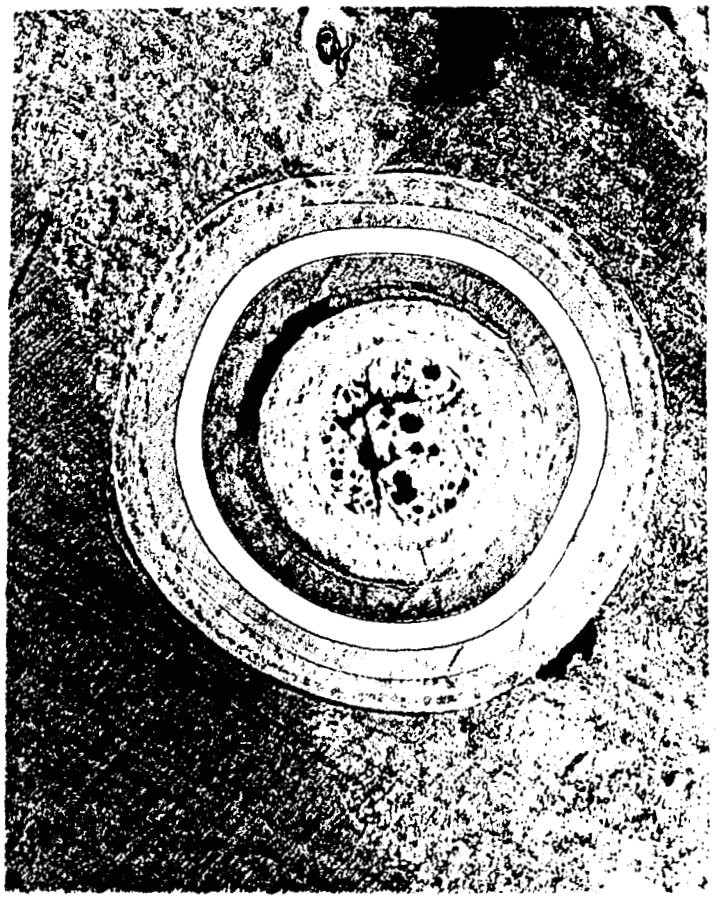

R81091 100μm

R81092 50μm

Figure 4.6.2.2.1. NPR-2 Compact A-4; Irradiation Conditions of 730°C, 3.7 x 10^{25} n/m^2, 80% FIMA. Remarks: Irradiation induced shrinkage of the buffer caused a gap to open between IPyC and buffer. Fission gas bubbles in the kernel indicate kernel swelling took place. The kernel was contained by the buffer.

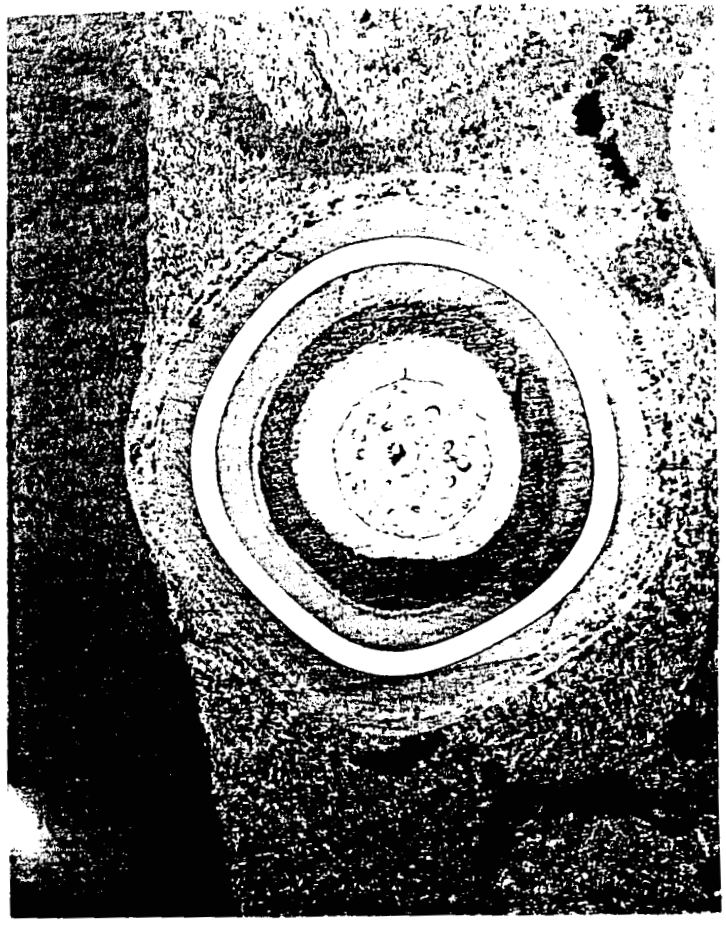

R81390 100μm

R81389 10μm

Figure 4.6.2.2.2 NPR-1 Compact A-8; Irradiation Conditions of 920°C, 2.3 x 10^{25} n/m^2, 72% FIMA. Remarks: A material which resembled densified buffer filled the kernel gas voids in some particles. These features may indicate carbon transport by gas or solid phase. No UC_2 should remain in the kernel at this high burnup. Bright irregular features in the kernel microstructure are probably fission product metals or carbides.

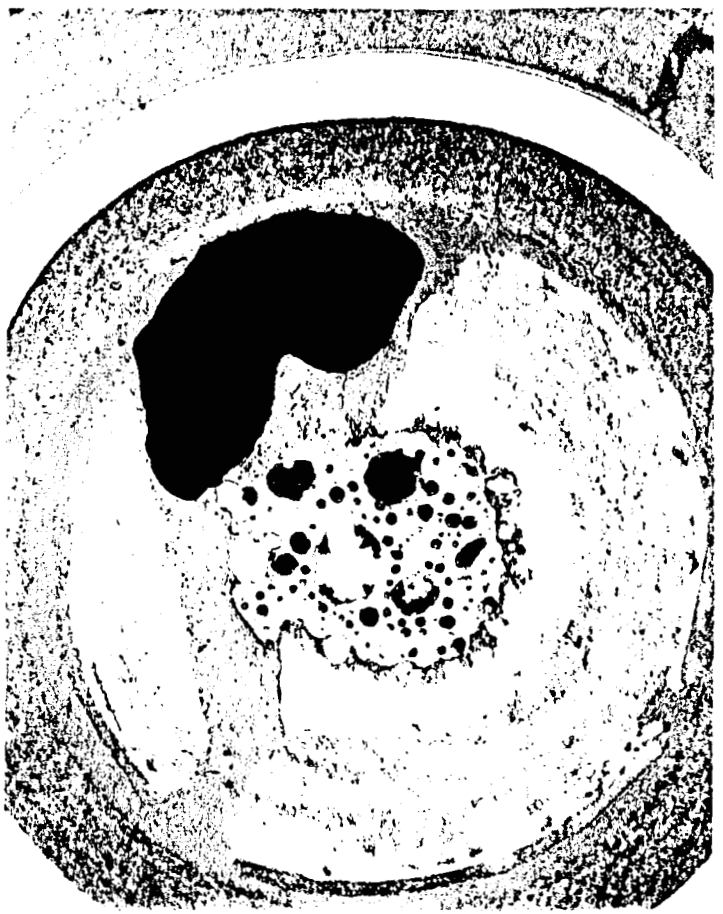

R81269

50μm

R81270

25μm

Figure 4.6.2.2.3 NPR-1 Compact A-5; Irradiation Conditions of 975°C, 3.7×10^{25} n/m^2, 80% FIMA. Remarks: The large gas voids in some UCO kernels were filled with a material which appeared similar to the fission recoil affected buffer material adjacent to the kernel. Gas or solid phase transport of carbon appeared to have taken place. The presence or absence of the material in kernel voids may have been related to the initial UC_2 and UO_2 content of the kernel.

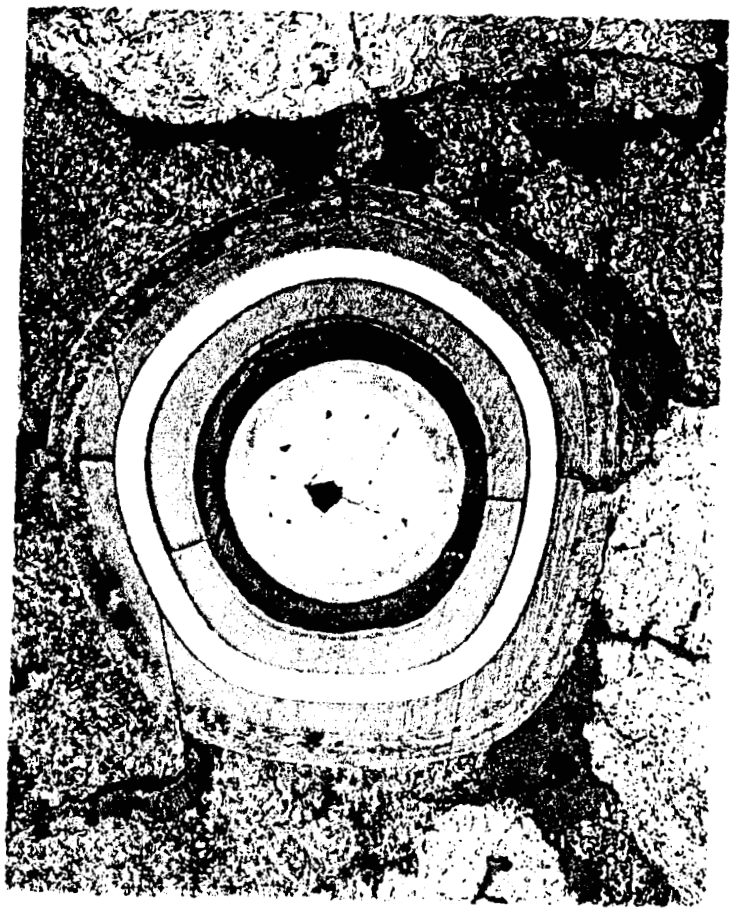

R81043 100μm

R81045 25μm

Figure 4.6.2.2.4 NPR-2 Compact A-4; Irradiation Conditions of 730°C, 3.7×10^{25} n/m^2, 80% FIMA. Remarks: Although extensive buffer shrinkage did not cause cracks completely through the buffer, fission recoil damage at kernel-buffer interface caused buffer cracks to initiate. The kernel expanded into the cracks in the buffer.

R81303 50μm

R81305 25μm

Figure 4.6.2.2.5 NPR-1 Compact A-5; Irradiation Conditions of 975°C, 3.7×10^{25} n/m^2, 80% FIMA. Remarks: Kernel swelling through a crack in the buffer coating was effectively contained by the IPyC layer. No evidence of SiC attack by fission products was evident. The bright white material adjacent to the kernel material was probably buffer material densified by fission fragment recoil effects.

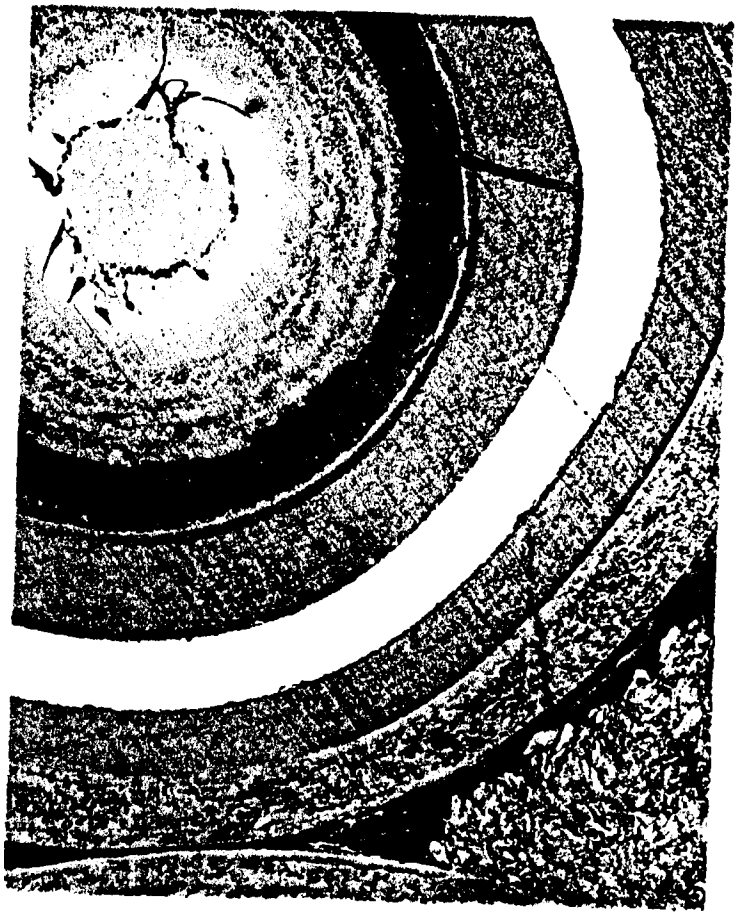

R81046

50μm

R81194

50μm

Figure 4.6.2.3.1 NPR-2 Compact A-4; Irradiation Conditions of 730°C, 3.7×10^{25} n/m^2, 80% FIMA. Remarks: Radial cracks in SiC were usually near a crack in the IPyC although IPyC cracks did not propagate into SiC.

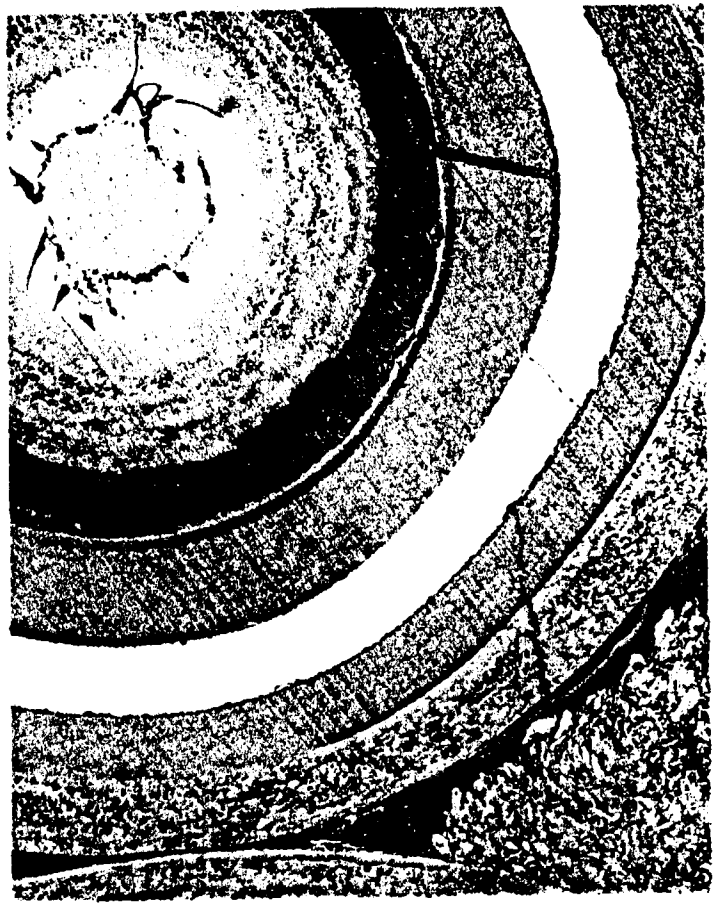

R81046

100μm

Figure 4.6.2.3.2 NPR-2 Compact A-4; Irradiation Conditions of 730°C, 3.7×10^{25} n/m^2, 80% FIMA. Remarks: The crack in SiC was near IPyC and OPyC/PPyC cracks. The buffer did not crack but shrunk radially.

R81172 25μm

R81164 25μm

Figure 4.6.2.3.3 NPR-2 Compact A-4; Irradiation Conditions of 730°C, 3.7×10^{25} n/m^2, 80% FIMA. Remarks: Circumferential cracks in SiC at the inner and outer surface of SiC. Porosity in SiC was associated with release of cesium in similar particles where fission product inventory was measured prior to metallographic examination.

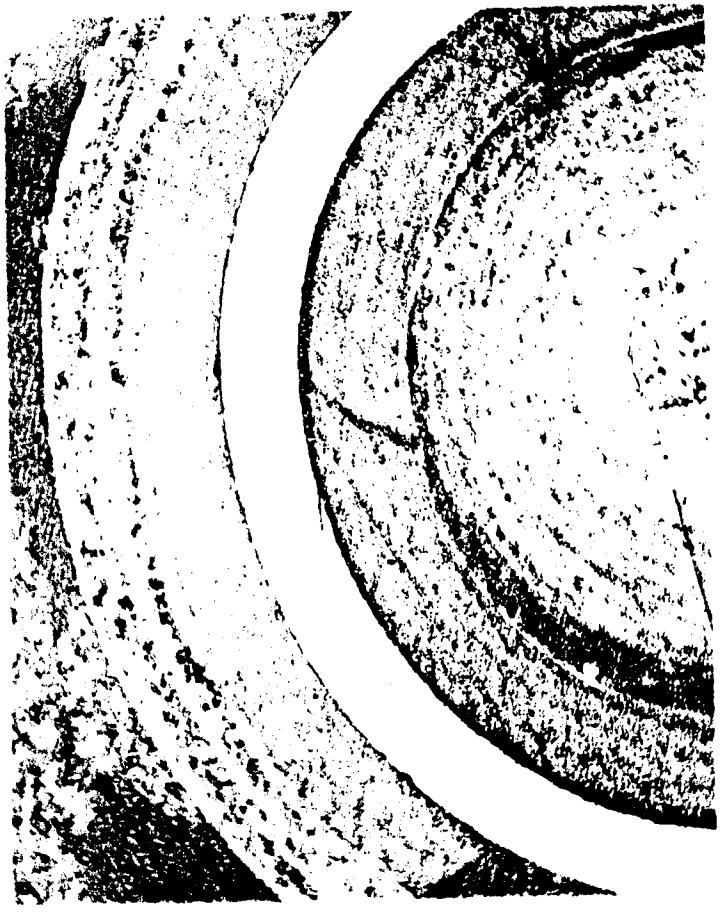

R81093 50μm

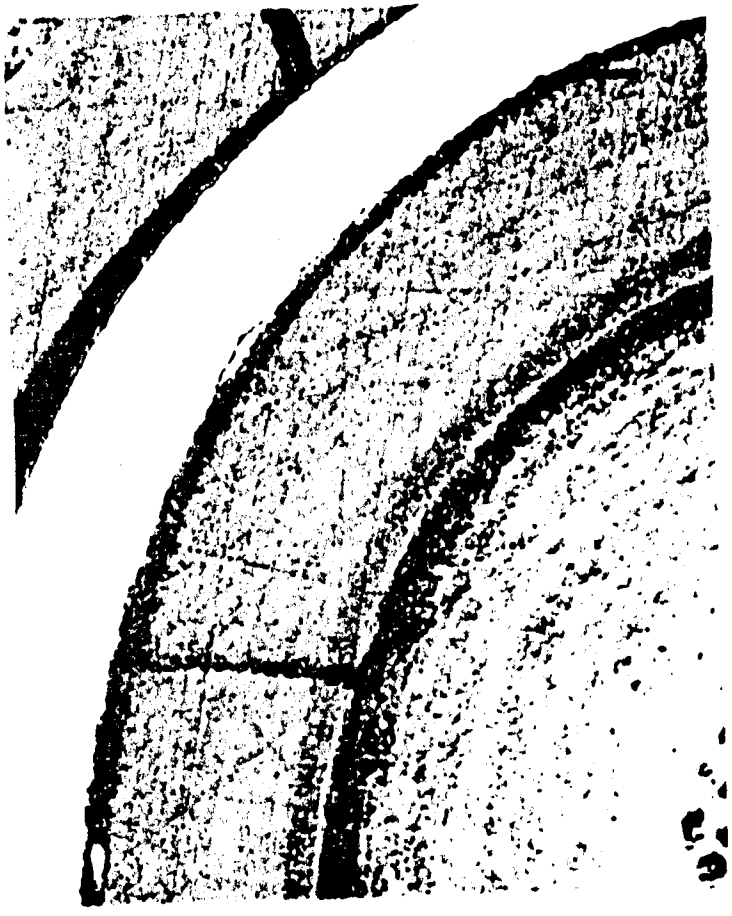

R81034 25μm

Figure 4.6.2.3.4 NPR-2 Compact A-4; Irradiation Conditions of 730°C, 3.7×10^{25} n/m^2, 80% FIMA. Remarks: Small SiC circumferential cracks were at the SiC inner surface in some particles.

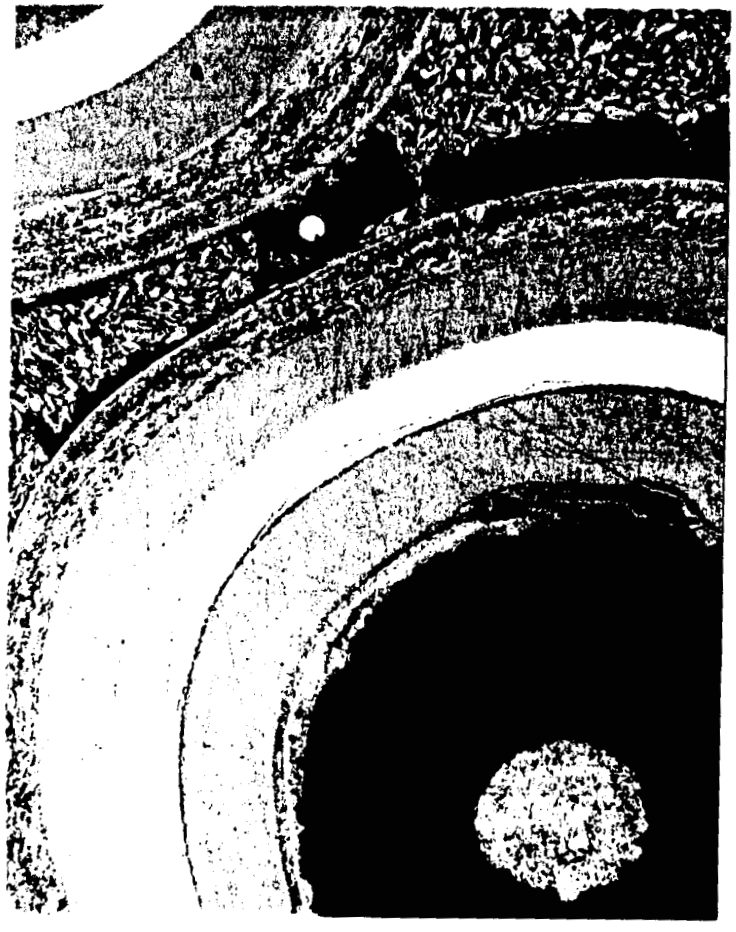

R81400 50μm

R81401 25μm

Figure 4.6.2.3.5 NPR-1 Compact A-8; Irradiation Conditions of 920°C, 2.3 x 10^{25} n/m^2, 72% FIMA. Remarks: Circumferential SiC cracks were more extensive in the compact with lower fast neutron exposure. The cracks did not propagate through the SiC wall.

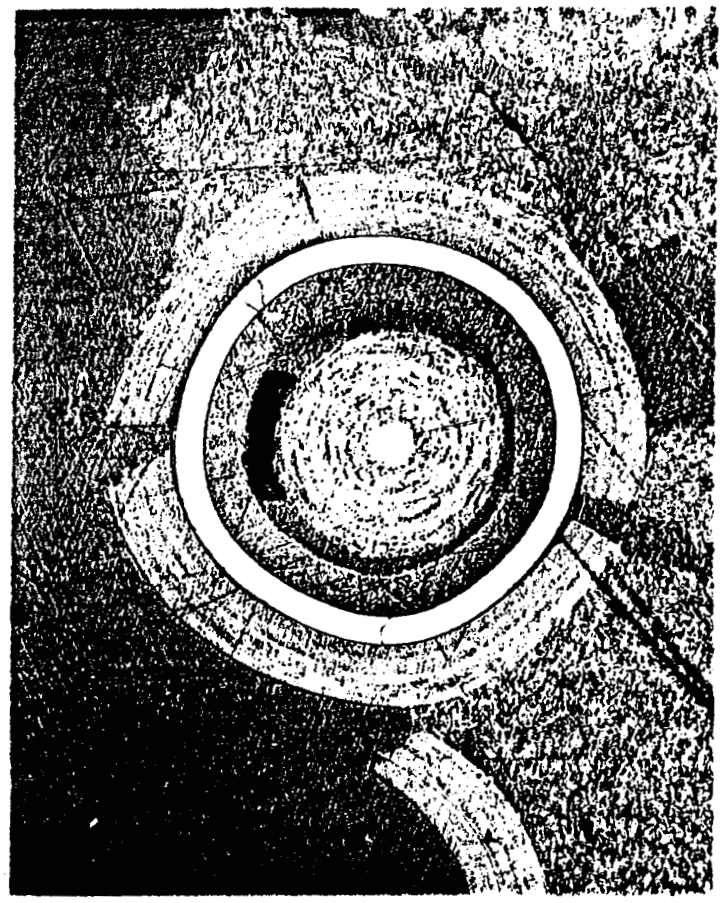

R81100 100μm

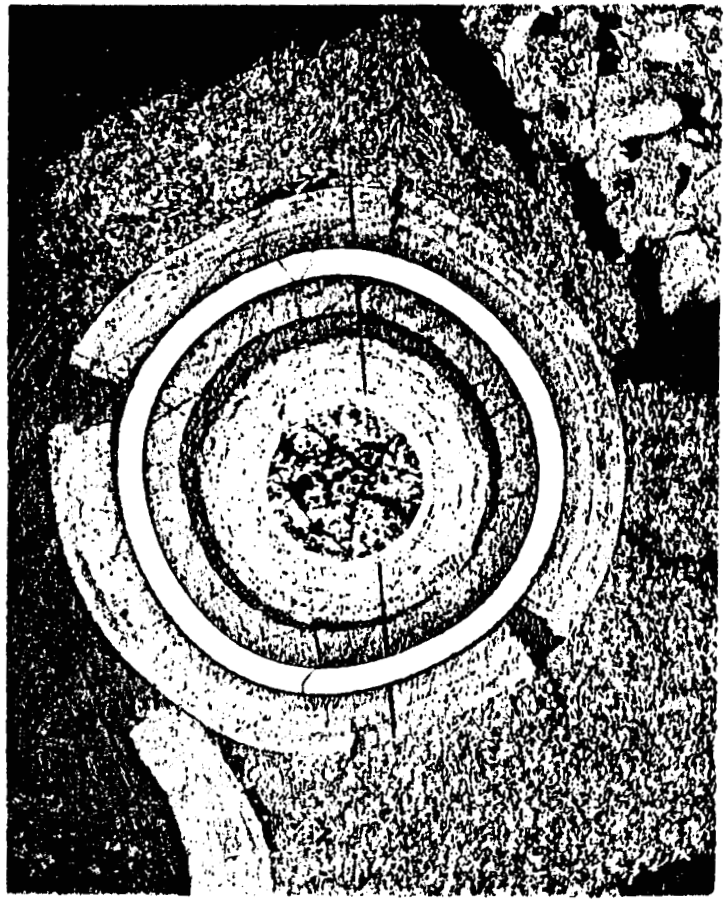

R81176 100μm

Figure 4.6.2.3.6 NPR-2 Compact A-4; Irradiation Conditions of 730°C, 3.7 x 10^{25} n/m^2, 80% FIMA. Remarks: Polished sections in the same particle at different location on the diameter revealed similar SiC crack pattern. This observation supports conclusion that metallographic grind and polish could be done without introducing SiC cracks.

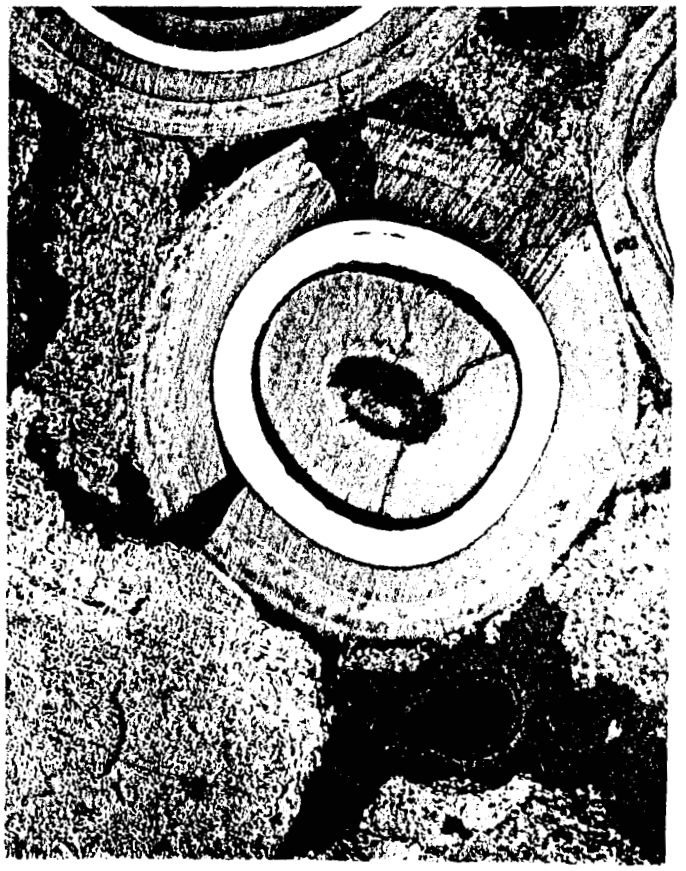

R81299 100μm

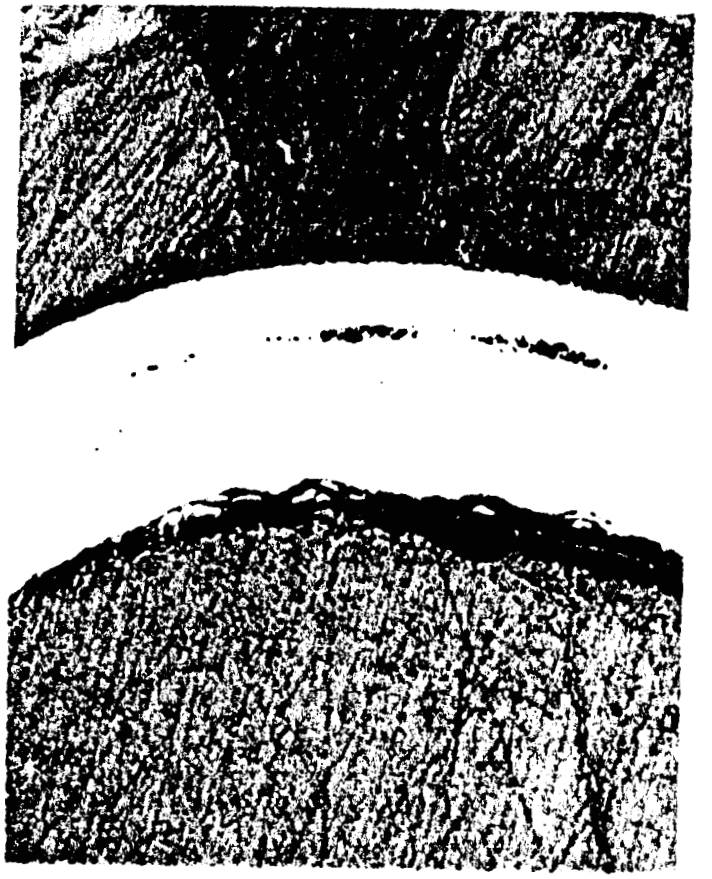

R81300 25μm

Figure 4.6.2.3.7 NPR-1 Compact A-5; Irradiation Conditions of 975°C, 3.7 x 10^{25} n/m^2, 80% FIMA. Remarks: Lenticular flaws in the SiC "Gold Spots" were not associated with cracks in the SiC. Cracks in the OPyC and IPyC did not cause cracks in the SiC.

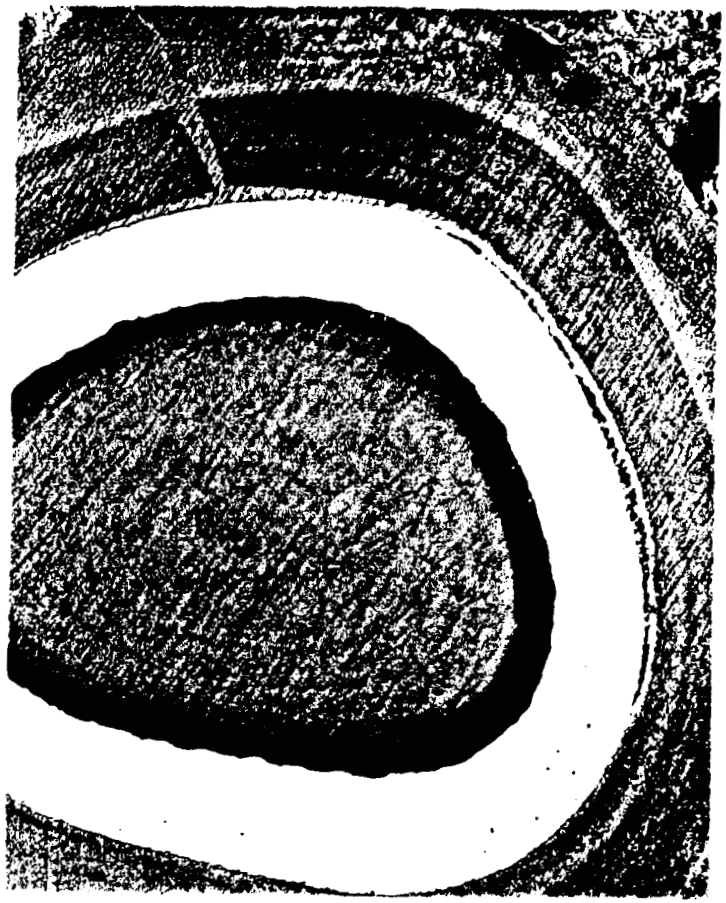

R81047 50μm

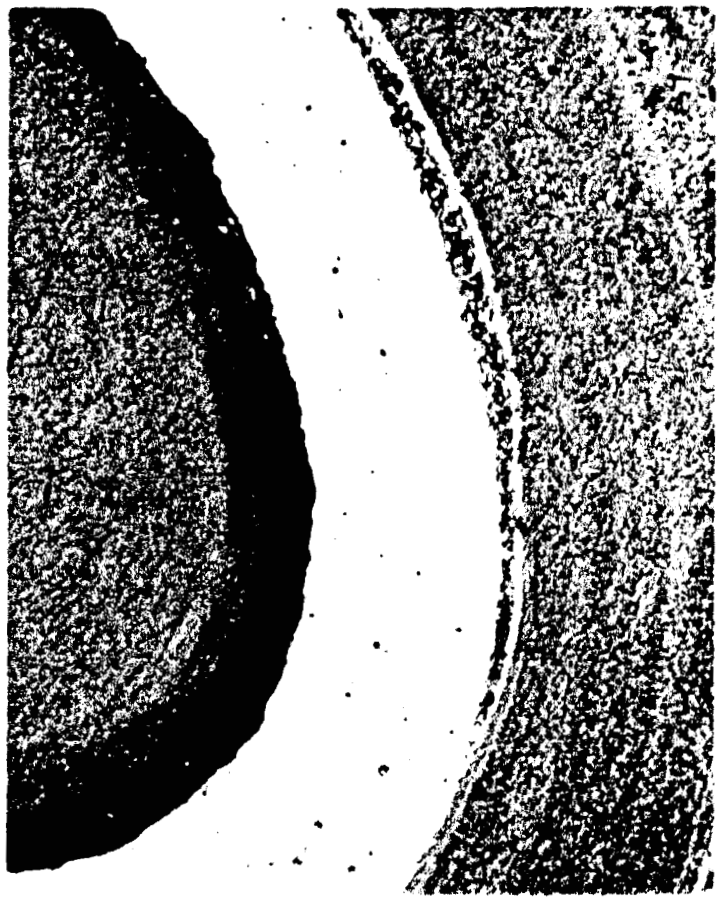

R81048 25μm

Figure 4.6.2.3.8 NPR-2 Compact A-4; Irradiation Conditions of 975°C, 3.7 x 10^{25} n/m^2, 80% FIMA. Remarks: Faceting of particles was evident but non spherical shape did not lead to SiC cracks. Lenticular flaws in the SiC "Gold Spots" were not associated with SiC cracks.

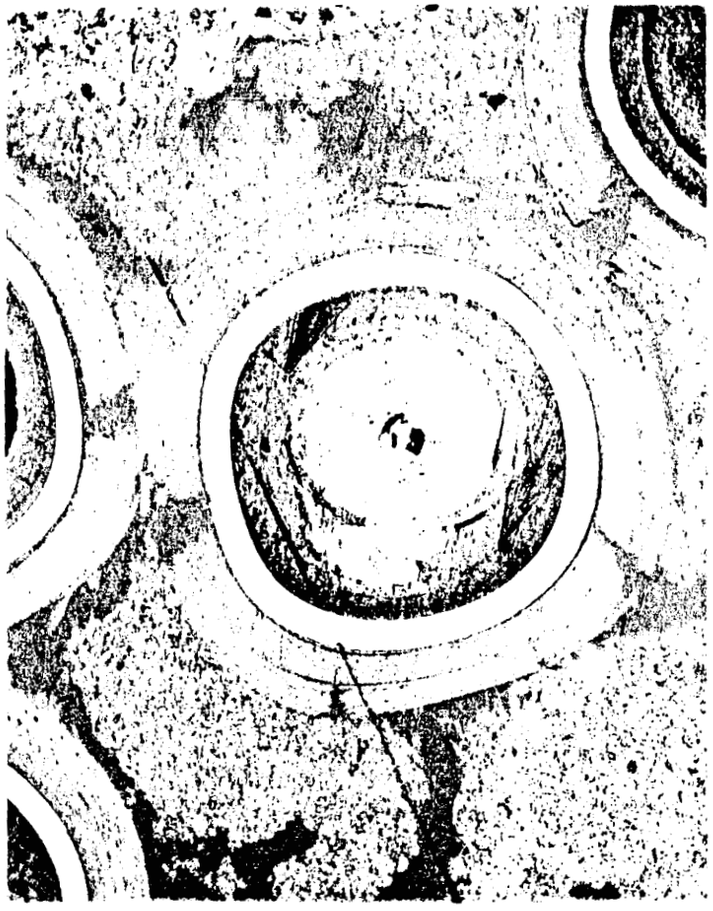

R81266 100μm

Bright Field

R81267 100μm

Polarized Light

Figure 4.6.2.3.9 NPR-1 Compact A-5; Irradiation Conditions of 975°C, 3.7 x 10^{25} n/m^2, 80% FIMA. Remarks: The UCO kernel material swelled out through a crack in the buffer and filled a void left by the shrinking buffer. The polarized light photograph shows the highly anisotropic PPyC seal coats as bright lines with interruptions where the seal coat was cracked by irradiation induced shrinkage. The absence of corresponding cracks in the OPyC and PPyC indicates that cracking of the seal coat did not initiate cracks in the OPyC and PPyC.

ORNL-DWG 93-8932R2

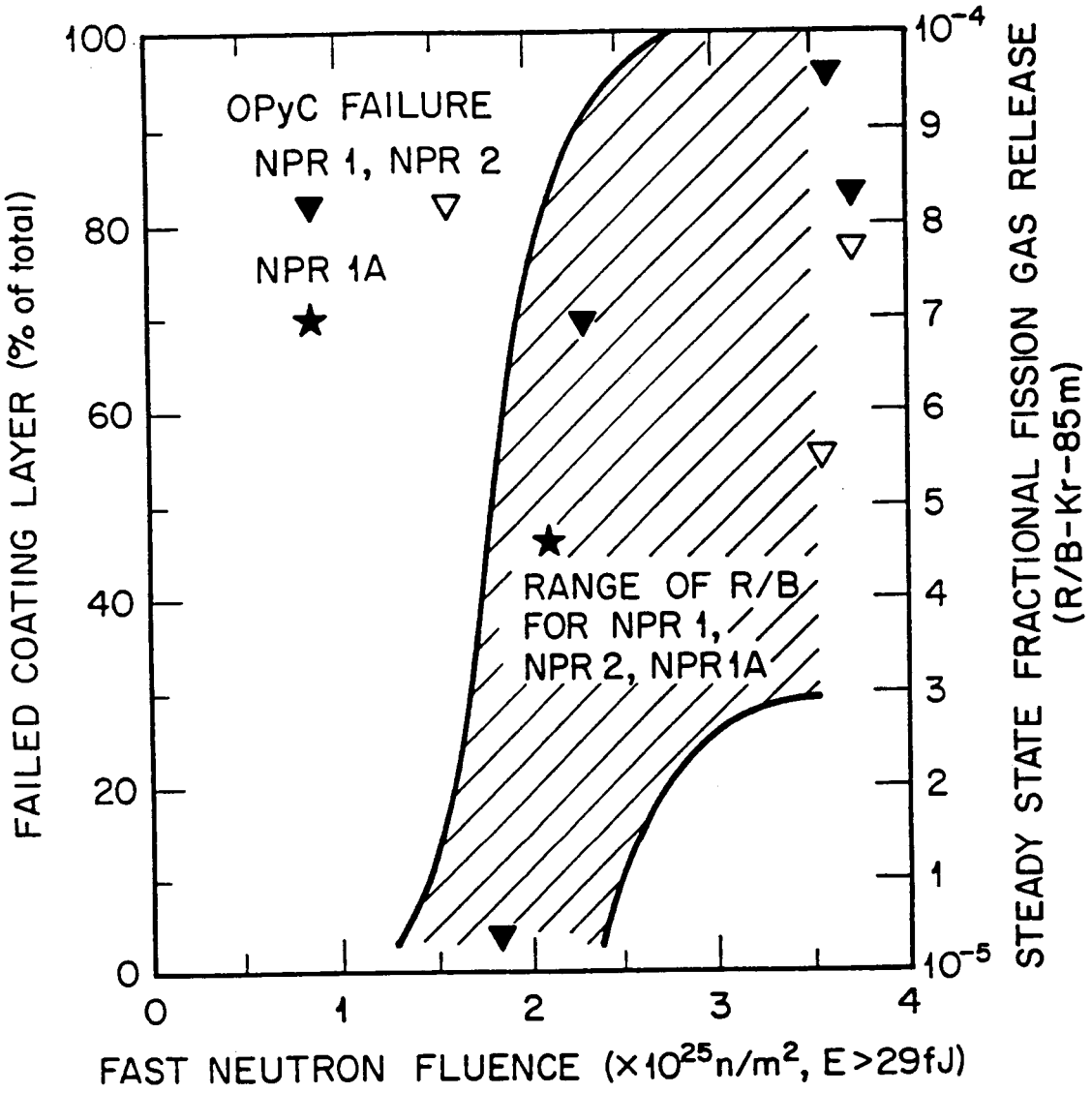

Figure 4.6.2.3.10
NPR 1, NPR 2, and NPR 1A Was a Strong Function of Fast Neutron Exposure and Correlated with Increasing Fission Gas Release

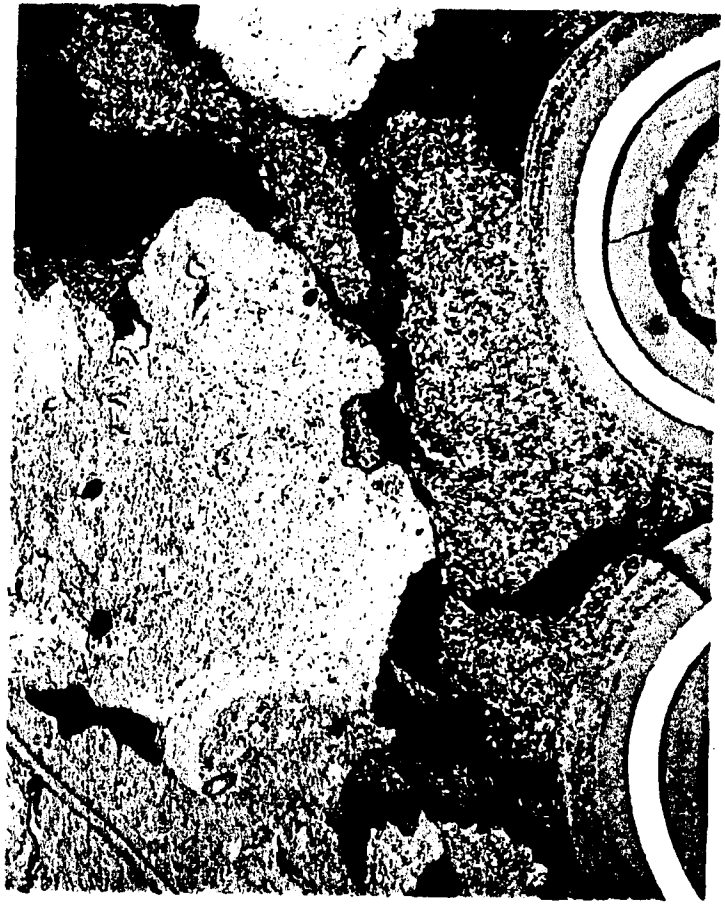

R81041

100μm

R81042

100μm

Figure 4.6.2.3.11 NPR-2 Compact A-4; Irradiation Conditions of 730°C, 3.7 x 10^{25} n/m^2, 80% FIMA. Remarks: There was no evidence of detrimental matrix-coating interaction. The matrix was very porous and weak.

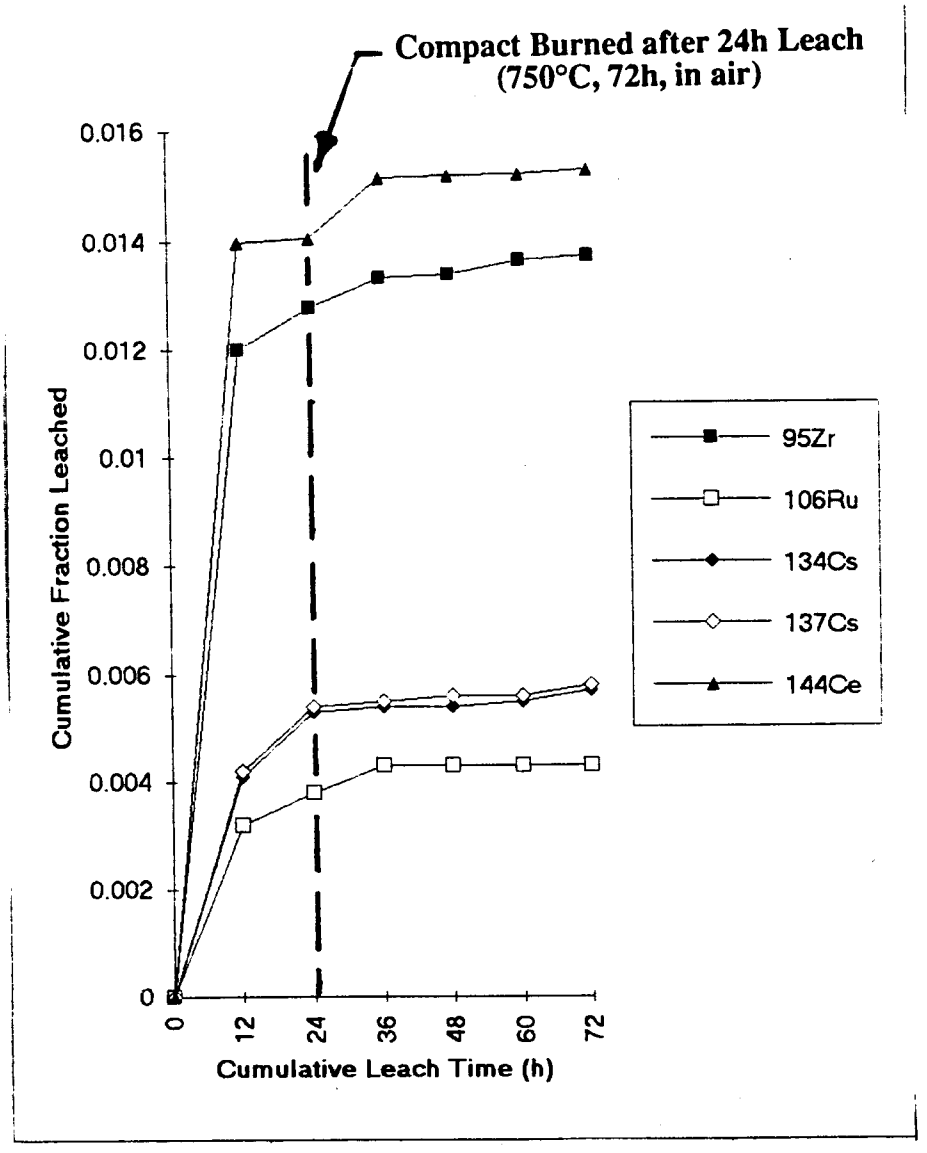

Figure 4.7.1.1

Compact NPR 1 B6 Leach Burn Leach
Fractional Fission Product Leach Versus Leach Time

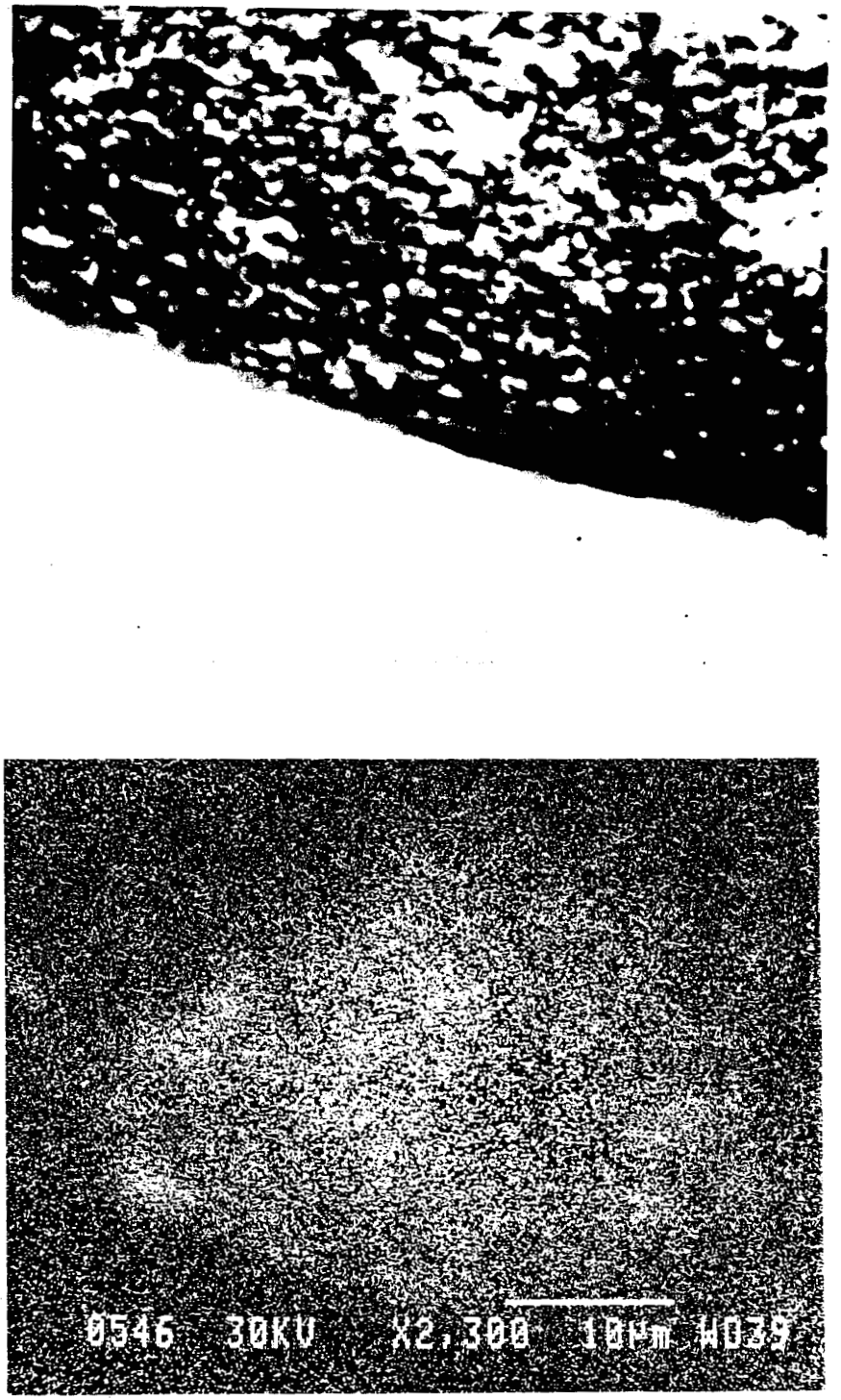

Fig. 4.8.1. Particle B4-P4 showing a Ba x-ray image of the inside surface of the SiC (upper half) and the polished section of the SiC (lower half). 2300X

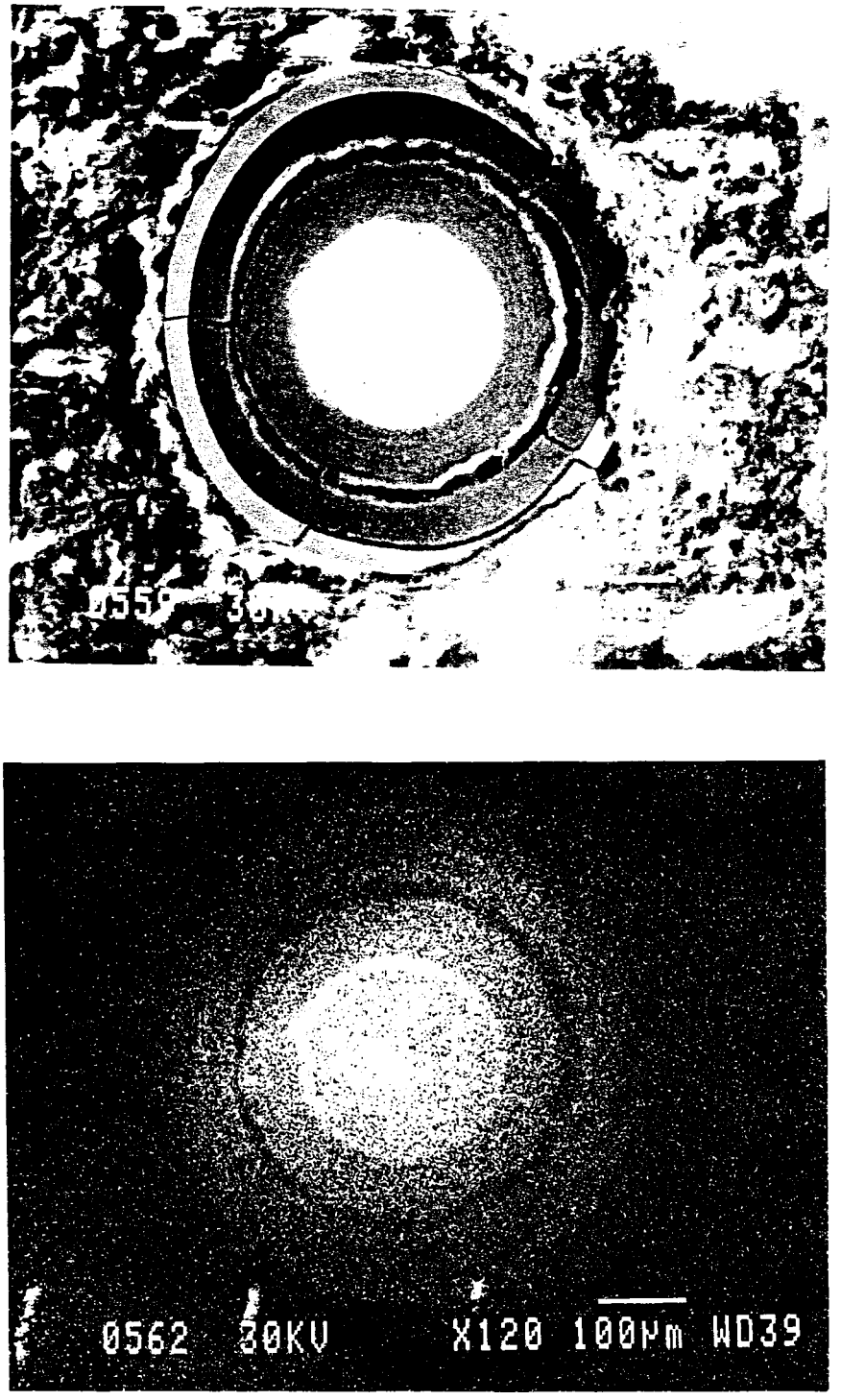

Fig. 4.8.2. Particle B5-P1 showing a Ba x-ray image of the entire particle, which contains a portion of the fuel kernel. 120X

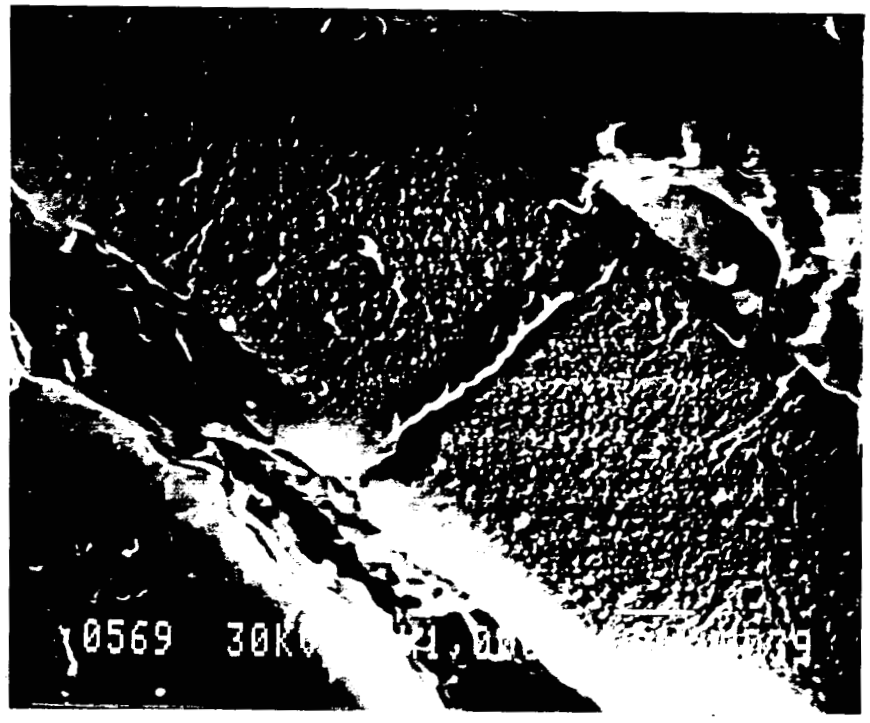

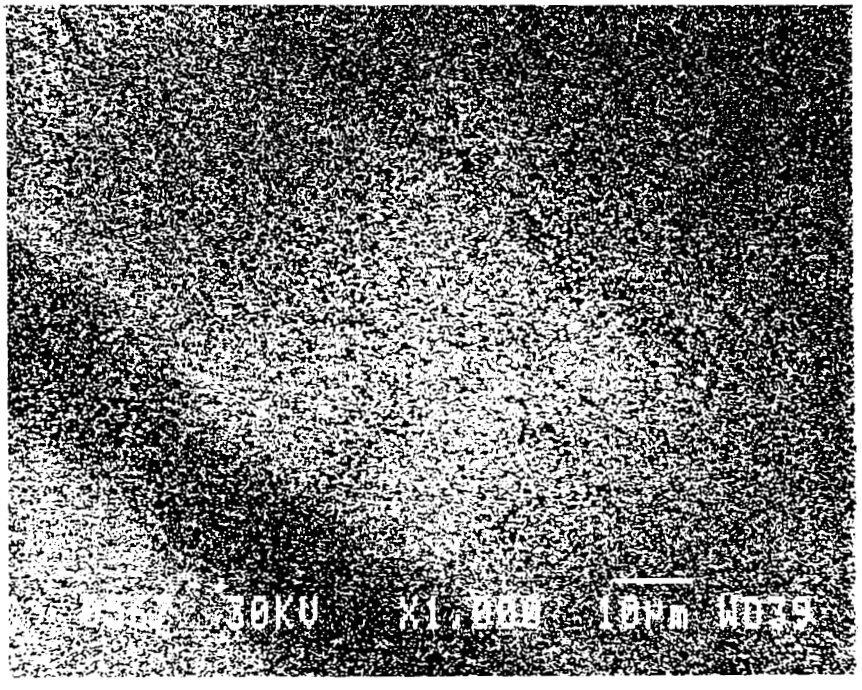

Fig. 4.8.3. Particle B5-P1 showing a Ba x-ray image of the IPyC in the region of a crack. 1000X

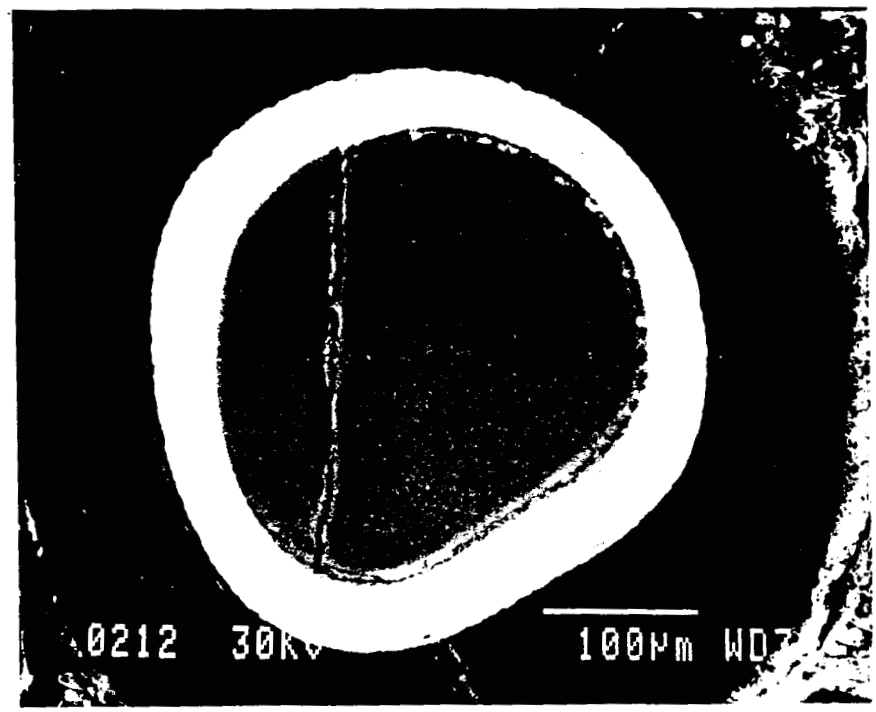

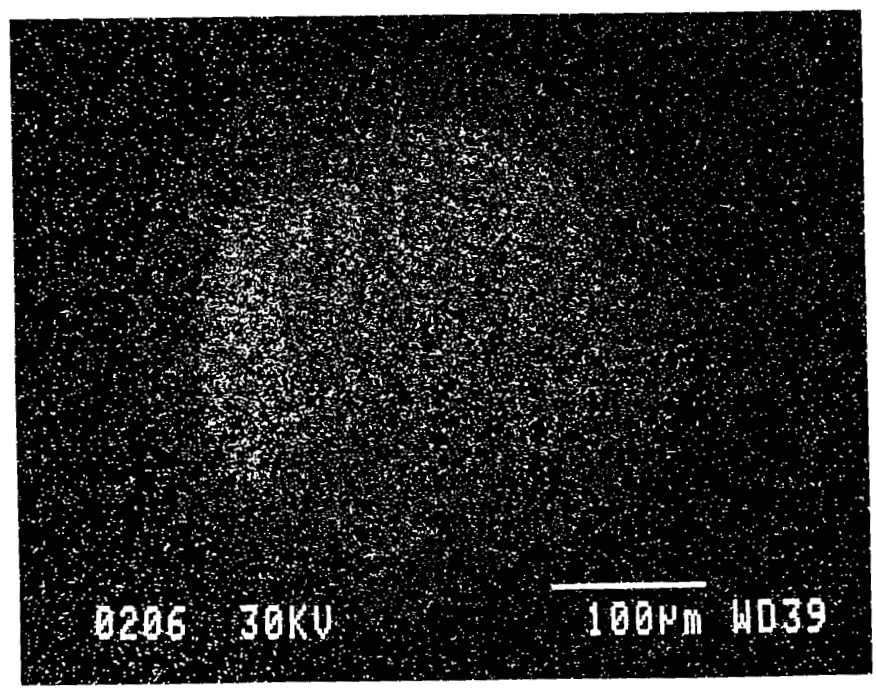

Fig. 4.8.4. Particle B4-P7 showing a Ba x-ray image of the entire particle. 200X

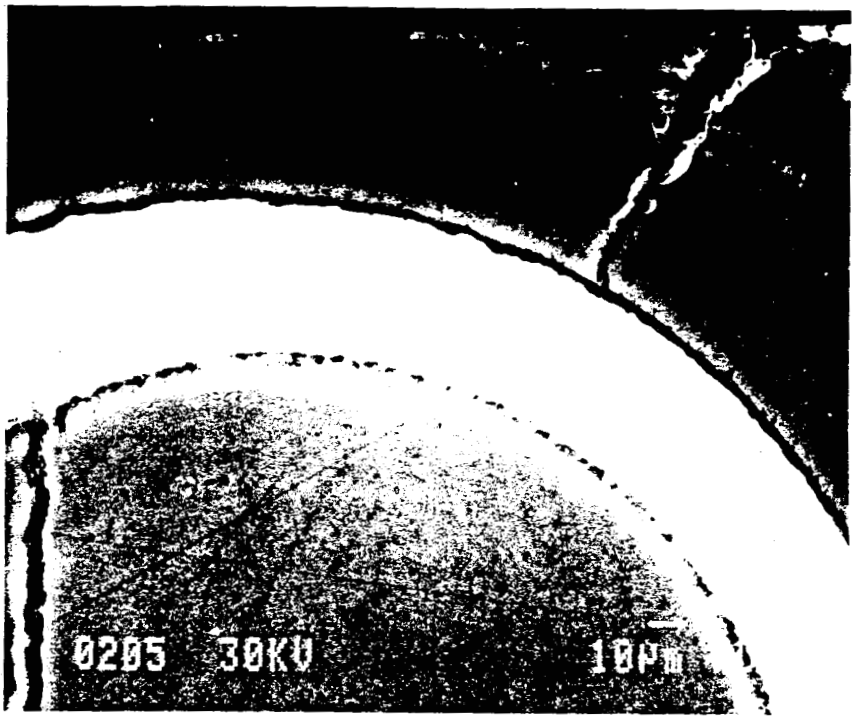

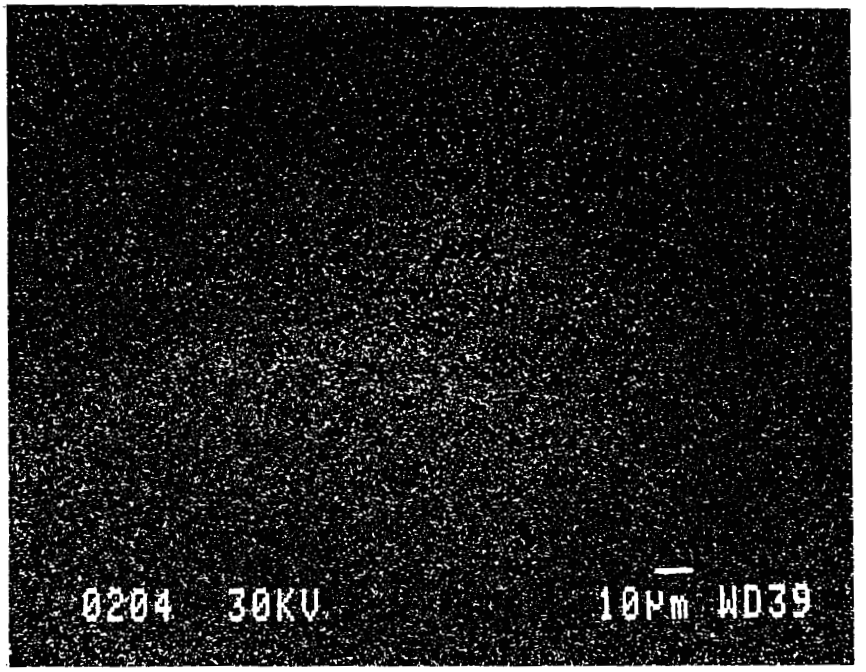

Fig. 4.8.5. Particle B4-P7 showing a Ba x-ray image of the SiC and surrounding layers in the vicinity of two cracks. 500X

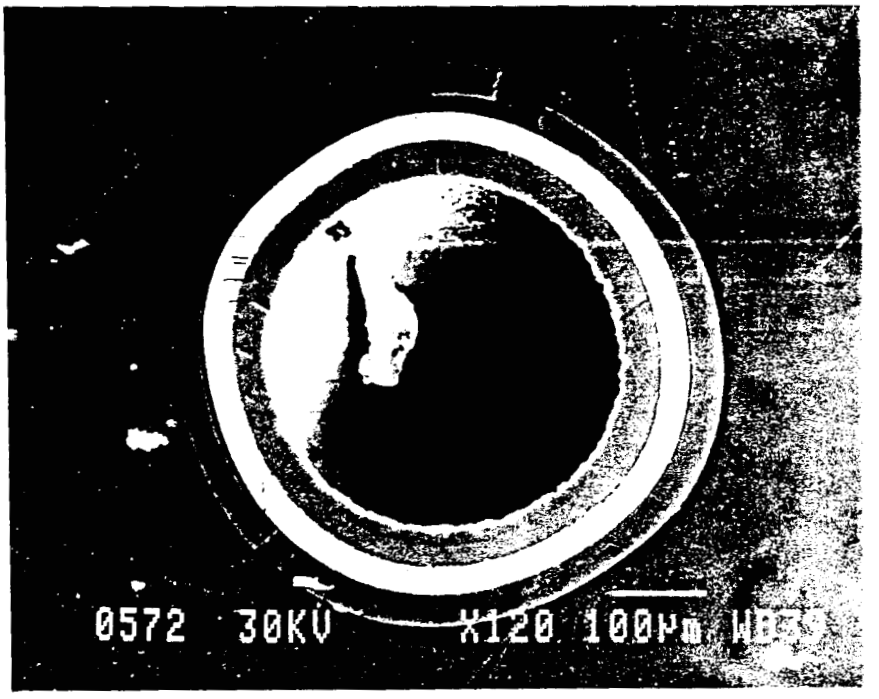

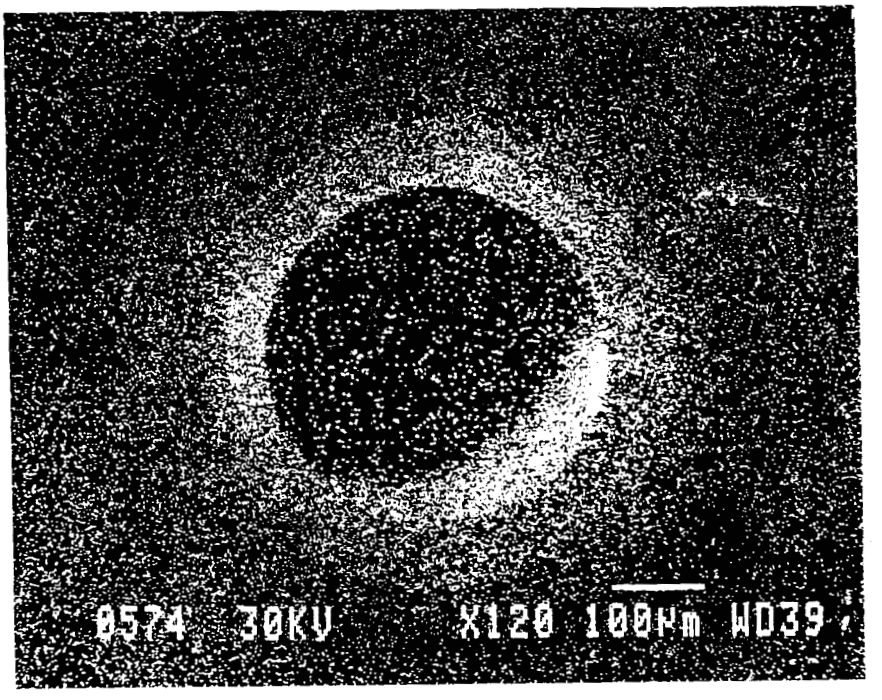

Fig. 4.8.6. Particle B5-P3 showing a Ba x-ray image of the entire particle. The concentration of Ba in the lower right is an artifact resulting from covering too wide an angle at low magnification. 120X

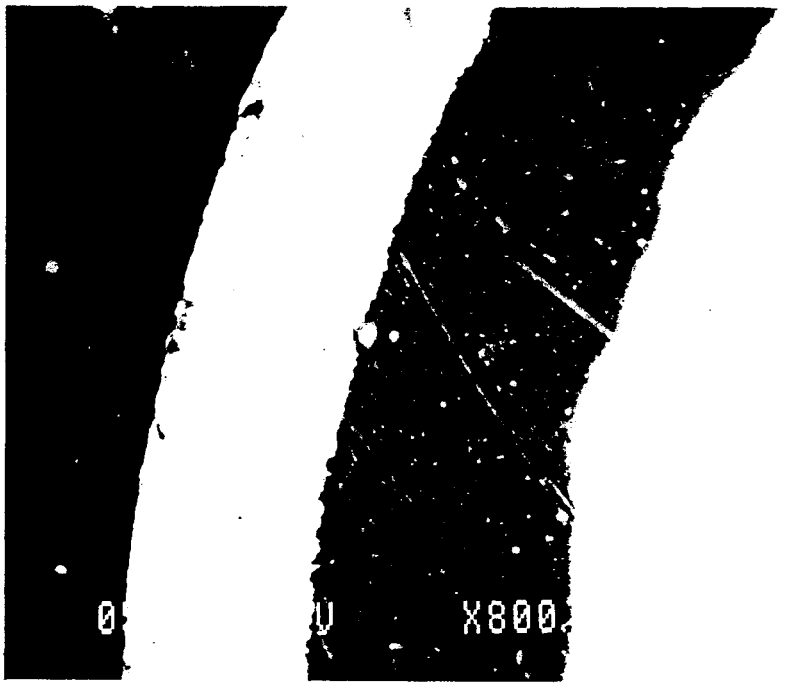

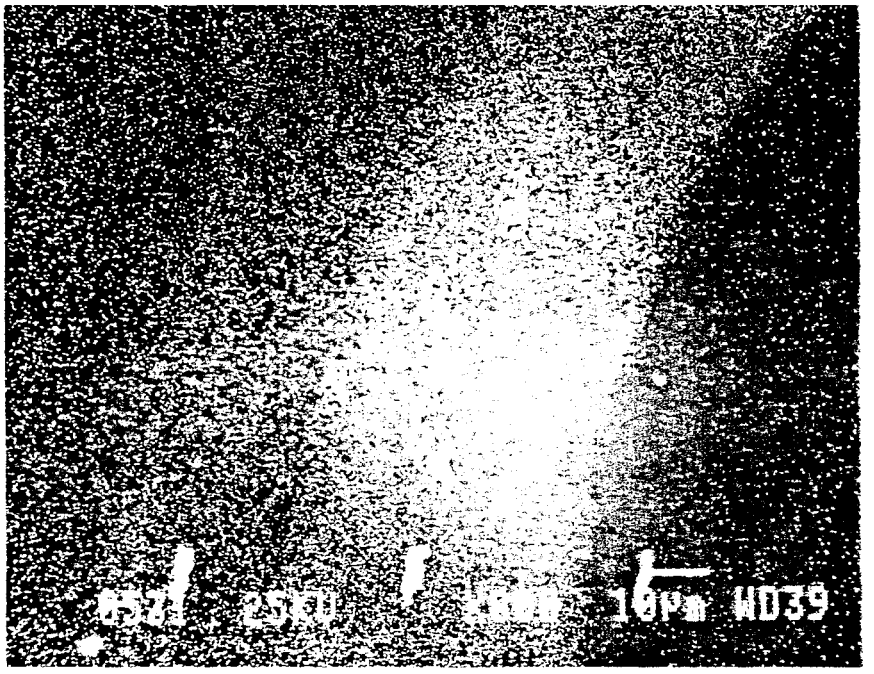

Fig. 4.8.7. Particle B5-P3 showing a Ba x-ray image of the SiC and surrounding layers. 800X

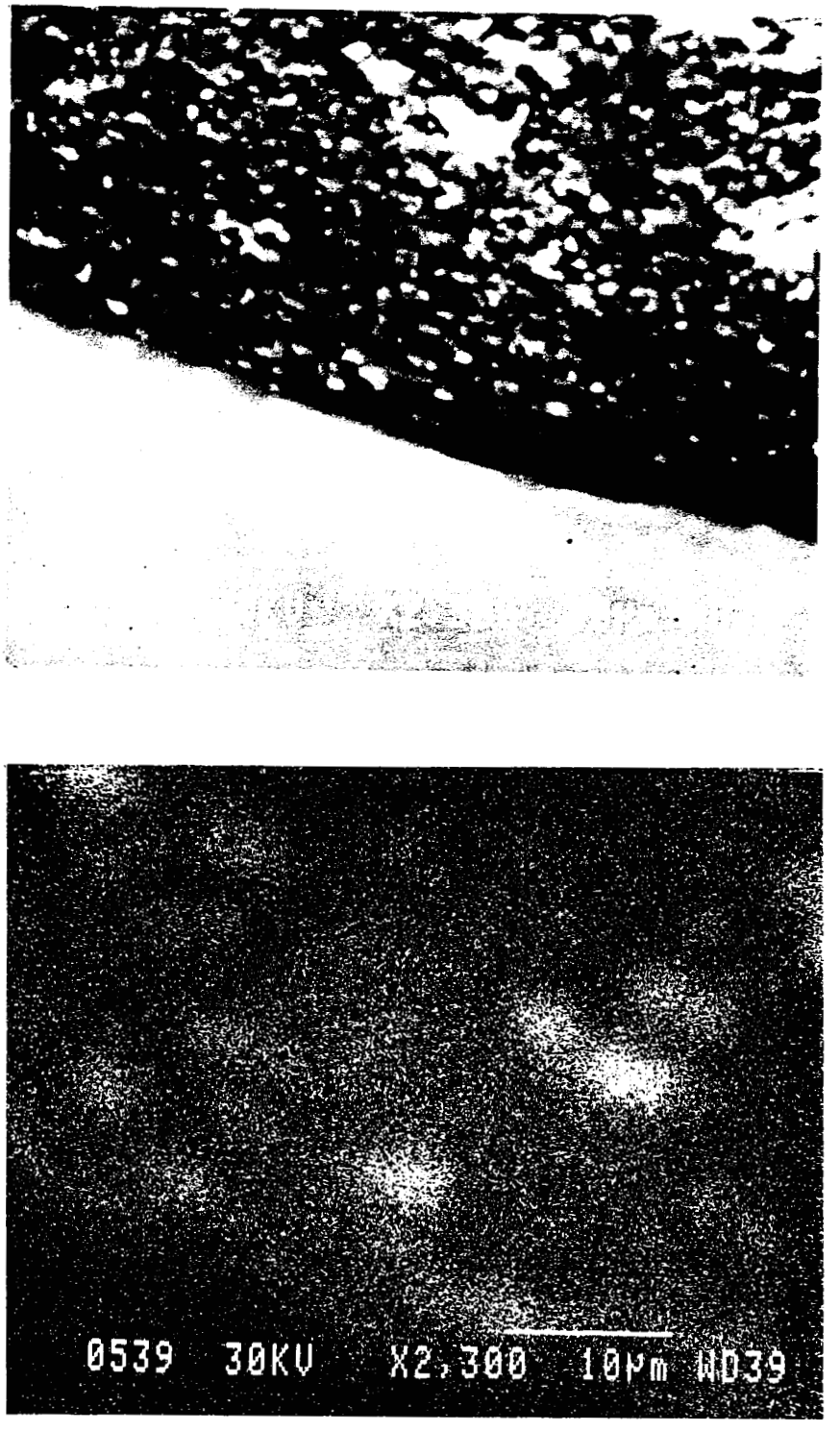

Fig. 4.8.8. Particle B4-P4 showing a Pd x-ray image of the SiC layer. The IPyC has fallen out exposing the inner surface of the SiC in the upper half of the figure. 2300X

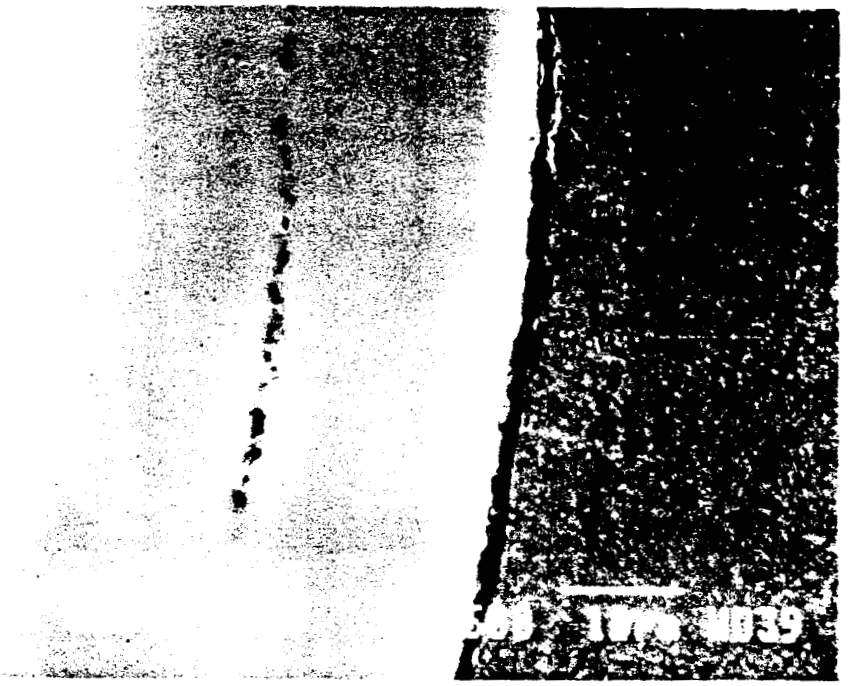

Fig. 4.8.9. Particle B4-P4 showing a "gold spot" defect in the SiC. 1500X

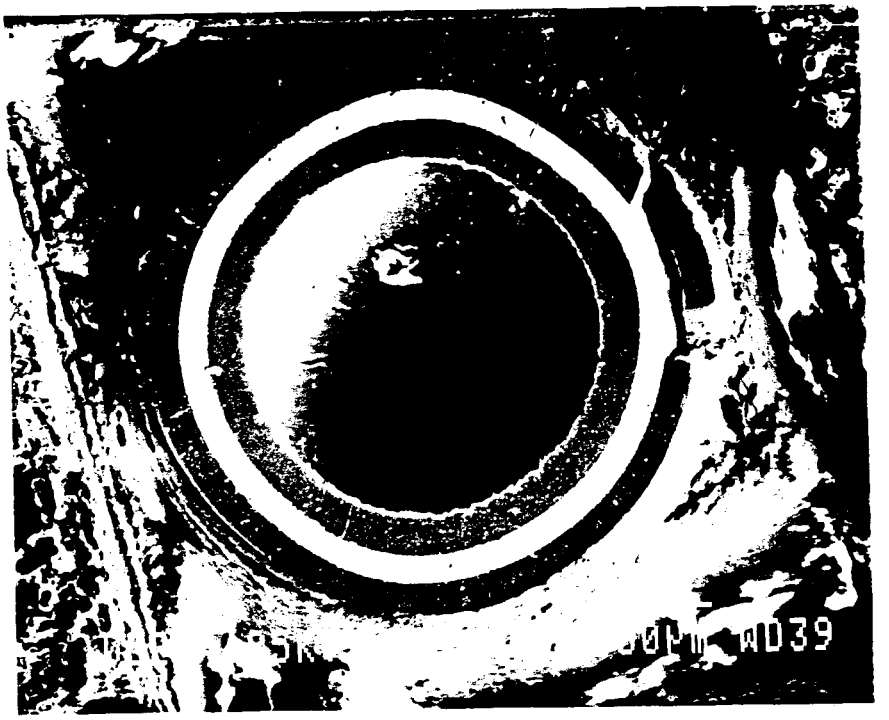

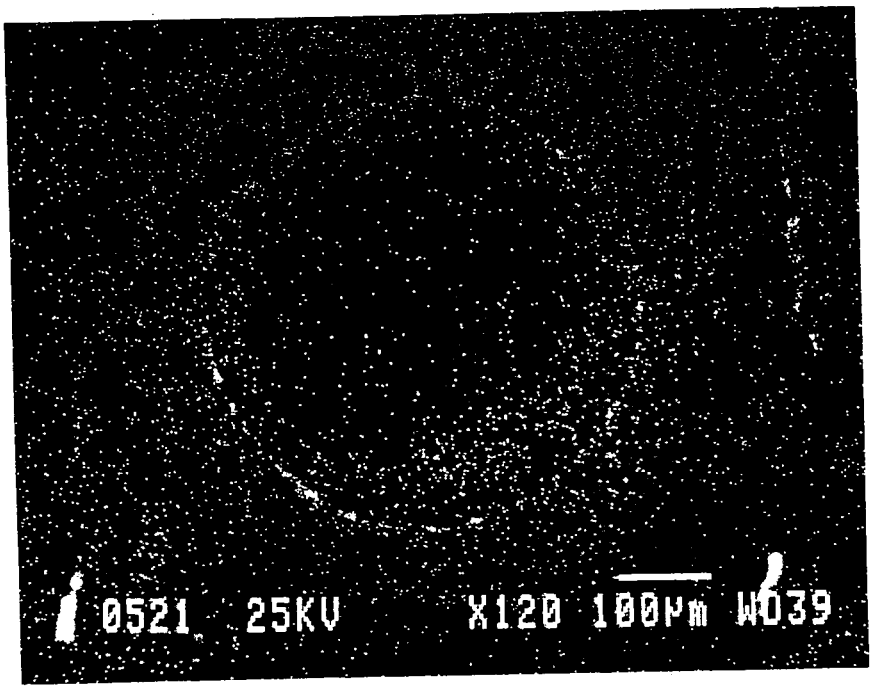

Fig. 4.8.10. Particle B5-P3 showing a Pd x-ray image of the entire particle. Pd is concentrated at the SiC/IPyC interface. 120X

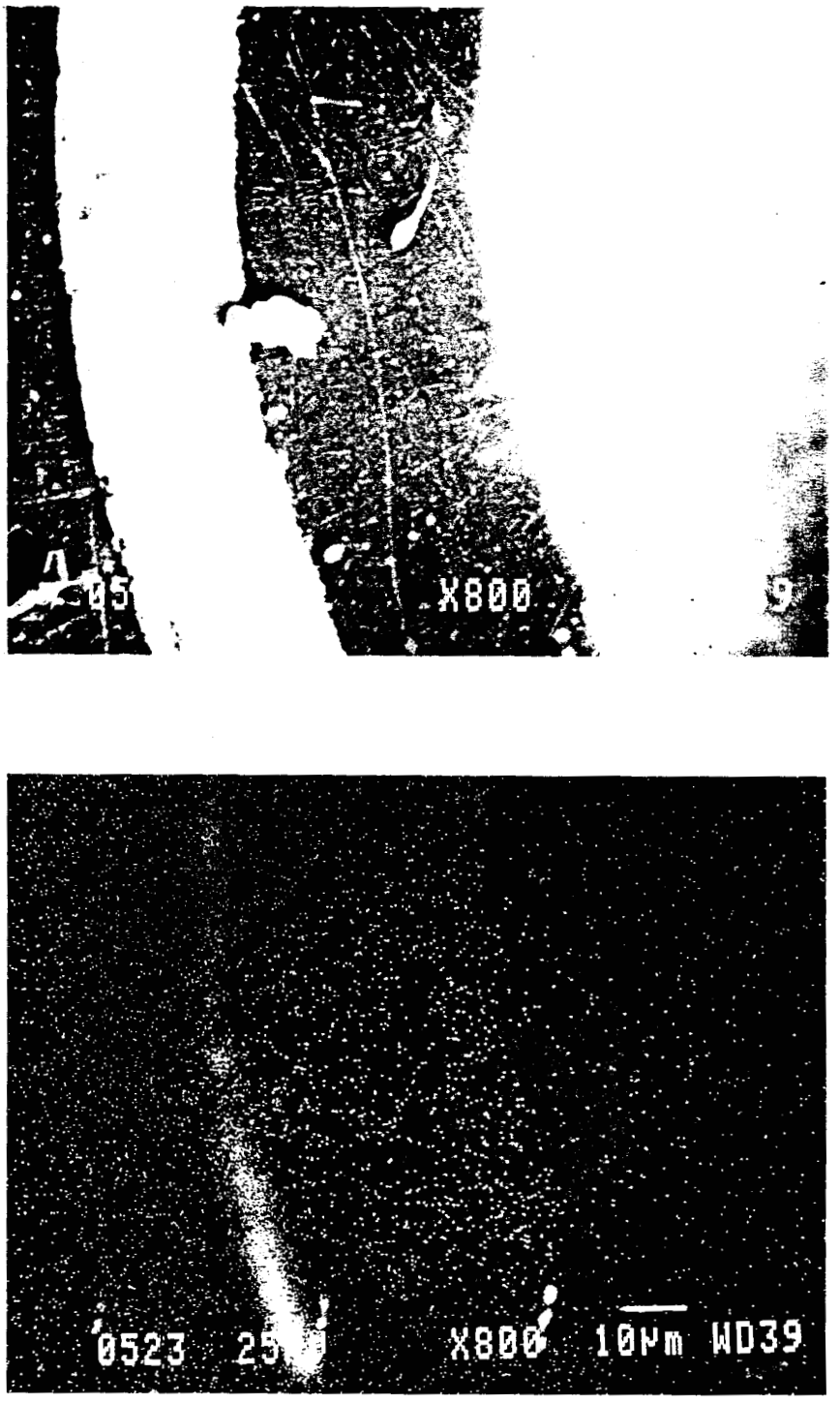

Fig. 4.8.11. Particle B5-P3 showing a Pd x-ray image of the SiC and surrounding layers. 800X.

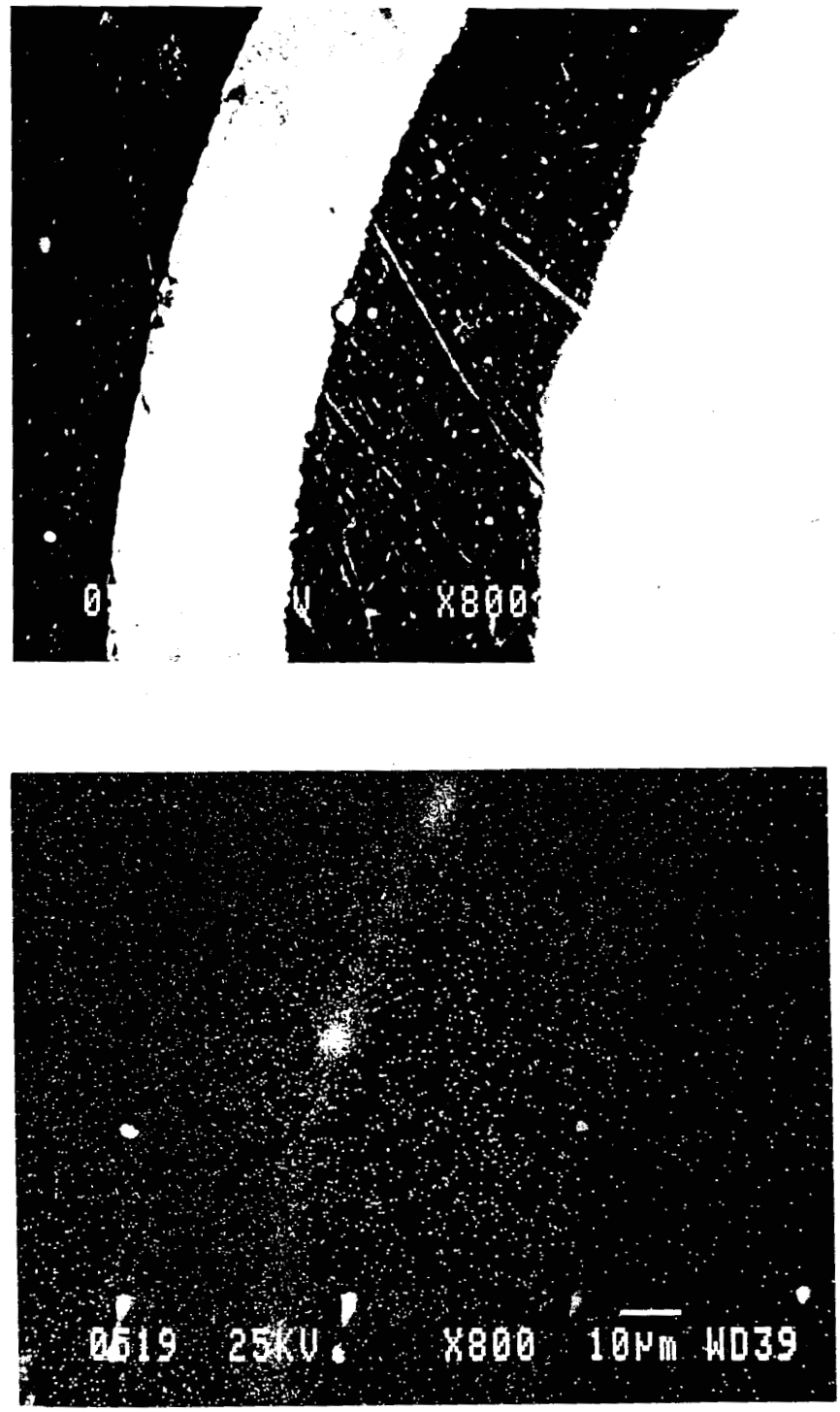

Fig. 4.8.12. Particle B5-P3 showing a Pd x-ray image of the SiC and adjacent layers. Pd is concentrated at the SiC/IPyC interface. A Pd-rich particle appears in the center along the SiC/IPyC interface. 800X

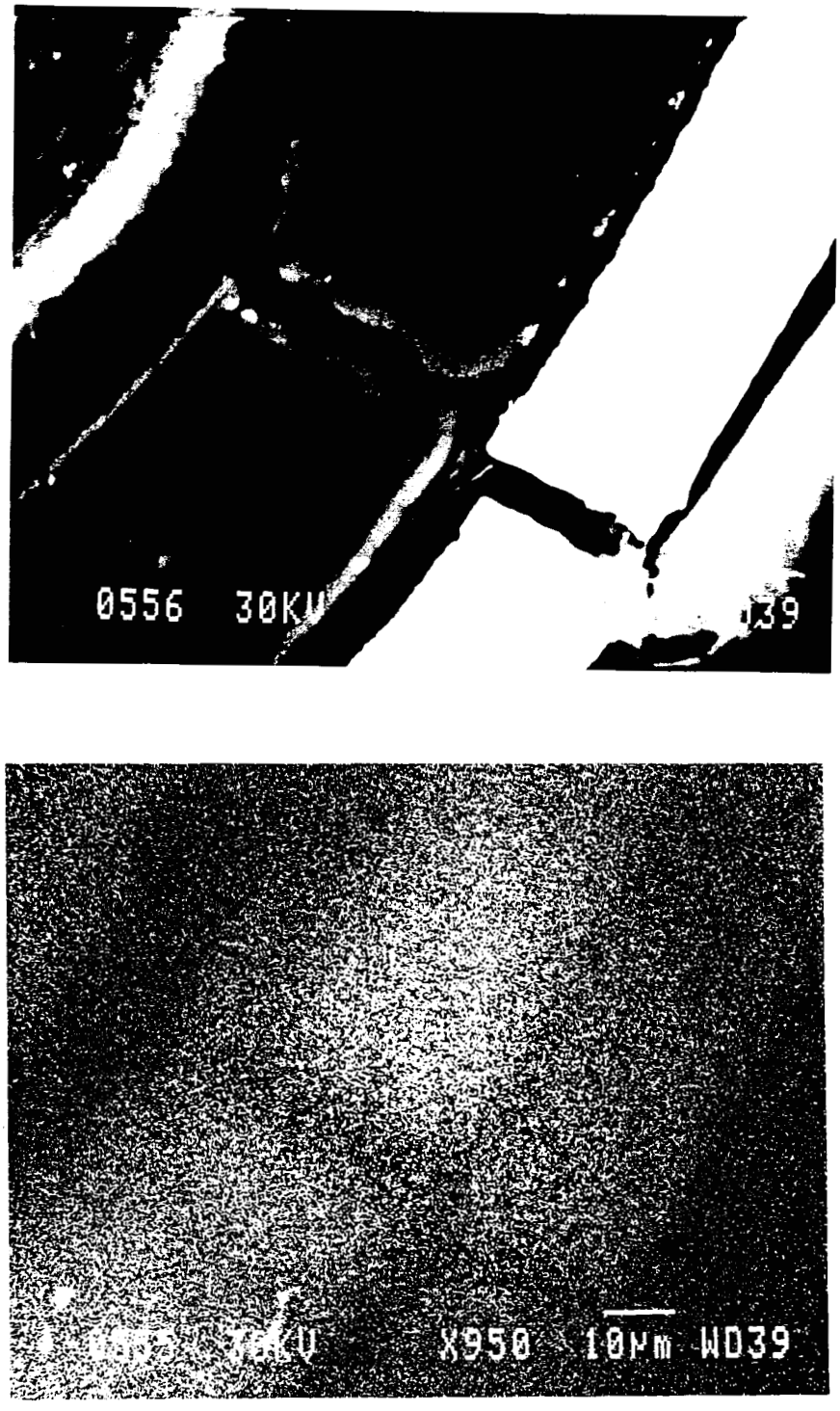

Fig. 4.8.13. Particle B5-P1 showing cracks in the IPyC and SiC and a Cs x-ray image of the region. No elements were found segregated at the crack. 950X

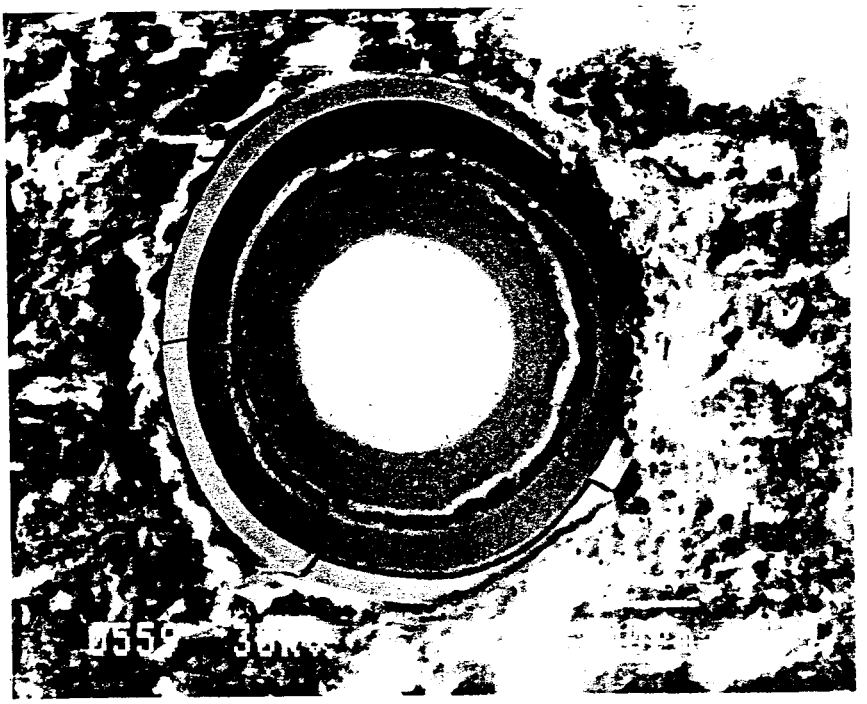

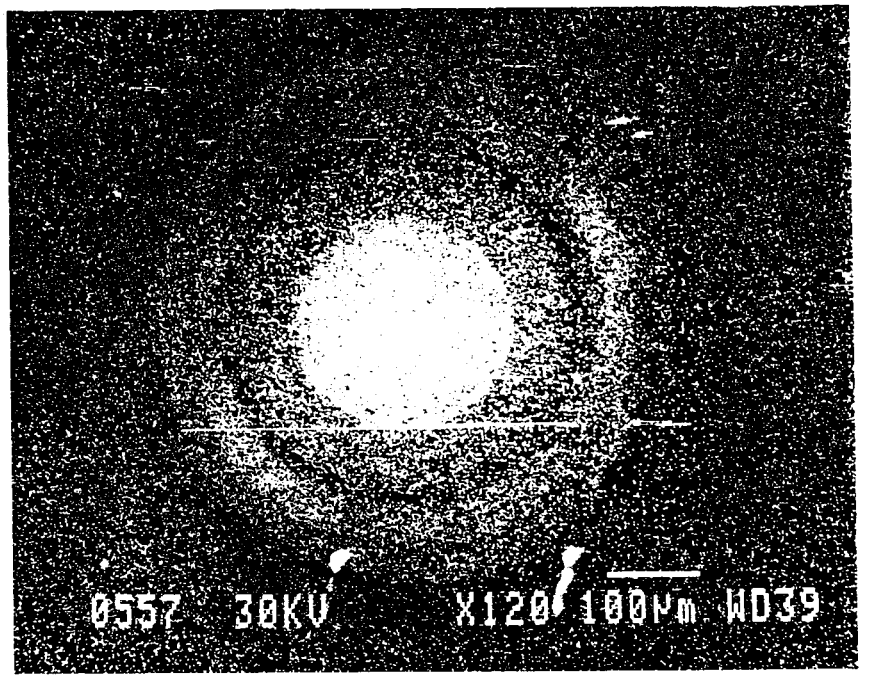

Fig. 4.8.14. Particle B5-P1 showing a Cs x-ray image of the entire particle. This section includes a portion of the fuel kernel. 120X

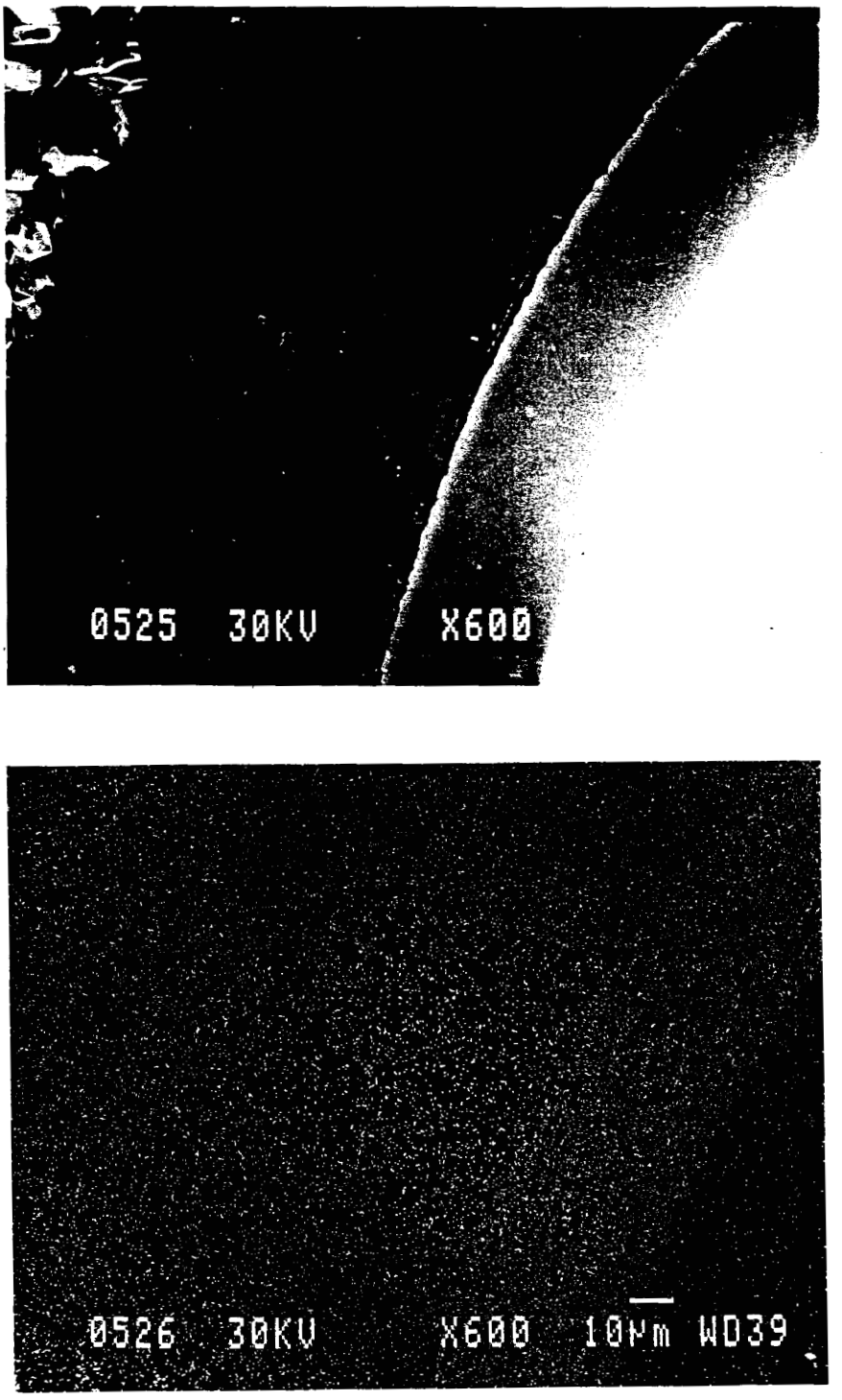

Fig. 4.8.15. Particle B4-P4 showing a Cs x-ray image of the SiC and outer layers. 600X

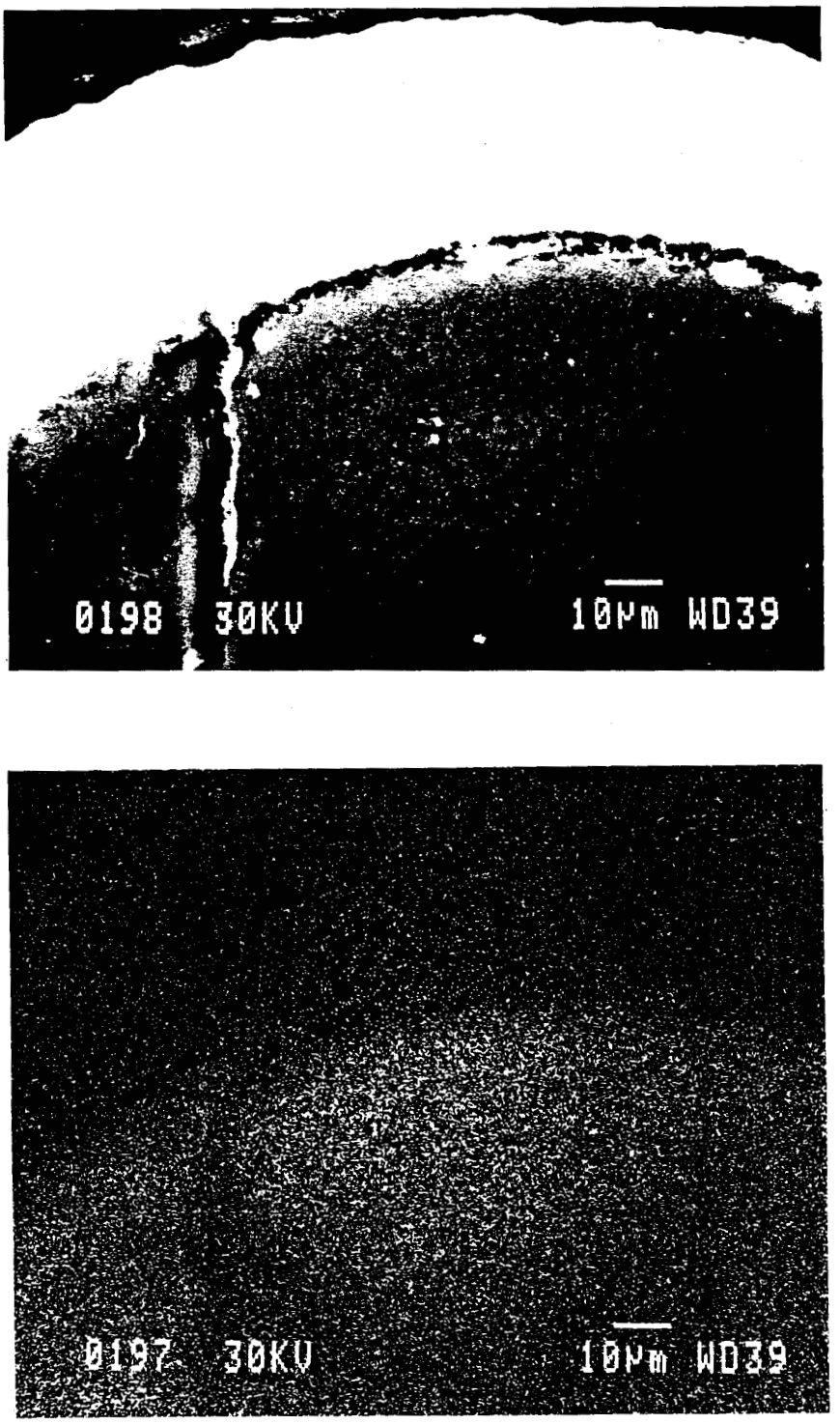

Fig. 4.8.16. Particle B4-P7 showing a Cs x-ray image of a section of the SiC and IPyC illustrating a lack of penetration of Cs into the SiC. 750X

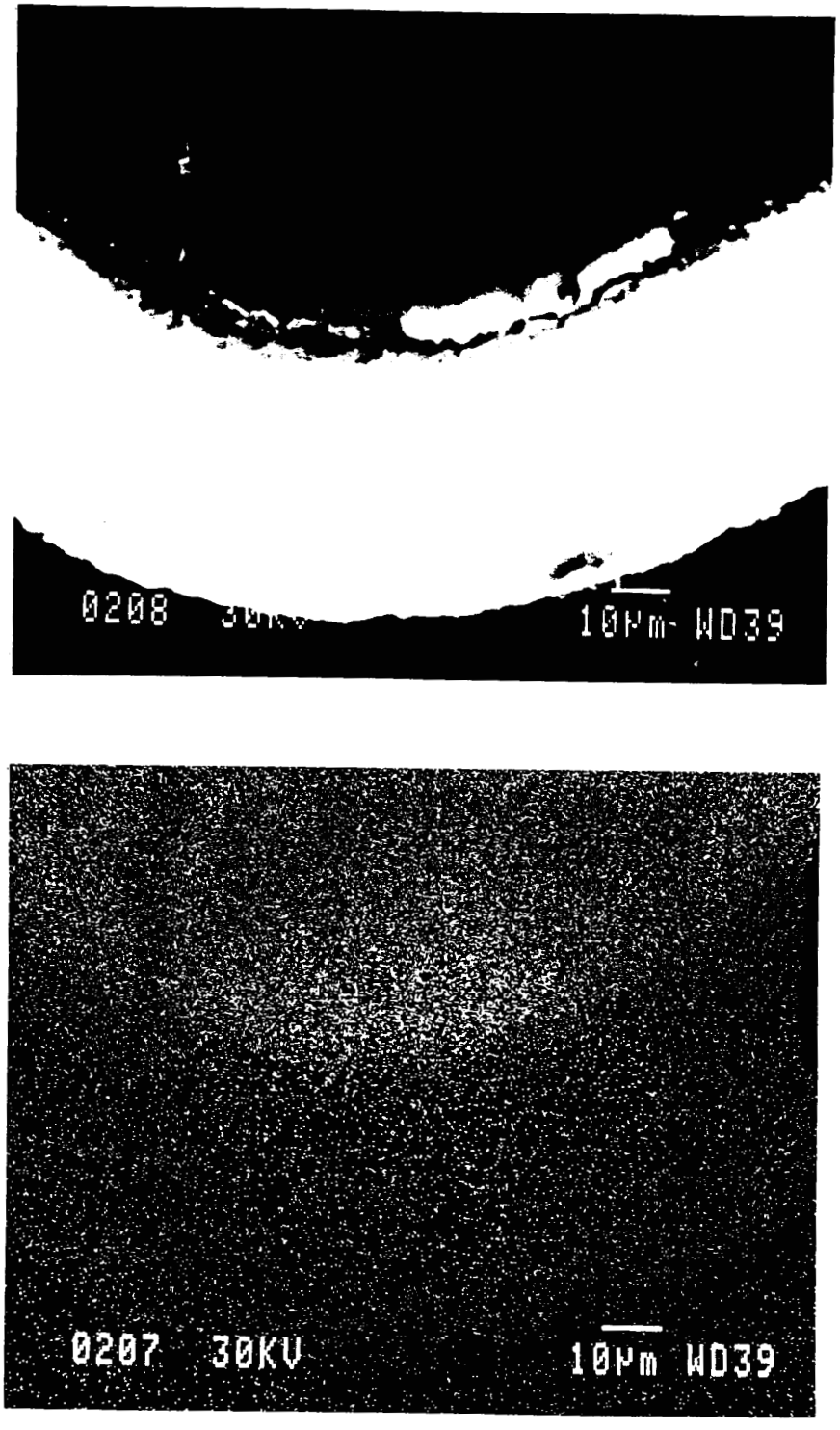

Fig. 4.8.17. Particle Br-P7 showing a Cs x-ray image in the region of a crack in the IPyC. Cs does not uppear to penetrate the SiC or segregate at the crack. 800X

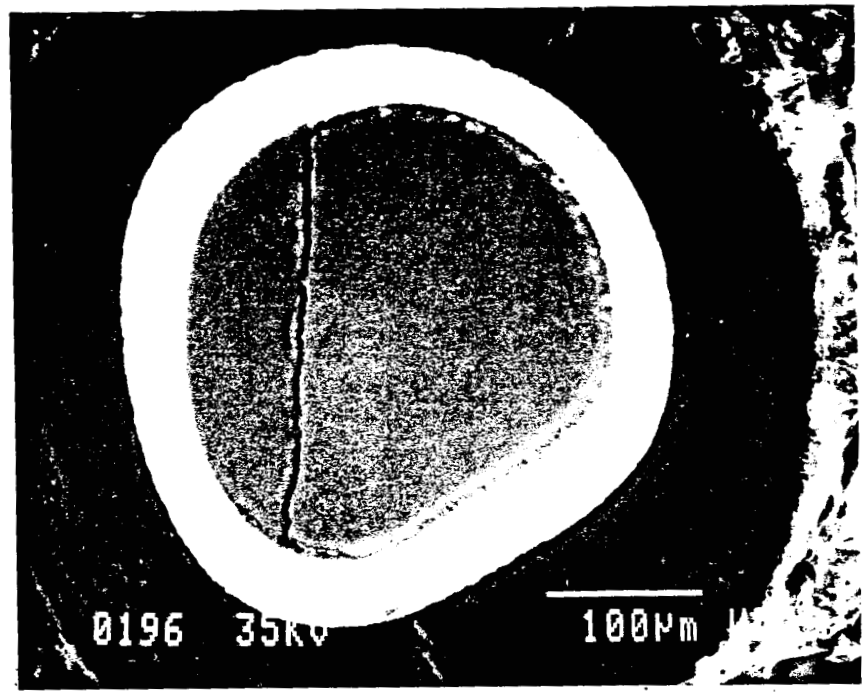

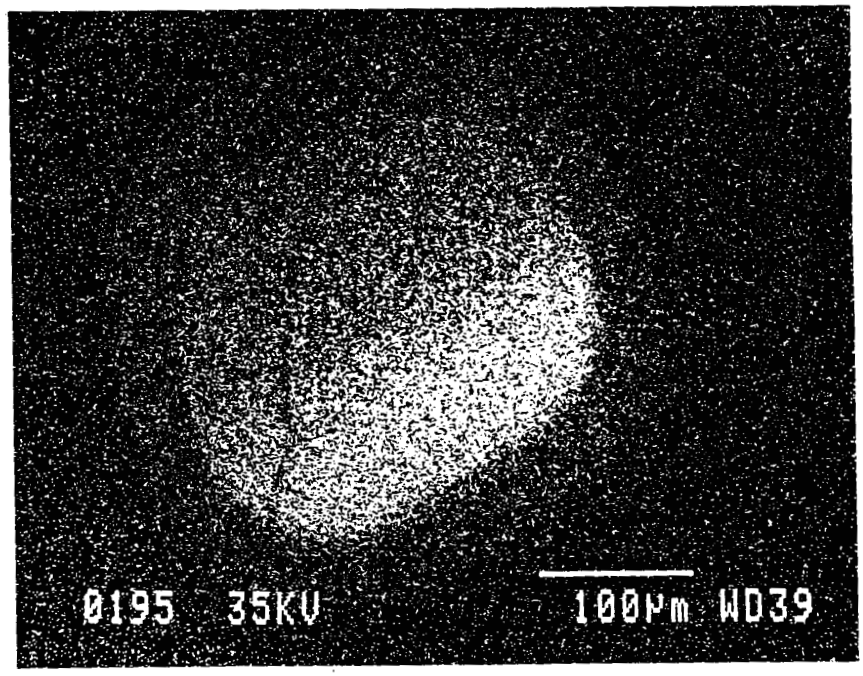

Fig. 4.8.18. Particle B4-P7 showing a Cs x-ray image of the entire particle. 200X

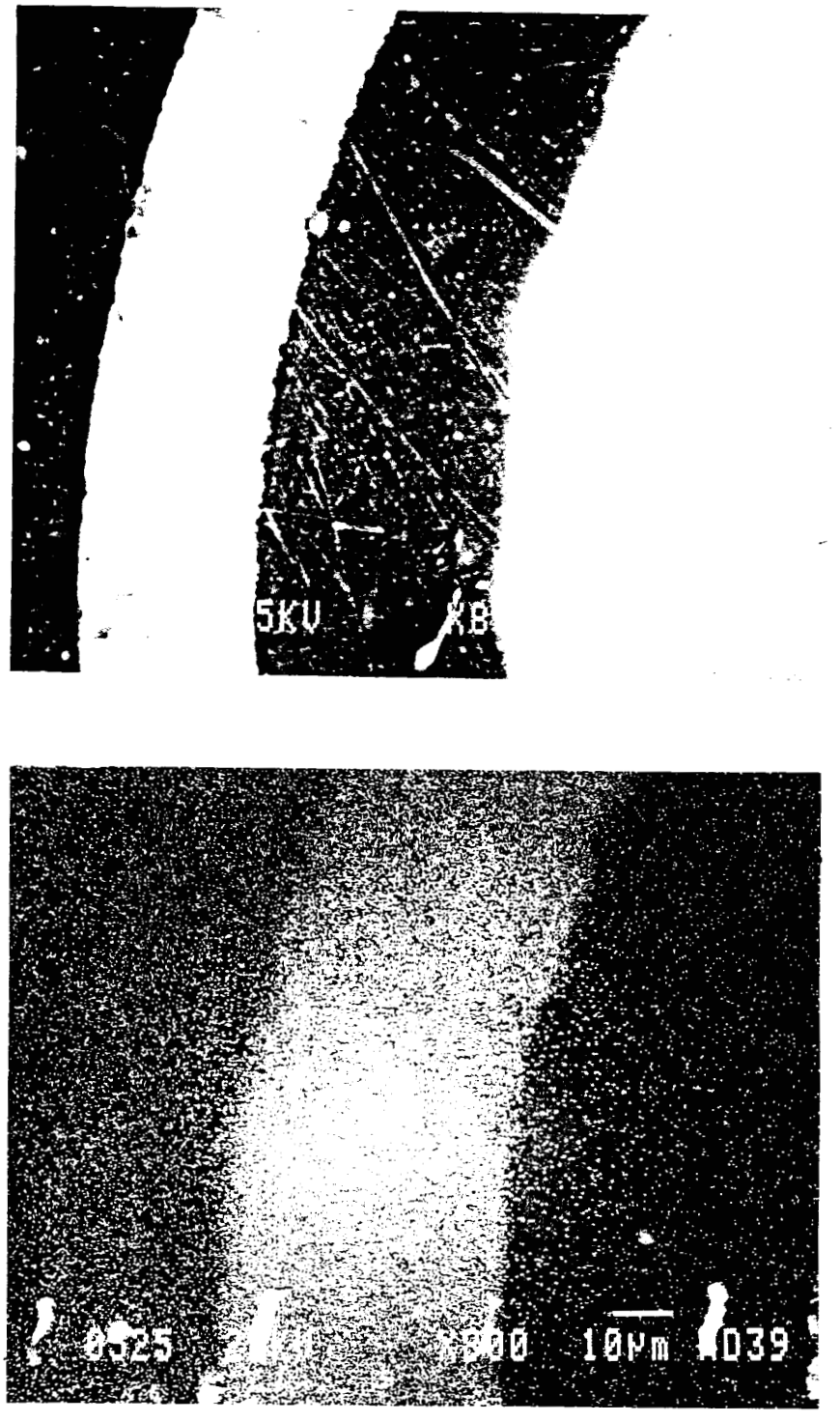

Fig. 4.8.19. Particle B5-P3 showing a Cs x-ray image of the SiC and surrounding layers. 800X.

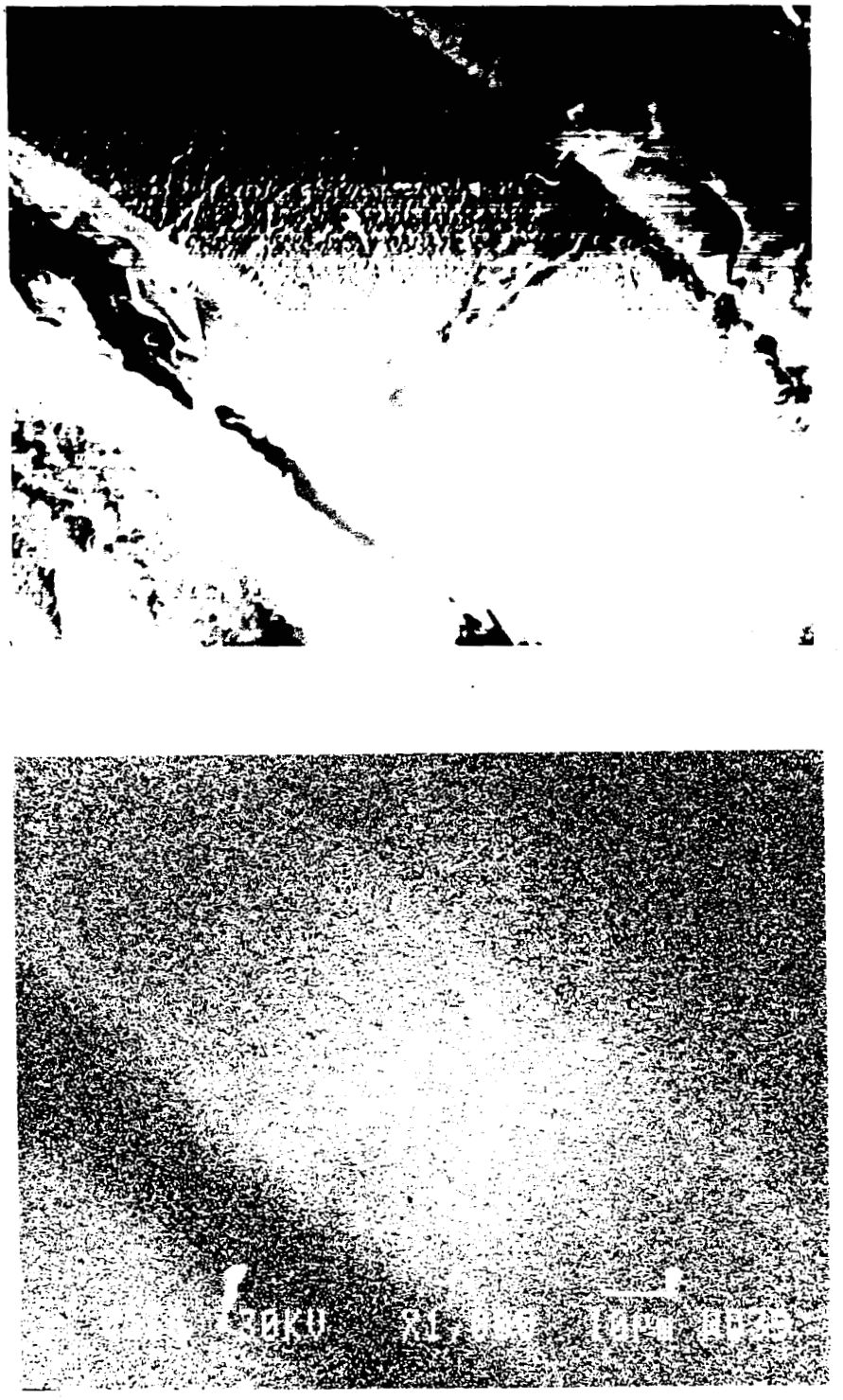

Fig. 4.8.20. Particle B5-P1 showing a Ce x-ray image exhibiting Ce in the IPyC. The SiC is partially covered by epoxy mounting medium in the upper right. The horizontal lines in the top of the upper photo resulted from changing of the epoxy. 1000X

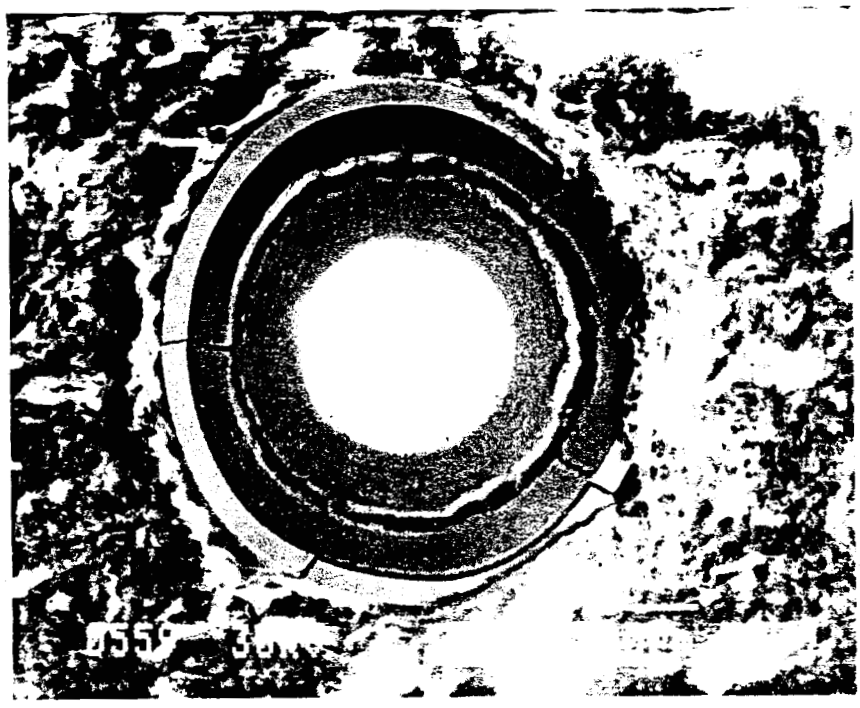

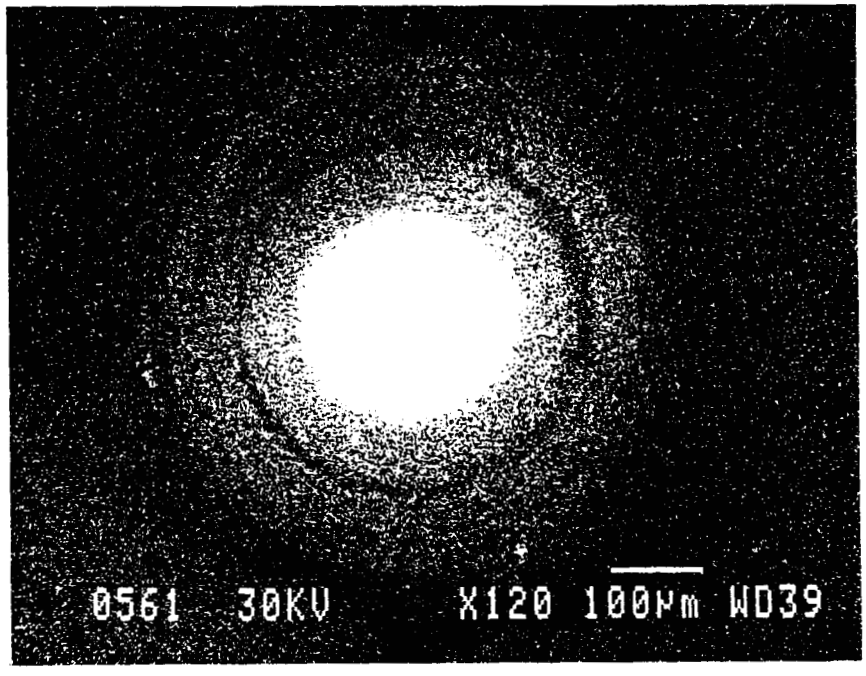

Fig. 4.8.21. Particle B5-P1 showing a Ce x-ray image of the entire particle. The Ce signal appears to be in all layers present. 120X

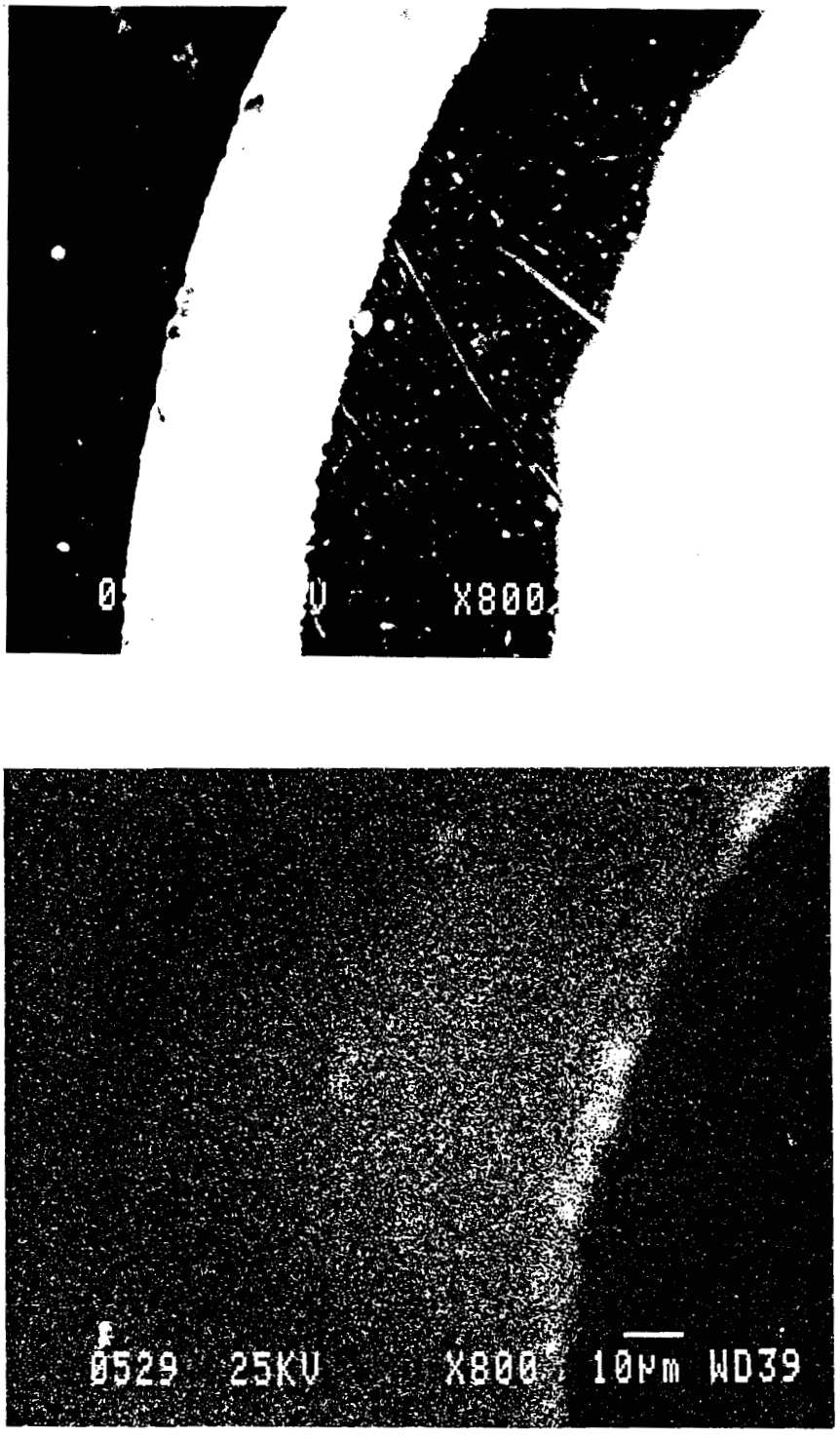

Fig. 4.8.22. Particle B5-P3 showing a Ce x-ray image of the SiC and surrounding layers in the same region as Fig. 4.8.7. The concentration is seen to be greater in the IPyC than in the SiC. 800X

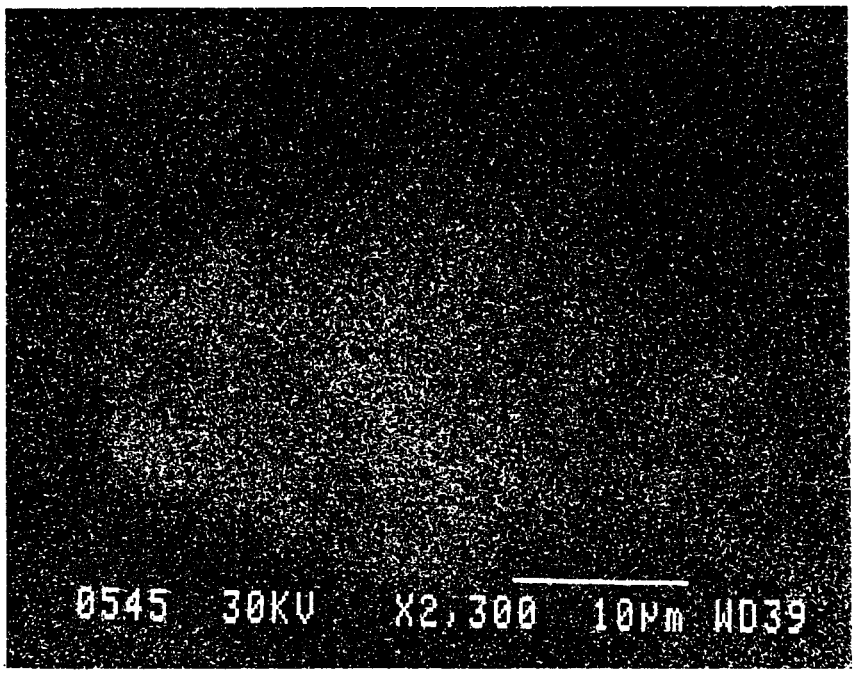

Fig. 4.8.23. Particle B4-P4 showing a Ce x-ray image of the inside of the SiC layer (upper half) and the polished surface of the SiC (lower half). 2300X

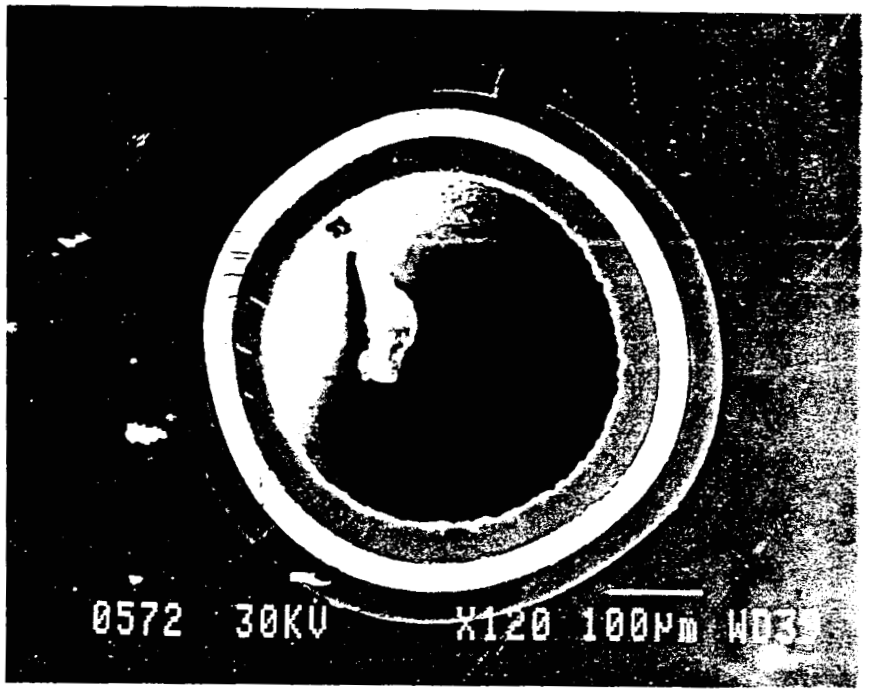

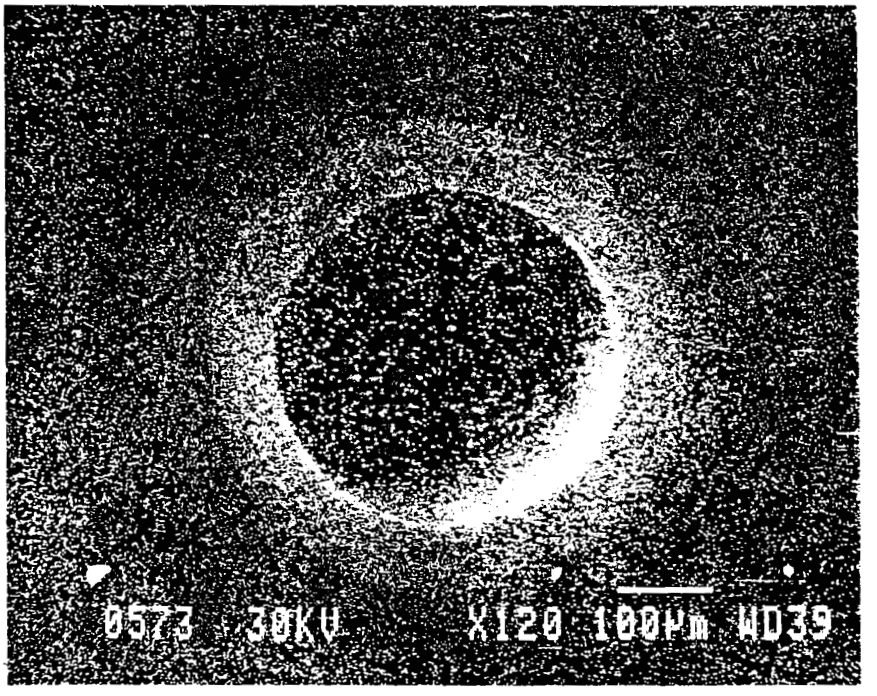

Fig. 4.8.24. (a) Overall views of particle B5-P3 showing the distribution of Ce in the SiC and adjacent layers. The high concentration at 5 o'clock is an artifact that results from covering too wide an angle at low magnification. 120X

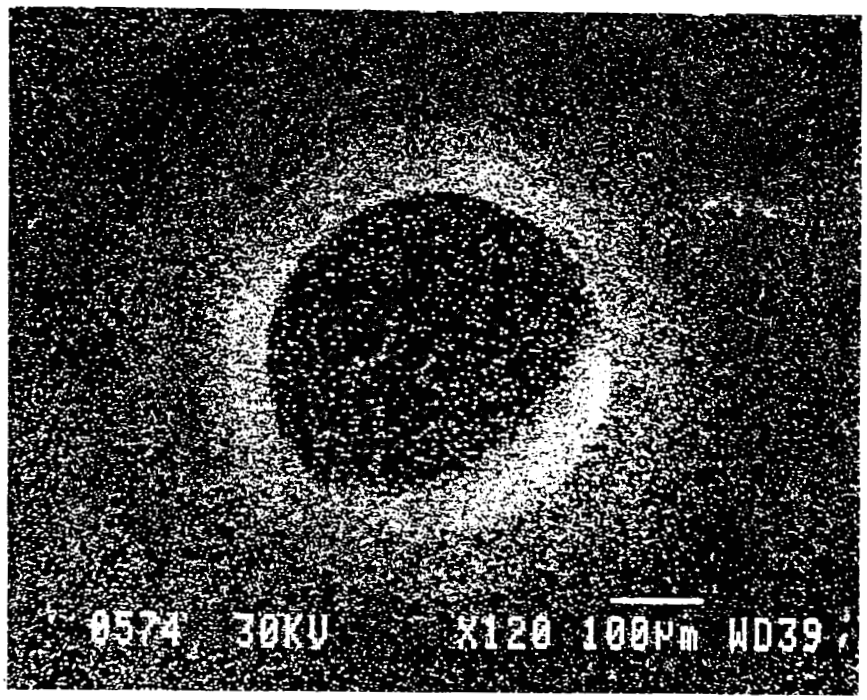

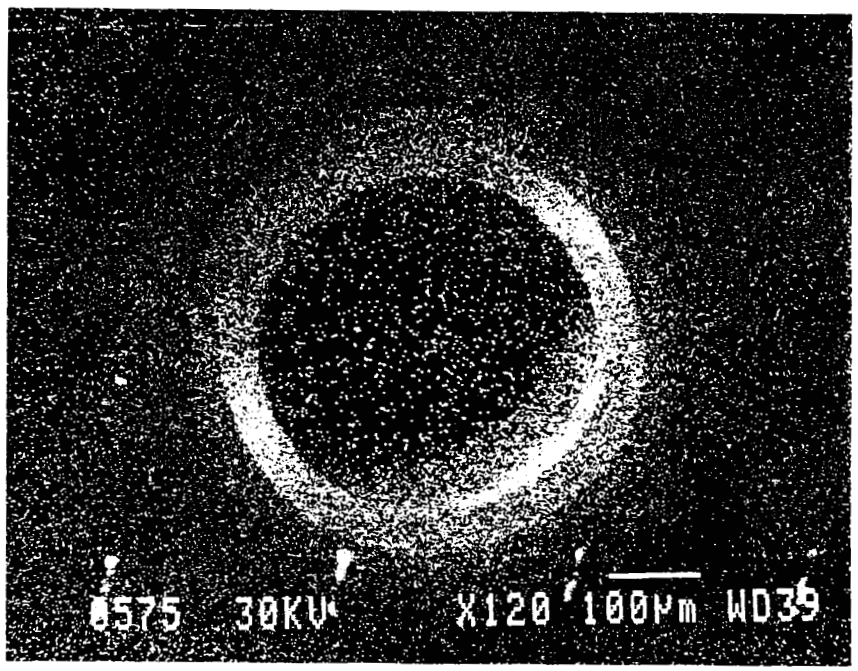

Fig. 4.8.24. (b) Complement to (a) showing x-ray images of Ba (top) and Cs (bottom). 120X

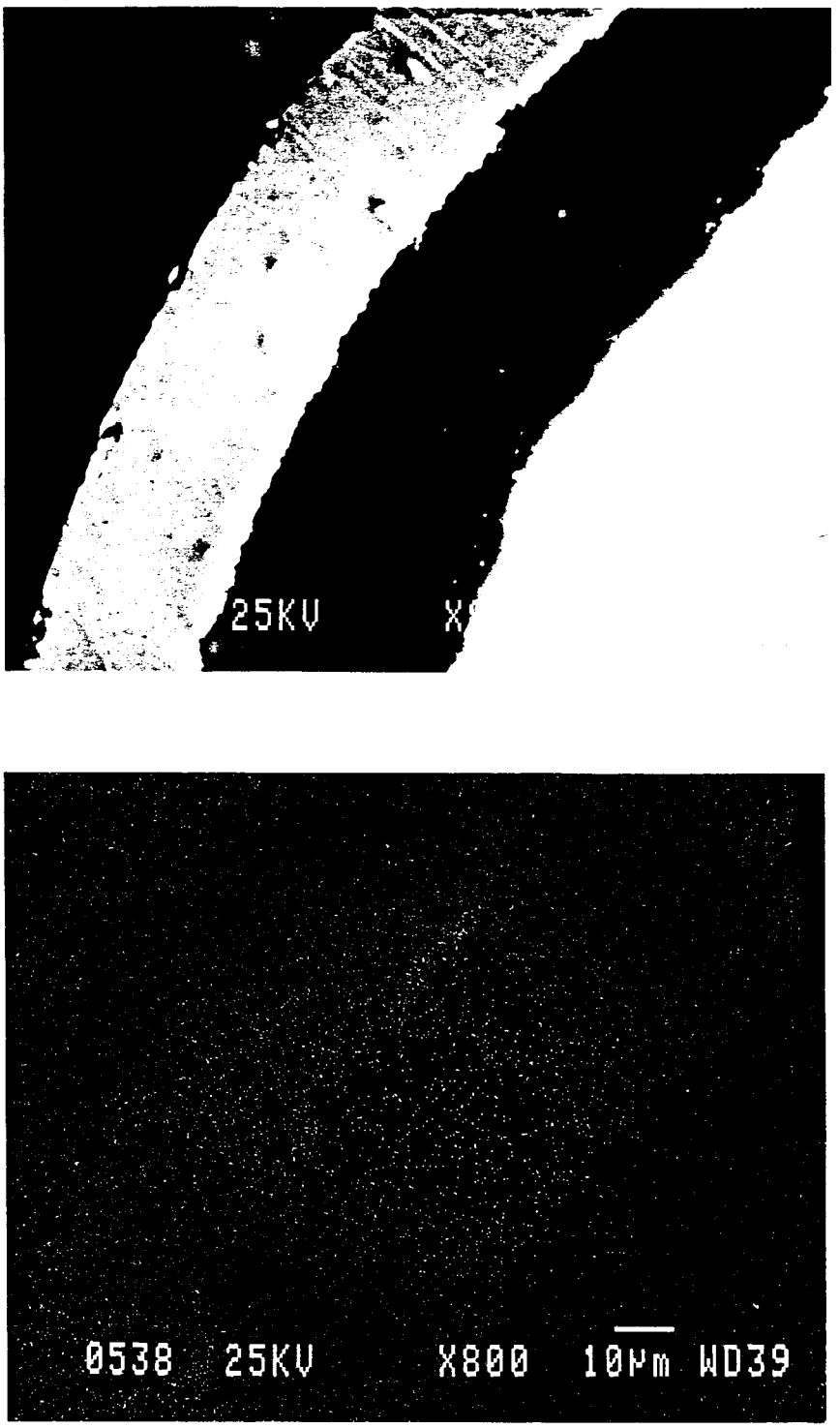

Fig. 4.8.25. Particle B5-P3 showing an Ag x-ray image of the SiC and IPyC layers. Only slight segregation is apparent at the SiC/IPyC interface. 800X

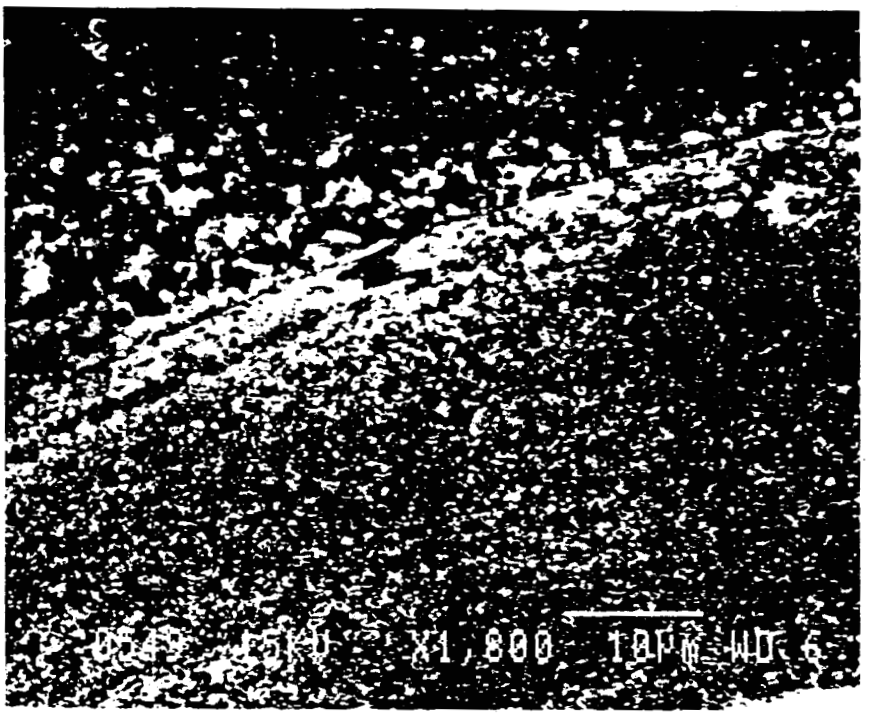

Fig. 4.8.26. Particle B4-P4 showing the seal coat on the OPyC. The feature in the center of the narrow seal coat appears to be a crack or other defect. 1800X

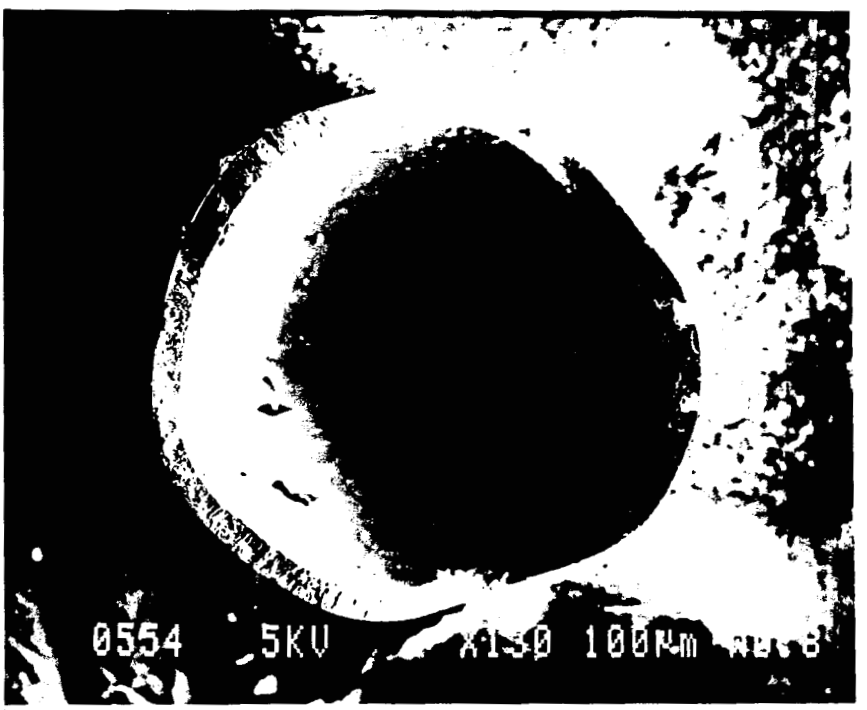

Fig. 4.8.27. Shard of SiC from a particle in compact B4. 130X

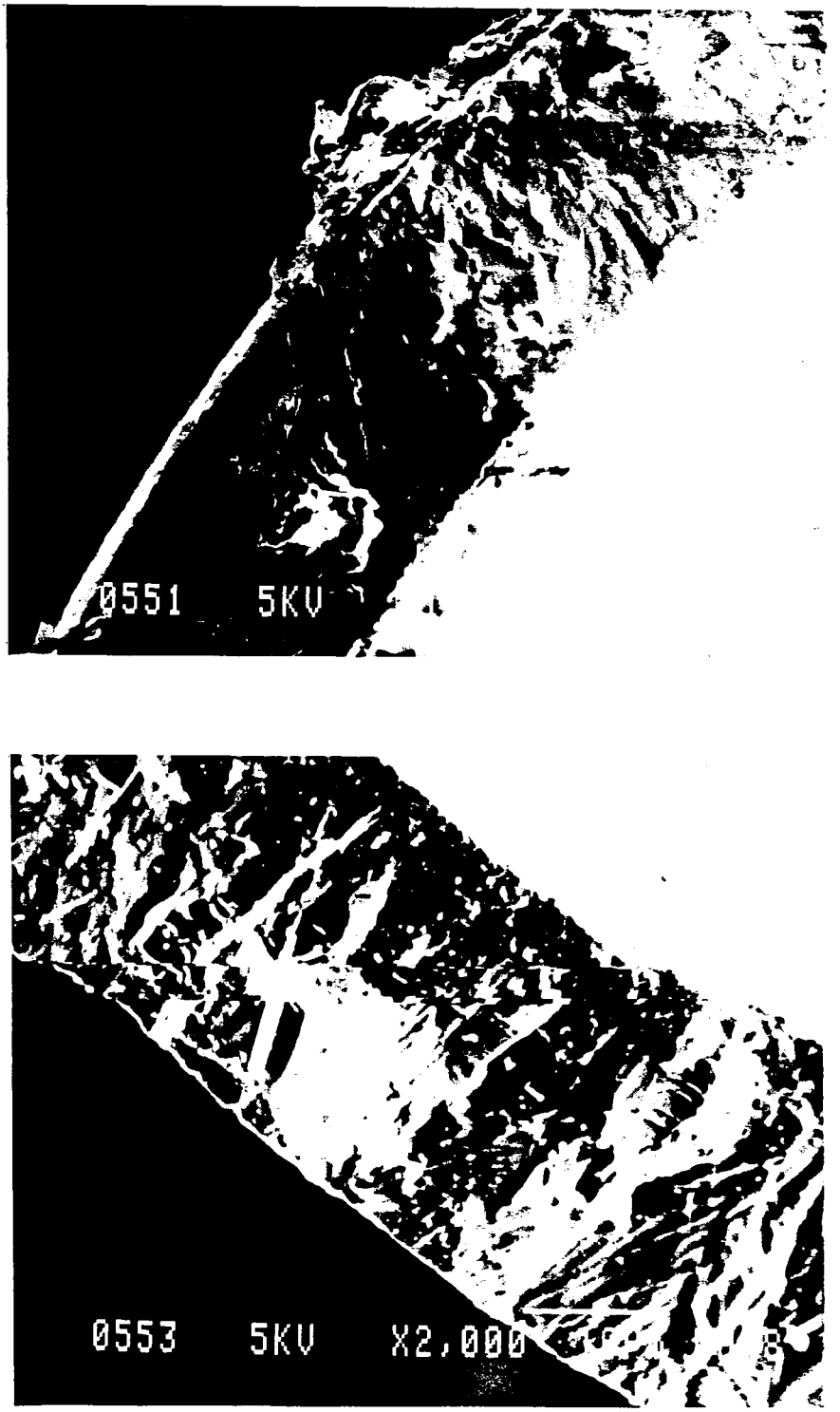

Fig. 4.8.28. Sections of the fracture surface of the shard from compact B4 that appears in Fig. 4.8.27.

4.9 REFERENCES

4.1.1. "NPR-1 and NPR-2 Capsule Disassembly, Visual Examination, and Component Metrology," Metals and Ceramics Division Procedure MET-FME-ESP-12, Rev. 1.

4.1.2 "Modified ORNL Loop Transport Cask HFIR Transport Cask HFIR Underwater Loading Procedure," Research Reactors Division Procedure RRD-TP-23, Rev. 0.

4.1.3 "Unloading Modified Loop Transport Cask 8S16-80," Metals and Ceramics Division Procedure MET-IFEL-OP-6, Rev. 0.

4.1.4 "Disconnection of MHTGR Capsules from MIF Instrumentation," Engineering Technology Division Procedure ETD-IE-23, Rev. 0.

4.1.5. "Gamma Scanning," Metals and Ceramics Division Procedure MET-FME-SOP-17, Rev. 0.

4.2.1. "NPR-1 and NPR-2 Piggyback Capsule Disassembly," Metals and Ceramics procedure MET-FME-ESP-13, Rev. 0. and 2.

4.3.1. "Determination of Diameters and Lengths of Cylindrical Objects Using Comparator Stand, Dial Gage, and V-Block," Metals and Ceramics procedure MET-FME-SOP-9, Rev. 1.

4.3.2. "QC Data Package, NPR-MHTGR Performance Test Fuel Test Capsules NPR-1, 1a, and -2, Compacts - Lot FM 23-00001," General Atomics, June 1991.

4.4.1 Clemmer, E. D., "Sweep Gas Sampling," ORNL Engineering Technology Division Procedure ETD-IE-SOP-005, December 1988.

4.4.2 Emerson, L. C., "HFIR Sweep Gas Counting and Analysis, MET-FMT-OG-002, Metals and Ceramics Division, ORNL, July 1993.

4.4.3 Allen, E. J., "CACA-2: Revised Version of CAA - A Heavy Isotope and Fission-Product Concentration Calculational Code for Experimental Irradiation Capsules," ORNL/TM-5266, UC-77-Gas Cooled Reactor Technology, February 1976, Oak Ridge National Laboratory.

4.4.3 Ketterer, J. W., and B. F. Myers, "Capsules HRB-17/18 PIE Report," U.S. Department of Energy Report HTGR-86-083, GA Technologies, September 1986.

4.4.5 Saurwein, J. J., and J. Greenwood, "Preliminary Test Report - Fission Gas Release Testing of Irradiated Compacts from NPR 1 and NPR 2.

4.4.6 Hill, D., General Atomics Chemistry Laboratory Gamma Spectrum Analysis reports.

4.4.7 Bell, G. L., J. T. Parks, K. R. Thoms, L. C. Emerson, G. L. Copeland, and B. F. Myers, "The New Production Reactor Fuel Irradiation Experiments NPR 1 and NPR 2 Irradiated Test Report, " U.S. Department of Energy Report ORNL/M-2663, Oak Ridge National Laboratory, February 1993

4.4.8 Goodin, D. T., NP-MHTGR Fuel Coordination Team Meeting, July 8, 1993, INEL, Idaho Falls, Idaho.

4.4.9 Meek, M. E. and B. F. Rider," Compilation of Fission Product Yields," General Electric Vallecitos Nuclear Center, NEDO-12143-1, January 26, 1974.

4.4.10 Olander, D. R., "Fundamental Aspects of Nuclear Reactor Fuel Elements," U.S. Department of Energy Report TID-26711-P1, pp 289-294.

4.4.11 Fuel Design Data Manual, General Atomics Document 901866, issue F, 1987, p 8-2.

4.4.12 Pointud, Marie-Louise, and Pierre Chenebault, "Emission of Fission Gases by Failed Coated Oxide Fuel Particles," Nuclear Technology 35 (2), 1977, pp. 494-500.

4.4.13 Montgomery, F. C., "Test Report on Steady State R/B of Hydrolyzed UC_2" 904929, issue/1, General Atomics Co., September 1980.

4.4.14 Kingery, W. D., H. K. Bowen, and D. R. Uhlmann, Introduction to Ceramics, 2nd ed., John Wiley & Sons, New York: 1976, p. 454.

4.4.15 Montgomery, F. C., and R. J. Precourt, "Test Status Report R/B Failed UCO Fuel," General Atomics document 906427, issue/1, March 1982.

4.4.16 Notley, M. J. F., and J. R. MacEwan, Nucl. Appl., 2, 1966, p- 447

4.4.17 Anderson, E. E., S. Langer, N. L. Baldwin, and F. E. Vanslager, "An In-core Furnace for the High-Temperature Irradiation Testing of Reactor Fuels," Nuclear Technology 11, 1971, pp 259-265.

4.4.18 Saurwein, J. and J. Greenwood, "Preliminary Test Report - Fission Gas Release Testing of Irradiated Compacts from the NPR-1 and NPR-2 Capsules," General Atomics Document 910588 Rev. 0, March 15, 1993.

4.4.19 Hofmann, T., CEGA memo to F. Montgomery, "A correlation for NPR TRIGA R/B tests with fluence," CEGA-M-93-1160, August 31, 1993.

4.4.20 Carroll, R. M., R. B. Perex, and O. Sisman, "Release of Fission Gas During Fissioning of UO_2," J. of the American Ceramic Society, 48, 1965, pp. 55-59.

4.4.21 Carroll, R. M., "Fission-Product Release from UO_2," Nuclear Safety, 5, 1964, pp. 356-60.

4.4.22 Burnette, R. D., and R. J. Precourt, "Test Status Report on R/B of Candidate HTGR Fuels," General Atomics Report 906044, issue/1, July 1981.

4.5.1 Valetine, K. H. and M. J. Kania," IMGA Operating Manual," Oak Ridge National Laboratory, ORNL/TM-6576, August 1979.

4.5.2 M. J. Kania and K. H. Valetine, "The Irradiated-Microsphere Gamma Analyzer (IMGA) - An Integrated System for HTGR Coated Particle Fuel Performance Assessment," Oak Ridge National Laboratory, Oak Ridge, TN, ORNL-5806, February 1980.

4.5.3 R. N. Morris, "MHTGR Fissile and Fertile Particle Burnup Determination by Gamma Spectroscopy," Oak Ridge National Laboratory, Oak Ridge, TN, ORNL-TM-12310 (to be published).

4.6.1.1 Clark, C. R. and J. Heaney, "Microstructural Evaluation of As- Manufactured Fuel Particles, Final Report." Babcock and Wilcox Report BWED-93-032 Rev. 01 August 1993.

4.6.2.1 Myers, B. F. "Fission Product Transport in Reactor Experiments," HTGR-85-115, September 1985.

4.6.2.2 Huddle, R. A. U., "The Influence in Fabrication Parameters on the Incidence of Spearhead Attack on Coated Particle Fuel," Dragon Report OPR 652, 1968

4.6.2.3 Wagner - Loffler, M., "Amoeba Behavior of UO_2 Coated Particle Fuel," Nuclear Technology, Vol 35, September 1977

4.7.1 Scott, C. B., D. P. Harmon, and J. F. Holzgraf, "Postirradiation Examination of Capsules P13R and P13S," GA-A13827 October 8, 1976.

4.7.2 Myers, B. F., W. J. Scheffel, A. W. Mehner, M. J. Kania, "Capsule R2-K13: Final Report on Cells 2 and 3," HTGR-85-068, GA Technologies Inc., September 1985.

4.7.4 Martin, R. C., "Acid Leach of Fuel Compacts," Procedure MET-FME-SOP-27, Rev. 0 with July - 1993 Field Change.

4.7.5 Martin, R. C., "Burn Leach of Fuel Compacts," Procedure MET-FME-SOP-27, Rev. 0 with July 1993 Field Change.

4.7.6 Parks, J. T. (ORNL), "Follow-up Evaluation of NPR-1 and -2 Fissile Inventories at End of Irradiation," Letter to J. J. Saurwein, General Atomics, July 21, 1993.

4.7.7 Price, R. J., "Properties of Silicon Carbide for Nuclear Fuel Particle Coatings," Nuclear Technology Vol. 35, September 1977.

5.0 DISCUSSION

5.1 Comparison With Prior Experience

There are two features of the NPR-1, NPR-2, and NPR-1A fuel performance that distinguish it from prior U.S. experience. The first feature is that the design change that introduced the protective PPyC coating was successful in achieving the desired low level of heavy metal contamination and low fission gas release. The fission gas release rate of $<10^{-8}$ R/B for Kr 85m was lower than in any prior U.S. capsule and similar to FRG irradiation tests.

The second feature was a rapid increase in fuel coating failure and fission gas release at relatively low fast neutron exposure of about 1.8×10^{-25} n/m^2. The release rate increased to a level of about 10^{-4} R/B for Kr 85m. Such behavior had been observed in a prior experiment, SSL-1 where nearly 100% failure of OPyC early in irradiation was coupled with a high level of as-manufactured defective SiC coatings (6 to 10%) (Refs. 5.1.1, 5.1.2, 5.1.3).

In the case of capsules NPR-1, NPR-2, NPR-1A, the PIE showed that failure of the PPyC and OPyC began at low fast neutron fluence and approached 100% at peak exposure, much like the SSL-1 experience. However, parallel fuel characterization work at General Atomics has shown that the as-manufactured SiC coating defects are on the order of 10^{-4} fraction (Ref. 5.1.4). While such a SiC defective fraction is higher than expected, it is not sufficient to explain the observed fission gas release in NPR-1, NPR-2, and NPR-1A. Failure of SiC coatings in addition to the initial as-manufactured SiC defect fraction must have taken place during irradiation to produce the high level of fission gas release observed.

5.2 Coating Failure Mechanism

At the present stage of MHTGR fuel particle development, there is no single technique for coating failure measurement which is an accepted standard. Several methods are utilized and the results must be utilized to reach a consensus on the estimated failure fraction. A summary of coating failure fraction increased by different techniques is given in Table 5.2.1 and Table 5.2.2.

Based on the data summarized in Table 5.2.1, the estimated coating failure fraction which resulted in exposed kernels and fission gas release ranged from 0.0007 to 0.07 for

Table 5.2.1
Total Coating Failure Estimates NPR 1, NPR 2, NPR 1A

Method	Failure Fraction Estimate (a)					
	NPR 1 Capsule	NPR 1 Compacts	NPR 2 Capsule	NPR 2 Compacts	NPR 1A Capsule	NPR 1A Compacts
In Reactor Steady State	0.013 (0.008R/Bf) (c)	(b)	0.0013 (0.008 R/Bf)	(b)	0.0022 (0.008R/Bf)	(b)
TRIGA FGR	0.07 (0.04R/Bf)	0.017-0.10 (0.04R/Bf)	0.06 (0.04R/Bf)	0.012-0.10 (0.04R/Bf)	0.0016 (0.04R/Bf)	$5x10^{-7}$ to $6x10^{-3}$ (0.04R/Bf)
In Reactor Cumm. Ion Gage Spikes	0.007 (526 spikes)	(b)	0.002 (135 spikes)	(b)	0.00069 (48 spikes)	(b)
Leach/Burn/Leach	(b)	0.015 (NPR 1 B6)	(b)	(b)	(b)	(b)

(a) All coatings Permeable due to fracture or porosity, Kernel exposed releasing fission gas to purge gas stream.
(b) not determined
(c) R/Bf = R/B fraction for particles with failed coatings

Table 5.2.2

SiC Coating Failure Estimates NPR 1, NPR 2, NPR 1A

Method	Failure Fraction Extimate (a)										
	NPR 1 Compacts						NPR 2 Compacts		NPR 1A Compacts		
	A5	A8	B4	B5	B6	B8	A4	B4	No 8	No. 9	No. 13
IMGA	(b)	(b)	0.04	0.02	(b)	0.002	(b)	0.005	0.002	(b)	(b)
Leach/Burn/Leach	(b)	(b)	(b)	(b)	0.015	(b)	(b)	(b)	(b)	(b)	(b)
Burn Visual	(b)	(b)	0.002	0.015	0.015	0.000	(b)	(b)	(b)	(b)	0.00
Ceramography nd	0.03	0.00	(b)	(b)	(b)	(b)	0.06	(b)	(b)	0.06	(b)

(a) SiC coatings Permeable due to fracture or porosity, OPyC or IPyC may or may not be intact.
(b) not determined

capsule average coating failure. The fission gas release rate measured prior to removal of the capsules from the test reactors provided the most consistent basis failure fraction estimate. Those results showed a capsule average coating failure fraction of 0.013, 0.0013, and 0.0022 for NPR-1, NPR-2, and NPR-1A, respectively. The failure fraction increased with increasing fast neutron exposure, temperature, and burnup. Fast neutron exposure was the most important variable and burnup the lease important.

For measurement of SiC coating failure the IMGA examination for cesium release provided the best estimate of failure fraction for compacts from each of the 3 capsules. Failure of SiC in individual compacts ranged from 0.002 to highest failure while NPR-2 and NPR-1A had the lower failure fraction, as shown in Table 5.2.2.

The failure of the PPyC/OPyC coatings in compacts was a strong function of fast neutron exposure. At a temperature of about 900° C, ceramography showed that the onset of OPyC failure was at about 1.8×10^{25} n/m^2. In fuel compacts with the lowest fast neutron exposure, there was significantly less OPyC failure than in the fuel with maximum exposure.

The unbonded particles at peak fast neutron exposure showed only surface cracks of the PyC seal coat and the cracks may not have penetrated to the SiC layer. On the other hand, particles bonded into the compacts showed cracks which penetrated to the SiC layer and were 20μm or more wide as a result of circumferential shrinkage after failure. The particles in the compacts were apparently acted upon by the carbonaceous matrix in a way that promoted cracking of the PPyC. Even in NPR-2, where compact temperatures were lower than in some unbonded particle samples, the cracking of the PPyC/OPyC layer was much more severe in compacts than in unbonded particles.

The SiC coating failure fraction showed no strong correlation with either fast neutron exposure or burnup. This observation may result from a rather narrow range of burnup and fast neutron exposure in these tests. The absence of significant attack of the SiC by fission products is consistent with a lack of dependence of SiC failure on burnup.

Penetration of the SiC layer by palladium fission product was observed in scanning electron microscopy microprobe examination of cross sections of particles which were known to have released cesium, as determined by IMGA. However, the palladium did not appear to follow grain boundaries or develop regions of high concentration as observed in prior tests.

In the ceramographic examination, there was no evidence that kernel or fission product attack contributed to mechanical failure of the SiC coating in a manner which would

release fission gases. From these observations, it was concluded that burnup had no detectable effect on coating failure within the burnup range of these experiments.

Particle shape and the existence of the lenticular SiC flaw known as a "gold spot" did not contribute to the observed failure of SiC or OPyC. Non-spherical particles performed as well as poorly shaped particles. Cracks in the SiC were never seen to connect with or be associated with the gold spot discontinuity in the SiC. The source of stress causing SiC failure acted independent of these shape and flaw features. Apparently, the margin for failure due to pressure vessel effects is very large in MHTGR particle design. However, features which degrade pressure vessel performance should be removed because they can be expected to become limiting when the non-pressure vessel source of failure in these particles is identified and eliminated.

The buffer coatings did not usually crack radially but underwent a uniform radial shrinkage down around the HEU UCO kernel. The radial shrinkage in buffer thickness was often more than 50%. Swelling of the UCO kernel was observed in several particles where the buffer had been breached and the kernel swelled into the gap between shrinking buffer and the IPyC which remained attached to the SiC. However, no fission product attack of the SiC was observed even when the swelling kernel contacted the inner surface of the IPyC which was only 40μm from the SiC.

The observation of extensive kernel swelling upon failure of the buffer layer indicated that the buffer has significant strength which restrained kernel swelling in most particles. The buffer pulled away from the IPyC as a result of irradiation induced shrinkage, and during initial irradiation there may have been sufficient strength in the buffer to cause damage to the IPyC prior to separation of the two layers.

The IPyC coating was firmly bonded to the SiC except in the vicinity of SiC cracks where debonding was observed. The cracked IPyC tended to curl inward toward the buffer and away from the SiC. The inward movement of the IPyC may have been assisted by the buffer coating which underwent more than 50% radial contraction during irradiation. As a result of the radial buffer contraction, the buffer material parted in the buffer layer near the outer diameter leaving fragments of the buffer and the PyC seal coat attached to the IPyC.

The fact that the crack in the SiC was associated with a crack in the IPyC suggests that the mechanism of failure involves both coatings. Since the IPyC crack was not observed to be aligned with the SiC crack and the IPyC was typically debonded from the SiC in the vicinity of the crack, the conclusion was drawn that cracks in one coating did not propagate

into the other. While this conclusion seems likely, the data are not conclusive since only a two dimensional view of the particle cross section was observed. Perhaps in a plane of the particle not observed, the IPyC and SiC crack were aligned at the point where the crack was initiated. The data obtained here does not provide the required evidence to resolve this issue.

Analysis of fission gas release rates indicated the particle coating failure was not more than 1.3% in NPR-1 and 0.13% in NPR-2. There is significant uncertainty in the estimate because per failed particles is not well known for high burnup HEU UCO.

The IMGA and ceramography results indicated that particles in all but the lowest exposure compacts had 1% to 6% cracked or porous SiC coatings. These coatings were shown to have released cesium during irradiation. However, if any one of the PyC coatings was intact, the fission gases would be retained by such particles.

In order to measure the fraction of exposed kernels which could release fission gas, the initial leach of the leach-burn-leach procedure was carried out on compact NPR-1 B6 with relatively high TRIGA fission gas release measurement ($2x10^{-3}$ R/B Kr 85m). The results of that work showed that about 1.5% of the particles in compact NPR-1 B6 had complete failure of all coatings which exposed the kernel and allowed it to be leached out prior to burning away the PyC coatings. Burning the compact did not result in more exposed kernels. This observation suggests failure of all three coatings (OPyC/SiC/IPyC) are connected in the failure mechanism.

5.3 References

5.1.1 Stansfield, O. M., Ballogny, D. D. Jensen, D. P. Harmon, "SSL-1 Spitfire Loop Experiment Post Irradiation Examination and Analysis, Dossier No. 6," General Atomics Document GA-A14628, July 1978.

5.1.2 Goodin, D. T., "TRISO Fuel Performance Model Modifications," GA Document 907395, DOE-HTGR-88359, January 1991.

5.1.3 Kovacs, W. J., "Characterization of Defective SiC Evaluation in TRISO HTGR Fuel Particles," Jour. American Ceramic Society, Vol. 66, No. 3, March 1982.

5.1.4 Saurwein, J. J., "Measurement of SiC Defect Fractions in As-Manufactured Fuel Particles," Fuel Coordination Meeting, INEL, Idaho Falls, ID, July 8, 1993.

6.0 CONCLUSIONS

The primary objective of the NPR 1, NPR 2, and NPR 1A irradiation tests was to demonstrate that HEU UCO TRISO particles in fuel compacts fabricated to NP MHTGR specification would perform as expected under moderate and peak design exposure. Initial performance at or above the required level of fission product retention was expected because of the PPyC design improvement which protected the particle from damage during compact fabrication. While there was some concern that the previously untested PPyC/OPyC coating system might fail during irradiation, the SiC layer was expected to perform satisfactorily without the PPyC/OPyC coatings. There were also process improvements yielding more spherical particles through tabling and elutriation and more uniform coatings through use of a draft tube coater design. These improvements were expected to produce a superior performing SiC.

During irradiation of the capsules, the fuel was exposed at about NP-MHTGR core average temperature and also near peak temperature. Under both of these conditions the coating failure and fission gas release were higher than expected by at least two orders of magnitude. Although the primary programmatic objective regarding fuel performance was not achieved, fabrication of fuel with extremely low contamination and conduct of complex irradiation experiments in compliance with rigorous quality assurance requirements was successfully carried out.

The coating failure resulted in kernel exposure and fission gas release from about 1.5% of the coated particles in the high temperature tests and about 0.1% failure in the lower temperature test near expected core average temperature. This conclusion was based on acid leaching data and end of irradiation fission gas release rate in HFIR. Failure of the SiC coating with release of cesium, as detected by IMGA, was about 2% for high temperature and 0.5% for low temperature exposure. The observed failure in these tests was high enough that detection and observation of failed particles was readily accomplished.

The SiC coating was deposited with relatively large columnar grain size of 10 to 20μm length as determined on unirradiated coatings. Scanning electron microscopy of SiC coating fracture surfaces revealed transgranular fracture, as normally observed in SiC materials and no nucleation sites for SiC fracture were identified. Therefore, the large SiC grain size did not result in unexpected fracture behavior.

The observed failure of coatings was not caused by unexpected dimensional changes in the kernel or coatings during irradiation. This conclusion was based on the observation that dimensional change of particle components during irradiation was qualitatively consistent with prior experience. All PyC coatings densified and underwent irradiation induced shrinkage. The low density coatings contracted much more than the dense PyC coatings. The high burnup HEU UCO kernel was restrained from swelling by shrinkage of the buffer, except in rare cases where the buffer failed and allowed the kernel to swell into the gap which developed between the buffer and IPyC. The SiC coating dimensions remained relatively constant and may have expanded 0.5% as expected for beta SiC. This latter conclusion was based on measurement of SiC diameter at the outer surface of the SiC and comparison with dimensions obtained using the same procedures for unirradiated particles.

As a result of the observations conducted during PIE it was concluded that the coating failure which took place was caused by deleterious mechanical interaction of SiC and PyC coating layers of the TRISo particle. Specifically, the SiC and IPyC appeared to be intimately bonded and fractured SiC was accompanied by fractured IPyC. The PIE results do not indicate which coating failed first and contributed to failure in the other coating. However, all particles with failed SiC had failed IPyC, but only 15% of the particles with failed IPyC had failed SiC. From this observation, it appears reasonable conjecture that the IPyC failed first and in a small portion of the population with failed IPyC, the geometry or exposure conditions were favorable for high SiC stress and subsequent SiC failure.

Failure of the PPyC resulted from tensile stress resulting from irradiation induced densification and shrinkage down around more rigid OPyC and SiC layers. Cracks in the PPyC appeared to initiate at the outer surface and propagate inward through the PyC seal coat into the OPyC. Although matrix intrusion into the PPyC was not observed in this work, penetration of the PPyC was observed at the as-manufactured stage. Some interaction of the matrix and PPyC may have taken place to enhance PPyC failure in compacts. This conclusion was based on the observation that large PPyC cracks were observed in all compacts. In unbonded piggyback particle specimen that were not exposed to compact matrix, cracks which developed were superficial in nature and restricted to particles at the highest temperature and fast neutron exposure.

Irradiation induced failure of the PPyC led to the failure of OPyC coatings. The OPyC coating was not strongly bonded to the SIC so that the failed OPyC readily separated from the SiC. The high failure fraction of OPyC at high exposure allowed fission gases to

escape into the capsule purge gas stream and revealed total coating failure by detection of increased purge gas activity. However, the failure of the OPyC coating did not initiate failure of the SiC coating. This conclusion was based on the observation that nearly 100% OPyC failure determined by ceramography in compacts with high exposure did not result in SiC failure fraction greater that in compacts where OPyC failure was much lower.

In order to gain a complete understanding of fission product release from coated particle fuel, it may be necessary to consider release pathways more subtle than mechanical cracks. For example, connected porosity in the SiC may be present as-manufactured or develop during irradiation and is difficult to detect but still significant with regards to fission product release. Evidence for such porosity was obtained from the burning of compact NPR 1A #13 which had a relatively high TRIGA fission gas release rate of 3.3×10^{-4} R/B Kr-85m. Examination of the exposed SiC surface at 25x of all the particles in the compact after burning off the PPyC/OPyC coating did not reveal any cracked SiC or other types of flaws through which the fission gas escaped. Supporting evidence was also obtained from ceramography of particles known to have released cesium during irradiation which did not have cracked SiC but did have evidence of porosity in the SIC. More complete characterization of SIC microstructure before and after irradiation would contribute significantly to understanding of fuel performance and point the way to improved materials.

List of Appendices

Appendix A: NPR 1 Fission Gas Release

R/B Measurements for NPR 1 ..... A-1

Fuel Parameters for NPR1 R/B Measurements A-6

Fission Gas Concentrations for NPR1 R/B Samples A-11

Appendix B: NPR 2 Fission Gas Release

R/B Values for NPR 2 ..... B-1

Fuel Parameters for NPR 2 R/B Measurements B-6

Fission Gas Concentrations for NPR 2 R/B Samples B11

Appendix C: TRIGA R/B Measurements C-1

APPENDIX A1: R/B Measurements for NPR1

sample I.D.	Release Rate/Birth Rate (R/B) corrected to capsule exit time							
	Kr-85m	Kr-87	Kr-88	Kr-89	Xe-133	Xe-135m	Xe-135	Xe-138
NPR1_1	7.2e-09	5.5e-09	8.0e-09	nd(1)	nd	nd	nd	1.8e-09
NPR1_2	8.4e-09	8.3e-09	7.7e-09	9.3E-10(2)	nd	nd	nd	1.4e-09
NPR1_3	1.4e-08	9.9e-09	1.2e-08	1.3E-09(2)	nd	3.0e-09	5.2e-09	1.5e-09
NPR1_4	1.5e-08	9.6e-09	1.3e-08	1.4e-09	nd	2.0e-09	5.0e-09	1.2e-09
NPR1_5	1.6e-08	8.2e-09	1.2e-08	8.6E-10(2)	nd	2.7e-09	4.6e-09	8.0e-10
NPR1_6	1.5e-08	8.4e-09	1.2e-08	nd	nd	2.8e-09	4.6e-09	1.3e-09
NPR1_7	1.3e-08	8.7e-09	1.1e-08	nd	nd	3.5e-09	4.0e-09	8.6e-10
NPR1_8	1.4e-08	8.1e-09	1.1e-08	7.4E-10(2)	nd	2.9e-09	4.0e-09	1.1e-09
NPR1_9	1.5e-08	9.3e-09	1.2e-08	6.0E-10(2)	7.7e-09	2.4e-09	4.3e-09	1.1e-09
NPR1_10	9.9e-09	6.4e-09	9.4e-09	3.9E-10(2)	nd	1.7e-09	2.5e-09	6.8e-10
NPR1_11	1.1e-08	6.5e-09	9.5e-09	nd	1.3e-08	2.2e-09	3.2e-09	7.8e-10
NPR1_12	1.2e-08	7.0e-09	9.5e-09	nd	3.8e-08	2.0e-09	3.2e-08	1.3e-09
NPR1_13	1.3e-08	7.6e-09	1.2e-08	nd	1.2e-08	2.3e-09	3.0e-09	1.0e-09
NPR1_14	1.1e-08	6.6e-09	9.8e-09	1.2E-09(2)	2.1e-08	1.7e-09	3.1e-09	1.4e-09
NPR1_15	3.6e-09	3.5e-09	3.7e-09	1.6E-09(2)	nd	nd	nd	7.9e-10
NPR1_16	5.8e-09	4.5e-09	7.3e-09	1.5E-09(2)	nd	nd	nd	9.7e-10
NPR1_17	6.7e-09	4.4e-09	4.7e-09	nd	nd	2.1e-09	1.9e-09	6.6e-10
NPR1_18	1.0e-08	6.6e-09	9.2e-09	nd	1.8e-08	1.8e-09	1.8e-09	8.6e-10
NPR1_19	9.5e-09	6.8e-09	7.8e-09	nd	2.7e-08	1.5e-09	3.0e-09	7.7e-10
NPR1_20	1.1e-08	6.9e-09	9.5e-09	1.2E-09(2)	1.6e-08	1.8e-09	3.4e-09	1.0e-09
NPR1_21	1.2e-08	7.6e-09	1.1e-08	1.5E-09(2)	1.7e-08	2.4e-09	3.4e-09	1.2e-09
NPR1_22	1.0e-08	6.4e-09	8.2e-09	nd	2.0e-08	2.0e-09	2.3e-09	8.3e-10
NPR1_23	1.1e-08	7.3e-09	9.2e-09	1.4E-09(2)	7.7e-09	2.6e-09	3.1e-09	8.6e-10
NPR1_24	1.2e-08	6.8e-09	1.0e-08	1.4E-09(2)	1.9e-08	2.5e-09	2.9e-09	1.0e-09
NPR1_25	1.1e-08	6.8e-09	9.3e-09	nd	7.5e-09	2.3e-09	3.1e-09	9.4e-10
NPR1_26	1.2e-08	6.7e-09	1.0e-08	1.2E-09(2)	8.0e-09	2.2e-09	3.0e-09	1.2e-09
NPR1_27	1.1e-08	7.1e-09	1.0e-08	7.4E-10(2)	6.3e-09	1.9e-09	2.5e-09	9.5e-10
NPR1_28	1.2e-08	7.4e-09	1.0e-08	1.3E-09(2)	3.0e-08	1.8e-09	3.0e-09	9.8e-10

APPENDIX A1: R/B Measurements for NPR1

sample I.D.	Release Rate/Birth Rate (R/B) corrected to capsule exit time							
	Kr-85m	Kr-87	Kr-88	Kr-89	Xe-133	Xe-135m	Xe-135	Xe-138
NPR1_29	1.2e-08	7.5e-09	1.0e-08	9.6E-10(2)	2.4e-08	2.5e-09	2.9e-09	9.8e-10
NPR1_30	0.0	1.5e-09	2.9e-09	nd	nd	nd	nd	8.1e-10
NPR1_31	2.3e-09	1.9e-09	1.4e-09	8.7E-10(2)	nd	nd	nd	5.6e-10
NPR1_32	3.2e-09	2.5e-09	2.2e-09	nd	nd	1.3e-09	9.5e-10	6.2e-10
NPR1_33	1.8e-08	8.5e-09	1.3e-08	nd	1.4e-07	1.4e-09	3.0e-09	1.1e-09
NPR1_34	1.2e-08	6.8e-09	1.0e-08	1.3E-09(2)	2.0e-08	2.0e-09	2.8e-09	1.2e-09
NPR1_35	1.4e-08	7.3e-09	1.2e-08	2.0E-09(2)	3.2e-08	2.0e-09	2.8e-09	1.2e-09
NPR1_36	1.2e-08	7.2e-09	1.0e-08	nd	2.0e-08	2.1e-09	3.0e-09	1.1e-09
NPR1_37	1.1e-08	7.4e-09	9.6e-09	2.8E-09(2)	2.1e-08	2.6e-09	3.0e-09	1.1e-09
NPR1_38	1.2e-08	8.0e-09	1.2e-08	2.6E-09(2)	2.9e-08	2.8e-09	2.7e-09	1.3e-09
NPR1_39	1.1e-08	9.1e-09	1.0e-08	3.6E-09(2)	7.8e-08	2.5e-09	2.9e-09	1.4e-09
NPR1_41	1.2e-08	7.2e-09	1.0e-08	nd	2.8e-08	3.7e-09	2.7e-09	1.1e-09
NPR1_42	1.5e-08	1.0e-08	1.4e-08	3.2E-09(2)	1.2e-07	2.7e-09	3.3e-09	2.0e-09
NPR1_43	1.2e-08	8.0e-09	1.1e-08	nd	2.9e-08	2.5e-09	3.4e-09	1.4e-09
NPR1_44	1.3e-08	7.7e-09	1.5e-09	2.3e-10	3.5e-08	2.6e-09	2.9e-09	1.2e-09
NPR1_45	1.3e-08	7.7e-09	1.0e-08	2.3E-09(2)	3.8e-08	2.3e-09	2.3e-09	1.1e-09
NPR1-46	5.5e-09	3.4e-09	4.3e-09	nd	8.5e-06	5.8e-09	nd	6.6e-10
NPR1-47	6.7e-09	3.6e-09	6.3e-09	nd	3.0e-06	nd	nd	7.5e-10
NPR1-48	8.2e-09	5.1e-09	6.4e-09	5.8E-10(2)	2.2e-07	1.1e-09	1.4e-09	8.0e-10
NPR1-49	8.0e-09	5.3e-09	6.9e-09	nd	1.2e-07	nd	1.7e-09	9.2e-10
NPR1-50	1.1e-08	6.7e-09	9.7e-09	nd	1.9e-07	1.5e-09	1.7e-09	7.8e-10
NPR1-51	1.2e-08	7.2e-09	9.8e-09	1.4E-09(2)	2.0e-07	1.6e-09	1.7e-09	9.7e-10
NPR1-52	9.8e-09	5.8e-09	9.0e-09	1.4E-09(2)	1.5e-07	nd	2.0e-09	1.1e-09
NPR1-53	9.6e-09	6.2e-09	8.3e-09	nd	1.5e-07	nd	1.8e-09	1.0e-09
NPR1-54	8.7e-09	5.3e-09	7.1e-09	1.5E-09(2)	1.5e-07	1.0e-09	1.9e-09	9.8e-10
NPR1-55	8.8e-09	5.7e-09	6.8e-09	6.1E-10(2)	1.5e-07	1.3e-09	1.8e-09	9.2e-10
NPR1-56	1.0e-08	6.5e-09	9.1e-09	1.4E-05(2)	2.6e-07	1.8e-09	1.6e-09	8.9e-10

APPENDIX A1: R/B Measurements for NPR1

sample I.D.	Release Rate/Birth Rate (R/B) corrected to capsule exit time							
	Kr-85m	Kr-87	Kr-88	Kr-89	Xe-133	Xe-135m	Xe-135	Xe-138
NPR1-57	1.3e-08	8.1e-09	1.1e-08	1.5E-09(2)	3.7e-07	2.2e-09	2.8e-09	9.0e-10
NPR1-59	1.3e-08	8.2e-09	1.0e-08	1.6E-09(2)	3.0e-07	1.5e-09	2.3e-09	1.2e-09
NPR1-60	1.6e-08	9.0e-09	1.1e-08	nd	3.4e-07	nd	2.2e-09	1.3e-09
NPR1-61	6.2e-09	3.5e-09	4.8e-09	nd	2.0e-07	2.2e-09	1.7e-09	1.1e-09
NPR1-62	1.4e-08	8.1e-09	1.2e-08	1.5E-09(2)	8.2e-07	2.2e-09	2.7e-09	1.3e-09
NPR1-63	1.3e-08	7.9e-09	1.2e-08	2.5E-09(2)	6.0e-07	2.1e-09	2.9e-09	1.6e-09
NPR1-64	1.5e-08	9.8e-09	1.3e-08	7.2E-10(2)	5.1e-07	2.7e-09	3.2e-09	1.5e-09
NPR1-65	1.5e-08	9.0e-09	1.2e-08	1.9E-09(2)	5.8e-07	2.7e-09	3.0e-09	1.5e-09
NPR1-66	1.4e-08	8.1e-09	1.0e-08	8.8E-10(2)	5.0e-07	2.3e-09	3.0e-09	1.5e-09
NPR1-67	1.8e-08	1.1e-08	1.4e-08	2.5E-09(2)	7.5e-07	3.0e-09	3.9e-09	1.8e-09
NPR1-68	1.4e-08	9.9e-09	1.2e-08	1.5E-09(2)	6.3e-07	2.4e-09	3.0e-09	1.8e-09
NPR1-69	1.5e-08	9.3e-09	1.4e-08	1.4E-09(2)	6.8e-07	2.3e-09	3.2e-09	1.7e-09
NPR1-70	2.1e-08	1.1e-08	1.4e-08	2.4E-09(2)	8.0e-07	3.3e-09	3.4e-09	2.3e-09
NPR1-71	2.0e-08	1.3e-08	1.6e-08	2.1E-09(2)	8.4e-07	3.7e-09	4.4e-09	2.4e-09
NPR1-72	2.0e-08	1.3e-08	1.8e-08	2.1E-09(2)	8.2e-07	3.7e-09	4.9e-09	2.8e-09
NPR1-73	4.6e-09	2.2e-09	2.3e-09	9.4E-10(2)	1.6e-07	2.3e-09	2.9e-09	1.2e-09
NPR1-74	4.2e-09	2.8e-09	3.9e-09	nd	9.6e-08	2.1e-09	3.2e-09	1.0e-09
NPR1-75	1.7e-07	8.5e-08	1.3e-07	7.9E-09(2)	1.5e-06	5.3e-08	8.2e-08	1.1e-08
NPR1-76	1.7e-07	8.3e-08	1.3e-07	1.1E-08(2)	1.2e-06	3.2e-08	4.4e-08	1.1e-08
NPR1-77	1.4e-07	6.9e-08	1.0e-07	9.0E-09(2)	1.1e-06	1.9e-08	3.3e-08	7.6e-09
NPR1-78	9.0e-07	5.5e-07	7.5e-07	6.2e-08	1.9e-06	3.7e-07	5.6e-07	1.1e-07
NPR1-79	6.5e-07	4.3e-07	5.6e-07	6.2e-08	2.3e-06	2.7e-07	4.0e-07	1.0e-07
NPR1-80	5.2e-06	2.7e-06	4.0e-06	2.8e-07	2.3e-05	3.0e-06	4.6e-06	4.2e-07
NPR1-81	1.4e-05	8.4e-06	1.1e-05	9.7e-07	4.4e-05	6.8e-06	1.0e-05	1.8e-06
NPR1-82	1.4e-05	7.6e-06	1.0e-05	1.3e-06	8.4e-05	9.0e-06	1.2e-05	1.6e-06
NPR1-83	4.4e-06	2.9e-06	3.9e-06	2.8e-07	6.5e-06	7.7e-07	1.1e-06	4.4e-07

APPENDIX A1: R/B Measurements for NPR1

sample I.D.	Release Rate/Birth Rate (R/B) corrected to capsule exit time							
	Kr-85m	Kr-87	Kr-88	Kr-89	Xe-133	Xe-135m	Xe-135	Xe-138
NPR1-84	4.9e-05	3.0e-05	3.9e-05	5.4e-06	1.1e-04	2.1e-05	2.5e-05	7.0e-06
NPR1-85	4.2e-05	2.4e-05	3.3e-05	4.2e-06	1.2e-04	1.6e-05	1.9e-05	5.1e-06
NPR1-86	4.0e-05	2.1e-05	3.0e-05	4.1e-06	1.4e-04	1.5e-05	1.9e-05	4.6e-06
NPR1-87	3.6e-05	2.1e-05	2.7e-05	4.2e-06	1.0e-04	1.5e-05	1.8e-05	4.8e-06
NPR1-88	3.4e-06	3.1e-06	3.4e-06	5.7e-07	nd	1.9e-06	2.5e-06	1.2e-06
NPR1-89	8.2e-05	4.5e-05	6.1e-05	5.1E-06(2)	9.4e-05	2.2e-05	3.7e-05	9.6e-06
NPR1-90	7.4e-05	3.9e-05	5.6e-05	3.9e-06	8.7e-05	2.0e-05	2.5e-05	6.7e-06
NPR1-91	5.2e-05	2.9e-05	4.0e-05	3.6E-06(2)	7.3e-05	1.3e-05	1.8e-05	4.3e-06
NPR1-92	6.1e-05	3.3e-05	4.7e-05	3.8E-06(2)	1.0e-04	1.5e-05	2.1e-05	4.8e-06
NPR1-93	5.3e-05	3.1e-05	4.2e-05	4.6e-06	1.2e-04	1.9e-05	2.6e-05	4.9e-06
NPR1-94	7.1e-05	4.2e-05	5.6e-05	4.9e-06	1.7e-04	2.6e-05	3.6e-05	6.9e-06
NPR1-95	2.1e-04	7.1e-05	1.3e-04	5.9E-06(2)	5.1e-03	2.8e-05	3.6e-05	1.1e-05
NPR1-96	9.3e-06	8.2e-06	9.1e-06	2.1E-06(2)	4.5e-05	1.0e-06	1.1e-06	3.0e-06
NPR1-97	2.8e-05	2.0e-05		3.5E-06(2)	4.4e-05	6.2e-06	7.5e-06	4.4e-06
NPR1-98	1.7e-04	9.0e-05	1.3e-04	2.0E-05(2)	7.9e-04	2.7e-05	3.2e-05	2.2e-05
NPR1-99	1.0e-05	7.2e-06	9.5e-06	1.3E-06(2)	1.5e-05	1.8e-06	2.1e-06	1.7e-06
NPR1-100	8.3e-05	4.4e-05	6.2e-05	6.1E-06(2)	2.4e-04	2.1e-05	2.7e-05	8.8e-06
NPR1-101	6.1e-05	3.5e-05	4.8e-05	5.3E-06(3)	1.1e-04	1.6e-05	2.0e-05	5.7e-06
NPR1-102	5.4e-05	3.1e-05	4.3e-05	3.7E-06(2)	1.8e-04	1.4e-05	2.0e-05	5.0e-06
NPR1-103	1.0e-05	7.0e-06	9.0e-06	8.6E-07(2)	4.5e-05	2.6e-06	3.9e-06	1.9e-06
NPR1-104	4.0e-05	2.7e-05	3.5e-05	2.1E-06(2)	1.4e-04	6.8e-06	1.0e-05	5.1e-06
NPR1-105	4.9e-04	2.9e-04	3.7e-04	3.4e-05	2.3e-03	1.2e-04	1.4e-04	9.3e-05
NPR1-106	3.3e-04	1.8e-04	2.6e-04	2.3E-05(3)	1.4e-03	8.9e-05	1.2e-04	3.8e-05
NPR1-107	3.3e-04	2.1e-04	2.6e-04	2.7e-05	9.5e-04	1.3e-04	1.7e-04	4.5e-05
NPR1-108	3.1e-04	1.8e-04	2.5e-04	2.1e-05	9.9e-04	1.0e-04	1.3e-04	3.1e-05

APPENDIX A1: R/B Measurements for NPR1

sample I.D.	Release Rate/Birth Rate (R/B) corrected to capsule exit time							
	Kr-85m	Kr-87	Kr-88	Kr-89	Xe-133	Xe-135m	Xe-135	Xe-138
NPR1-109	2.5e-04	1.5e-04	2.0e-04	1.8E-05(2)	6.3e-04	7.2e-05	9.4e-05	2.3e-05
NPR1-110	1.6e-04	7.9e-05	1.2e-04	1.4e-05	4.8e-04	3.6e-05	4.6e-05	1.6e-05
NPR1-111	1.4e-04	6.9e-05	1.0e-04	8.9E-06(3)	3.7e-04	2.2e-05	3.3e-05	1.0e-05
NPR1-112	7.2e-05	2.8e-05	5.1e-05	3.7E-06(2)	4.7e-03	5.8e-06	7.3e-06	5.3e-06
NPR1-113	3.1e-04	1.7e-04	2.3e-04	2.1e-05	1.5e-03	8.0e-05	1.0e-04	3.5e-05
NPR1-114	4.0e-05	2.8e-05	3.5e-05	4.8E-06(2)	7.2e-05	1.0e-05	1.2e-05	6.9e-06
NPR1-115	2.0e-04	1.2e-04	1.6e-04	1.5e-05	3.7e-04	6.7e-05	8.6e-05	2.3e-05

(1) nd: none detected
(2) based on Rb-89 concentration since no Kr-89 gamma peak
(3) based on Rb-89 concentration since Kr-89 gamma peak too small to be reliable

APPENDIX A2: Fuel Parameters for NPR1 R/B Measurements

RB SAMPLE				zone 4 compact parameters			
I.D.	Date	Time	efpd	fluence ($x10^{25}n/m^2$)	burnup (%FIMA)	temp (°C)	flow (cc/min)
NPR1_1	25-Jul-91	22:27	0.01	0.000	0.0	1078	77.4
NPR1_2	25-Jul-91	23:52	0.07	0.000	0.1	1094	78.8
NPR1_3	26-Jul-91	09:45	0.48	0.002	0.7	1125	79.1
NPR1_4	27-Jul-91	10:09	1.50	0.005	2.0	1132	63.5
NPR1_5	28-Jul-91	09:39	2.48	0.008	3.3	1131	63.9
NPR1_6	29-Jul-91	11:41	3.56	0.012	4.7	1127	63.3
NPR1_7	30-Jul-91	14:29	4.68	0.016	6.1	1121	65.2
NPR1_8	31-Jul-91	10:56	5.53	0.019	7.2	1116	64.1
NPR1_9	02-Aug-91	09:38	7.48	0.025	9.6	1104	65.5
NPR1_10	05-Aug-91	10:51	10.53	0.036	13.1	1087	65.8
NPR1_11	07-Aug-91	10:22	12.51	0.042	15.3	1076	65.2
NPR1_12	09-Aug-91	10:35	14.52	0.049	17.5	1065	65.1
NPR1_13	12-Aug-91	11:14	17.55	0.060	20.6	1052	65.9
NPR1_14	14-Aug-91	17:09	19.79	0.067	22.8	1036	66.9
NPR1_15	28-Aug-91	12:43	20.49	0.069	23.5	960	89.8
NPR1_16	28-Aug-91	14:01	20.54	0.070	23.6	966	90.4
NPR1_17	29-Aug-91	10:07	21.38	0.072	24.3	995	86.4
NPR1_18	29-Aug-91	13:57	21.54	0.073	24.5	1053	69.7
NPR1_19	30-Aug-91	09:09	22.34	0.076	25.2	1049	68.0
NPR1_20	31-Aug-91	08:10	23.30	0.079	26.1	1064	68.9
NPR1_21	01-Sep-91	09:19	24.35	0.083	27.1	1056	71.9
NPR1_22	03-Sep-91	09:52	26.37	0.089	28.9	1043	71.6
NPR1_23	04-Sep-91	13:57	27.54	0.093	29.9	1061	70.5
NPR1_24	06-Sep-91	09:12	29.34	0.099	31.4	1057	69.4
NPR1_25	09-Sep-91	09:41	32.36	0.110	33.8	1056	67.5
NPR1_26	11-Sep-91	09:04	34.34	0.116	35.3	1052	67.6
NPR1_27	13-Sep-91	08:22	36.31	0.123	36.8	1049	68.7

APPENDIX A2: Fuel Parameters for NPR1 R/B Measurements

RB SAMPLE				zone 4 compact parameters			
I.D.	Date	Time	efpd	fluence ($x10^{25}n/m^2$)	burnup (%FIMA)	temp (°C)	flow (cc/min)
NPR1_28	16-Sep-91	09:28	39.35	0.133	38.9	1045	68.8
NPR1_29	17-Sep-91	09:29	40.35	0.137	39.6	1051	67.9
NPR1_30	27-Sep-91	21:56	40.72	0.138	39.9	823	69.2
NPR1_31	27-Sep-91	23:16	40.78	0.138	39.9	829	66.8
NPR1_32	28-Sep-91	08:38	41.17	0.139	40.2	868	63.6
NPR1_33	28-Sep-91	11:42	41.30	0.140	40.2	1053	71.3
NPR1_34	29-Sep-91	08:53	42.18	0.143	40.8	1058	68.8
NPR1_35	30-Sep-91	09:23	43.20	0.146	41.5	1051	68.6
NPR1_36	01-Oct-91	08:26	44.16	0.150	42.1	1046	68.6
NPR1_37	02-Oct-91	08:56	45.18	0.153	42.8	1040	67.7
NPR1_38	04-Oct-91	09:06	47.19	0.160	44.0	1042	71.2
NPR1_39	07-Oct-91	12:46	50.34	0.170	45.9	1032	109.8
NPR1_41	09-Oct-91	12:02	52.31	0.177	47.0	1031	89.7
NPR1_42	11-Oct-91	09:21	54.20	0.184	48.0	1017	88.6
NPR1_43	14-Oct-91	08:53	57.18	0.194	49.5	1032	67.2
NPR1_44	16-Oct-91	09:08	59.19	0.200	50.5	1023	67.6
NPR1_45	18-Oct-91	09:01	61.19	0.208	51.6	1010	69.2
NPR1-46	30-Oct-91	12:50	62.58	0.213	52.2	1000	68.5
NPR1-47	30-Oct-91	14:24	62.64	0.215	52.2	1015	68.2
NPR1-48	31-Oct-91	09:20	63.43	0.240	52.9	1022	67.6
NPR1-49	01-Nov-91	10:50	64.49	0.273	53.8	1025	67.9
NPR1-50	02-Nov-91	08:42	65.41	0.303	54.5	1061	65.6
NPR1-51	03-Nov-91	09:45	66.45	0.338	55.3	1056	64.4
NPR1-52	04-Nov-91	09:46	67.45	0.371	56.0	1044	63.3
NPR1-53	06-Nov-91	09:50	69.45	0.436	57.4	1032	66.8
NPR1-54	08-Nov-91	08:47	71.41	0.500	58.7	1016	66.9

APPENDIX A2: Fuel Parameters for NPR1 R/B Measurements

RB SAMPLE				zone 4 compact parameters			
I.D.	Date	Time	efpd	fluence ($x10^{25}n/m^2$)	burnup (%FIMA)	temp (°C)	flow (cc/min)
NPR1-55	11-Nov-91	08:53	74.41	0.599	60.6	1000	65.8
NPR1-56	13-Nov-91	09:00	76.42	0.663	61.7	1019	69.2
NPR1-57	15-Nov-91	10:45	78.49	0.730	62.9	1035	72.2
NPR1-59	18-Nov-91	09:01	81.42	0.826	64.3	1013	72.2
NPR1-60	20-Nov-91	08:31	83.40	0.891	65.2	1001	69.8
NPR1-61	02-Dec-91	09:12	85.02	0.947	65.9	894	70.1
NPR1-62	03-Dec-91	08:37	86.00	0.979	66.3	1043	70.9
NPR1-63	04-Dec-91	08:40	87.00	1.010	66.7	1039	69.8
NPR1-64	05-Dec-91	08:32	88.00	1.040	67.1	1030	69.5
NPR1-65	06-Dec-91	08:38	89.00	1.080	67.5	1035	70.7
NPR1-66	09-Dec-91	10:39	92.08	1.180	68.6	1018	70.2
NPR1-67	11-Dec-91	08:34	94.00	1.240	69.2	1037	72.0
NPR1-68	13-Dec-91	14:00	96.22	1.310	69.9	1015	72.1
NPR1-69	16-Dec-91	09:40	99.04	1.401	70.7	1024	76.2
NPR1-70	18-Dec-91	09:12	101.02	1.470	71.2	1010	77.7
NPR1-71	20-Dec-91	09:01	103.01	1.528	71.7	995	76.7
NPR1-72	22-Dec-91	09:12	105.02	1.592	72.2	963	73.2
NPR1-73	01-Jan-92	08:36	106.26	1.631	72.4	765	68.8
NPR1-74	02-Jan-92	11:09	107.37	1.670	72.7	767	71.6
NPR1-75	03-Jan-92	08:38	108.26	1.701	72.9	999	69.7
NPR1-76	04-Jan-92	08:46	109.27	1.730	73.1	1002	78.7
NPR1-77	05-Jan-92	09:27	110.29	1.760	73.3	994	78.0
NPR1-78	06-Jan-92	09:14	111.29	1.795	73.5	988	76.9
NPR1-79	08-Jan-92	08:42	113.26	1.860	73.8	1007	71.9
NPR1-80	10-Jan-92	08:41	115.26	1.920	74.2	998	68.3
NPR1-81	13-Jan-92	08:28	118.25	2.020	74.6	990	63.0

APPENDIX A2: Fuel Parameters for NPR1 R/B Measurements

RB SAMPLE				zone 4 compact parameters			
I.D.	Date	Time	efpd	fluence ($x10^{25}n/m^2$)	burnup (%FIMA)	temp (°C)	flow (cc/min)
NPR1-82	15-Jan-92	08:53	120.27	2.081	74.9	989	61.5
NPR1-83	20-Jan-92	08:40	122.58	2.160	75.3	716	68.1
NPR1-84	21-Jan-92	08:37	123.58	2.191	75.4	979	71.4
NPR1-85	22-Jan-92	08:38	124.58	2.230	75.5	975	71.1
NPR1-86	23-Jan-92	08:38	125.58	2.260	75.6	972	69.4
NPR1-87	24-Jan-92	10:22	126.65	2.293	75.8	961	69.9
NPR1-88	31-Mar-92	14:21	127.04	2.320	75.8	615	69.2
NPR1-89	01-Apr-92	18:40	128.22	2.350	76.0	978	60.7
NPR1-90	02-Apr-92	11:17	128.91	2.380	76.0	1010	52.9
NPR1-91	03-Apr-92	09:40	129.84	2.410	76.1	1010	51.4
NPR1-92	04-Apr-92	08:57	130.81	2.439	76.3	1017	50.1
NPR1-93	06-Apr-92	09:56	132.81	2.510	76.4	1014	50.4
NPR1-94	08-Apr-92	09:17	134.79	2.571	76.6	1026	49.3
NPR1-95	10-Apr-92	08:01	136.73	2.640	76.8	1019	49.7
NPR1-96	14-Apr-92	14:00	138.36	2.690	77.0	620	66.9
NPR1-97	16-Apr-92	09:23	140.17	2.751	77.1	654	66.8
NPR1-98	16-Apr-92	16:55	140.48	2.760	77.2	960	52.1
NPR1-99	22-Apr-92	11:23	143.61	2.870	77.4	639	69.8
NPR1-100	23-Apr-92	15:24	144.78	2.902	77.5	929	57.1
NPR1-101	24-Apr-92	10:40	145.58	2.933	77.5	924	59.2
NPR1-102	27-Apr-92	09:58	148.56	3.034	77.7	899	57.3
NPR1-103	02-May-92	10:13	149.12	3.050	77.8	619	33.2
NPR1-104	03-May-92	08:51	150.07	3.080	77.8	634	33.0

APPENDIX A2: Fuel Parameters for NPR1 R/B Measurements

RB SAMPLE				zone 4 compact parameters			
I.D.	Date	Time	efpd	fluence ($x10^{25}n/m^2$	burnup (%FIMA)	temp (°C)	flow (cc/min)
NPR1-105	04-May-92	15:07	151.32	3.131	77.9	980	58.2
NPR1-106	05-May-92	11:45	152.18	3.153	78.0	1019	58.5
NPR1-107	06-May-92	09:55	153.11	3.190	78.0	1041	56.0
NPR1-108	08-May-92	09:52	155.11	3.253	78.2	1046	58.8
NPR1-109	11-May-92	09:14	158.08	3.352	78.3	1037	57.7
NPR1-110	13-May-92	10:37	160.14	3.420	78.4	988	60.3
NPR1-111	15-May-92	08:32	162.05	3.481	78.5	982	59.4
NPR1-112	19-May-92	09:04	163.20	3.520	78.6	625	60.1
NPR1-113	20-May-92	12:19	164.33	3.560	78.6	975	54.1
NPR1-114	26-May-92	09:10	167.47	3.668	78.8	606	61.2
NPR1-115	27-May-92	09:15	168.48	3.700	78.8	899	57.8

APPENDIX A3: Fission Gas Concentrations for NPR1 R/B Samples

Sample I.D.	Concentration in sweep gas (uCi/cc) corrected to capsule exit time							
	Kr-85m	Kr-87	Kr-88	Kr-89	Xe-133	Xe-135m	Xe-135	Xe-138
NPR1_1	7.49e-05	3.87e-04	3.59e-04	nd(1)	nd	nd	nd	1.71e-03
NPR1_2	8.59e-05	5.77e-04	3.40e-04	2.82E-03(2)	nd	nd	nd	1.33e-03
NPR1_3	1.38e-04	6.84e-04	5.23e-04	3.96E-03(2)	nd	3.05e-04	7.94e-05	1.37e-03
NPR1_4	1.84e-04	8.05e-04	7.15e-04	5.29e-03	nd	3.30e-04	1.29e-04	1.35e-03
NPR1_5	1.89e-04	6.78e-04	6.50e-04	3.12E-03(2)	nd	4.47e-04	1.20e-04	9.14e-04
NPR1_6	1.76e-04	6.95e-04	6.48e-04	nd	nd	4.75e-04	1.20e-04	1.51e-03
NPR1_7	1.51e-04	6.85e-04	5.72e-04	nd	nd	5.67e-04	9.79e-05	9.36e-04
NPR1_8	1.62e-04	6.46e-04	5.79e-04	2.56E-03(2)	nd	4.68e-04	1.00e-04	1.16e-03
NPR1_9	1.66e-04	7.02e-04	5.98e-04	1.98E-03(2)	1.54e-05	3.62e-04	1.03e-04	1.12e-03
NPR1_10	1.06e-04	4.68e-04	4.39e-04	1.24E-03(2)	nd	2.55e-04	5.80e-05	6.78e-04
NPR1_11	1.15e-04	4.70e-04	4.42e-04	nd	2.49e-05	3.29e-04	7.40e-05	7.74e-04
NPR1_12	1.25e-04	5.07e-04	4.41e-04	nd	7.49e-05	3.10e-04	7.57e-04	1.28e-03
NPR1_13	1.43e-04	5.54e-04	5.59e-04	nd	2.36e-05	3.47e-04	7.12e-05	1.01e-03
NPR1_14	1.16e-04	4.76e-04	4.47e-04	3.78E-03(2)	4.09e-05	2.54e-04	7.25e-05	1.36e-03
NPR1_15	2.37e-05	1.55e-04	1.07e-04	3.21E-03(2)	nd	nd	nd	4.86e-04
NPR1_16	3.78e-05	2.00e-04	2.09e-04	2.95E-03(2)	nd	nd	nd	5.89e-04
NPR1_17	4.50e-05	2.03e-04	1.38e-04	nd	nd	1.88e-04	2.62e-05	4.13e-04
NPR1_18	8.46e-05	3.74e-04	3.34e-04	nd	1.65e-05	1.99e-04	3.16e-05	6.69e-04
NPR1_19	8.03e-05	3.89e-04	2.88e-04	nd	3.31e-05	1.85e-04	5.55e-05	6.07e-04
NPR1_20	9.03e-05	3.87e-04	3.41e-04	3.05E-03(2)	2.15e-05	2.08e-04	6.15e-05	7.78e-04
NPR1_21	9.59e-05	4.02e-04	3.57e-04	3.51E-03(2)	2.39e-05	2.63e-04	5.88e-05	8.55e-04
NPR1_22	7.69e-05	3.33e-04	2.71e-04	nd	2.83e-05	2.22e-04	3.87e-05	5.87e-04
NPR1_23	8.03e-05	3.77e-04	3.04e-04	3.25E-03(2)	1.09e-05	2.78e-04	5.19e-05	6.12e-04
NPR1_24	8.74e-05	3.53e-04	3.33e-04	3.14E-03(2)	2.62e-05	2.73e-04	4.92e-05	7.39e-04
NPR1_25	8.37e-05	3.56e-04	3.14e-04	nd	1.07e-05	2.58e-04	5.27e-05	6.77e-04
NPR1_26	9.62e-05	3.56e-04	3.49e-04	2.72E-03(2)	1.13e-05	2.42e-04	5.08e-05	8.37e-04
NPR1_27	8.23e-05	3.70e-04	3.41e-04	1.70E-03(2)	8.94e-06	2.11e-04	4.30e-05	6.87e-04
NPR1_28	9.58e-05	3.91e-04	3.42e-04	3.04E-03(2)	4.32e-05	1.95e-04	5.12e-05	7.13e-04
NPR1_29	9.43e-05	4.04e-04	3.45e-04	2.28E-03(2)	3.51e-05	2.79e-04	5.12e-05	7.26e-04

APPENDIX A3: Fission Gas Concentrations for NPR1 R/B Samples

Sample I.D.	Concentration in sweep gas (uCi/cc) corrected to capsule exit time							
	Kr-85m	Kr-87	Kr-88	Kr-89	Xe-133	Xe-135m	Xe-135	Xe-138
NPR1_30	nd0	6.52e-05	8.14e-05	nd	nd	nd	nd	4.90e-04
NPR1_31	1.50e-05	8.69e-05	4.05e-05	1.74E-03(2)	nd	nd	nd	3.46e-04
NPR1_32	2.28e-05	1.20e-04	6.80e-05	nd	nd	9.21e-05	1.03e-05	4.09e-04
NPR1_33	1.10e-04	3.62e-04	3.62e-04	nd	6.32e-05	1.01e-04	3.26e-05	6.63e-04
NPR1_34	7.82e-05	2.96e-04	2.89e-04	2.56E-03(2)	1.66e-05	1.79e-04	3.80e-05	6.92e-04
NPR1_35	8.60e-05	3.17e-04	3.22e-04	3.77E-03(2)	3.23e-05	1.80e-04	3.92e-05	6.94e-04
NPR1_36	7.59e-05	3.08e-04	2.83e-04	nd	2.23e-05	1.90e-04	4.14e-05	6.49e-04
NPR1_37	6.94e-05	3.16e-04	2.60e-04	5.22E-03(2)	2.33e-05	2.32e-04	4.09e-05	6.50e-04
NPR1_38	6.91e-05	3.15e-04	3.01e-04	4.44E-03(2)	3.16e-05	2.28e-04	3.39e-05	7.22e-04
NPR1_39	4.14e-05	2.24e-04	1.61e-04	3.94E-03(2)	5.24e-05	1.27e-04	2.33e-05	4.67e-04
NPR1_41	5.36e-05	2.17e-04	1.97e-04	nd	2.31e-05	2.35e-04	2.65e-05	4.54e-04
NPR1_42	6.78e-05	3.20e-04	2.73e-04	4.31E-03(2)	9.63e-05	1.73e-04	3.30e-05	8.27e-04
NPR1_43	7.26e-05	3.25e-04	2.89e-04	nd	3.24e-05	2.18e-04	4.45e-05	7.64e-04
NPR1_44	7.90e-05	3.13e-04	3.87e-05	4.14e-04	3.87e-05	2.20e-04	3.82e-05	6.79e-04
NPR1_45	7.69e-05	3.09e-04	2.61e-04	4.01E-03(2)	4.13e-05	1.92e-04	3.07e-05	6.08e-04
NPR1-46	4.79e-05	2.01e-04	1.63e-04	nd	4.04e-04	9.23e-05	nd	5.43e-04
NPR1-47	5.94e-05	2.19e-04	2.41e-04	nd	3.85e-04	nd	nd	6.20e-04
NPR1-48	7.13e-05	2.99e-04	2.43e-04	1.51E-03(2)	1.85e-04	1.29e-04	2.50e-05	6.51e-04
NPR1-49	6.78e-05	3.06e-04	2.54e-04	nd	1.58e-04	nd	3.27e-05	7.24e-04
NPR1-50	9.49e-05	3.89e-04	3.59e-04	nd	2.86e-04	1.93e-04	3.28e-05	6.20e-04
NPR1-51	1.01e-04	4.15e-04	3.60e-04	3.61E-03(2)	3.07e-04	2.02e-04	3.30e-05	7.71e-04
NPR1-52	8.22e-05	3.29e-04	3.29e-04	3.48E-03(2)	2.47e-04	nd	3.80e-05	8.37e-04
NPR1-53	7.31e-05	3.21e-04	2.74e-04	nd	2.17e-04	nd	3.20e-05	7.19e-04
NPR1-54	6.35e-05	2.63e-04	2.24e-04	3.24E-03(2)	2.08e-04	1.09e-04	3.08e-05	6.67e-04
NPR1-55	6.30e-05	2.79e-04	2.11e-04	1.30E-03(2)	2.10e-04	1.39e-04	2.90e-05	6.13e-04
NPR1-56	7.01e-05	2.98e-04	2.64e-04	2.85E+01(2)	3.26e-04	1.76e-04	2.44e-05	5.53e-04
NPR1-57	8.00e-05	3.47e-04	3.10e-04	2.82E-03(2)	4.44e-04	2.00e-04	4.00e-05	5.36e-04
NPR1-59	7.96e-05	3.50e-04	2.82e-04	2.90E-03(2)	3.59e-04	1.37e-04	3.30e-05	7.16e-04

APPENDIX A3: Fission Gas Concentrations for NPR1 R/B Samples

Sample I.D.	Concentration in sweep gas (uCi/cc) corrected to capsule exit time							
	Kr-85m	Kr-87	Kr-88	Kr-89	Xe-133	Xe-135m	Xe-135	Xe-138
NPR1-60	1.02e-04	3.91e-04	3.17e-04	nd	4.16e-04	nd	3.12e-05	8.03e-04
NPR1-61	3.12e-05	1.19e-04	1.05e-04	nd	9.65e-05	1.47e-04	1.69e-05	5.34e-04
NPR1-62	6.93e-05	2.66e-04	2.60e-04	2.23E-03(2)	5.84e-04	1.55e-04	2.91e-05	6.07e-04
NPR1-63	6.36e-05	2.59e-04	2.50e-04	3.56E-03(2)	4.96e-04	1.50e-04	3.16e-05	7.41e-04
NPR1-64	6.99e-05	3.16e-04	2.65e-04	1.01E-03(2)	4.40e-04	1.85e-04	3.37e-05	6.76e-04
NPR1-65	6.58e-05	2.77e-04	2.45e-04	2.62E-03(2)	4.95e-04	1.76e-04	3.08e-05	6.25e-04
NPR1-66	5.85e-05	2.33e-04	1.93e-04	1.11E-03(2)	4.04e-04	1.40e-04	2.81e-05	6.08e-04
NPR1-67	7.03e-05	2.86e-04	2.48e-04	2.99E-03(2)	5.69e-04	1.75e-04	3.49e-05	6.76e-04
NPR1-68	5.47e-05	2.61e-04	2.10e-04	1.76E-03(2)	4.61e-04	1.33e-04	2.62e-05	6.54e-04
NPR1-69	5.48e-05	2.26e-04	2.15e-04	1.56E-03(2)	4.60e-04	1.22e-04	2.61e-05	5.67e-04
NPR1-70	7.46e-05	2.63e-04	2.21e-04	2.52E-03(2)	5.30e-04	1.69e-04	2.66e-05	7.50e-04
NPR1-71	7.07e-05	3.09e-04	2.50e-04	2.28E-03(2)	5.64e-04	1.91e-04	3.49e-05	8.09e-04
NPR1-72	7.37e-05	3.15e-04	2.87e-04	2.30E-03(2)	5.71e-04	2.00e-04	4.10e-05	9.63e-04
NPR1-73	1.41e-05	4.62e-05	3.02e-05	8.53E-04(2)	4.01e-05	8.82e-05	1.68e-05	3.54e-04
NPR1-74	1.21e-05	5.47e-05	4.84e-05	nd	4.01e-05	8.73e-05	2.04e-05	2.75e-04
NPR1-75	4.97e-04	1.66e-03	1.62e-03	6.77E-03(2)	7.15e-04	2.26e-03	5.37e-04	2.94e-03
NPR1-76	4.10e-04	1.40e-03	1.36e-03	8.13E-03(2)	5.53e-04	1.16e-03	2.49e-04	2.68e-03
NPR1-77	3.38e-04	1.15e-03	1.09e-03	6.54E-03(2)	5.07e-04	6.73e-04	1.83e-04	1.75e-03
NPR1-78	2.19e-03	9.08e-03	7.92e-03	4.50e-02	9.04e-04	1.32e-02	3.09e-03	2.44e-02
NPR1-79	1.60e-03	7.24e-03	6.01e-03	4.57e-02	1.09e-03	9.91e-03	2.28e-03	2.35e-02
NPR1-80	1.31e-02	4.67e-02	4.36e-02	2.08e-01	1.10e-02	1.10e-01	2.65e-02	9.95e-02
NPR1-81	3.73e-02	1.51e-01	1.31e-01	7.65e-01	2.22e-02	2.67e-01	6.22e-02	4.56e-01
NPR1-82	3.65e-02	1.38e-01	1.20e-01	1.01e+00	4.28e-02	3.60e-01	7.09e-02	4.09e-01
NPR1-83	1.07e-02	4.77e-02	4.10e-02	2.03e-01	3.02e-03	2.78e-02	6.22e-03	9.99e-02
NPR1-84	1.13e-01	4.67e-01	3.91e-01	3.73e+00	4.74e-02	7.21e-01	1.33e-01	1.53e+00
NPR1-85	9.72e-02	3.78e-01	3.28e-01	2.87e+00	5.31e-02	5.66e-01	1.03e-01	1.11e+00
NPR1-86	9.49e-02	3.39e-01	3.09e-01	2.91e+00	6.51e-02	5.40e-01	1.01e-01	1.04e+00

APPENDIX A3: Fission Gas Concentrations for NPR1 R/B Samples

Sample I.D.	Concentration in sweep gas (uCi/cc) corrected to capsule exit time							
	Kr-85m	Kr-87	Kr-88	Kr-89	Xe-133	Xe-135m	Xe-135	Xe-138
NPR1-87	8.34e-02	3.27e-01	2.76e-01	2.94e+00	4.71e-02	5.24e-01	9.66e-02	1.06e+00
NPR1-88	6.23e-03	3.88e-02	2.68e-02	3.09e-01	nd	8.02e-03	1.27e-03	2.09e-01
NPR1-89	1.66e-01	6.22e-01	5.40e-01	3.08E+00(2)	2.32e-02	6.66e-01	1.66e-01	1.86e+00
NPR1-90	1.68e-01	6.08e-01	5.55e-01	2.67e+00	3.07e-02	6.80e-01	1.34e-01	1.46e+00
NPR1-91	1.20e-01	4.58e-01	3.98e-01	2.45E+00(2)	2.99e-02	4.77e-01	9.56e-02	9.36e-01
NPR1-92	1.42e-01	5.22e-01	4.65e-01	2.58E+00(2)	4.57e-02	5.31e-01	1.14e-01	1.05e+00
NPR1-93	1.19e-01	4.70e-01	4.07e-01	3.05e+00	5.02e-02	6.36e-01	1.33e-01	1.04e+00
NPR1-94	1.56e-01	6.25e-01	5.28e-01	3.17e+00	7.30e-02	8.71e-01	1.83e-01	1.45e+00
NPR1-95	4.38e-01	1.01e+00	1.18e+00	3.66E+00(2)	2.11e+00	8.87e-01	1.75e-01	2.18e+00
NPR1-96	1.41e-02	8.50e-02	6.01e-02	9.36E-01(2)	1.35e-02	2.39e-02	4.04e-03	4.35e-01
NPR1-97	4.27e-02	2.09e-01	1.67e-01	1.58E+00(2)	1.30e-02	1.44e-01	2.65e-02	6.41e-01
NPR1-98	3.39e-01	1.18e+00	1.09e+00	1.18E+01(2)	2.99e-01	7.96e-01	1.45e-01	4.08e+00
NPR1-99	1.52e-02	7.11e-02	5.98e-02	5.83E-01(2)	4.31e-03	3.88e-02	7.17e-03	2.41e-01
NPR1-100	1.48e-01	5.29e-01	4.78e-01	3.24E+00(2)	8.25e-02	5.75e-01	1.13e-01	1.50e+00
NPR1-101	1.04e-01	4.14e-01	3.58e-01	2.70E+00(3)	3.78e-02	4.11e-01	8.06e-02	9.36e-01
NPR1-102	9.64e-02	3.81e-01	3.30e-01	1.98E+00(2)	6.22e-02	3.82e-01	8.09e-02	8.56e-01
NPR1-103	2.33e-02	1.11e-01	9.06e-02	5.93E-01(2)	6.89e-03	6.96e-02	1.49e-02	4.36e-01
NPR1-104	9.08e-02	4.24e-01	3.50e-01	1.45E+00(2)	4.32e-02	2.38e-01	5.30e-02	1.13e+00
NPR1-105	6.16e-01	2.47e+00	2.06e+00	1.26e+01	5.20e-01	2.34e+00	4.21e-01	1.14e+01
NPR1-106	4.10e-01	1.56e+00	1.37e+00	8.62E+00(3)	3.29e-01	1.73e+00	3.49e-01	4.48e+00
NPR1-107	4.22e-01	1.76e+00	1.42e+00	1.00e+01	2.37e-01	2.65e+00	5.10e-01	5.46e+00
NPR1-108	3.63e-01	1.44e+00	1.23e+00	7.08e+00	2.29e-01	1.84e+00	3.54e-01	3.41e+00
NPR1-109	2.80e-01	1.11e+00	9.45e-01	5.86E+00(2)	1.43e-01	1.28e+00	2.53e-01	2.45e+00
NPR1-110	1.68e-01	5.59e-01	5.31e-01	4.21e+00	9.98e-02	5.96e-01	1.15e-01	1.60e+00
NPR1-111	1.48e-01	4.95e-01	4.76e-01	2.79E+00(3)	7.71e-02	3.62e-01	8.45e-02	1.06e+00

APPENDIX A3: Fission Gas Concentrations for NPR1 R/B Samples

Sample I.D.	Concentration in sweep gas (uCi/cc) corrected to capsule exit time							
	Kr-85m	Kr-87	Kr-88	Kr-89	Xe-133	Xe-135m	Xe-135	Xe-138
NPR1-112	7.54e-02	1.99e-01	2.31e-01	1.15E+00(2)	9.81e-01	9.56e-02	1.83e-02	5.38e-01
NPR1-113	3.67e-01	1.31e+00	1.18e+00	7.31e+00	3.49e-01	1.48e+00	2.83e-01	3.95e+00
NPR1-114	4.17e-02	1.99e-01	1.60e-01	1.47E+00(2)	1.49e-02	1.67e-01	3.11e-02	7.02e-01
NPR1-115	2.22e-01	9.20e-01	7.72e-01	5.03e+00	8.06e-02	1.19e+00	2.27e-01	2.47e+00

(1) nd: none detected
(2) based on Rb-89 concentration since no Kr-89 gamma peak
(3) based on Rb-89 concentration since Kr-89 gamma peak too small to be reliable

APPENDIX B1: R/B Values for NPR2

Sample I.D.	Release Rate/Birth Rate (R/B)							
	Kr-85m	Kr-87	Kr-88	Kr-89	Xe-133	Xe-135m	Xe-135	Xe-138
NPR2_1	nd[1]	nd	nd	nd	nm[3]	nd	nd	1.1e-09
NPR2_2	nd	nd	nd	nd	nm	nd	nd	nd
NPR2_3	5.2e-09	3.7e-09	5.5e-09	nd	nm	nd	1.8e-09	6.9e-10
NPR2_4	5.4e-09	3.5e-09	5.7e-09	nd	nm	nd	1.9e-09	1.2e-09
NPR2_5	6.2e-09	3.3e-09	5.2e-09	nd	nm	nd	1.3e-09	6.1e-10
NPR2_6	5.3e-09	3.4e-09	4.1e-09	nd	nm	nd	1.0e-09	5.4e-10
NPR2_7	4.8e-09	3.2e-09	4.0e-09	8.1E-10[2]	2.8e-09	nd	1.4e-09	7.7e-10
NPR2_8	4.3e-09	1.8e-09	3.4e-09	nd	2.5e-09	1.7e-10	1.4e-09	2.9e-11
NPR2_9	3.8e-09	2.4e-09	4.1e-09	nd	1.8e-09	nd	1.2e-09	6.2e-10
NPR2_10	4.2e-09	3.1e-09	3.6e-09	8.4E-10[2]	nm	nd	1.4e-09	6.5e-10
NPR2_11	4.4e-09	3.1e-09	4.5e-09	nd	3.1e-09	nd	1.3e-09	5.3e-10
NPR2_12	4.4e-09	2.6e-09	3.3e-09	nd	2.2e-09	4.3e-10	1.0e-09	5.1e-10
NPR2_14	3.3e-09	2.5e-09	3.7e-09	nd	nm	nd	1.3e-09	5.6e-10
NPR2_15	3.6e-09	2.5e-09	2.9e-09	nd	nm	nd	1.0e-09	6.8e-10
NPR2_16	nd	2.0e-09	1.8e-09	nd	nm	nd	nd	4.8e-10
NPR2_17	nd	1.2e-09	1.8e-09	nd	nm	nd	nd	5.0e-10
NPR2_18	3.2e-09	1.9e-09	3.1e-09	nd	nm	nd	6.4e-09	5.3e-10
NPR2_19	3.2e-09	2.4e-09	3.0e-09	nd	nm	nd	1.0e-09	5.4e-10
NPR2_20	3.1e-09	2.1e-09	2.4e-09	nd	nm	nd	1.1e-09	4.2e-10
NPR2_21	3.0e-09	1.8e-09	2.6e-09	5.3E-10[2]	nm	nd	9.0e-10	5.7e-10
NPR2_22	2.7e-09	2.6e-09	2.5e-09	nd	nm	nd	1.0e-09	5.6e-10
NPR2_23	2.3e-09	2.2e-09	2.4e-09	nd	nm	nd	8.1e-10	5.9e-10
NPR2_24	2.7e-09	2.0e-09	2.3e-09	nd	nm	nd	1.0e-09	nd
NPR2_25	2.6e-09	1.4e-09	1.8e-09	nd	nm	nd	7.6e-10	5.2e-10
NPR2_26	3.7e-09	1.7e-09	2.8e-09	nd	nm	nd	1.6e-09	4.7e-10
NPR2_27	2.0e-09	1.7e-09	2.5e-09	nd	nm	nd	7.9e-10	nd
NPR2_28	2.4e-09	2.2e-09	2.9e-09	nd	nm	nd	nd	6.9e-10
NPR2_29	3.1e-09	1.8e-09	2.4e-09	nd	nm	nd	8.4e-10	6.3e-10

APPENDIX B1: R/B Values for NPR2

Sample I.D.	Release Rate/Birth Rate (R/B)							
	Kr-85m	Kr-87	Kr-88	Kr-89	Xe-133	Xe-135m	Xe-135	Xe-138
NPR2-30	nd	nd	nd	nd	nm	nd	nd	3.6e-10
NPR2-32	9.2e-10	1.2e-09	1.2e-09	nd	nm	nd	nd	nd
NPR2-33	1.2e-09	1.2e-09	1.7e-09	nd	nm	nd	nd	nd
NPR2-34	1.2e-09	1.2e-09	1.1e-09	nd	nm	nd	nd	6.1e-10
NPR2-35	3.2e-09	1.1e-09	2.8e-09	nd	nm	nd	1.1e-09	4.9e-10
NPR2-36	nd	nd	nd	nd	nm	nd	8.2e-10	4.5e-10
NPR2-38	3.9e-09	2.1e-09	nd	nd	nm	nd	nd	8.6e-10
NPR2-40	2.6e-09	3.4e-09	2.3e-09	nd	nm	1.4e-09	1.2e-09	9.3e-10
NPR2-41	3.3e-09	1.9e-09	2.6e-09	nd	nm	nd	1.1e-09	8.3e-10
NPR2-42	2.9e-09	1.8e-09	2.2e-09	nd	nm	1.2e-09	1.1e-09	6.8e-10
NPR2-43	2.9e-09	2.0e-09	2.3e-09	nd	nm	nd	1.6e-09	5.6e-10
NPR2-44	4.3e-09	2.7e-09	3.3e-09	nd	nm	nd	2.5e-09	5.0e-10
NPR2-45	3.5e-09	2.5e-09	3.7e-09	nd	nm	nd	1.2e-09	6.9e-10
NPR2-46	2.7e-09	1.7e-09	1.7e-09	nd	3.5e-08	nd	nd	5.6e-10
NPR2-47	2.5e-09	1.7e-09	1.9e-09	nd	3.0e-08	7.8e-10	8.3e-10	4.9e-10
NPR2-48	2.8e-09	1.9e-09	1.8e-09	nd	3.8e-08	nd	8.2e-10	6.1e-10
NPR2-49	3.0e-09	1.8e-09	2.4e-09	nd	4.9e-08	nd	1.1e-09	5.2e-10
NPR2-50	2.9e-09	2.0e-09	3.0e-09	nd	1.7e-08	1.2e-09	1.2e-09	6.0e-10
NPR2-51	2.4e-09	1.7e-09	1.8e-09	nd	2.6e-08	nd	1.3e-09	4.9e-10
NPR2-52	2.9e-09	1.6e-09	1.9e-09	nd	1.7e-08	1.0e-09	7.4e-10	4.9e-10
NPR2-53	2.1e-09	1.2e-09	1.8e-09	nd	1.6e-08	8.7e-10	9.1e-10	5.2e-10
NPR2-54	2.1e-09	1.3e-09	1.5e-09	nd	3.0e-08	4.3e-10	9.9e-10	4.4e-10
NPR2-55	2.5e-09	1.6e-09	1.9e-09	nd	2.3e-08	8.5e-10	1.3e-09	5.9e-11
NPR2-56	2.7e-09	1.9e-09	2.7e-09	nd	2.7e-08	1.1e-09	9.2e-10	5.1e-10
NPR2-57	2.2e-09	1.5e-09	1.9e-09	nd	1.6e-08	nd	9.3e-10	4.7e-10
NPR2-58	1.8e-09	1.5e-09	1.7e-09	nd	3.6e-08	1.0e-09	nd	0.0

APPENDIX B1: R/B Values for NPR2

Sample I.D.	Release Rate/Birth Rate (R/B)							
	Kr-85m	Kr-87	Kr-88	Kr-89	Xe-133	Xe-135m	Xe-135	Xe-138
NPR2-59	1.5e-09	1.6e-09	2.1e-09	nd	3.0e-08	8.4e-10	1.4e-09	5.2e-10
NPR2-60	2.1e-09	2.0e-09	1.9e-09	nd	4.0e-08	1.5e-09	1.4e-10	7.9e-10
NPR2-61	2.6e-09	1.2e-09	1.5e-09	7.8E-10(2)	3.2e-08	nd	1.2e-09	8.2e-10
NPR2-62	2.7e-09	1.5e-09	1.1e-09	nd	3.5e-08	9.9e-10	1.0e-09	1.0e-09
NPR2-63	1.9e-09	2.0e-09	2.5e-09	nd	nd	nd	2.0e-09	6.6e-10
NPR2-64	2.2e-09	1.8e-09	3.6e-09	nd	3.7e-08	1.5e-09	1.7e-09	9.7e-10
NPR2-65	2.9e-09	1.7e-09	2.7e-09	9.2E-10(2)	4.0e-08	1.2e-09	1.3e-09	7.7e-10
NPR2-66	2.8e-09	2.2e-09	2.4e-09	nd	nd	1.9e-09	1.9e-09	8.1e-10
NPR2-67	3.3e-09	1.9e-09	2.6e-09	nd	4.4e-08	1.3e-09	2.0e-09	8.2e-10
NPR2-68	1.8e-09	2.2e-09	1.6e-09	nd	nd	1.8e-09	1.7e-09	7.9e-10
NPR2-69	4.3e-09	3.2e-09	3.8e-09	nd	4.3e-08	1.8e-09	2.5e-09	1.1e-09
NPR2-70	5.3e-09	3.7e-09	4.1e-09	nd	7.6e-08	1.8e-09	2.1e-09	1.3e-09
NPR2-71	3.7e-09	2.5e-09	3.2e-09	nd	2.6e-07	1.6e-09	3.4e-09	1.1e-09
NPR2-72	4.7e-09	3.9e-09	6.3e-09	nd	2.4e-07	2.1e-09	3.0e-09	1.5e-09
NPR2-73	3.5e-09	2.3e-09	2.5e-09	1.1E-09(2)	1.0e-07	1.7e-09	1.6e-09	1.4e-09
NPR2-74	4.3e-09	4.5e-09	3.8e-09	nd	9.3e-08	2.5e-09	2.6e-09	1.5e-09
NPR2-75	6.4e-09	3.6e-09	5.1e-09	nd	1.6e-07	3.0e-09	3.1e-09	1.2e-09
NPR2-76	6.1e-09	4.3e-09	4.6e-09	nd	2.3e-07	2.5e-09	2.7e-09	1.6e-09
NPR2-77	8.4e-09	6.2e-09	7.8e-09	nd	4.1e-07	2.8e-09	2.6e-09	1.5e-09
NPR2-78	8.1e-09	5.9e-09	7.7e-09	nd	3.5e-07	4.0e-09	3.5e-09	2.1e-09
NPR2-79	3.9e-08	2.5e-08	3.5e-08	6.5E-09(2)	1.3e-06	2.7e-07	3.9e-07	4.2e-09
NPR2-80	3.2e-08	2.0e-08	2.8e-08	5.4E-09(2)	1.4e-06	4.9e-08	7.0e-08	3.1e-09
NPR2-81	7.0e-07	3.2e-07	5.1e-07	nd	5.1e-06	5.2e-07	8.1e-07	2.9e-08
NPR2-82	7.1e-07	3.4e-07	5.2e-07	6.9e-08	1.3e-06	1.4e-07	2.1e-07	3.8e-08
NPR2-83	2.9e-07	1.6e-07	2.4e-07	3.6e-08	5.6e-07	6.4e-08	9.4e-08	2.1e-08

APPENDIX B1: R/B Values for NPR2

Sample I.D.	Release Rate/Birth Rate (R/B)							
	Kr-85m	Kr-87	Kr-88	Kr-89	Xe-133	Xe-135m	Xe-135	Xe-138
NPR2-84	1.8e-07	1.0e-07	1.5e-07	nd	5.4e-07	4.4e-08	6.6e-08	1.7e-08
NPR2-85	6.4e-07	5.3e-07	6.0e-07	1.1E-07(2)	nd	2.6e-07	3.8e-07	2.2e-07
NPR2-86	3.7e-05	2.2e-05	3.1e-05	3.8e-06	5.1e-05	5.9e-06	7.7e-06	4.6e-06
NPR2-87	2.2e-05	1.3e-05	1.8e-05	1.7e-06	3.5e-05	5.0e-06	6.2e-06	2.3e-06
NPR2-88	1.6e-05	1.0e-05	1.3e-05	2.4e-06	2.3e-05	4.3e-06	5.4e-06	1.8e-06
NPR2-89	1.5e-05	9.5e-06	1.3e-05	9.5E-07(2)	2.5e-05	3.9e-06	4.9e-06	1.6e-06
NPR2-90	1.1e-05	5.8e-06	8.6e-06	5.0E-07(2)	2.4e-05	2.4e-06	3.1e-06	7.2e-07
NPR2-91	4.5e-06	2.3e-06	3.6e-06	2.5E-07(2)	1.2e-05	1.2e-06	1.6e-06	3.2e-07
NPR2-92	5.3e-06	2.7e-06	4.0e-06	2.5E-07(2)	1.8e-05	1.9e-06	2.6e-06	3.3e-07
NPR2-93	1.8e-06	1.5e-06	1.8e-06	2.9E-07(2)	8.1e-06	2.8e-07	2.4e-07	4.9e-07
NPR2-94	1.1e-05	7.2e-06	9.5e-06	1.5e-06	3.2e-05	1.2e-06	1.3e-06	1.3e-06
NPR2-95	2.0e-04	1.0e-04	1.5e-04	1.3E-05(2)	9.2e-04	3.0e-05	3.7e-05	2.4e-05
NPR2-96	6.2e-06	4.4e-06	5.5e-06	8.7E-07(2)	1.7e-05	1.3e-06	1.7e-06	1.3e-06
NPR2-97	3.5e-05	1.8e-05	2.7e-05	2.0E-06(2)	8.6e-05	4.5e-06	6.0e-06	2.8e-06
NPR2-98	2.8e-05	1.8e-05	2.4e-05	2.4E-06(2)	5.6e-05	7.5e-06	9.7e-06	3.8e-06
NPR2-99	1.1e-05	6.9e-06	9.4e-06	9.7E-07(2)	2.0e-05	2.4e-06	3.2e-06	1.1e-06
NPR2-100	1.2e-05	1.1e-05	1.2e-05	3.5E-06(2)	5.9e-05	5.4e-06	8.5e-06	6.3e-06
NPR2-101	1.3e-05	1.0e-05	1.2e-05	2.6E-06(2)	3.0e-05	4.0e-06	7.2e-06	3.5e-06
NPR2-102	1.7e-04	8.9e-05	1.3e-04	1.7e-05	7.5e-04	2.2e-05	2.8e-05	1.9e-05
NPR2-103	5.0e-05	3.4e-05	4.4e-05	5.9e-06	9.7e-05	1.4e-05	1.8e-05	7.7e-06
NPR2-104	3.3e-05	2.2e-05	2.9e-05	5.1e-06	6.2e-05	8.1e-06	1.1e-05	4.6e-06
NPR2-105	2.1e-05	1.4e-05	1.8e-05	2.3E-06(2)	3.6e-05	5.2e-06	7.0e-06	2.8e-06
NPR2-106	1.4e-05	9.7e-06	1.3e-05	1.8E-06(2)	2.6e-05	4.0e-06	5.1e-06	2.1e-06
NPR2-108	1.3e-05	8.8e-06	1.1e-05	1.5E-06(2)	2.5e-05	2.9e-06	4.3e-06	1.7e-06
NPR2-109	9.5e-06	5.8e-06	8.0e-06	8.9E-07(2)	3.3e-05	1.6e-06	2.6e-06	9.3e-07

APPENDIX B1: R/B Values for NPR2

Sample I.D.	Release Rate/Birth Rate (R/B)							
	Kr-85m	Kr-87	Kr-88	Kr-89	Xe-133	Xe-135m	Xe-135	Xe-138
NPR2-110	6.2e-06	4.7e-06	5.3e-06	1.4E-06(2)	5.9e-05	2.2e-06	2.8e-06	2.2e-06
NPR2-111	5.4e-05	2.3e-05	3.6e-05	2.8E-06(2)	1.2e-03	5.5e-06	7.5e-06	3.5e-06
NPR2-112	6.9e-06	5.2e-06	6.2e-06	1.3E-06(2)	1.2e-05	2.3e-06	2.8e-06	1.6e-06
NPR2-113	3.8e-05	2.4e-05	3.3e-05	3.2E-06(2)	7.0e-05	6.9e-06	8.8e-06	4.0e-06

(1) nd: none detected
(2) based on Rb-89 concentration since no Kr-89 gamma peak
(3) nm: did not attempt to measure Xe-133

APPENDIX B2: Fuel Parameters for NPR2 R/B Measurements

RB SAMPLE				zone 4 compact parameters			flow (cc/min)
I.D.	Date	Time at capsule	efpd	burnup %FIMA	Fluence ($x10^{25}n/m^2$)	temp (°C)	
NPR2_1	28-Aug-91	13:10	0.059	0.0	0.000	891	73.9
NPR2_2	28-Aug-91	14:26	0.11	0.1	0.000	897	73.2
NPR2_3	29-Aug-91	11:20	0.98	1.1	0.003	926	78.4
NPR2_4	30-Aug-91	10:59	1.97	2.4	0.006	925	81.2
NPR2_5	31-Aug-91	09:05	2.89	2.6	0.007	922	82.4
NPR2_6	01-Sep-91	10:19	3.94	3.8	0.010	919	74.4
NPR2_7	03-Sep-91	11:16	5.98	6.3	0.016	909	73.2
NPR2_8	04-Sep-91	16:41	7.20	8.8	0.023	905	70.4
NPR2_9	06-Sep-91	11:34	8.99	10.0	0.027	897	78.7
NPR2_10	09-Sep-91	11:19	11.98	14.6	0.040	885	77.2
NPR2_11	11-Sep-91	10:15	13.94	16.8	0.047	877	75.2
NPR2_12	13-Sep-91	11:03	15.97	18.9	0.054	866	73.4
NPR2_14	16-Sep-91	11:06	18.97	21.9	0.064	851	69.9
NPR2_15	17-Sep-91	11:14	19.98	22.1	0.064	846	68.1
NPR2_16	27-Sep-91	22:25	20.30	23.3	0.069	797	74.8
NPR2_17	27-Sep-91	23:39	20.35	23.3	0.069	803	75.1
NPR2_18	28-Sep-91	10:32	20.80	23.4	0.069	830	75.8
NPR2_19	29-Sep-91	10:03	21.78	23.8	0.071	836	74.8
NPR2_20	30-Sep-91	10:28	22.80	25.6	0.077	830	75.6
NPR2_21	1-Oct-91	10:48	23.81	26.5	0.080	825	72.4
NPR2_22	2-Oct-91	10:06	24.78	26.6	0.081	818	73.8
NPR2_23	4-Oct-91	10:19	26.79	28.1	0.087	807	73.1
NPR2_24	7-Oct-91	10:33	29.80	29.6	0.093	790	74.8
NPR2_25	9-Oct-91	10:46	31.81	33.3	0.108	777	68.2
NPR2_26	11-Oct-91	11:17	33.83	34.8	0.114	792	77.9
NPR2_27	14-Oct-91	11:30	36.84	36.3	0.121	781	101.3
NPR2_28	16-Oct-91	10:40	38.80	38.0	0.128	795	98.8

APPENDIX B2: Fuel Parameters for NPR2 R/B Measurements

RB SAMPLE				zone 4 compact parameters			flow (cc/min)
I.D.	Date	Time at capsule	efpd	burnup %FIMA	Fluence ($x10^{25}n/m^2$)	temp (°C)	
NPR2_1	28-Aug-91	13:10	0.059	0.0	0.000	891	73.9
NPR2_29	18-Oct-91	10:19	40.79	39.1	0.135	781	92.3
NPR2-30	30-Oct-91	13:18	42.15	40.8	0.143	649	81.8
NPR2-32	31-Oct-91	10:36	43.04	40.8	0.143	649	78.5
NPR2-33	1-Nov-91	09:35	43.99	41.4	0.146	646	80.8
NPR2-34	2-Nov-91	10:08	45.02	42.0	0.149	674	84.1
NPR2-35	3-Nov-91	11:05	46.06	42.7	0.152	669	85.5
NPR2-36	4-Nov-91	11:08	47.06	43.3	0.156	660	82.7
NPR2-38	6-Nov-91	11:41	49.08	44.0	0.160	781	80.9
NPR2-40	8-Nov-91	10:05	51.01	45.6	0.169	776	81.3
NPR2-41	11-Nov-91	10:36	54.04	47.3	0.179	772	73.6
NPR2-42	13-Nov-91	10:25	56.03	48.6	0.188	779	75.7
NPR2-43	15-Nov-91	11:59	58.09	49.5	0.194	781	74.1
NPR2-44	18-Nov-91	10:52	61.05	50.9	0.203	774	75.8
NPR2-45	20-Nov-91	09:45	63.001	52.0	0.211	786	79.3
NPR2-46	02-Dec-91	10:30	64.63	53.8	0.245	779	74.8
NPR2-47	03-Dec-91	09:55	65.60	53.9	0.247	778	88.2
NPR2-48	04-Dec-91	9:59	66.61	54.6	0.279	776	92.7
NPR2-49	05-Dec-91	09:56	67.60	55.4	0.313	768	93.8
NPR2-50	06-Dec-91	10:02	68.61	56.1	0.346	760	75.5
NPR2-51	09-Dec-91	11:44	71.68	58.2	0.441	739	67.9
NPR2-52	11-Dec-91	10:04	73.61	59.5	0.506	729	72.2
NPR2-53	13-Dec-91	15:15	75.83	60.7	0.569	711	69.1
NPR2-54	16-Dec-91	11:08	78.65	62.3	0.666	696	70.9
NPR2-55	18-Dec-91	10:53	80.64	63.4	0.730	686	68.6
NPR2-56	20-Dec-91	10:29	82.637	64.5	0.804	693	74.1

APPENDIX B2: Fuel Parameters for NPR2 R/B Measurements

RB SAMPLE				zone 4 compact parameters			flow (cc/min)
I.D.	Date	Time at capsule	efpd	burnup %FIMA	Fluence ($x10^{25}n/m^2$)	temp (°C)	
NPR2_1	28-Aug-91	13:10	0.059	0.0	0.000	891	73.9
NPR2-57	22-Dec-91	10:37	84.63	65.5	0.879	678	75.9
NPR2-58	01-Jan-92	10:10	85.88	66.0	0.911	648	80.1
NPR2-59	02-Jan-92	12:56	86.99	66.6	0.961	642	77.1
NPR2-60	03-Jan-92	10:08	87.88	67.0	0.996	698	79.4
NPR2-61	04-Jan-92	10:26	88.89	67.0	0.999	687	87.7
NPR2-62	05-Jan-92	10:59	89.91	67.4	1.030	678	88.2
NPR2-63	06-Jan-92	10:37	90.90	67.8	1.061	670	91.7
NPR2-64	08-Jan-92	10:21	92.88	68.6	1.131	672	74.4
NPR2-65	10-Jan-92	10:10	94.876	69.2	1.200	681	75.4
NPR2-66	13-Jan-92	09:22	97.84	70.1	1.283	661	74.4
NPR2-67	15-Jan-92	09:39	99.85	70.7	1.360	671	79.6
NPR2-68	20-Jan-92	10:01	102.18	71.2	1.422	573	77.9
NPR2-69	22-Jan-92	09:20	104.16	71.7	1.491	663	70.4
NPR2-70	24-Jan-92	10:58	106.23	72.3	1.578	669	73.8
NPR2-71	31-Jan-92	12:06	107.11	72.6	1.620	675	87.4
NPR2-72	1-Feb-92	08:43	107.97	72.7	1.630	751	81.2
NPR2-73	2-Feb-92	08:44	108.97	72.8	1.650	735	83.9
NPR2-74	3-Feb-92	08:45	109.97	73.0	1.681	727	86.0
NPR2-75	4-Feb-92	08:42	110.97	73.3	1.731	750	93.8
NPR2-76	5-Feb-92	08:38	111.96	73.5	1.763	776	88.4
NPR2-77	7-Feb-92	09:51	114.00	73.9	1.840	816	80.0
NPR2-78	10-Feb-92	10:45	117.03	74.4	1.940	790	81.8
NPR2-79	11-Feb-92	15:18	118.22	74.6	1.974	789	97.7

APPENDIX B2: Fuel Parameters for NPR2 R/B Measurements

RB SAMPLE				zone 4 compact parameters			flow (cc/min)
I.D.	Date	Time at capsule	efpd	burnup %FIMA	Fluence ($x10^{25}n/m^2$)	temp (°C)	
NPR2_1	28-Aug-91	13:10	0.059	0.0	0.000	891	73.9
NPR2-80	12-Feb-92	08:40	118.95	74.6	1.981	820	92.3
NPR2-81	14-Feb-92	14:10	121.18	75.0	2.071	823	63.7
NPR2-82	23-Feb-92	08:43	124.58	75.3	2.150	755	77.4
NPR2-83	24-Feb-92	10:58	125.67	75.7	2.220	703	73.6
NPR2-84	26-Feb-92	08:30	127.57	75.8	2.260	669	64.0
NPR2-85	31-Mar-92	15:56	128.68	76.0	2.320	450	77.9
NPR2-86	01-Apr-92	17:14	129.73	76.1	2.350	767	72.3
NPR2-87	02-Apr-92	12:14	130.52	76.2	2.380	775	73.7
NPR2-88	03-Apr-92	11:08	131.48	76.2	2.391	774	60.1
NPR2-89	04-Apr-92	10:41	132.46	76.3	2.401	775	60.5
NPR2-90	06-Apr-92	11:17	134.44	76.5	2.482	773	61.6
NPR2-91	08-Apr-92	14:45	136.58	76.7	2.540	767	63.9
NPR2-92	10-Apr-92	09:54	138.38	76.9	2.613	766	64.6
NPR2-93	14-Apr-92	15:39	140.00	77.1	2.700	459	76.6
NPR2-94	16-Apr-92	11:12	141.82	77.2	2.720	484	87.8
NPR2-95	16-Apr-92	15:22	141.99	77.3	2.770	761	56.6
NPR2-96	22-Apr-92	13:35	145.28	77.5	2.871	481	87.7
NPR2-97	23-Apr-92	17:02	146.42	77.6	2.910	750	59.2
NPR2-98	24-Apr-92	15:08	147.34	77.6	2.937	745	59.5
NPR2-99	27-Apr-92	11:10	150.18	77.8	3.028	698	71.6
NPR2-100	02-May-92	11:51	150.76	77.9	3.040	468	80.9
NPR2-101	03-May-92	10:34	151.7	77.9	3.060	476	82.4

APPENDIX B2: Fuel Parameters for NPR2 R/B Measurements

RB SAMPLE				zone 4 compact parameters			flow (cc/min)
I.D.	Date	Time at capsule	efpd	burnup %FIMA	Fluence ($x10^{25}n/m^2$)	temp (°C)	
NPR2_1	28-Aug-91	13:10	0.059	0.0	0.000	891	73.9
NPR2-102	04-May-92	15:56	152.93	78.0	3.130	748	62.8
NPR2-103	05-May-92	9:59	153.68	78.0	3.132	734	68.9
NPR2-104	06-May-92	10:52	154.72	78.1	3.163	732	65.9
NPR2-105	08-May-92	11:12	156.73	78.2	3.224	728	67.0
NPR2-106	11-May-92	10:48	159.71	78.4	3.325	724	70.3
NPR2-108	13-May-92	14:26	161.87	78.5	3.420	727	70.8
NPR2-109	15-May-92	09:32	163.66	78.6	3.460	708	64.3
NPR2-110	19-May-92	10:26	164.82	78.6	3.501	466	65.1
NPR2-111	20-May-92	11:21	165.86	78.7	3.560	716	56.9
NPR2-112	26-May-92	10:32	169.1	78.8	3.640	472	75.6
NPR2-113	27-May-92	10:46	170.11	78.9	3.680	697	64.7

APPENDIX B3: Release Rates for NPR2 R/B Samples

Sample I.D.	Concentration in sweep gas (uCi/cc) corrected to capsule exit time							
	Kr-85m	Kr-87	Kr-88	Kr-89	Xe-133	Xe-135m	Xe-135	Xe-138
NPR2_1	nd(1)	nd	nd	nd	nm(3)	nd	nd	1.0e-03
NPR2_2	nd	nd	nd	nd	nm	nd	nd	nd
NPR2_3	5.2e-05	2.5e-04	2.4e-04	nd	nm	nd	3.6e-05	6.0e-04
NPR2_4	5.2e-05	2.3e-04	2.4e-04	nd	nm	nd	3.9e-05	1.0e-03
NPR2_5	5.8e-05	2.1e-04	2.1e-04	nd	nm	nd	2.5e-05	5.2e-04
NPR2_6	5.4e-05	2.4e-04	1.8e-04	nd	nm	nd	2.3e-05	5.0e-04
NPR2_7	4.9e-05	2.2e-04	1.8e-04	1.6E-03(2)	5.0e-06	nd	3.1e-05	7.0e-04
NPR2_8	4.4e-05	1.3e-04	1.5e-04	nd	4.7e-06	2.4e-05	3.0e-05	2.7e-05
NPR2_9	3.4e-05	1.5e-04	1.6e-04	nd	3.0e-06	nd	2.3e-05	5.0e-04
NPR2_10	3.8e-05	1.9e-04	1.4e-04	1.9E-03(2)	nm	nd	2.7e-05	5.4e-04
NPR2_11	4.0e-05	1.9e-04	1.8e-04	nd	5.1e-06	nd	2.5e-05	4.3e-04
NPR2_12	4.1e-05	1.6e-04	1.3e-04	nd	3.8e-06	5.5e-05	2.1e-05	4.3e-04
NPR2_14	3.3e-05	1.7e-04	1.6e-04	nd	nm	nd	2.7e-05	5.0e-04
NPR2_15	3.7e-05	1.8e-04	1.3e-04	nd	nm	nd	2.3e-05	6.3e-04
NPR2_16	nd	1.1e-04	6.2e-05	nd	nm	nd	nd	3.4e-04
NPR2_17	nd	6.6e-05	5.9e-05	nd	nm	nd	nd	3.5e-04
NPR2_18	2.5e-05	1.0e-04	1.0e-04	nd	nm	nd	8.3e-05	3.7e-04
NPR2_19	2.5e-05	1.3e-04	1.0e-04	nd	nm	nd	1.7e-05	3.8e-04
NPR2_20	2.4e-05	1.1e-04	8.0e-05	nd	nm	nd	1.9e-05	2.9e-04
NPR2_21	2.4e-05	9.8e-05	8.6e-05	7.9E-04(2)	nm	nd	1.5e-05	4.0e-04
NPR2_22	2.0e-05	1.3e-04	8.2e-05	nd	nm	nd	1.7e-05	3.8e-04
NPR2_23	1.7e-05	1.1e-04	7.8e-05	nd	nm	nd	1.3e-05	3.9e-04
NPR2_24	1.9e-05	9.8e-05	7.1e-05	nd	nm	nd	1.6e-05	
NPR2_25	2.0e-05	7.6e-05	6.0e-05	nd	nm	nd	1.3e-05	3.5e-04
NPR2_26	2.5e-05	7.7e-05	8.0e-05	nd	nm	nd	2.3e-05	2.9e-04
NPR2_27	1.1e-05	6.1e-05	5.6e-05	nd	nm	nd	8.9e-06	nd
NPR2_28	1.3e-05	8.2e-05	6.7e-05	nd	nm	nd	nd	3.4e-04

APPENDIX B3: Release Rates for NPR2 R/B Samples

Sample I.D.	Concentration in sweep gas (uCi/cc) corrected to capsule exit time							
	Kr-85m	Kr-87	Kr-88	Kr-89	Xe-133	Xe-135m	Xe-135	Xe-138
NPR2_29	1.8e-05	7.3e-05	6.0e-05	nd	nm	nd	1.0e-05	3.3e-04
NPR2-30	nd	nd	nd	nd	nm	nd	nd	1.7e-04
NPR2-32	5.1e-06	4.5e-05	3.0e-05	nd	nm	nd	nd	nd
NPR2-33	6.5e-06	4.4e-05	4.0e-05	nd	nm	nd	nd	nd
NPR2-34	5.8e-06	4.3e-05	2.4e-05	nd	nm	nd	nd	2.8e-04
NPR2-35	1.6e-05	3.6e-05	5.9e-05	nd	nm	nd	1.2e-05	2.1e-04
NPR2-36	nd	nd	nd	nd	nm	nd	8.9e-06	2.0e-04
NPR2-38	1.9e-05	7.0e-05	nd	nd	nm	nd	nd	3.8e-04
NPR2-40	1.2e-05	1.1e-04	4.7e-05	nd	nm	9.0e-05	1.2e-05	4.1e-04
NPR2-41	1.7e-05	6.8e-05	5.8e-05	nd	9.0e-05	nd	1.2e-05	3.9e-04
NPR2-42	1.5e-05	6.3e-05	5.0e-05	nd	nm	8.1e-05	1.2e-05	3.1e-04
NPR2-43	1.6e-05	7.3e-05	5.2e-05	nd	nm	nd	1.8e-05	2.7e-04
NPR2-44	2.3e-05	9.7e-05	7.5e-05	nd	nm	nd	2.8e-05	2.4e-04
NPR2-45	1.8e-05	8.5e-05	8.0e-05	nd	nm	nd	1.3e-05	3.1e-04
NPR2-46	2.1e-05	9.4e-05	5.7e-05	nd	2.7e-05	nd	nd	4.0e-04
NPR2-47	1.7e-05	7.7e-05	5.5e-05	nd	2.9e-05	7.1e-05	1.2e-05	2.9e-04
NPR2-48	1.7e-05	7.9e-05	4.7e-05	nd	3.8e-05	nd	1.1e-05	3.4e-04
NPR2-49	1.8e-05	7.3e-05	6.0e-05	nd	5.1e-05	nd	1.4e-05	2.8e-04
NPR2-50	2.1e-05	9.8e-05	9.0e-05	nd	2.2e-05	1.2e-04	1.9e-05	3.8e-04
NPR2-51	1.7e-05	8.5e-05	5.7e-05	nd	3.5e-05	nd	2.1e-05	3.1e-04
NPR2-52	1.9e-05	7.3e-05	5.3e-05	nd	2.1e-05	9.1e-05	1.1e-05	2.9e-04
NPR2-53	1.4e-05	5.5e-05	5.1e-05	nd	2.0e-05	8.0e-05	1.3e-05	3.1e-04
NPR2-54	1.4e-05	5.5e-05	4.1e-05	nd	3.5e-05	3.8e-05	1.4e-05	2.5e-04
NPR2-55	1.6e-05	7.4e-05	5.5e-05	nd	2.7e-05	7.6e-05	1.8e-05	3.5e-05
NPR2-56	1.7e-05	7.8e-05	7.0e-05	nd	2.9e-05	9.0e-05	1.2e-05	2.8e-04
NPR2-57	1.3e-05	6.1e-05	4.9e-05	nd	1.7e-05	nd	1.2e-05	2.4e-04

APPENDIX B3: Release Rates for NPR2 R/B Samples

Sample I.D.	Concentration in sweep gas (uCi/cc) corrected to capsule exit time							
	Kr-85m	Kr-87	Kr-88	Kr-89	Xe-133	Xe-135m	Xe-135	Xe-138
NPR2-58	7.9e-06	4.5e-05	3.2e-05	nd	1.3e-05	5.4e-05	nd	nd
NPR2-59	6.4e-06	4.8e-05	4.0e-05	nd	1.9e-05	5.1e-05	1.4e-05	2.0e-04
NPR2-60	8.9e-06	5.7e-05	3.5e-05	nd	2.8e-05	8.7e-05	1.3e-06	3.0e-04
NPR2-61	9.6e-06	3.1e-05	2.4e-05	5.9E-04(2)	2.1e-05	nd	9.6e-06	2.8e-04
NPR2-62	9.6e-06	3.6e-05	1.6e-05	nd	2.3e-05	5.0e-05	8.0e-06	3.3e-04
NPR2-63	6.4e-06	4.5e-05	3.6e-05	nd	nm	nd	1.5e-05	2.0e-04
NPR2-64	8.7e-06	4.9e-05	6.1e-05	nd	2.7e-05	8.2e-05	1.5e-05	3.5e-04
NPR2-65	1.1e-05	4.4e-05	4.3e-05	7.6E-4(2)	2.8e-05	6.3e-05	1.0e-05	2.6e-04
NPR2-66	1.0e-05	5.5e-05	3.7e-05	nd	nm	1.0e-04	1.5e-05	2.7e-04
NPR2-67	1.1e-05	4.4e-05	3.7e-05	nd	2.7e-05	6.2e-05	1.5e-05	2.5e-04
NPR2-68	6.2e-06	5.3e-05	2.4e-05	nd	nm	8.7e-05	1.3e-05	2.5e-04
NPR2-69	1.6e-05	8.3e-05	6.2e-05	nd	2.9e-05	9.3e-05	2.1e-05	3.7e-04
NPR2-70	1.9e-05	9.0e-05	6.4e-05	nd	5.0e-05	9.3e-05	1.7e-05	4.2e-04
NPR2-71	9.0e-06	4.1e-05	3.3e-05	nd	4.2e-05	4.3e-05	1.3e-05	2.4e-04
NPR2-72	1.2e-05	6.9e-05	7.0e-05	nd	7.5e-05	7.2e-05	1.6e-05	3.5e-04
NPR2-73	8.5e-06	3.9e-05	2.7e-05	6.0E-4(2)	3.9e-05	5.6e-05	8.4e-06	3.1e-04
NPR2-74	1.0e-05	7.2e-05	3.8e-05	nd	3.7e-05	8.0e-05	1.3e-05	3.3e-04
NPR2-75	1.3e-05	5.2e-05	4.6e-05	nd	5.7e-05	8.6e-05	1.4e-05	2.4e-04
NPR2-76	1.3e-05	6.3e-05	4.3e-05	nd	8.9e-05	7.6e-05	1.3e-05	3.1e-04
NPR2-77	1.9e-05	9.6e-05	7.7e-05	nd	1.7e-04	8.9e-05	1.3e-05	3.1e-04
NPR2-78	1.7e-05	8.4e-05	7.0e-05	nd	1.3e-04	1.2e-04	1.6e-05	4.0e-04
NPR2-79	6.7e-05	2.9e-04	2.6e-04	2.6E-3(2)	4.1e-04	6.4e-03	1.5e-03	6.6e-04
NPR2-80	5.9e-05	2.5e-04	2.2e-04	2.3E-3(2)	4.5e-04	1.3e-03	2.7e-04	5.3e-04
NPR2-81	1.8e-03	5.7e-03	5.7e-03	nd	2.4e-03	1.8e-02	4.6e-03	6.8e-03
NPR2-82	1.5e-03	4.9e-03	4.8e-03	3.3e-02	5.1e-04	4.2e-03	9.6e-04	7.5e-03

APPENDIX B3: Release Rates for NPR2 R/B Samples

Sample I.D.	Concentration in sweep gas (uCi/cc) corrected to capsule exit time							
	Kr-85m	Kr-87	Kr-88	Kr-89	Xe-133	Xe-135m	Xe-135	Xe-138
NPR2-83	6.5e-04	2.4e-03	2.3e-03	1.8e-02	2.3e-04	2.0e-03	4.6e-04	4.5e-03
NPR2-84	4.7e-04	1.8e-03	1.6e-03	nd	2.5e-04	1.6e-03	3.7e-04	4.0e-03
NPR2-85	1.0e-03	5.7e-03	4.0e-03	3.8e-02	nm	2.0e-03	3.6e-04	3.1e-02
NPR2-86	6.1e-02	2.5e-01	2.2e-01	1.3e+00	9.8e-03	1.4e-01	2.7e-02	7.0e-01
NPR2-87	3.5e-02	1.4e-01	1.2e-01	6.0e-01	8.5e-03	1.2e-01	2.2e-02	3.4e-01
NPR2-88	3.1e-02	1.3e-01	1.1e-01	9.2e-01	7.7e-03	1.2e-01	2.4e-02	3.2e-01
NPR2-89	2.8e-02	1.2e-01	1.0e-01	3.6E-01(2)	8.4e-03	1.0e-01	2.1e-02	2.8e-01
NPR2-90	1.9e-02	7.0e-02	6.6e-02	1.8E-01(2)	8.0e-03	6.2e-02	1.2e-02	1.2e-01
NPR2-91	7.3e-03	2.5e-02	2.5e-02	8.2E-02(2)	3.7e-03	2.8e-02	5.9e-03	4.7e-02
NPR2-92	8.3e-03	2.9e-02	2.7e-02	7.9E-02(2)	5.5e-03	4.3e-02	9.3e-03	4.8e-02
NPR2-93	2.3e-03	1.3e-02	9.7e-03	8.1E-02(2)	2.0e-03	5.3e-03	6.9e-04	5.8e-02
NPR2-94	1.2e-02	5.5e-02	4.6e-02	3.8e-01	6.7e-03	2.0e-02	3.4e-03	1.4e-01
NPR2-95	3.4e-01	1.2e+00	1.1e+00	4.4E+00(2)	3.0e-01	7.4e-01	1.5e-01	3.8e+00
NPR2-96	7.0e-03	3.3e-02	2.7e-02	2.2E-01(2)	3.5e-03	2.2e-02	4.3e-03	1.4e-01
NPR2-97	5.9e-02	2.0e-01	1.9e-01	6.5E-01(2)	2.7e-02	1.1e-01	2.3e-02	4.3e-01
NPR2-98	4.7e-02	2.0e-01	1.7e-01	7.8E-01(2)	1.7e-02	1.9e-01	3.6e-02	5.8e-01
NPR2-99	1.5e-02	6.5e-02	5.6e-02	2.9E-01(2)	5.3e-03	4.9e-02	9.8e-03	1.4e-01
NPR2-100	1.2e-02	6.7e-02	4.9e-02	7.1E-01(2)	3.8e-03	7.7e-02	1.3e-02	5.5e-01
NPR2-101	1.1e-02	6.3e-02	4.5e-02	5.2E-01(2)	3.7e-03	5.6e-02	1.4e-02	3.0e-01
NPR2-102	1.9e-01	6.9e-01	6.3e-01	4.0e+00	1.5e-01	3.9e-01	7.3e-02	2.0e+00
NPR2-103	5.2e-02	2.4e-01	1.9e-01	1.3e+00	1.8e-02	2.2e-01	4.3e-02	7.5e-01
NPR2-104	3.6e-02	1.6e-01	1.3e-01	1.1e+00	1.2e-02	1.3e-01	2.7e-02	4.5e-01
NPR2-105	2.1e-02	9.2e-02	7.6e-02	4.9E-01(2)	6.9e-03	8.1e-02	1.6e-02	2.7e-01
NPR2-106	1.3e-02	5.9e-02	4.9e-02	3.3E-01(2)	4.6e-03	5.6e-02	1.1e-02	1.7e-01

APPENDIX B3: Release Rates for NPR2 R/B Samples

Sample I.D.	Concentration in sweep gas (uCi/cc) corrected to capsule exit time							
	Kr-85m	Kr-87	Kr-88	Kr-89	Xe-133	Xe-135m	Xe-135	Xe-138
NPR2-108	1.1e-02	5.2e-02	4.1e-02	2.8E-01(2)	4.1e-03	4.0e-02	8.6e-03	1.4e-01
NPR2-109	9.0e-03	3.7e-02	3.3e-02	1.7E-01(2)	6.0e-03	2.4e-02	5.7e-03	8.3e-02
NPR2-110	5.9e-03	3.0e-02	2.1e-02	2.8E-01(2)	1.1e-02	3.2e-02	6.1e-03	1.9e-01
NPR2-111	5.9e-02	1.7e-01	1.6e-01	5.8E-01(2)	2.4e-01	9.3e-02	1.9e-02	3.6e-01
NPR2-112	5.7e-03	2.9e-02	2.2e-02	2.4E-01(2)	1.9e-03	3.1e-02	5.4e-03	1.3e-01
NPR2-113	3.7e-02	1.6e-01	1.4e-01	6.4E-01(2)	1.3e-02	1.0e-01	2.0e-02	3.7e-01

(1) nd: none detected
(2) based on Rb-89 since no Kr-89 gamma peak
(3) nm: did not attempt to measure Xe-133

APPENDIX C: Triga R/B Measurements

Test	compact	Temp (°C)	fluence $x10^{25}$	R/B based on stearate, not corrected for steady-state				
				Kr-85m	Kr-87	Kr-88	Kr-89	Xe-138
NPR1	5A	1100	3.76	0.0037	0.0032	0.0031	0.0016	0.0012
	5A	1100	3.76	0.0039	0.0037	0.0034	0.0019	0.0014
	5B	1100	3.76	0.0068	0.006	0.0053	0.0033	0.0021
	5B	900	3.76	0.0029	0.0026	0.0025	0.0016	0.0011
	5B	1300	3.76	0.025	0.022	0.02	0.013	0.011
	6A	1100	3.48	0.0038	0.0036	0.0033	0.0019	0.0014
	6B	1100	3.48	0.0046	0.0042	0.0036	0.0022	0.0013
	7A	1100	2.98	0.0022	0.002	0.0018	0.0011	0.00078
	7B	1100	2.98	0.0023	0.0022	0.0022	0.0014	0.00093
	8A	1100	2.33	0.0007	0.00065	0.00062	0.00038	0.00023
	8B	1100	2.33	0.00069	0.00064	0.00058	0.00039	0.00027
	8B	900	2.33	0.00033	0.00028	0.00025	0.00018	0.00011
	8B	1300	2.33	0.0026	0.0024	0.0021	0.0013	0.00096
NPR2	5A	1100	3.76	0.0067	0.007	0.0068	0.0026	0.0032
	5B	1100	3.76	0.0025	0.0026	0.0026	0.00078	0.0014
	5B	1100	3.76	0.0047	0.0048	0.0043	0.0029	0.0026
	5B	900	3.76	0.0022	0.0021	0.0022	0.0011	0.0012
	5B	1300	3.76	0.0071	0.0068	0.0068	0.003	0.004
	6A	1100	3.48	0.0045	0.0044	0.005	0.0017	0.0026
	6B	1100	3.48	0.002	0.0021	0.0022	0.00081	0.0012
	7A	1100	2.98	0.0028	0.003	0.0032	0.0017	0.00016
	7B	1100	2.98	0.0019	0.002	0.0023	0.0012	0.00096
	8A	1100	2.33	0.0006	0.00065	0.00061	0.00037	0.00034
	8B	1100	2.33	0.00044	0.00043	0.00042	0.00025	0.00021
	8B	900	2.33	0.0003	0.00028	0.00025	0.00019	0.00015
	8B	1300	2.33	0.0015	0.00013	0.0011	0.00065	0.00064